Multipoles, symmetry representations and thermal fluctuations in elastic systems

Siddhartha Sarkar

A Dissertation
Presented to the Faculty
of Princeton University
in Candidacy for the Degree
of Doctor of Philosophy

Recommended for Acceptance
by the Department of
Electrical and Computer Engineering
Adviser: Andrej Košmrlj

September 2021

Abstract

In recent years, we have seen an exciting new development in research on mechanical metamaterials, topological phononics, and mechanics of atomically thin 2D materials. In this thesis, I present how methods from physics can help us in understanding the mechanical properties of these systems as well as gaining further intuition. First, we develop a multipole expansion method to describe the deformation of infinite as well as finite solid structures with cylindrical holes and inclusions by borrowing concepts from electrostatics, such as induction and method of image charges. Our method shows excellent agreement with finite element simulations and experiments. Next, using representation theory, I show how symmetries of phononic crystals affect the degeneracies in their phononic band structures. Deformation of phononic crystals under external load that causes breaking of some symmetries can lead to the lifting of degeneracies for bands and creating gaps such that waves of certain frequencies become disallowed. Finally, using methods from statistical physics, I present how the mechanical properties of atomically thin 2D sheets and shells get modified due to thermal fluctuations. Freely suspended sheets subject to such fluctuations are much harder to bend, but easier to stretch, compress and shear, beyond a characteristic thermal length scale, which is on the order of nanometers for graphene at room temperatures. Just like in critical phenomena, these renormalized elastic constants become scale dependent with universal power-law exponents. In nanotubes, competition between stretching and bending costs associated with radial fluctuations introduces another characteristic elastic length scale, which is proportional to the geometric mean of the radius and effective thickness. Beyond this elastic length scale, bending rigidities and in-plane elastic constants of nanotubes become anisotropic.

Acknowledgements

I would like to thank my adviser Prof. Andrej Košmrlj for giving me the opportunity to work with him as a Ph.D. student. Even though I did not have a physics background, he put his trust in me. He gave me a lot of independence to learn things on my own and apply them in my research. I am thankful for his guidance, encouragement, and patience that made these six years such a rewarding experience.

I am grateful to Prof. Mikko Haataja for giving valuable advice and suggestions during the course of the research presented in this thesis. I am also grateful to Prof. Hakan Türeci for serving in my FPO committee. I would like to thank Prof. Alejandro Rodriguez for not only serving as my thesis reader, but also recommending me to join Prof. Košmrlj's group all those years ago. My thanks also go to our collaborator Prof. Miha Brojan at University of Ljubljana for not only helping me shape my first project as a Ph.D. student, but also great discussions on movies, songs, etc.

I want to express my gratitude to my group mates. I have not come across a more helpful person than Mohamed in my life. As a friend and as a human being, 'he is of the highest kind, quality and order; supreme' in the words of Michael Scott, a character we both came to love. My time in the group would not have been so enjoyable without Sijie, Sheng and Matt. Thank you Sijie for bearing with me all those years we shared an office. I also thank Tejas for helping with research.

I would like to thank Priyabrata, Sumit, Susnata, Debdoot, Abhay, and Shuvrangsu. Although they are not at Princeton, they were always there whenever I needed to talk. I am also grateful to Mouktik, Rajkrishna, and Amir; I could not have asked for better housemates and friends than them.

I want to acknowledge the efforts of my teachers Joydeep Ghosh (Rana Sir) and Anadi Pradhan from school days for impressing upon me the importance of physics and mathematics and providing a lot of encouragement along the way.

Finally, I thank my parents, my sister, and my late uncle for their unconditional love and support over the years. Without them, nothing would be possible. Thank you Baba, Ma, Chhotomama, and Bu for everything.

To my parents and sister.

Contents

List of Tables

List of Figures

Chapter 1

Introduction

Motivated by recent explosion in research in mechanical metamaterials [2, 3, 4, 5, 6, 7], bio-physics and bio-mechanics [8, 9, 10], nano-scale origami [11] and kirigami [12] structures, and micro-robots [13, 14, 15], this work focuses on using concepts and techniques from physics to understand elasticity and mechanics problem. In particular, we use electrostatic induction and image charges, representation theory of symmetry groups, and renormalization group theory from statistical mechanics, and apply to problems of deformation of 2D inhomogeneous elastic structures, elastic wave propagation in periodic elastic media, and effect of thermal fluctuations on the mechanical properties atomically thin structures respectively. A broad perspective of the specific problems and how ideas from physics can help us in the respective areas is given below.

1.1 Inhomogeneous elastic materials

Elastic materials with holes and inclusions have been studied extensively in materials science. Typically, the goal is to homogenize the microscale distribution of holes and inclusions to obtain effective material properties on the macroscale [16, 17, 18, 19], where the detailed micropattern of deformations and stresses is ignored. On the

other hand, it has recently been recognized that the microscale interactions between proteins embedded in biological membranes can promote the assembly of ordered protein structures [20, 8, 9] and can also facilitate the entry of virus particles into cells [10]. Furthermore, in mechanical metamaterials [2], the geometry, symmetry, topology and contrasting elastic properties of different materials are exploited to achieve extraordinary functionalities, such as shape morphing [3, 21], mechanical cloaking [4, 22, 23], negative Poisson's ratio [24, 25, 26, 27, 28], negative thermal expansion [5, 29], effective negative swelling [6, 30, 31], and tunable phononic band gaps [32, 7, 33]. At the heart of these functionalities are deformation patterns of such materials with holes and inclusions. Therefore, understanding how these structures deform under applied external load and how symmetries of these structures affect their functionalities are crucial for the design of novel metamaterials. A significant part of this thesis is dedicated to investigating these two topics using methods from electrostatics and representation theory.

1.1.1 Elastic deformation of 2D solids with circular inclusions using concepts from electrostatics

Linear deformations of infinite thin plates with circular holes under external load have been studied extensively over the years [34, 35, 36, 37, 38]. The solution for one hole can be easily obtained using standard techniques [1] and the solution for two holes can be constructed with conformal maps and complex analysis [35]. Green demonstrated how to construct a solution for infinite thin plates with any number of holes [34] by expanding the Airy stress function around each hole in terms of the Michell solution for biharmonic functions [39]. However, it remained unclear how this procedure could be generalized to finite structures with boundaries.

Deformations of thin membranes with infinitely rigid inclusions have also received a lot of attention, especially in the context of rigid proteins embedded in biological

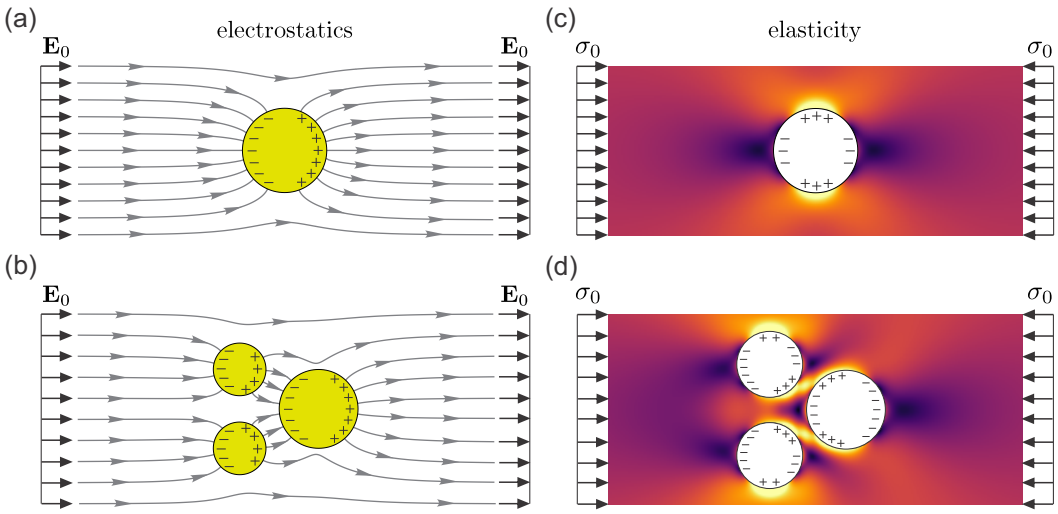

Figure 1.1: Induction in electrostatics and elasticity. (a,b) Induced polarization resulting from the charge (−, +) redistribution due to the external electric field $\mathbf{E}_0$ of (a) a single and (b) multiple conducting spheres (yellow). The resultant electric field lines are shown in grey color. (c,d) Induced quadrupoles resulting from the charge (−, +) redistribution due to external uniaxial compressive stress σ_0 in (c) a single and (d) multiple circular holes (white disks) embedded in an elastic matrix. Heat maps show the von Mises stress field, where yellow and dark purple colors indicate regions of high and low von Mises stress, respectively.

membranes [40, 41, 42, 43, 44, 8, 45, 46, 9, 10, 47]. Several different approaches were developed to study the elastic and entropic interactions between inclusions, such as multipole expansion [40], the effective field theory approach [45, 46], and homogenization [10]. Even though these articles considered membrane bending, the governing equation for the out-of-plane displacement is also biharmonic to the lowest order. Hence these methods could be adapted to investigate the in-plane deformations of plates with rigid inclusions.

The analogies with electrostatics can help us to describe the linear response of a thin elastic plate (plane stress) or an infinitely thick elastic matrix (plane strain) with embedded cylindrical holes and inclusions, which can be treated as a 2D problem with circular holes and inclusions. Just like a polarized conductive object in an external electric field can be described by an induced dipole (see Fig. 1.1a), a hole deformed by the external load can be described by induced elastic quadrupoles (see

Fig. 1.1c). [1] Circular inclusions in the elastic matrix under external load are analogous to dielectric objects in an external electric field. When multiple conductive objects are placed in an external electric field, the induced polarizations generate additional electric fields, which lead to further charge redistribution on the surface of conductive objects (see Fig. 1.1b). Similarly, induced quadrupoles in deformed holes generate additional stresses in the elastic matrix, which lead to further deformations of holes (see Fig. 1.1d). Note that the effect of the induced charge distributions outside the conductive objects and inclusions can be interpreted as the induced multipoles at their centers.

When there are conductive boundaries in the system, charges in electrostatics induce image charges near conductive boundaries and an external electric field induces polarization (dipoles, quadrupoles, and other multipoles) of conductive and dielectric objects. When such a polarized object is near a conductive plate, it is also influenced by the electric field generated by its image, which leads to further charge redistribution on the surface of this object (see Fig. 1.2a). Moreover, when multiple conductive objects in an external electric field are placed near conductive plates, they interact with each other as well as with their images via the electric fields generated by induced polarizations and induced image charges (see Fig. 1.2b).

Similarly, charges in elasticity induce image charges near boundaries and external stress induces polarization (quadrupoles and other multipoles) inside deformed holes and inclusions. When such a deformed inclusion is near a boundary it is also influenced by the stress fields produced by its image, which leads to further deformation of the inclusion (see Fig. 1.2c). When multiple deformed holes and inclusions are located near boundaries, they interact with each other as well as with their images via the

[1] Note that the lowest order multipole that is induced in elasticity is quadrupole unlike in electrostatics where the lowest order induced multipole is a dipole because the governing equation in 2D elasticity is biharmonic unlike the harmonic equation in electrostatics. This will be discussed in Chapter 2 in detail.

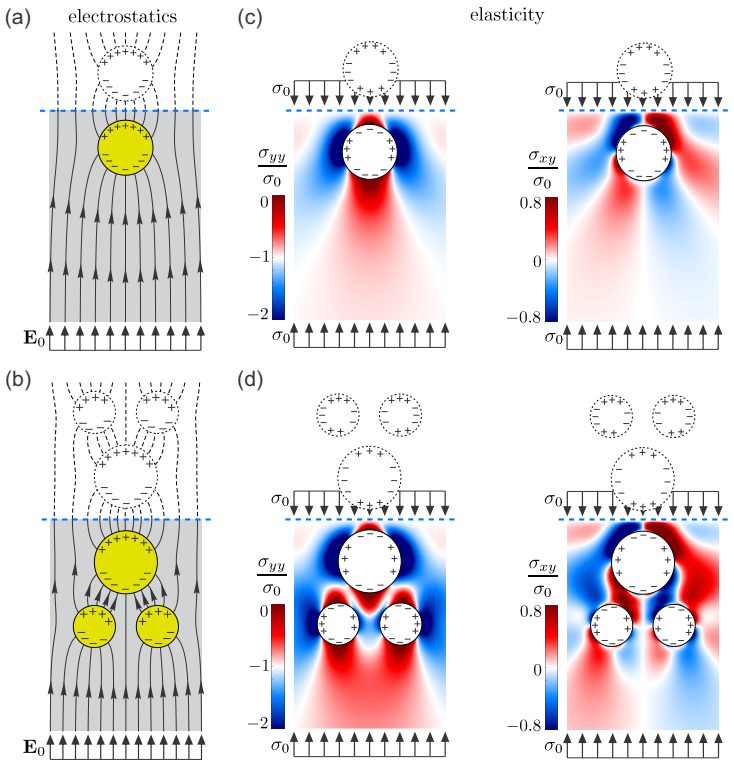

Figure 1.2: Induction and image charges in electrostatics and elasticity. (a,b) Induced polarization due to external electric field $\mathbf{E}_0$ of (a) a single and (b) multiple conducting spheres (yellow disks) near a conductive wall (dashed blue line), which induces image charges (dashed circles). The induced charge distribution on conductive spheres is influenced by interactions between the spheres as well as by interactions with their images. The resultant electric field lines are shown in grey color. (c,d) Induced quadrupoles due to external uniaxial compressive stress σ_0 in (c) a single and (d) multiple circular holes (white disks) embedded in an elastic matrix near an edge with prescribed tractions (dashed blue line), which induces image charges (dashed circles). The induced charge distribution inside holes is affected by interactions between holes as well as by interactions with their images. Heat maps show the resultant stress fields σ_{yy} and σ_{xy}.

stress fields generated by induced elastic multipoles and induced image charges (see Fig. 1.2d).

These analogies with electrostatics allow us to write down these charge distributions induced by applied mechanical load at the circumference of the holes and at the boundary in terms of multipoles at center of the holes and image multipoles just as we do for conductors in the case of electrostatics [48]. In Chapters 2 and 3, I make these analogies concrete and develop an elastic multipole method to describe

deformations of 2D infinite (Chapter 2), semi-infinite and finite (Chapter 3) elastic solids with circular holes and inclusions. Our collaborators Matjaž Čebron and Miha Brojan at University of Ljubljana, Slovenia helped us by providing with finite element simulations and experimental results. The contents of these two chapters have been published in the journal *Physical Review E* [49, 50].

1.1.2 Understanding effects of symmetry on elastic wave propagation in periodic metamaterials using group theory

Over the past decade periodic elastic structures, called phononic crystals, have gained great attention in the research community [3, 4, 5, 6, 7, 51, 52, 33]. Bragg scattering of elastic waves from periodic structure of these crystals prevent waves of particular ranges of frequencies, called band gaps, from propagating through these crystals [53, 54, 55]. Note that this property of periodic media is not limited to phononic crystals, rather it is seen in any wave propagation problem such as electron waves in condensed matter systems [56, 57] and electromagnetic waves in photonic crystals [58]. Because of this property, they have been used in a variety of applications, such as noise reduction [59], vibration control [60, 61], wave guides [62], frequency modulators [63] to name a few. This has led to increasing interest in controlling the frequency range of the band gaps of these structures for specific applications [51, 52, 64, 33, 7, 65, 66]. To this end, it has been shown that the openning and closing of band gaps can be changed by changing temperature [64] or applying deformation [51, 52, 33, 7, 65, 66]. While the former of these methods changes the speed of elastic wave inside the materials using a ferroelectric phase transition, the later relies on changing the periodic structure upon deformation induced by mechanical loading. To control the change in band gaps

by modifying the periodic structure, it is important to understand how structural changes affect the band structure of an elastic system.

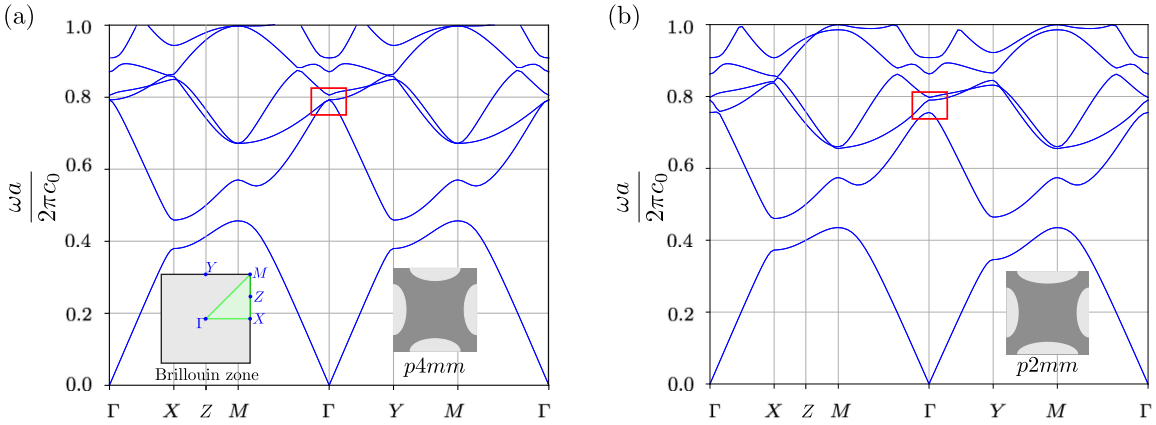

Figure 1.3: Anti-plane shear wave band structures of elastic systems with space group symmetry $p4mm$ (a), and $p2mm$ (b). The unit cells are shown inset with the band structures. The elastic matrix with shear modulus μ_0 and densityρ_0 is shown in dark grey and the elliptic inclusions with shear modulus μ_i and densityρ_i are shown in light grey, where $\mu_i/\mu_0 = 1/10$ and $\rho_i/\rho_0 = 1/2$. The ellipses in (a) have major axes $0.3a$ and minor axes $0.15a$, where a is length of the sides of the unit cells. In (b), only change from (a) is that the top and bottom ellipses have major axes $0.37a$. The eigenfrequency ω was normalized by $2\pi c_0/a$ where $c_0 = \sqrt{\mu_0/\rho_0}$ is the speed of shear wave inside the elastic matrix. The red boxes highlight certain region where a degeneracy has been lifted from (a) to (b).

One aspect of a periodic medium (electronic [67, 68], photonic [69, 70] or phononic) that influences the band structure is the symmetry of medium. If the periodic medium has certain rotational, mirror or glide symmetries on top of the discrete translational symmetry, there can be degeneracies in its wave propagation eigenfrequencies. Under perturbative change (more so when the change is large) of the structure, if some of the symmetries are broken, the degeneracies can be lifted and a directional band gap can open up at that position. For example, consider the elastic structures in Fig. 1.3. The unit cell (the smallest piece which upon repeating in horizontal and vertical direction gives the whole periodic structure) in Fig. 1.3(a) is symmetric under $\pi/2$ rotation around the center and reflection about horizontal, vertical and diagonal lines passing through the center. It's band structure has degeneracy (pointed out

with red box in Fig. 1.3(a)). However, once the major axes of the top and bottom ellipses are elongated to break the $\pi/2$ rotation and the diagonal mirror symmetries (see Fig. 1.3(b)), that degeneracy is lifted and we see directional band gap at that position. In Chapter 4, using techniques from group theory, well-known to researchers in the field of condensed matter [67, 68], I show how spatial and time-reversal symmetries give rise to degeneracies in band structures of anti-plane shear wave (anti-plane shear waves are chosen as example because of simplicity) band structures and how breaking of these symmetries sometimes result in opening of directional band gaps. The contents of this chapter is under preparation to be submitted for publication. The author of the thesis acknowledges the efforts of Tejas Dethe, Polona Zhilkina, Matevz Marinčič for their help with the simulations and PI Andrej Košmrlj for helpful discussions.

1.2 Effect of thermal fluctuations in microscopic elastic structures

Atomically thin membranes are subject of interest over the last few decades [71, 72, 73, 74, 75] for their promising electronic properties. Thin solid membranes are also ubiquitous in soft condensed matter [76, 77, 78] and biological systems [79, 80, 81, 82, 83, 84, 85, 86, 87]. In these contexts, the statistical mechanics of freely suspended elastic membranes have been studied extensively [88, 89, 90, 91, 92, 93, 94, 95, 96, 97, 98, 99, 100, 101]. Theoretical studies of these membranes suggest that due to long-range interaction between out-of-plane undulations mediated by in-plane phonons (see Fig. 1.4(a)), arbitrarily large elastic membranes can remain flat at low enough temperatures [88, 89, 90, 91, 92, 93]. In such membranes, the thermal fluctuations stiffen the bending rigidity κ in scale (ℓ) dependent fashion $\kappa(\ell) \sim \ell^{\eta}$ and reduce the Young's modulus $Y(\ell) \sim \ell^{-\eta_u}$ beyond a temperature T dependent length $\ell_{\text{th}} \sim$

$\sqrt{\kappa_0^2/(k_B T Y_0)}$, where κ_0 and Y_0 are the microscopic bending rigidity and Young's modulus respectively. This result has been obtained using various methods such as perturbative renormalization group with ϵ-expansion [92, 94, 95], $1/d$-expansion [93], self consistent screening approximation [96, 97] and nonperturbative renormalization group [98, 99, 100], verified with numerical simulations [102, 103, 104], and being studied in experiments [105, 12].

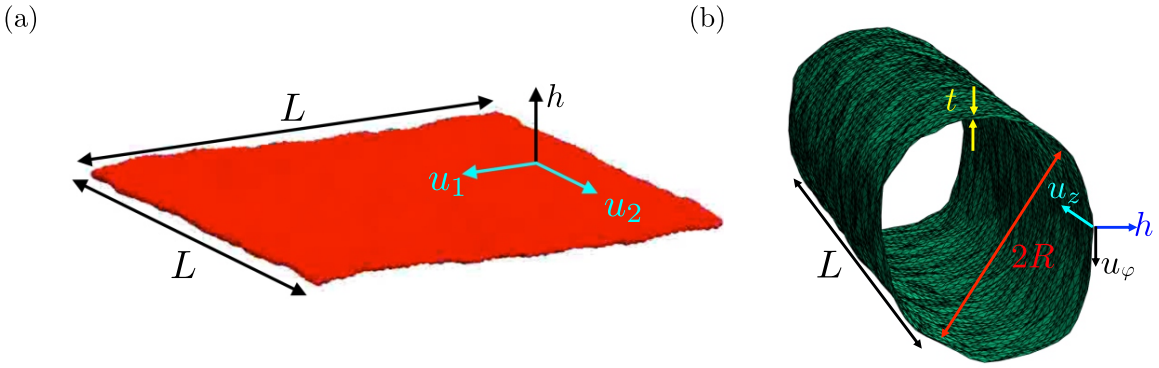

Figure 1.4: Schematic pictures of thermally fluctuating flat sheet (a) and cylindrical shell (b). The geometric dimensions of the sheet and the shell are shown. In-plane displacements are shown as u_i whereas the out-of-plane (radial in case of the shell) displacement is shown as h.

However, much less is known about the mechanical behavior of thin curved shell under thermal fluctuations. There have been works [106, 107] on mechanical properties of thermalized spherical shells, where it was found that at any temperature, if radius of the shell is large enough it spontaneously buckles. Still, little is known about mechanical properties of thermalized cylindrical shells. Atomically thin cylindrical shell-like structures are important in the context of carbon nanotubes. Since its invention in 1991 [72], carbon nanotubes have gained significant research interest due to their electronic properties [108], high tensile strength [109, 110], thermal conductivity [110] and their ability to absorb gases [111]. They have been used in field-effect transistors [112], composite materials [113], environmental monitoring [111] etc. For these applications, it is important to study the effect of thermal fluctuations on the

mechanical properties of nanotubes. In Chapter 5, using renormalization group technique, we investigate how the presence of the anisotropic curvature in nanotubes affect their mechanical properties under thermal fluctuations, and show that unlike in the case flat membranes, the linear response elastic moduli of the nanotubes become anisotropic above a length scale $\ell_{\text{el}} \sim \sqrt{Rt}$, R and t being the radius and effective thickness of the nanotube respectively (see Fig. 1.4(b)). The contents of this chapter is under preparation to be submitted for publication. The author of the thesis acknowledges Mohamed El Hedi Bahri and PI Andrej Košmrlj for helpful discussions.

1.3 Thesis outline

The remaining part of the thesis is organized as follows. In Chapter 2, using the analogy with electrostatics, we develop a method based on multipole expansion for describing deformation of 2D elastic solid with circular inclusions. In Chapter 3, starting from the method of Chapter 2, we add image charges to take flat and circular boundaries with different boundary conditions into account. In Chapter 4, using group theory techniques, we describe how symmetries influence wave propagation properties in periodic elastic media. Chapter 5 describes the mechanical properties nanotubes under thermal fluctuations. Chapter 6 summarizes these works and presents possible future directions.

Chapter 2

Elastic multipole method for describing deformation of infinite 2D solids with circular inclusions

In this chapter, we present a method to describe linear deformations of circular holes and inclusions embedded in an *infinite* 2D elastic matrix under small external loads by systematically expanding induced polarization of each hole/inclusion in terms of elastic multipoles that are related to terms in the Michell solution for biharmonic functions [39]. Note that various multipole expansion techniques have previously been used to describe point defects, such as vacancies and interstitials [114, 115, 116], dislocation defects in piezoelectric composite materials [117, 118, 119], and dynamics of dislocation loops [120]. However, most of these studies were limited to the leading order in multipole expansion. Here we show that as the maximum degree of elastic multipoles is increased, the error decreases exponentially. Moreover, the results of this method are shown to be in excellent agreement with linear finite element simulations and experiments. In the next chapter, we describe how this method can be generalized

Table 2.1: Comparison between equations in electrostatics and 2D linear elasticity. Note that in electrostatics $\mathbf{E}$ is the electric field, while in elasticity E is the 2D Young's modulus.

	Electrostatics	**Elasticity**
Scalar potentials	U	χ
Fields	$\mathbf{E} = -\boldsymbol{\nabla} U$	$\sigma_{ij} = \epsilon_{ik}\epsilon_{jl}\frac{\partial^2 \chi}{\partial x_k \partial x_l}$
Properties of scalar functions	$\boldsymbol{\nabla} \times \mathbf{E} = -\boldsymbol{\nabla} \times \boldsymbol{\nabla} U = \mathbf{0}$	$\frac{\partial \sigma_{ij}}{\partial x_j} = \epsilon_{ik}\epsilon_{jl}\frac{\partial}{\partial x_j}\frac{\partial^2 \chi}{\partial x_k \partial x_l} = 0$
Governing equations	$\Delta U = -\rho_e/\epsilon_e$	$\Delta\Delta\chi = E\rho$

to *finite size* structures by employing ideas of image charges, which become important for holes and inclusions near boundaries.

2.1 Analogy between electrostatics and 2D linear elasticity

The analogy between electrostatics and 2D linear elasticity can be recognized, when the governing equations are formulated in terms of the electric potential U [121] and the Airy stress function χ [1], respectively, which are summarized in Table 2.1. The measurable fields, namely the electric field $\mathbf{E}$ and the stress tensor field σ_{ij}, are obtained by taking spatial derivatives of these scalar functions as $\mathbf{E} = -\boldsymbol{\nabla} U$ and $\sigma_{ij} = \epsilon_{ik}\epsilon_{jl}\frac{\partial^2 \chi}{\partial x_k \partial x_l}$, where ϵ_{ij} is the permutation symbol ($\epsilon_{12} = -\epsilon_{21} = 1, \epsilon_{11} = \epsilon_{22} = 0$) and summation over repeated indices is implied. The most compelling aspect of the formulations in terms of scalar functions U and χ is that Faraday's law in electrostatics ($\boldsymbol{\nabla} \times \mathbf{E} = \mathbf{0}$) and the force balance in elasticity ($\frac{\partial \sigma_{ij}}{\partial x_j} = 0$) are automatically satisfied. Moreover, the governing equations for these scalar functions take simple forms. Equation $\Delta U = -\rho_e/\epsilon_e$ describes the well known Gauss's law, where ρ_e is the electric charge density and ϵ_e is the permittivity of the material. The analogous

equation in elasticity $\Delta\Delta\chi = E\rho$ describes the (in)compatibility conditions [122, 123], where E is the 2D Young's modulus and ρ is the elastic charge density associated with defects, which are sources of incompatibility. Note that a strain field is said to be compatible if it is continuous and its integral over any loop is identically equal to zero [124]. This is, however, not the case for the integrals of strain field over a loop around disclination and dislocation defects [122, 123]. Note also that in the absence of electric charges ($\rho_e = 0$) the electric potential U is a harmonic function, while in the absence of defects ($\rho = 0$) the Airy stress function χ is a biharmonic function.

When a conductive object is placed in an external electric field, it gets polarized due to the redistribution of charges (see Fig. 1.1a). This induced polarization generates an additional electric field outside the conductive object, which can be expanded in terms of fictitious multipoles (dipole, quadrupole, and other multipoles) located at the center of the conductive object [121]. Note that the induced polarization does not include a monopole charge, because the total topological charge is conserved [121]. Similarly, a hole or inclusion embedded in an elastic matrix gets polarized when the external load is applied (see Fig. 1.1c). The additional stresses in the elastic matrix due to this induced polarization can again be expanded in terms of fictitious *elastic multipoles* (quadrupoles and other multipoles) located at the center of hole/inclusion. In elasticity, the induced polarization does not include disclinations (topological monopole) and dislocations (topological dipole), which are topological defects [122]. In order to demonstrate this, we first briefly present the multipoles and induction in electrostatics and describe the meaning of their counterparts in elasticity.

2.1.1 Monopoles

In electrostatics, a *topological monopole* is defined as the electric charge density distribution proportional to the Dirac delta function, i.e. $\rho_e = q\delta(\mathbf{x} - \mathbf{x}_0)$, where q is the charge and $\mathbf{x}_0$ denotes its position. The electric potential $U_m(\mathbf{x} - \mathbf{x}_0|q)$ in 2D is then

obtained by solving the governing equation as [121]

$$\begin{aligned} \Delta U_m &= -\frac{q}{\epsilon_e}\delta(\mathbf{x}-\mathbf{x}_0), \\ U_m(\mathbf{x}-\mathbf{x}_0|q) &= -\frac{q}{2\pi\epsilon_e}\ln|\mathbf{x}-\mathbf{x}_0|. \end{aligned} \tag{2.1}$$

For the positive monopole charge, the electric field $\mathbf{E}_m = -\boldsymbol{\nabla} U_m$ is pointing radially outward (see Fig. 2.1a). Note that the total charge is topologically conserved [121].

Similarly, we can define a *topological monopole* in 2D elasticity as the charge density proportional to the Dirac delta function, i.e. $\rho = s\delta(\boldsymbol{x}-\boldsymbol{x}_0)$, where s is the charge and $\mathbf{x}_0$ denotes its position. Topological monopoles are called disclinations and their Airy stress function $\chi_m^s(\mathbf{x}-\mathbf{x}_0|s)$ can be obtained by solving the governing equation as [122, 125]

$$\begin{aligned} \Delta\Delta\chi_m^s &= Es\delta(\mathbf{x}-\mathbf{x}_0), \\ \chi_m^s(\mathbf{x}-\mathbf{x}_0|s) &= \frac{Es}{8\pi}|\mathbf{x}-\mathbf{x}_0|^2\big(\ln|\mathbf{x}-\mathbf{x}_0|-1/2\big). \end{aligned} \tag{2.2}$$

The physical interpretation of topological monopoles in 2D elasticity comes from condensed matter theory. When a wedge with angle s is cut out from a 2D elastic material and the newly created boundaries of the remaining material are glued together, a positive disclination defect of charge s is formed (see Fig. 2.1b). The negative disclination with charge $s<0$ corresponds to the insertion of a wedge with angle $|s|$. The stresses generated by these operations are described with the Airy stress function in Eq. (2.2). [122, 125]

Unlike in electrostatics, we can also define a *non-topological monopole* in 2D elasticity as the charge density proportional to $\rho = p\Delta_0\delta(\boldsymbol{x}-\boldsymbol{x}_0)$, where p is the charge, $\mathbf{x}_0$ denotes its position, and Δ_0 corresponds to the Laplace operator with respect to $\mathbf{x}_0$. The corresponding Airy stress function $\chi_m^p(\mathbf{x}-\mathbf{x}_0|p)$ can be obtained by solving the governing equation as [125]

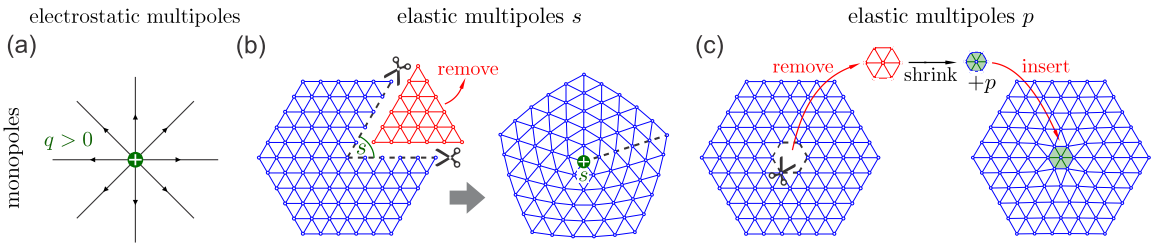

Figure 2.1: Monopoles in electrostatics and 2D elasticity. (a) An electrostatic monopole with positive charge q (green) generates an outward radial electric field (black lines). For a monopole with negative charge, the direction of the electric field is reversed. (b) In 2D elasticity a disclination defect (topological monopole) with charge s forms upon removal ($s > 0$) or insertion ($s < 0$) of a wedge of material (red), where $|s|$ is the wedge angle. (c) In 2D elasticity, a non-topological monopole $p > 0$ ($p < 0$) corresponds to a local isotropic contraction (expansion) of the material.

$$\begin{aligned} \Delta\Delta\chi_m^p &= Ep\Delta_0\delta(\mathbf{x}-\mathbf{x}_0), \\ \chi_m^p(\mathbf{x}-\mathbf{x}_0|p) &= \frac{Ep}{2\pi}(\ln(|\mathbf{x}-\mathbf{x}_0|)+1/2). \end{aligned} \tag{2.3}$$

Note that the Airy stress functions for the non-topological monopole p and for the topological monopole s are related via $\chi_m^p(\mathbf{x}-\mathbf{x}_0|p) = \Delta_0\chi_m^s(\mathbf{x}-\mathbf{x}_0|p)$. The constant term in Eq. (2.3) does not generate any stresses and can thus be omitted. A positive (negative) non-topological monopole with charge $p > 0$ ($p < 0$) is related to a local isotropic contraction (expansion) of the material (see Fig 2.1c). [126, 125]

2.1.2 Dipoles

An electrostatic dipole is formed at $\mathbf{x}_0$ when two opposite charges $\pm q$ are located at $\mathbf{x}_\pm = \mathbf{x}_0 \pm \mathbf{a}/2$ (see Fig. 2.2a). The electric potential for a dipole in 2D is thus

$$\begin{aligned} U_d(\mathbf{x}-\mathbf{x}_0|\mathbf{p}) &= U_m(\mathbf{x}-\mathbf{x}_+|q) + U_m(\mathbf{x}-\mathbf{x}_-|-q), \\ U_d(\mathbf{x}-\mathbf{x}_0|\mathbf{p}) &\xrightarrow{|\mathbf{a}|\to 0} \frac{\mathbf{p}\cdot(\mathbf{x}-\mathbf{x}_0)}{2\pi\epsilon_e|\mathbf{x}-\mathbf{x}_0|^2}, \end{aligned} \tag{2.4}$$

where we introduced the dipole moment $\mathbf{p} = q\mathbf{a}$. [121] Note that in electrostatics dipoles and all higher-order multipoles are *non-topological* [121].

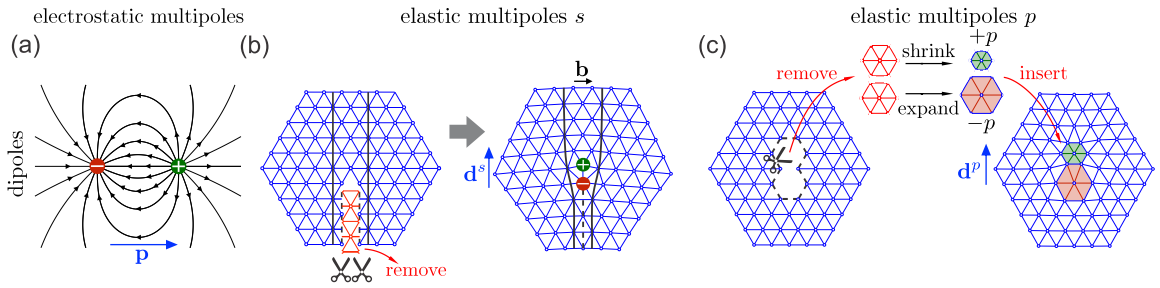

Figure 2.2: Dipoles in electrostatics and 2D elasticity. (a) An electrostatic dipole $\mathbf{p}$ is formed when a positive (green) and a negative (red) charge of equal magnitude are brought close together. The resulting electric field lines are shown with black lines. (b) In 2D elasticity, a dislocation (topological dipole) forms upon removal or insertion of a semi-infinite strip of material of width $|\mathbf{b}|$ and is represented by the Burgers vector $\mathbf{b}$. In a triangular lattice, the dislocation corresponds to two adjacent disclinations of opposite charges. The two black lines indicate the positions of points before and after the removal of a semi-infinite strip (red) from crystal. A dipole moment $\mathbf{d}^s$ can be defined in the direction from negative to positive disclination and its magnitude is equal to the distance between two disclinations times the magnitude of charge of each disclination. (c) In 2D elasticity, a non-topological dipole $\mathbf{d}^p$ is formed when a positive (green) and a negative (red) non-topological charge of equal magnitude are brought close together.

Similarly, a dipole $\mathbf{d}^s = s\mathbf{a}$ in 2D elasticity is formed when two disclination defects of opposite charges $\pm s$ are located at $\mathbf{x}_\pm = \mathbf{x}_0 \pm \mathbf{a}/2$ (see Fig. 2.2b). Dipoles are called dislocations and their Airy stress function is [122]

$$\begin{aligned} \chi_d^s(\mathbf{x}-\mathbf{x}_0|\mathbf{d}^s) &= \chi_m^s(\mathbf{x}-\mathbf{x}_+|s) + \chi_m^s(\mathbf{x}-\mathbf{x}_-|-s), \\ \chi_d^s(\mathbf{x}-\mathbf{x}_0|\mathbf{d}^s) &\xrightarrow{|\mathbf{a}|\to 0} -\frac{E}{4\pi}\mathbf{d^s}\cdot(\mathbf{x}-\mathbf{x}_0)\ln|\mathbf{x}-\mathbf{x}_0|. \end{aligned} \tag{2.5}$$

Dislocation is a *topological* defect, which forms upon removal or insertion of a semi-infinite strip of material of width $|\mathbf{b}|$ (see Fig. 2.2b). Note that dislocations are conventionally represented by the Burgers vector $\mathbf{b}$, which is equal to the dipole moment $\mathbf{d}^s$ rotated by 90°, i.e. $b_i = \epsilon_{ij} d_j^s$. [122, 125]

In 2D elasticity, we can define another *non-topological* dipole $\mathbf{d}^p = p\mathbf{a}$, which is formed when two non-topological monopoles of opposite charges $\pm p$ are located at

$\mathbf{x}_\pm = \mathbf{x}_0 \pm \mathbf{a}/2$ (see Fig. 2.2c). Their Airy stress function is

$$\begin{aligned} \chi_d^p(\mathbf{x}-\mathbf{x}_0|\mathbf{d}^p) &= \chi_m^p(\mathbf{x}-\mathbf{x}_+|p) + \chi_m^p(\mathbf{x}-\mathbf{x}_-|-p), \\ \chi_d^p(\mathbf{x}-\mathbf{x}_0|\mathbf{d}^p) &\xrightarrow{|\mathbf{a}|\to 0} -\frac{E}{2\pi}\frac{\mathbf{d}^p\cdot(\mathbf{x}-\mathbf{x}_0)}{|\mathbf{x}-\mathbf{x}_0|^2}. \end{aligned} \tag{2.6}$$

2.1.3 Quadrupoles

An electrostatic quadrupole $\mathbf{Q}$ in 2D is formed when two positive and negative charges are placed symmetrically around $\mathbf{x}_0$, such that charges $q_i = q(-1)^i$ are placed at positions $\mathbf{x}_i = \mathbf{x}_0 + a\big(\cos(\theta + i\pi/2), \sin(\theta + i\pi/2)\big)$, where $i \in \{0,1,2,3\}$ and angle θ describes the orientation of quadrupole (see Fig. 2.3a). The electric potential of the quadrupole is thus

$$\begin{aligned} U_Q(r,\varphi|Q,\theta) &= \sum_{i=0}^{3} U_m(\mathbf{x}-\mathbf{x}_i|q_i), \\ U_Q(r,\varphi|Q,\theta) &\xrightarrow{a\to 0} \frac{Q\cos\big(2(\varphi-\theta)\big)}{\pi\epsilon_e r^2}, \end{aligned} \tag{2.7}$$

where we introduced the quadrupole moment $Q = qa^2$ and polar coordinates ($r = \sqrt{(x-x_0)^2+(y-y_0)^2}$, $\varphi = \arctan[(y-y_0)/(x-x_0)]$) centered at $\mathbf{x}_0$.

Similarly, an elastic quadrupole $\mathbf{Q}^s$ is formed when two positive and negative disclinations are placed symmetrically around $\mathbf{x}_0$, such that disclinations with charges $s_i = s(-1)^i$ are placed at positions $\mathbf{x}_i = \mathbf{x}_0 + a\big(\cos(\theta + i\pi/2), \sin(\theta + i\pi/2)\big)$, where $i \in \{0,1,2,3\}$ and angle θ describes the orientation of quadrupole (see Fig. 2.3b). The Airy stress function for quadrupole $\mathbf{Q}^s$ in polar coordinates is thus

$$\begin{aligned} \chi_Q^s(r,\varphi|Q^s,\theta) &= \sum_{i=0}^{3} \chi_m^s(\mathbf{x}-\mathbf{x}_i|s_i), \\ \chi_Q^s(r,\varphi|Q^s,\theta) &\xrightarrow{a\to 0} \frac{EQ^s\cos\big(2(\varphi-\theta)\big)}{4\pi}, \end{aligned} \tag{2.8}$$

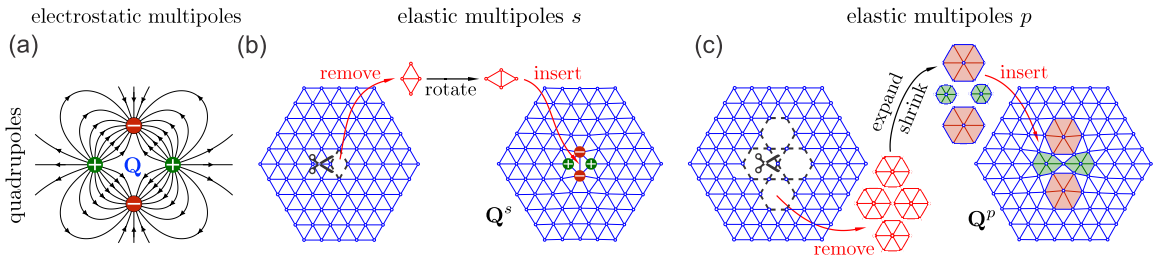

Figure 2.3: Quadrupoles in electrostatics and 2D elasticity. ((a) An electrostatic quadrupole $\mathbf{Q}$ consisting of four charges at the vertices of a square with opposite charges at the adjacent vertices. The resulting electric field lines are shown with black lines. (b) In 2D elasticity, a quadrupole $\mathbf{Q}^s$ is represented by four disclinations at the vertices of a square with opposite charges at the adjacent vertices. Due to the quadrupole $\mathbf{Q}^s$, material locally expands in the direction of positive disclinations and locally contracts in the direction of negative disclinations, while the total area remains locally unchanged. (c) In 2D elasticity, a quadrupole $\mathbf{Q}^p$ is represented by four non-topological monopoles at the vertices of a square with opposite charges at the adjacent vertices.

where we introduced the quadrupole moment $Q^s = sa^2$. The elastic quadrupole $\mathbf{Q}^s$ causes the material to locally expand in the θ direction and locally contract in the orthogonal direction (see Fig. 2.3b). Note that the quadrupole $\mathbf{Q}^s$ is *non-topological* [126, 125].

In elasticity, we can define another quadrupole $\mathbf{Q}^p$, which is formed when two positive and negative non-topological monopoles are placed symmetrically around $\mathbf{x}_0$, such that non-topological charges $p_i = p(-1)^i$ are placed at positions $\mathbf{x}_i = \mathbf{x}_0 + a\big(\cos(\theta + i\pi/2), \sin(\theta + i\pi/2)\big)$, where $i \in \{0, 1, 2, 3\}$ and angle θ describes the orientation of quadrupole (see Fig. 2.3c). The Airy stress function for quadrupole $\mathbf{Q}^p$ in polar coordinates is thus

$$\begin{aligned} \chi_Q^p(r, \varphi | Q^p, \theta) &= \sum_{i=0}^{3} \chi_m^p(\mathbf{x} - \mathbf{x}_i | p_i), \\ \chi_Q^p(r, \varphi | Q^p, \theta) &\xrightarrow{a \to 0} \frac{E Q^p \cos\big(2(\varphi - \theta)\big)}{\pi r^2}, \end{aligned} \tag{2.9}$$

where we introduced the quadrupole moment $Q^p = pa^2$.

2.1.4 Higher-order multipoles

The procedure described in the previous sections can be generalized to define higher-order multipoles $\mathbf{Q}_n^s$ and $\mathbf{Q}_n^p$. In 2D the quadrupole $\mathbf{Q}^s$ is generalized by placing n positive and n negative disclinations symmetrically around $\mathbf{x}_0$, such that disclinations of charges $s_i = s(-1)^i$ are placed at positions $\mathbf{x}_i = \mathbf{x}_0 + a\big(\cos(\theta + i\pi/n), \sin(\theta + i\pi/n)\big)$, where $i \in \{0, 1, \ldots, 2n-1\}$ and angle θ describes the orientation of multipole. The Airy stress functions for such multipoles $\mathbf{Q}_n^s$ in polar coordinates are

$$\begin{aligned} \chi_n^s(r, \varphi | Q_n^s, \theta) &= \sum_{i=0}^{2n-1} \chi_m^s(\mathbf{x} - \mathbf{x}_i | s_i), \\ \chi_n^s(r, \varphi | Q_n^s, \theta) &\xrightarrow{a \to 0} \frac{E Q_n^s \cos\big(n(\varphi - \theta)\big)}{4(n-1)\pi r^{n-2}}, \end{aligned} \tag{2.10}$$

where we introduced the multipole moment $Q_n^s = sa^n$.

The quadrupole $\mathbf{Q}^p$ is generalized to higher-order multipoles by placing n positive and n negative non-topological monopoles symmetrically around $\mathbf{x}_0$, such that charges of strength $p_i = p(-1)^i$ are placed at positions $\mathbf{x}_i = \mathbf{x}_0 + a\big(\cos(\theta + i\pi/n), \sin(\theta + i\pi/n)\big)$, where $i \in \{0, 1, \ldots, 2n-1\}$ and angle θ describes the orientation of multipole. The Airy stress functions for such multipoles $\mathbf{Q}_n^p$ in polar coordinates are

$$\begin{aligned} \chi_n^p(r, \varphi | Q_n^p, \theta) &= \sum_{i=0}^{2n-1} \chi_m^p(\mathbf{x} - \mathbf{x}_i | p_i), \\ \chi_n^p(r, \varphi | Q_n^p, \theta) &\xrightarrow{a \to 0} -\frac{E Q_n^p \cos\big(n(\varphi - \theta)\big)}{\pi r^n}, \end{aligned} \tag{2.11}$$

where we introduced the multipole moment $Q_n^p = pa^n$.

2.1.5 Multipoles vs. the Michell solution for biharmonic functions

The elastic multipoles of types s and p introduced in the previous sections are closely related to the general solution of the biharmonic equation $\Delta\Delta\chi = 0$, due to Michell [39], which is given in polar coordinates (r, φ) as

$$\begin{aligned}\chi(r,\varphi) = {} & A_0 r^2 + B_0 r^2 \ln r + C_0 \ln r + I\varphi \\ & + (A_1 r + \frac{B_1}{r} + B_1' r\varphi + C_1 r^3 + D_1 r \ln r)\cos\varphi \\ & + (E_1 r + \frac{F_1}{r} + F_1' r\varphi + G_1 r^3 + H_1 r \ln r)\sin\varphi \\ & + \sum_{n=2}^{\infty}(A_n r^n + \frac{B_n}{r^n} + C_n r^{n+2} + \frac{D_n}{r^{n-2}})\cos(n\varphi) \\ & + \sum_{n=2}^{\infty}(E_n r^n + \frac{F_n}{r^n} + G_n r^{n+2} + \frac{H_n}{r^{n-2}})\sin(n\varphi).\end{aligned} \tag{2.12}$$

The Michell solution above contains the Airy stress functions corresponding to multipoles located at the origin: disclination ($r^2 \ln r$), dislocation ($r \ln r \cos\varphi$, $r \ln r \sin\varphi$), non-topological monopole ($\ln r$), non-topological dipole ($\cos\varphi/r$, $\sin\varphi/r$), quadrupole $\mathbf{Q}^s$ ($\cos(2\varphi)$, $\sin(2\varphi)$), quadrupole $\mathbf{Q}^p$ ($\cos(2\varphi)/r^2$, $\sin(2\varphi)/r^2$), as well as all higher-order multipoles $\mathbf{Q}_n^s$ and $\mathbf{Q}_n^p$ (see Eqs. (2.10, 2.11)). Note that the Michell solution also contains terms that increase faster than r^2 far away from the origin. These terms are associated with stresses that increase away from the origin and can be interpreted as multipoles located at infinity [127]. Due to the connection with elastic multipoles we refer to coefficients $A_i, B_i, \ldots, H_i$ in the Michell solution as the amplitudes of multipoles.

2.1.6 Induction

As mentioned previously, the external electric field induces polarization in conducting and dielectric objects. Similarly, external stress induces elastic quadrupoles inside

holes and inclusions. To make this analogy concrete, we first demonstrate how external electric field in 2D polarizes a single conductive or dielectric disk, and then discuss how external stress induces quadrupoles inside a circular hole or inclusion.

Let us consider a perfectly conductive disk of radius R in a uniform external electric field ($\mathbf{E} = E_0\hat{\mathbf{x}}$) in 2D. This electric field provides a driving force for mobile charges on the disk, which are redistributed until the resulting tangential component of the total electric field at the circumference of the disk is zero. This means that the electric potential is constant on the circumference ($r = R$). Assuming that the electric potential is zero on the circumference of the disk and that the resultant electric field approaches the background field far away from the disk, we can solve the governing equation $\Delta U = 0$ in polar coordinates to find that the electric potential is $U_{\text{in}}^{\text{tot}}(r, \varphi) = 0$ inside the conductive disk ($r < R$) and that the electric potential $U_{\text{out}}^{\text{tot}}(r, \varphi)$ outside the conductive disk ($r > R$) is given by [48]

$$U_{\text{out}}^{\text{tot}}(r, \varphi) = -E_0 r \cos\varphi + E_0 \frac{R^2}{r} \cos\varphi, \tag{2.13}$$

where the origin of the coordinate system is at the center of the conductive disk. The first term in the above Eq. (2.13) for the electric potential $U_{\text{out}}^{\text{tot}}(r, \varphi)$ outside the conductive disk is due to the external electric field and the second term can be interpreted as the electric potential of an induced electrostatic dipole at the center of the disk (see Eq. (2.4) and Fig. 1.1a). This analysis can be generalized to a dielectric disk with dielectric constant ϵ_{in} that is embedded in a material with the dielectric constant ϵ_{out} in a uniform external electric field ($\mathbf{E} = E_0\hat{\mathbf{x}}$). The electric potentials inside and outside the disk are then given by [48]

$$U_{\text{in}}^{\text{tot}}(r, \varphi) = -E_0 r \cos\varphi + E_0 \frac{(\epsilon_{\text{in}} - \epsilon_{\text{out}})}{(\epsilon_{\text{in}} + \epsilon_{\text{out}})} r \cos\varphi, \tag{2.14a}$$

$$U_{\text{out}}^{\text{tot}}(r, \varphi) = -E_0 r \cos\varphi + E_0 \frac{(\epsilon_{\text{in}} - \epsilon_{\text{out}})}{(\epsilon_{\text{in}} + \epsilon_{\text{out}})} \frac{R^2}{r} \cos\varphi. \tag{2.14b}$$

The first terms in both $U_{\text{in}}^{\text{tot}}$ and $U_{\text{out}}^{\text{tot}}$ correspond to the external electric field, whereas the second terms can be interpreted as induced dipoles. The expression in Eq. (2.13) for the conductive disk is recovered in the limit $\epsilon_{\text{in}}/\epsilon_{\text{out}} \to \infty$. Note that the resulting electric field inside the dielectric disk is uniform $\mathbf{E}_{\text{in}}^{\text{tot}} = -\boldsymbol{\nabla} U_{\text{in}}^{\text{tot}} = 2E_0\epsilon_{\text{out}}/(\epsilon_{\text{in}} + \epsilon_{\text{out}})\hat{\mathbf{x}}$.

Similarly, external stress induces multipoles in elastic systems. For example, consider a circular hole of radius R embedded in an infinite elastic matrix. Under external stress $\sigma_{xx}^{\text{ext}} = -\sigma_0$, the resultant Airy stress function is obtained by solving the governing equation $\Delta\Delta\chi = 0$ with the traction-free boundary condition ($\sigma_{rr} = \sigma_{r\varphi} = 0$) at the circumference of the hole. The Airy stress function outside the hole ($r > R$) in polar coordinates is given by [128]

$$\begin{aligned}\chi_{\text{out}}^{\text{tot}}(r,\varphi) = &-\frac{\sigma_0 r^2}{4}\big(1-\cos(2\varphi)\big) + \frac{\sigma_0 R^2}{2}\ln r \\ &- \frac{\sigma_0 R^2}{2}\cos(2\varphi) + \frac{\sigma_0 R^4}{4r^2}\cos(2\varphi).\end{aligned} \tag{2.15}$$

The above equation for the Airy stress function reveals that the external stress induces a non-topological monopole p (Eq. (2.3)), and quadrupoles $\mathbf{Q}^s$ and $\mathbf{Q}^p$ (Eqs. (2.8, 2.9)) at the center of the hole (see Fig. 1.1c). Note that unlike in electrostatics, dipoles $\mathbf{d}^s$ are not induced in elasticity. This is because isolated disclinations (topological monopoles) and dislocations (topological dipoles) are formed by insertion or removal of material, which makes them topological defects [122]. On the other hand, elastic non-topological monopole p and quadrupoles $\mathbf{Q}^s$ and $\mathbf{Q}^p$ can be obtained by local material rearrangement and can thus be induced by external loads [126, 125].

The above analysis can be generalized to the case with a circular inclusion of radius R made from material with the Young's modulus E_{in} and the Poisson's ratio ν_{in} that is embedded in an infinite elastic matrix made from material with the Young's modulus E_{out} and the Poisson's ratio ν_{out}. Under uniaxial compressive stress $\sigma_{xx}^{\text{ext}} = -\sigma_0$, the Airy stress function corresponding to the external stress is $\chi_{\text{ext}} = -\sigma_0 y^2/2 =$

Table 2.2: Stresses σ_{ij} and displacements u_i corresponding to different terms for the Airy stress function χ [see Eq. (2.12)] in the Michell solution [1]. The value of Kolosov's constant for plane stress is $\kappa = (3-\nu)/(1+\nu)$ and for plane strain is $\kappa = 3-4\nu$. Here, μ is the shear modulus and ν is the Poisson's ratio.

χ	σ_{rr}	$\sigma_{r\varphi}$	$\sigma_{\varphi\varphi}$	$2\mu \begin{pmatrix} u_r \\ u_\varphi \end{pmatrix}$
r^2	2	0	2	$r \begin{pmatrix} \kappa-1 \\ 0 \end{pmatrix}$
$\ln r$	r^{-2}	0	$-r^{-2}$	$r^{-1} \begin{pmatrix} -1 \\ 0 \end{pmatrix}$
$r^{n+2}\cos(n\varphi)$	$-(n+1)(n-2)r^n\cos(n\varphi)$	$n(n+1)r^n\sin(n\varphi)$	$(n+1)(n+2)r^n\cos(n\varphi)$	$r^{n+1} \begin{pmatrix} (\kappa-n-1)\cos(n\varphi) \\ (\kappa+n+1)\sin(n\varphi) \end{pmatrix}$
$r^{n+2}\sin(n\varphi)$	$-(n+1)(n-2)r^n\sin(n\varphi)$	$-n(n+1)r^n\cos(n\varphi)$	$(n+1)(n+2)r^n\sin(n\varphi)$	$r^{n+1} \begin{pmatrix} (\kappa-n-1)\sin(n\varphi) \\ -(\kappa+n+1)\cos(n\varphi) \end{pmatrix}$
$r^{-n+2}\cos(n\varphi)$	$-(n+2)(n-1)r^{-n}\cos(n\varphi)$	$-n(n-1)r^{-n}\sin(n\varphi)$	$(n-1)(n-2)r^{-n}\cos(n\varphi)$	$r^{-n+1} \begin{pmatrix} (\kappa+n-1)\cos(n\varphi) \\ -(\kappa-n+1)\sin(n\varphi) \end{pmatrix}$
$r^{-n+2}\sin(n\varphi)$	$-(n+2)(n-1)r^{-n}\sin(n\varphi)$	$n(n-1)r^{-n}\cos(n\varphi)$	$(n-1)(n-2)r^{-n}\sin(n\varphi)$	$r^{-n+1} \begin{pmatrix} (\kappa+n-1)\sin(n\varphi) \\ (\kappa-n+1)\cos(n\varphi) \end{pmatrix}$
$r^n\cos(n\varphi)$	$-n(n-1)r^{n-2}\cos(n\varphi)$	$n(n-1)r^{n-2}\sin(n\varphi)$	$n(n-1)r^{n-2}\cos(n\varphi)$	$r^{n-1} \begin{pmatrix} -n\cos(n\varphi) \\ n\sin(n\varphi) \end{pmatrix}$
$r^n\sin(n\varphi)$	$-n(n-1)r^{n-2}\sin(n\varphi)$	$-n(n-1)r^{n-2}\cos(n\varphi)$	$n(n-1)r^{n-2}\sin(n\varphi)$	$r^{n-1} \begin{pmatrix} -n\sin(n\varphi) \\ -n\cos(n\varphi) \end{pmatrix}$
$r^{-n}\cos(n\varphi)$	$-n(n+1)r^{-n-2}\cos(n\varphi)$	$-n(n+1)r^{-n-2}\sin(n\varphi)$	$n(n+1)r^{-n-2}\cos(n\varphi)$	$r^{-n-1} \begin{pmatrix} n\cos(n\varphi) \\ n\sin(n\varphi) \end{pmatrix}$
$r^{-n}\sin(n\varphi)$	$-n(n+1)r^{-n-2}\sin(n\varphi)$	$n(n+1)r^{-n-2}\cos(n\varphi)$	$n(n+1)r^{-n-2}\sin(n\varphi)$	$r^{-n-1} \begin{pmatrix} n\sin(n\varphi) \\ -n\cos(n\varphi) \end{pmatrix}$

$-\sigma_0 r^2\big(1-\cos(2\varphi)\big)/4$. Since the Airy stress function due to external stress contains both the axisymmetric and the $\cos(2\varphi)$ term, the Airy stress function due to induced multipoles should have the same angular dependence. Furthermore stresses should remain finite at the center of the inclusion ($r=0$) and also far away from the inclusion ($r\to\infty$). The total Airy stress function $\chi_{\text{in}}^{\text{tot}}(r,\varphi)$ inside ($r<R$) and $\chi_{\text{out}}^{\text{tot}}(r,\varphi)$ outside ($r>R$) the inclusion can thus be written in the following form

$$\chi_{\text{in}}^{\text{tot}}(r,\varphi) = -\frac{\sigma_0 r^2}{4}\big(1-\cos(2\varphi)\big) + c_0 r^2 + a_2 r^2\cos(2\varphi) + c_2\frac{r^4}{R^2}\cos(2\varphi), \tag{2.16a}$$

$$\chi_{\text{out}}^{\text{tot}}(r,\varphi) = -\frac{\sigma_0 r^2}{4}\big(1-\cos(2\varphi)\big) + A_0 R^2\ln\left(\frac{r}{R}\right) + C_2 R^2\cos(2\varphi) + A_2 R^4 r^{-2}\cos(2\varphi). \tag{2.16b}$$

The last three terms in Eq. (2.16b) correspond to the induced non-topological monopole p and quadrupoles $\mathbf{Q}^s$ and $\mathbf{Q}^p$ at the center of the inclusion, similar to

induced multipoles at the center of the hole in Eq. (2.15). The last three terms in Eq. (2.16a) can also be interpreted as induced multipoles that are located far away from the inclusion. The unknown coefficients are determined from the boundary conditions, which require that tractions (σ_{rr} and $\sigma_{r\varphi}$) and displacements (u_r and u_φ) are continuous at the circumference of the inclusion ($r = R$). Stresses corresponding to the Airy stress function $\chi(r,\varphi)$ can be calculated as $\sigma_{rr} = r^{-1}(\partial\chi/\partial r) + r^{-2}(\partial^2\chi/\partial\varphi^2)$, $\sigma_{\varphi\varphi} = \partial^2\chi/\partial r^2$, and $\sigma_{r\varphi} = -\partial(r^{-1}\partial\chi/\partial\varphi)/\partial r$. Table 2.2 summarizes the stresses corresponding to different terms in the Michell solution [1]. The boundary conditions for tractions at the circumference of inclusion are thus $\sigma^{\text{tot}}_{\text{in},rr} = \sigma^{\text{tot}}_{\text{out},rr}$ and $\sigma^{\text{tot}}_{\text{in},r\varphi} = \sigma^{\text{tot}}_{\text{out},r\varphi}$, where

$$\sigma^{\text{tot}}_{\text{in},rr} = -\frac{\sigma_0}{2} + 2c_0 - \left(\frac{\sigma_0}{2} + 2a_2\right)\cos(2\varphi), \tag{2.17a}$$

$$\sigma^{\text{tot}}_{\text{out},rr} = -\frac{\sigma_0}{2} + A_0 - \left(\frac{\sigma_0}{2} + 4C_2 + 6A_2\right)\cos(2\varphi), \tag{2.17b}$$

$$\sigma^{\text{tot}}_{\text{in},r\varphi} = \left(\frac{\sigma_0}{2} + 2a_2 + 6c_2\right)\sin(2\varphi), \tag{2.17c}$$

$$\sigma^{\text{tot}}_{\text{out},r\varphi} = \left(\frac{\sigma_0}{2} - 2C_2 - 6A_2\right)\sin(2\varphi). \tag{2.17d}$$

In order to obtain displacements, we first calculate the strains $\varepsilon_{rr} = \left((\kappa+1)\sigma_{rr} - (3-\kappa)\sigma_{\varphi\varphi}\right)/(8\mu)$, $\varepsilon_{r\varphi} = \sigma_{r\varphi}/(2\mu)$ and $\varepsilon_{\varphi\varphi} = \left((\kappa+1)\sigma_{\varphi\varphi} - (3-\kappa)\sigma_{rr}\right)/(8\mu)$, where $\mu = E/[2(1+\nu)]$ is the shear modulus and we introduced the Kolosov's constant $\kappa = (3-\nu)/(1+\nu)$ for plane stress and $\kappa = 3-4\nu$ for plane strain condition [1]. Displacements u_r and u_φ are then obtained by integrating the strains. Table 2.2 summarizes the displacements corresponding to different terms in the Michell solution [1]. The boundary conditions for displacements at the circumference of inclusion are thus $u^{\text{tot}}_{\text{in},r} = u^{\text{tot}}_{\text{out},r}$ and $u^{\text{tot}}_{\text{in},\varphi} = u^{\text{tot}}_{\text{out},\varphi}$, where

$$u^{\text{tot}}_{\text{in},r} = \left(-\frac{\sigma_0}{4} + c_0\right)\frac{R(\kappa_{\text{in}}-1)}{2\mu_{\text{in}}}$$

$$+\left(-\frac{\sigma_0}{2}-2a_2+c_2(\kappa_{\text{in}}-3)\right)\frac{R\cos(2\varphi)}{2\mu_{\text{in}}}, \tag{2.18a}$$

$$u^{\text{tot}}_{\text{out},r}=-\frac{R}{2\mu_{\text{out}}}\left(\frac{1}{4}\sigma_0(\kappa_{\text{out}}-1)+A_0\right)$$
$$+\left(-\frac{\sigma_0}{2}+C_2(\kappa_{\text{out}}+1)+2A_2\right)\frac{R\cos(2\varphi)}{2\mu_{\text{out}}}, \tag{2.18b}$$

$$u^{\text{tot}}_{\text{in},\varphi}=\left(\frac{\sigma_0}{2}+2a_2+c_2(\kappa_{\text{in}}+3)\right)\frac{R\sin(2\varphi)}{2\mu_{\text{in}}}, \tag{2.18c}$$

$$u^{\text{tot}}_{\text{out},\varphi}=\left(\frac{\sigma_0}{2}-C_2(\kappa_{\text{out}}-1)+2A_2\right)\frac{R\sin(2\varphi)}{2\mu_{\text{out}}}. \tag{2.18d}$$

The boundary conditions in Eqs. (2.17) and (2.18) have to be satisfied at every point (φ) on the circumference of the inclusion. Thus the coefficients of the Fourier components have to match on both sides of these equations, which allows us to rewrite the boundary conditions as a matrix equation

$$\begin{pmatrix}\mathbf{M}^{\text{trac}}_{\text{out}}, & \mathbf{M}^{\text{trac}}_{\text{in}}\\ \mathbf{M}^{\text{disp}}_{\text{out}}, & \mathbf{M}^{\text{disp}}_{\text{in}}\end{pmatrix}\begin{pmatrix}\mathbf{a}_{\text{out}}\\ \mathbf{a}_{\text{in}}\end{pmatrix}=\begin{pmatrix}\mathbf{0}\\ \mathbf{b}^{\text{disp}}\end{pmatrix}. \tag{2.19}$$

The top and bottom rows of the matrix in the above equation are obtained from the boundary conditions for tractions (superscript 'trac') and displacements (superscript 'disp'), respectively, where

$$\mathbf{M}^{\text{trac}}_{\text{out}}=\begin{pmatrix}1 & 0 & 0\\ 0 & -6 & -4\\ 0 & -6 & -2\end{pmatrix}, \tag{2.20a}$$

$$\mathbf{M}^{\text{trac}}_{\text{in}}=\begin{pmatrix}-2 & 0 & 0\\ 0 & 2 & 0\\ 0 & -2 & -6\end{pmatrix}, \tag{2.20b}$$

$$\mathbf{M}_{\text{out}}^{\text{disp}} = \begin{pmatrix} -\frac{R}{2\mu_{\text{out}}} & 0 & 0 \\ 0 & \frac{R}{\mu_{\text{out}}} & \frac{R(\kappa_{\text{out}}+1)}{2\mu_{\text{out}}} \\ 0 & \frac{R}{\mu_{\text{out}}} & -\frac{R(\kappa_{\text{out}}-1)}{2\mu_{\text{out}}} \end{pmatrix}, \tag{2.20c}$$

$$\mathbf{M}_{\text{in}}^{\text{disp}} = \begin{pmatrix} -\frac{R(\kappa_{\text{in}}-1)}{2\mu_{\text{in}}} & 0 & 0 \\ 0 & \frac{R}{\mu_{\text{in}}} & -\frac{R(\kappa_{\text{in}}-3)}{2\mu_{\text{in}}} \\ 0 & -\frac{R}{\mu_{\text{in}}} & -\frac{R(\kappa_{\text{in}}+3)}{2\mu_{\text{in}}} \end{pmatrix}. \tag{2.20d}$$

The left and right columns of the matrix in Eq. (2.19) describe the effect of the induced multipoles $\mathbf{a}_{\text{out}}$ outside and $\mathbf{a}_{\text{in}}$ inside the inclusion, respectively, where

$$\mathbf{a}_{\text{out}} = \begin{pmatrix} A_0 \\ A_2 \\ C_2 \end{pmatrix}, \quad \mathbf{a}_{\text{in}} = \begin{pmatrix} c_0 \\ a_2 \\ c_2 \end{pmatrix}. \tag{2.21}$$

The right hand side of the Eq. (2.19) describes the effect of external load as

$$\mathbf{b}^{\text{disp}} = \begin{pmatrix} \frac{\sigma_0 R}{8}\left(\frac{(\kappa_{\text{out}}-1)}{\mu_{\text{out}}} - \frac{(\kappa_{\text{in}}-1)}{\mu_{\text{in}}}\right) \\ \frac{\sigma_0 R}{4}\left(\frac{1}{\mu_{\text{out}}} - \frac{1}{\mu_{\text{in}}}\right) \\ \frac{\sigma_0 R}{4}\left(-\frac{1}{\mu_{\text{out}}} + \frac{1}{\mu_{\text{in}}}\right) \end{pmatrix}. \tag{2.22}$$

By solving the set of equations in Eq. (2.19) we find that the Airy stress functions $\chi_{\text{in}}^{\text{tot}}(r,\varphi)$ inside $(r < R)$ and $\chi_{\text{out}}^{\text{tot}}(r,\varphi)$ outside $(r > R)$ the inclusion are given by

$$\begin{aligned} \chi_{\text{in}}^{\text{tot}}(r,\varphi) = &-\frac{\sigma_0 r^2}{4}\big(1-\cos(2\varphi)\big) \\ &+\frac{(\mu_{\text{out}}(\kappa_{\text{in}}-1)-\mu_{\text{in}}(\kappa_{\text{out}}-1))}{4(\mu_{\text{out}}(\kappa_{\text{in}}-1)+2\mu_{\text{in}})}\,\sigma_0 r^2 \\ &-\frac{(\mu_{\text{out}}-\mu_{\text{in}})}{4(\mu_{\text{out}}+\mu_{\text{in}}\kappa_{\text{out}})}\,\sigma_0 r^2\cos(2\varphi), \end{aligned} \tag{2.23a}$$

$$\chi_{\text{out}}^{\text{tot}}(r,\varphi) = -\frac{\sigma_0 r^2}{4}\big(1-\cos(2\varphi)\big)$$

$$+\frac{(\mu_{\text{out}}(\kappa_{\text{in}}-1)-\mu_{\text{in}}(\kappa_{\text{out}}-1))}{2(\mu_{\text{out}}(\kappa_{\text{in}}-1)+2\mu_{\text{in}})}\sigma_0 R^2\ln r$$
$$-\frac{(\mu_{\text{out}}-\mu_{\text{in}})}{2(\mu_{\text{out}}+\mu_{\text{in}}\kappa_{\text{out}})}\sigma_0 R^2\cos(2\varphi)$$
$$+\frac{(\mu_{\text{out}}-\mu_{\text{in}})}{4(\mu_{\text{out}}+\mu_{\text{in}}\kappa_{\text{out}})}\sigma_0 R^4 r^{-2}\cos(2\varphi). \tag{2.23b}$$

In the above Eq. (2.23) for the Airy stress functions the last three terms can again be interpreted as induced non-topological monopole p and quadrupoles $\mathbf{Q}^s$ and $\mathbf{Q}^p$. The expression in Eq. (2.15) for the hole is recovered in the limit $\mu_{\text{in}} \to 0$. Note that similar to the Eshelby inclusions in 3D [16], the stress field inside the inclusion in 2D is uniform and is given by

$$\sigma_{xx}^{\text{in}} = -\sigma_0\frac{\mu_{\text{in}}(1+\kappa_{\text{out}})(\mu_{\text{out}}\kappa_{\text{in}}+\mu_{\text{in}}(2+\kappa_{\text{out}}))}{2(\mu_{\text{out}}(\kappa_{\text{in}}-1)+2\mu_{\text{in}})(\mu_{\text{out}}+\mu_{\text{in}}\kappa_{\text{out}})}, \tag{2.24a}$$
$$\sigma_{yy}^{\text{in}} = \sigma_0\frac{\mu_{\text{in}}(1+\kappa_{\text{out}})(\mu_{\text{out}}(\kappa_{\text{in}}-2)-\mu_{\text{in}}(\kappa_{\text{out}}-2))}{2(\mu_{\text{out}}(\kappa_{\text{in}}-1)+2\mu_{\text{in}})(\mu_{\text{out}}+\mu_{\text{in}}\kappa_{\text{out}})}, \tag{2.24b}$$
$$\sigma_{xy}^{\text{in}} = 0. \tag{2.24c}$$

By comparing the above analyses in elasticity and electrostatics, we conclude that holes and inclusions in elasticity are analogous to perfect conductors and dielectrics in electrostatics, respectively.

The problem of induction becomes much more involved when multiple dielectric objects are considered in electrostatics or multiple inclusions in elasticity. This is because dielectric objects and inclusions interact with each other via induced electric fields and stress fields, respectively. In the next Section, we describe how such interactions can be systematically taken into account in elasticity, which enabled us to calculate the magnitudes of induced multipoles in the presence of external load.

2.2 Elastic multipole method

Building on the concepts described above, we have developed a method for calculating the linear deformation of circular inclusions and holes embedded in an infinite elastic matrix under external stress. External stress induces elastic multipoles at the centers of inclusions and holes, and their amplitudes are obtained from the boundary conditions between different materials (continuity of tractions and displacements). In the following Section 2.2.1, we describe the method for the general case where circular inclusions can have different sizes and material properties (holes correspond to zero shear modulus). Note that our method applies to the deformation of cylindrical holes and inclusions embedded in thin plates (plane stress) as well as to cylindrical holes and inclusions embedded in an infinitely thick elastic matrix (plane strain) by appropriately setting the values of the Kolosov's constant. In Section 2.2.2 we compare the results of our method to the finite element simulations and in Section 2.2.3 they are compared to experiments.

2.2.1 Method

Let us consider a 2D infinite elastic matrix with the Young's modulus E_0 and the Poisson's ratio ν_0. Embedded in the matrix are N circular inclusions with radii R_i centered at positions $\mathbf{x}_i = (x_i, y_i)$ with Young's moduli E_i and Poisson's ratios ν_i, where $i \in \{1, \ldots, N\}$. Holes are described with zero Young's modulus ($E_i = 0$). External stress, represented with the Airy stress function

$$\chi_{\text{ext}}(x, y) = \frac{1}{2}\sigma_{xx}^{\text{ext}} y^2 + \frac{1}{2}\sigma_{yy}^{\text{ext}} x^2 - \sigma_{xy}^{\text{ext}} xy, \tag{2.25}$$

induces non-topological monopoles (p), non-topological dipoles ($\mathbf{d}^p$), quadrupoles ($\mathbf{Q}^s$, $\mathbf{Q}^p$), and higher-order multipoles ($\mathbf{Q}_n^s$, $\mathbf{Q}_n^p$) at the centers of inclusions, as was discussed in Section 2.1.6. Thus the Airy stress function outside the i^{th} inclusion due

to the induced multipoles can be expanded as

$$\begin{aligned}\chi_{\text{out}}\big(r_i,\varphi_i|\mathbf{a}_{i,\text{out}}\big) =& A_{i,0}R_i^2\ln\left(\frac{r_i}{R_i}\right)\\ &+\sum_{n=1}^{\infty}R_i^2\left(\frac{r_i}{R_i}\right)^{-n}\Big[A_{i,n}\cos(n\varphi_i)+B_{i,n}\sin(n\varphi_i)\Big]\\ &+\sum_{n=2}^{\infty}R_i^2\left(\frac{r_i}{R_i}\right)^{-n+2}\Big[C_{i,n}\cos(n\varphi_i)+D_{i,n}\sin(n\varphi_i)\Big],\end{aligned}\tag{2.26}$$

where the origin of polar coordinates ($r_i=\sqrt{(x-x_i)^2+(y-y_i)^2}, \varphi_i=\arctan[(y-y_i)/(x-x_i)]$) is at the center $\mathbf{x}_i$ of the i^{th} inclusion and $\mathbf{a}_{i,\text{out}}=\{A_{i,0}, A_{i,1}, \dots, B_{i,1}, B_{i,2}, \dots, C_{i,2}, C_{i,3}, \dots, D_{i,2}, D_{i,3}, \dots\}$ is the set of amplitudes of induced multipoles. The total Airy stress function outside all inclusions can then be written as

$$\begin{aligned}\chi^{\text{tot}}_{\text{out}}\big(x,y|\mathbf{a}_{\text{out}}\big) =& \chi_{\text{ext}}(x,y)\\ &+\sum_{i=1}^{N}\chi_{\text{out}}\big(r_i(x,y),\varphi_i(x,y)|\mathbf{a}_{i,\text{out}}\big),\end{aligned}\tag{2.27}$$

where the first term is due to external stress and the summation describes contributions due to induced multipoles at the centers of inclusions. The set of amplitudes of induced multipoles for all inclusions is defined as $\mathbf{a}_{\text{out}}=\{\mathbf{a}_{1,\text{out}},\cdots,\mathbf{a}_{N,\text{out}}\}$.

Similarly, we expand the induced Airy stress function inside the i^{th} inclusion as

$$\begin{aligned}\chi_{\text{in}}\big(r_i,\varphi_i|\mathbf{a}_{i,\text{in}}\big) =& c_{i,0}r_i^2\\ &+\sum_{n=2}^{\infty}R_i^2\left(\frac{r_i}{R_i}\right)^{n}\big[a_{i,n}\cos(n\varphi_i)+b_{i,n}\sin(n\varphi_i)\big]\\ &+\sum_{n=1}^{\infty}R_i^2\left(\frac{r_i}{R_i}\right)^{n+2}\big[c_{i,n}\cos(n\varphi_i)+d_{i,n}\sin(n\varphi_i)\big],\end{aligned}\tag{2.28}$$

where we kept only the terms that generate finite stresses at the center of inclusion and omitted constant and linear terms $\{1, r_i\cos\varphi_i, r_i\sin\varphi_i\}$ that correspond to zero stresses. The set of amplitudes of induced multipoles is represented as

$\mathbf{a}_{i,\text{in}} = \{a_{i,2}, a_{i,3}, \ldots, b_{i,2}, b_{i,3}, \ldots, c_{i,0}, c_{i,1}, \ldots, d_{i,1}, d_{i,2}, \ldots\}$. The total Airy stress function inside the i^{th} inclusion is thus

$$\begin{aligned}\chi_{\text{in}}^{\text{tot}}\big(x, y|\mathbf{a}_{i,\text{in}}\big) =& \chi_{\text{ext}}(x, y) \\ &+ \chi_{\text{in}}\big(r_i(x, y), \varphi_i(x, y)|\mathbf{a}_{i,\text{in}}\big),\end{aligned} \tag{2.29}$$

where the first term is due to external stress and the second term is due to induced multipoles.

The amplitudes of induced multipoles $\mathbf{a}_{i,\text{out}}$ and $\mathbf{a}_{i,\text{in}}$ are obtained by satisfying the boundary conditions that tractions and displacements are continuous across the circumference of each inclusion

$$\sigma_{\text{in},rr}^{\text{tot}}\big(r_i = R_i, \varphi_i|\mathbf{a}_{i,\text{in}}\big) = \sigma_{\text{out},rr}^{\text{tot}}\big(r_i = R_i, \varphi_i|\mathbf{a}_{\text{out}}\big), \tag{2.30a}$$

$$\sigma_{\text{in},r\varphi}^{\text{tot}}\big(r_i = R_i, \varphi_i|\mathbf{a}_{i,\text{in}}\big) = \sigma_{\text{out},r\varphi}^{\text{tot}}\big(r_i = R_i, \varphi_i|\mathbf{a}_{\text{out}}\big), \tag{2.30b}$$

$$u_{\text{in},r}^{\text{tot}}\big(r_i = R_i, \varphi_i|\mathbf{a}_{i,\text{in}}\big) = u_{\text{out},r}^{\text{tot}}\big(r_i = R_i, \varphi_i|\mathbf{a}_{\text{out}}\big), \tag{2.30c}$$

$$u_{\text{in},\varphi}^{\text{tot}}\big(r_i = R_i, \varphi_i|\mathbf{a}_{i,\text{in}}\big) = u_{\text{out},\varphi}^{\text{tot}}\big(r_i = R_i, \varphi_i|\mathbf{a}_{\text{out}}\big), \tag{2.30d}$$

where stresses and displacements are obtained from the total Airy stress functions $\chi_{\text{in}}^{\text{tot}}\big(x, y|\mathbf{a}_{i,\text{in}}\big)$ inside the i^{th} inclusion (see Eq. (2.29)) and $\chi_{\text{out}}^{\text{tot}}\big(x, y|\mathbf{a}_{\text{out}}\big)$ outside all inclusions (see Eq. (2.27)). In the boundary conditions for the i^{th} inclusion in the above Eq. (2.30), we can easily take into account contributions due to the induced multipoles $\mathbf{a}_{i,\text{in}}$ and $\mathbf{a}_{i,\text{out}}$ in this inclusion and due to external stresses σ_{xx}^{ext}, σ_{yy}^{ext}, and σ_{xy}^{ext} after rewriting the corresponding Airy stress function $\chi_{\text{ext}}(x, y)$ in Eq. (2.25) in polar coordinates centered at the i^{th} inclusion as

$$\begin{aligned}\chi_{\text{ext}}(r_i, \varphi_i) = &\frac{1}{4}(\sigma_{xx}^{\text{ext}} + \sigma_{yy}^{\text{ext}})r_i^2 \\ &- \frac{1}{4}(\sigma_{xx}^{\text{ext}} - \sigma_{yy}^{\text{ext}})r_i^2 \cos(2\varphi_i) \\ &- \frac{1}{2}\sigma_{xy}^{\text{ext}} r_i^2 \sin(2\varphi_i).\end{aligned} \tag{2.31}$$

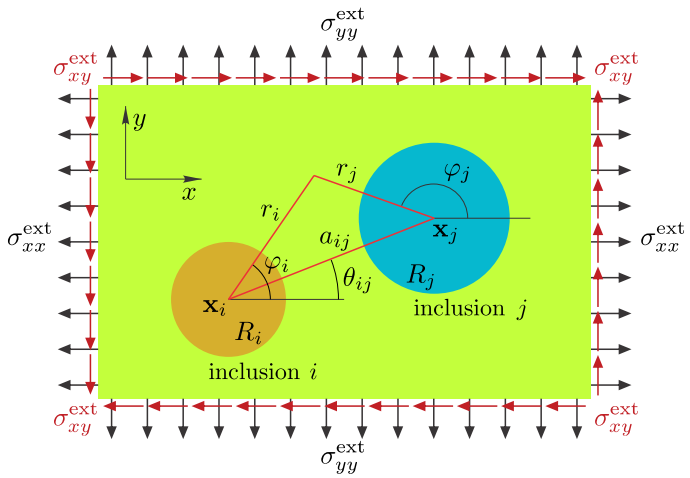

Figure 2.4: Illustration of external load (σ_{xx}^{ext}, σ_{yy}^{ext}, σ_{xy}^{ext}) and polar coordinates (r_i, φ_i) and (r_j, φ_j) relative to the centers $\mathbf{x}_i$ of the i^{th} inclusion (orange disk) with radius R_i and $\mathbf{x}_j$ of the j^{th} inclusion (blue disk) with radius R_j, respectively. Here, a_{ij} is the separation distance between the i^{th} and j^{th} inclusion and θ_{ij} is the angle between the line joining their centers and the x-axis.

Contributions to stresses and displacements in the boundary conditions for the i^{th} inclusion in Eq. (2.30) due to the Airy stress functions $\chi_{\text{in}}\big(r_i, \varphi_i|\mathbf{a}_{i,\text{in}}\big)$, $\chi_{\text{out}}\big(r_i, \varphi_i|\mathbf{a}_{i,\text{out}}\big)$, and $\chi_{\text{ext}}(r_i, \varphi_i)$ can be taken into account with the help of Table 2.2. However, it is not straightforward to consider the contributions due to the induced multipoles $\mathbf{a}_{j,\text{out}}$ for other inclusions ($j \neq i$), because the corresponding Airy stress functions $\chi_{\text{out}}\big(r_j, \varphi_j|\mathbf{a}_{j,\text{out}}\big)$ in Eq. (2.26) are written in the polar coordinates centered at $\mathbf{x}_j$. The polar coordinates (r_j, φ_j) centered at the j^{th} inclusion can be expressed in terms of polar coordinates (r_i, φ_i) centered at the i^{th} inclusion as

$$\begin{aligned} r_j(r_i, \varphi_i) &= \sqrt{r_i^2 + a_{ij}^2 - 2r_i a_{ij}\cos(\varphi_i - \theta_{ij})}, \\ \varphi_j(r_i, \varphi_i) &= \pi + \theta_{ij} - \arctan\left[\frac{r_i \sin(\varphi_i - \theta_{ij})}{\big(a_{ij} - r_i\cos(\varphi_i - \theta_{ij})\big)}\right], \end{aligned} \tag{2.32}$$

where $a_{ij} = \sqrt{(x_i - x_j)^2 + (y_i - y_j)^2}$ is the distance between the centers of the i^{th} and j^{th} inclusion and $\theta_{ij} = \arctan[(y_j - y_i)/(x_j - x_i)]$ is the angle between the line joining the centers of inclusions and the x-axis, as shown in Fig. 2.4.

The Airy stress function due to the induced multipoles centered at the j^{th} inclusion can be expanded in Taylor series around the center of the i^{th} inclusion as [34]

$$\begin{aligned}\chi_{\text{out}}\big(r_j(r_i,\varphi_i),\varphi_j(r_i,\varphi_i)|\mathbf{a}_{\text{j,out}}\big) = \quad & \sum_{n=2}^{\infty} R_j^2 \frac{r_i^n}{a_{ij}^n}\Big[\cos(n\varphi_i) f_c^n\left(R_j/a_{ij},\theta_{ij}|\mathbf{a}_{j,\text{out}}\right) \\ & \qquad + \sin(n\varphi_i) f_s^n\left(R_j/a_{ij},\theta_{ij}|\mathbf{a}_{j,\text{out}}\right)\Big] \\ & + \sum_{n=0}^{\infty} R_j^2 \frac{r_i^{n+2}}{a_{ij}^{n+2}}\Big[\cos(n\varphi_i) g_c^n\left(R_j/a_{ij},\theta_{ij}|\mathbf{a}_{j,\text{out}}\right) \\ & \qquad + \sin(n\varphi_i) g_s^n\left(R_j/a_{ij},\theta_{ij}|\mathbf{a}_{j,\text{out}}\right)\Big],\end{aligned} \tag{2.33}$$

where we omitted constant and linear terms $\{1, r_i\cos\varphi_i, r_i\sin\varphi_i\}$ that correspond to zero stresses and we introduced functions

$$\begin{aligned} f_c^n\left(R_j/a_{ij},\theta_{ij}|\mathbf{a}_{j,\text{out}}\right) = \sum_{m=0}^{\infty}\Bigg(& \frac{R_j^m}{a_{ij}^m}\Big[A_{j,m}\mathcal{A}_n^m(\theta_{ij}) + B_{j,m}\mathcal{B}_n^m(\theta_{ij})\Big] \\ & + \frac{R_j^{m-2}}{a_{ij}^{m-2}}\Big[C_{j,m}\mathcal{C}_n^m(\theta_{ij}) + D_{j,m}\mathcal{D}_n^m(\theta_{ij})\Big]\Bigg), \end{aligned} \tag{2.34a}$$

$$\begin{aligned} f_s^n\left(R_j/a_{ij},\theta_{ij}|\mathbf{a}_{j,\text{out}}\right) = \sum_{m=0}^{\infty}\Bigg(& \frac{R_j^m}{a_{ij}^m}\Big[A_{j,m}\mathcal{B}_n^m(\theta_{ij}) - B_{j,m}\mathcal{A}_n^m(\theta_{ij})\Big] \\ & + \frac{R_j^{m-2}}{a_{ij}^{m-2}}\Big[C_{j,m}\mathcal{D}_n^m(\theta_{ij}) - D_{j,m}\mathcal{C}_n^m(\theta_{ij})\Big]\Bigg), \end{aligned} \tag{2.34b}$$

$$g_c^n\left(R_j/a_{ij},\theta_{ij}|\mathbf{a}_{j,\text{out}}\right) = \sum_{m=2}^{\infty}\frac{R_j^{m-2}}{a_{ij}^{m-2}}\Big[C_{j,m}\mathcal{E}_n^m(\theta_{ij}) + D_{j,m}\mathcal{F}_n^m(\theta_{ij})\Big], \tag{2.34c}$$

$$g_s^n\left(R_j/a_{ij},\theta_{ij}|\mathbf{a}_{j,\text{out}}\right) = \sum_{m=2}^{\infty}\frac{R_j^{m-2}}{a_{ij}^{m-2}}\Big[C_{j,m}\mathcal{F}_n^m(\theta_{ij}) - D_{j,m}\mathcal{E}_n^m(\theta_{ij})\Big]. \tag{2.34d}$$

In the above Eq. (2.34), we set $B_{j,0} = C_{j,0} = D_{j,0} = C_{j,1} = D_{j,1} = 0$ and introduced coefficients $\mathcal{A}_n^m(\theta_{ij})$, $\mathcal{B}_n^m(\theta_{ij})$, $\mathcal{C}_n^m(\theta_{ij})$, $\mathcal{D}_n^m(\theta_{ij})$, $\mathcal{E}_n^m(\theta_{ij})$, and $\mathcal{F}_n^m(\theta_{ij})$ that are summarized in Table 2.3.

Table 2.3: Coefficients for the expansion of the Airy stress function $\chi_{\text{out}}\big(r_j(r_i,\varphi_i),\varphi_j(r_i,\varphi_i)|\mathbf{a}_{\text{j,out}}\big)$ in Eqs. (2.33-2.34).

$n\geq 2$	$\mathcal{A}_n^0(\theta_{ij})=-\frac{1}{n}\cos(n\theta_{ij})$	$\mathcal{B}_n^0(\theta_{ij})=-\frac{1}{n}\sin(n\theta_{ij})$
$n\geq 2, m\geq 1$	$\mathcal{A}_n^m(\theta_{ij})=(-1)^m\binom{m+n-1}{n}\cos\big((m+n)\theta_{ij}\big)$	$\mathcal{B}_n^m(\theta_{ij})=(-1)^m\binom{m+n-1}{n}\sin\big((m+n)\theta_{ij}\big)$
$n\geq 0, m\geq 2$	$\mathcal{C}_n^m(\theta_{ij})=(-1)^m\binom{m+n-2}{n}\cos\big((m+n)\theta_{ij}\big)$	$\mathcal{D}_n^m(\theta_{ij})=(-1)^m\binom{m+n-2}{n}\sin\big((m+n)\theta_{ij}\big)$
$n\geq 0, m\geq 2$	$\mathcal{E}_n^m(\theta_{ij})=(-1)^{m-1}\binom{m+n-1}{n+1}\cos\big((m+n)\theta_{ij}\big)$	$\mathcal{F}_n^m(\theta_{ij})=(-1)^{m-1}\binom{m+n-1}{n+1}\sin\big((m+n)\theta_{ij}\big)$

Next, we calculate stresses and displacements at the circumference of the i^{th} inclusion by using expressions for the Airy stress functions $\chi_{\text{ext}}(r_i,\varphi_i)$ in Eq. (2.31) due to external stresses, $\chi_{\text{in}}\big(r_i,\varphi_i|\mathbf{a}_{i,\text{in}}\big)$ and $\chi_{\text{out}}\big(r_i,\varphi_i|\mathbf{a}_{i,\text{out}}\big)$ in Eqs. (2.28) and (2.26) due to induced multipoles for the i^{th} inclusion, and $\chi_{\text{out}}\big(r_j,\varphi_j|\mathbf{a}_{j,\text{out}}\big)$ in Eq. (2.33) due to the induced multipoles for the j^{th} inclusion $(j\neq i)$. With the help of Table 2.2, which shows how to convert each term of the Airy stress function to stresses and displacements, we obtain

$$\sigma^{\text{tot}}_{\text{in},rr}\big(r_i=R_i,\varphi_i|\mathbf{a}_{i,\text{in}}\big)=\frac{1}{2}(\sigma^{\text{ext}}_{xx}+\sigma^{\text{ext}}_{yy})+\frac{1}{2}(\sigma^{\text{ext}}_{xx}-\sigma^{\text{ext}}_{yy})\cos(2\varphi_i)+\sigma^{\text{ext}}_{xy}\sin(2\varphi_i)+2c_{i,0}$$
$$-\sum_{n=1}^{\infty}\Big[n(n-1)\big(a_{i,n}\cos(n\varphi_i)+b_{i,n}\sin(n\varphi_i)\big)+(n+1)(n-2)\big(c_{i,n}\cos(n\varphi_i)+d_{i,n}\sin(n\varphi_i)\big)\Big], \tag{2.35a}$$

$$\sigma^{\text{tot}}_{\text{out},rr}\big(r_i=R_i,\varphi_i|\mathbf{a}_{\text{out}}\big)=\frac{1}{2}(\sigma^{\text{ext}}_{xx}+\sigma^{\text{ext}}_{yy})+\frac{1}{2}(\sigma^{\text{ext}}_{xx}-\sigma^{\text{ext}}_{yy})\cos(2\varphi_i)+\sigma^{\text{ext}}_{xy}\sin(2\varphi_i)+A_{i,0}$$
$$-\sum_{n=1}^{\infty}\Big[n(n+1)\big(A_{i,n}\cos(n\varphi_i)+B_{i,n}\sin(n\varphi_i)\big)+(n+2)(n-1)\big(C_{i,n}\cos(n\varphi_i)+D_{i,n}\sin(n\varphi_i)\big)\Big]$$
$$-\sum_{j\neq i}\sum_{n=2}^{\infty}\frac{R_j^2R_i^{n-2}}{a_{ij}^n}n(n-1)\Big[\cos(n\varphi_i)f_c^n\big(R_j/a_{ij},\theta_{ij}|\mathbf{a}_{j,\text{out}}\big)+\sin(n\varphi_i)f_s^n\big(R_j/a_{ij},\theta_{ij}|\mathbf{a}_{j,\text{out}}\big)\Big]$$
$$-\sum_{j\neq i}\sum_{n=0}^{\infty}\frac{R_j^2R_i^{n}}{a_{ij}^{n+2}}(n+1)(n-2)\Big[\cos(n\varphi_i)g_c^n\big(R_j/a_{ij},\theta_{ij}|\mathbf{a}_{j,\text{out}}\big)+\sin(n\varphi_i)g_s^n\big(R_j/a_{ij},\theta_{ij}|\mathbf{a}_{j,\text{out}}\big)\Big], \tag{2.35b}$$

$$\sigma^{\text{tot}}_{\text{in},r\varphi}\big(r_i=R_i,\varphi_i|\mathbf{a}_{i,\text{in}}\big)=-\frac{1}{2}(\sigma^{\text{ext}}_{xx}-\sigma^{\text{ext}}_{yy})\sin(2\varphi_i)+\sigma^{\text{ext}}_{xy}\cos(2\varphi_i)$$
$$+\sum_{n=1}^{\infty}\Big[n(n-1)\big(a_{i,n}\sin(n\varphi_i)-b_{i,n}\cos(n\varphi_i)\big)+n(n+1)\big(c_{i,n}\sin(n\varphi_i)-d_{i,n}\cos(n\varphi_i)\big)\Big], \tag{2.35c}$$

$$\sigma^{\text{tot}}_{\text{out},r\varphi}(r_i = R_i, \varphi_i|\mathbf{a}_{\text{out}}) = -\frac{1}{2}(\sigma^{\text{ext}}_{xx} - \sigma^{\text{ext}}_{yy})\sin(2\varphi_i) + \sigma^{\text{ext}}_{xy}\cos(2\varphi_i)$$
$$- \sum_{n=1}^{\infty}\Big[n(n+1)\big(A_{i,n}\sin(n\varphi_i) - B_{i,n}\cos(n\varphi_i)\big) + n(n-1)\big(C_{i,n}\sin(n\varphi_i) - D_{i,n}\cos(n\varphi_i)\big)\Big]$$
$$+ \sum_{j\neq i}\sum_{n=2}^{\infty}\frac{R_j^2 R_i^{n-2}}{a_{ij}^n}n(n-1)\Big[\sin(n\varphi_i)f_c^n\big(R_j/a_{ij}, \theta_{ij}|\mathbf{a}_{j,\text{out}}\big) - \cos(n\varphi_i)f_s^n\big(R_j/a_{ij}, \theta_{ij}|\mathbf{a}_{j,\text{out}}\big)\Big]$$
$$+ \sum_{j\neq i}\sum_{n=0}^{\infty}\frac{R_j^2 R_i^{n}}{a_{ij}^{n+2}}n(n+1)\Big[\sin(n\varphi_i)g_c^n\big(R_j/a_{ij}, \theta_{ij}|\mathbf{a}_{j,\text{out}}\big) - \cos(n\varphi_i)g_s^n\big(R_j/a_{ij}, \theta_{ij}|\mathbf{a}_{j,\text{out}}\big)\Big], \tag{2.35d}$$

$$\frac{2\mu_i}{R_i}u^{\text{tot}}_{\text{in},r}(r_i = R_i, \varphi_i|\mathbf{a}_{i,\text{in}}) = -\frac{1}{4}(\sigma^{\text{ext}}_{xx} + \sigma^{\text{ext}}_{yy})(1-\kappa_i) + \frac{1}{2}(\sigma^{\text{ext}}_{xx} - \sigma^{\text{ext}}_{yy})\cos(2\varphi_i) + \sigma^{\text{ext}}_{xy}\sin(2\varphi_i) + c_{i,0}(\kappa_i - 1)$$
$$- \sum_{n=1}^{\infty}\Big[n\big(a_{i,n}\cos(n\varphi_i) + b_{i,n}\sin(n\varphi_i)\big) + (n+1-\kappa_i)\big(c_{i,n}\cos(n\varphi_i) + d_{i,n}\sin(n\varphi_i)\big)\Big], \tag{2.35e}$$

$$\frac{2\mu_0}{R_i}u^{\text{tot}}_{\text{out},r}(r_i = R_i, \varphi_i|\mathbf{a}_{\text{out}}) = -\frac{1}{4}(\sigma^{\text{ext}}_{xx} + \sigma^{\text{ext}}_{yy})(1-\kappa_0) + \frac{1}{2}(\sigma^{\text{ext}}_{xx} - \sigma^{\text{ext}}_{yy})\cos(2\varphi_i) + \sigma^{\text{ext}}_{xy}\sin(2\varphi_i) - A_{i,0}$$
$$+ \sum_{n=1}^{\infty}\Big[n\big(A_{i,n}\cos(n\varphi_i) + B_{i,n}\sin(n\varphi_i)\big) + (n-1+\kappa_0)\big(C_{i,n}\cos(n\varphi_i) + D_{i,n}\sin(n\varphi_i)\big)\Big]$$
$$- \sum_{j\neq i}\sum_{n=2}^{\infty}\frac{R_j^2 R_i^{n-2}}{a_{ij}^n}n\Big[\cos(n\varphi_i)f_c^n\big(R_j/a_{ij}, \theta_{ij}|\mathbf{a}_{j,\text{out}}\big) + \sin(n\varphi_i)f_s^n\big(R_j/a_{ij}, \theta_{ij}|\mathbf{a}_{j,\text{out}}\big)\Big]$$
$$- \sum_{j\neq i}\sum_{n=0}^{\infty}\frac{R_j^2 R_i^{n}}{a_{ij}^{n+2}}(n+1-\kappa_0)\Big[\cos(n\varphi_i)g_c^n\big(R_j/a_{ij}, \theta_{ij}|\mathbf{a}_{j,\text{out}}\big) + \sin(n\varphi_i)g_s^n\big(R_j/a_{ij}, \theta_{ij}|\mathbf{a}_{j,\text{out}}\big)\Big], \tag{2.35f}$$

$$\frac{2\mu_i}{R_i}u^{\text{tot}}_{\text{in},\varphi}(r_i = R_i, \varphi_i|\mathbf{a}_{i,\text{in}}) = -\frac{1}{2}(\sigma^{\text{ext}}_{xx} - \sigma^{\text{ext}}_{yy})\sin(2\varphi_i) + \sigma^{\text{ext}}_{xy}\cos(2\varphi_i)$$
$$+ \sum_{n=1}^{\infty}\Big[n\big(a_{i,n}\sin(n\varphi_i) - b_{i,n}\cos(n\varphi_i)\big) + (n+1+\kappa_i)\big(c_{i,n}\sin(n\varphi_i) - d_{i,n}\cos(n\varphi_i)\big)\Big], \tag{2.35g}$$

$$\frac{2\mu_0}{R_i}u^{\text{tot}}_{\text{out},\varphi}(r_i = R_i, \varphi_i|\mathbf{a}_{\text{out}}) = -\frac{1}{2}(\sigma^{\text{ext}}_{xx} - \sigma^{\text{ext}}_{yy})\sin(2\varphi_i) + \sigma^{\text{ext}}_{xy}\cos(2\varphi_i)$$
$$+ \sum_{n=1}^{\infty}\Big[n\big(A_{i,n}\sin(n\varphi_i) - B_{i,n}\cos(n\varphi_i)\big) + (n-1-\kappa_0)\big(C_{i,n}\sin(n\varphi_i) - D_{i,n}\cos(n\varphi_i)\big)\Big]$$
$$+ \sum_{j\neq i}\sum_{n=2}^{\infty}\frac{R_j^2 R_i^{n-2}}{a_{ij}^n}n\Big[\sin(n\varphi_i)f_c^n\big(R_j/a_{ij}, \theta_{ij}|\mathbf{a}_{j,\text{out}}\big) - \cos(n\varphi_i)f_s^n\big(R_j/a_{ij}, \theta_{ij}|\mathbf{a}_{j,\text{out}}\big)\Big]$$
$$+ \sum_{j\neq i}\sum_{n=0}^{\infty}\frac{R_j^2 R_i^{n}}{a_{ij}^{n+2}}(n+1+\kappa_0)\Big[\sin(n\varphi_i)g_c^n\big(R_j/a_{ij}, \theta_{ij}|\mathbf{a}_{j,\text{out}}\big) - \cos(n\varphi_i)g_s^n\big(R_j/a_{ij}, \theta_{ij}|\mathbf{a}_{j,\text{out}}\big)\Big]. \tag{2.35h}$$

In the above equations, terms with coefficients $\sigma_{xx}^{\text{ext}}, \sigma_{yy}^{\text{ext}}$ and σ_{xy}^{ext} correspond to $\chi_{\text{ext}}(r_i, \varphi_i)$, terms with coefficients $a_{i,n}, b_{i,n}, c_{i,n}, d_{i,n}$ correspond to $\chi_{\text{in}}(r_i, \varphi_i|\mathbf{a}_{i,\text{in}})$, terms with coefficients $A_{i,n}, B_{i,n}, C_{i,n}, D_{i,n}$ correspond to $\chi_{\text{out}}(r_i, \varphi_i|\mathbf{a}_{i,\text{in}})$, and terms with coefficients $A_{j,n}, B_{j,n}, C_{j,n}, D_{j,n}$ correspond to $\chi_{\text{out}}(r_j, \varphi_j|\mathbf{a}_{j,\text{out}})$. We introduced the shear modulus $\mu_i = E_i/[2(1+\nu_i)]$ and the Kolosov's constant κ_i for the i^{th} inclusion, where the value of Kolosov's constant is $\kappa_i = (3-\nu_i)/(1+\nu_i)$ for plane stress and $\kappa_i = 3-4\nu_i$ for plane strain conditions [1]. Similarly, we define the shear modulus $\mu_0 = E_0/[2(1+\nu_0)]$ and the Kolosov's constant κ_0 for the elastic matrix. The boundary conditions in Eq. (2.30) have to be satisfied at every point (φ_i) on the circumference of the i^{th} inclusion. Thus the coefficients of the Fourier modes $\{1, \cos(n\varphi_i), \sin(n\varphi_i)\}$ have to match in the expansions of tractions and displacements in Eq. (2.35), similar to what was done for the case with the single inclusion in Section 2.1.6. This enables us to construct a matrix equation for the set of amplitudes $\{\mathbf{a}_{i,\text{out}}, \mathbf{a}_{i,\text{in}}\}$ of induced multipoles in the form (see also Fig. 2.5)

$$\begin{pmatrix} \mathbf{M}_{\text{out},ij}^{\text{trac}}, & \mathbf{M}_{\text{in},ij}^{\text{trac}} \\ \mathbf{M}_{\text{out},ij}^{\text{disp}}, & \mathbf{M}_{\text{in},ij}^{\text{disp}} \end{pmatrix} \begin{pmatrix} \mathbf{a}_{j,\text{out}} \\ \mathbf{a}_{j,\text{in}} \end{pmatrix} = \begin{pmatrix} \mathbf{0} \\ \mathbf{b}_i^{\text{disp}} \end{pmatrix}, \tag{2.36}$$

where the summation over inclusions j is implied.

The top and bottom rows of the matrix $\mathbf{M}$ in the above equation are obtained from the boundary conditions in Eq. (2.30) for tractions (superscript 'trac') and displacements (superscript 'disp'), respectively. The left and right columns of the matrix $\mathbf{M}$ describe the effect of the induced multipoles $\mathbf{a}_{j,\text{out}}$ and $\mathbf{a}_{j,\text{in}}$, respectively. The entries in matrices $\mathbf{M}_{\text{out},ii}^{\text{trac}}$ and $\mathbf{M}_{\text{in},ii}^{\text{trac}}$ for the i^{th} inclusion are numbers that depend on the degrees of induced multipoles. The entries in matrices $\mathbf{M}_{\text{out},ii}^{\text{disp}}$ and $\mathbf{M}_{\text{in},ii}^{\text{disp}}$ for the i^{th} inclusion depend on the degrees of induced multipoles, the radius of inclusion R_i and the material properties of the inclusion (μ_i, κ_i) and elastic matrix (μ_0, κ_0). Matrices $\mathbf{M}_{\text{out},ij}^{\text{trac}}$ and $\mathbf{M}_{\text{out},ij}^{\text{disp}}$ encode interactions between the inclusions i and j. The

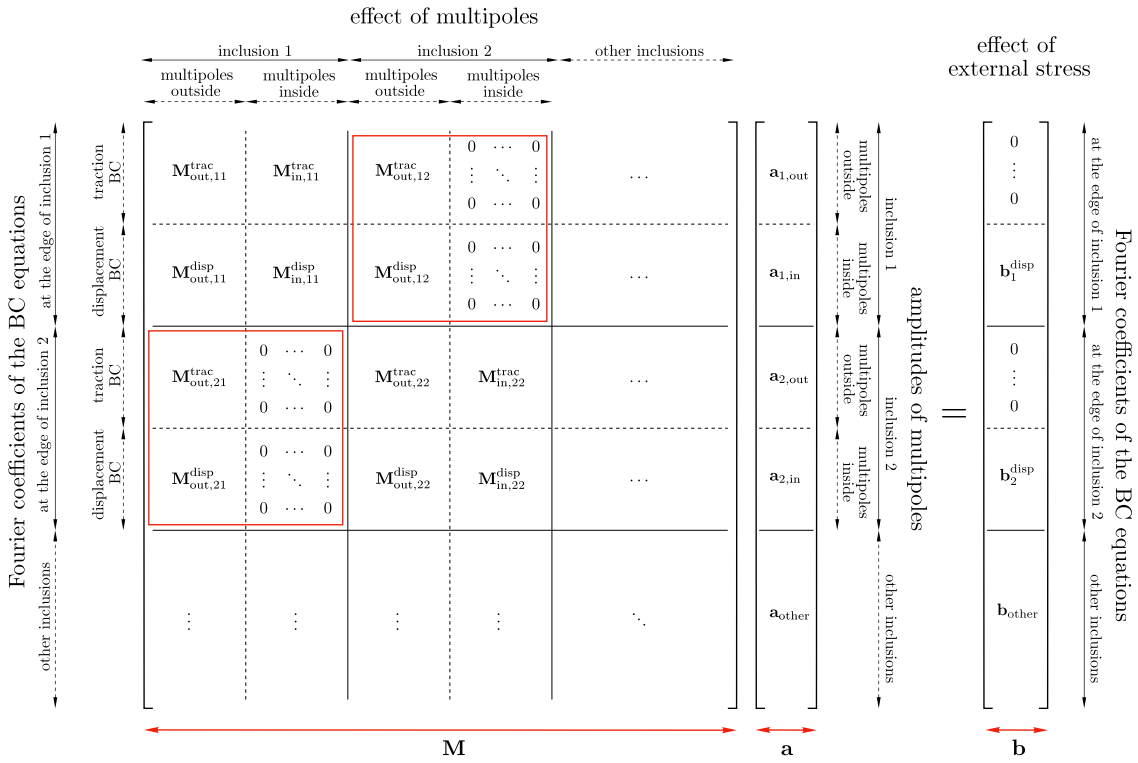

Figure 2.5: Structure of the system of Equations (2.36) for the amplitudes $\mathbf{a}_{i,\text{out}}$ and $\mathbf{a}_{i,\text{in}}$ of the induced multipoles for inclusions $i \in \{1, \ldots, N\}$. The matrix $\mathbf{M}$ is divided into $4N^2$ blocks, where the blocks $\mathbf{M}^{\text{trac}}_{\text{out},ij}$ and $\mathbf{M}^{\text{trac}}_{\text{in},ij}$ correspond to the boundary conditions for tractions around the circumference of the i^{th} inclusion in Eq. (2.30a, 2.30b), and the blocks $\mathbf{M}^{\text{disp}}_{\text{out},ij}$ and $\mathbf{M}^{\text{disp}}_{\text{in},ij}$ correspond to the boundary conditions for displacements around the circumference of the i^{th} inclusion in Eq. (2.30c, 2.30d). The red boxes mark the blocks with $i \neq j$ that account for the interactions between different inclusions. The effect of external stresses is contained in vectors $\mathbf{b}^{\text{disp}}_i$. See text for detailed description of elements represented in this system of equations.

entries in these matrices depend on the degrees of induced multipoles, the radii R_i and R_j of inclusions, the angle θ_{ij}, and the separation distance a_{ij} between the inclusions (see Fig. 2.4). In addition to that, the entries in matrix $\mathbf{M}^{\text{disp}}_{\text{out},ij}$ also depend on the material properties of the elastic matrix (μ_0, κ_0). Note that the other matrices are zero, i.e. $\mathbf{M}^{\text{trac}}_{\text{in},ij} = \mathbf{M}^{\text{disp}}_{\text{in},ij} = 0$. The entries in vector $\mathbf{b}^{\text{disp}}_i$ depend on the magnitude of external stresses $(\sigma^{\text{ext}}_{xx}, \sigma^{\text{ext}}_{yy}, \sigma^{\text{ext}}_{xy})$, the degrees of induced multipoles, the radius of inclusion R_i, and the material properties of the inclusion (μ_i, κ_i) and elastic matrix

(μ_0, κ_0). Note that in $\mathbf{b}_i^{\text{disp}}$ the only nonzero entries are the ones that correspond to Fourier modes 1, $\cos(2\varphi_i)$, and $\sin(2\varphi_i)$.

To numerically solve the system of equations for induced multipoles in Eq. (2.36) we truncate the multipole expansion at degree $n_{\max}$. For each inclusion i, there are $4n_{\max} - 1$ unknown amplitudes of multipoles $\mathbf{a}_{i,\text{out}} = \{A_{i,0}, A_{i,1}, \ldots, A_{i,n_{\max}}, B_{i,1}, B_{i,2}, \ldots, B_{i,n_{\max}}, C_{i,2}, C_{i,3}, \ldots, C_{i,n_{\max}}, D_{i,2}, D_{i,3}, \ldots, D_{i,n_{\max}}\}$ and $4n_{\max} - 1$ unknown amplitudes of multipoles $\mathbf{a}_{i,\text{in}} = \{a_{i,2}, a_{i,3}, \ldots, a_{i,n_{\max}}, b_{i,2}, b_{i,3}, \ldots, b_{i,n_{\max}}, c_{i,0}, c_{i,1}, \ldots, c_{i,n_{\max}}, d_{i,1}, d_{i,2}, \ldots, d_{i,n_{\max}}\}$. Furthermore, we truncate the Taylor expansion for the Airy stress function $\chi_{\text{out}}\big(r_j(r_i, \varphi_i), \varphi_j(r_i, \varphi_i) | \mathbf{a}_{j,\text{out}}\big)$ in Eq. (2.33) at the same order $n_{\max}$. By matching the coefficients of the Fourier modes $\{1, \cos\varphi_i, \sin\varphi_i, \ldots, \cos(n_{\max}\varphi_i), \sin(n_{\max}\varphi_i)\}$ in the expansions for tractions and displacements in Eq. (2.35) around the circumference of the i^{th} inclusion, we in principle get $2(2n_{\max} + 1)$ equations from tractions and $2(2n_{\max} + 1)$ equations from displacements. However, the zero Fourier modes for $\sigma_{r\varphi}$ and u_φ are equal to zero. Furthermore, the coefficients of Fourier modes $\cos\varphi_i$ and $\sin\varphi_i$ are identical for each of the σ_{rr}, $\sigma_{r\varphi}$, u_r, and u_φ in Eq. (2.35). By removing the equations that do not provide new information, the dimensions of matrices $\mathbf{M}^{\text{trac}}_{\text{out},ij}$, $\mathbf{M}^{\text{trac}}_{\text{in},ij}$, $\mathbf{M}^{\text{disp}}_{\text{out},ij}$, and $\mathbf{M}^{\text{disp}}_{\text{in},ij}$, become $(4n_{\max} - 1) \times (4n_{\max} - 1)$. Thus Eq. (2.36) describes the system of $N(8n_{\max} - 2)$ equations for the amplitudes of the induced multipoles $\{\mathbf{a}_{1,\text{out}}, \mathbf{a}_{1,\text{in}}, \ldots, \mathbf{a}_{N,\text{out}}, \mathbf{a}_{N,\text{in}}\}$. The solution of this system of equations gives amplitudes of induced multipoles, which are linear functions of applied loads σ^{ext}_{xx}, σ^{ext}_{yy}, and σ^{ext}_{xy}. These amplitudes are then used to obtain the Airy stress functions $\chi^{\text{tot}}_{\text{in}}\big(x, y | \mathbf{a}_{i,\text{in}}\big)$ in Eq. (2.29) inside inclusions and $\chi^{\text{tot}}_{\text{out}}\big(x, y | \mathbf{a}_{\text{out}}\big)$ in Eq. (2.27) outside inclusions, which enables us to calculate stresses and displacements everywhere in the structure. The accuracy of the obtained results depends on the number $n_{\max}$ for the maximum degree of induced multipoles, where larger $n_{\max}$ yields more accurate

results. In the next two Sections, we compare the results of the elastic multipole method described above with linear finite element simulations and experiments.

2.2.2 Comparison with linear finite element simulations

First, we tested the elastic multipole method for two circular inclusions embedded in an infinite plate subjected to uniaxial stress (Fig. 2.6) and shear stress (Fig. 2.7). The two inclusions had identical diameters d and they were centered at $(\pm a/2, 0)$. Three different values of the separation distance a between the inclusions were considered: $a = 2d$, $a = 1.4d$, and $a = 1.1d$. The left and right inclusions were chosen to be more flexible ($E_1/E_0 = 0.25$) and stiffer ($E_2/E_0 = 4$) than the outer elastic matrix with the Young's modulus E_0, respectively. We used plane stress condition with Kolosov's constants $\kappa_i = (3-\nu_i)/(1+\nu_i)$, where Poisson's ratios of the left and right inclusions, and the outer material were $\nu_1 = 0.45$, $\nu_2 = 0.15$, and $\nu_0 = 0.3$, respectively. The values of the applied uniaxial stress and shear stress were $\sigma_{xx}^{\text{ext}}/E_0 = -0.25$ (Fig. 2.6) and $\sigma_{xy}^{\text{ext}}/E_0 = 0.1$ (Fig. 2.7), respectively. Such large values of external loads were used only to exaggerate deformations. Note that in practical experiments these loads would cause nonlinear deformation.

In Figs. 2.6 and 2.7 we show contours of deformed inclusions and spatial distributions of stresses for different values of the separation distance a between the inclusions, where the results from elastic multipole method were compared with linear finite element simulations on a square domain of size $400d \times 400d$ (see Appendix A for details). When the inclusions are far apart, they interact weakly, as can be seen from the expansion of stresses and displacements in Eq. (2.35), where the terms describing interactions between the inclusions i and j contain powers of $R_i/a_{ij} \ll 1$ and $R_j/a_{ij} \ll 1$. This is the case for the separation distance $a = 2d$, where we find that the contours of deformed inclusions have elliptical shapes (see Figs. 2.6b and 2.7b) and stresses inside the inclusions are uniform (see Figs. 2.6e,h and 2.7e,h), which is

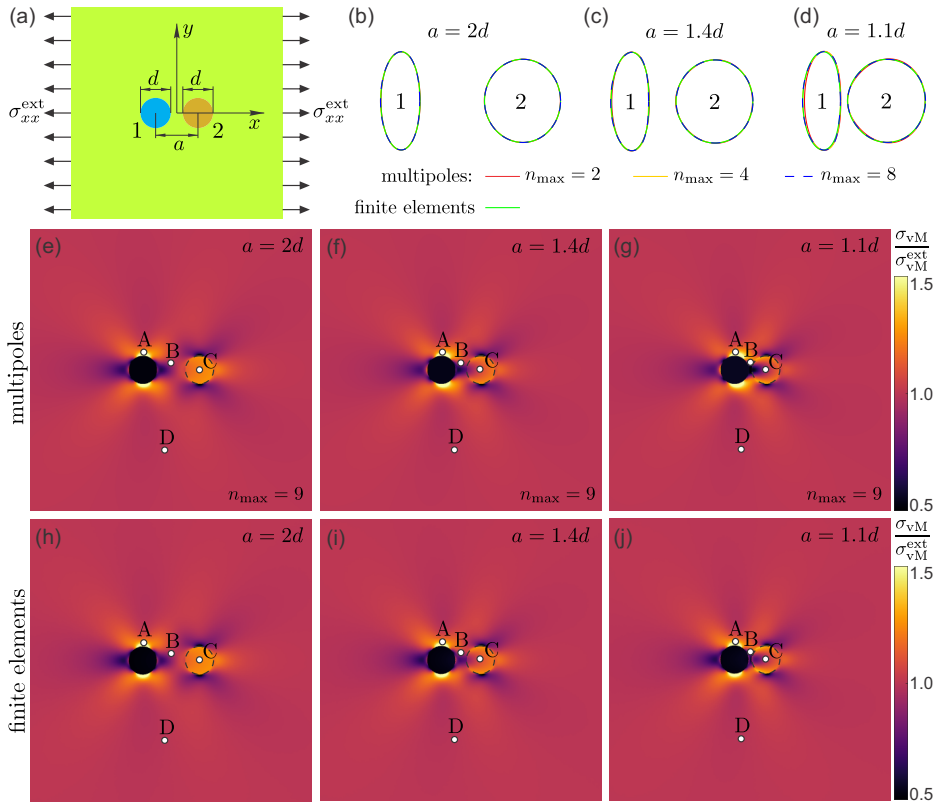

Figure 2.6: Deformation of an infinite elastic plate with two circular inclusions under uniaxial stress $\sigma_{xx}^{\mathrm{ext}}$ and plane stress condition. (a) Schematic image describing the initial undeformed shape of the structure and applied load $\sigma_{xx}^{\mathrm{ext}} = -0.25E_0$. The diameters of both inclusions (blue and orange disks) are d and the separation distance between their centers is a. The Young's moduli of the left and right inclusions are $E_1/E_0 = 0.25$ and $E_2/E_0 = 4$, respectively, where E_0 is the Young's modulus of the outer material. Poisson's ratios of the left and right inclusions and the outer material are $\nu_1 = 0.45$, $\nu_2 = 0.15$, and $\nu_0 = 0.3$, respectively. (b-d) Contours of the deformed inclusions for different values of the separation distance $a/d = 2$, 1.4, and 1.1. The solid red, yellow and dashed blue lines show the contours obtained with elastic multipole method for $n_{\max} = 2$, 4, and 8, respectively. Green solid lines show the contours obtained with linear finite element simulations. (e-j) von Mises stress (σ_{vM}) distributions obtained with (e-g) elastic multipole method ($n_{\max} = 9$) and (h-j) linear finite element simulations for different separation distances of inclusions a/d. von Mises stress distributions are normalized with the value of von Mises stress $\sigma_{\mathrm{vM}}^{\mathrm{ext}} = |\sigma_{xx}^{\mathrm{ext}}|$ due to the applied load. Four marked points A-D were chosen for the quantitative comparison of stresses and displacements between elastic multipole method and finite element simulations. See Table 2.4 for details.

characteristic for isolated inclusions (see Eq. (2.24) and [16]). Furthermore, the von Mises stress distribution ($\sigma_{\mathrm{vM}} = \sqrt{\sigma_{xx}^2 - \sigma_{xx}\sigma_{yy} + \sigma_{yy}^2 + 3\sigma_{xy}^2}$) around the more flex-

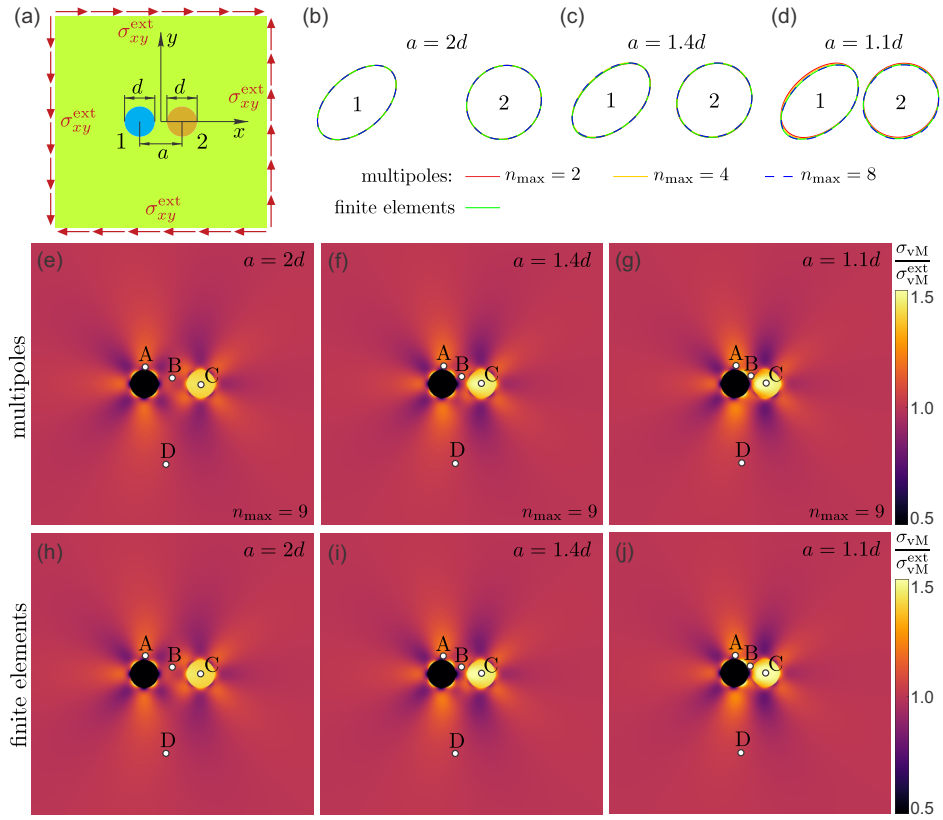

Figure 2.7: Deformation of an infinite elastic plate with two circular inclusions under shear stress $\sigma_{xy}^{\mathrm{ext}}$ and plane stress condition. (a) Schematic image describing the initial undeformed shape of the structure and applied load $\sigma_{xy}^{\mathrm{ext}} = 0.1E_0$, where E_0 is the Young's modulus of the outer material. The diameter of both inclusions (blue and orange disks) is d and the separation distance between their centers is a. Material properties are the same as in Fig. 2.6. (b-d) Contours of the deformed inclusions for different values of the separation distance $a/d = 2$, 1.4, and 1.1. The solid red, yellow and dashed blue lines show the contours obtained with elastic multipole method for $n_{\max} = 2$, 4, and 8, respectively. Green solid lines show the contours obtained with finite element simulations. (e-j) von Mises stress (σ_{vM}) distributions obtained with (e-g) elastic multipole method ($n_{\max} = 9$) and (h-j) linear finite element simulations for different separation distances of inclusions a/d. von Mises stress distributions are normalized with the value of von Mises stress $\sigma_{\mathrm{vM}}^{\mathrm{ext}} = \sqrt{3}|\sigma_{xy}^{\mathrm{ext}}|$ due to the applied load. Four marked points A-D were chosen for the quantitative comparison of stresses and displacements between elastic multipole method and finite element simulation. See Table 2.5 for details.

ible left inclusion (see Fig. 2.6e,h) is similar to that of an isolated hole under uniaxial stress (see Fig. 1.1c). For the stiffer right inclusion, the locations of the maxima and

minima in the von Mises stress distribution are reversed (see Fig. 2.6e,h) because the amplitudes of induced multipoles have the opposite sign (see Eq. (2.23)).

Similar patterns in the von Mises stress distribution are observed when the structure is under external shear, but they are rotated by 45° (see Fig. 2.7e,h). When inclusions are far apart ($a = 2d$), the contours of deformed inclusions can be accurately

Table 2.4: Quantitative comparison for the values of von Mises stresses σ_{vM} and displacements $\mathbf{u}$ at points A-D (defined in Fig. 2.6) obtained with the elastic multipole method (EMP) and finite element method simulations (FEM) for uniaxially compressed samples with two inclusions of diameter d for different values of their separation distance a. von Mises stresses σ_{vM} are normalized with the value of von Mises stress $\sigma_{\text{vM}}^{\text{ext}} = |\sigma_{xx}^{\text{ext}}|$ due to the applied uniaxial compression. Displacements $\mathbf{u}$ are normalized with the characteristic scale of deformation $d\sigma_{\text{vM}}^{\text{ext}}/E_0$, where E_0 is the Young's modulus of the elastic matrix. The relative percent errors ϵ between the two methods are calculated as $100 \times (\sigma_{\text{vM}}^{\text{EMP}} - \sigma_{\text{vM}}^{\text{FEM}})/\sigma_{\text{vM}}^{\text{FEM}}$ and $100 \times (|\mathbf{u}|^{\text{EMP}} - |\mathbf{u}|^{\text{FEM}})/|\mathbf{u}|^{\text{FEM}}$.

	separation $a = 2d$					
	stress $\sigma_{\text{vM}}/\sigma_{\text{vM}}^{\text{ext}}$			disp. $\lvert\mathbf{u}\rvert/[d\sigma_{\text{vM}}^{\text{ext}}/E_0]$		
	EMP	FEM	ϵ (%)	EMP	FEM	ϵ(%)
A	1.419	1.416	0.2	1.442	1.442	0.0
B	0.940	0.947	0.7	0.082	0.081	0.5
C	1.213	1.216	0.3	0.654	0.653	0.1
D	0.997	0.997	0.0	1.144	1.144	0.0
	separation $a = 1.4d$					
	stress $\sigma_{\text{vM}}/\sigma_{\text{vM}}^{\text{ext}}$			disp. $\lvert\mathbf{u}\rvert/[d\sigma_{\text{vM}}^{\text{ext}}/E_0]$		
	EMP	FEM	ϵ (%)	EMP	FEM	ϵ(%)
A	1.424	1.419	0.5	1.265	1.264	0.1
B	0.940	0.959	1.9	0.116	0.116	0.7
C	1.083	1.092	0.8	0.275	0.274	0.3
D	0.994	0.994	0.0	1.250	1.250	0.0
	separation $a = 1.1d$					
	stress $\sigma_{\text{vM}}/\sigma_{\text{vM}}^{\text{ext}}$			disp. $\lvert\mathbf{u}\rvert/[d\sigma_{\text{vM}}^{\text{ext}}/E_0]$		
	EMP	FEM	ϵ (%)	EMP	FEM	ϵ(%)
A	1.439	1.426	0.9	1.223	1.220	0.3
B	0.887	0.91	2.7	0.127	0.126	1.0
C	0.933	0.948	1.5	0.122	0.122	0.3
D	0.992	0.992	0.0	1.363	1.363	0.0

Table 2.5: Quantitative comparison for the values of von Mises stresses σ_{vM} and displacements $\mathbf{u}$ at points A-D (defined in Fig. 2.7) obtained with the elastic multipole method (EMP) and finite element method simulations (FEM) for sheared samples with two inclusions of diameter d for different values of their separation distance a. von Mises stresses σ_{vM} are normalized with the value of von Mises stress $\sigma_{\mathrm{vM}}^{\mathrm{ext}} = \sqrt{3}|\sigma_{xy}^{\mathrm{ext}}|$ due to the applied shear. Displacements $\mathbf{u}$ are normalized with the characteristic scale of deformation $d\sigma_{\mathrm{vM}}^{\mathrm{ext}}/E_0$, where E_0 is the Young's modulus of the elastic matrix. The relative percent errors ϵ between the two methods are calculated as $100 \times (\sigma_{\mathrm{vM}}^{\mathrm{EMP}} - \sigma_{\mathrm{vM}}^{\mathrm{FEM}})/\sigma_{\mathrm{vM}}^{\mathrm{FEM}}$ and $100 \times (|\mathbf{u}|^{\mathrm{EMP}} - |\mathbf{u}|^{\mathrm{FEM}})/|\mathbf{u}|^{\mathrm{FEM}}$.

	separation $a = 2d$					
	stress $\sigma_{\mathrm{vM}}/\sigma_{\mathrm{vM}}^{\mathrm{ext}}$			disp. $\lvert\mathbf{u}\rvert/[d\sigma_{\mathrm{vM}}^{\mathrm{ext}}/E_0]$		
	EMP	FEM	ϵ (%)	EMP	FEM	ϵ (%)
A	1.027	1.026	0.1	1.167	1.166	0.1
B	1.045	1.050	0.5	0.387	0.387	0.2
C	1.415	1.419	0.2	0.159	0.159	0.0
D	1.016	1.016	0.0	4.235	4.235	0.0
	separation $a = 1.4d$					
	stress $\sigma_{\mathrm{vM}}/\sigma_{\mathrm{vM}}^{\mathrm{ext}}$			disp. $\lvert\mathbf{u}\rvert/[d\sigma_{\mathrm{vM}}^{\mathrm{ext}}/E_0]$		
	EMP	FEM	ϵ (%)	EMP	FEM	ϵ (%)
A	1.051	1.047	0.4	1.132	1.131	0.1
B	1.065	1.081	1.5	0.379	0.377	0.5
C	1.469	1.481	0.8	0.280	0.279	0.2
D	1.016	1.016	0.0	4.265	4.265	0.0
	separation $a = 1.1d$					
	stress $\sigma_{\mathrm{vM}}/\sigma_{\mathrm{vM}}^{\mathrm{ext}}$			disp. $\lvert\mathbf{u}\rvert/[d\sigma_{\mathrm{vM}}^{\mathrm{ext}}/E_0]$		
	EMP	FEM	ϵ (%)	EMP	FEM	ϵ (%)
A	1.085	1.076	0.9	1.159	1.156	0.2
B	1.106	1.134	2.5	0.371	0.368	0.8
C	1.512	1.533	1.4	0.407	0.405	0.4
D	1.020	1.020	0.0	4.275	4.275	0.0

described already with multipoles up to degree $n_{\max} = 2$ (see Figs. 2.6b and 2.7b). This degree of multipoles is sufficient because external stresses $\sigma_{xx}^{\mathrm{ext}}$ and $\sigma_{xy}^{\mathrm{ext}}$ couple only to the Fourier modes 1, $\cos 2\varphi_i$, and $\sin 2\varphi_i$ in the expansion for stresses and displacements in Eq. (2.35). As the inclusions are moved closer together ($a = 1.4d$ and $a = 1.1d$), they interact more strongly. As a consequence, the contours of deformed inclusions become progressively more non-elliptical and higher order of multipoles

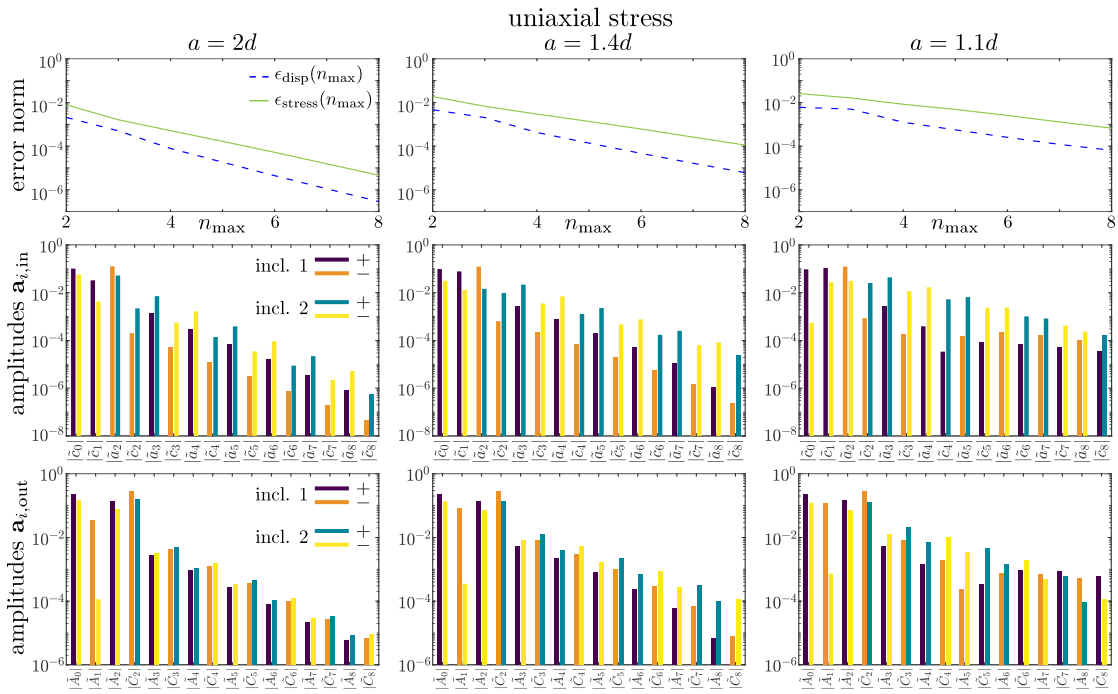

Figure 2.8: Normalized errors and amplitudes of induced multipoles for the structures with two inclusions with diameters d and the separation distance a under uniaxial stress σ_{xx}^{ext} (see Fig. 2.6). The normalized errors for displacements $\epsilon_{\text{disp}}(n_{\max})$ (blue lines) and stresses $\epsilon_{\text{stress}}(n_{\max})$ (red lines) are defined in Eq. (2.37). Absolute values of the amplitudes of induced multipoles $\{\mathbf{a}_{1,\text{out}}, \mathbf{a}_{2,\text{out}}\}$ for $n_{\max} = 9$. The amplitudes are normalized as $\tilde{a}_n = a_n/\sigma_{xx}^{\text{ext}}$, $\tilde{c}_n = c_n/\sigma_{xx}^{\text{ext}}$, $\tilde{A}_n = A_n/\sigma_{xx}^{\text{ext}}$, and $\tilde{C}_n = C_n/\sigma_{xx}^{\text{ext}}$. The dark and light blue colored bars correspond to the positive $(a_n, c_n, A_n, C_n > 0)$ and negative $(a_n, c_n, A_n, C_n < 0)$ amplitudes for inclusion 1, respectively. Similarly, the red and orange colored bars correspond to the positive and negative amplitudes for inclusion 2, respectively. Note that the amplitudes of multipoles b_i, d_i, B_i, and D_i are zero due to the symmetry of the problem.

are needed to accurately describe their shapes (see Figs. 2.6c,d and 2.7c,d). Furthermore, the stress distribution inside the right inclusion becomes nonuniform (see Figs. 2.6f,g,i,j and 2.7f,g,i,j). Note that von Mises stress distributions look similar far from inclusions regardless of the separation distance a (see Figs. 2.6 and 2.7), because they are dictated by the lowest order induced multipoles, i.e. by non-topological monopoles (p), non-topological dipoles ($\mathbf{d}^p$) and quadrupoles ($\mathbf{Q}^s$, $\mathbf{Q}^p$).

To determine the proper number for the maximum degree $n_{\max}$ of induced multipoles we performed a convergence analysis for the spatial distributions of displacements $\mathbf{u}^{(n_{\max})}(x, y)$ and von Mises stresses $\sigma_{\text{vM}}^{(n_{\max})}(x, y)$. Displacements and von Mises

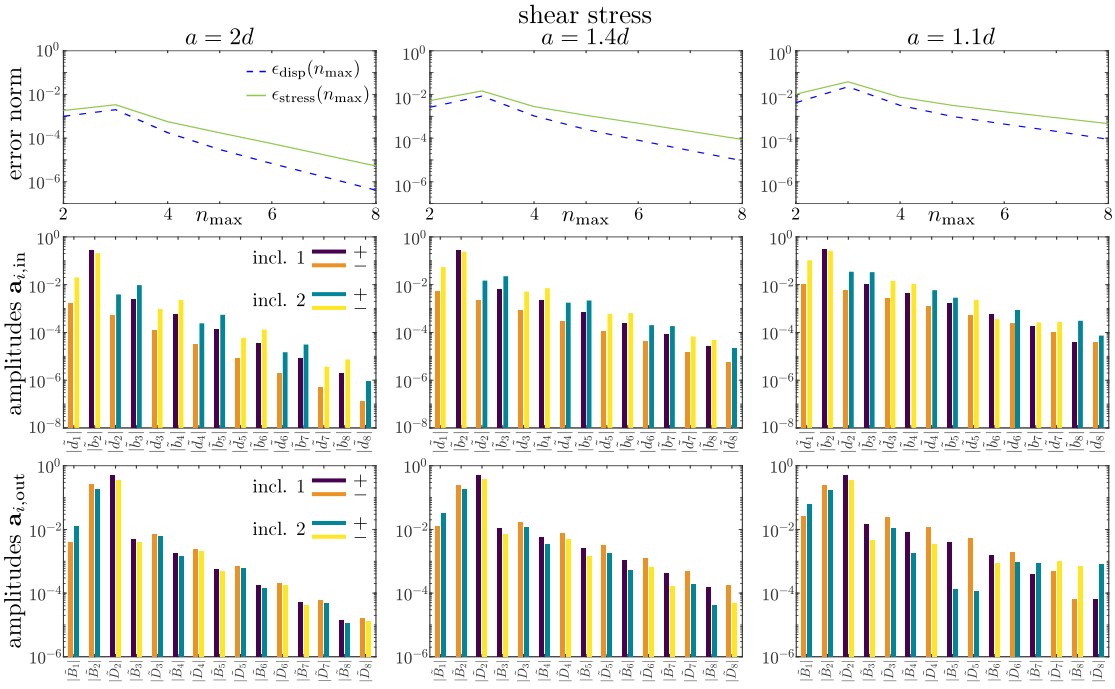

Figure 2.9: Normalized errors and amplitudes of induced multipoles for the structures with two inclusions with diameters d and the separation distance a under shear stress $\sigma_{xy}^{\rm ext}$ (see Fig. 2.7). The normalized errors for displacements $\epsilon_{\rm disp}(n_{\rm max})$ (blue lines) and stresses $\epsilon_{\rm stress}(n_{\rm max})$ (red lines) are defined in Eq. (2.37). Absolute values of the amplitudes of induced multipoles $\{\mathbf{a}_{1,\rm out}, \mathbf{a}_{2,\rm out}\}$ for $n_{\rm max} = 9$. The amplitudes are normalized as $\tilde{b}_n = b_n/\sigma_{xy}^{\rm ext}$, $\tilde{d}_n = d_n/\sigma_{xy}^{\rm ext}$, $\tilde{B}_n = B_n/\sigma_{xy}^{\rm ext}$, and $\tilde{D}_n = D_n/\sigma_{xy}^{\rm ext}$. The dark purple and orange blue colored bars correspond to the positive $(b_n, d_n, B_n, D_n > 0)$ and negative $(b_n, d_n, B_n, D_n < 0)$ amplitudes for inclusion 1, respectively. Similarly, the green and yellow colored bars correspond to the positive and negative amplitudes for inclusion 2, respectively. Note that the amplitudes of multipoles a_i, c_i, A_i, and C_i are zero due to the symmetry of the problem.

stresses were evaluated at $N_p = 1001 \times 1001$ points on a square grid of size $10d \times 10d$ surrounding the inclusions, i.e. at the points $(x_i, y_j) = (id/100, jd/100)$, where $i, j \in \{-500, -499, \ldots, 500\}$. The normalized errors for displacements $\epsilon_{\rm disp}(n_{\rm max})$ and stresses $\epsilon_{\rm stress}(n_{\rm max})$ were obtained by calculating the relative changes of the spatial distributions of displacements and von Mises stresses when the maximum degree $n_{\rm max}$ of induced multipoles is increased by one. The normalized errors are given by [129]

$$\epsilon_{\rm disp}(n_{\rm max}) = \sqrt{\sum_{i,j} \frac{\left(\mathbf{u}^{(n_{\rm max}+1)}(x_i, y_j) - \mathbf{u}^{(n_{\rm max})}(x_i, y_j)\right)^2}{N_p (d\, \sigma_{\rm vM}^{\rm ext}/E_0)^2}}, \tag{2.37a}$$

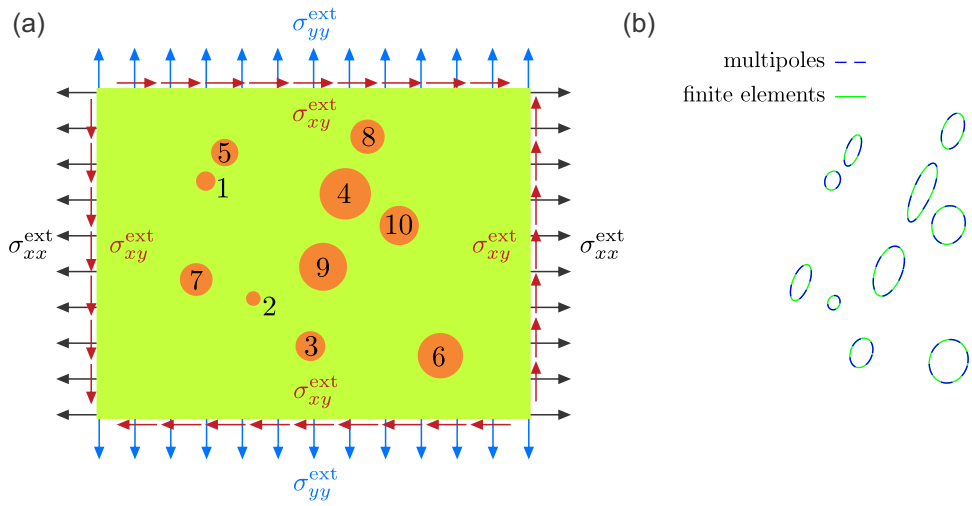

inclusion	1	2	3	4	5	6	7	8	9	10
radius	0.38	0.28	0.58	1.00	0.53	0.88	0.64	0.38	0.67	0.77
E_i/E_0	2.10	3.00	1.50	0.25	0.40	3.75	0.50	2.10	0.60	3.20
ν_i	0.22	0.28	0.16	0.24	0.44	0.10	0.30	0.22	0.24	0.32

Figure 2.10: Deformation of an infinite elastic plate with ten circular inclusions (orange disks) under general external stress. (a) Schematic image describing the initial undeformed shape of the structure and applied external loads: $\sigma_{xx}^{\text{ext}}/E_0 = -0.25$, $\sigma_{yy}^{\text{ext}}/E_0 = 0.05$, and $\sigma_{xy}^{\text{ext}}/E_0 = 0.10$, where E_0 is the Young's modulus of the outer material. The plane stress condition was used. The radii and material properties (Young's moduli E_i and Poisson's ratios ν_i) of inclusions are provided in the table below the schematic image. The radii of inclusions are normalized by the radius of the largest inclusion. The Young's moduli are normalized by the Young's modulus of the outer material E_0. The value of Poisson's ratio for the outer material was $\nu_0 = 0.3$. (b) Contours of deformed inclusions. The blue dashed lines show the results obtained with the elastic multipole method ($n_{\max} = 6$). The green solid lines correspond to the deformed contours obtained with linear finite element simulations.

$$\epsilon_{\text{stress}}(n_{\max}) = \sqrt{\sum_{i,j} \frac{\left(\sigma_{\text{vM}}^{(n_{\max}+1)}(x_i, y_j) - \sigma_{\text{vM}}^{(n_{\max})}(x_i, y_j)\right)^2}{N_p(\sigma_{\text{vM}}^{\text{ext}})^2}}. \tag{2.37b}$$

Here, displacements and von Mises stresses are normalized by the characteristic scales $d\sigma_{\text{vM}}^{\text{ext}}/E_0$ and $\sigma_{\text{vM}}^{\text{ext}}$, respectively, where d is the diameter of inclusions, $\sigma_{\text{vM}}^{\text{ext}}$ is the value of the von Mises stress due to external load, and E_0 is the Young's modulus of the surrounding elastic matrix. The normalized errors are plotted in Figs. 2.8 and 2.9. As the maximum degree $n_{\max}$ of induced multipoles is increased, the normalized errors for displacements $\epsilon_{\text{disp}}(n_{\max})$ and stresses $\epsilon_{\text{stress}}(n_{\max})$ decrease exponentially. Since

the induced elastic multipoles form the basis for the biharmonic equation, this is akin to the spectral method, which is exponentially convergent when the functions and the boundaries are smooth [129]. The normalized errors for displacements are lower than the errors for stresses (see Figs. 2.8 and 2.9) because stresses are related to spatial derivatives of displacements. Note that the normalized errors decrease more slowly when inclusions are brought close together and their interactions become important (see Figs. 2.8 and 2.9). This is also reflected in the amplitudes $\mathbf{a}_{1,\mathrm{in}}$, $\mathbf{a}_{2,\mathrm{in}}$, $\mathbf{a}_{1,\mathrm{out}}$, and $\mathbf{a}_{2,\mathrm{out}}$ of the induced multipoles, which decrease exponentially with the degree of multipoles and they decrease more slowly when inclusions are closer (see Figs. 2.8 and 2.9).

Results from the elastic multipole method were compared with linear finite element simulations, and very good agreement is achieved already for $n_{\max} = 9$ even when inclusions are very close together ($a = 1.1d$, see Figs. 2.6 and 2.7). To make the comparison with finite elements more quantitative, we compared the values of displacements and stresses at 4 different points: A – at the edge of the left inclusion, B – in between the inclusions, C – at the center of the right inclusion, and D – far away from both inclusions (see Figs. 2.6 and 2.7). For all 4 points, the error increases when inclusions are brought closer together (see Tables 2.4 and 2.5). Of the 4 different points, we find that the errors are the largest at point B, which is strongly influenced by induced multipoles from both inclusions. For the smallest separation distance $a = 1.1d$ between the inclusions, the errors for the von Mises stress at point B are 2.7% and 2.5% for the uniaxial and shear loads, respectively. These errors can be further reduced by increasing the number $n_{\max}$ for the maximum degree of multipoles, e.g. for $n_{\max} = 14$ the errors for von Mises stress at point B are reduced to 1.2% and 1.1% for the uniaxial and shear loads, respectively.

To demonstrate the full potential of the elastic multipole method, we also considered the deformation of an infinite plate with $N = 10$ inclusions of different sizes and

material properties subjected to general external stress load under plane stress condition (see Fig. 2.10). The contours of deformed inclusions obtained with finite element simulations (green solid lines) and elastic multipole method with $n_{\max} = 6$ (blue dashed lines) are in very good agreement. Note that the results for the elastic multipole method were obtained by solving the linear system of only $N(8n_{\max} - 2) = 460$ equations for the amplitudes of the induced multipoles described in Eq. (2.36), which is significantly smaller than the number of degrees of freedom required for finite element simulations.

2.2.3 Comparison with experiments

Finally, we also tested the elastic multipole method against experiments. Experimental samples were prepared by casting Elite Double 32 (Zhermack) elastomers with the measured Young's modulus $E_0 = 0.97$ MPa and assumed Poisson's ratio $\nu = 0.49$ [28]. Molds were fabricated from 5 mm thick acrylic plates with laser-cut circular holes, which were then filled with acrylic cylinders in the assembled molds to create cylindrical holes in the elastomer samples. Approximately 30 min after casting, the molds were disassembled and the solid samples were placed in a convection oven at 40 °C for 12 hours for further curing. The cylindrical inclusions made from acrylic (Young's modulus $E = 2.9$ GPa, Poisson's ratio $\nu = 0.37$ [130]) were inserted into the holes of the elastomer samples and they were glued by a cyanoacrylate adhesive.

We designed two compressive testing systems (see Fig. 2.11) to compare the contours of deformed holes and inclusions and strain fields with predictions made by the elastic multipole method. In Fig. 2.11a, we first present an experimental system for extracting the contours of deformed holes and inclusions in compressed experimental samples. The system comprises a custom-made loading mechanism and a flatbed photo scanner. Displacement loading is applied in 0.5 mm increments via 180° turns of the M10x1 screw (metric thread with 10 mm diameter and 1 mm pitch)

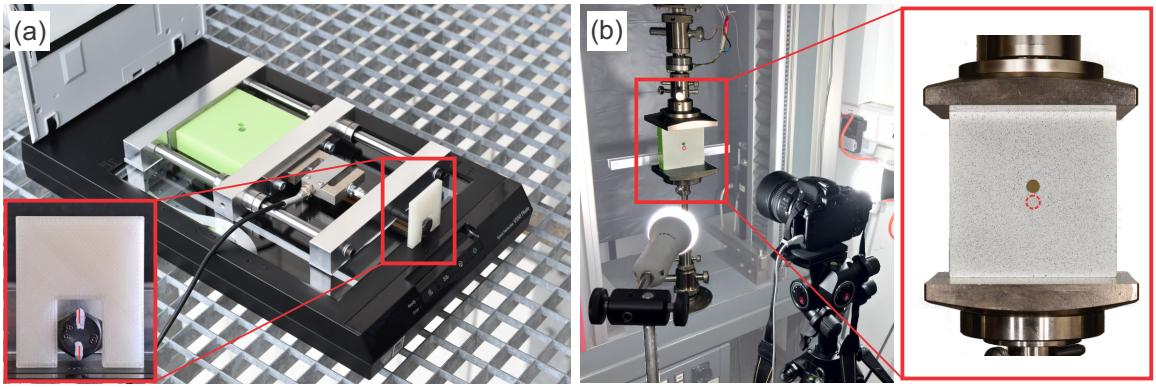

Figure 2.11: Experimental systems for displacement controlled compressive tests. (a) A mechanism for compression of rubber samples (green slab) sits on top of a flatbed photo scanner, which is used to extract the contours of deformed holes/inclusions. The zoomed-in photo on the left shows a 3D-printed plastic wrench that was used for the precise control of screw turns. (b) Setup for extracting strain fields via digital image correlation (DIC). The surface of the sample was painted with speckle patterns. The sample was then compressed with steel plates of the testing machine and photos of speckle patterns were used to extract the displacement field on the front surface of the slab. The zoomed-in photo on the right shows the rubber sample with one hole and one inclusion (indicated with a red dashed circle) mounted between two parallel plates of the testing machine.

in the mechanism, which is controlled by a 3D-printed plastic wrench (see the inset of Fig. 2.11a). The loading mechanism was placed on an Epson V550 photo scanner to scan the surface of deformed samples and silicone oil was applied between the sample and the glass surface of the scanner to reduce friction between them. Scanned images were post-processed with Corel PHOTO-PAINT X8 and the Image Processing Toolbox in MATLAB 2018b. First, the dust particles and air bubbles trapped in a thin film of silicone oil were digitally removed from the scanned images. Scanned grayscale images were then converted to black and white binary images from which the contours were obtained with MATLAB.

Second, we present a system for capturing the displacement and strain fields in compressed samples via digital image correlation (DIC) technique (see Fig. 2.11b). Black and white speckle patterns were spray-painted onto the surface of samples with slow-drying acrylic paint to prevent the speckle pattern from hardening too quickly,

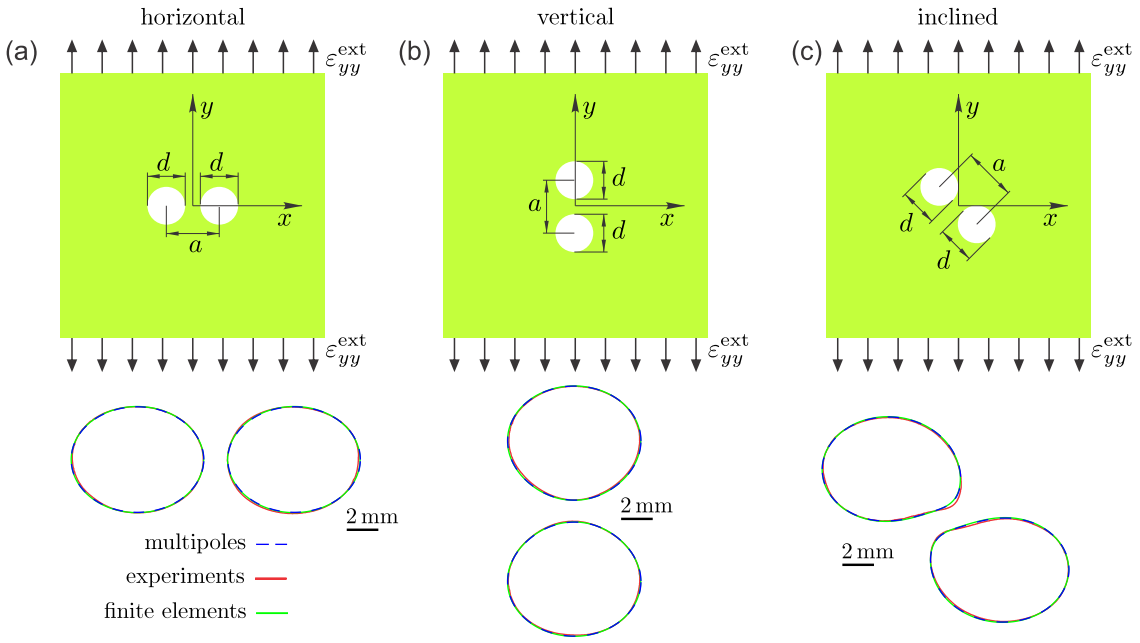

Figure 2.12: Uniaxial vertical compression of elastic structures with holes. (a-c) Schematic images describing the initial undeformed shapes of structures with two holes (white disks) in three different configurations (horizontal, vertical and inclined at 45°) and applied external strain $\varepsilon_{yy}^{\text{ext}} = -0.05$. Deformed contours of holes obtained with elastic multipole method ($n_{\max} = 10$, blue dashed lines), experiments (red solid lines), and finite element simulations (solid green lines). In all cases, the size of samples was 100 mm × 100 mm × 25 mm, the diameters of each hole/inclusion were $d = 8.11$ mm, and their separation distances were $a = 9.50$ mm.

which could lead to delamination under applied compressive loads. Using a Zwick Z050 universal material testing machine, we applied a compressive displacement in 0.2 mm increments, where again a silicone oil was applied between the steel plates and the elastomer samples to prevent sticking and to reduce friction. A Nikon D5600 photo camera was used at each step to take a snapshot of the compressed sample (see Fig. 2.11b). These photos were then used to calculate the displacements and strain fields with Ncorr, an open-source 2D DIC MATLAB based software. [131]

We analyzed uniaxially compressed 100 mm × 100 mm × 25 mm elastomer structures with three different configurations (horizontal, vertical and inclined at 45° angle) of two holes with identical diameters $d = 8.11$ mm and their separation distance $a = 9.50$ mm (see Fig. 2.12a-c). Holes were placed near the centers of elastomer

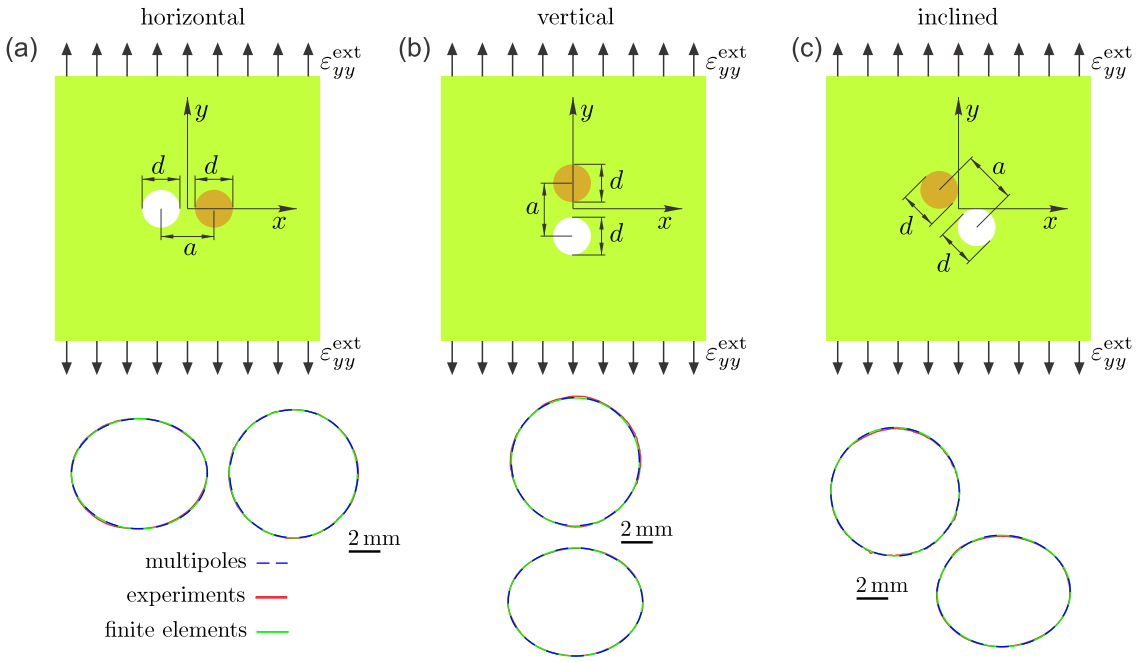

Figure 2.13: Uniaxial vertical compression of elastic structures with holes and inclusions. (a-c) Schematic images describing the initial undeformed shapes of structures with one hole (white disks) and one inclusion (orange disks) in three different configurations (horizontal, vertical and inclined at 45°), and applied external strain $\varepsilon_{yy}^{\text{ext}} = -0.05$. Deformed contours of holes and inclusions obtained with elastic multipole method ($n_{\max} = 10$, blue dashed lines), experiments (red solid lines), and finite element simulations (solid green lines). In all cases, the size of samples was 100 mm × 100 mm × 25 mm, the diameters of each hole/inclusion were $d = 8.11$ mm, and their separation distances were $a = 9.50$ mm.

structures to minimize the effects of boundaries. The structures were relatively thick (25 mm) to prevent the out-of-plane buckling. The contours of deformed holes in compressed experimental samples under external strain $\varepsilon_{yy}^{\text{ext}} = -0.05$ were compared with those obtained with elastic multipole method and finite element simulations (see Fig. 2.13a-c). For the elastic multipole method, we used external stress $\sigma_{yy}^{\text{ext}} = E_0 \varepsilon_{yy}^{\text{ext}}$ ($\sigma_{xx}^{\text{ext}} \approx \sigma_{xy}^{\text{ext}} \approx 0$ due to reduced friction) and plane stress condition was assumed since the experimental samples were free to expand in the out-of-plane direction. Linear finite element simulations were performed for finite-size (100 mm × 100 mm) 2D structures with circular holes under plane stress condition. In finite element simulations, samples were compressed by prescribing a uniform displacement in the y-direction on

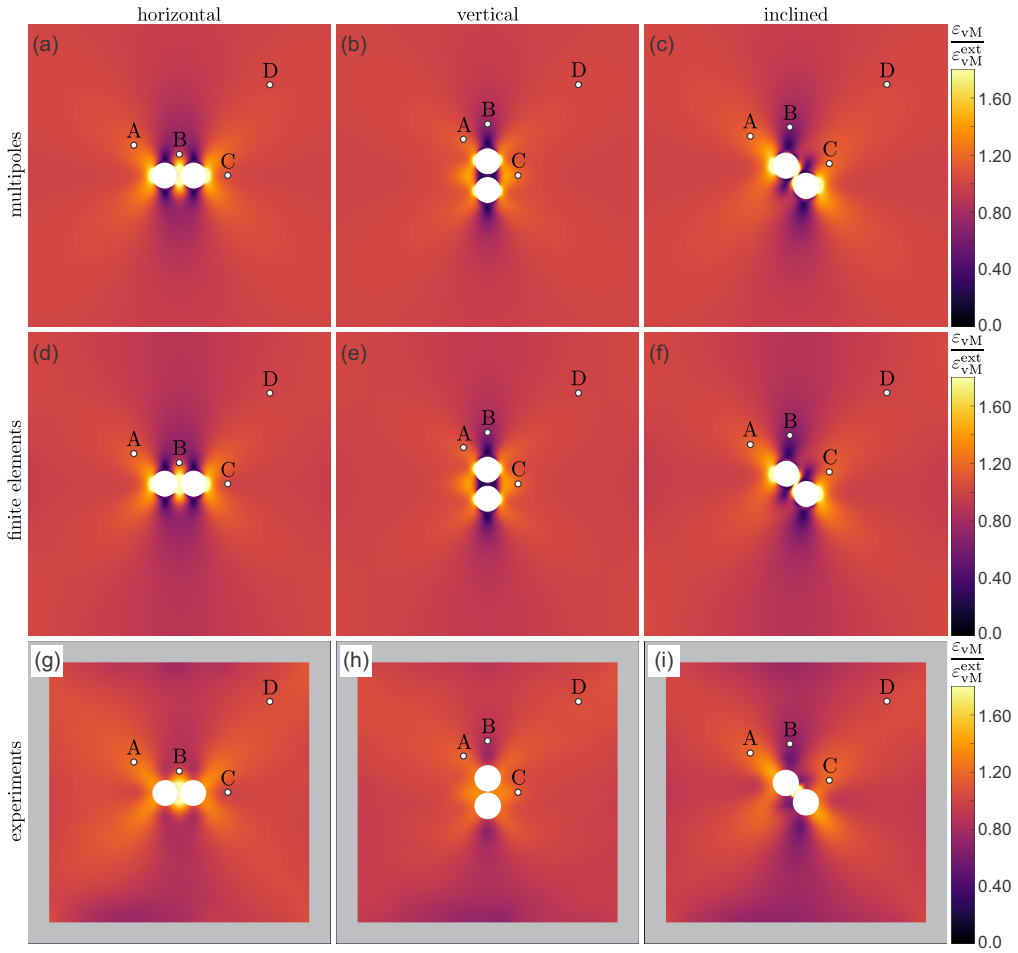

Figure 2.14: Equivalent von Mises strain fields $\varepsilon_{\mathrm{vM}}$ (see Eq. (2.38)) for uniaxially vertically compressed elastic structures with two holes (white disks) in three different configurations (horizontal, vertical, inclined at 45°) introduced in Fig. 2.12. Equivalent von Mises strain fields $\varepsilon_{\mathrm{vM}}$ were obtained with (a-c) elastic multipole method ($n_{\max} = 10$), (d-f) finite element simulations, and (g-i) DIC analysis of experiments. Note that the strain data was corrupted near the edges for some samples due to oil stains on the speckle patterns near the boundary. For this reason, we omitted the affected border regions (grey frames) in heat maps (g-i). Four marked points A-D were chosen for the quantitative comparison of strains $\varepsilon_{\mathrm{vM}}$. See Table 2.6 for details.

the upper and lower surfaces, while allowing nodes on these surfaces to move freely in the x-direction. The midpoint of the bottom edge was constrained to prevent rigid body translations in the x-direction.

The contours of deformed holes obtained in experiments agree very well with those obtained with elastic multipole method ($n_{\max} = 10$) and linear finite element

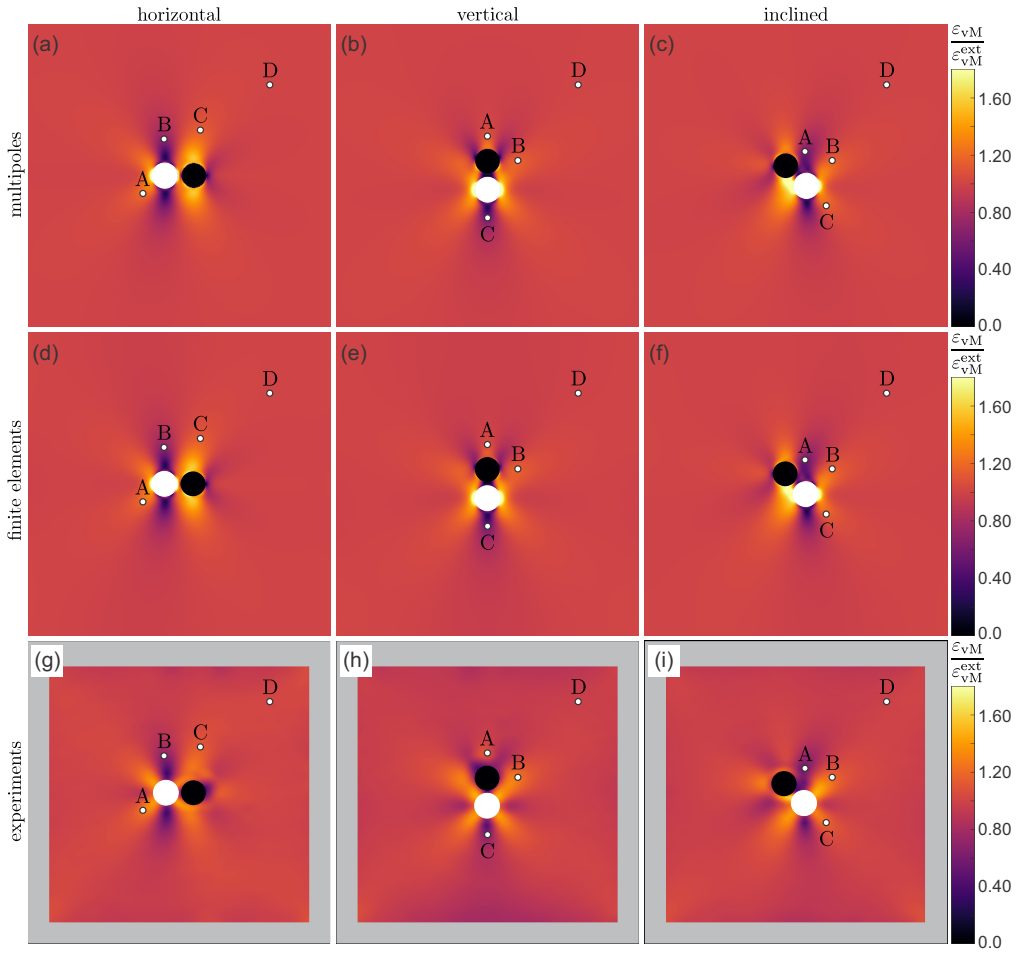

Figure 2.15: Equivalent von Mises strain fields $\varepsilon_{\mathrm{vM}}$ (see Eq. (2.38)) for uniaxially vertically compressed elastic structures with one hole (white disks) and one inclusion (blue disks) in three different configurations (horizontal, vertical, inclined at 45°) introduced in Fig. 2.13. Equivalent von Mises strain fields $\varepsilon_{\mathrm{vM}}$ were obtained with (a-c) elastic multipole method ($n_{\max} = 10$), (d-f) linear finite element simulations, and (g-i) DIC analysis of experiments. Note that the strain data was corrupted near the edges for some samples due to oil stains on the speckle patterns near the boundary. For this reason, we omitted the affected border regions (grey frames) in heat maps (g-i). Four marked points A-D were chosen for the quantitative comparison of strains $\varepsilon_{\mathrm{vM}}$. See Table 2.7 for details.

simulations for all three configurations of holes (see Fig. 2.12a-c). We also compared the equivalent von Mises strain fields defined as $\varepsilon_{\mathrm{vM}} = \sigma_{\mathrm{vM}}/E$ [1] with

$$\varepsilon_{\mathrm{vM}} = \frac{\sqrt{\varepsilon_{xx}^2 - \varepsilon_{xx}\varepsilon_{yy} + \varepsilon_{yy}^2 + 3\varepsilon_{xy}^2 + \frac{\nu}{(1-\nu)^2}(\varepsilon_{xx} + \varepsilon_{yy})^2}}{1+\nu} \tag{2.38}$$

Table 2.6: Quantitative comparison for the values of equivalent von Mises strains $\varepsilon_{\mathrm{vM}}$ normalized with the value for the applied external load $\varepsilon_{\mathrm{vM}}^{\mathrm{ext}}$ at points A-D (defined in Fig. 2.14) in compressed samples with two holes in three different configurations (horizontal, vertical, inclined) obtained with elastic multipole method (EMP), finite element method simulations (FEM) and DIC analysis of experiments (EXP). The relative percent errors between EMP and FEM were calculated as $100 \times (\varepsilon_{\mathrm{vM}}^{(\mathrm{EMP})} - \varepsilon_{\mathrm{vM}}^{(\mathrm{FEM})})/\varepsilon_{\mathrm{vM}}^{(\mathrm{FEM})}$. The relative percent errors between EMP and EXP were calculated as $100 \times (\varepsilon_{\mathrm{vM}}^{(\mathrm{EMP})} - \varepsilon_{\mathrm{vM}}^{(\mathrm{EXP})})/\varepsilon_{\mathrm{vM}}^{(\mathrm{EXP})}$.

points	horizontal				
	strain $\varepsilon_{\mathrm{vM}}/\epsilon_{\mathrm{vM}}^{\mathrm{ext}}$			error of EMP (%)	
	EMP	FEM	EXP	FEM	EXP
A	1.17	1.14	1.17	2.6	0.2
B	1.07	1.04	1.11	2.7	3.8
C	1.05	1.03	0.92	2.5	14.1
D	1.03	1.00	0.98	2.8	4.5
points	vertical				
	strain $\varepsilon_{\mathrm{vM}}/\epsilon_{\mathrm{vM}}^{\mathrm{ext}}$			error of EMP (%)	
	EMP	FEM	EXP	FEM	EXP
A	1.14	1.12	1.12	2.0	2.3
B	0.71	0.69	0.73	2.0	3.3
C	1.23	1.21	1.12	1.7	10.2
D	1.02	1.00	1.00	1.6	2.0
points	inclined				
	strain $\varepsilon_{\mathrm{vM}}/\epsilon_{\mathrm{vM}}^{\mathrm{ext}}$			error of EMP (%)	
	EMP	FEM	EXP	FEM	EXP
A	1.19	1.16	1.18	2.6	0.7
B	0.63	0.61	0.63	3.9	0.3
C	1.21	1.18	1.15	2.7	4.9
D	1.03	1.00	0.99	2.8	4.2

that were obtained with elastic multipole method ($n_{\max} = 10$), finite element simulations, and DIC analyses of experiments (see Fig. 2.14). For all three configurations of holes, the strain fields agree very well between the elastic multipole method (Fig. 2.14a-c) and finite element simulations (Fig. 2.14d-f). The strain fields for experimental samples are qualitatively similar, but they differ quantitatively near the holes as can be seen from heat maps in Fig. 2.14g-i. The quantitative comparison of strains at four different points A-D (marked in Fig. 2.14) showed a relative error of 2–4% between elastic multipole method and finite elements, and a relative

Table 2.7: Quantitative comparison for the values of equivalent von Mises strains $\varepsilon_{\mathrm{vM}}$ normalized with the value for the applied external load $\varepsilon_{\mathrm{vM}}^{\mathrm{ext}}$ at points A-D (defined in Fig. 2.15) in compressed samples with one hole and one inclusion in three different configurations (horizontal, vertical, inclined) obtained with elastic multipole method (EMP), finite element method simulations (FEM) and DIC analysis of experiments (EXP). The relative percent errors between EMP and FEM were calculated as $100 \times (\varepsilon_{\mathrm{vM}}^{(\mathrm{EMP})} - \varepsilon_{\mathrm{vM}}^{(\mathrm{FEM})})/\varepsilon_{\mathrm{vM}}^{(\mathrm{FEM})}$. The relative percent errors between EMP and EXP were calculated as $100 \times (\varepsilon_{\mathrm{vM}}^{(\mathrm{EMP})} - \varepsilon_{\mathrm{vM}}^{(\mathrm{EXP})})/\varepsilon_{\mathrm{vM}}^{(\mathrm{EXP})}$.

points	horizontal				
	strain $\varepsilon_{\mathrm{vM}}/\epsilon_{\mathrm{vM}}^{\mathrm{ext}}$			error of EMP (%)	
	EMP	FEM	EXP	FEM	EXP
A	1.21	1.20	1.23	0.7	1.1
B	0.70	0.70	0.62	0.6	11.9
C	1.14	1.13	1.09	0.7	4.0
D	1.01	1.00	0.97	0.2	3.7
points	vertical				
	strain $\varepsilon_{\mathrm{vM}}/\epsilon_{\mathrm{vM}}^{\mathrm{ext}}$			error of EMP (%)	
	EMP	FEM	EXP	FEM	EXP
A	1.11	1.07	1.06	3.9	4.5
B	1.14	1.14	1.27	0.5	10.1
C	0.57	0.56	0.61	1.4	6.3
D	1.00	0.99	0.97	1.0	3.3
points	inclined				
	strain $\varepsilon_{\mathrm{vM}}/\epsilon_{\mathrm{vM}}^{\mathrm{ext}}$			error of EMP (%)	
	EMP	FEM	EXP	FEM	EXP
A	0.61	0.59	0.57	4.8	7.0
B	1.18	1.15	1.18	2.4	0.5
C	1.16	1.15	1.17	0.7	1.2
D	1.00	0.99	0.96	0.8	4.0

error of 0–14% between elastic multipole method and experiments (see Table 2.6). The discrepancy between elastic multipole method and finite element simulations is attributed to the finite size effects. For elastic multipole method, we assumed an infinite domain, while finite domains were modeled in finite element simulations to mimic experiments. Since the domains are relatively small, interactions of induced elastic multipoles with boundaries become important, which is discussed in detail in the next chapter 3. The discrepancy between experiments and elastic multipole method is also attributed to the confounding effects of nonlinear deformation due

to moderately large compression ($\varepsilon_{yy}^{\text{ext}} = -0.05$), 3D deformation due to relatively thick samples, fabrication imperfections, nonzero friction between the sample and the mounting grips of the testing machine, the alignment of camera with the sample (2D DIC system was used), and the errors resulting from the choice of DIC parameters (see e.g. [132, 133]).

Experiments were repeated with relatively rigid inclusions ($E_{\text{inc}}/E_0 = 3000$), where the samples described above were reused. Acrylic (PMMA) rods were inserted into one of the holes and glued with a cyanoacrylate adhesive for each of the samples. The contours of deformed holes obtained in experiments matched very well with those obtained with elastic multipole method ($n_{\max} = 10$) and finite element simulations for all three configurations of holes and inclusions (see Fig. 2.13a-c). A relatively good agreement was also obtained for strain fields (see Fig. 2.15), where the strains inside rigid inclusions are very small (black). The quantitative comparison of strains at four different points A-D (marked in Fig. 2.15) showed a relative error of 0-5% between elastic multipole method and finite elements, and a relative error of 0-12% between elastic multipole method and experiments (see Table 2.7).

2.3 Conclusion

In this chapter, we demonstrated how induction and multipole expansion, which are common concepts in electrostatics, can be effectively used also for analyzing the linear deformation of infinite 2D elastic structures with circular holes and inclusions for both plane stress and plane strain conditions. Unlike in electrostatics, there are two different types of multipoles $\mathbf{Q}_n^s$ and $\mathbf{Q}_n^p$ in elasticity, which are derived from topological monopoles s (disclinations) and non-topological monopoles p. This is due to the biharmonic nature of the Airy stress function. The external load can induce all

of these multipoles except for the topological defects called disclinations (topological monopole s) and dislocations (topological dipole $\mathbf{d}^s$).

The multipole expansion is a so-called *far-field* method and is thus extremely efficient when holes and inclusions are far apart. In this case, very accurate results can be obtained by considering only induced quadrupoles, because the effect of higher-order multipoles decays more rapidly at large distances. When holes and inclusions are closer together, their interactions via induced higher-order multipoles become important as well. The accuracy of the results increases exponentially with the maximum degree of elastic multipoles, which is also the case in electrostatics, and this is characteristic for spectral methods [129].

Note that the Stokes flows in 2D can also be described in terms of the biharmonic equations of the stream function [134]. Hence, it may seem that the multipole method described above could be adapted for Stokes flows around rigid and deformable obstacles. However, this is not possible due to the Stokes' paradox, which is the phenomenon that there can be no creeping flow of a fluid around a disk in 2D [134].

The elastic multipole method presented here was limited to deformations of infinite structures with holes and inclusions of circular shapes. It can be generalized to deformations of finite size structures by employing the concept of image charges from electrostatics, which is discussed in detail in the next chapter 3. This method can also be adapted to describe deformations of structures with non-circular holes and inclusions. One still needs to use the boundary conditions that tractions and displacements are continuous across the boundary of the inclusion [see Eq. (2.30)] to obtain a set of linear equations for the amplitudes of multipoles. One option is to expand tractions and displacements in terms of the Fourier modes up to order $n_{\max}$ both outside and inside inclusions and match their coefficients. An alternative option

is to satisfy the continuity of tractions and displacements at $2n_{\max}$ different points on the boundary of each inclusion.

Chapter 3

Method of image charges for describing deformation of bounded 2D solids with circular inclusions

In the last chapter 2, we presented a method to describe linear deformations of circular holes and inclusions embedded in an *infinite* 2D elastic matrix under small external loads, by systematically expanding induced polarization of each hole/inclusion in terms of elastic multipoles, which are related to terms in the Michell solution for biharmonic functions [39]. Here, we generalize this method to describe linear deformation of *finite* and *semi-infinite* 2D structures with circular holes and inclusions by taking into account also the interaction with induced images near boundaries. The results of this method are compared with linear finite element simulations and experiments. We show that the error decreases exponentially as the maximum degree of elastic multipoles is increased.

3.1 Image charges in electrostatics and elasticity

The method of image charges is commonly used in electrostatics to satisfy various boundary conditions [121]. Similarly, image charges can be introduced in 2D elasticity to satisfy boundary conditions. Below we first discuss image charges in electrostatics for charges near a straight conductive edge and then demonstrate how image charges can be constructed in elasticity for charges near a straight traction-free edge. In Sections 3.2.3 and 3.2.4 we also show how to construct image charges near a straight rigid edge (Sec. 3.2.3) and near a curved edge (Sec. 3.2.4) with three different types of boundary conditions.

Let us consider a 2D semi-infinite dielectric medium with permittivity ϵ_e filling half-space $y < y_b$ and with a monopole with charge q at position $\mathbf{x}_0 = (x_0, y_0) = (x_0, y_b - h)$, which is at the distance h from an infinite perfectly conducting straight edge at $y = y_b$, as shown in Fig. 3.1a. The electric potential $U(\mathbf{x})$ for this case can be found by solving the governing equation $\Delta U = -\frac{q}{\epsilon_e}\delta(\mathbf{x} - \mathbf{x}_0)$ subject to the boundary condition imposed by the conducting edge, i.e. $E_x(x, y_b) = 0$, where the electric field $\mathbf{E}(\mathbf{x}) = (E_x(\mathbf{x}), E_y(\mathbf{x}))$ is related to the electric potential $U(\mathbf{x})$ as

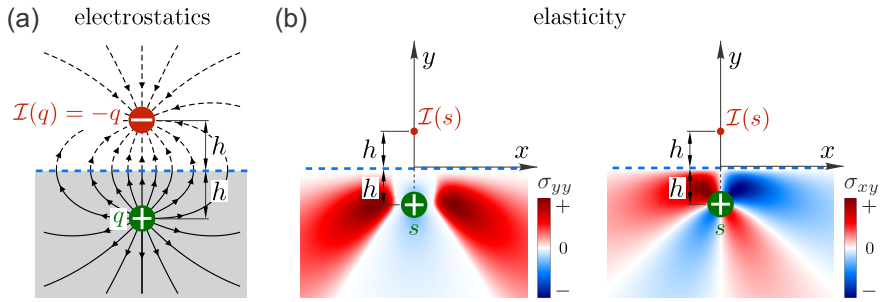

Figure 3.1: Image charges in electrostatics and elasticity. (a) A point electric charge q (green) near an infinite conducting plate (dashed blue line) induces an opposite image charge $\mathcal{I}(q) = -q$ (red) to satisfy the boundary condition that the electric field lines (black lines) are orthogonal to the conductive plate. (b) A point disclination with charge s (green) embedded in a semi-infinite elastic material near a traction-free edge (dashed blue line) induces an image charge $\mathcal{I}(s)$ (red) to satisfy boundary conditions at the traction-free edge ($\sigma_{xy} = \sigma_{yy} = 0$). Heat maps show the resultant stress fields σ_{yy} and σ_{xy}.

$\mathbf{E} = -\boldsymbol{\nabla} U$. [121] The solution for the governing equation in an infinite 2D dielectric medium is $U_m(\mathbf{x}-\mathbf{x}_0|q) = -\frac{q}{2\pi\epsilon_e}\ln|\mathbf{x}-\mathbf{x}_0|$, but the corresponding electric field does not satisfy boundary conditions at the conducting edge. The boundary conditions can be satisfied by placing an image monopole charge $-q$ on the opposite side of the conducting edge at position $\mathbf{x}_0^* = (x_0^*, y_0^*) = (x_0, y_b + h)$ (see Fig. 3.1a) with the corresponding electric potential $\mathcal{I}[U_m(\mathbf{x}-\mathbf{x}_0|q)] = +\frac{q}{2\pi\epsilon_e}\ln|\mathbf{x}-\mathbf{x}_0^*|$. The total electric potential is thus $U^{\text{tot}}(\mathbf{x}) = U_m(\mathbf{x}-\mathbf{x}_0|q) + \mathcal{I}[U_m(\mathbf{x}-\mathbf{x}_0|q)] = -\frac{q}{2\pi\epsilon_e}\ln|\mathbf{x}-\mathbf{x}_0| + \frac{q}{2\pi\epsilon_e}\ln|\mathbf{x}-\mathbf{x}_0^*|$. [121] It is straightforward to check that the corresponding electric field $\mathbf{E}^{\text{tot}} = -\boldsymbol{\nabla} U^{\text{tot}}$ satisfies the boundary condition at the conducting edge (see Fig. 3.1a). Note that the image of the image charge is the original charge itself, i.e. $\mathcal{I}\big[\mathcal{I}[U_m(\mathbf{x}-\mathbf{x}_0|q)]\big] = U_m(\mathbf{x}-\mathbf{x}_0|q)$. [121]

Let us consider a related problem in 2D elasticity for a semi-infinite elastic medium with the Young's modulus E filling half-space $y < y_b$ with a topological monopole (disclination) with charge s at position $\mathbf{x}_0 = (x_0, y_0) = (x_0, y_b - h)$, which is at the distance h from the traction-free edge ($t_i \equiv 0$) at $y = y_b$ (see Fig. 3.1b). Note that tractions t_i are defined as the force per unit length on the boundary, which are related to the stress tensor σ_{ij} as $t_i = \sigma_{ij} n_j$, where n_j is the unit normal vector to the boundary. The Airy stress function $\chi(\mathbf{x})$ for this case can be found by solving the governing equation $\Delta\Delta\chi = Es\delta(\mathbf{x}-\mathbf{x}_0)$ subject to the boundary condition imposed by the traction-free edge, i.e. $\sigma_{xy}(x, y_b) = \sigma_{yy}(x, y_b) = 0$, where stress fields $\sigma_{ij}(\mathbf{x})$ are related to the Airy stress function $\chi(\mathbf{x})$ as $\sigma_{xx} = \frac{\partial^2\chi}{\partial y^2}$, $\sigma_{yy} = \frac{\partial^2\chi}{\partial x^2}$, and $\sigma_{xy} = -\frac{\partial^2\chi}{\partial x \partial y}$. The solution for the governing equation in an infinite 2D elastic medium is $\chi_m^s(\mathbf{x}-\mathbf{x}_0|s) = \frac{Es}{8\pi}|\mathbf{x}-\mathbf{x}_0|^2\big(\ln|\mathbf{x}-\mathbf{x}_0| - 1/2\big)$, [122, 125] but the corresponding stress fields do not satisfy boundary conditions at the traction-free edge. Inspired by electrostatics we try placing an image disclination with charge $-s$ on the opposite side of the traction-free edge at position $\mathbf{x}_0^* = (x_0^*, y_0^*) = (x_0, y_b + h)$. The trial Airy stress function is thus $\chi^{\text{tr}}(\mathbf{x}) = \chi_m^s(\mathbf{x}-\mathbf{x}_0|s) + \chi_m^s(\mathbf{x}-\mathbf{x}_0^*|-s) = \frac{Es}{8\pi}|\mathbf{x}-\mathbf{x}_0|^2\big(\ln|\mathbf{x}-\mathbf{x}_0| -$

$1/2\big) - \frac{Es}{8\pi}|\mathbf{x}-\mathbf{x}_0^*|^2\big(\ln|\mathbf{x}-\mathbf{x}_0^*| - 1/2\big)$. This trial Airy stress function $\chi^{\rm tr}(\mathbf{x})$ satisfies one of the boundary conditions, $\sigma_{yy}^{\rm tr}(x,y_b) = 0$, at the traction-free edge, but the other boundary condition is violated because $\sigma_{xy}^{\rm tr}(x,y_b) = -\frac{Es(x-x_0)h}{2\pi((x-x_0)^2+h^2)} \neq 0$. Thus in elasticity additional image multipoles have to be included to satisfy both boundary conditions. This difference between electrostatics and elasticity stems from the fact that the electric potential $U(\mathbf{x})$ is a harmonic function [121], while the Airy stress function $\chi(\mathbf{x})$ is a biharmonic function [1]. The additional image multipoles can be found by calculating the Airy stress function $\chi^a(\mathbf{x})$ that corresponds to distributed tractions $f_x(x) = -\sigma_{xy}^{\rm tr}(x,y_b) = \frac{Es(x-x_0)h}{2\pi((x-x_0)^2+h^2)}$ and $f_y(x) = -\sigma_{yy}^{\rm tr}(x,y_b) = 0$ along the edge (x,y_b). This can be done with the help of the solution of the Boussinesq problem in 2D, where the response to a concentrated force $\mathbf{F} = (1,0)$ in the x-direction at point (x',y_b) on the edge is described with the Airy stress function $\chi_B(\mathbf{x}|x',y_b) = -(1/\pi)(y-y_b)\arctan[(y-y_b)/(x-x')]$, where $\mathbf{x} = (x,y)$. [135] The Airy stress function of the additional elastic image multipoles can then be obtained as $\chi^a(\mathbf{x}) = \int_{-\infty}^{\infty} dx' f_x(x')\chi_B(\mathbf{x}|x',y_b) = -(Esh/2\pi)(y-y_0^*+h)\ln|\mathbf{x}-\mathbf{x}_0^*|$. Thus the Airy stress functions $\chi_m^s(\mathbf{x}-\mathbf{x}_0|s)$ for the monopole disclination and for its image $\mathcal{I}[\chi_m^s(\mathbf{x}-\mathbf{x}_0|s)]$ can be expressed as

$$\chi_m^s(\mathbf{x}-\mathbf{x}_0|s) = +\frac{Es}{8\pi}r^2\big(\ln r - 1/2\big), \tag{3.1a}$$

$$\begin{aligned}\mathcal{I}[\chi_m^s(\mathbf{x}-\mathbf{x}_0|s)] = &-\frac{Es}{8\pi}r^{*2}\big(\ln r^* - 1/2\big)\\ &-\frac{Esh}{2\pi}r^*\sin\varphi^*\ln r^* - \frac{Esh^2}{2\pi}\ln r^*,\end{aligned} \tag{3.1b}$$

where we introduced polar coordinates (r,φ) and (r^*,φ^*) centered at the disclination ($r = \sqrt{(x-x_0)^2+(y-y_0)^2}$, $\varphi = \arctan[(y-y_0)/(x-x_0)]$) and the position of its image ($r^* = \sqrt{(x-x_0^*)^2+(y-y_0^*)^2}$, $\varphi^* = \arctan[(y-y_0^*)/(x-x_0^*)]$), respectively. It is straightforward to check that the stress fields resulting from the Airy stress function $\chi^{\rm tot} = \chi_m^s + \mathcal{I}[\chi_m^s]$ satisfy the boundary conditions along the edge (see Fig. 3.1b). Just

like in electrostatics, the image of the image disclination is the original disclination itself, i.e. $\mathcal{I}\big[\mathcal{I}[\chi_m^s(\mathbf{x}-\mathbf{x}_0|s)]\big] = \chi_m^s(\mathbf{x}-\mathbf{x}_0|s)$.

The Airy stress function for the disclination χ_m^s can be used to systematically construct the Airy stress functions for all other elastic multipoles, as discussed in detail in the previous chapter 2. Here, we repeat this procedure to construct the images for all other elastic multipoles. First, we show how to construct an image for a topological dipole (dislocation), which is formed at $\mathbf{x}_0 = (x_0, y_0) = (x_0, y_b - h)$, when two opposite disclinations with charges $\pm s$ are located at $\mathbf{x}_\pm = \mathbf{x}_0 \pm a(\cos\theta, \sin\theta)$, where the angle θ describes the orientation of dislocation. Thus the Airy stress functions $\chi_d^s(\mathbf{x}-\mathbf{x}_0)$ for the dislocation and $\mathcal{I}[\chi_d^s(\mathbf{x}-\mathbf{x}_0)]$ for its image at position $\mathbf{x}_0^* = (x_0^*, y_0^*) = (x_0, y_b + h)$ can be expressed as [**?**, 136]

$$
\begin{aligned}
\chi_d^s(\mathbf{x}-\mathbf{x}_0|sa,\theta) &= \chi_m^s(\mathbf{x}-\mathbf{x}_+|s) + \chi_m^s(\mathbf{x}-\mathbf{x}_-|-s),\\
\chi_d^s(\mathbf{x}-\mathbf{x}_0|sa,\theta) &\xrightarrow{a\to 0} \frac{Esa}{2\pi} r\ln r\cos(\varphi-\theta),
\end{aligned}
\tag{3.2a}
$$

$$
\begin{aligned}
\mathcal{I}[\chi_d^s(\mathbf{x}-\mathbf{x}_0|sa,\theta)] &= \mathcal{I}[\chi_m^s(\mathbf{x}-\mathbf{x}_+|s)]\\
&\quad + \mathcal{I}[\chi_m^s(\mathbf{x}-\mathbf{x}_-|-s)],\\
\mathcal{I}[\chi_d^s(\mathbf{x}-\mathbf{x}_0|sa,\theta)] &\xrightarrow{a\to 0} + \frac{Esa}{2\pi} r^*\ln r^*\cos(\varphi^*-\theta)\\
&\quad + \frac{Esah}{2\pi}\sin(2\varphi^*+\theta)\\
&\quad + \frac{Esah}{\pi}\sin\theta\left(\ln r^* - \frac{1}{2}\right)\\
&\quad + \frac{Esah^2}{\pi}\frac{\cos(\varphi^*+\theta)}{r^*},
\end{aligned}
\tag{3.2b}
$$

where we again used polar coordinates (r, φ) centered at the dislocation and (r^*, φ^*) centered at its image.

The Airy stress functions for a quadrupole and higher-order multipoles and their images can be constructed similarly. The multipole $\mathbf{Q}_n^s$ of order n is constructed by placing n positive and n negative disclinations symmetrically around $\mathbf{x}_0 = (x_0, y_0) =$

$(x_0, y_b - h)$, such that disclinations of charges $s_i = s(-1)^i$ are placed at positions $\mathbf{x}_i = \mathbf{x}_0 + a\big(\cos(\theta + i\pi/n), \sin(\theta + i\pi/n)\big)$, where $i \in \{0, 1, \ldots, 2n-1\}$ and the angle θ describes the orientation of elastic multipole. The Airy stress functions for such multipoles χ_n^s and their images $\mathcal{I}[\chi_n^s]$ at positions $\mathbf{x}_0^* = (x_0^*, y_0^*) = (x_0, y_b + h)$ are expressed in polar coordinates as

$$\begin{aligned}
\chi_n^s(\mathbf{x} - \mathbf{x}_0 | sa^n, \theta) &= \sum_{i=0}^{2n-1} \chi_m^s(\mathbf{x} - \mathbf{x}_i | s_i), \\
\chi_n^s(\mathbf{x} - \mathbf{x}_0 | sa^n, \theta) &\xrightarrow{a\to 0} + \frac{Esa^n}{4(n-1)\pi} \frac{\cos\big(n(\varphi - \theta)\big)}{r^{n-2}},
\end{aligned} \tag{3.3a}$$

$$\begin{aligned}
\mathcal{I}[\chi_n^s(\mathbf{x} - \mathbf{x}_0 | sa^n, \theta)] &= \sum_{i=0}^{2n-1} \mathcal{I}[\chi_m^s(\mathbf{x} - \mathbf{x}_i | s_i)], \\
\mathcal{I}[\chi_n^s(\mathbf{x} - \mathbf{x}_0 | sa^n, \theta)] &\xrightarrow{a\to 0} + \frac{Esa^n}{4\pi} \frac{\cos\big(n\varphi^* + n\theta\big)}{r^{*n-2}} \\
&\quad - \frac{Esa^n}{4(n-1)\pi} \frac{n\cos\big((n-2)\varphi^* + n\theta\big)}{r^{*n-2}} \\
&\quad + \frac{Esa^n h}{2\pi} \frac{\sin\big((n+1)\varphi^* + n\theta\big)}{r^{*n-1}} \\
&\quad - \frac{Esa^n h}{2(n-1)\pi} \frac{(2n-1)\sin\big((n-1)\varphi^* + n\theta\big)}{r^{*n-1}} \\
&\quad + \frac{Esa^n h^2}{\pi} \frac{\cos\big(n\varphi^* + n\theta\big)}{r^{*n}}.
\end{aligned} \tag{3.3b}$$

In 2D elasticity, there is another type of monopole besides disclinations. This is a non-topological monopole with charge p that describes local contraction of material at point $\mathbf{x}_0 = (x_0, y_0) = (x_0, y_b - h)$ and the corresponding Airy stress function χ_m^p can be obtained as the solution of equation $\Delta\Delta\chi_m^p = Ep\Delta_0\delta(\mathbf{x} - \mathbf{x}_0)$, where Δ_0 corresponds to the Laplace operator with respect to $\mathbf{x}_0$. [125, 49] The Airy stress functions χ_m^p for this non-topological monopole and $\mathcal{I}[\chi_m^p]$ for its image at position $\mathbf{x}_0^* = (x_0^*, y_0^*) = (x_0, y_b + h)$ can thus be obtained from the Airy stress function χ_m^s for

disclination as

$$\begin{aligned}
\chi_m^p(\mathbf{x}-\mathbf{x}_0|p) &= \Delta_0 \chi_m^s(\mathbf{x}-\mathbf{x}_0|p), \\
\chi_m^p(\mathbf{x}-\mathbf{x}_0|p) &= +\frac{Ep}{4\pi}\left(1+2\ln r\right), \qquad (3.4a) \\
\mathcal{I}[\chi_m^p(\mathbf{x}-\mathbf{x}_0|p)] &= \Delta_0 \mathcal{I}[\chi_m^s(\mathbf{x}-\mathbf{x}_0|p)], \\
\mathcal{I}[\chi_m^p(\mathbf{x}-\mathbf{x}_0|p)] &= +\frac{Ep}{4\pi}\left[1-2\ln r^* - 2\cos(2\varphi^*)\right] \\
&\quad + \frac{Eph}{\pi}\frac{\sin\varphi^*}{r^*}. \qquad (3.4b)
\end{aligned}$$

The Airy stress functions for a dipole, a quadrupole, and higher-order multipoles that arise from non-topological monopoles p and their images can be constructed similarly as for higher-order multipoles arising from disclinations. The multipole $\mathbf{Q}_n^p$ of order n is constructed by placing n positive and n negative non-topological monopoles symmetrically around $\mathbf{x}_0 = (x_0, y_0) = (x_0, y_b - h)$, such that non-topological monopoles of charges $p_i = p(-1)^i$ are placed at positions $\mathbf{x}_i = \mathbf{x}_0 + a\big(\cos(\theta + i\pi/n), \sin(\theta + i\pi/n)\big)$, where $i \in \{0, 1, \ldots, 2n-1\}$ and the angle θ describes the orientation of multipole. Airy stress functions χ_n^p for such multipoles and $\mathcal{I}[\chi_n^p]$ for their images at positions $\mathbf{x}_0^* = (x_0^*, y_0^*) = (x_0, y_b + h)$ are expressed in polar coordinates as

$$\begin{aligned}
\chi_n^p(\mathbf{x}-\mathbf{x}_0|pa^n,\theta) &= \sum_{i=0}^{2n-1} \chi_n^p(\mathbf{x}-\mathbf{x}_i|p_i), \\
\chi_n^p(\mathbf{x}-\mathbf{x}_0|pa^n,\theta) &\xrightarrow{a\to 0} -\frac{Epa^n}{\pi}\,\frac{\cos\big(n(\varphi-\theta)\big)}{r^n}, \qquad (3.5a) \\
\mathcal{I}[\chi_n^p(\mathbf{x}-\mathbf{x}_0|pa^n,\theta)] &= \sum_{i=0}^{2n-1} \mathcal{I}[\chi_m^p(\mathbf{x}-\mathbf{x}_i|p_i)], \\
\mathcal{I}[\chi_n^p(\mathbf{x}-\mathbf{x}_0|pa^n,\theta)] &\xrightarrow{a\to 0} \\
&\quad + \frac{Epa^n}{\pi}\,\frac{(n+1)\cos\big(n\varphi^*+\theta\big)}{r^{*n}} \\
&\quad - \frac{Epa^n}{\pi}\,\frac{n\cos\big((n+2)\varphi^*+n\theta\big)}{r^{*n}}
\end{aligned}$$

$$+\frac{Epa^n h}{\pi}\,\frac{2n\sin\big((n+1)\varphi^*+n\theta\big)}{r^{*n+1}}. \tag{3.5b}$$

Note that the elastic multipoles described above are related to the terms in the Michell solution [39] for the biharmonic equation, which is discussed in detail in the previous chapter 2. The operator $\mathcal{I}$ for constructing the Airy stress functions of images can be written in a compact form as was previously shown by Adeerogba [137]

$$\begin{aligned}\mathcal{I}\big[\chi_0(x,y)\big] =& -\chi_0(x,2y_b-y)+2(y-y_b)\frac{\partial\chi_0(x,2y_b-y)}{\partial y}\\ &-(y-y_b)^2\Delta\chi_0(x,2y_b-y).\end{aligned} \tag{3.6}$$

Note that the above operator works for all elastic multipoles except for the disclination (topological monopole), for which it produces additional uniform stress that has to be subtracted. Adeerogba derived this expression for eigenstresses in the elastic matrix, which correspond to all non-topological multipoles.

3.2 Elastic multipole method with image charges

Using the concept of image charges described in Section 3.1 and procedures that were presented in the previous chapter 2, we describe a method for calculating the linear deformation of circular inclusions and holes embedded either in a semi-infinite ($y < y_b$) elastic matrix, in an infinite elastic strip ($y_a < y < y_b$), or in an elastic disk with radius R. External load induces elastic multipoles at the centers of inclusions and holes, which further induce image multipoles in order to satisfy boundary condition at the edges. The amplitudes of induced multipoles are obtained from boundary conditions (continuity of tractions and displacements) between different materials in the elastic matrix.

In the following subsections, we describe the method for the general case where circular inclusions can have different sizes and material properties (holes correspond to zero shear modulus). Note that our method applies to the deformation of cylindrical holes and inclusions embedded in a thin plate (plane stress) as well as of cylindrical inclusions and holes embedded in an infinitely thick elastic matrix (plane strain) by appropriately setting the values of Kolosov's constants [1]. In Section 3.2.1, we describe the method for a semi-infinite elastic matrix ($y < y_b$) subject to uniform tractions along the boundary. In Section 3.2.2, we adapt this method for the case of an infinite elastic strip ($y_a < y < y_b$) subject to uniform tractions along the boundary. In Section 3.2.3, we use our method to describe the deformation of a semi-infinite elastic matrix ($y < y_b$) subject to displacement control boundary conditions. Finally, in Section 3.2.4, we describe the deformation of a circular disk subject to either hydrostatic stress, no-slip (displacement control), and slip boundary conditions. In all of these sections, we compare the results of our method with linear finite element simulations and experiments.

3.2.1 Inclusions in a semi-infinite elastic matrix with uniform tractions along the outer boundary of the elastic matrix

Method

Let us consider a 2D semi-infinite elastic matrix with the Young's modulus E_0 and Poisson's ratio ν_0 filling the half-space $y < y_b$ subject to external stresses (σ_{xx}^{ext}, σ_{yy}^{ext}, σ_{xy}^{ext}). Embedded in the elastic matrix are N circular inclusions with radii R_i centered at positions $\mathbf{x}_i = (x_i, y_i) = (x_i, y_b - h_i)$ with Young's moduli E_i and Poisson's ratios ν_i, where $i \in \{1, \ldots, N\}$ and h_i is the distance from the center of the i^{th} inclusion to the traction controlled edge at $y = y_b$ (see Fig. 3.2). Holes are described with the zero Young's modulus ($E_i = 0$).

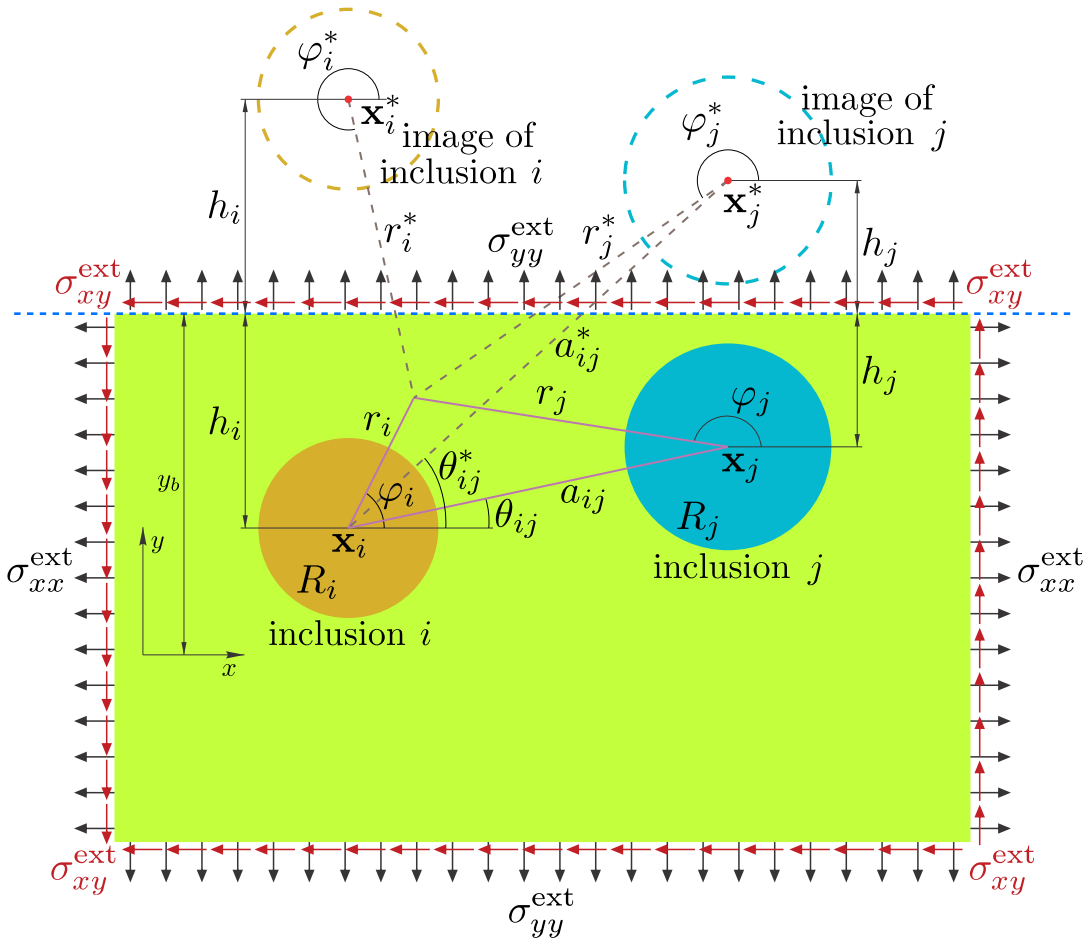

Figure 3.2: Illustration of external loading (σ_{xx}^{ext}, σ_{yy}^{ext}, σ_{xy}^{ext}) for the semi-infinite structure ($y < y_b$) with circular inclusions (colored disks) with uniform tractions along the edge (dashed blue line). Images of inclusions are represented with dashed circles. The schematic describes polar coordinates (r_i, φ_i) and (r_j, φ_j) relative to the centers $\mathbf{x}_i$ of the i^{th} inclusion with radius R_i and $\mathbf{x}_j$ of the j^{th} inclusion with radius R_j, respectively. Similarly, we define polar coordinates (r_i^*, φ_i^*) and (r_j^*, φ_j^*) relative to the centers $\mathbf{x}_i^*$ of the image of the i^{th} inclusion and $\mathbf{x}_j^*$ of the image of the j^{th} inclusion, respectively. Here, a_{ij} (a_{ij}^*) is the separation distance between the centers of the i^{th} inclusion and the j^{th} inclusion (the image of the j^{th} inclusion) and θ_{ij} (θ_{ij}^*) is the angle between the line joining their centers and the x-axis.

External stress, represented with the Airy stress function

$$\chi_{\text{ext}}(x, y) = \frac{1}{2}\sigma_{xx}^{\text{ext}} y^2 + \frac{1}{2}\sigma_{yy}^{\text{ext}} x^2 - \sigma_{xy}^{\text{ext}} xy, \tag{3.7}$$

induces non-topological monopoles, non-topological dipoles, quadrupoles and higher-order multipoles at the centers of inclusions, while topological defects (disclination, dislocation) cannot be induced, as was discussed in the previous chapter 2. Thus the Airy stress function $\chi_{\text{out}}\big(r_i, \varphi_i|\mathbf{a}_{i,\text{out}}\big)$ outside the i^{th} inclusion due to the induced multipoles can be expanded as

$$\begin{aligned}\chi_{\text{out}}\big(r_i, \varphi_i|\mathbf{a}_{i,\text{out}}\big) =& A_{i,0}R_i^2 \ln\left(\frac{r_i}{R_i}\right) \\ &+ \sum_{n=1}^{\infty} R_i^2 \left(\frac{r_i}{R_i}\right)^{-n} \big[A_{i,n}\cos(n\varphi_i) + B_{i,n}\sin(n\varphi_i)\big] \\ &+ \sum_{n=2}^{\infty} R_i^2 \left(\frac{r_i}{R_i}\right)^{-n+2} \big[C_{i,n}\cos(n\varphi_i) + D_{i,n}\sin(n\varphi_i)\big],\end{aligned} \tag{3.8}$$

where the origin of polar coordinates ($r_i = \sqrt{(x-x_i)^2 + (y-y_i)^2}, \varphi_i = \arctan[(y - y_i)/(x - x_i)]$) is at the center $\mathbf{x}_i = (x_i, y_i) = (x_i, y_b - h_i)$ of the i^{th} inclusion with radius R_i and the set of amplitudes of induced multipoles is $\mathbf{a}_{i,\text{out}} = \{A_{i,0}, A_{i,1}, \ldots, B_{i,1}, B_{i,2}, \ldots, C_{i,2}, C_{i,3}, \ldots, D_{i,2}, D_{i,3}, \ldots\}$. The induced elastic multipoles at the center of the i^{th} inclusion then further induce image multipoles at position $\mathbf{x}_i^* = (x_i^*, y_i^*) = (x_i, y_b + h_i)$ to satisfy boundary conditions at the edge ($\sigma_{yy}(x, y_b) = \sigma_{yy}^{\text{ext}}$, $\sigma_{xy}(x, y_b) = \sigma_{xy}^{\text{ext}}$). The Airy stress functions of image multipoles due to the i^{th} inclusion can be expanded as

$$\begin{aligned}\mathcal{I}[\chi_{\text{out}}\big(r_i, \varphi_i|\mathbf{a}_{i,\text{out}}\big)] =& \chi_{\text{out}}^*\big(r_i^*, \varphi_i^*|\mathbf{a}_{i,\text{out}}^*\big), \\ \chi_{\text{out}}^*\big(r_i^*, \varphi_i^*|\mathbf{a}_{i,\text{out}}^*\big) =& A_{i,0}^* R_i^2 \ln\left(\frac{r_i^*}{R_i}\right) + B_{i,0}^* R_i^2 \varphi_i^* \\ &+ \sum_{n=1}^{\infty} R_i^2 \left(\frac{r_i^*}{R_i}\right)^{-n} \big[A_{i,n}^*\cos(n\varphi_i^*) + B_{i,n}^*\sin(n\varphi_i^*)\big] \\ &+ \sum_{n=2}^{\infty} R_i^2 \left(\frac{r_i^*}{R_i}\right)^{-n+2} \big[C_{i,n}^*\cos(n\varphi_i^*) + D_{i,n}^*\sin(n\varphi_i^*)\big],\end{aligned} \tag{3.9}$$

where the origin of polar coordinates ($r_i^* = \sqrt{(x-x_i^*)^2+(y-y_i^*)^2}, \varphi_i^* = \arctan[(y-y_i^*)/(x-x_i^*)]$) is at the center $\mathbf{x}_i^*$ of the image of the i^{th} inclusion. Note that in the above expansion in Eq. (3.9) we included the term proportional to $B_{i,0}^*\varphi_i^*$, which is absent in the expansion for the Airy stress function $\chi_{\text{out}}\big(r_i,\varphi_i|\mathbf{a}_{i,\text{out}}\big)$ of the i^{th} inclusion in Eq. (3.8). This term is not allowed for inclusions located inside the elastic matrix because the Airy stress function $\chi_{\text{out}}\big(r_i,\varphi_i|\mathbf{a}_{i,\text{out}}\big)$ must be continuous as the angle φ_i spans the range of values from 0 to 2π. On the other hand, the images of inclusions are located outside the elastic matrix (see Fig. 3.2) and thus the angle φ_i^* cannot attain values in the whole range from 0 to 2π. The amplitudes $\mathbf{a}_{i,\text{out}}^* = \{A_{i,0}^*, A_{i,1}^*, \dots, B_{i,0}^*, B_{i,1}^*, \dots, C_{i,2}^*, C_{i,3}^*, \dots, D_{i,2}^*, D_{i,3}^*, \dots\}$ of image multipoles are related to the amplitudes $\mathbf{a}_{i,\text{out}}$ of induced multipoles for the i^{th} inclusion as

$$A_{i,n}^* = \begin{cases} -A_{i,0}, & n=0, \\ -(n+1)A_{i,n} - (n+2)C_{i,n+2} \\ \quad -2(n-1)\frac{h_i}{R_i}B_{i,n-1} \\ \quad -2(2n+1)\frac{h_i}{R_i}D_{i,n+1} & n\geq 1, \\ \quad +4(n-1)\frac{h_i^2}{R_i^2}C_{i,n}, \end{cases} \tag{3.10a}$$

$$B_{i,n}^* = \begin{cases} 0, & n=0, \\ +2B_{i,1} + 3D_{i,3} \\ \quad +2\frac{h_i}{R_i}A_{i,0} - 6\frac{h_i}{R_i}C_{i,2}, & n=1, \\ +(n+1)B_{i,n} + (n+2)D_{i,n+2} \\ \quad -2(n-1)\frac{h_i}{R_i}A_{i,n-1} \\ \quad -2(2n+1)\frac{h_i}{R_i}C_{i,n+1} & n\geq 2, \\ \quad -4(n-1)\frac{h_i^2}{R_i^2}D_{i,n}, \end{cases} \tag{3.10b}$$

$$C^*_{i,n} = \begin{cases} +C_{i,2} - A_{i,0}, & n = 2, \\ +(n-1)C_{i,n} + (n-2)A_{i,n-2} & \\ \qquad +2(n-2)\frac{h_i}{R_i}D_{i,n-1}, & n \geq 3, \end{cases} \tag{3.10c}$$

$$D^*_{i,n} = \begin{cases} -(n-1)D_{i,n} - (n-2)B_{i,n-2} & \\ \qquad +2(n-2)\frac{h_i}{R_i}C_{i,n-1}, & n \geq 2, \end{cases} \tag{3.10d}$$

where we used results for the image multipoles derived in Section 3.1. The total Airy stress function outside all inclusions can then be written as

$$\begin{aligned} \chi^{\text{tot}}_{\text{out}}\big(x, y|\mathbf{a}_{\text{out}}\big) &= \chi_{\text{ext}}(x, y) \\ &+ \sum_{i=1}^{N} \chi_{\text{out}}\big(r_i(x, y), \varphi_i(x, y)|\mathbf{a}_{i,\text{out}}\big) \\ &+ \sum_{i=1}^{N} \mathcal{I}\left[\chi_{\text{out}}\big(r_i(x, y), \varphi_i(x, y)|\mathbf{a}_{i,\text{out}}\big)\right], \end{aligned} \tag{3.11}$$

where the first term is due to external stress and the two summations describe contributions due to induced multipoles at the centers of inclusions and due to their images. The set of amplitudes of induced multipoles for all inclusions is defined as $\mathbf{a}_{\text{out}} = \{\mathbf{a}_{1,\text{out}}, \ldots, \mathbf{a}_{N,\text{out}}\}$.

Similarly, we expand the induced Airy stress function inside the i^{th} inclusion as [49]

$$\begin{aligned} \chi_{\text{in}}\big(r_i, \varphi_i|\mathbf{a}_{i,\text{in}}\big) =& c_{i,0}r_i^2 \\ &+ \sum_{n=2}^{\infty} R_i^2 \left(\frac{r_i}{R_i}\right)^n \left[a_{i,n}\cos(n\varphi_i) + b_{i,n}\sin(n\varphi_i)\right] \\ &+ \sum_{n=1}^{\infty} R_i^2 \left(\frac{r_i}{R_i}\right)^{n+2} \left[c_{i,n}\cos(n\varphi_i) + d_{i,n}\sin(n\varphi_i)\right], \end{aligned} \tag{3.12}$$

where we kept only terms that generate finite stresses at the center of inclusion and we omitted constant and linear terms $\{1, r_i\cos\varphi_i, r_i\sin\varphi_i\}$ that correspond to zero stresses. The set of amplitudes of induced multipoles is represented as $\mathbf{a}_{i,\text{in}} = \{a_{i,2}, a_{i,3}, \dots, b_{i,2}, b_{i,3}, \dots, c_{i,0}, c_{i,1}, \dots, d_{i,1}, d_{i,2}, \dots\}$. The total Airy stress function inside the i^{th} inclusion is thus

$$\begin{aligned}\chi_{\text{in}}^{\text{tot}}\big(x, y|\mathbf{a}_{i,\text{in}}\big) =& \chi_{\text{ext}}(x, y) \\ &+ \chi_{\text{in}}\big(r_i(x, y), \varphi_i(x, y)|\mathbf{a}_{i,\text{in}}\big),\end{aligned} \tag{3.13}$$

where the first term is due to external stress and the second term is due to induced multipoles.

The amplitudes of induced multipoles $\mathbf{a}_{i,\text{out}}$ and $\mathbf{a}_{i,\text{in}}$ are obtained by satisfying boundary conditions that tractions and displacements are continuous across the circumference of each inclusion [49]

$$\sigma_{\text{in},rr}^{\text{tot}}\big(r_i = R_i, \varphi_i|\mathbf{a}_{i,\text{in}}\big) = \sigma_{\text{out},rr}^{\text{tot}}\big(r_i = R_i, \varphi_i|\mathbf{a}_{\text{out}}\big), \tag{3.14a}$$

$$\sigma_{\text{in},r\varphi}^{\text{tot}}\big(r_i = R_i, \varphi_i|\mathbf{a}_{i,\text{in}}\big) = \sigma_{\text{out},r\varphi}^{\text{tot}}\big(r_i = R_i, \varphi_i|\mathbf{a}_{\text{out}}\big), \tag{3.14b}$$

$$u_{\text{in},r}^{\text{tot}}\big(r_i = R_i, \varphi_i|\mathbf{a}_{i,\text{in}}\big) = u_{\text{out},r}^{\text{tot}}\big(r_i = R_i, \varphi_i|\mathbf{a}_{\text{out}}\big), \tag{3.14c}$$

$$u_{\text{in},\varphi}^{\text{tot}}\big(r_i = R_i, \varphi_i|\mathbf{a}_{i,\text{in}}\big) = u_{\text{out},\varphi}^{\text{tot}}\big(r_i = R_i, \varphi_i|\mathbf{a}_{\text{out}}\big), \tag{3.14d}$$

where stresses and displacements are obtained from the total Airy stress functions $\chi_{\text{in}}^{\text{tot}}\big(x, y|\mathbf{a}_{i,\text{in}}\big)$ inside the i^{th} inclusion (see Eq. (3.13)) and $\chi_{\text{out}}^{\text{tot}}\big(x, y|\mathbf{a}_{\text{out}}\big)$ outside all inclusions (see Eq. (3.11)). In the boundary conditions for the i^{th} inclusion in the above Eq. (3.14), we can easily take into account contributions due to the induced multipoles $\mathbf{a}_{i,\text{in}}$ and $\mathbf{a}_{i,\text{out}}$ in this inclusion and due to external stresses σ_{xx}^{ext}, σ_{yy}^{ext}, and σ_{xy}^{ext} after rewriting the corresponding Airy stress function $\chi_{\text{ext}}(x, y)$ in Eq. (3.7) in

Table 3.1: Stresses σ_{ij} and displacements u_i corresponding to different terms for the Airy stress function χ in the Michell solution [1]. The value of Kolosov's constant for plane stress is $\kappa = (3-\nu)/(1+\nu)$ and for plane strain is $\kappa = 3-4\nu$. Here, μ is the shear modulus and ν is the Poisson's ratio.

χ	σ_{rr}	$\sigma_{r\varphi}$	$\sigma_{\varphi\varphi}$	$2\mu \begin{pmatrix} u_r \\ u_\varphi \end{pmatrix}$
r^2	2	0	2	$r \begin{pmatrix} \kappa-1 \\ 0 \end{pmatrix}$
$\ln r$	r^{-2}	0	$-r^{-2}$	$r^{-1} \begin{pmatrix} -1 \\ 0 \end{pmatrix}$
$r^{n+2}\cos(n\varphi)$	$-(n+1)(n-2)r^n\cos(n\varphi)$	$n(n+1)r^n\sin(n\varphi)$	$(n+1)(n+2)r^n\cos(n\varphi)$	$r^{n+1} \begin{pmatrix} (\kappa-n-1)\cos(n\varphi) \\ (\kappa+n+1)\sin(n\varphi) \end{pmatrix}$
$r^{n+2}\sin(n\varphi)$	$-(n+1)(n-2)r^n\sin(n\varphi)$	$-n(n+1)r^n\cos(n\varphi)$	$(n+1)(n+2)r^n\sin(n\varphi)$	$r^{n+1} \begin{pmatrix} (\kappa-n-1)\sin(n\varphi) \\ -(\kappa+n+1)\cos(n\varphi) \end{pmatrix}$
$r^{-n+2}\cos(n\varphi)$	$-(n+2)(n-1)r^{-n}\cos(n\varphi)$	$-n(n-1)r^{-n}\sin(n\varphi)$	$(n-1)(n-2)r^{-n}\cos(n\varphi)$	$r^{-n+1} \begin{pmatrix} (\kappa+n-1)\cos(n\varphi) \\ -(\kappa-n+1)\sin(n\varphi) \end{pmatrix}$
$r^{-n+2}\sin(n\varphi)$	$-(n+2)(n-1)r^{-n}\sin(n\varphi)$	$n(n-1)r^{-n}\cos(n\varphi)$	$(n-1)(n-2)r^{-n}\sin(n\varphi)$	$r^{-n+1} \begin{pmatrix} (\kappa+n-1)\sin(n\varphi) \\ (\kappa-n+1)\cos(n\varphi) \end{pmatrix}$
$r^n\cos(n\varphi)$	$-n(n-1)r^{n-2}\cos(n\varphi)$	$n(n-1)r^{n-2}\sin(n\varphi)$	$n(n-1)r^{n-2}\cos(n\varphi)$	$r^{n-1} \begin{pmatrix} -n\cos(n\varphi) \\ n\sin(n\varphi) \end{pmatrix}$
$r^n\sin(n\varphi)$	$-n(n-1)r^{n-2}\sin(n\varphi)$	$-n(n-1)r^{n-2}\cos(n\varphi)$	$n(n-1)r^{n-2}\sin(n\varphi)$	$r^{n-1} \begin{pmatrix} -n\sin(n\varphi) \\ -n\cos(n\varphi) \end{pmatrix}$
$r^{-n}\cos(n\varphi)$	$-n(n+1)r^{-n-2}\cos(n\varphi)$	$-n(n+1)r^{-n-2}\sin(n\varphi)$	$n(n+1)r^{-n-2}\cos(n\varphi)$	$r^{-n-1} \begin{pmatrix} n\cos(n\varphi) \\ n\sin(n\varphi) \end{pmatrix}$
$r^{-n}\sin(n\varphi)$	$-n(n+1)r^{-n-2}\sin(n\varphi)$	$n(n+1)r^{-n-2}\cos(n\varphi)$	$n(n+1)r^{-n-2}\sin(n\varphi)$	$r^{-n-1} \begin{pmatrix} n\sin(n\varphi) \\ -n\cos(n\varphi) \end{pmatrix}$

polar coordinates centered at the i^{th} inclusion as

$$\begin{aligned} \chi_{\text{ext}}(r_i,\varphi_i) = &\frac{1}{4}(\sigma_{xx}^{\text{ext}}+\sigma_{yy}^{\text{ext}})r_i^2 \\ &-\frac{1}{4}(\sigma_{xx}^{\text{ext}}-\sigma_{yy}^{\text{ext}})r_i^2\cos(2\varphi_i) \\ &-\frac{1}{2}\sigma_{xy}^{\text{ext}}r_i^2\sin(2\varphi_i). \end{aligned} \tag{3.15}$$

This can be done with the help of Table 3.1, which shows the values of stresses and displacements corresponding to each term in the Michell solution [1]. In order to calculate the contributions from induced multipoles in other inclusions as well as all the contributions from image multipoles from the i^{th} and other inclusions, we need to expand expressions for the Airy stress functions $\chi_{\text{out}}\big(r_j,\varphi_j|\mathbf{a}_{j,\text{out}}\big)$ and $\mathcal{I}[\chi_{\text{out}}\big(r_j,\varphi_j|\mathbf{a}_{j,\text{out}}\big)]$ around the center $\mathbf{x}_i$ of the i^{th} inclusion. Polar coordinates (r_j,φ_j) centered at the j^{th} inclusion can be expressed in terms of polar coordinates

(r_i, φ_i) centered at the i^{th} inclusion as

$$\begin{aligned} r_j(r_i, \varphi_i) &= \sqrt{r_i^2 + a_{ij}^2 - 2 r_i a_{ij} \cos(\varphi_i - \theta_{ij})}, \\ \varphi_j(r_i, \varphi_i) &= \pi + \theta_{ij} - \arctan\left[\frac{r_i \sin(\varphi_i - \theta_{ij})}{\big(a_{ij} - r_i \cos(\varphi_i - \theta_{ij})\big)}\right], \end{aligned} \tag{3.16}$$

where $a_{ij} = \sqrt{(x_i - x_j)^2 + (y_i - y_j)^2}$ is the distance between the centers of the i^{th} and j^{th} inclusions and $\theta_{ij} = \arctan[(y_j - y_i)/(x_j - x_i)]$ is the angle between the line joining the centers of inclusions and the x-axis, as shown in Fig. 3.2. Similarly, polar coordinates (r_j^*, φ_j^*) centered at the image of the j^{th} inclusion can be expressed in terms of polar coordinates (r_i, φ_i) centered at the i^{th} inclusion as

$$\begin{aligned} r_j^*(r_i, \varphi_i) &= \sqrt{r_i^2 + {a_{ij}^*}^2 - 2 r_i a_{ij}^* \cos(\varphi_i - \theta_{ij}^*)}, \\ \varphi_j^*(r_i, \varphi_i) &= \pi + \theta_{ij}^* - \arctan\left[\frac{r_i \sin(\varphi_i - \theta_{ij}^*)}{\big(a_{ij}^* - r_i \cos(\varphi_i - \theta_{ij}^*)\big)}\right], \end{aligned} \tag{3.17}$$

where $a_{ij}^* = \sqrt{(x_i - x_j^*)^2 + (y_i - y_j^*)^2}$ is the distance between the centers of the i^{th} inclusion and the image of the j^{th} inclusion and $\theta_{ij}^* = \arctan[(y_j^* - y_i)/(x_j^* - x_i)]$ is the angle between the line joining these centers and the x-axis as shown in Fig. 3.2. The Airy stress functions $\chi_{\text{out}}\big(r_j, \varphi_j | \mathbf{a}_{j,\text{out}}\big)$ and $\mathcal{I}[\chi_{\text{out}}\big(r_j, \varphi_j | \mathbf{a}_{j,\text{out}}\big)]$ due to induced multi-

poles centered at the j^{th} inclusion and due to their image multipoles, respectively, can be expanded in Taylor series around the center of the i^{th} inclusion as [34, 49]

$$\begin{aligned}\chi_{\text{out}}\big(r_j(r_i,\varphi_i),\varphi_j(r_i,\varphi_i)|\mathbf{a}_{j,\text{out}}\big) =& \sum_{n=2}^{\infty} R_j^2 \frac{r_i^n}{a_{ij}^n}\Big[\cos(n\varphi_i) f_c^n\big(R_j/a_{ij},\theta_{ij}|\mathbf{a}_{j,\text{out}}\big) \\ &+ \sin(n\varphi_i) f_s^n\big(R_j/a_{ij},\theta_{ij}|\mathbf{a}_{j,\text{out}}\big)\Big] \\ &+ \sum_{n=0}^{\infty} R_j^2 \frac{r_i^{n+2}}{a_{ij}^{n+2}}\Big[\cos(n\varphi_i) g_c^n\big(R_j/a_{ij},\theta_{ij}|\mathbf{a}_{j,\text{out}}\big) \\ &+ \sin(n\varphi_i) g_s^n\big(R_j/a_{ij},\theta_{ij}|\mathbf{a}_{j,\text{out}}\big)\Big],\end{aligned} \tag{3.18a}$$

$$\begin{aligned}\mathcal{I}\left[\chi_{\text{out}}\big(r_j(r_i,\varphi_i),\varphi_j(r_i,\varphi_i)|\mathbf{a}_{j,\text{out}}\big)\right] =& \sum_{n=2}^{\infty} R_j^2 \frac{r_i^n}{a_{ij}^{*n}}\Big[\cos(n\varphi_i) f_c^n\big(R_j/a_{ij}^*,\theta_{ij}^*|\mathbf{a}_{j,\text{out}}^*\big) \\ &+ \sin(n\varphi_i) f_s^n\big(R_j/a_{ij}^*,\theta_{ij}^*|\mathbf{a}_{j,\text{out}}^*\big)\Big] \\ &+ \sum_{n=0}^{\infty} R_j^2 \frac{r_i^{n+2}}{a_{ij}^{*n+2}}\Big[\cos(n\varphi_i) g_c^n\big(R_j/a_{ij}^*,\theta_{ij}^*|\mathbf{a}_{j,\text{out}}^*\big) \\ &+ \sin(n\varphi_i) g_s^n\big(R_j/a_{ij}^*,\theta_{ij}^*|\mathbf{a}_{j,\text{out}}^*\big)\Big],\end{aligned} \tag{3.18b}$$

where we omitted constant and linear terms $\{1, r_i\cos\varphi_i, r_i\sin\varphi_i\}$ that correspond to zero stresses and we introduced functions

$$\begin{aligned}f_c^n\left(R_j/a_{ij},\theta_{ij}|\mathbf{a}_{j,\text{out}}\right) =& \sum_{m=0}^{\infty}\left(\frac{R_j^m}{a_{ij}^m}\Big[A_{j,m}\mathcal{A}_n^m(\theta_{ij}) + B_{j,m}\mathcal{B}_n^m(\theta_{ij})\Big]\right. \\ &\left.+ \frac{R_j^{m-2}}{a_{ij}^{m-2}}\Big[C_{j,m}\mathcal{C}_n^m(\theta_{ij}) + D_{j,m}\mathcal{D}_n^m(\theta_{ij})\Big]\right),\end{aligned} \tag{3.19a}$$

$$\begin{aligned}f_s^n\left(R_j/a_{ij},\theta_{ij}|\mathbf{a}_{j,\text{out}}\right) =& \sum_{m=0}^{\infty}\left(\frac{R_j^m}{a_{ij}^m}\Big[A_{j,m}\mathcal{B}_n^m(\theta_{ij}) - B_{j,m}\mathcal{A}_n^m(\theta_{ij})\Big]\right. \\ &\left.+ \frac{R_j^{m-2}}{a_{ij}^{m-2}}\Big[C_{j,m}\mathcal{D}_n^m(\theta_{ij}) - D_{j,m}\mathcal{C}_n^m(\theta_{ij})\Big]\right),\end{aligned} \tag{3.19b}$$

Table 3.2: Coefficients for the expansion of the Airy stress functions $\chi_{\text{out}}\big(r_j(r_i,\varphi_i),\varphi_j(r_i,\varphi_i)|\mathbf{a}_{j,\text{out}}\big)$ and $\mathcal{I}\left[\chi_{\text{out}}\big(r_j(r_i,\varphi_i),\varphi_j(r_i,\varphi_i)|\mathbf{a}_{j,\text{out}}\big)\right]$ in Eqs. (3.18-3.19).

$n\geq 2$	$\mathcal{A}_n^0(\theta_{ij})=-\frac{1}{n}\cos(n\theta_{ij})$	$\mathcal{B}_n^0(\theta_{ij})=-\frac{1}{n}\sin(n\theta_{ij})$
$n\geq 2, m\geq 1$	$\mathcal{A}_n^m(\theta_{ij})=(-1)^m\binom{m+n-1}{n}\cos\big((m+n)\theta_{ij}\big)$	$\mathcal{B}_n^m(\theta_{ij})=(-1)^m\binom{m+n-1}{n}\sin\big((m+n)\theta_{ij}\big)$
$n\geq 0, m\geq 2$	$\mathcal{C}_n^m(\theta_{ij})=(-1)^m\binom{m+n-2}{n}\cos\big((m+n)\theta_{ij}\big)$	$\mathcal{D}_n^m(\theta_{ij})=(-1)^m\binom{m+n-2}{n}\sin\big((m+n)\theta_{ij}\big)$
$n\geq 0, m\geq 2$	$\mathcal{E}_n^m(\theta_{ij})=(-1)^{m-1}\binom{m+n-1}{n+1}\cos\big((m+n)\theta_{ij}\big)$	$\mathcal{F}_n^m(\theta_{ij})=(-1)^{m-1}\binom{m+n-1}{n+1}\sin\big((m+n)\theta_{ij}\big)$

$$g_c^n\left(R_j/a_{ij},\theta_{ij}|\mathbf{a}_{j,\text{out}}\right)=\sum_{m=2}^{\infty}\frac{R_j^{m-2}}{a_{ij}^{m-2}}\Big[C_{j,m}\mathcal{E}_n^m(\theta_{ij})+D_{j,m}\mathcal{F}_n^m(\theta_{ij})\Big], \tag{3.19c}$$

$$g_s^n\left(R_j/a_{ij},\theta_{ij}|\mathbf{a}_{j,\text{out}}\right)=\sum_{m=2}^{\infty}\frac{R_j^{m-2}}{a_{ij}^{m-2}}\Big[C_{j,m}\mathcal{F}_n^m(\theta_{ij})-D_{j,m}\mathcal{E}_n^m(\theta_{ij})\Big]. \tag{3.19d}$$

In the above Eq. (3.19), we set $C_{j,0}=D_{j,0}=C_{j,1}=D_{j,1}=0$ and introduced coefficients $\mathcal{A}_n^m(\theta_{ij})$, $\mathcal{B}_n^m(\theta_{ij})$, $\mathcal{C}_n^m(\theta_{ij})$, $\mathcal{D}_n^m(\theta_{ij})$, $\mathcal{E}_n^m(\theta_{ij})$, and $\mathcal{F}_n^m(\theta_{ij})$ that are summarized in Table 3.2.

Next, we calculate stresses and displacements at the circumference of the i^{th} inclusion by using expressions for the Airy stress functions $\chi_{\text{ext}}(r_i,\varphi_i)$ in Eq. (3.15) due to external stresses, $\chi_{\text{in}}\big(r_i,\varphi_i|\mathbf{a}_{i,\text{in}}\big)$ and $\chi_{\text{out}}\big(r_i,\varphi_i|\mathbf{a}_{i,\text{out}}\big)$ in Eqs. (3.12) and Eq. (3.8) due to induced multipoles for the i^{th} inclusion, $\chi_{\text{out}}\big(r_j,\varphi_j|\mathbf{a}_{j,\text{out}}\big)$ in Eq. (3.18a) due to induced multipoles for the j^{th} inclusion ($j\neq i$), and $\mathcal{I}[\chi_{\text{out}}\big(r_j,\varphi_j|\mathbf{a}_{j,\text{out}}\big)]$ in Eq. (3.18b) due to image multipoles for the j^{th} inclusion ($j=1,\ldots,N$). With the help of Table 3.1, which shows how to convert each term of the Airy stress function to stresses and displacements, we obtain

$$\begin{aligned}\sigma_{\text{in},rr}^{\text{tot}}\big(r_i=R_i,\varphi_i|\mathbf{a}_{i,\text{in}}\big)=&\frac{1}{2}(\sigma_{xx}^{\text{ext}}+\sigma_{yy}^{\text{ext}})+\frac{1}{2}(\sigma_{xx}^{\text{ext}}-\sigma_{yy}^{\text{ext}})\cos(2\varphi_i)+\sigma_{xy}^{\text{ext}}\sin(2\varphi_i)+2c_{i,0}\\&-\sum_{n=1}^{\infty}\Big[n(n-1)\big(a_{i,n}\cos(n\varphi_i)+b_{i,n}\sin(n\varphi_i)\big)+(n+1)(n-2)\big(c_{i,n}\cos(n\varphi_i)+d_{i,n}\sin(n\varphi_i)\big)\Big],\end{aligned} \tag{3.20a}$$

$$\begin{aligned}\sigma_{\text{out},rr}^{\text{tot}}\big(r_i=R_i,\varphi_i|\mathbf{a}_{\text{out}}\big)=&\frac{1}{2}(\sigma_{xx}^{\text{ext}}+\sigma_{yy}^{\text{ext}})+\frac{1}{2}(\sigma_{xx}^{\text{ext}}-\sigma_{yy}^{\text{ext}})\cos(2\varphi_i)+\sigma_{xy}^{\text{ext}}\sin(2\varphi_i)+A_{i,0}\\&-\sum_{n=1}^{\infty}\Big[n(n+1)\big(A_{i,n}\cos(n\varphi_i)+B_{i,n}\sin(n\varphi_i)\big)+(n+2)(n-1)\big(C_{i,n}\cos(n\varphi_i)+D_{i,n}\sin(n\varphi_i)\big)\Big]\\&-\sum_{j\neq i}\sum_{n=2}^{\infty}\frac{R_j^2R_i^{n-2}}{a_{ij}^n}n(n-1)\Big[\cos(n\varphi_i)f_c^n\left(R_j/a_{ij},\theta_{ij}|\mathbf{a}_{j,\text{out}}\right)+\sin(n\varphi_i)f_s^n\left(R_j/a_{ij},\theta_{ij}|\mathbf{a}_{j,\text{out}}\right)\Big]\end{aligned}$$

$$
\begin{aligned}
&- \sum_{j\neq i}\sum_{n=0}^{\infty} \frac{R_j^2 R_i^n}{a_{ij}^{n+2}}(n+1)(n-2)\Big[\cos(n\varphi_i) g_c^n\big(R_j/a_{ij},\theta_{ij}|\mathbf{a}_{j,\text{out}}\big) + \sin(n\varphi_i) g_s^n\big(R_j/a_{ij},\theta_{ij}|\mathbf{a}_{j,\text{out}}\big)\Big] \\
&- \sum_{j=1}^{N}\sum_{n=2}^{\infty} \frac{R_j^2 R_i^{n-2}}{a_{ij}^{*n}} n(n-1)\Big[\cos(n\varphi_i) f_c^n\big(R_j/a_{ij}^*,\theta_{ij}^*|\mathbf{a}_{j,\text{out}}^*\big) + \sin(n\varphi_i) f_s^n\big(R_j/a_{ij}^*,\theta_{ij}^*|\mathbf{a}_{j,\text{out}}^*\big)\Big] \\
&- \sum_{j=1}^{N}\sum_{n=0}^{\infty} \frac{R_j^2 R_i^n}{a_{ij}^{*n+2}}(n+1)(n-2)\Big[\cos(n\varphi_i) g_c^n\big(R_j/a_{ij}^*,\theta_{ij^*}|\mathbf{a}_{j,\text{out}}^*\big) + \sin(n\varphi_i) g_s^n\big(R_j/a_{ij}^*,\theta_{ij}^*|\mathbf{a}_{j,\text{out}}^*\big)\Big],
\end{aligned}
\tag{3.20b}
$$

$$
\begin{aligned}
\sigma_{\text{in},r\varphi}^{\text{tot}}\big(r_i = R_i,\varphi_i|\mathbf{a}_{i,\text{in}}\big) &= -\frac{1}{2}(\sigma_{xx}^{\text{ext}} - \sigma_{yy}^{\text{ext}})\sin(2\varphi_i) + \sigma_{xy}^{\text{ext}}\cos(2\varphi_i) \\
&+ \sum_{n=1}^{\infty}\Big[n(n-1)\big(a_{i,n}\sin(n\varphi_i) - b_{i,n}\cos(n\varphi_i)\big) + n(n+1)\big(c_{i,n}\sin(n\varphi_i) - d_{i,n}\cos(n\varphi_i)\big)\Big],
\end{aligned}
\tag{3.20c}
$$

$$
\begin{aligned}
\sigma_{\text{out},r\varphi}^{\text{tot}}\big(r_i = R_i,\varphi_i|\mathbf{a}_{\text{out}}\big) &= -\frac{1}{2}(\sigma_{xx}^{\text{ext}} - \sigma_{yy}^{\text{ext}})\sin(2\varphi_i) + \sigma_{xy}^{\text{ext}}\cos(2\varphi_i) \\
&- \sum_{n=1}^{\infty}\Big[n(n+1)\big(A_{i,n}\sin(n\varphi_i) - B_{i,n}\cos(n\varphi_i)\big) + n(n-1)\big(C_{i,n}\sin(n\varphi_i) - D_{i,n}\cos(n\varphi_i)\big)\Big] \\
&+ \sum_{j\neq i}\sum_{n=2}^{\infty} \frac{R_j^2 R_i^{n-2}}{a_{ij}^{n}} n(n-1)\Big[\sin(n\varphi_i) f_c^n\big(R_j/a_{ij},\theta_{ij}|\mathbf{a}_{j,\text{out}}\big) - \cos(n\varphi_i) f_s^n\big(R_j/a_{ij},\theta_{ij}|\mathbf{a}_{j,\text{out}}\big)\Big] \\
&+ \sum_{j\neq i}\sum_{n=0}^{\infty} \frac{R_j^2 R_i^{n}}{a_{ij}^{n+2}} n(n+1)\Big[\sin(n\varphi_i) g_c^n\big(R_j/a_{ij},\theta_{ij}|\mathbf{a}_{j,\text{out}}\big) - \cos(n\varphi_i) g_s^n\big(R_j/a_{ij},\theta_{ij}|\mathbf{a}_{j,\text{out}}\big)\Big] \\
&+ \sum_{j=1}^{N}\sum_{n=2}^{\infty} \frac{R_j^2 R_i^{n-2}}{a_{ij}^{*n}} n(n-1)\Big[\sin(n\varphi_i) f_c^n\big(R_j/a_{ij}^*,\theta_{ij}^*|\mathbf{a}_{j,\text{out}}^*\big) - \cos(n\varphi_i) f_s^n\big(R_j/a_{ij}^*,\theta_{ij}^*|\mathbf{a}_{j,\text{out}}^*\big)\Big] \\
&+ \sum_{j=1}^{N}\sum_{n=0}^{\infty} \frac{R_j^2 R_i^{n}}{a_{ij}^{*n+2}} n(n+1)\Big[\sin(n\varphi_i) g_c^n\big(R_j/a_{ij}^*,\theta_{ij}^*|\mathbf{a}_{j,\text{out}}^*\big) - \cos(n\varphi_i) g_s^n\big(R_j/a_{ij}^*,\theta_{ij}^*|\mathbf{a}_{j,\text{out}}^*\big)\Big],
\end{aligned}
\tag{3.20d}
$$

$$
\begin{aligned}
\frac{2\mu_i}{R_i}\, u_{\text{in},r}^{\text{tot}}\big(r_i = R_i,\varphi_i|\mathbf{a}_{i,\text{in}}\big) &= -\frac{1}{4}(\sigma_{xx}^{\text{ext}} + \sigma_{yy}^{\text{ext}})(1-\kappa_i) + \frac{1}{2}(\sigma_{xx}^{\text{ext}} - \sigma_{yy}^{\text{ext}})\cos(2\varphi_i) + \sigma_{xy}^{\text{ext}}\sin(2\varphi_i) + c_{i,0}(\kappa_i - 1) \\
&- \sum_{n=1}^{\infty}\Big[n\big(a_{i,n}\cos(n\varphi_i) + b_{i,n}\sin(n\varphi_i)\big) + (n+1-\kappa_i)\big(c_{i,n}\cos(n\varphi_i) + d_{i,n}\sin(n\varphi_i)\big)\Big],
\end{aligned}
\tag{3.20e}
$$

$$
\begin{aligned}
\frac{2\mu_0}{R_i}\, u_{\text{out},r}^{\text{tot}}\big(r_i = R_i,\varphi_i|\mathbf{a}_{\text{out}}\big) &= -\frac{1}{4}(\sigma_{xx}^{\text{ext}} + \sigma_{yy}^{\text{ext}})(1-\kappa_0) + \frac{1}{2}(\sigma_{xx}^{\text{ext}} - \sigma_{yy}^{\text{ext}})\cos(2\varphi_i) + \sigma_{xy}^{\text{ext}}\sin(2\varphi_i) - A_{i,0} \\
&+ \sum_{n=1}^{\infty}\Big[n\big(A_{i,n}\cos(n\varphi_i) + B_{i,n}\sin(n\varphi_i)\big) + (n-1+\kappa_0)\big(C_{i,n}\cos(n\varphi_i) + D_{i,n}\sin(n\varphi_i)\big)\Big] \\
&- \sum_{j\neq i}\sum_{n=2}^{\infty} \frac{R_j^2 R_i^{n-2}}{a_{ij}^{n}} n\Big[\cos(n\varphi_i) f_c^n\big(R_j/a_{ij},\theta_{ij}|\mathbf{a}_{j,\text{out}}\big) + \sin(n\varphi_i) f_s^n\big(R_j/a_{ij},\theta_{ij}|\mathbf{a}_{j,\text{out}}\big)\Big] \\
&- \sum_{j\neq i}\sum_{n=0}^{\infty} \frac{R_j^2 R_i^{n}}{a_{ij}^{n+2}} (n+1-\kappa_0)\Big[\cos(n\varphi_i) g_c^n\big(R_j/a_{ij},\theta_{ij}|\mathbf{a}_{j,\text{out}}\big) + \sin(n\varphi_i) g_s^n\big(R_j/a_{ij},\theta_{ij}|\mathbf{a}_{j,\text{out}}\big)\Big]
\end{aligned}
$$

$$
\begin{aligned}
&-\sum_{j=1}^{N}\sum_{n=2}^{\infty}\frac{R_j^2 R_i^{n-2}}{a_{ij}^{*n}}n\Big[\cos(n\varphi_i)f_c^n\big(R_j/a_{ij}^*,\theta_{ij}^*|\mathbf{a}_{j,\mathrm{out}}^*\big)+\sin(n\varphi_i)f_s^n\big(R_j/a_{ij}^*,\theta_{ij}^*|\mathbf{a}_{j,\mathrm{out}}^*\big)\Big]\\
&-\sum_{j=1}^{N}\sum_{n=0}^{\infty}\frac{R_j^2 R_i^{n}}{a_{ij}^{*n+2}}(n+1-\kappa_0)\Big[\cos(n\varphi_i)g_c^n\big(R_j/a_{ij}^*,\theta_{ij}^*|\mathbf{a}_{j,\mathrm{out}}^*\big)+\sin(n\varphi_i)g_s^n\big(R_j/a_{ij}^*,\theta_{ij}^*|\mathbf{a}_{j,\mathrm{out}}^*\big)\Big],
\end{aligned}
\tag{3.20f}
$$

$$
\begin{aligned}
\frac{2\mu_i}{R_i}\,u_{\mathrm{in},\varphi}^{\mathrm{tot}}\big(r_i=R_i,\varphi_i|\mathbf{a}_{i,\mathrm{in}}\big)&=-\frac{1}{2}(\sigma_{xx}^{\mathrm{ext}}-\sigma_{yy}^{\mathrm{ext}})\sin(2\varphi_i)+\sigma_{xy}^{\mathrm{ext}}\cos(2\varphi_i)\\
&+\sum_{n=1}^{\infty}\Big[n\big(a_{i,n}\sin(n\varphi_i)-b_{i,n}\cos(n\varphi_i)\big)+(n+1+\kappa_i)\big(c_{i,n}\sin(n\varphi_i)-d_{i,n}\cos(n\varphi_i)\big)\Big],
\end{aligned}
\tag{3.20g}
$$

$$
\begin{aligned}
\frac{2\mu_0}{R_i}\,u_{\mathrm{out},\varphi}^{\mathrm{tot}}\big(r_i=R_i,\varphi_i|\mathbf{a}_{\mathrm{out}}\big)&=-\frac{1}{2}(\sigma_{xx}^{\mathrm{ext}}-\sigma_{yy}^{\mathrm{ext}})\sin(2\varphi_i)+\sigma_{xy}^{\mathrm{ext}}\cos(2\varphi_i)\\
&+\sum_{n=1}^{\infty}\Big[n\big(A_{i,n}\sin(n\varphi_i)-B_{i,n}\cos(n\varphi_i)\big)+(n-1-\kappa_0)\big(C_{i,n}\sin(n\varphi_i)-D_{i,n}\cos(n\varphi_i)\big)\Big]\\
&+\sum_{j\neq i}\sum_{n=2}^{\infty}\frac{R_j^2 R_i^{n-2}}{a_{ij}^{n}}n\Big[\sin(n\varphi_i)f_c^n\big(R_j/a_{ij},\theta_{ij}|\mathbf{a}_{j,\mathrm{out}}\big)-\cos(n\varphi_i)f_s^n\big(R_j/a_{ij},\theta_{ij}|\mathbf{a}_{j,\mathrm{out}}\big)\Big]\\
&+\sum_{j\neq i}\sum_{n=0}^{\infty}\frac{R_j^2 R_i^{n}}{a_{ij}^{n+2}}(n+1+\kappa_0)\Big[\sin(n\varphi_i)g_c^n\big(R_j/a_{ij},\theta_{ij}|\mathbf{a}_{j,\mathrm{out}}\big)-\cos(n\varphi_i)g_s^n\big(R_j/a_{ij},\theta_{ij}|\mathbf{a}_{j,\mathrm{out}}\big)\Big]\\
&+\sum_{j=1}^{N}\sum_{n=2}^{\infty}\frac{R_j^2 R_i^{n-2}}{a_{ij}^{*n}}n\Big[\sin(n\varphi_i)f_c^n\big(R_j/a_{ij}^*,\theta_{ij}^*|\mathbf{a}_{j,\mathrm{out}}^*\big)-\cos(n\varphi_i)f_s^n\big(R_j/a_{ij}^*,\theta_{ij}^*|\mathbf{a}_{j,\mathrm{out}}^*\big)\Big]\\
&+\sum_{j=1}^{N}\sum_{n=0}^{\infty}\frac{R_j^2 R_i^{n}}{a_{ij}^{*n+2}}(n+1+\kappa_0)\Big[\sin(n\varphi_i)g_c^n\big(R_j/a_{ij}^*,\theta_{ij}^*|\mathbf{a}_{j,\mathrm{out}}^*\big)-\cos(n\varphi_i)g_s^n\big(R_j/a_{ij}^*,\theta_{ij}^*|\mathbf{a}_{j,\mathrm{out}}^*\big)\Big].
\end{aligned}
\tag{3.20h}
$$

Colors in the above equations correspond to the Airy stress functions $\chi_{\mathrm{ext}}(r_i,\varphi_i)$, $\chi_{\mathrm{in}}\big(r_i,\varphi_i|\mathbf{a}_{i,\mathrm{in}}\big)$, $\chi_{\mathrm{out}}\big(r_i,\varphi_i|\mathbf{a}_{i,\mathrm{out}}\big)$, $\chi_{\mathrm{out}}\big(r_j,\varphi_j|\mathbf{a}_{j,\mathrm{out}}\big)$, and $\mathcal{I}\left[\chi_{\mathrm{out}}\big(r_j,\varphi_j|\mathbf{a}_{j,\mathrm{out}}\big)\right]$. We introduced the shear modulus $\mu_i=E_i/[2(1+\nu_i)]$ and the Kolosov's constant κ_i for the i^{th} inclusion, where the value of Kolosov's constant is $\kappa_i=(3-\nu_i)/(1+\nu_i)$ for plane stress and $\kappa_i=3-4\nu_i$ for plane strain conditions [1]. Similarly, we define the shear modulus $\mu_0=E_0/[2(1+\nu_0)]$ and the Kolosov's constant κ_0 for the elastic matrix.

The boundary conditions in Eq. (3.14) have to be satisfied at every point (φ_i) on the circumference of the i^{th} inclusion. Thus the coefficients of Fourier modes

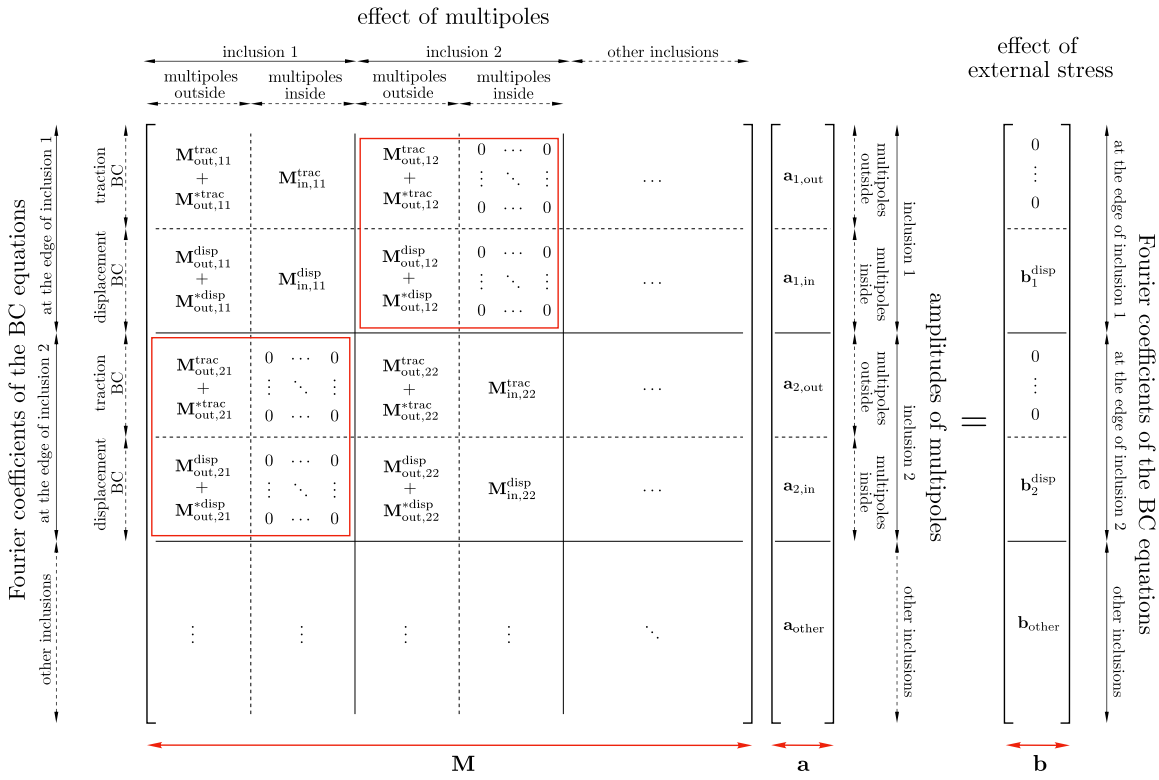

Figure 3.3: Structure of the system of Eqs. (3.21) for the amplitudes of induced multipoles $\mathbf{a}_{i,\mathrm{out}}$, $\mathbf{a}_{i,\mathrm{in}}$ for inclusions $i \in \{1, \ldots, N\}$. The matrix $\mathbf{M}$ is divided into $4N^2$ blocks, where blocks $\mathbf{M}^{\mathrm{trac}}_{\mathrm{in},ij}$ and $\mathbf{M}^{\mathrm{trac}}_{\mathrm{out},ij} + \mathbf{M}^{*\mathrm{trac}}_{\mathrm{out},ij}$ correspond to the boundary conditions for tractions around the circumference of the i^{th} inclusion in Eq. (3.14a, 3.14b), and blocks $\mathbf{M}^{\mathrm{disp}}_{\mathrm{in},ij}$ and $\mathbf{M}^{\mathrm{disp}}_{\mathrm{out},ij} + \mathbf{M}^{*\mathrm{disp}}_{\mathrm{out},ij}$ correspond to the boundary conditions for displacements around the circumference of the i^{th} inclusion in Eq. (3.14c, 3.14d). The red boxes mark blocks with $i \neq j$ that account for the interactions between different inclusions. The effect of external stresses is contained in vectors $\mathbf{b}^{\mathrm{disp}}_i$. See text for the detailed description of elements represented in this system of equations.

$\{1, \cos(n\varphi_i), \sin(n\varphi_i)\}$ have to match in the expansions of tractions and displacements in Eq. (3.20). This enables us to construct a matrix equation for the set of induced multipoles $\{\mathbf{a}_{i,\mathrm{out}}, \mathbf{a}_{i,\mathrm{in}}\}$ in the form (see also Fig. 3.3)

$$\begin{pmatrix} \mathbf{M}^{\mathrm{trac}}_{\mathrm{out},ij} + \mathbf{M}^{*\mathrm{trac}}_{\mathrm{out},ij}, & \mathbf{M}^{\mathrm{trac}}_{\mathrm{in},ij} \\ \mathbf{M}^{\mathrm{disp}}_{\mathrm{out},ij} + \mathbf{M}^{*\mathrm{disp}}_{\mathrm{out},ij}, & \mathbf{M}^{\mathrm{disp}}_{\mathrm{in},ij} \end{pmatrix} \begin{pmatrix} \mathbf{a}_{j,\mathrm{out}} \\ \mathbf{a}_{j,\mathrm{in}} \end{pmatrix} = \begin{pmatrix} \mathbf{0} \\ \mathbf{b}^{\mathrm{disp}}_i \end{pmatrix}, \tag{3.21}$$

where the summation over inclusions j is implied. The top and bottom rows of matrix $\mathbf{M}$ in the above equation are obtained from the boundary conditions in Eq. (3.14) for

tractions (superscript 'trac') and displacements (superscript 'disp'), respectively. The left and right columns of matrix $\mathbf{M}$ describe the effect of induced multipoles $\mathbf{a}_{j,\text{out}}$ and $\mathbf{a}_{j,\text{in}}$, respectively. Matrices $\mathbf{M}^{*}_{ij}$ describe interactions between the i^{th} inclusion and the image of the j^{th} inclusion; these are new compared to the previous chapter 2. Note that each inclusion interacts with its image as well as with images of other inclusions. The entries in matrices $\mathbf{M}^{\text{trac}}_{\text{out},ii}$, $\mathbf{M}^{*\text{trac}}_{\text{out},ii}$, and $\mathbf{M}^{\text{trac}}_{\text{in},ii}$ for the i^{th} inclusion are numbers that depend on the degrees of induced multipoles. The entries in matrices $\mathbf{M}^{\text{disp}}_{\text{out},ii}$, $\mathbf{M}^{*\text{disp}}_{\text{out},ii}$, and $\mathbf{M}^{\text{disp}}_{\text{in},ii}$ for the i^{th} inclusion depend on the degrees of induced multipoles, the radius of inclusion R_i and the material properties of the inclusion (μ_i, κ_i) and elastic matrix (μ_0, κ_0). Additionally, the entries in matrices $\mathbf{M}^{*\text{trac}}_{\text{out},ii}$ and $\mathbf{M}^{*\text{disp}}_{\text{out},ii}$ also depend on the distance h_i from the center of the i^{th} inclusion to the boundary. Matrices $\mathbf{M}^{\text{trac}}_{\text{out},ij}$ and $\mathbf{M}^{\text{disp}}_{\text{out},ij}$ encode the interactions between inclusions i and j. The entries in these matrices depend on the degrees of induced multipoles, the radii R_i and R_j of inclusions, the angle θ_{ij}, and the separation distance a_{ij} between inclusions (see Fig. 3.2). In addition to that, the entries in matrix $\mathbf{M}^{\text{disp}}_{\text{out},ij}$ also depend on the material properties of the elastic matrix (μ_0, κ_0). Matrices $\mathbf{M}^{*\text{trac}}_{\text{out},ij}$ and $\mathbf{M}^{*\text{disp}}_{\text{out},ij}$ describe the interaction between the i^{th} inclusion and the image of the j^{th} inclusion. These matrices depend on the degrees of image multipoles, the radii R_i and R_j of inclusions, the distance h_j from the center of the j^{th} inclusion to the boundary, the angle θ^{*}_{ij}, and the separation distance a^{*}_{ij} between the i^{th} inclusion and the image of the j^{th} inclusion (see Fig. 3.2). Matrices $\mathbf{M}^{*\text{disp}}_{\text{out},ij}$ additionally depend on the material properties of the elastic matrix (μ_0, κ_0). Note that the other matrices are zero, i.e. $\mathbf{M}^{\text{trac}}_{\text{in},ij} = \mathbf{M}^{\text{disp}}_{\text{in},ij} = 0$. The entries in vector $\mathbf{b}^{\text{disp}}_{i}$ depend on the magnitude of external stresses $(\sigma^{\text{ext}}_{xx}, \sigma^{\text{ext}}_{yy}, \sigma^{\text{ext}}_{xy})$, the degrees of induced multipoles, the radius of inclusion R_i, and the material properties of the inclusion (μ_i, κ_i) and elastic matrix (μ_0, κ_0). Note that in $\mathbf{b}^{\text{disp}}_{i}$ the only nonzero entries are the ones that correspond to Fourier modes 1, $\cos(2\varphi_i)$, and $\sin(2\varphi_i)$.

To numerically solve the system of equations for induced multipoles in Eq. (3.21) we truncate the multipole expansion at degree $n_{\max}$. For each inclusion i, there are $4n_{\max}-1$ unknown amplitudes of multipoles $\mathbf{a}_{i,\text{out}} = \{A_{i,0}, A_{i,1}, \ldots, A_{i,n_{\max}}, B_{i,1}, B_{i,2}, \ldots, B_{i,n_{\max}}, C_{i,2}, C_{i,3}, \ldots, C_{i,n_{\max}}, D_{i,2}, D_{i,3}, \ldots, D_{i,n_{\max}}\}$ and $4n_{\max}-1$ unknown amplitudes of multipoles $\mathbf{a}_{i,\text{in}} = \{a_{i,2}, a_{i,3}, \ldots, a_{i,n_{\max}}, b_{i,2}, b_{i,3}, \ldots, b_{i,n_{\max}}, c_{i,0}, c_{i,1}, \ldots, c_{i,n_{\max}}, d_{i,1}, d_{i,2}, \ldots, d_{i,n_{\max}}\}$. Furthermore, we truncate the series for the Airy stress function of image multipoles $\mathcal{I}\left[\chi_{\text{out}}\left(r_i, \varphi_i|\mathbf{a}_{i,\text{out}}\right)\right]$ in Eq. (3.9) as well as the Taylor expansions for the Airy stress functions $\chi_{\text{out}}\left(r_j(r_i,\varphi_i), \varphi_j(r_i,\varphi_i)|\mathbf{a}_{j,\text{out}}\right)$ and $\mathcal{I}\left[\chi_{\text{out}}\left(r_j(r_i,\varphi_i), \varphi_j(r_i,\varphi_i)|\mathbf{a}_{j,\text{out}}\right)\right]$ in Eq. (3.18) at the same order $n_{\max}$. By matching the coefficients of Fourier modes $\{1, \cos\varphi_i, \sin\varphi_i, \ldots, \cos(n_{\max}\varphi_i), \sin(n_{\max}\varphi_i)\}$ in the expansions for tractions and displacements in Eq. (3.20) around the circumference of the i^{th} inclusion, we in principle get $2(2n_{\max}+1)$ equations from tractions and $2(2n_{\max}+1)$ equations from displacements. However, the zero Fourier modes for $\sigma_{r\varphi}$ and u_φ are equal to zero. Furthermore, the coefficients of Fourier modes $\cos\varphi_i$ and $\sin\varphi_i$ are identical for each of the σ_{rr}, $\sigma_{r\varphi}$, u_r, and u_φ in Eq. (3.20). By removing the equations, which do not provide any new information, the dimensions of matrices $\mathbf{M}^{\text{trac}}_{\text{out},ij}$, $\mathbf{M}^{*\text{trac}}_{\text{out},ij}$, $\mathbf{M}^{\text{trac}}_{\text{in},ij}$, $\mathbf{M}^{\text{disp}}_{\text{out},ij}$, $\mathbf{M}^{*\text{disp}}_{\text{out},ij}$, and $\mathbf{M}^{\text{disp}}_{\text{in},ij}$, become $(4n_{\max}-1)\times(4n_{\max}-1)$. Thus Eq. (3.21) describes the system of $N(8n_{\max}-2)$ equations for the amplitudes of induced multipoles $\{\mathbf{a}_{1,\text{out}}, \mathbf{a}_{1,\text{in}}, \ldots, \mathbf{a}_{N,\text{out}}, \mathbf{a}_{N,\text{in}}\}$. The solution of this system of equations gives amplitudes of induced multipoles, which are linear functions of applied loads σ^{ext}_{xx}, σ^{ext}_{yy}, and σ^{ext}_{xy}. These amplitudes are then used to obtain the Airy stress functions $\chi^{\text{tot}}_{\text{in}}\left(x, y|\mathbf{a}_{i,\text{in}}\right)$ in Eq. (3.13) inside inclusions and $\chi^{\text{tot}}_{\text{out}}\left(x, y|\mathbf{a}_{\text{out}}\right)$ in Eq. (3.11) outside all inclusions, which enables us to calculate stresses and displacements everywhere in the structure. The accuracy of obtained results depends on the number $n_{\max}$ for the maximum degree of induced multipoles, where larger number $n_{\max}$ yields more accurate results. In the next sections, we compare results obtained with the method described above with linear finite element simulations and experiments.

Comparison with linear finite element simulations and experiments

First, we tested the elastic multipole method for one circular hole of radius R embedded in a semi-infinite plate ($y < 0$) subjected to uniaxial stress σ_{xx}^{ext} (see Fig. 3.4). This way we investigated how a single hole interacts with its image near a traction-free edge ($\sigma_{xy}^{\text{ext}}(x,0) = \sigma_{yy}^{\text{ext}}(x,0) = 0$). Three different values of the separation distance h between the center of the hole and the traction-free edge were considered: $h = 4R$, $h = 2R$, and $h = 1.25R$. The value of applied uniaxial stress was $\sigma_{xx}^{\text{ext}} = -0.11E_0$, where E_0 is the Young's modulus of the elastic matrix, and we used the plane stress condition with the value of Kolosov's constant $\kappa_0 = (3-\nu_0)/(1+\nu_0)$ and the Poisson's ratio $\nu_0 = 0.3$. Such large values of external loads were used only to exaggerate deformations. Note that in practical experiments these loads would cause nonlinear deformation.

In Fig. 3.4 we show the contours of deformed holes and the amplitudes of induced multipoles $\mathbf{a}_{\text{out}}$ for different values of the separation distance h between the center of the hole and the traction-free edge, where we set $n_{\max} = 10$. Note that the amplitudes $\mathbf{a}_{\text{in}} = \mathbf{0}$ because the Young's modulus is zero for the hole. Results from the elastic multipole method are compared with linear finite element simulations on a rectangular domain of size $800R \times 400R$ (see Appendix B.1 for details). When the hole is far from the traction-free edge ($h \gg R$) it interacts very weakly with its image, which can be seen from the expansion of stresses and displacements in Eq. (3.20), where terms describing interactions between the i^{th} inclusions and its image contain powers of $R_i/a_{ii}^* \ll 1$, where $a_{ii}^* = 2h$. This is the case for the separation distance $h = 4R$, where we find that the contour of the hole has elliptical shape (see Fig. 3.4b), which is characteristic for deformed holes embedded in an infinite elastic matrix [16, 49]. When the hole is moved closer to the traction-free edge ($h = 2R$, $h = 1.25R$) it interacts more strongly with its image. As a consequence, the contour of the deformed hole becomes progressively more non-elliptical, approaching a teardrop shape, and the

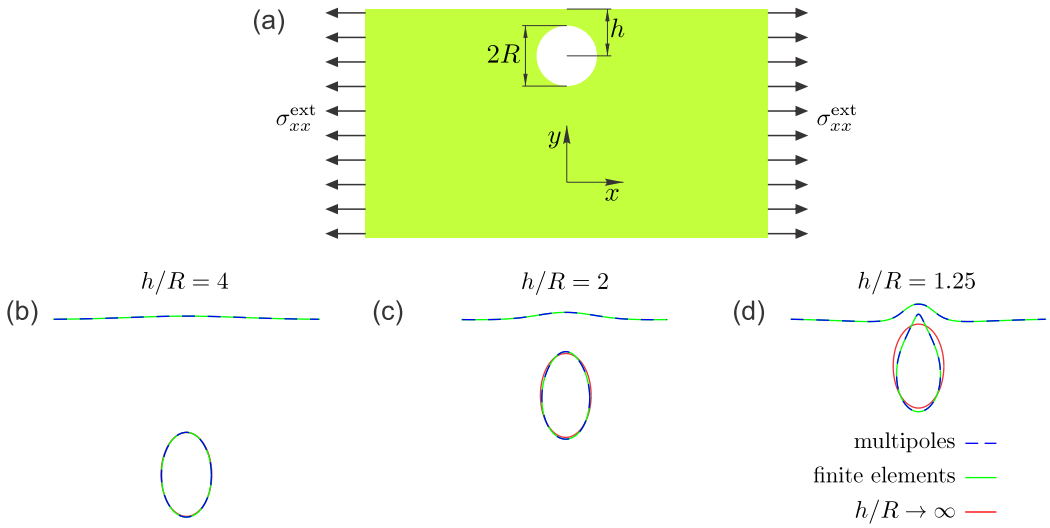

Figure 3.4: Uniaxial deformation of a semi-infinite elastic plate with a hole near a traction free edge. (a) Schematic image describing the initial undeformed shape of the structure and the direction of applied load $\sigma_{xx}^{\text{ext}} = -0.11E_0$, where E_0 is the Young's modulus of the elastic matrix, it's Poisson's ratio is $\nu_0 = 0.3$, and plane stress condition was used. The radius of the circular hole is R, which is at the distance h from the traction-free edge. (b)-(d) Contours of deformed holes and deformed boundaries for $h/R = 4$, 2 and 1.25. Dashed blue lines show the contours obtained with elastic multipole method for $n_{\max} = 10$ and green solid lines show the contours obtained from finite element simulations. As a reference, we include red solid lines that correspond to shapes of holes that are far away from edges ($h/R \to \infty$).

traction-free edge bulges out near the hole (see Fig. 3.4c,d). This is also reflected in the amplitudes $\mathbf{a}_{\text{out}}$ of induced multipoles. They decrease exponentially with the degree of multipoles and decrease more slowly when the hole is closer to the traction-free edge (Fig. 3.5a-c).

To determine the proper number for the maximum degree $n_{\max}$ of induced multipoles, we performed a convergence analysis for the spatial distributions of displacements $\mathbf{u}^{(n_{\max})}(x, y)$ and von Mises stress $\sigma_{\text{vM}}^{(n_{\max})}(x, y)$, where $\sigma_{\text{vM}} = (\sigma_{xx}^2 - \sigma_{xx}\sigma_{yy} + \sigma_{yy}^2 + 3\sigma_{xy}^2)^{1/2}$. Displacements and von Mises stresses were evaluated at N_p discrete points $(x_i, y_j) = (iR/50, jR/50)$, where $i \in \{-500, -499, \ldots, 500\}$ and $j \in \{-1000, -999, \ldots, 0\}$ and grid points that lie inside the hole were excluded. The normalized errors for displacements $\epsilon_{\text{disp}}(n_{\max})$ and stresses $\epsilon_{\text{stress}}(n_{\max})$ were obtained by calculating the relative changes of spatial distributions of displacements

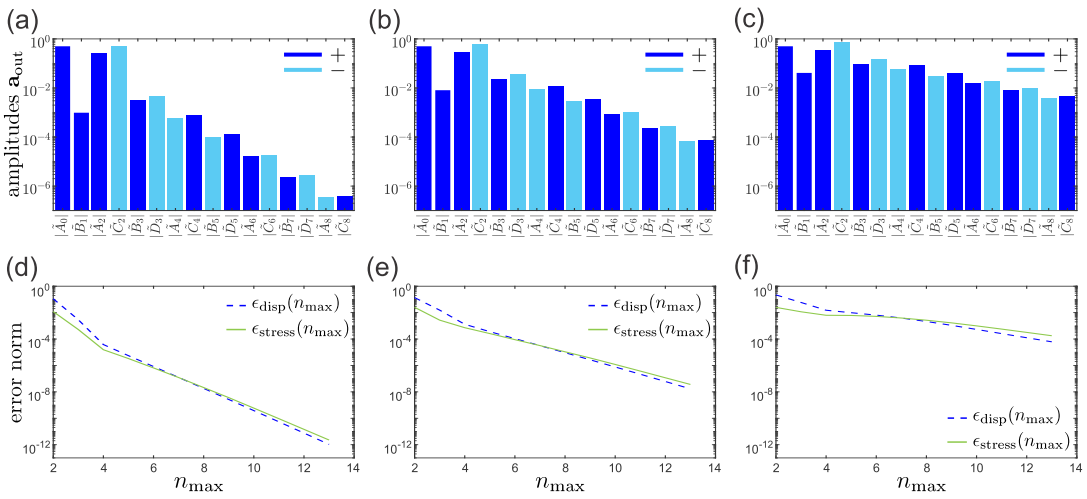

Figure 3.5: Amplitudes of the multipoles and normalized errors for the deformation of the structure with one hole near a traction free edge considered in Fig. 3.4. (a-c) Absolute values of the amplitudes of induced multipoles $\mathbf{a}_{\text{out}}$ at the center of the hole for $n_{\max} = 10$. Amplitudes are normalized, such that $\tilde{A}_n = A_n/\sigma_{xx}^{\text{ext}}$, $\tilde{B}_n = B_n/\sigma_{xx}^{\text{ext}}$, $\tilde{C}_n = C_n/\sigma_{xx}^{\text{ext}}$, $\tilde{D}_n = D_n/\sigma_{xx}^{\text{ext}}$. The dark and light blue colored bars correspond to the positive $(A_n, B_n, C_n, D_n > 0)$ and negative $(A_n, B_n, C_n, D_n < 0)$ amplitudes, respectively. Note that the amplitudes $B_{2m} = D_{2m} = A_{2m+1} = C_{2m+1} = 0$ due to the symmetry of the problem. (d-f) The normalized errors for displacements $\epsilon_{\text{disp}}(n_{\max})$ (blue dashed lines) and stresses $\epsilon_{\text{stress}}(n_{\max})$ (green solid lines) obtained from Eq. (3.22). The left column corresponds to results for $h/R = 4$, the middle column to $h/R = 2$ and the right column to $h/R = 1.25$.

and von Mises stresses when the maximum degree $n_{\max}$ of induced multipoles is increased by one. The normalized errors are given by [129]

$$\epsilon_{\text{disp}}(n_{\max}) = \sqrt{\sum_{i,j} \frac{\left(\mathbf{u}^{(n_{\max}+1)}(x_i, y_j) - \mathbf{u}^{(n_{\max})}(x_i, y_j)\right)^2}{N_p (d\,\sigma_{\text{vM}}^{\text{ext}}/E_0)^2}}, \tag{3.22a}$$

$$\epsilon_{\text{stress}}(n_{\max}) = \sqrt{\sum_{i,j} \frac{\left(\sigma_{\text{vM}}^{(n_{\max}+1)}(x_i, y_j) - \sigma_{\text{vM}}^{(n_{\max})}(x_i, y_j)\right)^2}{N_p (\sigma_{\text{vM}}^{\text{ext}})^2}}. \tag{3.22b}$$

Here, displacements and von Mises stresses are normalized by the characteristic scales $d\sigma_{\text{vM}}^{\text{ext}}/E_0$ and $\sigma_{\text{vM}}^{\text{ext}}$, respectively, where $d = 2R$ is the diameter of the hole, $\sigma_{\text{vM}}^{\text{ext}} = |\sigma_{xx}^{\text{ext}}|$ is the value of von Mises stress due to applied load, and E_0 is the Young's modulus of surrounding elastic matrix. The normalized errors are plotted in Fig. 3.5d-f. As the maximum degree $n_{\max}$ of induced multipoles is increased, the normalized errors for

displacements $\epsilon_{\text{disp}}(n_{\max})$ and stresses $\epsilon_{\text{stress}}(n_{\max})$ decrease exponentially, because the induced elastic multipoles form the basis for the biharmonic equation. This is akin to the spectral method, which is exponentially convergent when the functions and the shapes of boundaries are smooth [129]. Note that the normalized errors decrease more slowly when the hole is moved closer to the traction-free edge and the interaction of hole with its image becomes important (see Fig. 3.5d-f), which is reflected in larger magnitudes of amplitudes of higher-order multipoles (Fig. 3.5a-c).

Additionally, we compared the results of the elastic multipole method with experiments (see Appendix B.2 for details). The size of the elastomer sample in the experiment was 100 mm $\times$ 100 mm $\times$ 25 mm with the hole of diameter $2R = 8.11$ mm, and the distance between the center of the hole and the traction-free edge was $h = 6.25$ mm (see Fig. 3.6a). The contour of the deformed hole in the compressed experimental sample under external strain $\varepsilon_{xx}^{\text{ext}} = -0.05$ ($\sigma_{xy}^{\text{ext}} \approx 0$ due to applied silicone oil to reduce friction) was compared with those obtained with elastic multipole method and linear finite element simulation (see Fig. 3.6b). For the elastic multipole method, we used external stress $\sigma_{yy}^{\text{ext}} = E_0 \varepsilon_{yy}^{\text{ext}}$ and plane stress condition was assumed since the experimental sample was free to expand in the out-of-plane direction. Linear finite element simulation was performed for a 100 mm $\times$ 100 mm 2D structure with a circular hole located at the center under plane stress condition. In finite element simulation, the sample was compressed by imposing a uniform displacement in the x-direction on the left and right edges, while allowing the nodes on these edges to move freely in the y-direction. The midpoints of the left and right edge were constrained to prevent rigid body translations in the y-direction.

The contour of the deformed hole obtained with the experiment matched very well to those obtained with elastic multipole method ($n_{\max} = 10$) and finite element simulations (see Fig. 3.6b). We also compared the equivalent von Mises strain field

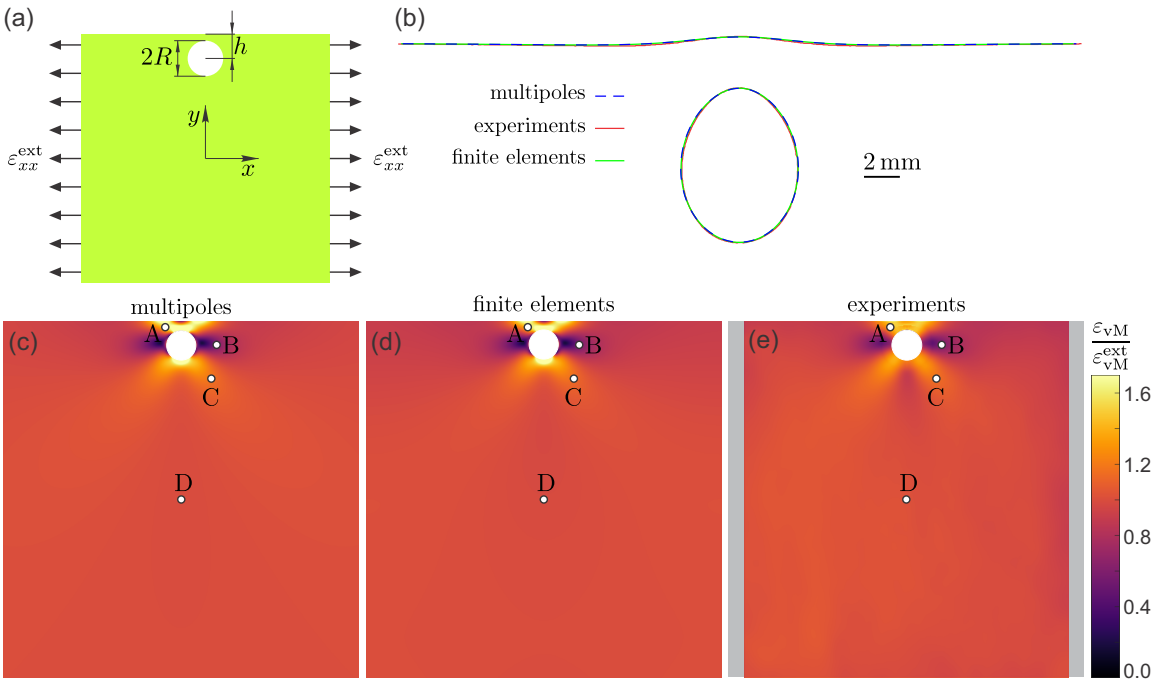

Figure 3.6: Uniaxial horizontal compression of an elastic structure with a hole near a traction-free edge. (a) Schematic image describing the initial undeformed shape of the structure and applied strain $\epsilon_{xx}^{\text{ext}} = -0.05$. The size of the experimental sample was 100 mm × 100 mm × 25 mm with the hole of diameter $2R = 8.11$ mm, and the distance between the center of the hole and the traction-free edge was $h = 6.25$ mm. The Young's modulus of the elastic matrix was $E_0 = 0.97\,\text{MPa}$ and the Poisson's ratio was $\nu_0 = 0.49$. For linear finite element simulations, we used a 2D structure of size 100 mm × 100 mm under plane stress condition. The elastic multiple method describes the deformation of a semi-infinite 2D elastic matrix, where we used the load $\sigma_{xx}^{\text{ext}} = \epsilon_{xx}^{\text{ext}} E_0$ and plane stress condition. (b) Contours of deformed holes and traction-free edges obtained with elastic multipole method (dashed blue lines, $n_{\max} = 10$), experiments (solid red lines) and finite element simulations (solid green lines). (c-e) Equivalent von Mises strain fields ϵ_{vM} were obtained with (c) elastic multipole method ($n_{\max} = 10$), (d) finite element simulations, and (e) DIC (digital image correlation) analysis of experiments. Strain fields were normalized with the value of the equivalent von Mises strain $\epsilon_{\text{vM}}^{\text{ext}} = |\epsilon_{xx}^{\text{ext}}|$ imposed by the applied load. Note that the strain data was corrupted near the edges for this experimental sample due to oil stains on the speckle patterns near the boundary. For this reason, we omitted the affected border regions (grey) in the heat map (e). Four marked points A-D were chosen for the quantitative comparison of strains ϵ_{vM}. See Table 3.3 for details.

defined as $\varepsilon_{\text{vM}} = \sigma_{\text{vM}}/E$ [1] with

$$\varepsilon_{\text{vM}} = \frac{\sqrt{\varepsilon_{xx}^2 - \varepsilon_{xx}\varepsilon_{yy} + \varepsilon_{yy}^2 + 3\varepsilon_{xy}^2 + \frac{\nu}{(1-\nu)^2}(\varepsilon_{xx} + \varepsilon_{yy})^2}}{1+\nu} \tag{3.23}$$

that were obtained with elastic multipole method ($n_{\max} = 10$), finite element simulations and digital image correlation (DIC) analysis of experiment (see Appendix B.2). Strain fields show characteristic features of the induced quadrupoles (see Fig. 3.6c-e), because they have the largest amplitude and because the effect of higher-order multipoles decays faster away from holes and images. The effect of higher-order multipoles is most pronounced in the region between the hole and the traction-free edge, where contributions from both the hole and from its image are important. The strain fields agree very well between the elastic multipole method (Fig. 3.6c) and linear finite element simulations (Fig. 3.6d). The strain fields for experimental samples are qualitatively similar, but they deviate quantitatively near the hole, as can be seen from the heat map in Fig. 3.6e. The quantitative comparison of strains at four different points A-D (marked in Fig. 3.6) showed a relative error of 1-4% between elastic multipole method and finite elements, and a relative error of 1-10% between elastic multipole method and experiments (see Table 3.3). The discrepancy between elastic multipole method and finite element simulations is attributed to the finite size effects. For the elastic multipole method, we assumed a semi-infinite domain, while finite domains were modeled in finite element simulations to mimic experiments. The discrepancy between experiments and elastic multipole method is attributed to the confounding effects of nonlinear deformation due to moderately large compression ($\varepsilon_{xx}^{\text{ext}} = -0.05$), 3D deformation due to relatively thick samples, fabrication imperfections, nonzero friction between the sample and the mounting grips of the testing machine, the alignment of camera with the sample (2D DIC system was used), and the errors resulting from the choice of DIC parameters (see e.g. [132, 133]).

Table 3.3: Quantitative comparison for the values of equivalent von Mises strains $\varepsilon_{\rm vM}$ normalized with the value for the applied external load $\varepsilon_{\rm vM}^{\rm ext} = |\varepsilon_{xx}^{\rm ext}|$ at points A-D (defined in Fig. 3.6) in compressed samples with one hole near a traction-free edge obtained with elastic multipole method (EMP), finite element simulations (FEM) and DIC analysis of experiments (EXP). The relative percent errors between the EMP and FEM were calculated as $100 \times (\varepsilon_{\rm vM}^{\rm (EMP)} - \varepsilon_{\rm vM}^{\rm (FEM)})/\varepsilon_{\rm vM}^{\rm (FEM)}$. The relative percent errors between the EMP and EXP were calculated as $100 \times (\varepsilon_{\rm vM}^{\rm (EMP)} - \varepsilon_{\rm vM}^{\rm (EXP)})/\varepsilon_{\rm vM}^{\rm (EXP)}$.

points	strain $\varepsilon_{\rm vM}/\epsilon_{\rm vM}^{\rm ext}$			error of EMP (%)	
	EMP	FEM	DIC	FEM	DIC
A	1.5390	1.4868	1.3998	3.5	9.9
B	0.5782	0.5586	0.5506	3.5	5.0
C	1.1760	1.1406	1.1586	3.1	1.5
D	0.9932	0.9836	0.9792	1.0	1.4

3.2.2 Inclusions in an infinite elastic strip with prescribed tractions along the outer boundary of the strip

In this section, we consider the deformation of an infinite elastic strip ($y_a < y < y_b$) with embedded circular holes and inclusions by prescribing uniform tractions along the outer boundary of an elastic strip. The deformation of the elastic matrix again induces elastic multipoles at the center of holes and inclusions. However, in this case, the induced multipoles generate an infinite number of image multipoles, similar to an infinite number of images for charges between parallel conductive plates in electrostatics [121]. The effect of all images can be captured with the integrals introduced by Howland [138], who considered deformation of an infinite elastic strip in response to a localized force. Here, however, we take a different approach, because we would like to explicitly show the contribution of each image.

To demonstrate how to enumerate all images let us first consider an elastic multipole with the Airy stress function χ_0 that is at position $\mathbf{x}_0 = (x_0, y_0)$ between the two traction-free edges a and b at $y = y_a$ and $y = y_b$ (see Fig. 3.7). To satisfy the boundary conditions at the edge a, we first place an image multipole $\mathcal{I}^a[\chi_0] \equiv \mathcal{I}^{a,1}[\chi_0]$ at position $\mathbf{x}_0^{*a,1} = (x_0^{*a,1}, y_0^{*a,1}) = (x_0, 2y_a - y_0)$ as discussed in Section 3.2.1. This first image

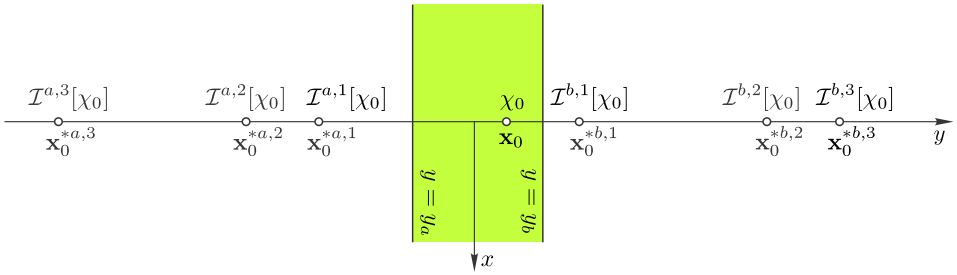

Figure 3.7: Images of an elastic multipole with the Airy stress function χ_0 at position $\mathbf{x_0}$ between the two parallel traction-free edges at $y = y_a$ and $y = y_b$. See text for the detailed description.

ensures that the boundary conditions at the edge a are satisfied, but the boundary conditions at the edge b are still violated. To correct this, we need to place two more images with the Airy stress functions $\mathcal{I}^b[\chi_0] \equiv \mathcal{I}^{b,1}[\chi_0]$ and $\mathcal{I}^b[\mathcal{I}^a[\chi_0]] \equiv \mathcal{I}^{b,2}[\chi_0]$ at positions $\mathbf{x}_0^{*b,1} = (x_0^{*b,1}, y_0^{*b,1}) = (x_0, 2y_b - y_0)$ and $\mathbf{x}_0^{*b,2} = (x_0^{*b,2}, y_0^{*b,2}) = (x_0, 2y_b - y_0^{*a,1})$, respectively. These two additional images ensure that the boundary conditions at the edge b are satisfied, but now the boundary conditions at the edge a are violated. Thus we need to add two more images with the Airy stress functions $\mathcal{I}^a[\mathcal{I}^b[\chi_0]] \equiv \mathcal{I}^{a,2}[\chi_0]$ and $\mathcal{I}^a[\mathcal{I}^b[\mathcal{I}^a[\chi_0]]] \equiv \mathcal{I}^{a,3}[\chi_0]$ at positions $\mathbf{x}_0^{*a,2} = (x_0^{*a,2}, y_0^{*a,2}) = (x_0, 2y_a - y_0^{*b,1})$ and $\mathbf{x}_0^{*a,3} = (x_0^{*a,3}, y_0^{*a,3}) = (x_0, 2y_a - y_0^{*b,2})$, respectively. These two additional images ensure that the boundary conditions at the edge a are satisfied, but now the boundary conditions at the edge b are violated. Thus, we need to keep adding more and more images, which are getting further and further away from the edges of the strip (see Fig. 3.7). The infinite set of images can be constructed recursively with the Airy stress functions $\mathcal{I}^{a,k+1}[\chi_0] = \mathcal{I}^a[\mathcal{I}^{b,k}[\chi_0]]$ and $\mathcal{I}^{b,k+1}[\chi_0] = \mathcal{I}^b[\mathcal{I}^{a,k}[\chi_0]]$ that are at positions $\mathbf{x}_0^{*a,k+1} = (x_0^{*a,k+1}, y_0^{*a,k+1}) = (x_0, 2y_a - y_0^{*b,k})$ and $\mathbf{x}_0^{*b,k+1} = (x_0^{*b,k+1}, y_0^{*b,k+1}) = (x_0, 2y_b - y_0^{*a,k})$, respectively. The initial conditions for the recursive relations are $\mathcal{I}^{a,0}[\chi_0] = \mathcal{I}^{b,0}[\chi_0] = \chi_0$ and $\mathbf{x}_0^{*a,0} = \mathbf{x}_0^{*b,0} = (x_0, y_0)$. Below we show how to use this approach to analyze the deformation of elastic strips with circular inclusions and holes.

Consider a 2D infinite elastic strip with the Young's modulus E_0 and the Poisson's ratio ν_0 filling the space $y_a < y < y_b$ subject to external stress σ_{xx}^{ext} with traction-free edges a and b, where the boundary conditions are $\sigma_{yy} = \sigma_{xy} = 0$ at $y = y_a$ and $y = y_b$. Embedded in the elastic matrix are N circular inclusions with radii R_i centered at positions $\mathbf{x}_i = (x_i, y_i)$ with Young's moduli E_i and Poisson's ratios ν_i, where $i \in \{1, \ldots, N\}$. Holes are described with the zero Young's modulus ($E_i = 0$).

The external load σ_{xx}^{ext}, represented with the Airy stress function $\chi_{\text{ext}}(x, y) = \sigma_{xx}^{\text{ext}} y^2/2$, induces elastic multipoles at the centers of inclusions and holes. The Airy stress function $\chi_{\text{out}}\big(r_i, \varphi_i | \mathbf{a}_{i,\text{out}}\big)$ outside the i^{th} inclusion due to the induced multipoles can be expanded as shown in Eq. (3.8), where the origin of polar coordinates (r_i, φ_i) is at the center $\mathbf{x}_i$ of i^{th} inclusion and the set of induced multipoles is $\mathbf{a}_{i,\text{out}} = \{A_{i,0}, A_{i,1}, \ldots, B_{i,1}, B_{i,2}, \ldots, C_{i,2}, C_{i,3}, \ldots, D_{i,2}, D_{i,3}, \ldots\}$. The induced multipoles $\mathbf{a}_{i,\text{out}}$ at the center of the i^{th} inclusion then further induce an infinite set of image multipoles at positions $\mathbf{x}_i^{*a,k}$ and $\mathbf{x}_i^{*b,k}$, where $k \in \{1, 2, \ldots\}$, to satisfy the boundary conditions at the traction-free edges a and b. The positions of these image multipoles can be generated recursively as $\mathbf{x}_i^{*a,k+1} = (x_i^{*a,k+1}, y_i^{*a,k+1}) = (x_i, 2y_a - y_i^{*b,k})$ and $\mathbf{x}_i^{*b,k+1} = (x_i^{*b,k+1}, y_i^{*b,k+1}) = (x_i, 2y_b - y_i^{*a,k})$ with the initial conditions $\mathbf{x}_i^{*a,0} = \mathbf{x}_i^{*b,0} = \mathbf{x_i} = (x_i, y_i)$. The Airy stress functions $\mathcal{I}^{a,k}[\chi_{\text{out}}]$ and $\mathcal{I}^{b,k}[\chi_{\text{out}}]$ of image multipoles for the i^{th} inclusion can be expanded as

$$\mathcal{I}^{a,k}[\chi_{\text{out}}\big(r_i, \varphi_i | \mathbf{a}_{i,\text{out}}\big)] = \chi^*_{\text{out}}\big(r_i^{*a,k}, \varphi_i^{*a,k} | \mathbf{a}_{i,\text{out}}^{*a,k}\big), \tag{3.24a}$$

$$\mathcal{I}^{b,k}[\chi_{\text{out}}\big(r_i, \varphi_i | \mathbf{a}_{i,\text{out}}\big)] = \chi^*_{\text{out}}\big(r_i^{*b,k}, \varphi_i^{*b,k} | \mathbf{a}_{i,\text{out}}^{*b,k}\big), \tag{3.24b}$$

where the function χ^*_{out} is defined in Eq. (3.9), the origins of polar coordinates $(r_i^{*a,k}, \varphi_i^{*a,k})$ and $(r_i^{*b,k}, \varphi_i^{*b,k})$ are at $\mathbf{x}_i^{*a,k}$ and $\mathbf{x}_i^{*b,k}$, respectively, and the sets of amplitudes of image multipoles are $\mathbf{a}_{i,\text{out}}^{*a,k} = \{A_{i,0}^{*a,k}, A_{i,1}^{*a,k}, \ldots, B_{i,0}^{*a,k}, B_{i,1}^{*a,k}, \ldots, C_{i,2}^{*a,k}, C_{i,3}^{*a,k}, \ldots, D_{i,2}^{*a,k}, D_{i,3}^{*a,k}, \ldots\}$ and $\mathbf{a}_{i,\text{out}}^{*b,k} = \{A_{i,0}^{*b,k}, A_{i,1}^{*b,k}, \ldots, B_{i,0}^{*b,k}, B_{i,1}^{*b,k}, \ldots, C_{i,2}^{*b,k}, C_{i,3}^{*b,k},$

$\dots, D_{i,2}^{*b,k}, D_{i,3}^{*b,k}, \dots\}$. The amplitudes of image multipoles $\mathbf{a}_{i,\text{out}}^{*a,k}$ and $\mathbf{a}_{i,\text{out}}^{*b,k}$ are related to the amplitudes $\mathbf{a}_{i,\text{out}}$ of induced multipoles at the center of the i^{th} inclusion and they can be generated recursively. The initial conditions for recursive relations are $\mathbf{a}_{i,\text{out}}^{*a,0} = \mathbf{a}_{i,\text{out}}^{*b,0} = \mathbf{a}_{i,\text{out}}$, and the amplitudes of image multipoles $\mathbf{a}_{i,\text{out}}^{*a,k+1}$ and $\mathbf{a}_{i,\text{out}}^{*b,k+1}$ are related to the amplitudes of image multipoles $\mathbf{a}_{i,\text{out}}^{*b,k}$ and $\mathbf{a}_{i,\text{out}}^{*a,k}$ as

$$A_{i,n}^{*a,k+1} = \begin{cases} -A_{i,0}^{*b,k}, & n = 0, \\ -(n+1)A_{i,n}^{*b,k} - (n+2)C_{i,n+2}^{*b,k} \\ \quad -2(n-1)\alpha_i^{*b,k} B_{i,n-1}^{*b,k} \\ \quad -2(2n+1)\alpha_i^{*b,k} D_{i,n+1}^{*b,k} \\ \quad +4(n-1)(\alpha_i^{*b,k})^2 C_{i,n}^{*b,k}, & n \geq 1, \end{cases} \tag{3.25a}$$

$$B_{i,n}^{*a,k+1} = \begin{cases} 0, & n = 0, \\ +2B_{i,1}^{*b,k} + 3D_{i,3}^{*b,k} + 2\alpha_i^{*b,k} A_{i,0}^{*b,k} \\ \quad -6\alpha_i^{*b,k} C_{i,2}^{*b,k}, & n = 1, \\ +(n+1)B_{i,n}^{*b,k} + (n+2)D_{i,n+2}^{*b,k} \\ \quad -2(n-1)\alpha_i^{*b,k} A_{i,n-1}^{*b,k} \\ \quad -2(2n+1)\alpha_i^{*b,k} C_{i,n+1}^{*b,k} \\ \quad -4(n-1)(\alpha_i^{*b,k})^2 D_{i,n}^{*b,k}, & n \geq 2, \end{cases} \tag{3.25b}$$

$$C_{i,n}^{*a,k+1} = \begin{cases} +C_{i,2}^{*b,k} - A_{i,0}^{*b,k}, & n = 2, \\ +(n-1)C_{i,n}^{*b,k} + (n-2)A_{i,n-2}^{*b,k} \\ \quad +2(n-2)\alpha_i^{*b,k} D_{i,n-1}^{*b,k}, & n \geq 3, \end{cases} \tag{3.25c}$$

$$D_{i,n}^{*a,k+1} = \begin{cases} -(n-1)D_{i,n}^{*b,k} - (n-2)B_{i,n-2}^{*b,k} \\ \quad +2(n-2)\alpha_i^{*b,k} C_{i,n-1}^{*b,k}, & n \geq 2, \end{cases} \tag{3.25d}$$

$$A_{i,n}^{*b,k+1} = \begin{cases} -A_{i,0}^{*a,k}, & n = 0, \\ -(n+1)A_{i,n}^{*a,k} - (n+2)C_{i,n+2}^{*a,k} \\ \quad -2(n-1)\alpha_i^{*a,k} B_{i,n-1}^{*a,k} \\ \quad -2(2n+1)\alpha_i^{*a,k} D_{i,n+1}^{*a,k} \\ \quad +4(n-1)(\alpha_i^{*a,k})^2 C_{i,n}^{*a,k}, & n \geq 1, \end{cases} \tag{3.25e}$$

$$B_{i,n}^{*b,k+1} = \begin{cases} 0, & n = 0, \\ +2B_{i,1}^{*a,k} + 3D_{i,3}^{*a,k} + 2\alpha_i^{*a,k} A_{i,0}^{*a,k} \\ \quad -6\alpha_i^{*a,k} C_{i,2}^{*a,k}, & n = 1, \\ +(n+1)B_{i,n}^{*a,k} + (n+2)D_{i,n+2}^{*a,k} \\ \quad -2(n-1)\alpha_i^{*a,k} A_{i,n-1}^{*a,k} \\ \quad -2(2n+1)\alpha_i^{*a,k} C_{i,n+1}^{*a,k} \\ \quad -4(n-1)(\alpha_i^{*a,k})^2 D_{i,n}^{*a,k}, & n \geq 2, \end{cases} \tag{3.25f}$$

$$C_{i,n}^{*b,k+1} = \begin{cases} +C_{i,2}^{*a,k} - A_{i,0}^{*a,k}, & n = 2, \\ +(n-1)C_{i,n}^{*a,k} + (n-2)A_{i,n-2}^{*a,k} \\ \quad +2(n-2)\alpha_i^{*a,k} D_{i,n-1}^{*a,k}, & n \geq 3, \end{cases} \tag{3.25g}$$

$$D_{i,n}^{*b,k+1} = \begin{cases} -(n-1)D_{i,n}^{*a,k} - (n-2)B_{i,n-2}^{*a,k} \\ \quad +2(n-2)\alpha_i^{*a,k} C_{i,n-1}^{*a,k}, & n \geq 2, \end{cases} \tag{3.25h}$$

where $\alpha_i^{*a,k} = (y_b - y_i^{*a,k})/R_i$ and $\alpha_i^{*b,k} = (y_a - y_i^{*b,k})/R_i$.

The total Airy stress function outside all inclusions can then be written as

$$\begin{aligned}\chi_{\text{out}}^{\text{tot}}\left(x,y|\mathbf{a}_{\text{out}}\right) =&\chi_{\text{ext}}(x,y)\\ &+\sum_{i=1}^{N}\chi_{\text{out}}\left(r_i(x,y),\varphi_i(x,y)|\mathbf{a}_{i,\text{out}}\right)\\ &+\sum_{i=1}^{N}\sum_{k=1}^{\infty}\mathcal{I}^{a,k}\left[\chi_{\text{out}}\left(r_i(x,y),\varphi_i(x,y)|\mathbf{a}_{i,\text{out}}\right)\right]\\ &+\sum_{i=1}^{N}\sum_{k=1}^{\infty}+\mathcal{I}^{b,k}\left[\chi_{\text{out}}\left(r_i(x,y),\varphi_i(x,y)|\mathbf{a}_{i,\text{out}}\right)\right],\end{aligned} \tag{3.26}$$

where the first term is due to external stress, the first summation describes contributions due to induced multipoles at the centers of inclusions and the last two summations describe contributions due to images of induced multipoles. The set of amplitudes of induced multipoles for all inclusions is defined as $\mathbf{a}_{\text{out}} = \{\mathbf{a}_{1,\text{out}},\dots,\mathbf{a}_{N,\text{out}}\}$.

We also expand the induced Airy stress function $\chi_{\text{in}}\left(r_i,\varphi_i|\mathbf{a}_{i,\text{in}}\right)$ inside the i^{th} inclusion, as shown in Eq. (3.12), where the set of amplitudes of induced multipoles is $\mathbf{a}_{i,\text{in}} = \{a_{i,2},a_{i,3},\dots,b_{i,2},b_{i,3},\dots,c_{i,0},c_{i,1},\dots,d_{i,1},d_{i,2},\dots\}$. We again define the total Airy stress function $\chi_{\text{in}}^{\text{tot}}\left(x,y|\mathbf{a}_{i,\text{in}}\right)$ inside the i^{th} inclusion, which also includes the effect of the external load (χ_{ext}) as shown in Eq. (3.13). The rest of the steps are the same as the ones described in Section 3.2.1. The amplitudes of induced multipoles $\mathbf{a}_{i,\text{out}}$ and $\mathbf{a}_{i,\text{in}}$ are obtained by satisfying the boundary conditions that tractions and displacements are continuous across the circumference of each inclusion in Eq. (3.14), which can be converted to the matrix equation similar to that in Eq. (3.21). To numerically solve the matrix equation we truncate the degrees of multipoles at $n_{\max}$ as discussed in Section 3.2.1. Furthermore, we truncate the summation for the number of images at $k_{\max}$ in Eq. (3.26).

The elastic multipole method described above was compared with linear finite element simulations and experiments. Three different configurations of elastic strips with length $L = 100$ mm and thickness 25 mm were considered: $w = 12.75$ mm wide

strips with one hole, $w = 19.97$ mm wide strips with two holes placed orthogonal to the long axis of the strip and $w = 20.72$ mm wide strips with two holes at 45° angle relative to the long axis of the strip (see Fig. 3.8). The diameter of all holes was $d = 8.00$ mm. Experiments were carried out using displacement controlled compressive and tensile loading (strain $\varepsilon_{xx}^{\text{ext}}$), where both ends of the strip were glued to aluminum plates, while the outer edges of the strip were free to move (see Appendix B.2). For the elastic multipole method, we set the external load to $\sigma_{xx}^{\text{ext}} = E_0 \varepsilon_{xx}^{\text{ext}}$, $\sigma_{yy}^{\text{ext}} = \sigma_{xy}^{\text{ext}} = 0$ and assumed plane stress condition. For 2D linear finite element simulations we used plane stress condition with the same external loads as for elastic multipole method (see Appendix B.1). Note that the elastic multipole method considers infinitely long strips ($L \to \infty$), while the length L is finite in experiments and simulations. In experiments and simulations, we observed a slight bending of strips under both compression and tension because holes were placed asymmetrically. However, this bending is not captured by the elastic multipole method. Bending could in principle be captured by adding additional terms to the Airy stress functions, such as y^3 and xy^3 [1], which were omitted in our expansion for the induced multipoles. Note that the coefficients of these additional terms cannot be obtained from the continuity of tractions and displacements across the circumference of inclusions in Eq. (3.14), but additional equations would be needed, such as the boundary conditions at the two ends of the strip. This is beyond the scope of this chapter and hence we expect to observe some errors for the elastic multipole method due to the neglected bending.

In Fig. 3.8, we show contours of deformed holes obtained with elastic multipole method ($n_{\max} = 10$, $k_{\max} = 6$), linear finite elements, and experiments. The results for all 3 different approaches agree very well in the vicinity of holes where the effect of bending is small. In Fig. 3.8a, we observe more pronounced deformations of the hole and the outer edges of the strip in the regions where they approach each other due to the strong interaction between the hole and its images. This is similar to the

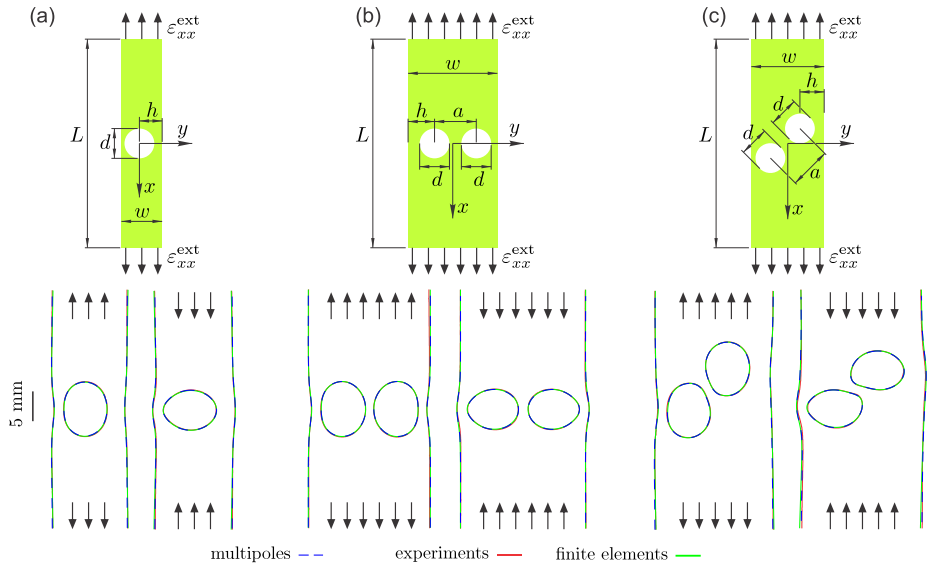

Figure 3.8: Deformation of elastic strips with holes and inclusions. (a-c) Schematic images describing the initial undeformed shapes of structures with holes and the direction of applied strain $\varepsilon_{xx}^{\text{ext}}$. The Young's modulus of the elastic matrix is $E_0 = 0.97$ MPa and Poisson's ratio is $\nu_0 = 0.49$. Holes are represented with white circles. (a-c) For each structure, we show contours of deformed holes, inclusions and traction-free edges under tensile (left) and compressive (right) loads. Note that contours are only shown in the vicinity of deformed holes and inclusions and they do not span the whole length of samples. Dashed blue lines show the contours obtained with elastic multipole method for $n_{\max} = 10$ and $k_{\max} = 6$. Red and green solid lines show the contours obtained with experiments and linear finite element simulations, respectively. For all samples the length was $L = 100$ mm and the thickness was 25 mm. The diameters of all inclusions and holes were $d = 8.00$ mm. Other geometrical properties were: (a) $h = 7.06$ mm, $w = 12.75$ mm, (b) $h = 5.67$ mm, $a = 9.49$ mm, $w = 20.72$ mm, and (c) $h = 7.56$ mm, $a = 9.57$ mm, $w = 19.97$ mm. Tensile and compressive loads were: (a) $\varepsilon_{xx}^{\text{ext}} = +0.027$ and $\varepsilon_{xx}^{\text{ext}} = -0.033$, (b) $\varepsilon_{xx}^{\text{ext}} = +0.027$ and $\varepsilon_{xx}^{\text{ext}} = -0.029$, (c) $\varepsilon_{xx}^{\text{ext}} = +0.020$ and $\varepsilon_{xx}^{\text{ext}} = -0.030$.

deformation of the hole near the single traction-free edge in Figs. 3.4 and 3.6, but here such deformation is observed on both sides (Fig. 3.8a). Note that deformations are more pronounced near the left edge because the hole is closer to the left edge and thus the interactions between the hole and its images become more dominant. In Figs. 3.8b-c, we observe interactions between holes as well as interactions between holes and their images, which is reflected in more pronounced deformations in the

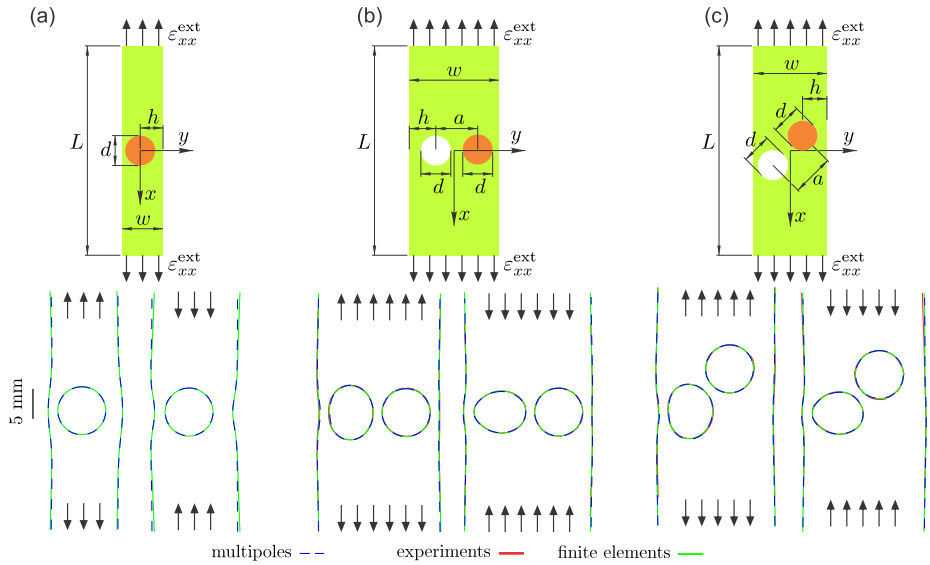

Figure 3.9: Deformation of elastic strips with holes and inclusions. (a-c) Schematic images describing the initial undeformed shapes of structures with holes and the direction of applied strain $\varepsilon_{xx}^{\text{ext}}$. The Young's modulus of the elastic matrix is $E_0 = 0.97\,\text{MPa}$ and Poisson's ratio is $\nu_0 = 0.49$. Holes are represented with white circles and inclusions with orange circles ($E_{\text{inc}} = 2.9\,\text{GPa}$, $\nu_{\text{inc}} = 0.37$). (a-c) For each structure, we show contours of deformed holes, inclusions and traction-free edges under tensile (left) and compressive (right) loads. Note that contours are only shown in the vicinity of deformed holes and inclusions and they do not span the whole length of samples. Dashed blue lines show the contours obtained with elastic multipole method for $n_{\text{max}} = 10$ and $k_{\text{max}} = 6$. Red and green solid lines show the contours obtained with experiments and linear finite element simulations, respectively. For all samples the length was $L = 100$ mm and the thickness was 25 mm. The diameters of all inclusions and holes were $d = 8.00$ mm. Other geometrical properties were: (a) $h = 7.06$ mm, $w = 12.75$ mm, (b) $h = 5.67$ mm, $a = 9.49$ mm, $w = 20.72$ mm, and (c) $h = 7.56$ mm, $a = 9.57$ mm, $w = 19.97$ mm. Tensile and compressive loads were: (a) $\varepsilon_{xx}^{\text{ext}} = +0.250$ and $\varepsilon_{xx}^{\text{ext}} = -0.250$, (b) $\varepsilon_{xx}^{\text{ext}} = +0.034$ and $\varepsilon_{xx}^{\text{ext}} = -0.033$, (c) $\varepsilon_{xx}^{\text{ext}} = +0.038$ and $\varepsilon_{xx}^{\text{ext}} = -0.033$.

regions, where holes are close to each other, and in the regions, where holes are close to the outer edges of the strip.

In Fig. 3.9 we repeated the analysis, where for each sample one of the holes was filled with a PMMA rod that was glued to the elastic matrix with a cyanoacrylate adhesive. Compared to the base elastic matrix with Young's modulus $E_0 = 0.97$ MPa, the PMMA inclusion is very rigid ($E_{\text{inc}} = 2.9$ GPa). This is reflected in the contours of deformed samples, where inclusions remain circular, while holes and traction-free

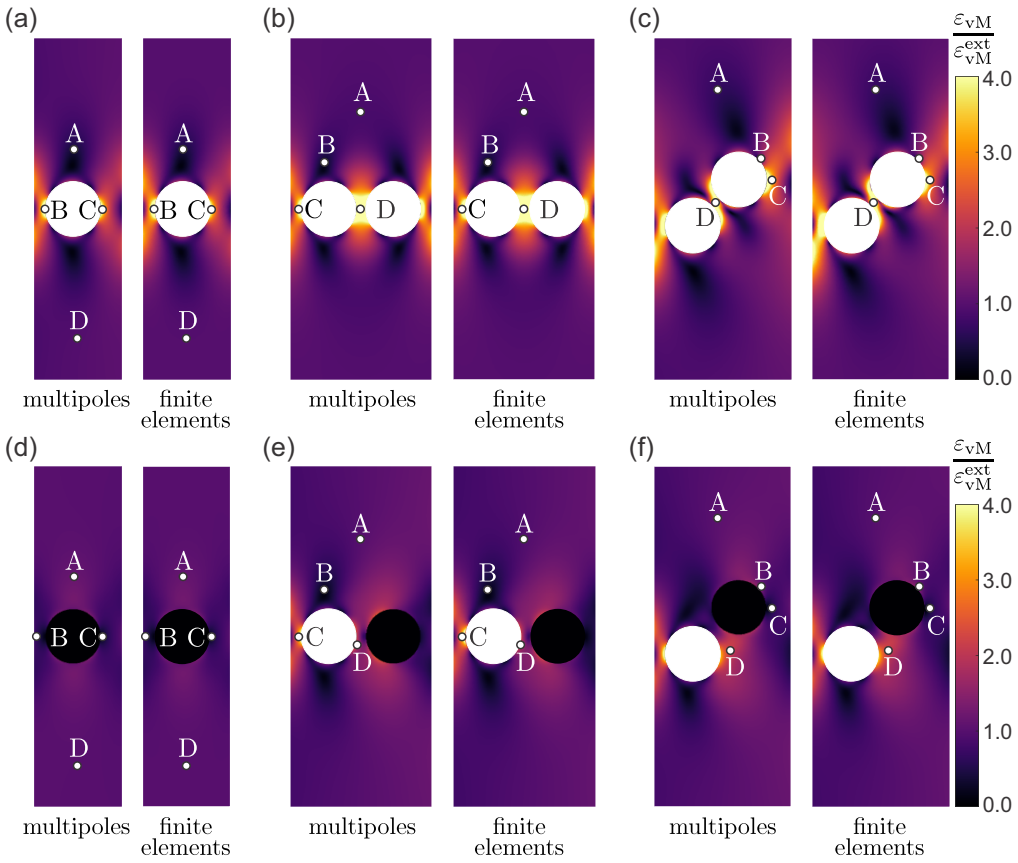

Figure 3.10: Equivalent von Mises strain fields $\varepsilon_{\mathrm{vM}}$ were obtained with elastic multipole method ($n_{\max} = 10$, $k_{\max} = 6$) and linear finite element simulations. The values of the strain fields $\varepsilon_{\mathrm{vM}}$ were normalized with the value of the equivalent von Mises strain $\varepsilon_{\mathrm{vM}}^{\mathrm{ext}} = |\varepsilon_{xx}^{\mathrm{ext}}|$ due to the external load. The geometrical properties and the magnitudes of applied loads for the samples in (a-f) were the same as in Figs. 3.8 and 3.9. For each of the samples in (a-f), four marked points A-D were chosen for the quantitative comparison of strains $\varepsilon_{\mathrm{vM}}$. See Table 3.4 for details.

edges are deformed (see Fig. 3.9a-c). We observe interactions between holes and inclusions as well as interactions between them and their images, which is reflected in more pronounced deformations in the regions, where holes are close to inclusions, and in the regions, where holes and inclusions are close to the outer edges of the strip. Note that for a narrow elastic strip with a single inclusion (see Fig. 3.9a) we had to apply a very large compressive/tensile strain of $\varepsilon_{xx}^{\mathrm{ext}} = \pm 25\%$ to observe a notable deformation of the outer edges of the strip in the vicinity of inclusion. At such large compressive/tensile loads there was a failure of the glue between the PMMA rod

Table 3.4: Quantitative comparison for the values of equivalent von Mises strains $\varepsilon_{\mathrm{vM}}$ normalized with the value for the applied external load $\varepsilon_{\mathrm{vM}}^{\mathrm{ext}} = |\varepsilon_{xx}^{\mathrm{ext}}|$ at points A-D for 6 different samples defined in Fig. 3.10 obtained with elastic multipole method (EMP) and finite element simulations (FEM). The relative percent errors between the EMP and FEM were calculated as $\epsilon = 100 \times |\varepsilon_{\mathrm{vM}}^{(\mathrm{EMP})} - \varepsilon_{\mathrm{vM}}^{(\mathrm{FEM})}|/\varepsilon_{\mathrm{vM}}^{(\mathrm{FEM})}$.

points	sample (a)			sample (b)			sample (c)		
	strain $\epsilon_{\mathrm{vM}}/\epsilon_{\mathrm{vM}}^{\mathrm{ext}}$			strain $\epsilon_{\mathrm{vM}}/\epsilon_{\mathrm{vM}}^{\mathrm{ext}}$			strain $\epsilon_{\mathrm{vM}}/\epsilon_{\mathrm{vM}}^{\mathrm{ext}}$		
	EMP	FEM	$\epsilon(\%)$	EMP	FEM	$\epsilon(\%)$	EMP	FEM	$\epsilon(\%)$
A	0.439	0.454	3.3	0.875	0.883	0.9	0.675	0.692	2.4
B	5.740	6.077	5.5	0.331	0.330	0.2	1.301	1.245	4.5
C	3.783	3.746	1.0	4.561	4.562	0.0	3.311	3.203	3.4
D	0.971	0.984	1.3	5.760	5.803	0.7	4.188	4.308	2.8
points	sample (d)			sample (e)			sample (f)		
	strain $\epsilon_{\mathrm{vM}}/\epsilon_{\mathrm{vM}}^{\mathrm{ext}}$			strain $\epsilon_{\mathrm{vM}}/\epsilon_{\mathrm{vM}}^{\mathrm{ext}}$			strain $\epsilon_{\mathrm{vM}}/\epsilon_{\mathrm{vM}}^{\mathrm{ext}}$		
	EMP	FEM	$\epsilon(\%)$	EMP	FEM	$\epsilon(\%)$	EMP	FEM	$\epsilon(\%)$
A	1.168	1.154	1.2	1.002	0.952	5.3	1.045	1.005	4.0
B	0.643	0.612	5.0	0.231	0.223	3.6	1.190	1.135	4.9
C	0.273	0.283	3.6	3.443	3.497	1.5	0.496	0.524	5.3
D	1.014	1.004	0.9	1.955	2.020	3.2	2.166	2.141	1.2

and the elastic matrix as well as between the elastic matrix and the outer aluminum plates at the two ends of the strip. Thus we were not able to perform experiments in this case. Note that the strip edges near the rigid inclusion (Fig. 3.9a) bulge in the opposite direction than the strip edges near holes (e.g. Fig. 3.8a), which is related to the opposite sign of amplitudes of induced quadrupoles as discussed in the previous chapter 2.

Furthermore, in Fig. 3.10 we compared the equivalent von Mises strain obtained with elastic multipole method and linear finite element simulations for all 6 samples described above (see Figs. 3.8 and. 3.9). The strain fields obtained with the two methods agree very well. Note that we were unable to obtain strain fields in experiments because of the delamination of the spray-painted speckle pattern near the edges of the strip, which is required for DIC analysis. We observe large strain concentrations in regions where holes are close to the traction-free edges, inclusions and other holes. In contrast, we observe reduced strains in regions where inclusions are close to free

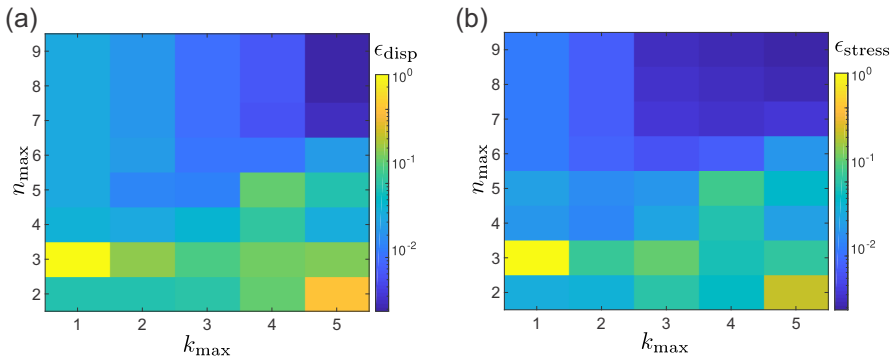

Figure 3.11: The normalized errors for (a) displacements $\epsilon_{\mathrm{disp}}(n_{\mathrm{max}}, k_{\mathrm{max}})$ and (b) stresses $\epsilon_{\mathrm{stress}}(n_{\mathrm{max}}, k_{\mathrm{max}})$ as defined in Eq. (3.27) for the deformation of an elastic strip with a single hole (see Fig. 3.8a).

edges. The quantitative comparison of strains at four different point A-D (marked in Fig. 3.10) showed a relative error of 0-6% (see Table 3.4). The relative error was the largest in the regions that were affected by the bending of strips in finite element simulations, which was neglected in the elastic multipole method.

Finally, we also comment on the convergence analysis for spatial distributions of displacements $\mathbf{u}^{(n_{\mathrm{max}},k_{\mathrm{max}})}(x,y)$ and von Mises stresses $\sigma_{\mathrm{vM}}^{(n_{\mathrm{max}},k_{\mathrm{max}})}(x,y)$ as a function of the numbers n_{max} for the maximum degree of induced multipoles and k_{max} for the maximum number of images. Displacements and von Mises stresses were evaluated at N_p discrete points $(x_i, y_j) = (iR/50, jw/200)$, where $i \in \{-250, -249, \ldots, 250\}$ and $j \in \{-100, -99, \ldots, 100\}$ and grid points that lie inside holes and inclusions were excluded. Here, R is the radius of holes and w is the width of the strip. The normalized errors for displacements $\epsilon_{\mathrm{disp}}(n_{\mathrm{max}}, k_{\mathrm{max}})$ and stresses $\epsilon_{\mathrm{stress}}(n_{\mathrm{max}}, k_{\mathrm{max}})$ were obtained by calculating the relative changes of spatial distributions of displacements and von Mises stresses when the maximum degree n_{max} of induced multipoles and the maximum number k_{max} of images are both increased by one. The normalized errors are given by [129]

$$\epsilon_{\mathrm{disp}}(n_{\mathrm{max}}, k_{\mathrm{max}}) = \sqrt{\sum_{i,j} \frac{\left(\mathbf{u}^{(n_{\mathrm{max}}+1,k_{\mathrm{max}}+1)}(x_i,y_j) - \mathbf{u}^{(n_{\mathrm{max}},k_{\mathrm{max}})}(x_i,y_j)\right)^2}{N_p (d\,\sigma_{\mathrm{vM}}^{\mathrm{ext}}/E_0)^2}}, \tag{3.27a}$$

$$\epsilon_{\text{stress}}(n_{\max}, k_{\max}) = \sqrt{\sum_{i,j} \frac{\left(\sigma_{\text{vM}}^{(n_{\max}+1,k_{\max}+1)}(x_i, y_j) - \sigma_{\text{vM}}^{(n_{\max},k_{\max})}(x_i, y_j)\right)^2}{N_p(\sigma_{\text{vM}}^{\text{ext}})^2}}. \tag{3.27b}$$

Here, displacements and von Mises stresses are normalized with the characteristic scales $d\sigma_{\text{vM}}^{\text{ext}}/E_0$ and $\sigma_{\text{vM}}^{\text{ext}}$, respectively, where d is the diameter of holes, $\sigma_{\text{vM}}^{\text{ext}} = |\sigma_{xx}^{\text{ext}}|$ is the value of von Mises stress due to external load, and E_0 is the Young's modulus of the surrounding elastic matrix. The normalized errors are plotted in Fig. 3.11 for the elastic strip with one hole (see Fig. 3.8a). As the maximum degree $n_{\max}$ of induced multipoles and the maximum number $k_{\max}$ of images are increased, the normalized errors for displacements $\epsilon_{\text{disp}}(n_{\max}, k_{\max})$ and stresses $\epsilon_{\text{stress}}(n_{\max}, k_{\max})$ decrease exponentially. As discussed in Section 3.2.1 and in Ref. [49] a higher number $n_{\max}$ is needed when either holes and inclusions are close to each other or when holes and inclusions are close to the boundary. For sufficiently large $n_{\max}$, the errors are quite low already for $k_{\max} = 1$ (see Fig. 3.11), because the most dominant interactions occur with the nearest image. The errors can then be further reduced by increasing the number of images $k_{\max}$.

3.2.3 Inclusions in a semi-infinite elastic matrix with prescribed displacements along the outer boundary of the elastic matrix

In this section, we consider the deformation of a semi-infinite elastic matrix ($y < y_b$) with embedded circular holes and inclusions by prescribing uniform displacements along the outer boundary of the elastic matrix. We follow the same procedure as described in Section 3.2.1 for prescribed uniform tractions along the outer boundary of the elastic matrix. Deformation of the elastic matrix induces elastic multipoles at the centers of holes and inclusions, which further induce image multipoles in order

to satisfy boundary conditions at the outer edge. The first step is thus to find the appropriate Airy stress functions for image multipoles. As described in Section 3.1, it is sufficient to find the Airy stress function for the image of disclination, which can then be used to derive expressions for the Airy stress functions that correspond to images for all other elastic multipoles.

Thus we first consider a semi-infinite elastic medium with Young's modulus E_0 and Poisson's ratio ν_0 filling half-space $y < y_b$ with a disclination with charge s at position $\mathbf{x}_0 = (x_0, y_0) = (x_0, y_b - h)$, which is at the distance h from the fixed edge at $y = y_b$. The Airy stress function $\chi(\mathbf{x})$ for this case can be found by solving the equation $\Delta\Delta\chi = E_0 s\delta(\mathbf{x} - \mathbf{x_0})$ with the boundary conditions $u_x(x, y_b) = u_y(x, y_b) = 0$. This boundary condition can be achieved by bonding the elastic matrix to an infinitely rigid material ($E \to \infty$) on the half-plane ($y > y_b$) at $y = y_b$. Such a problem was previously considered by Adeerogba in Ref. [137], who demonstrated that for the eigenstresses in the elastic matrix described with the Airy stress function $\chi_0(x, y)$, boundary conditions at the fixed edge can be satisfied with the addition of the image Airy stress function

$$\begin{aligned}\mathcal{I}\big[\chi_0(x,y)\big] = \frac{1}{4}\left(\frac{1}{\kappa_0} - \kappa_0\right)\int dy \int dy\, \Delta\chi_0\big(x, 2y_b - y\big) \\ + \frac{1}{\kappa_0}\chi_0\big(x, 2y_b - y\big) - \frac{2}{\kappa_0}(y - y_b)\frac{\partial\chi_0\big(x, 2y_b - y\big)}{\partial y} \\ + \frac{1}{\kappa_0}(y - y_b)^2\Delta\chi_0\big(x, 2y_b - y\big),\end{aligned} \tag{3.28}$$

where the value of Kolosov's constant κ_0 is $(3 - \nu_0)/(1 + \nu_0)$ for plane stress and $3 - 4\nu_0$ for plane strain condition [1]. The above operator in Eq. (3.28) works for all elastic multipoles except for the disclination (topological monopole), for which it produces additional uniform stress that has to be subtracted. For the disclination with charge s at position $\mathbf{x}_0$ with the Airy stress function $\chi_m(\mathbf{x} - \mathbf{x}_0|s) = \frac{E_0 s}{8\pi}|\mathbf{x} - \mathbf{x}_0|^2\big(\ln|\mathbf{x} - \mathbf{x}_0| - 1/2\big)$, we obtain the Airy stress function for its image at position

$\mathbf{x}_0^* = (x_0^*, y_0^*) = (x_0, y_b + h)$ as

$$\begin{aligned}\frac{8\pi\kappa_0}{E_0 s}\mathcal{I}\big[\chi_m(\mathbf{x}-\mathbf{x}_0|s)\big] =& r^{*2}\ln r^* + \frac{(5+2\kappa_0+\kappa_0^2)}{8}r^{*2} \\ &+ \frac{(-9-\kappa_0-7\kappa_0^2+\kappa_0^3)}{16}r^{*2}\cos(2\varphi^*) \\ &- \frac{(1-\kappa_0^2)}{2}r^{*2}\ln r^*\cos(2\varphi^*) \\ &+ \frac{(1-\kappa_0^2)}{2}r^{*2}\varphi^*\sin(2\varphi^*) \\ &+ 4hr^*\ln r^*\sin\varphi^* + 4h^2\ln r^*,\end{aligned} \tag{3.29}$$

where ($r_i^* = \sqrt{(x-x_0^*)^2+(y-y_0^*)^2}, \varphi_i^* = \arctan[(y-y_0^*)/(x-x_0^*)]$) are polar coordinates centered at the image of the disclination. Note that the terms $r^{*2}\ln r^*\cos(2\varphi^*)$ and $r^{*2}\varphi^*\sin(2\varphi^*)$ are absent in the Michell solution for the biharmonic equation [39], but their difference $r^{*2}\cos(2\varphi^*)\ln r^* - r^{*2}\varphi^*\sin(2\varphi^*)$ is harmonic and thus satisfies the biharmonic equation. The images for all other multipoles can be obtained by using the operator in Eq. (3.28) or by taking appropriate derivatives of the Airy stress function for the image of disclination as demonstrated in Section 3.1.

Now, let us consider a 2D semi-infinite elastic matrix with the Young's modulus E_0 and the Poisson's ratio ν_0 filling the half-space $y < y_b$ subjected to external strain ($\varepsilon_{xx}^{\text{ext}}$, $\varepsilon_{yy}^{\text{ext}}$). Embedded in the elastic matrix are N circular inclusions with radii R_i centered at positions $\mathbf{x}_i = (x_i, y_i) = (x_i, y_b - h_i)$ with Young's moduli E_i and Poisson's ratios ν_i, where $i \in \{1, \ldots, N\}$ and h_i is the distance between the center of the i^{th} inclusion and the displacement-controlled edge at $y = y_b$. Holes are described with the zero Young's modulus ($E_i = 0$).

The external strain ($\varepsilon_{xx}^{\text{ext}}$, $\varepsilon_{yy}^{\text{ext}}$) can be described with the equivalent external stresses $\sigma_{xx}^{\text{ext}} = \frac{E_0}{(1-\nu_0^2)}\left[\varepsilon_{xx}^{\text{ext}} + \nu_0\varepsilon_{yy}^{\text{ext}}\right]$, $\sigma_{yy}^{\text{ext}} = \frac{E_0}{(1-\nu_0^2)}\left[\varepsilon_{yy}^{\text{ext}} + \nu_0\varepsilon_{xx}^{\text{ext}}\right]$ for plane stress condition and with stresses $\sigma_{xx}^{\text{ext}} = \frac{E_0}{(1+\nu_0)(1-2\nu_0)}\left[(1-\nu_0)\varepsilon_{xx}^{\text{ext}} + \nu_0\varepsilon_{yy}^{\text{ext}}\right]$, $\sigma_{yy}^{\text{ext}} = \frac{E_0}{(1+\nu_0)(1-2\nu_0)}\left[(1-\nu_0)\varepsilon_{yy}^{\text{ext}} + \nu_0\varepsilon_{xx}^{\text{ext}}\right]$ for plane strain condition. External load represented with the Airy stress function $\chi_{\text{ext}}(x,y) = \frac{1}{2}\sigma_{xx}^{\text{ext}}y^2 + \frac{1}{2}\sigma_{yy}^{\text{ext}}x^2$ then induces

elastic multipoles at the centers of inclusions and holes. The Airy stress function $\chi_{\text{out}}\big(r_i, \varphi_i|\mathbf{a}_{i,\text{out}}\big)$ outside the i^{th} inclusion due to the induced multipoles can be expanded as shown in Eq. (3.8), where the origin of polar coordinates (r_i, φ_i) is at the center $\mathbf{x}_i$ of the i^{th} inclusion and the set of amplitudes of induced multipoles is $\mathbf{a}_{i,\text{out}} = \{A_{i,0}, A_{i,1}, \dots, B_{i,1}, B_{i,2}, \dots, C_{i,2}, C_{i,3}, \dots, D_{i,2}, D_{i,3}, \dots\}$. The induced elastic multipoles at the center of the i^{th} inclusion then further induce image multipoles at position $\mathbf{x}_i^* = (x_i^*, y_i^*) = (x_i, y_b + h_i)$ to satisfy boundary conditions at the edge ($u_x(x, y_b) = x\varepsilon_{xx}^{\text{ext}}$, $u_y(x, y_b) = y_b\varepsilon_{yy}^{\text{ext}}$). The Airy stress function $\mathcal{I}\left[\chi_{\text{out}}\big(r_i, \varphi_i|\mathbf{a}_{i,\text{out}}\big)\right]$ of image multipoles due to the i^{th} inclusion can be expanded as shown in Eq. (3.9), where the set of amplitudes of image multipoles is $\mathbf{a}_{i,\text{out}}^* = \{A_{i,0}^*, A_{i,1}^*, \dots, B_{i,0}^*, B_{i,1}^*, \dots, C_{i,2}^*, C_{i,3}^*, \dots, D_{i,2}^*, D_{i,3}^*, \dots\}$. The amplitudes $\mathbf{a}_{i,\text{out}}^*$ of image multipoles can be obtained with the help of the image operator in Eq. (3.28) and they are related to the amplitudes of induced multipoles $\mathbf{a}_{i,\text{out}}$ for the i^{th} inclusion as

$$A_{i,n}^* = \begin{cases} +\frac{1}{\kappa_0}A_{i,0} + \left(-\frac{1}{\kappa_0} + \kappa_0\right)C_{i,2}, & n = 0, \\ +\frac{(n+1)}{\kappa_0}A_{i,n} + \frac{1}{n}\left(\frac{(n+1)^2}{\kappa_0} - \kappa_0\right)C_{i,n+2} \\ \quad +\frac{2(n-1)}{\kappa_0}\frac{h_i}{R_i}B_{i,n-1} & n \geq 1, \\ \quad +\frac{2(2n+1)}{\kappa_0}\frac{h_i}{R_i}D_{i,n+1} \\ \quad -\frac{4(n-1)}{\kappa_0}\frac{h_i^2}{R_i^2}C_{i,n}, \end{cases} \tag{3.30a}$$

$$B^*_{i,n} = \begin{cases} \left(-\frac{1}{\kappa_0} + \kappa_0\right) D_{i,2}, & n = 0, \\ -\frac{2}{\kappa_0} B_{i,1} - \left(\frac{4}{\kappa_0} - \kappa_0\right) D_{i,3} \\ \qquad -\frac{2}{\kappa_0}\frac{h_i}{R_i} A_{i,0} & n = 1, \\ \qquad +\frac{6}{\kappa_0}\frac{h_i}{R_i} C_{i,2}, \\ -\frac{(n+1)}{\kappa_0} B_{i,n} - \frac{1}{n}\left(\frac{(n+1)^2}{\kappa_0} - \kappa_0\right) D_{i,n+2} \\ \qquad +\frac{2(n-1)}{\kappa_0}\frac{h_i}{R_i} A_{i,n-1} \\ \qquad +\frac{2(2n+1)}{\kappa_0}\frac{h_i}{R_i} C_{i,n+1} & n \geq 2, \\ \qquad +\frac{4(n-1)}{\kappa_0}\frac{h_i^2}{R_i^2} D_{i,n}, \end{cases} \tag{3.30b}$$

$$C^*_{i,n} = \begin{cases} -\frac{1}{\kappa_0} C_{i,2} + \frac{1}{\kappa_0} A_{i,0}, & n = 2, \\ -\frac{(n-1)}{\kappa_0} C_{i,n} - \frac{(n-2)}{\kappa_0} A_{i,n-2} \\ \qquad -\frac{2(n-2)}{\kappa_0}\frac{h_i}{R_i} D_{i,n-1}, & n \geq 3, \end{cases} \tag{3.30c}$$

$$D^*_{i,n} = \begin{cases} +\frac{(n-1)}{\kappa_0} D_{i,n} + \frac{(n-2)}{\kappa_0} B_{i,n-2} \\ \qquad -\frac{2(n-2)}{\kappa_0}\frac{h_i}{R_i} C_{i,n-1}, & n \geq 2. \end{cases} \tag{3.30d}$$

The total Airy stress function $\chi^{\text{tot}}_{\text{out}}\left(x, y|\mathbf{a}_{\text{out}}\right)$ outside all inclusions is then the sum of contributions due to external load, $\chi_{\text{ext}}(x, y)$, due to induced multipoles at the center of the i^{th} inclusion, $\chi_{\text{out}}\left(r_i, \varphi_i|\mathbf{a}_{i,\text{out}}\right)$, and due to their images, $\mathcal{I}\left[\chi_{\text{out}}\left(r_i, \varphi_i|\mathbf{a}_{i,\text{out}}\right)\right]$, as shown in Eq. (3.11). We also expand the induced Airy stress function inside the i^{th} inclusion $\chi_{\text{in}}\left(r_i, \varphi_i|\mathbf{a}_{i,\text{in}}\right)$, as shown in Eq. (3.12), and define the total Airy stress function $\chi^{\text{tot}}_{\text{in}}\left(r_i, \varphi_i|\mathbf{a}_{i,\text{in}}\right)$ inside the i^{th} inclusion, which also includes the effect of external load, $\chi_{\text{ext}}(x, y)$ as shown in Eq. (3.13). The rest of the steps are the same as those described in Section 3.2.1. The amplitudes of induced multipoles $\mathbf{a}_{i,\text{out}}$ and $\mathbf{a}_{i,\text{in}}$ are obtained by satisfying the boundary conditions that tractions and displacements

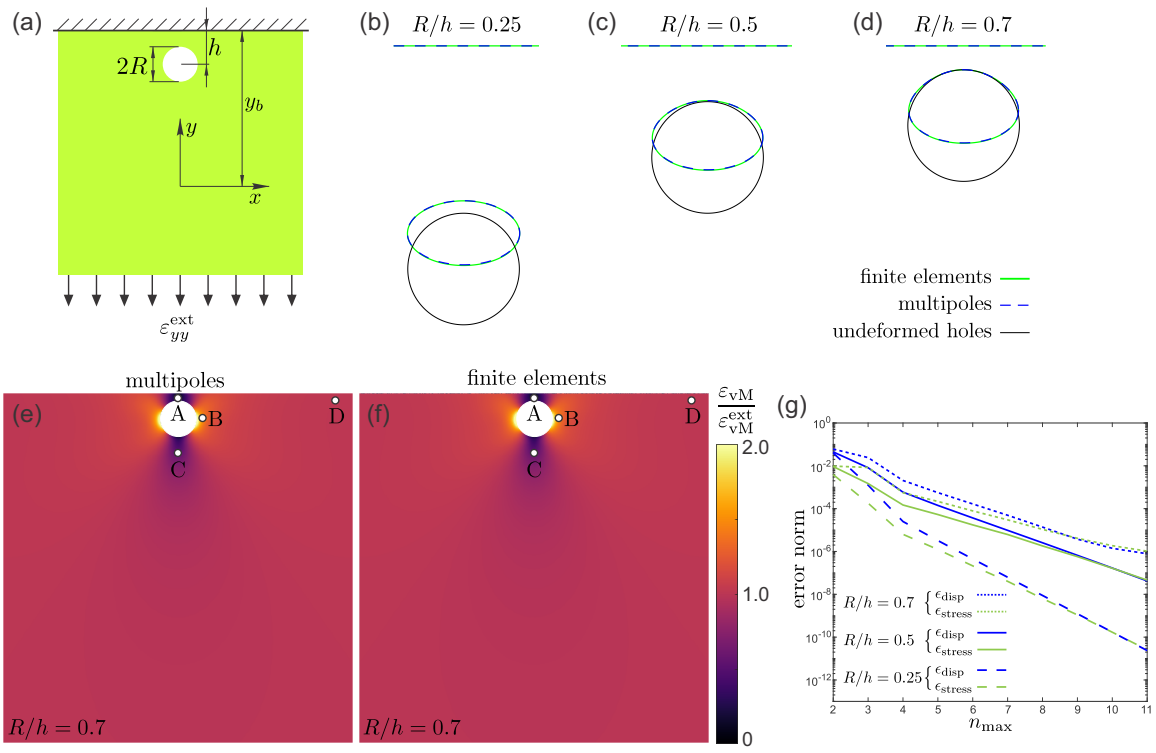

Figure 3.12: Deformation of a circular hole near a straight rigid edge under external strain. (a) Schematic image describing the initial undeformed shape of the structure and the direction of applied strain $\varepsilon_{yy}^{\text{ext}} = -0.15$ ($\varepsilon_{xx}^{\text{ext}} = 0$). The Poisson's ratio for the elastic matrix was $\nu_0 = 0.30$. (b-d) Contours of deformed holes for $R/h = 0.25$, 0.5, and 0.7, where R is the hole radius and h is the distance between the center of the hole and the rigid edge. Dashed blue lines show the contours obtained with elastic multipole method for $n_{\max} = 10$. Green solid lines show the contours obtained with linear finite element simulations. As a reference, we include black solid lines that correspond to the undeformed configurations of holes at their original positions. (e-f) Equivalent von Mises strain fields ε_{vM} for the case with $R/h = 0.7$ were obtained with (e) elastic multipole method ($n_{\max} = 10$) and (f) linear finite element simulations. Strain fields were normalized with the value of the equivalent von Mises strain $\varepsilon_{\text{vM}}^{\text{ext}} = |\varepsilon_{yy}^{\text{ext}}|$ imposed by external loads. Four marked points A-D were chosen for the quantitative comparison of strains ε_{vM}. See Table 3.5 for details. (g) The normalized errors for displacements $\epsilon_{\text{disp}}(n_{\max})$ (blue lines) and stresses $\epsilon_{\text{stress}}(n_{\max})$ (green lines) are defined in Eq. (3.22).

are continuous across the circumference of each inclusion in Eq. (3.14), which can be converted to the matrix equation similar to that in Eq. (3.21).

The elastic multipole method described above was tested for one circular hole of radius R embedded in a semi-infinite plate ($y < 0$) subjected to uniaxial strain

$\varepsilon_{yy}^{\text{ext}} = -0.15$ under plane stress condition (see Fig. 3.12a). Three different values of the separation distance h between the center of the hole and the rigid edge were considered: $h = 4R$, $h = 2R$, and $h = R/0.7$. In Fig. 3.12b-d, we show the contours of deformed holes for different values of the separation distance h of the hole from the rigid edge, where we set $n_{\max} = 10$. When the hole is far away from the edge ($h = 4R$) its deformed shape is elliptical because the interaction of hole with its image is very weak (see Fig. 3.12b). However, when the hole is moved closer to the rigid edge ($h = 2R$, $h = R/0.7$), its deformed shape deviates from the ellipse, because the hole interacts more strongly with its image (see Fig. 3.12c,d). In particular, for $h = R/0.7$, the portion of the contour of the deformed hole facing the rigid edge overlaps with that of the undeformed hole, whereas the portion of the circumference of the deformed hole facing away from the rigid edge is still elliptical. This occurs because displacements near the rigid edge are very small.

The normalized errors obtained from the convergence analysis for displacements $\epsilon_{\text{disp}}(n_{\max})$ and stresses $\epsilon_{\text{stress}}(n_{\max})$ are evaluated according to Eq. (3.22) and they are plotted in Fig. 3.12g. As the maximum degree $n_{\max}$ of induced multipoles is increased, the normalized errors decrease exponentially and they decrease more slowly when the hole is brought close to the rigid edge and their interaction with its image becomes important (see Fig. 3.12d).

Results from the elastic multipole method are compared with linear finite element simulations on a rectangular domain of size $800R \times 400R$ with prescribed displacements along the boundary (see Appendix B.1 for details). The contours of deformed holes in simulations matched very well with those obtained with the elastic multipole method with $n_{\max} = 10$ (Fig. 3.12b-d). We also compared the equivalent von Mises strain fields ε_{vM} (see Eq. (3.23)) obtained with elastic multipole method (Fig. 3.12e) and linear finite elements (Fig. 3.12f). The agreement between the two strain fields is very good and the quantitative comparison of strains at four different points A-

Table 3.5: Quantitative comparison for the values of equivalent von Mises strains $\varepsilon_{\rm vM}$ normalized with the value for the applied external load $\varepsilon_{\rm vM}^{\rm ext} = |\varepsilon_{yy}^{\rm ext}|$ at points A-D (defined in Fig. 3.12) in compressed samples with one hole near a rigid edge obtained with elastic multipole method (EMP) and finite element simulations (FEM). The relative percent errors between EMP and FEM were calculated as $100 \times (\varepsilon_{\rm vM}^{\rm (EMP)} - \varepsilon_{\rm vM}^{\rm (FEM)})/\varepsilon_{\rm vM}^{\rm (FEM)}$.

points	strain $\varepsilon_{\rm vM}/\varepsilon_{\rm vM}^{\rm ext}$		
	EMP	FEM	$\epsilon(\%)$
A	0.22208	0.22232	0.11
B	1.48299	1.48307	0.02
C	0.55360	0.55369	0.01
D	1.01509	1.01508	0.00

D (marked in Fig. 3.12e,f) showed a relative error of only $\sim 0.1\%$ (see Table 3.5), which is much smaller than errors for the example with one hole near the traction-free edge in Section 3.2.1. This is because the sample of size $\approx 25R \times 25R$ was used for linear finite element simulations to match the size of the experimental sample for the traction-free edge case, but here we used a much larger sample of size $800R \times 400R$, which better approximates semi-infinite elastic matrix that is analyzed with the elastic multipole method. Moreover, the hole was further away from the rigid edge than for the traction-free case in Section 3.2.1, which results in lower amplitudes of induced higher-order multipoles.

Note that we tried to perform experiments for this case as well by gluing the edge to aluminum plates. Upon compression of the sample, we observed a pronounced out-of-plane deformation in the vicinity of the hole, which is not captured by the elastic multipole method and by 2D linear finite element simulations. Hence, we skipped the comparison with experiments in this case.

3.2.4 Inclusions in deformed elastic disks

In this section we consider the deformation of an elastic disk with embedded circular holes and inclusions by prescribing three different types of boundary conditions at

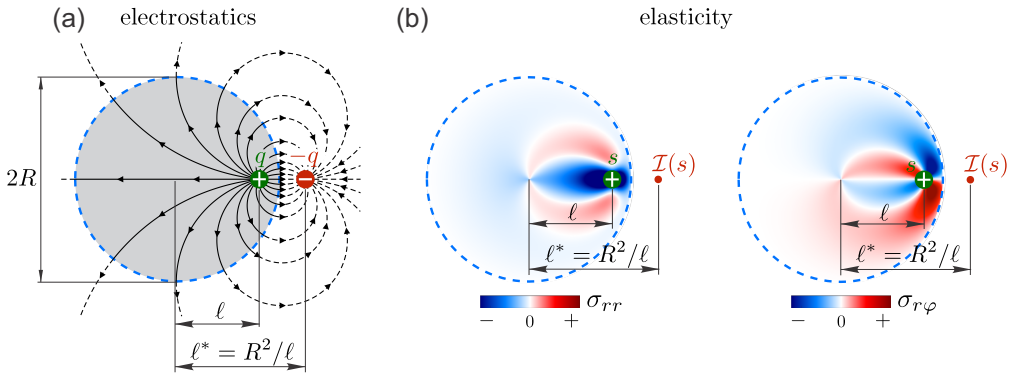

Figure 3.13: Image charges in electrostatics and elasticity for circular geometry. (a) A point electric charge q (green) at distance ℓ from the center of a circular conductive shell with radius R (dashed blue line) induces an opposite image charge $\mathcal{I}(q) = -q$ (red) at the inverse point at distance $\ell^* = R^2/\ell$ to satisfy the boundary condition that the electric field lines (black lines) are orthogonal to the conductive shell. (b) A disclination with charge s (green) embedded in an elastic disk near a traction-free edge induces an image charge $\mathcal{I}(s)$ (red) at the inverse point to satisfy the boundary conditions at the edge, where tractions must vanish ($\sigma_{rr} = \sigma_{r\varphi} = 0$).

the outer edge of the disk: hydrostatic stress ($\sigma_{rr} \neq 0$, $\sigma_{r\varphi} = 0$), no-slip condition ($u_r \neq 0$, $u_\varphi = 0$), and slip condition ($u_r \neq 0$, $\sigma_{r\varphi} = 0$). Physically, the hydrostatic boundary condition corresponds to the uniform pressure applied on the boundary. The no-slip boundary condition corresponds to prescribing a uniform radial displacement without any slipping in the tangential direction, i.e. tangential displacements are zero. Finally, the slip boundary condition corresponds to the uniform radial displacement with slipping in the tangential direction, i.e. the boundary tangential force is zero. As described in previous sections, the deformation of the elastic matrix induces elastic multipoles at the centers of holes and inclusions, which further induce image multipoles to satisfy boundary conditions at the outer edge of the disk.

Image charges in circular geometries have been considered in electrostatics, where it is known that a charge q inside a conductive circular shell of radius R induces an image charge $-q$ at the inverse point (see Fig. 3.13a) [121, 48], where the charge and the image charge are located along the same radial line and their distances to the center of the conductive circular shell are ℓ and $\ell^* = R^2/\ell$, respectively. Similarly, a

disclination with charge s embedded inside an elastic disk induces image disclination at the inverse point to satisfy boundary conditions at the edge of the elastic disk (see Fig. 3.13b). Using the method described below, we can show that for a disclination with the Airy stress function $\chi_m(r_0, \varphi_0|s) = \frac{E_0 s}{8\pi} r_0^2(\ln r_0 - 1/2)$ embedded inside an elastic disk with Young's modulus E_0 and traction-free boundary ($\sigma_{rr} = \sigma_{r\varphi} = 0$), the induced image charge is described with the Airy stress function $\mathcal{I}[\chi_m(r_0, \varphi_0|s)] = \frac{E_0 s}{8\pi}\big[- r_0^{*2}(\ln r_0^* - 1/2) - 2(\ell^* - \ell) r_0^* \ln r_0^* \cos(\varphi^* - \theta) - (\ell^* - \ell)^2 \ln r_0^* - (1 - \ell^2/R^2 + 2\ln(\ell/R)) r_0^{*2}/2\big]$. Here, the origins of polar coordinates (r, φ), (r_0, φ_0), and (r_0^*, φ_0^*) are at the center of the elastic disk, at the position of disclination ($r = \ell, \varphi = \theta$), and at the position of its image ($r = \ell^*, \varphi = \theta$), respectively. The expressions for the Airy stress functions for images of all other multipoles can then be obtained similarly as discussed in Section 3.1 or by using the compact expression for the image operator $\mathcal{I}$ that was derived by Ogbonna in Ref. [139]. While compact analytical expressions for the images of disclination are possible to obtain for traction-free and no-slip boundary conditions, this is not possible for the slip boundary condition. Below we describe how images multipoles can be systematically obtained for all boundary conditions by following the standard procedure from electrostatics [48].

Now, let us consider a 2D elastic disk of radius R with the Young's modulus E_0 and the Poisson's ratio ν_0. Embedded in the disk are N circular inclusions of radii R_i with Young's moduli E_i, Poisson's ratios ν_i, where $i \in \{1, \ldots, N\}$. They are centered at positions $\mathbf{x}_i = (r = \ell_i, \varphi = \theta_i)$, where ℓ_i is the distance from the center of the i^{th} inclusion to the center of the disk. Holes are described with the zero Young's modulus ($E_i = 0$). As discussed above, we consider three different loading conditions: hydrostatic stress ($\sigma_{rr}(r = R, \varphi) = \sigma_{rr}^{\text{ext}}$, $\sigma_{r\varphi}(r = R, \varphi) = 0$), no-slip condition ($u_r(r = R, \varphi) = u_r^{\text{ext}}$, $u_\varphi(r = R, \varphi) = 0$), and slip condition ($u_r(r = R, \varphi) = u_r^{\text{ext}}$, $\sigma_{r\varphi}(r = R, \varphi) = 0$). In the absence of inclusions, all 3 loading conditions are equivalent, i.e., they produce identical isotropic deformation (displacements, stresses)

of disk described with the Airy stress function $\chi_{\rm ext}(r,\varphi)=\frac{1}{2}\sigma_{rr}^{\rm ext}r^2$, where the radial displacement $u_r^{\rm ext}$ at the edge of the disk is related to the radial stress $\sigma_{rr}^{\rm ext}$ as $u_r^{\rm ext}=(\kappa_0-1)\sigma_{rr}^{\rm ext}R/(4\mu_0)$. Here $\mu_0=E_0/[2(1+\nu_0)]$ is the shear modulus and the value of Kolosov's constant κ_0 for plane stress is $\kappa_0=(3-\nu_0)/(1+\nu_0)$ and for plane strain is $\kappa_0=3-4\nu_0$.

External stress induces elastic multipoles at the centers of inclusions. Thus the Airy stress function outside the $i^{\rm th}$ inclusion due to the induced multipoles can be expanded as

$$\begin{aligned}\chi_{\rm out}\big(r_i,\varphi_i|\mathbf{a}_{i,\rm out}\big)=&A_{i,0}R_i^2\ln\left(\frac{r_i}{R_i}\right)\\&+\sum_{n=1}^{\infty}R_i^2\left(\frac{r_i}{R_i}\right)^{-n}\big[A_{i,n}\cos(n\varphi_i)+B_{i,n}\sin(n\varphi_i)\big]\\&+\sum_{n=2}^{\infty}R_i^2\left(\frac{r_i}{R_i}\right)^{-n+2}\big[C_{i,n}\cos(n\varphi_i)+D_{i,n}\sin(n\varphi_i)\big],\end{aligned}\tag{3.31}$$

where the origin of polar coordinates (r_i,φ_i) is at the center $\mathbf{x}_i$ of the $i^{\rm th}$ inclusion with radius R_i and the set of amplitudes of induced multipoles is $\mathbf{a}_{i,\rm out}=\{A_{i,0},A_{i,1},\dots,B_{i,1},B_{i,2},\dots,C_{i,2},C_{i,3},\dots,D_{i,2},D_{i,3},\dots\}$. To satisfy boundary conditions at the outer edge of disk these multipoles further induce image multipoles $\mathcal{I}\left[\chi_{\rm out}\big(r_i,\varphi_i|\mathbf{a}_{i,\rm out}\big)\right]$. Since the boundary conditions have to be satisfied at the outer edge of the elastic disk, it is more convenient to expand all Airy stress functions with respect to the polar coordinates (r,φ) centered at the origin of the disk. Polar coordinates (r_i,φ_i) centered at the $i^{\rm th}$ inclusion can be expressed in terms of polar coordinates centered at the disk as $r_i(r,\varphi)=\big(r^2+\ell_i^2-2r\ell_i\cos(\varphi-\theta_i)\big)^{1/2}$ and $\varphi_i(r,\varphi)=\pi+\theta_i-\arctan\left[\big(r\sin(\varphi-\theta_i)\big)/\big(\ell-r\cos(\varphi-\theta_i)\big)\right]$. Since we are interested in the region where $r\to R$ we expand the Airy stress functions $\chi_{\rm out}\big(r_i(r,\varphi),\varphi_i(r,\varphi)|\mathbf{a}_{i,\rm out}\big)$ in terms of powers of $\ell_i/r<1$ as

$$\chi_{\rm out}\big(r_i(r,\varphi),\varphi_i(r,\varphi)|\mathbf{a}_{i,\rm out}\big)=\chi_{\rm out}\big(r,\varphi|\mathbf{a}_{i,\rm out}^d\big),\tag{3.32}$$

$$\begin{aligned}\chi_{\text{out}}\big(r_i(r,\varphi),\varphi_i(r,\varphi)|\mathbf{a}_{i,\text{out}}\big) =& A^d_{i,0}R_i^2\ln\left(\frac{r}{R_i}\right)\\ &+\sum_{n=1}^{\infty}R_i^2\left(\frac{r}{R_i}\right)^{-n}\big[A^d_{i,n}\cos(n\varphi)+B^d_{i,n}\sin(n\varphi)\big]\\ &+\sum_{n=2}^{\infty}R_i^2\left(\frac{r}{R_i}\right)^{-n+2}\big[C^d_{i,n}\cos(n\varphi)+D^d_{i,n}\sin(n\varphi)\big],\end{aligned}$$

where the amplitudes $\mathbf{a}^d_{i,\text{out}}=\{A^d_{i,0},A^d_{i,1},\dots,B^d_{i,1},B^d_{i,2},\dots,C^d_{i,2},C^d_{i,3},\dots,D^d_{i,2},C^d_{i,3},\dots\}$ relative to the center of disk are related to the amplitudes $\mathbf{a}_{i,\text{out}}$ relative to the center of the i^{th} inclusion as

$$A^d_{i,n}=\begin{cases}A_{i,0}, & n=0,\\ +\displaystyle\sum_{m=1}^{n}\binom{n-1}{m-1}\left(\frac{\ell_i}{R_i}\right)^{n-m}\Big[A_{i,m}\cos\big((n-m)\theta_i\big)-B_{i,m}\sin\big((n-m)\theta_i\big)\Big]\\ +\displaystyle\sum_{m=2}^{n+1}\binom{n-1}{m-2}\left(\frac{\ell_i}{R_i}\right)^{n-m+2}\Big[-C_{i,m}\cos\big((n-m)\theta_i\big)+D_{i,m}\sin\big((n-m)\theta_i\big)\Big] & n\geq 1,\\ -\dfrac{1}{n}\left(\dfrac{\ell_i}{R_i}\right)^{n}A_{i,0}\cos(n\theta_i),\end{cases}$$

(3.33a)

$$B^d_{i,n}=\begin{cases}+\displaystyle\sum_{m=1}^{n}\binom{n-1}{m-1}\left(\frac{\ell_i}{R_i}\right)^{n-m}\Big[A_{i,m}\sin\big((n-m)\theta_i\big)+B_{i,m}\cos\big((n-m)\theta_i\big)\Big]\\ +\displaystyle\sum_{m=2}^{n+1}\binom{n-1}{m-2}\left(\frac{\ell_i}{R_i}\right)^{n-m+2}\Big[-C_{i,m}\sin\big((n-m)\theta_i\big)-D_{i,m}\cos\big((n-m)\theta_i\big)\Big] & n\geq 1\ ,\\ -\dfrac{1}{n}\left(\dfrac{\ell_i}{R_i}\right)^{n}A_{i,0}\sin(n\theta_i),\end{cases}$$

(3.33b)

$$C^d_{i,n}=\begin{cases}\displaystyle\sum_{m=2}^{n}\binom{n-2}{m-2}\left(\frac{\ell_i}{R_i}\right)^{n-m}\Big[C_{i,m}\cos\big((n-m)\theta_i\big)-D_{i,m}\sin\big((n-m)\theta_i\big)\Big], & n\geq 2\ ,\end{cases}$$

(3.33c)

$$D_{i,n}=\begin{cases}\displaystyle\sum_{m=2}^{n}\binom{n-2}{m-2}\left(\frac{\ell_i}{R_i}\right)^{n-m}\Big[C_{i,m}\sin\big((n-m)\theta_i\big)+D_{i,m}\cos\big((n-m)\theta_i\big)\Big], & n\geq 2\ .\end{cases}$$

(3.33d)

Image multipoles $\mathcal{I}[\chi_{\text{out}}\big(r_i(r,\varphi),\varphi_i(r,\varphi)|\mathbf{a}_{i,\text{out}}\big)]$ for the i^{th} inclusion are at positions $\mathbf{x}^*_i=(r=\ell^*_i,\varphi=\theta_i)$, where $\ell^*_i=R^2/\ell_i>R$. Thus their Airy stress function is

expanded in terms of powers r/ℓ_i^* as

$$\begin{aligned}
\mathcal{I}[\chi_{\text{out}}\big(r_i(r,\varphi),\varphi_i(r,\varphi)|\mathbf{a}_{i,\text{out}}\big)] =& \chi_{\text{in}}\big(r,\varphi|\mathbf{a}^{*d}_{i,\text{out}}\big),\\
\mathcal{I}[\chi_{\text{out}}\big(r_i(r,\varphi),\varphi_i(r,\varphi)|\mathbf{a}_{i,\text{out}}\big)] =& c^{*d}_{i,0}r^2 + \sum_{n=2}^{\infty} R_i^2\left(\frac{r}{R_i}\right)^n \left[a^{*d}_{i,n}\cos(n\varphi) + b^{*d}_{i,n}\sin(n\varphi)\right]\\
&+ \sum_{n=1}^{\infty} R_i^2\left(\frac{r}{R_i}\right)^{n+2} \left[c^{*d}_{i,n}\cos(n\varphi_i) + d^{*d}_{i,n}\sin(n\varphi)\right],
\end{aligned} \tag{3.34}$$

where the amplitudes of image multipoles relative to the disk center are $\mathbf{a}^{*d}_{i,\text{out}} = \{a^{*d}_{i,2}, a^{*d}_{i,3}, \ldots, b^{*d}_{i,2}, b^{*d}_{i,3}, \ldots, c^{*d}_{i,0}, c^{*d}_{i,1}, \ldots, d^{*d}_{i,1}, d^{*d}_{i,2}, \ldots\}$ and factors of ℓ_i^*/R_i are absorbed in the amplitudes $\mathbf{a}^{*d}_{i,\text{out}}$. The amplitudes of image multipoles $\mathbf{a}^{*d}_{i,\text{out}}$ are related to the amplitudes of induced multipoles $\mathbf{a}^{d}_{i,\text{out}}$, such that the boundary conditions for tractions and displacements at the edge of the disk are satisfied. To evaluate tractions and displacements at the edge we define the total Airy stress function outside all inclusions as

$$\begin{aligned}
\chi^{\text{tot}}_{\text{out}}\big(r,\varphi|\mathbf{a}_{\text{out}}\big) =& \chi_{\text{ext}}(r,\varphi) + \sum_{i=1}^{N} \chi_{\text{out}}\big(r_i(r,\varphi),\varphi_i(r,\varphi)|\mathbf{a}_{i,\text{out}}\big)\\
&+ \sum_{i=1}^{N} \mathcal{I}\left[\chi_{\text{out}}\big(r_i(r,\varphi),\varphi_i(r,\varphi)|\mathbf{a}_{i,\text{out}}\big)\right],\\
\chi^{\text{tot}}_{\text{out}}\big(r,\varphi|\mathbf{a}_{\text{out}}\big) =& \chi_{\text{ext}}(r,\varphi) + \sum_{i=1}^{N} R_i^2\left[A^d_{i,0}\ln\left(\frac{r}{R_i}\right) + c^{*d}_{i,0}\left(\frac{r}{R_i}\right)^2\right]\\
&+ \sum_{i=1}^{N}\sum_{n=1}^{\infty} R_i^2\left[A^d_{i,n}\left(\frac{r}{R_i}\right)^{-n} + C^d_{i,n}\left(\frac{r}{R_i}\right)^{-n+2}\right.\\
&\left. + a^{*d}_{i,n}\left(\frac{r}{R_i}\right)^{n} + c^{*d}_{i,n}\left(\frac{r}{R_i}\right)^{n+2}\right]\cos(n\varphi)\\
&+ \sum_{i=1}^{N}\sum_{n=1}^{\infty} R_i^2\left[B^d_{i,n}\left(\frac{r}{R_i}\right)^{-n} + D^d_{i,n}\left(\frac{r}{R_i}\right)^{-n+2}\right.\\
&\left. + b^{*d}_{i,n}\left(\frac{r}{R_i}\right)^{n} + d^{*d}_{i,n}\left(\frac{r}{R_i}\right)^{n+2}\right]\sin(n\varphi),
\end{aligned}$$

where we set $a^{*d}_{i,1} = b^{*d}_{i,1} = C^{d}_{i,1} = D^{d}_{i,1} = 0$. With the help of Table 3.1, we then evaluate tractions and displacements as

$$\begin{aligned}\sigma^{\text{out}}_{\text{tot},rr}(r=R,\varphi|\mathbf{a}_{\text{out}}) =& \sigma^{\text{ext}}_{rr} + \sum_{i=1}^{N}\left[A^{d}_{i,0}\left(\frac{R}{R_i}\right)^{-2} + 2c^{*d}_{i,0}\right] \\ &+ \sum_{i=1}^{N}\sum_{n=1}^{\infty}\left[-n(n+1)A^{d}_{i,n}\left(\frac{R}{R_i}\right)^{-n-2} - (n-1)(n+2)C^{d}_{i,n}\left(\frac{R}{R_i}\right)^{-n}\right. \\ &\qquad \left. -n(n-1)a^{*d}_{i,n}\left(\frac{R}{R_i}\right)^{n-2} - (n+1)(n-2)c^{*d}_{i,n}\left(\frac{R}{R_i}\right)^{n}\right]\cos(n\varphi) \\ &+ \sum_{i=1}^{N}\sum_{n=1}^{\infty}\left[-n(n+1)B^{d}_{i,n}\left(\frac{R}{R_i}\right)^{-n-2} - (n-1)(n+2)D^{d}_{i,n}\left(\frac{R}{R_i}\right)^{-n}\right. \\ &\qquad \left. -n(n-1)b^{*d}_{i,n}\left(\frac{R}{R_i}\right)^{n-2} - (n+1)(n-2)d^{*d}_{i,n}\left(\frac{R}{R_i}\right)^{n}\right]\sin(n\varphi),\end{aligned} \tag{3.35a}$$

$$\begin{aligned}\sigma^{\text{out}}_{\text{tot},r\varphi}(r=R,\varphi|\mathbf{a}_{\text{out}}) =& + \sum_{i=1}^{N}\sum_{n=1}^{\infty}\left[-n(n+1)A^{d}_{i,n}\left(\frac{R}{R_i}\right)^{-n-2} - n(n-1)C^{d}_{i,n}\left(\frac{R}{R_i}\right)^{-n}\right. \\ &\qquad \left. +n(n-1)a^{*d}_{i,n}\left(\frac{R}{R_i}\right)^{n-2} + n(n+1)c^{*d}_{i,n}\left(\frac{R}{R_i}\right)^{n}\right]\sin(n\varphi) \\ &+ \sum_{i=1}^{N}\sum_{n=1}^{\infty}\left[n(n+1)B^{d}_{i,n}\left(\frac{R}{R_i}\right)^{-n-2} + n(n-1)D^{d}_{i,n}\left(\frac{R}{R_i}\right)^{-n}\right. \\ &\qquad \left. -n(n-1)b^{*d}_{i,n}\left(\frac{R}{R_i}\right)^{n-2} - n(n+1)d^{*d}_{i,n}\left(\frac{R}{R_i}\right)^{n}\right]\cos(n\varphi),\end{aligned} \tag{3.35b}$$

$$\begin{aligned}\frac{2\mu_0}{R}u^{\text{out}}_{\text{tot},r}(r=R,\varphi|\mathbf{a}_{\text{out}}) =& \frac{2\mu_0}{R}\left(u^{\text{ext}}_{r} + u_x\cos\varphi + u_y\sin\varphi\right) + \sum_{i=1}^{N}\left[-A^{d}_{i,0}\left(\frac{R}{R_i}\right)^{-2} + (\kappa_0-1)c^{*d}_{i,0}\right] \\ &+ \sum_{i=1}^{N}\sum_{n=1}^{\infty}\left[nA^{d}_{i,n}\left(\frac{R}{R_i}\right)^{-n-2} + (\kappa_0+n-1)C^{d}_{i,n}\left(\frac{R}{R_i}\right)^{-n}\right. \\ &\qquad \left. -na^{*d}_{i,n}\left(\frac{R}{R_i}\right)^{n-2} + (\kappa_0-n-1)c^{*d}_{i,n}\left(\frac{R}{R_i}\right)^{n}\right]\cos(n\varphi) \\ &+ \sum_{i=1}^{N}\sum_{n=1}^{\infty}\left[nB^{d}_{i,n}\left(\frac{R}{R_i}\right)^{-n-2} + (\kappa_0+n-1)D^{d}_{i,n}\left(\frac{R}{R_i}\right)^{-n}\right. \\ &\qquad \left. -nb^{*d}_{i,n}\left(\frac{R}{R_i}\right)^{n-2} + (\kappa_0-n-1)d^{*d}_{i,n}\left(\frac{R}{R_i}\right)^{n}\right]\sin(n\varphi)\end{aligned} \tag{3.35c}$$

$$\begin{aligned}\frac{2\mu_0}{R}u^{\text{out}}_{\text{tot},\varphi}(r=R,\varphi|\mathbf{a}_{\text{out}}) =& \frac{2\mu_0}{R}\left(-u_x\sin\varphi + u_y\cos\varphi\right) \\ &+ \sum_{i=1}^{N}\sum_{n=1}^{\infty}\left[nA^{d}_{i,n}\left(\frac{R}{R_i}\right)^{-n-2} - (\kappa_0-n+1)C^{d}_{i,n}\left(\frac{R}{R_i}\right)^{-n}\right.\end{aligned}$$

$$+na_{i,n}^{*d}\left(\frac{R}{R_i}\right)^{n-2}+(\kappa_0+n+1)c_{i,n}^{*d}\left(\frac{R}{R_i}\right)^{n}\Bigg]\sin(n\varphi)$$
$$+\sum_{i=1}^{N}\sum_{n=1}^{\infty}\Bigg[-nB_{i,n}^{d}\left(\frac{R}{R_i}\right)^{-n-2}+(\kappa_0-n+1)D_{i,n}^{d}\left(\frac{R}{R_i}\right)^{-n}$$
$$-nb_{i,n}^{*d}\left(\frac{R}{R_i}\right)^{n-2}-(\kappa_0+n+1)d_{i,n}^{*d}\left(\frac{R}{R_i}\right)^{n}\Bigg]\cos(n\varphi), \tag{3.35d}$$

where terms containing σ_{rr}^{ext} and u_r^{ext} correspond to $\chi_{\text{ext}}(r,\varphi)$, terms containing $A_{i,n}^d, B_{i,n}^d, C_{i,n}^d, D_{i,n}^d$ correspond to $\chi_{\text{out}}\big(r_i,\varphi_i|\mathbf{a}_{i,\text{out}}\big)$, and terms containing $a_{i,n}^{*d}, b_{i,n}^{*d}, c_{i,n}^{*d}, d_{i,n}^{*d}$ correspond to $\mathcal{I}\left[\chi_{\text{out}}\big(r_i,\varphi_i|\mathbf{a}_{i,\text{out}}\big)\right]$. We also included displacements u_x and u_y due to a rigid body translation and introduced the shear modulus $\mu_i = E_i/[2(1+\nu_i)]$ and the Kolosov's constant κ_i for the i^{th} inclusion, where the value of Kolosov's constants is $\kappa_i = (3-\nu_i)/(1+\nu_i)$ for plane stress and $\kappa_i = 3-4\nu_i$ for plane strain conditions [1]. Similarly, we define the shear modulus $\mu_0 = E_0/[2(1+\nu_0)]$ and the Kolosov's constant κ_0 for the elastic matrix of the disk.

For the hydrostatic stress boundary condition, we require that $\sigma_{\text{tot},rr}^{\text{out}}(r = R,\varphi|\mathbf{a}_{\text{out}}) = \sigma_{rr}^{\text{ext}}$ in Eq. (3.35a) and that $\sigma_{\text{tot},r\varphi}^{\text{out}}(r = R,\varphi|\mathbf{a}_{\text{out}}) = 0$ in Eq. (3.35b). From this system of equations we obtain

$$a_{i,n}^{*d} = \begin{cases} -(n+1)\left(\dfrac{R_i}{R}\right)^{2n}A_{i,n}^{d} - n\left(\dfrac{R_i}{R}\right)^{2n-2}C_{i,n}^{d}, & n\geq 2, \end{cases} \tag{3.36a}$$

$$b_{i,n}^{*d} = \begin{cases} -(n+1)\left(\dfrac{R_i}{R}\right)^{2n}B_{i,n}^{d} - n\left(\dfrac{R_i}{R}\right)^{2n-2}D_{i,n}^{d}, & n\geq 2, \end{cases} \tag{3.36b}$$

$$c_{i,n}^{*d} = \begin{cases} -\dfrac{1}{2}\left(\dfrac{R_i}{R}\right)^{2}A_{i,0}^{d}, & n=0, \\ n\left(\dfrac{R_i}{R}\right)^{2n+2}A_{i,n}^{d} + (n-1)\left(\dfrac{R_i}{R}\right)^{2n}C_{i,n}^{d}, & n\geq 1, \end{cases} \tag{3.36c}$$

$$d_{i,n}^{*d} = \begin{cases} n\left(\dfrac{R_i}{R}\right)^{2n+2}B_{i,n}^{d} + (n-1)\left(\dfrac{R_i}{R}\right)^{2n}D_{i,n}^{d}, & n\geq 1. \end{cases} \tag{3.36d}$$

For the no-slip boundary condition, we require that $u_{\text{tot},r}^{\text{out}}(r = R,\varphi|\mathbf{a}_{\text{out}}) = u_r^{\text{ext}}$ in Eq. (3.35c) and that $u_{\text{tot},\varphi}^{\text{out}}(r = R,\varphi|\mathbf{a}_{\text{out}}) = 0$ in Eq. (3.35d). From this system of

equations we obtain

$$a_{i,n}^{*d} = \begin{cases} \frac{1}{\kappa_0}(n+1)\left(\frac{R_i}{R}\right)^{2n} A_{i,n}^d \\ \quad + \frac{1}{n\kappa_0}\left(n^2+\kappa_0^2-1\right)\left(\frac{R_i}{R}\right)^{2n-2} C_{i,n}^d \end{cases}, \quad n \geq 2, \tag{3.37a}$$

$$b_{i,n}^{*d} = \begin{cases} \frac{1}{\kappa_0}(n+1)\left(\frac{R_i}{R}\right)^{2n} B_{i,n}^d \\ \quad + \frac{1}{n\kappa_0}\left(n^2+\kappa_0^2-1\right)\left(\frac{R_i}{R}\right)^{2n-2} D_{i,n}^d \end{cases}, \quad n \geq 2, \tag{3.37b}$$

$$c_{i,n}^{*d} = \begin{cases} \frac{1}{(\kappa_0-1)} A_{i,0}^d \left(\frac{R_i}{R}\right)^2, & n = 0, \\ -\frac{1}{\kappa_0} n \left(\frac{R_i}{R}\right)^{2n+2} A_{i,n}^d \\ \quad - \frac{1}{\kappa_0}(n-1)\left(\frac{R_i}{R}\right)^{2n} C_{i,n}^d, & n \geq 1, \end{cases} \tag{3.37c}$$

$$d_{i,n}^{*d} = \begin{cases} -\frac{1}{\kappa_0} n \left(\frac{R_i}{R}\right)^{2n+2} B_{i,n}^d \\ \quad - \frac{1}{\kappa_0}(n-1)\left(\frac{R_i}{R}\right)^{2n} D_{i,n}^d \end{cases}, \quad n \geq 1, \tag{3.37d}$$

$$u_x = \sum_{i=1}^{N} -\frac{2}{\kappa_0}\frac{R_i}{2\mu_0}\left(\frac{R_i}{R}\right)^2 A_{i,1}^d, \tag{3.37e}$$

$$u_y = \sum_{i=1}^{N} -\frac{2}{\kappa_0}\frac{R_i}{2\mu_0}\left(\frac{R_i}{R}\right)^2 B_{i,1}^d, \tag{3.37f}$$

For the slip boundary conditions, we require that $u_{\mathrm{tot},r}^{\mathrm{out}}(r = R, \varphi|\mathbf{a}_{\mathrm{out}}) = u_r^{\mathrm{ext}}$ in Eq. (3.35c) and that $\sigma_{\mathrm{tot},r\varphi}^{\mathrm{out}}(r = R, \varphi|\mathbf{a}_{\mathrm{out}}) = 0$ in Eq. (3.35b). From this system of equations we obtain

$$a_{i,n}^{*d} = \begin{cases} \frac{(n+1)(\kappa_0-1)}{(\kappa_0(n-1)+n+1)}\left(\frac{R_i}{R}\right)^{2n} A_{i,n}^d \\ \quad + \frac{2n\kappa_0}{(\kappa_0(n-1)+n+1)}\left(\frac{R_i}{R}\right)^{2n-2} C_{i,n}^d \end{cases}, \quad n \geq 2, \tag{3.38a}$$

$$b_{i,n}^{*d} = \begin{cases} \frac{(n+1)(\kappa_0-1)}{(\kappa_0(n-1)+n+1)}\left(\frac{R_i}{R}\right)^{2n} B_{i,n}^d \\ \quad + \frac{2n\kappa_0}{(\kappa_0(n-1)+n+1)}\left(\frac{R_i}{R}\right)^{2n-2} D_{i,n}^d \end{cases}, \quad n \geq 2, \tag{3.38b}$$

$$c_{i,n}^{*d} = \begin{cases} \frac{1}{(\kappa_0-1)} A_{i,0}^{d} \left(\frac{R_i}{R}\right)^2 , & n=0, \\ \frac{2n}{(\kappa_0(n-1)+n+1)} \left(\frac{R_i}{R}\right)^{2n+2} A_{i,n}^{d} & \\ \quad + \frac{(n-1)(1-\kappa_0)}{(\kappa_0(n-1)+n+1)} \left(\frac{R_i}{R}\right)^{2n} C_{i,n}^{d} , & n \geq 1, \end{cases} \tag{3.38c}$$

$$d_{i,n}^{*d} = \begin{cases} \frac{2n}{(\kappa_0(n-1)+n+1)} \left(\frac{R_i}{R}\right)^{2n+2} B_{i,n}^{d} & \\ \quad + \frac{(n-1)(1-\kappa_0)}{(\kappa_0(n-1)+n+1)} \left(\frac{R_i}{R}\right)^{2n} D_{i,n}^{d} , & n \geq 1, \end{cases} \tag{3.38d}$$

$$u_x = \sum_{i=1}^{N} (1-\kappa_0) \frac{R_i}{2\mu_0} \left(\frac{R_i}{R}\right)^2 A_{i,1}^{d}, \tag{3.38e}$$

$$u_y = \sum_{i=1}^{N} (1-\kappa_0) \frac{R_i}{2\mu_0} \left(\frac{R_i}{R}\right)^2 B_{i,1}^{d}. \tag{3.38f}$$

Above we showed how the amplitudes for image multipoles $\mathbf{a}_{i,\text{out}}^{*d}$ relative to the center of the disk are related to the amplitudes of induced multipoles $\mathbf{a}_{i,\text{out}}^{d}$, which can be further expressed in terms of the amplitudes of induced multipoles $\mathbf{a}_{i,\text{out}}$ relative to the center of the i^{th} inclusion by using Eq. (3.33). In principle we could also expand the Airy stress function for the image multipoles $\mathcal{I}\left[\chi_{\text{out}}\left(r_i, \varphi_i | \mathbf{a}_{i,\text{out}}\right)\right] = \chi_{\text{out}}^{*}\left(r_i^{*}, \varphi_i^{*} | \mathbf{a}_{i,\text{out}}^{*}\right)$ in terms of polar coordinates (r_i^{*}, φ_i^{*}) relative to the center $\mathbf{x}_i^{*}$ of the image of the i^{th} inclusion as shown in Eq. (3.9) and we could also relate the amplitudes $\mathbf{a}_{i,\text{out}}^{*d}$ to the amplitudes $\mathbf{a}_{i,\text{out}}^{*}$. However, we omit this step, because we never actually need to evaluate the Airy stress functions $\mathcal{I}\left[\chi_{\text{out}}\left(r_j, \varphi_j | \mathbf{a}_{j,\text{out}}\right)\right]$ with respect to $\mathbf{x}_i^{*}$, but we need to expand them around the center $\mathbf{x}_i$ of the i^{th} inclusion to evaluate boundary conditions at the edge of that inclusion as was discussed in details in Section 3.2.1.

The resulting expression is

$$
\begin{aligned}
&\mathcal{I}\left[\chi_{\text{out}}\big(r_j(r_i,\varphi_i),\varphi_j(r_i,\varphi_i)|\mathbf{a}_{j,\text{out}}\big)\right] = \chi_{\text{in}}\big(r_i,\varphi_i|\mathbf{a}^{*i}_{j,\text{out}}\big),\\
&\mathcal{I}\left[\chi_{\text{out}}\big(r_j(r_i,\varphi_i),\varphi_j(r_i,\varphi_i)|\mathbf{a}_{j,\text{out}}\big)\right] = c^{*i}_{j,0} r_i^2\\
&\qquad + \sum_{n=2}^{\infty} R_j^2 \left(\frac{r_i}{R_j}\right)^n \left[a^{*i}_{j,n}\cos(n\varphi_i) + b^{*i}_{j,n}\sin(n\varphi_i)\right]\\
&\qquad + \sum_{n=1}^{\infty} R_j^2 \left(\frac{r_i}{R_j}\right)^{n+2} \left[c^{*i}_{j,n}\cos(n\varphi_i) + d^{*i}_{j,n}\sin(n\varphi_i)\right],
\end{aligned}
\tag{3.39}
$$

where the amplitudes $\mathbf{a}^{*i}_{j,\text{out}}$ of image multipoles relative to the center $\mathbf{x}_i = (r = \ell_i, \varphi = \theta_i)$ of fifth i^{th} inclusion are related to the amplitudes $\mathbf{a}^{*d}_{j,\text{out}}$ relative to the center of disk as

$$
\begin{aligned}
a^{*i}_{j,n} =& + \sum_{m=n}^{\infty} \binom{m}{n} \left(\frac{\ell_i}{R_j}\right)^{m-n} \Big[a^{*d}_{j,m}\cos\big((n-m)\theta_i\big) - b^{*d}_{j,m}\sin\big((n-m)\theta_i\big)\Big]\\
&+ \sum_{m=n-1}^{\infty} \binom{m+1}{n} \left(\frac{\ell_i}{R_j}\right)^{m-n+2} \Big[c^{*d}_{j,m}\cos\big((n-m)\theta_i\big) - d^{*d}_{j,m}\sin\big((n-m)\theta_i\big)\Big],
\end{aligned}
\tag{3.40a}
$$

$$
\begin{aligned}
b^{*i}_{j,n} =& + \sum_{m=n}^{\infty} \binom{m}{n} \left(\frac{\ell_i}{R_j}\right)^{m-n} \Big[a^{*d}_{j,m}\sin\big((n-m)\theta_i\big) + b^{*d}_{j,m}\cos\big((n-m)\theta_i\big)\Big]\\
&+ \sum_{m=n-1}^{\infty} \binom{m+1}{n} \left(\frac{\ell_i}{R_j}\right)^{m-n+2} \Big[c^{*d}_{j,m}\sin\big((n-m)\theta_i\big) + d^{*d}_{j,m}\cos\big((n-m)\theta_i\big)\Big],
\end{aligned}
\tag{3.40b}
$$

$$
c^{*i}_{j,n} = \sum_{m=n}^{\infty} \binom{m+1}{n+1} \left(\frac{\ell_i}{R_j}\right)^{m-n} \Big[c^{*d}_{j,m}\cos\big((n-m)\theta_i\big) - d^{*d}_{j,m}\sin\big((n-m)\theta_i\big)\Big],
\tag{3.40c}
$$

$$
d^{*i}_{j,n} = \sum_{m=n}^{\infty} \binom{m+1}{n+1} \left(\frac{\ell_i}{R_j}\right)^{m-n} \Big[c^{*d}_{j,m}\sin\big((n-m)\theta_i\big) + d^{*d}_{j,m}\cos\big((n-m)\theta_i\big)\Big].
\tag{3.40d}
$$

The rest of the steps are the same as in Section 3.2.1. We expand the induced Airy stress function inside i^{th} inclusion $\chi_{\text{in}}\big(r_i,\varphi_i|\mathbf{a}_{i,\text{in}}\big)$ as shown in Eq. (3.12),

where the set of amplitudes of induced multipoles is represented as $\mathbf{a}_{i,\text{in}} = \{a_{i,2}, a_{i,3}, \ldots, b_{i,2}, b_{i,3}, \ldots, c_{i,0}, c_{i,1}, \ldots, d_{i,1}, d_{i,2}, \ldots\}$. We again define the total Airy stress function $\chi_{\text{in}}^{\text{tot}}\big(x, y|\mathbf{a}_{i,\text{in}}\big)$ inside the i^{th} inclusion, which also includes the effect of the external load (χ_{ext}) as shown in Eq. (3.13). The amplitudes of induced multipoles $\mathbf{a}_{i,\text{out}}$ and $\mathbf{a}_{i,\text{in}}$ are obtained by satisfying the boundary conditions that tractions and displacements are continuous across the circumference of each inclusion in Eq. (3.14), which can be converted to a matrix equation similar to that in Eq. (3.21). The only difference in this procedure is that we use the above Eq. (3.39) instead of Eq. (3.18b) when expanding the Airy stress functions $\mathcal{I}\left[\chi_{\text{out}}\big(r_j, \varphi_j|\mathbf{a}_{j,\text{out}}\big)\right]$ for the image multipoles around the center $\mathbf{x}_i$ of the i^{th} inclusion. To solve the matrix equation numerically, we truncate the degrees of multipoles at $n_{\max}$ as discussed in Section 3.2.1.

The elastic multipole method described above was tested for a compressed elastic disk of diameter D with a single circular hole with diameter $d = 0.20D$ for all 3 different boundary conditions discussed above under plane stress condition (see Fig. 3.14). The distance between the center of the hole and the edge of disk was $h = 0.14D$. In Fig. 3.14b-d, we show contours of deformed holes and disk boundaries for (b) hydrostatic stress, (c) no-slip, and (d) slip boundary conditions obtained with the elastic multipole method ($n_{\max} = 10$), which match very well with the contours obtained with linear finite element simulations (see Appendix B.1 for details). For easier comparison between different boundary conditions, we chose the value of the hydrostatic stress $\sigma_{rr}^{\text{ext}} = 8\mu_0 u_r^{\text{ext}}/[D(\kappa_0 - 1)]$ such that the pristine elastic disk without holes would have the same displacement of the edge u_r^{ext} as was used for the no-slip and slip boundary conditions, where $\mu_0 = E_0/[2(1+\nu_0)]$ is the shear modulus and $\kappa_0 = (3-\nu_0)/(1+\nu_0)$ is the Kolosov's constant for plane stress condition. For the hydrostatic stress boundary condition in Fig. 3.14b, we observe a pronounced deformation in the region where the hole is close to the outer edge of the disk, which is

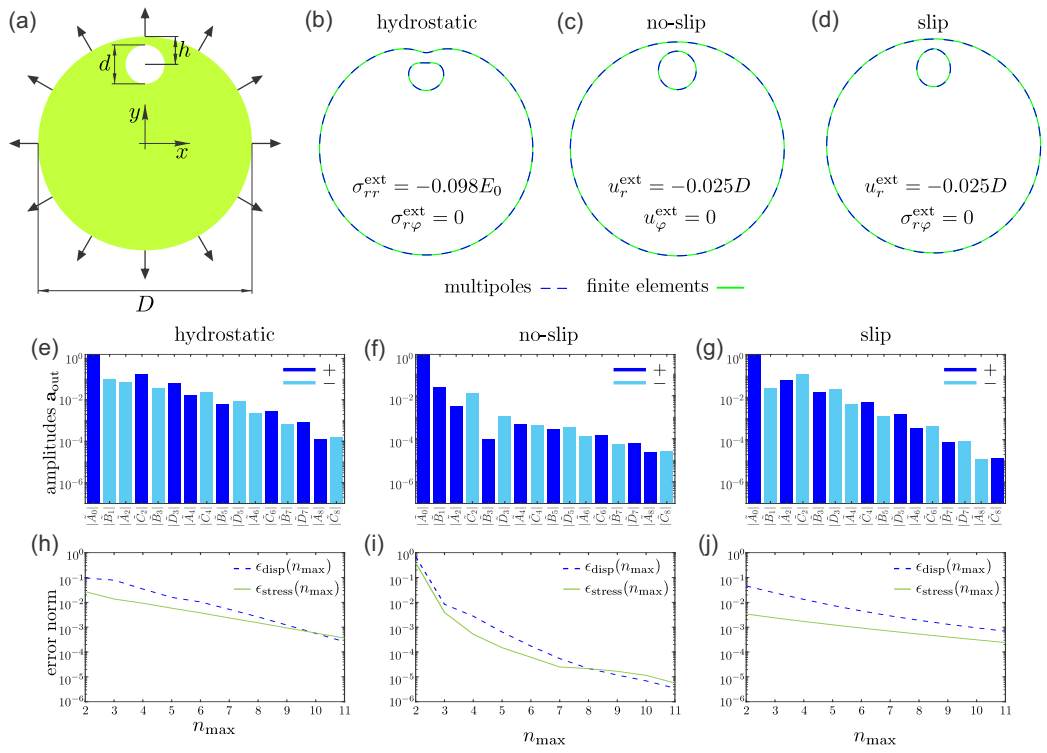

Figure 3.14: Deformation of a circular hole near the edge of a deformed elastic disk. (a) Schematic image describing the initial undeformed shape of the structure and the direction of applied deformation. The Poisson's ratio for the elastic matrix was $\nu_0 = 0.49$ and the Young's modulus was E_0. Hole is represented with the white circle. Geometrical parameters are $d/D = 0.20$ and $h/D = 0.14$. (b-d) Contours of deformed holes and disk boundaries for (b) hydrostatic stress ($\sigma_{rr}^{\rm ext} = -0.098E_0$, $\sigma_{r\varphi}^{\rm ext} = 0$), (c) no-slip ($u_r^{\rm ext} = -0.025D$, $u_\varphi^{\rm ext} = 0$), and (d) slip ($u_r^{\rm ext} = -0.025D$, $\sigma_{r\varphi}^{\rm ext} = 0$) boundary conditions. For all 3 cases, plane stress condition was used with the Kolosov's constant $\kappa_0 = (3-\nu_0)/(1+\nu_0)$. Dashed blue lines show the contours obtained with elastic multipole method for $n_{\rm max} = 10$. Green solid lines show the contours obtained from linear finite element simulations. (e-g) Absolute values of the amplitudes of induced multipoles $\mathbf{a}_{\rm out}$ at the center of hole obtained with $n_{\rm max} = 10$ for (e) hydrostatic stress, (f) no-slip, and (g) slip boundary conditions. The amplitudes are normalized, such that $\tilde{A}_n = A_n/\sigma_{rr}^{\rm ext}$, $\tilde{B}_n = B_n/\sigma_{rr}^{\rm ext}$, $\tilde{C}_n = C_n/\sigma_{rr}^{\rm ext}$, $\tilde{D}_n = D_n/\sigma_{rr}^{\rm ext}$. For the no-slip and slip boundary conditions we use the relation $\sigma_{rr}^{\rm ext} = 8\mu_0 u_r^{\rm ext}/[D(\kappa_0 - 1)]$, where $\mu_0 = E_0/[2(1+\nu_0)]$ is the shear modulus of elastic material. The dark and light blue colored bars correspond to the positive $(A_n, B_n, C_n, D_n > 0)$ and negative $(A_n, B_n, C_n, D_n < 0)$ amplitudes, respectively. Note that the amplitudes $B_{2m} = D_{2m} = A_{2m+1} = C_{2m+1} = 0$ due to the symmetry of the problem. (h-j) The normalized errors for displacements $\epsilon_{\rm disp}(n_{\rm max})$ (blue dashed lines) and stresses $\epsilon_{\rm stress}(n_{\rm max})$ (green solid lines) obtained from Eq. (3.41) for the (h) hydrostatic stress, (i) no-slip, and (j) slip boundary conditions.

similar to the case of one hole near the traction-free edge in Fig. 3.4. For the no-slip boundary condition in Fig. 3.14c we observe that the hole remains circular in the region where the hole is close to the outer edge of the disk, which is similar to the case for one hole near the straight rigid edge in Fig. 3.12. For the slip boundary condition in Fig. 3.14d we observe that the deformation of the hole is more pronounced in the region where the hole is close to the outer edge of the disk, but this deformation is not as striking as for the hydrostatic stress boundary condition in Fig. 3.14b.

These observations are also reflected in the amplitudes $\mathbf{a}_{\text{out}}$ of induced multipoles at the center of the hole (Fig. 3.14e-g). For the hydrostatic stress boundary condition, which results in the most pronounced deformation of the hole, the amplitudes of induced multipoles decrease very slowly with the degree of multipoles (see Fig. 3.14e). In contrast, the no-slip boundary condition results in the least pronounced deformation of the hole and the amplitudes of induced multipoles decrease much more rapidly with the degree of multipoles (see Fig. 3.14f). The results for the slip boundary condition are somewhere in between (see Fig. 3.14g).

The convergence analysis for the spatial distributions of displacements $\mathbf{u}^{(n_{\max})}(r,\varphi)$ and von Mises stress $\sigma_{\text{vM}}^{(n_{\max})}(r,\varphi)$ in the elastic multipole method was used to asses how many multipoles are needed. Displacements and von Mises stresses were evaluated at N_p discrete points $(r_i,\varphi_j) = (iR/500, 2\pi j/500)$, where $i \in \{1,2,\ldots,500\}$ and $j \in \{0,1,\ldots,499\}$ and grid points that lie inside the hole were excluded. The normalized errors for displacements $\epsilon_{\text{disp}}(n_{\max})$ and stresses $\epsilon_{\text{stress}}(n_{\max})$ were obtained by calculating the relative changes of spatial distributions of displacements and von Mises stresses when the maximum degree $n_{\max}$ of induced multipoles is increased by one. The normalized errors are given by [129]

$$\epsilon_{\text{disp}}(n_{\max}) = \sqrt{\sum_{i,j} \frac{\left(\mathbf{u}^{(n_{\max}+1)}(r_i,\varphi_j) - \mathbf{u}(n_{\max})(r_i,\varphi_j)\right)^2}{N_p (d\,\sigma_{\text{vM}}^{\text{ext}}/E_0)^2}}, \tag{3.41a}$$

$$\epsilon_{\text{stress}}(n_{\max}) = \sqrt{\sum_{i,j} \frac{\left(\sigma_{\text{vM}}^{(n_{\max}+1)}(r_i,\varphi_j) - \sigma_{\text{vM}}^{(n_{\max})}(r_i,\varphi_j)\right)^2}{N_p(\sigma_{\text{vM}}^{\text{ext}})^2}}. \tag{3.41b}$$

Here, displacements and von Mises stresses are normalized with the characteristic scales $d\sigma_{\text{vM}}^{\text{ext}}/E_0$ and $\sigma_{\text{vM}}^{\text{ext}}$, respectively, where $d = 2R$ is the diameter of the hole, $\sigma_{\text{vM}}^{\text{ext}}$ is the value of von Mises stress due to external load, and E_0 is the Young's modulus of surrounding elastic matrix. The normalized errors for displacements $\epsilon_{\text{disp}}(n_{\max})$ and stresses $\epsilon_{\text{stress}}(n_{\max})$ for all 3 boundary conditions are shown in Fig. 3.14h-j. The normalized errors decrease exponentially with the maximum degree of multipoles $n_{\max}$, which mimics the exponential decay of amplitude of induced multipoles in Fig. 3.14e-g. The normalized errors for the hydrostatic stress boundary condition were the largest (Fig. 3.14h), which is reflecting the observation that the amplitudes of multipoles decrease very slowly with the degree of multipoles (see Fig. 3.14e). In contrast, the normalized errors for the no-slip boundary condition reduced very quickly with the maximum degree of multipoles $n_{\max}$ (see Fig. 3.14i), which is again mimicking the distribution of amplitudes of induced multipoles (see Fig. 3.14f). The results for the slip boundary condition are somewhere in between (see Fig. 3.14j).

The elastic multipole method was also tested against experiments. We developed a simple experimental system for radial compressive loading of elastic disks with holes. The elastic disks were placed in rigid rings with smaller diameters made from polyethylene plastic (see Fig. 3.15). Elastic discs with diameter $D = 100$ mm and thickness 25 mm were pushed sequentially through the rigid rings of decreasing diameters ranging from 99 mm to 94 mm in steps of 1 mm (see Fig. 3.15a,c). Silicone oil was applied to reduce friction between the rubber sample and the walls of rigid rings. This experimental setup is thus approximating the slip boundary condition discussed above. The contours of deformed holes were then obtained by scanning the surface of compressed samples (see Fig. 3.15b).

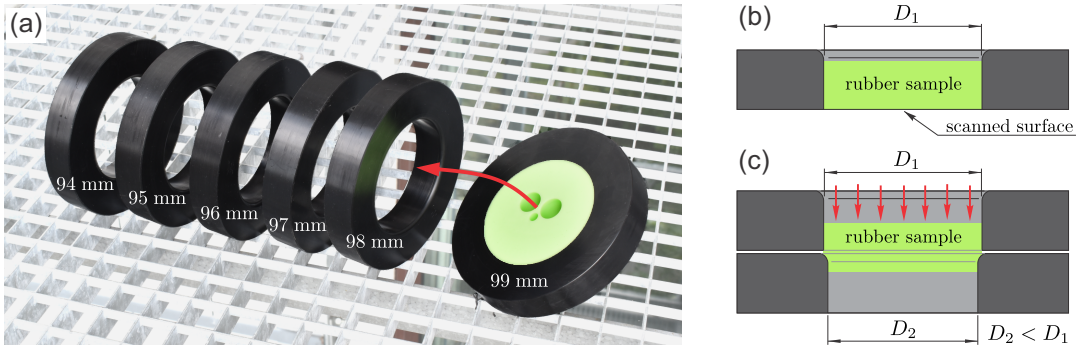

Figure 3.15: Experimental system for the compressive testing of disk samples. (a) A rubber disk sample with diameter 100 mm was placed in progressively smaller rigid rings made from polyethylene plastic. The inner diameters of rigid rings gradually decreased from 99 to 94 mm in steps of 1 mm. (b) A compressed rubber sample inside a rigid ring with diameter D_1 was placed on a flatbed photo scanner, which was used to extract the contours of deformed holes. (c) A schematic of a rubber sample pushed from a larger ring with diameter D_1 into a smaller ring with diameter $D_2 < D_1$. Silicone oil was applied to reduce friction between the rubber sample and the walls of the polyethylene ring.

In Fig. 3.16 we show initial and deformed configurations of disks with 4 different arrangements of holes. In experiments, disks were pushed through all 6 rigid rings. For each ring, the surface of disks was scanned and the contours of deformed holes were extracted with the Image Processing Toolbox in MATLAB 2018b. At higher compression, we observed a noticeable out-of-plane deformation in the vicinity of holes, which is not captured with the elastic multipole method. Therefore we used only those experimental results, where the out-of-plane deformation was minimal. The deformed contours of holes obtained with experiments were compared to the contours obtained with the elastic multiple method ($n_{\max} = 10$) and linear finite element simulations for the slip boundary condition and under plane stress condition. An excellent match was observed between the contours obtained with different methods (second row in Fig. 3.16). As in previous examples, we observed more pronounced deformations of holes in the regions where holes were close to each other and where holes were close to the edge of the disk. We have also compared the equivalent von Mises strain fields ε_{vM} (see Eq. (3.23)) obtained with the elastic multipole

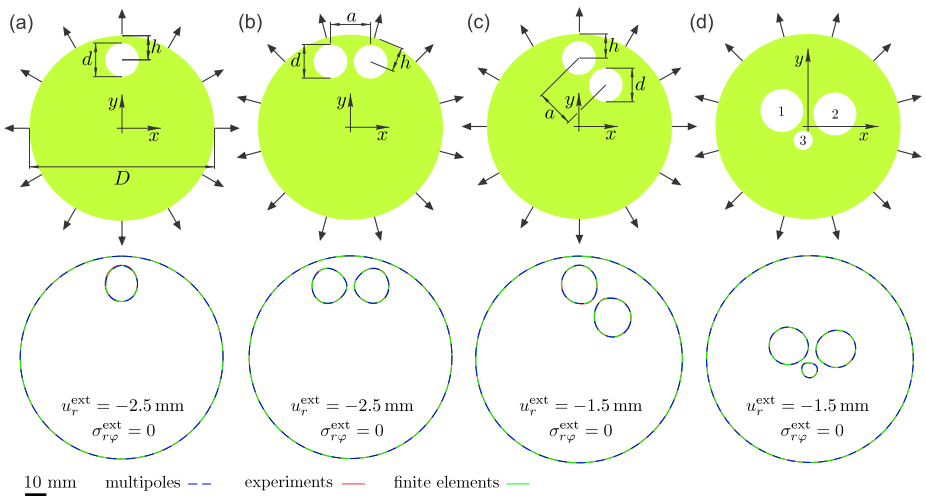

Figure 3.16: Deformation of elastic disks with holes. (a-d) Schematic images describing the initial undeformed shapes of structures with holes and the direction of applied deformation u_r^{ext} for the slip boundary condition. Holes are represented with white circles. For all elastic disks, the diameter was $D = 100$ mm and the thickness was 25 mm. They were made of rubber with the Young's modulus $E_0 = 0.97\,\text{MPa}$ and Poisson's ratio is $\nu_0 = 0.49$. For each structure we show the contours of deformed holes and disk boundaries and we report the value of applied compression u_r^{ext}. Plane stress condition was used for all cases with the Kolosov's constant $\kappa_0 = (3 - \nu_0)/(1 + \nu_0)$. Dashed blue lines show the contours obtained with elastic multipole method for $n_{\max} = 10$. Red and green solid lines show the contours obtained with experiments and linear finite element simulations, respectively. The diameters of holes in (a-c) were $d = 20.0$ mm. In (a-c) the distance h from the centers of holes to the edge of the elastic disk were (a) $h = 14.00$ mm, (b) $h = 13.95$ mm, and (c) $h = 14.00$ mm. In (b-c) the separation distance a between holes was (b) $a = 23.07$ mm and (c) $a = 23.10$ mm. In panel (d) the diameters of holes were $d_1 = d_2 = 20.0$ mm and $d_3 = 8.0$ mm and they were centered at $(x_1, y_1) = (-10.64\text{ mm}, 6.11\text{ mm})$, $(x_2, y_2) = (12.76\text{ mm}, 5.17\text{ mm})$ and $(x_3, y_3) = (-0.11\text{ mm}, -5.97\text{ mm})$.

method (first row in Fig. 3.17) and finite elements (second row in Fig. 3.17). Note that we were unable to obtain strain fields in experiments because the DIC analysis requires rather small compression increments to reliably track the movement of the speckle pattern, while in our experiments, the compression of samples was obtained in moderately large discrete steps (see Fig. 3.15). In strain fields, we observe strain concentration in regions where holes are close to each other and in regions where holes are close to the disk boundary, which is similar to the observations for holes near traction-free edges in Sections 3.2.1 and 3.2.2. The agreement between the strain

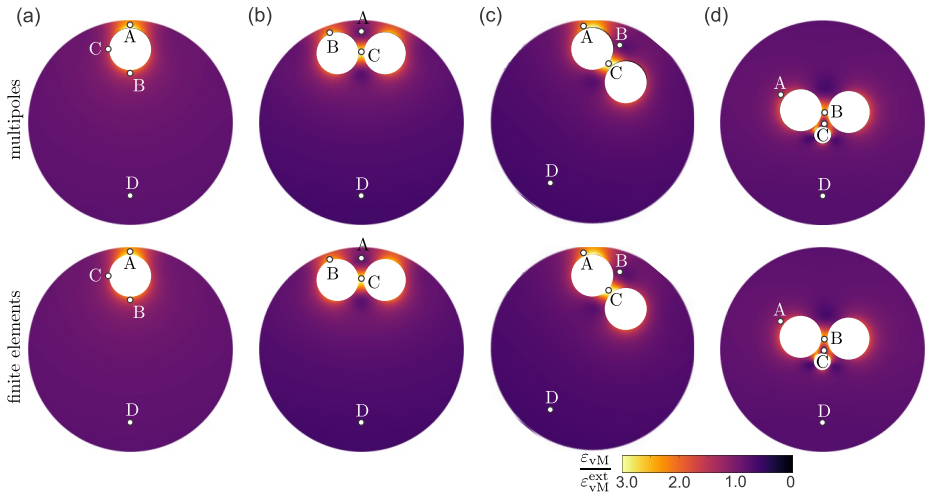

Figure 3.17: Equivalent von Mises strain fields for the deformation of elastic disks with holes in Fig. 3.16 (see Fig. 3.16 for the details of their geometry and applied deformation). (a-d) For each of the 4 structures in Fig. 3.16, we show equivalent von Mises strain fields $\varepsilon_{\mathrm{vM}}$ obtained with elastic multipole method ($n_{\max} = 10$) and finite element simulations. Strain fields were normalized with the value of the equivalent von Mises strain $\varepsilon_{\mathrm{vM}}^{\mathrm{ext}} = 4u_r^{\mathrm{ext}}/[D(1+\nu_0)(\kappa_0 - 1)]$ imposed by external loads. Four marked points A-D were chosen for the quantitative comparison of strains $\varepsilon_{\mathrm{vM}}$. See Table 3.6 for details.

fields obtained with two different methods is very good and the quantitative comparison of strains at four different points A-D (marked in Fig. 3.17) showed a relative error of $\sim 1\%$ (see Table 3.6). Note that the relative errors were so small because we used exactly the same geometry of elastic disks for both finite elements and elastic multipole method.

3.3 Conclusion

In this chapter, we demonstrated how image charges and induction, which are common concepts in electrostatics, can be effectively used also for the analysis of linear deformation of bounded 2D elastic structures with circular holes and inclusions for both plane stress and plane strain conditions. The multipole expansion of induced fields described in this work is a so-called *far-field* method and hence it is extremely efficient when holes and inclusions are far apart from each other and when they are far from

Table 3.6: Quantitative comparison for the values of equivalent von Mises strains $\varepsilon_{\mathrm{vM}}$ normalized with the value for the applied external load $\varepsilon_{\mathrm{vM}}^{\mathrm{ext}} = 4|u_r^{\mathrm{ext}}|/[D(1+\nu_0)(\kappa_0 - 1)]$ at points A-D for 4 different disk samples with holes defined in Fig. 3.17 obtained with the elastic multipole method (EMP) and linear finite element simulations (FEM). The relative percent errors between EMP and FEM were calculated as $\epsilon = 100 \times |\varepsilon_{\mathrm{vM}}^{(\mathrm{EMP})} - \varepsilon_{\mathrm{vM}}^{(\mathrm{FEM})}|/\varepsilon_{\mathrm{vM}}^{(\mathrm{FEM})}$.

points	sample (a)			sample (b)		
	strain $\epsilon_{\mathrm{vM}}/\epsilon_{\mathrm{vM}}^{\mathrm{ext}}$			strain $\epsilon_{\mathrm{vM}}/\epsilon_{\mathrm{vM}}^{\mathrm{ext}}$		
	EMP	FEM	$\epsilon(\%)$	EMP	FEM	$\epsilon(\%)$
A	2.5205	2.5396	0.75	0.8505	0.8475	0.36
B	1.5034	1.4946	0.59	2.3422	2.3406	0.07
C	1.7716	1.7723	0.04	2.8214	2.8076	0.49
D	0.8077	0.8075	0.03	0.6439	0.6441	0.03
points	sample (c)			sample (d)		
	strain $\epsilon_{\mathrm{vM}}/\epsilon_{\mathrm{vM}}^{\mathrm{ext}}$			strain $\epsilon_{\mathrm{vM}}/\epsilon_{\mathrm{vM}}^{\mathrm{ext}}$		
	EMP	FEM	$\epsilon(\%)$	EMP	FEM	$\epsilon(\%)$
A	2.2558	2.2703	0.64	1.3196	1.3227	0.23
B	0.9111	0.9047	0.71	2.3110	2.2805	1.34
C	3.3440	3.3368	0.19	0.7336	0.7248	1.21
D	0.6586	0.6584	0.03	0.7592	0.7593	0.01

the boundaries. In this case, very accurate results can be obtained by considering only induced quadrupoles, since the effect of higher-order multipoles decays more rapidly at large distances. When holes and inclusions are closer to each other or when they are closer to the boundaries, their interactions with each other via induced higher-order multipoles and their interactions with induced images become important as well. The accuracy of the results increases exponentially with the maximum degree of elastic multipoles, which is also the case in electrostatics, and this is characteristic for spectral methods [129]. The results of the elastic multipole method matched very well with both linear finite element simulations and experiments.

Chapter 4

Symmetry based classification of phonon bands in periodic elastic media

The aim of this chapter is to give a tutorial of the group theoretic description of how symmetries affect degeneracies. This theory has been used extensively in electronic and photonic systems [67, 68, 140, 69, 70]. Moreover, the group theoretic method presented in this article is applicable to systems in general dimensions. However, we restrict our examples to two dimensional (2D) systems for simplicity. In case of 2D systems, the in-plane longitudinal and shear waves decouple from antiplane shear waves since the antiplane shear wave is odd under reflection about the plane of propagation whereas the in-plane modes are even [141]. Additionally, even though the theory is equally applicable to in-plane waves, we restrict ourselves to antiplane waves because of two reasons. First, the displacement field in the latter case can be treated as a scalar field whereas the displacement field for in-plane waves is a vector field. Second, in the in-plane wave case, the longitudinal and shear waves (they are always

coupled due to scattering from boundaries between different materials) together give rise to twice as many bands as the antiplane shear waves.

4.1 Antiplane shear wave

Antiplane shear is a type of deformation of an effectively 2D elastic system spanning a region in $x-y$ plane, where the in-plane displacements $u_x = u_y = 0$, and only the out-of-plane displacement u_z is nonzero [1] in such a way that it is only a function of in-plane coordinates (x, y, t) and independent of z. For such a deformation, the system clearly needs to be homogeneous in the z direction. For small deformation (which we assume throughout the article), these restrictions on displacements mean that the diagonal elements of the strain tensor as the in-plane shear strain are zero: $\varepsilon_{xx} = \varepsilon_{yy} = \varepsilon_{zz} = \varepsilon_{xy} = 0$. The only nonzero elements of the strain tensors are $\varepsilon_{xz} = \varepsilon_{zx} = \partial_x u_z/2$ and $\varepsilon_{yz} = \varepsilon_{zy} = \partial_y u_z/2$ [1]. Assuming linear isotropic constitutive relation between stress (σ_{ij}) and strain (ε_{ij}) tensor everywhere,

$$\sigma_{ij} = \lambda\varepsilon_{kk}\delta_{ij} + 2\mu\varepsilon_{ij} \Rightarrow \sigma_{xx} = \sigma_{yy} = \sigma_{zz} = \sigma_{xy} = 0,\ \sigma_{xz} = \sigma_{zx} = \mu\partial_x u_z,\ \sigma_{yz} = \sigma_{zy} = \mu\partial_y u_z, \tag{4.1}$$

where summation is implied over repeated indices in the first equation. Above, λ and μ are the Lamé coefficients, μ is called the shear modulus. Then, the linear momentum equations become [1]

$$\partial_j\sigma_{ij} = \rho\partial_t^2 u_i \Rightarrow \partial_x(\mu\partial_x u_z) + \partial_y(\mu\partial_y u_z) = \rho\partial_t^2 u_z \Rightarrow \nabla\cdot\mu\nabla u_z = \rho\partial_t^2 u_z \tag{4.2}$$

where ρ is the density of the material and $\nabla = \hat{\mathbf{x}}\partial_x + \hat{\mathbf{y}}\partial_y$ is the in-plane gradient operator. Note that the material properties λ, μ and ρ can vary in-plane but cannot vary in the out-of-plane direction as mentioned above i.e., they are functions of in-plane coordinates (x, y). Let us denote $\nabla\cdot\mu\nabla \equiv \hat{H}$, we will call this operator

Hamiltonian. In the following, we analyze the properties of the master equation

$$\hat{H}u_z = \rho\partial_t^2 u_z. \tag{4.3}$$

Assuming that the material properties μ and ρ are independent of time, Eq. 4.3 is linear and time invariant. Since the eigenfunctions of a linear time invariant system are of the form $e^{-i\omega t}$, we plug the ansatz $u_z(x,y,t) = \tilde{u}_z(x,y)e^{-i\omega t}$ in Eq. 4.3 to obtain

$$\hat{H}\tilde{u}_z \equiv \nabla\cdot\mu\nabla\tilde{u}_z = -\rho\omega^2\tilde{u}_z. \tag{4.4}$$

The above equation is a generalized eigenvalue equation with eigenvalue ω^2. Let $\psi_0 \equiv \psi_0(x,y)$ be an eigenfunction with eigenvalue ω_0, i.e. $\hat{H}\psi_0 = -\rho\omega_0^2\psi_0$. Multiplying the complex conjugate ψ_0^* on both sides and integrating over the whole space, we get

$$\begin{aligned}
&\int dxdy\,\psi_0^*\nabla\cdot\mu\nabla\psi_0 = -\omega_0^2\int dxdy\,\psi_0^*\rho\psi_0 \\
\Rightarrow &-\int dxdy\,\mu|\nabla\psi_0|^2 + \text{Boundary terms} = -\omega_0^2\int dxdy\,\rho|\psi_0|^2 \\
\Rightarrow &\omega_0^2 = \frac{\int dxdy\,\mu|\nabla\psi_0|^2}{\int dxdy\,\rho|\psi_0|^2},
\end{aligned} \tag{4.5}$$

where from first to second line we performed integration by parts on the left hand side, and from second line to third line we ignored the boundary terms which is zero if either we employ periodic boundary condition in our system or the field dies out far away near the boundary. Let us define the inner product of any two functions $\phi(x,y)$ and $\psi(x,y)$ as $\langle\phi|\psi\rangle = \int dxdy\,\rho\,\phi^*\psi$ for later purposes. Note that the right hand side in the third line is positive as long as density ρ and shear modulus μ are positive. This implies that the frequency ω_0 is real. The purpose of this article is to give a detailed account of what can be said about the eigenvalues and eigenfunctions of Eq. 4.4 just from the symmetries (translations, rotations, glides and time reversal) of the system.

Before concluding this section, it is interesting to note the similarities between antiplane shear wave in a 2D elastic medium and electromagnetic wave in a 2D dielectric medium. The Maxwell equations [121] for electric ($\mathbf{E}$) and magnetic fields ($\mathbf{H}$) in a dielectric medium with no source charge or current are

$$\begin{aligned} \nabla \cdot \mathbf{H} = 0,\ \nabla \times \mathbf{E} = -\mu_0 \partial_t \mathbf{H}, \\ \nabla \cdot (\epsilon \mathbf{E}) = 0,\ \nabla \times \mathbf{H} = \epsilon \epsilon_0 \partial_t \mathbf{E}, \end{aligned} \tag{4.6}$$

where μ_0, ϵ_0 and ϵ are vacuum permeability, vacuum permittivity and dielectric constant respectively. Note that the fields $\mathbf{E}$ and $\mathbf{H}$ are 3D vectors but they are only functions of in-plane coordinates (x, y) and time t. As a consequence, the operator ∇ can be chosen to be the in-plane 2D gradient operator. Since, the equations are linear time invariant, we can plug in the ansatz $\mathbf{E}(x, y, t) = \tilde{\mathbf{E}}(x, y)e^{-i\omega t}$ and $\mathbf{H}(x, y, t) = \tilde{\mathbf{H}}(x, y)e^{-i\omega t}$ to get

$$\begin{aligned} \nabla \cdot \tilde{\mathbf{H}} = 0, \nabla \times \tilde{\mathbf{E}} = i\omega \mu_0 \tilde{\mathbf{H}}, \\ \nabla \cdot (\epsilon \tilde{\mathbf{E}}) = 0, \nabla \times \tilde{\mathbf{H}} = -i\omega \epsilon \epsilon_0 \tilde{\mathbf{E}}. \end{aligned} \tag{4.7}$$

Interestingly, in 2D the electric field and magnetic fields decouple two different modes, transverse electric (TE) and transverse magnetic (TM) field modes [58]. In the case of TE mode, the only nonzero fields are (E_x, E_y, H_z), whereas for TM mode, the nonzero components are (H_x, H_y, E_z). The reason for this separation of modes is the same to the reason behind separation of in-plane elastic waves and antiplane shear wave in 2D elastic media, and will be discussed later in Section 4.2. Then, after a

Table 4.1: Comparison between TE wave and antiplane shear wave when density ρ is constant

	TE mode	antiplane shear
out-of-plane field	magnetic field $\tilde{H}_z$	displacement $\tilde{u}_z$
field derivatives	electric field $\tilde{E}_y = -\frac{i}{\omega\epsilon\epsilon_0}\partial_x\tilde{H}_z$, $\tilde{E}_x = +\frac{i}{\omega\epsilon\epsilon_0}\partial_y\tilde{H}_z$	stress $\tilde{\sigma}_{xz} = \frac{1}{2}\mu\partial_x\tilde{u}_z$, $\tilde{\sigma_{yz}} = \frac{1}{2}\mu\partial_y\tilde{u}_z$
heterogeneous parameter	$\frac{1}{\epsilon}$	μ
governing equation	$\nabla\cdot\frac{1}{\epsilon}\nabla\tilde{H}_z = -\frac{\omega^2}{c_0^2}\tilde{H}_z$	$\nabla\cdot\mu\nabla\tilde{u}_z = -\rho\omega^2\tilde{u}_z$
interface conditions	$\tilde{H}_z^{(1)} = \tilde{H}_z^{(2)}$, $\mathbf{n}\times\tilde{\mathbf{E}}^{(1)} = \mathbf{n}\times\tilde{\mathbf{E}}^{(2)}$	$\tilde{u}_z^{(1)} = \tilde{u}_z^{(2)}$, $\mathbf{n}\cdot\tilde{\sigma}^{(1)} = \mathbf{n}\cdot\tilde{\sigma}^{(2)}$

little algebra the Eqs. 4.7 reduce to

$$\begin{aligned}
&\text{TE: } \nabla\times\frac{1}{\epsilon}\nabla\times\tilde{H}_z\hat{\mathbf{z}} = \frac{\omega^2}{c_0^2}\tilde{H}_z\hat{\mathbf{z}} \Rightarrow \nabla\cdot\frac{1}{\epsilon}\nabla\tilde{H}_z = -\frac{\omega^2}{c_0^2}\tilde{H}_z, \begin{cases}\tilde{E}_x = \frac{i}{\omega\epsilon\epsilon_0}\partial_y\tilde{H}_z,\\ \tilde{E}_y = -\frac{i}{\omega\epsilon\epsilon_0}\partial_x\tilde{H}_z\end{cases}\\
&\text{TM: } \nabla\times\nabla\times\tilde{E}_z\hat{\mathbf{z}} = \frac{\omega^2}{c_0^2}\epsilon\tilde{E}_z\hat{\mathbf{z}} \Rightarrow \nabla\cdot\nabla\tilde{E}_z = -\frac{\omega^2}{c_0^2}\epsilon\tilde{E}_z, \begin{cases}\tilde{H}_x = -\frac{i}{\omega\mu_0}\partial_y\tilde{E}_z,\\ \tilde{H}_y = \frac{i}{\omega\mu_0}\partial_x\tilde{E}_z\end{cases}
\end{aligned} \tag{4.8}$$

From the forms of the equations above, it can be seen that the antiplane shear wave behaves like TE (TM) mode when density ρ (shear modulus μ) is constant throughout the system. A thorough comparison between antiplane shear, TE and TM waves are given in Tables 4.1 and 4.2.

Table 4.2: Comparison between TM wave and antiplane shear wave when shear modulus μ is constant

	TM mode	antiplane shear
out-of-plane field	electric field $\tilde{E}_z$	displacement $\tilde{u}_z$
field derivatives	magnetic field $\tilde{H}_y = +\frac{i}{\omega\mu_0}\partial_x\tilde{E}_z$, $\tilde{H}_x = -\frac{i}{\omega\mu_0}\partial_y\tilde{E}_z$	stress $\tilde{\sigma}_{xz} = \frac{1}{2}\mu\partial_x\tilde{u}_z$, $\tilde{\sigma_{yz}} = \frac{1}{2}\mu\partial_y\tilde{u}_z$
heterogeneous parameter	ϵ	ρ
governing equation	$\nabla\cdot\nabla\tilde{E}_z = -\frac{\omega^2}{c_0^2}\epsilon\tilde{E}_z$	$\nabla\cdot\mu\nabla\tilde{u}_z = -\rho\omega^2\tilde{u}_z$
interface conditions	$\tilde{E}_z^{(1)} = \tilde{E}_z^{(2)}$, $\mathbf{n}\times\tilde{\mathbf{H}}^{(1)} = \mathbf{n}\times\tilde{\mathbf{H}}^{(2)}$	$\tilde{u}_z^{(1)} = \tilde{u}_z^{(2)}$, $\mathbf{n}\cdot\tilde{\sigma}^{(1)} = \mathbf{n}\cdot\tilde{\sigma}^{(2)}$

In the next section, we describe how the spatial symmetries of the system can affect the eigenvalues ω and the eigenfunctions $\tilde{u}_z(x, y)$ of the eigenproblem in Eq. 4.4.

4.2 Space group representations and symmetry protected degeneracies in band structures

A rotation, reflection or translation is a symmetry of a system, if after the transformation the system is identical to the system we started with. In other words, if, for example, for a system with a certain rotational symmetry there is an eigenfunction ψ_0 of Eq. 4.4 with eigenvalue ω_0, the rotated version ψ_0' of that eigenfunction is also an eigenfunction of Eq. 4.4 with the same eigenvalue. Now, if ψ_0 and ψ_0' are linearly independent functions, i.e. if one is not just a complex constant times the other, then we have a degeneracy at frequency ω_0. A systematic way of finding these *symmetry protected* degeneracies and classifying the eigenfunctions in terms their *characters* under symmetry operations is through group theory and group representations [68, 67, 69].

4.2.1 Group

A group is a set G with a binary operation, called product, such that (i) product of any two elements $A, B \in G$ their product AB is also in G, (ii) the product is associative, i.e., for any three elements $A, B, C \in G$, $A(BC) = (AB)C$, (iii) there exists a unique identity $E \in G$ such that for any element $A \in G$, $AE = EA = A$, (iv) for any element $A \in G$, there exists a unique element $A^{-1} \in E$, called the inverse of A, such that $AA^{-1} = A^{-1}A = E$. A point group is a group of symmetry operations that act on Euclidean space keeping a point (let us call that point O) in the n dimensional Euclidean space fixed and preserving all angles and distances. We

give a detailed account of the relevant definitions corresponding to groups and point groups in appendices C.1 and C.1.1. Here we describe space groups directly.

Space group

A discrete translational symmetry can be created in n dimensional Euclidean space by choosing n linearly independent vectors $\mathbf{t}_i$ with $i = 1, 2, \ldots n$ and making properties of the material periodic with periodicity $|\mathbf{t}_i|$ in direction $\mathbf{n}_i$, where $\mathbf{n}_i = \mathbf{t}_i/|\mathbf{t}_i|$. The set of points obtained by putting a mathematical point at each position vector $\mathbf{t} = \sum_{i=1}^{n} n_i \mathbf{t}_i$ where n_i goes over all integers is called a *Bravais lattice*. Here, $\mathbf{t}$ are called *lattice vectors* and $\mathbf{t}_i$ are called *fundamental lattice vectors*. Some examples of Bravais lattices are shown in Fig. 4.1(a) and (b). The set of translations $\mathbf{t}$ form an Abelian group T when the product is taken as the vector sum. Note that the sets $T_i = \{n_i \mathbf{t}_i | n_i \in \mathbb{Z}\}$ form Abelian subgroups of T. In $n = 2$ dimensions, T can be written as outer direct product of T_1 and T_2; $T = T_1 \otimes T_2$ (this is required to find representations of 2D discrete translation group). The Bravais lattice is invariant under these discrete translations. Therefore the symmetry group of the Bravais lattice consists of the translation operations $\mathbf{t}$. Moreover, depending on the relative of lengths of the fundamental lattice vectors and the angle between them, the Bravais lattices can be invariant under certain point group symmetries. In the example of Fig. 4.1(c), the lattice has the symmetry of the point group C_{6v} or $6mm$ shown in Fig. C.1. Depending on the point group symmetries, 2 dimensional Bravais lattices can be classified into 4 different families: monoclinic (point group C_2), orthorhombic (point group C_{2v})(Fig. 4.1(a) and (b)), square (point group C_{4v}) (Fig. 4.1(d)) and hexagonal (point group C_{6v})(Fig. 4.1(c)). Two different types of Bravais lattices can have the symmetry of point group C_{2v}: (i) if the fundamental lattice vectors are of same length ($|\mathbf{t}_1| = |\mathbf{t}_2|$) but they are not orthogonal ($\mathbf{t}_1 \cdot \mathbf{t}_2 \neq 0$); this is called a rhombic Bravais lattice (Fig. 4.1(b)) (ii) if the fundamental lattice vectors are not of same

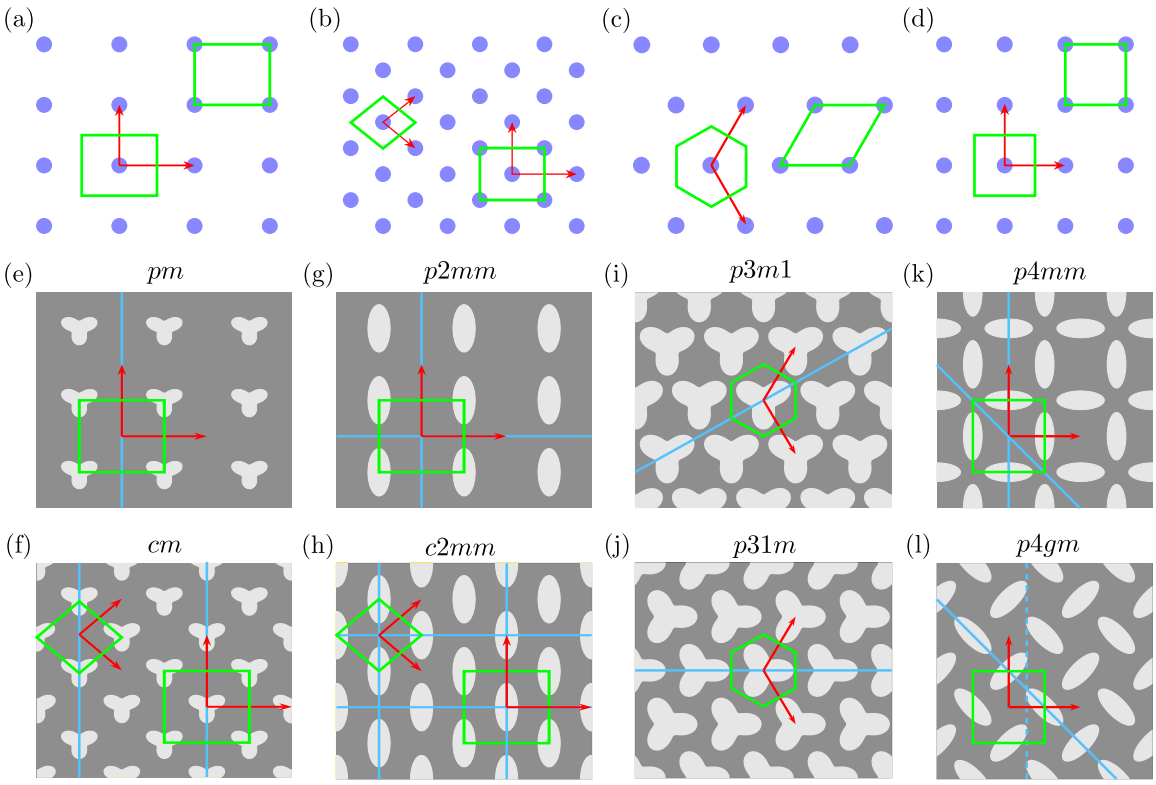

Figure 4.1: Different Bravais lattices (a-d) and examples of structures with different space group symmetries (e-l). (a), (b), (c) and (d) are rectangular, rhombic, hexagonal and square Bravais lattices, respectively, with blue dots showing the lattice points. The structures in (e), (f), (g), (h), (i), (j), (k) and (l) have pm, cm, $p2mm$, $c2mm$, $p3m1$, $p31m$, $p4mm$ and $p4gm$, respectively. In all panels the different unit cells are shown with regions outlined by solid green lines, whereas the fundamental lattice vectors are shown with red arrows. In (a-d), the unit cells that have only one lattice point and have them at their center are called Wigner-Seitz cell. The other unit cells which still have only one lattice point inside them are primitive unit cells. However, the unit cell on the bottom right corner in (b) has two lattice points and thus not primitive. In (e-l) the blue solid lines show the mirrors and blue dashed line is a glide plane. In (e) and (g), the mirrors are normal to fundamental lattice vectors, whereas in (f) and (h) they are not normal to fundamental lattice vectors (at the top left corner in each panel). However a choice of bigger unit cells in (f) and (h) (shown in bottom right corner in each panel) and hence larger lattice vectors can make the mirrors normal to lattice vectors. In (i) the mirror is perpendicular to a fundamental lattice vector, whereas in (j) it is not.

length ($|\mathbf{t}_1| \neq |\mathbf{t}_2|$) but they are orthogonal ($\mathbf{t}_1 \cdot \mathbf{t}_2 = 0$) (Fig. 4.1(a)); this is called a rectangular Bravais lattice. Therefore, there are five different Bravais lattice systems in 2D in total. Discrete translational symmetry breaks the n dimensional Euclidean

space into small repeating cells called *unit cell*. A *primitive unit cell* is a unit cell which has only one lattice point in it. Different types of unit cells are shown in Fig. 4.1(a-d).

Once we fill up the one unit cell of a Bravais lattice with elastic material and repeat that in the directions of fundamental lattice vectors, we get a phononic crystal. The set of all symmetries of a crystal form a group called *space group*. One type of symmetry of a crystal is a combination of a point group operation (rotation, inversion, reflection etc.) R followed by a lattice translation $\mathbf{t}$. If all the symmetries of a crystal are of this form, the space group of the crystal is called *symmorphic*. Clearly, in this case the symmetry group can be written as a semi-direct product of the translation group and the point group (it is easy to see that the translation group is a normal subgroup of the space group in this case). Since there are 10 crystallographic point groups in 2D dimensions, if we take semi-direct product of these with a translation group whose corresponding Bravais lattice is compatible with the point group, we get 10 different types of symmorphic space groups. However, a little thought leads to the following observations: (i) for a given hexagonal Bravais lattice there are two ways to insert the point group C_{3v} into it; in one case the normal to the mirror plane is parallel to a fundamental lattice vector (Fig. 4.1(i)), whereas in the other case the normal is at angle $\pi/6$ with a fundamental lattice vector (Fig. 4.1(j)). (ii) the insertion of C_{1v} and C_{2v} in a rectangular (or hexagonal) Bravais lattice (Fig. 4.1(e) and (g)) and a rhombic Bravais lattice (Fig. 4.1(f) and (h)) are different. In the first case, the normal of the mirror is parallel to one of the fundamental lattice vectors (Fig. 4.1(e) and (g), top left corner), in the second case it is not (Fig. 4.1(f) and (h)). (Note that in the case of Fig. 4.1(f) and (h), with the choice of the nonprimitive unit cell shown in Fig. 4.1(f) and(h) (bottom right corner), the normal of the mirror can be made parallel to a lattice vector; however, in that case, there will be a new kind of symmetry of the system which is a reflection followed by a translation equal to half

a fundamental lattice vector; this is discussed in the next paragraph.) In each of (i) and (ii), the multiplication tables change depending on direction of the normal to the mirror plane. Therefore, they lead to different space groups in each of (i) and (ii). Considering all this, there are 13 symmorphic space groups in 2 dimensions.

Since a symmorphic space group is a semi-direct product of the translation group and a point group, the point group operations and the translation operations are separable. However, there is another kind of symmetry that occurs, where the system remains invariant under a mirror reflection followed by a translation $\mathbf{v}$ (not a lattice vector). This translation $\mathbf{v}$ is often (not always) parallel to the plane of the mirror. Clearly, two successive application of this operation is equivalent to just a translation which has to be a (Bravais) lattice translation for this operation to be symmetry. Therefore the part of $\mathbf{v}$ which is parallel to mirror plane has to be half a lattice vector. This symmetry is called a glide symmetry. An example of this is shown in Fig. 4.1(l). Allowing this symmetry to be in a space group, it is possible to have 4 more space groups in 2 dimensions which can not be written as a semi-direct product of a translation group and a point group. These space groups are called *nonsymmorphic* space groups. (Note that there is a similar symmetry with a $2\pi/n$ rotation followed by a translation that can occur in 3 dimensions. This symmetry is called screw rotation. However, we will not discuss that in this text since it does not occur in 2 dimensions.) Therefore, in total there are 17 different space groups in 2 dimensions (one proof of this fact that there are only 17 space groups in 2 dimensions is using the fact that for a 2 dimensional periodic system, the Euler characteristic is 0, see [142]).

There are several different notations for space groups in literature. Here we are going to use the international notation. It starts with the letters p or c, which indicates if the unit cell of the Bravais lattice is primitive or centered (the rhombic Bravais lattice is also called centered rectangular because if we choose the nonprimitive unit cell shown in the bottom right corner of Fig. 4.1(b), (g) and (h), the unit cell

has a lattice point at its center). After that letter comes an integer showing the maximum order of rotational symmetry (1, 2, 3, 4 or 6). The next symbol indicates if there is a mirror (or a glide in the case of nonsymmorphic sapce group) plane perpendicular to one of the fundamental lattice translation vectors (called the "main" axis). If there is such a mirror (glide), the symbol is m (g), otherwise it is 1. The last symbol (again m, g or 1) shows if there is mirror or glide or none parallel or tilted to the "main" axis. The names of the space groups corresponding to the crystals in Figs. 4.1(e), (f), (g), (h), (i), (j), (k) and (l) are therefore pm, cm, $p2mm$, $c2mm$, $p3m1$, $p31m$, $p4mm$ and $p4gm$ respectively. As should be clear from the above discussion, the elements of the space groups are combinations of point group operations and translations. The standard notation for these elements is called the *Seitz* notation written as $\{R|\mathbf{v}\}$. It means a rotation R followed by a translation $\mathbf{v}$ ($\mathbf{v}$ can be lattice translation or not). The rule for multiplication of two operators $\{R_1|\mathbf{v}_1\}$ and $\{R_2|\mathbf{v}_2\}$ is $\{R_1|\mathbf{v}_1\}\{R_2|\mathbf{v}_2\} = \{R_1R_2|\mathbf{v}_1 + \mathbf{R}_1\mathbf{v}_2\}$. The identity element is denoted by $\{E|\mathbf{0}\}$. The inverse of an operator $\{R|\mathbf{v}\}$ is $\{R^{-1}| - \mathbf{R}^{-1}\mathbf{v}\}$. In this notation the glide plane shown in Fig. 4.1(l) can be written as $\{m|\mathbf{t}_2/2\}$ if call the mirror operation about the dashed line m. However, we can also write it down in terms of a parallel mirror plane passing through the center of the unit cell m_c followed by a different translation: $\{m_c|\mathbf{t}_1/2 + \mathbf{t}_2/2\}$. Although the first notation is more intuitive, the second notation is better for mathematical calculations. We will stick the second kind, i.e., we will choose the center of an unit cell to be our origin and write down any rotation (or reflection) about another point in terms of rotation (or reflection) about the origin and compensate for the difference in the translation that follows (and drop the subscript c here onward).

Clearly, the translation group T is a normal subgroup of space group G. Therefore, the coset decomposition of G with respect to T can be written as $G = \{R_1|\mathbf{v}_1\}T + \{R_2|\mathbf{v}_2\}T + \cdots + \{R_h|\mathbf{v}_h\}T$ (see appendix C.1 for definition of normal subgroup and

coset decomposition). In this decomposition we can choose $\{R_1|\mathbf{v}_1\} = \{E|\mathbf{0}\}$. The quotient group G/T is isomorphic to a point group F which contains the rotation and mirror parts of the coset representatives $F = \{R_1, R_2, \ldots, R_h\}$ (see appendix C.1 for definition of quotient group). This group F is called the *isogonal point group* of space group G. It is easy to see that if all coset representatives $\{R_i|\mathbf{v}_i\}$ of T in G can be chosen such that $\mathbf{v}_i = \mathbf{0}$, then the space group is symmorphic.

4.2.2 Representations of discrete translation group and space groups

Here we define representations, characters, reducible and irreducible representations, and give detailed accounts of how to obtain representations of the discrete translation group and space groups. The other important definitions, theorems and results can be found in appendix C.2.

Let there be a finite dimensional vector space V over the complex field. The set of all nonsingular linear operators on V forms a group called general linear group $GL(V)$. A *representation of a group* G is a homomorphism ρ from a group to the group of nonsingular linear operators $GL(V)$ on a finite dimensional vector space V. Since ρ is homomorphism, for any two elements $A, B \in G$, $\rho(A)\rho(B) = \rho(AB)$ meaning that for any vector $\mathbf{v} \in V$, $\rho(A)(\rho(B)\mathbf{v}) = \rho(AB)\mathbf{v}$. Moreover, $\rho(E)\mathbf{v} = \mathbf{v}$ where E is the identity element of G, and $\rho(A)^{-1}\mathbf{v} = \rho(A^{-1})\mathbf{v}$ for any $A \in G$ and $\mathbf{v} \in V$. Now, let a basis of the d dimensional vector space V be $V_b = \{\mathbf{v}_1, \mathbf{v}_2, \ldots, \mathbf{v}_d\}$. Then, for any element $A \in G$, since $\rho(A)\mathbf{v}_i \in V$, it can be written as a linear combination of all the vectors in the basis

$$\rho(A)\mathbf{v}_i = \mathbf{v}_j \mathbf{\Gamma}_\rho(A)_{ji}, \tag{4.9}$$

where $\mathbf{\Gamma}_\rho(A)_{ji}$ is the coefficient of $\mathbf{v}_j$ and obviously depends on the group element A. Note that sum over repeated index j is implied. We say that the square matrix

$\mathbf{\Gamma}_\rho(A)$ of dimension $d \times d$ is the matrix representing A in the basis V_b. Since for any $A \in G$, $\mathbf{\Gamma}_\rho(A) = \mathbf{\Gamma}_\rho(AE) = \mathbf{\Gamma}_\rho(A)\mathbf{\Gamma}_\rho(E)$, $\mathbf{\Gamma}_\rho(E) = \mathbb{1}$ the identity matrix of dimensionality d. Moreover, $\mathbb{1} = \mathbf{\Gamma}_\rho(E) = \mathbf{\Gamma}_\rho(AA^{-1}) = \mathbf{\Gamma}_\rho(A)\mathbf{\Gamma}_\rho(A^{-1})$ implies that $\mathbf{\Gamma}_\rho(A^{-1}) = \mathbf{\Gamma}_\rho(A)^{-1}$. It is not hard to realize that the set of all distinct matrices $\mathbf{\Gamma}_\rho(G)$ form a group Δ. Moreover, the mapping $\mathbf{\Gamma}_\rho : G \to \Delta$ is a homomorphism. The *character of a matrix group* Δ is a function $\chi : \Delta \to \mathbb{C}$, such that for any element $\mathbf{R} \in \Delta$, $\chi(\mathbf{R}) = \mathrm{tr}(\mathbf{R})$, where $\mathrm{tr}(\mathbf{R})$ is the trace of the matrix $\mathbf{R}$. If there is a subspace U of the vector space V such that for a representation ρ of a group G and any vector $\mathbf{u} \in U$, $\rho(A)\mathbf{u} \in U$ for all $A \in G$, U is called an *invariant subspace* of V under representation ρ of group G. In this case, the representation ρ is said to be *reducible*. If there are no invariant proper subspace of V under representation ρ of G, ρ is called *irreducible representation* of G. In this case the dimension of the vector space V is called the dimension of the representation ρ.

Representations of discrete translation group

Here, we describe the representations of the discrete translation group. We start with 1 dimensional discrete translation group T_1 with the generator of the group being fundamental lattice translation vector $\mathbf{t}_1$ of length $|\mathbf{t}_1| = a_1$. For convenience, we work with periodic boundary condition such that $\{E|\mathbf{t}_1\}^{N_1} = \{E|N_1\mathbf{t}_1\} \equiv \{E|\mathbf{0}\}$. Note that this assumption makes the group of finite order. Since this group is Abelian, each element of the group is in one conjugacy class by itself. Therefore, there are N_1 number of classes. Hence, there are N_1 number of irreps of the group which are all 1 dimensional (this comes from Schur's lemma described in Section C.2). Moreover, if the basis function for the m^{th} irrep is f_m, $\rho(\{E|\mathbf{t}_1\})f_m \propto f_m \implies \rho(\{E|\mathbf{t}_1\})f_m = c_m f_m$. This implies $\rho(\{E|\mathbf{t}_1\}^{N_1})f_m = c_m^{N_1} f_m = \rho(\{E|\mathbf{0}\})f_m = f_m$ or $c_m^{N_1} = 1$. Therefore, the representative matrices for each irrep are just N_1^{th} root of 1. This result along with the orthogonality relations of the characters means that

the only possible character table is 4.3. Hence, the character of $\{E|n_1\mathbf{t}_1\}$ in the m_1^{th} irrep is $\exp[-i\frac{2\pi m_1}{N_1}n_1] = \exp[-i\frac{2\pi m_1}{N_1 a_1}n_1 a_1]$. The irreps are denoted by the number

Table 4.3: Character table of 1 dimensional discrete translation group

	$\{E\|\mathbf{0}\}$	$\{E\|\mathbf{t}_1\}$	$\{E\|2\mathbf{t}_1\}$	...	$\{E\|(N_1-1)\mathbf{t}_1\}$
χ_0	$+1$	$+1$	$+1$	...	$+1$
χ_1	$+1$	$\exp[-i\frac{2\pi}{N_1}]$	$\exp[-i\frac{2\pi}{N_1}2]$	...	$\exp[-i\frac{2\pi}{N_1}(N_1-1)]$
χ_1	$+1$	$\exp[-i\frac{4\pi}{N_1}]$	$\exp[-i\frac{4\pi}{N_1}2]$	...	$\exp[-i\frac{4\pi}{N_1}(N_1-1)]$
$\vdots$	$\vdots$	$\vdots$	$\vdots$	$\ddots$	$\vdots$
χ_{N_1-1}	$+1$	$\exp[-i\frac{2(N_1-1)\pi}{N_1}]$	$\exp[-i\frac{2(N_1-1)\pi}{N_1}2]$	...	$\exp[-i\frac{2(N_1-1)\pi}{N_1}(N_1-1)]$

$m_1 = 0, 1, \ldots, N_1 - 1$ or equivalently can be characterized by $k = 0, \frac{2\pi}{N_1 a_1}, \ldots \frac{2\pi(N_1-1)}{N_1 a_1}$.

We have seen before that 2 dimensional discrete translation group T can be obtained by taking outer direct product of two 1 dimensional discrete translation group $T_1 = \{\{E|\mathbf{0}\}, \{E|\mathbf{t}_1\}, \ldots, \{E|(N_1-1)\mathbf{t}_1\}\}$ and $T_2 = \{\{E|\mathbf{0}\}, \{E|\mathbf{t}_2\}, \ldots, \{E|(N_2-1)\mathbf{t}_2\}\}$; $T = T_1 \otimes T_2$. The character table of T_2 is similar to character table of T_1, only difference is that we have to replace N_1 with N_2. From the discussion on outer direct product groups, we know that the number of conjugacy classes of T is $N_1 N_2$, hence the number of irreps is also $N_1 N_2$. We can construct the irreps of T from the irreps of T_1 and T_2 using the following intuitive *theorem on representations of outer direct product groups* (see [67] for a proof of the theorem). If $\Gamma_H^i(A)$ and $\Gamma_K^j(B)$ are the representative matrices of elements $A \in H$ and $B \in K$ of i^{th} and j^{th} irreps of dimensions d_H and d_K respectively, then the representative matrices of elements $AB = C \in G = H \otimes K$ of irrep ij of group G can be constructed as $\Gamma_G^{ij}(C) = \Gamma_H^i(A) \otimes \Gamma_K^j(B)$ where $\otimes$ between the matrices denotes Kronecker product of the matrices. This irrep ij of G is of dimension $d_H d_K$. The characters of these irreps are $\chi_G^{ij}(C) = \chi_H^i(A)\chi_K^j(B)$. Therefore, the character of an element $\{E|n_1\mathbf{t}_1 + n_2\mathbf{t}_2\}$ in the $m_1 m_2^{\text{th}}$ (that is Kronecker product of m_1^{th} irrep of T_1 and m_2^{th} irrep of T_2) irrep of T is given by the phase $\exp[-i(\frac{2\pi m_1}{N_1 a_1}(n_1 a_1) + \frac{2\pi m_2}{N_2 a_2}(n_2 a_2))]$ where $a_1 = |\mathbf{t}_1|$ and $a_2 = |\mathbf{t}_2|$ and $m_1 = 0, 1, \ldots, N_1 - 1$ and $m_2 = 0, 1, \ldots, N_2 - 1$. These

irreps of T are also 1 dimensional. A more compact way of writing this phase factor is: $\exp[-i(\frac{2\pi m_1}{N_1 a_1}(n_1 a_1) + \frac{2\pi m_2}{N_2 a_2}(n_2 a_2))] = \exp[-i(\frac{m_1}{N_1}\mathbf{K}_1 + \frac{m_2}{N_2}\mathbf{K}_2)\cdot(n_1\mathbf{t}_1 + n_2\mathbf{t}_2)]$ where the vectors $\mathbf{K}_1$ and $\mathbf{K}_2$ are called *fundamental reciprocal lattice vectors* and defined as $\mathbf{K}_i \cdot \mathbf{t}_j = 2\pi\delta_{ij}$. The fundamental reciprocal vectors can be evaluated easily as $\mathbf{K}_1 = 2\pi(\mathbf{t}_2 \times \hat{z})/(\hat{z}\cdot(\mathbf{t}_1 \times \mathbf{t}_2))$ and $\mathbf{K}_2 = 2\pi(\hat{z} \times \mathbf{t}_1)/(\hat{z}\cdot(\mathbf{t}_1 \times \mathbf{t}_2))$, where the vectors $\mathbf{t}_1$ and $\mathbf{t}_2$ are chosen to be in $x-y$ plane, and z is the direction perpendicular to $x-y$ plane in 3 dimensions. The two vectors $\mathbf{K}_1$ and $\mathbf{K}_2$ define a 2 dimensional space called *reciprocal space* or *momentum space* or simply $\mathbf{k}$-space. The vectors in this space are called *crystal momenta* and are of the form $\mathbf{k} = \frac{m_1}{N_1}\mathbf{K}_1 + \frac{m_2}{N_2}\mathbf{K}_2$, and the irreps of T can be labelled by these momenta $\mathbf{k}$. From the form of these vectors, it seems that the reciprocal space is discrete; however sending N_1 and N_2 we can make it continuous. Also, note that the characters do not change if we replace m_i with $m_i + N_i$. Therefore, we can let m_1 and m_2 to take any integer value as long as we remember $m_i \equiv m_i + c_i N_i$ for any integer c_i. In terms of the crystal momenta, this identification is $\mathbf{k} \equiv \mathbf{k} + c_1\mathbf{K}_1 + c_2\mathbf{K}_2$ where $c_1, c_2 \in \mathbb{Z}$. This defines a region in the reciprocal space called *Brillouin zone*, any momentum $\mathbf{k}$ outside of which can be brought inside the region using the identification $\mathbf{k} \equiv \mathbf{k} + c_1\mathbf{K}_1 + c_2\mathbf{K}_2$. Examples of Brillouin zone corresponding to square and hexagonal Bravais lattices are shown in Figs. 4.2(a) and 4.3(c). Let a basis function of the irrep labelled by $\mathbf{k}$ be $\tilde{u}_{\mathbf{k}}(\mathbf{r})$. Then under the action of the translation $\{E|n_1\mathbf{t}_1 + n_2\mathbf{t}_2\}$, the basis function transforms into $\rho(\{E|n_1\mathbf{t}_1 + n_2\mathbf{t}_2\})\tilde{u}_{\mathbf{k}}(\mathbf{r}) = \tilde{u}_{\mathbf{k}}(\mathbf{r} - n_1\mathbf{t}_1 - n_2\mathbf{t}_2) = e^{-i\mathbf{k}\cdot(n_1\mathbf{t}_1 + n_2\mathbf{t}_2)}\tilde{u}_{\mathbf{k}}(\mathbf{r})$ where the last equality comes from the representation (or character because the irrep is 1 dimensional). If we write $\tilde{u}_{\mathbf{k}}$ in the convenient $\tilde{u}_{\mathbf{k}}(\mathbf{r}) = \hat{u}_{\mathbf{k}}(\mathbf{r})e^{i\mathbf{k}\cdot\mathbf{r}}$, the equation in the previous sentence becomes $\hat{u}_{\mathbf{k}}(\mathbf{r} - n_1\mathbf{t}_1 - n_2\mathbf{t}_2)e^{i\mathbf{k}\cdot(\mathbf{r} - n_1\mathbf{t}_1 - n_2\mathbf{t}_2)} = e^{-i\mathbf{k}\cdot(n_1\mathbf{t}_1 + n_2\mathbf{t}_2)}\hat{u}_{\mathbf{k}}(\mathbf{r})e^{i\mathbf{k}\cdot\mathbf{r}}$ implying that $\hat{u}_{\mathbf{k}}(\mathbf{r} - n_1\mathbf{t}_1 - n_2\mathbf{t}_2) = \hat{u}_{\mathbf{k}}(\mathbf{r})$. Therefore, the basis function of the irrep labelled by crystal momentum $\mathbf{k}$ of the discrete translation

group is of the form $\hat{u}_{\mathbf{k}}(\mathbf{r})e^{i\mathbf{k}\cdot\mathbf{r}}$ where $\hat{u}_{\mathbf{k}}(\mathbf{r})$ is a periodic function with periodicity $\mathbf{t}_1$ and $\mathbf{t}_2$. The functions of this form are called *Bloch functions*.

What is a symmetry group and how do its representations affect the degeneracies of the eigenvalues of a Hamiltonian?

Before we discuss the consequence of the discrete translational symmetry on the eigenfunctions of Eq. 4.4, we have to discuss the mathematical definition of a symmetry properly. Let us rewrite Eq. 4.4 as following: $\frac{1}{\rho}\hat{H}\tilde{u}_z \equiv \tilde{H}\tilde{u}_z = -\omega^2\tilde{u}_z$, where we defined the modified Hamiltonian $\tilde{H} = \frac{1}{\rho}\hat{H}$. Let there be an arbitrary function $\psi(\mathbf{r})$. Further, let there be a group G such that under the action of the group elements $A \in G$ the function transforms as $\psi'(\mathbf{r}) = \rho(A)\psi(\mathbf{r}) = \psi(\mathbf{A}^{-1}\mathbf{r})$ where $\mathbf{A}$ is representation of group element A in the some chosen basis in 2 dimensional Euclidean plane. Then the function $\tilde{H}\psi(\mathbf{r})$ transforms to $\rho(A)\tilde{H}\psi(\mathbf{r})$ under the action of element $A \in G$. We can rewrite the this transformed function in the following way: $\rho(A)\tilde{H}\psi(\mathbf{r}) = \rho(A)\tilde{H}\rho(A)^{-1}\rho(A)\psi(\mathbf{r})$. Therefore, we say that the modified Hamiltonian $\tilde{H}$ transforms to $\tilde{H}' = \rho(A)\tilde{H}\rho(A)^{-1}$ under the action of A. The group G is called the *symmetry group* of the Hamiltonian (or the system) if for all $A \in G$, $\rho(A)\tilde{H}\rho(A)^{-1} = \tilde{H}$, or in other words if the Hamiltonian is invariant under the action of the group elements. Another way of writing this is $\rho(A)\tilde{H} = \tilde{H}\rho(A) \Rightarrow [\rho(A), \tilde{H}] = 0$ where $[,]$ is the commutator. Now, let there be an eigenfunction $\tilde{u}_z(\mathbf{r})$ of $\tilde{H}$ with eigenvalue ω^2; $\tilde{H}\tilde{u}_z = -\omega^2\tilde{u}_z$. Let G be the symmetry group of $\tilde{H}$. Then, for any $A \in G$, $\tilde{H}\rho(A)\tilde{u}_z = \rho(A)\tilde{H}\tilde{u}_z = \rho(A)(-\omega^2\tilde{u}_z) = -\omega^2\rho(A)\tilde{u}_z$ meaning that $\rho(A)\tilde{u}_z$ is also an eigenfunction of $\tilde{H}$ with the same eigenvalue. Now, we can construct the set V_{ω^2} of all degenerate eigenfunctions of $\tilde{H}$ with some eigenvalue ω^2. Note that V_{ω^2} is a vector space because if there are two eigenfunctions with same eigenvalue ω^2, then any linear combination of those two eigenfunction is also an eigenfunction with the same eigenvalue. The dimension of this vector space is equal to the degeneracy of the

eigenvalue ω^2. It is clear from the argument above that V_{ω^2} is invariant under the action of the group G. Therefore, we can form a representation of G on this vector space V_{ω^2}. This representation is either irreducible or can be reduced to irreducible components meaning that a basis of V_{ω^2} can be chosen such that the basis vectors can be written as $u_\alpha^{(i)}$, where $u_\alpha^{(i)}$ is the i^{th} basis vector of irrep α of group G. From this discussion, it should be clear that the eigenfunctions and eigenvalues of the Hamiltonian can be labelled by the irreps of the group G. And as a consequence, if an eigenvalue ω^2 is labelled by irrep label α, it should be (at least) d_α-fold degenerate, where d_α is the dimension of the irrep α of group G. One important point to note here is that if the vector space V_{ω^2} is reducible, the eigenvalue ω^2 has multiple irrep labels corresponding to the irreps in the reduction. This is generally as rare as having a equal eigenvalues of an arbitrary matrix [143]. Normally one eigenvalue corresponds to one irrep of the symmetry group G. When more than one irrep occur at the same eigenvalue, it is called *accidental degeneracy*.

Bloch's theorem

With the knowledge of the last two sub-sections, it is immediate that if the Hamiltonian $\tilde{H}$ is invariant under the discrete translation group, the eigenfunctions of $\tilde{H}$ are also the basis functions of the irreps of the discrete translation group T. However, we already know that the basis function of any irrep of the group T is a Bloch functions. This implies the statement of *Bloch's theorem*: the eigenfunctions of the Hamiltonian $\tilde{H}$ with discrete translation symmetry are Bloch functions i.e., of the form $\hat{u}_{\mathbf{k}}(\mathbf{r})e^{i\mathbf{k}\cdot\mathbf{r}}$ where $\hat{u}_{\mathbf{k}}(\mathbf{r})$ is periodic function: $\hat{u}_{\mathbf{k}}(\mathbf{r}+\mathbf{t}_1) = \hat{u}_{\mathbf{k}}(\mathbf{r}) = \hat{u}_{\mathbf{k}}(\mathbf{r}+\mathbf{t}_2)$. Moreover, the eigenvalues can also be labelled with $\mathbf{k}$: $\omega_{\mathbf{k}}^2$. The plot of eigenfrequencies $\omega_{\mathbf{k}}$ as a function of $\mathbf{k}$ is called *band structure*.

Space group representations

Having discussed the consequence of the discrete translation symmetry, now we are at a position to add other symmetries to obtain space group representations. We have already discussed that the Bloch functions $\tilde{u}_{\mathbf{k}}(\mathbf{r}) = \hat{u}_{\mathbf{k}}(\mathbf{r})e^{i\mathbf{k}\cdot\mathbf{r}}$, with periodic $\hat{u}_{\mathbf{k}}(\mathbf{r})$, form the basis of the translation group T. Let G be a space group with T being its translation normal subgroup. Now, the action of general space group element $\{R|\mathbf{v}\} \in G$ on the Bloch functions gives $\{R|\mathbf{v}\}\tilde{u}_{\mathbf{k}}(\mathbf{r}) = \tilde{u}_{\mathbf{k}}(\mathbf{R}^{-1}(\mathbf{r}-\mathbf{v})) = \hat{u}_{\mathbf{k}}(\mathbf{R}^{-1}(\mathbf{r}-\mathbf{v}))e^{i\mathbf{k}\cdot\mathbf{R}^{-1}(\mathbf{r}-\mathbf{v})} = \hat{u}_{\mathbf{k}}(\mathbf{R}^{-1}(\mathbf{r}-\mathbf{v}))e^{i(\mathbf{R}^{-T}\mathbf{k})\cdot(\mathbf{r}-\mathbf{v})} = \hat{u}_{\mathbf{k}}(\mathbf{R}^{-1}(\mathbf{r}-\mathbf{v}))e^{i(\mathbf{R}\mathbf{k})\cdot(\mathbf{r}-\mathbf{v})}$ where in the third equality we used $\mathbf{R}^{-1} = \mathbf{R}^T$ since $\mathbf{R}$ is a orthogonal matrix. Let us define $\hat{u}_{\mathbf{R}\mathbf{k}}(\mathbf{r}-\mathbf{v}) \equiv \hat{u}_{\mathbf{k}}(\mathbf{R}^{-1}\cdot(\mathbf{r}-\mathbf{v})) = \{R|\mathbf{v}\}\hat{u}_{\mathbf{k}}(\mathbf{r})$. Now, operating with a lattice translation on this function $\hat{u}_{\mathbf{R}\mathbf{k}}(\mathbf{r}-\mathbf{v})$, we get $\{E|\mathbf{t}\}\hat{u}_{\mathbf{R}\mathbf{k}}(\mathbf{r}-\mathbf{v}) = \{E|\mathbf{t}\}\{R|\mathbf{v}\}\hat{u}_{\mathbf{k}}(\mathbf{r}) = \{R|\mathbf{v}\}\hat{u}_{\mathbf{k}}(\mathbf{r}-\mathbf{t}) = \hat{u}_{\mathbf{k}}(\mathbf{R}^{-1}(\mathbf{r}-\mathbf{t}-\mathbf{v})) = \hat{u}_{\mathbf{k}}(\mathbf{R}^{-1}(\mathbf{r}-\mathbf{v})-\mathbf{R}^{-1}\mathbf{t}) = \hat{u}_{\mathbf{k}}(\mathbf{R}^{-1}(\mathbf{r}-\mathbf{v})-\mathbf{t}') = \hat{u}_{\mathbf{k}}(\mathbf{R}^{-1}(\mathbf{r}-\mathbf{v})) = \hat{u}_{\mathbf{R}\mathbf{k}}(\mathbf{r}-\mathbf{v})$ since $\mathbf{t}' = \mathbf{R}^{-1}\mathbf{t}$ is clearly a lattice translation and $\hat{u}_{\mathbf{k}}$ is invariant (periodic) under lattice translation. Therefore, $\{E|\mathbf{t}\}\{R|\mathbf{v}\}\tilde{u}_{\mathbf{k}}(\mathbf{r}) = \tilde{u}_{\mathbf{k}}(\mathbf{R}^{-1}(\mathbf{r}-\mathbf{v}-\mathbf{t})) = \hat{u}_{\mathbf{k}}(\mathbf{R}^{-1}(\mathbf{r}-\mathbf{v}-\mathbf{t}))e^{i\mathbf{k}\cdot\mathbf{R}^{-1}(\mathbf{r}-\mathbf{v}-\mathbf{t})} = \hat{u}_{\mathbf{R}\mathbf{k}}(\mathbf{r}-\mathbf{v})e^{i(\mathbf{R}\mathbf{k})\cdot(\mathbf{r}-\mathbf{v}-\mathbf{t})} = e^{-i(\mathbf{R}\mathbf{k})\cdot\mathbf{t}}\hat{u}_{\mathbf{R}\mathbf{k}}(\mathbf{r}-\mathbf{v})e^{i(\mathbf{R}\mathbf{k})\cdot(\mathbf{r}-\mathbf{v})} = e^{-i(\mathbf{R}\mathbf{k})\cdot\mathbf{t}}\{R|\mathbf{v}\}\tilde{u}_{\mathbf{k}}(\mathbf{r})$. This implies that $\{R|\mathbf{v}\}\tilde{u}_{\mathbf{k}}(\mathbf{r})$ is a Bloch function at $\mathbf{R}\mathbf{k}$.

Now, let ρ be an irrep of G with invariant vector space V of dimension d. Since all the irreps of the translation subgroup T are 1 dimensional with wave vector labels $\mathbf{k}$, we can choose the basis vectors of V as Bloch functions $\tilde{u}_{\mathbf{k}_i}(\mathbf{r})$ where $i = 1, 2, \ldots, d$. To see why more than one $\mathbf{k}$ vector arise in an irrep of G, let us start with one Bloch function $\tilde{u}_{\mathbf{k}_1}(\mathbf{r}) \in V$. Recall that G can be written as coset decomposition $G = \{R_1|\mathbf{v}_1\}T + \ldots \{R_h|\mathbf{v}_h\}T$. Under a application of any of these $\{R_i|\mathbf{v}_i\}$, $\{R_i|\mathbf{v}_i\}\tilde{u}_{\mathbf{k}_1}(\mathbf{r})$ becomes a Bloch function with wave vector label $\mathbf{R}_i\mathbf{k}_1$. Therefore, $\mathbf{R}_i\mathbf{k}_1$ is one of the wave vectors in $\{\mathbf{k}_1, \mathbf{k}_2, \ldots, \mathbf{k}_d\}$. This way as we go over all the elements of the quotient group G/T, the wave vector $\mathbf{k}_1$ transforms under corresponding elements of the isogonal point group F, and we get the whole vector space V (if we were to get

a subset of V, then V would be reducible). Note that not all of these wave vectors $\mathbf{k}_i$ have to be different. The reason is that a wave vector $\mathbf{k}$ is only distinguishable up to a reciprocal lattice vector, that is $\mathbf{R}_i\mathbf{k} \equiv \mathbf{k}$ if $\mathbf{R}_i\mathbf{k} = \mathbf{k} + c_1\mathbf{K}_1 + c_2\mathbf{K}_2$ where $\mathbf{K}_1$ and $\mathbf{K}_2$ are the fundamental reciprocal lattice vectors. The set of distinct (that is not equivalent) wave vectors $\mathbf{k}$ in the set $\{\mathbf{k}_1, \mathbf{k}_2, \ldots, \mathbf{k}_d\}$ is called the *star* of irrep ρ or equivalently of any wave vector in $\{\mathbf{k}_1, \mathbf{k}_2, \ldots, \mathbf{k}_d\}$. The elements R_i of the isogonal group F which transform a wave vector $\mathbf{k}$ into an equivalent wave vector $\mathbf{R}_i\mathbf{k} \equiv \mathbf{k}$ form a subgroup of F called the *little co-group* $\bar{G}^{\mathbf{k}}$ of $\mathbf{k}$. Examples of stars and little co-groups of different wave vectors of some space groups are shown in Figs. 4.2 and 4.3.

Since $\bar{G}^{\mathbf{k}}$ is a subgroup F, $|\bar{G}^{\mathbf{k}}|$ is a divisor of $|F|$. Now, let there be two distinct wave vectors $\mathbf{k}_1$ and $\mathbf{k}_2$ with some fixed element $R \in F$ such that $\mathbf{k}_2 = \mathbf{R}\mathbf{k}_1$. Then for every element $S_1 \in \bar{G}^{\mathbf{k}_1}$ (meaning $\mathbf{S}_1\mathbf{k}_1 \equiv \mathbf{k}_1$), $\mathbf{R}\mathbf{S}_1\mathbf{R}^{-1}\mathbf{k}_2 \equiv \mathbf{k}_2$ or $RS_1R^{-1} \in \bar{G}^{\mathbf{k}_2}$. This implies that $R\bar{G}^{\mathbf{k}_1}R^{-1} \subset \bar{G}^{\mathbf{k}_2}$. But, for every element $S_2 \in \bar{G}^{\mathbf{k}_2}$, $\mathbf{R}^{-1}S_2\mathbf{R}\mathbf{k}_1 \equiv \mathbf{k}_1$ implying $R^{-1}\bar{G}^{\mathbf{k}_2}R \subset \bar{G}^{\mathbf{k}_1}$ or $\bar{G}^{\mathbf{k}_2} \subset R\bar{G}^{\mathbf{k}_1}R^{-1}$. This means that $\bar{G}^{\mathbf{k}_2} = R\bar{G}^{\mathbf{k}_1}R^{-1}$, or in other words the little co-groups of two different wave vectors in the star of an irrep ρ of the space group G are conjugate of each other and have same number of elements. From this it is easy to see then that the number of elements $h \equiv |F|$ in F is just the number of elements $b \equiv |\bar{G}^{\mathbf{k}}|$ in the little co-group $\bar{G}^{\mathbf{k}}$ of a wave vector $\mathbf{k}$ in the star of irrep ρ times the number of distinct wave vectors q in the star of ρ. Moreover, the isogonal group F can be coset decomposed in the following manner $F = R_1\bar{G}^{\mathbf{k}} + R_2\bar{G}^{\mathbf{k}} + \cdots + R_q\bar{G}^{\mathbf{k}}$ with $\mathbf{R}_\alpha\mathbf{k} \equiv \mathbf{k}_\alpha$. With this definition of the star of each wave vector $\mathbf{k}$ in the Brillouin zone, we can choose a region in the Brillouin zone such that only one wave vector from the star of each irrep ρ is in that region. This region in the Brillouin zone is called the *representation domain* or *irreducible Brillouin zone* in the Physics community. The irreducible Brillouin zone for some the space groups are shown in Figs. 4.2 and 4.3. Now, for the wave vector $\mathbf{k}$, let the little co-group be $\bar{G}^{\mathbf{k}}$ with elements $\{S_1, S_2, \ldots, S_b\}$ where $b = |\bar{G}^{\mathbf{k}}|$. Then, if we

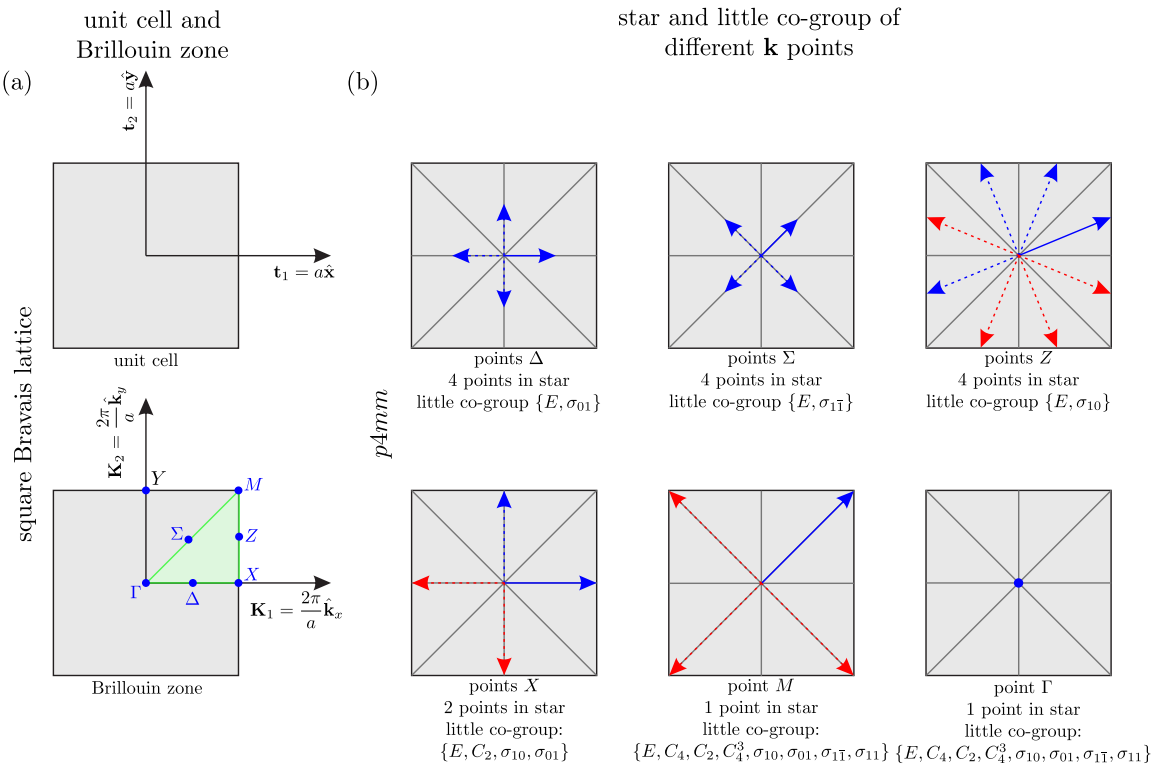

Figure 4.2: Figure showing unit cells and Brillouin zones for square (a) Bravais lattice (left) and star and little co-groups of different points in Brillouin zone for $p4mm$ (b) space group. Note that $p4mm$ space group can only be realized from square Bravais lattice. In (a), $\mathbf{t}_1$ and $\mathbf{t}_2$ are fundamental lattice vectors, $\mathbf{K}_1$ and $\mathbf{K}_2$ are fundamental reciprocal lattice vectors. The different high symmetry points Γ, X and M, and high symmetry lines Δ, Σ and Z are shown in (a). The regions shaded in green in (a) are the irreducible Brillouin zone corresponding to $p4mm$. In (b), these points (blue solid arrows), points in their stars (blue dashed arrows), and their equivalent points (red dashed arrows) are shown. For convenience, we also show the mirrors with dark grey lines.

look at the coset decomposition $G = \{R_1|\mathbf{v}_1\}T + \{R_2|\mathbf{v}_2\}T + \cdots + \{R_h|\mathbf{v}_h\}T$ and pick only the cosets for which the rotation (or mirror) parts are $S_1, S_2, \ldots, S_b$ and form the set theoretical sum of those, we get a subgroup of the space group G. This subgroup $G^{\mathbf{k}} = \{S_1|\mathbf{w}_1\}T + \{S_2|\mathbf{w}_2\}T + \cdots + \{S_b|\mathbf{w}_b\}T$ is called the *little group* of wave vector $\mathbf{k}$. Moreover, just like the isogonal group F can be coset decomposed in terms of the little co-group $\bar{G}^{\mathbf{k}}$, the space group G can be coset decomposed in terms of the little group: $G = \{R_1|\mathbf{v}_1\}G^{\mathbf{k}} + \{R_2|\mathbf{v}_2\}G^{\mathbf{k}} + \cdots + \{R_q|\mathbf{v}_q\}G^{\mathbf{k}}$, where q is the number of wave vectors in the star of $\mathbf{k}$. Furthermore, since the little co-group $\bar{G}^{\mathbf{k}_\alpha}$

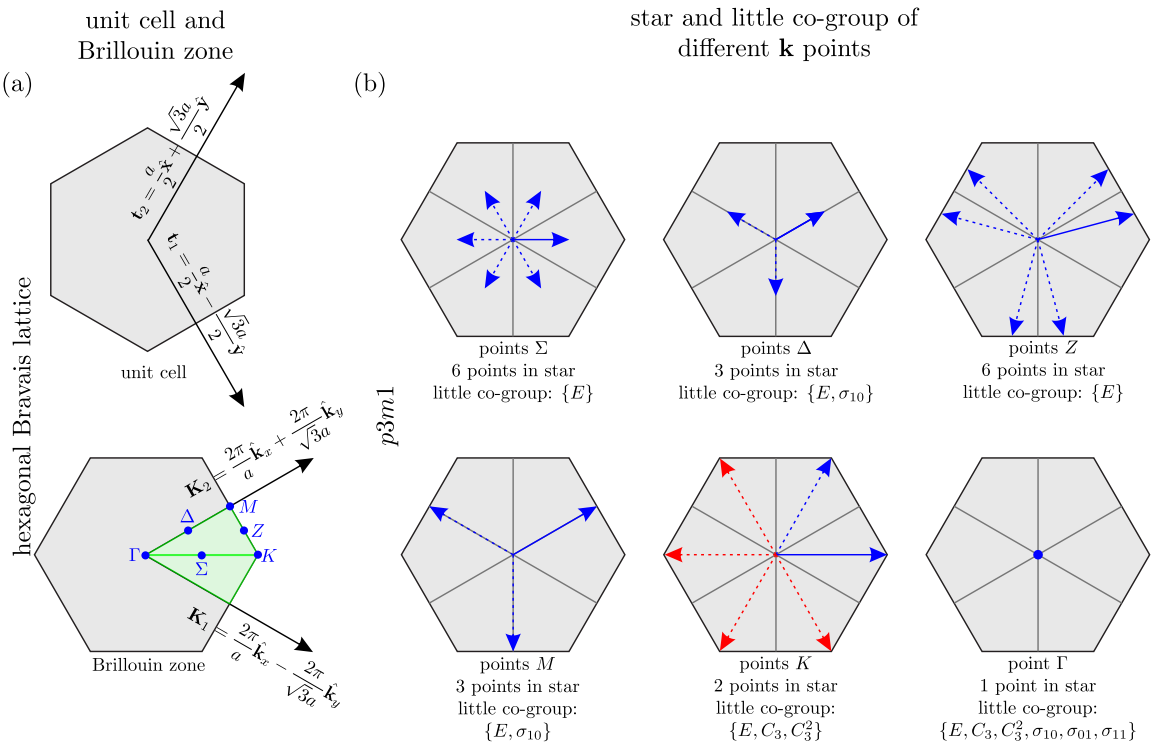

Figure 4.3: Figure showing unit cells and Brillouin zones for hexagonal (a) Bravais lattice (left) and star and little co-groups of different points in Brillouin zone for $p3m1$ (b) space group. Note that $p3m1$ space group can only be realized from hexagonal Bravais lattice. In (a), $\mathbf{t}_1$ and $\mathbf{t}_2$ are fundamental lattice vectors, $\mathbf{K}_1$ and $\mathbf{K}_2$ are fundamental reciprocal lattice vectors. The different high symmetry points Γ, K and M, and high symmetry lines Δ, Σ and Z are shown in (a). The regions shaded in green in (a) are the irreducible Brillouin zone corresponding to $p3m1$. In (b), these points (blue solid arrows), points in their stars (blue dashed arrows), and their equivalent points (red dashed arrows) are shown. For convenience, we also show the mirrors with dark grey lines.

of wave vector $\mathbf{k}_\alpha \equiv \mathbf{R}_\alpha \mathbf{k}$ ($\alpha = 1, \ldots, q$) is conjugate of $\bar{G}^{\mathbf{k}}$ ($\bar{G}^{\mathbf{k}_\alpha} = R_\alpha \bar{G}^{\mathbf{k}} R_\alpha^{-1}$), it is easy to see that the little group of wave vector $\mathbf{k}_\alpha$ is $G^{\mathbf{k}_\alpha} = \{R_\alpha|\mathbf{v}_\alpha\} G^{\mathbf{k}} \{R_\alpha|\mathbf{v}_\alpha\}^{-1}$.

Now, let there be a wave vector $\mathbf{k}$ with b elements in $\bar{G}^{\mathbf{k}} = \{S_1, S_2, \ldots, S_b\}$, and q elements in the star: $\mathbf{k}_1 \equiv \mathbf{R}_1\mathbf{k}, \mathbf{k}_2 \equiv \mathbf{R}_2\mathbf{k}, \ldots, \mathbf{k}_q \equiv \mathbf{R}_q\mathbf{k}$ (with $R_1 = E$). Moreover, let there be a Bloch function $\tilde{u}_{\mathbf{k}}(\mathbf{r})$ at wave vector $\mathbf{k}$. Acting on this Bloch functions, the only elements of G that can generate another Bloch function at $\mathbf{k}$ are the elements of the little group $G^{\mathbf{k}}$. The elements of $G^{\mathbf{k}} = \{S_1|\mathbf{w}_1\}T + \{S_2|\mathbf{w}_2\}T + \cdots + \{S_b|\mathbf{w}_b\}T$ are of the of the form $\{S_i|\mathbf{w}_i\}\{E|\mathbf{t}\} = \{S_i|\mathbf{w}_i + \mathbf{S}_i\mathbf{t}\} = \{E|\mathbf{t}'\}\{S_i|\mathbf{w}_i\}$ where $\mathbf{t}$ and

$\mathbf{t}' = \mathbf{S}_i\mathbf{t}$ are lattice translations. Since $\{E|\mathbf{t}'\}\{S_i|\mathbf{w}_i\}$ and $\{S_i|\mathbf{w}_i\}$ generate same function up to a over all phase factor when acting on $\tilde{u}_{\mathbf{k}}(\mathbf{r})$, the maximum number of linearly independent functions that can be generated from $\tilde{u}_{\mathbf{k}}(\mathbf{r})$ acting the elements of $G^{\mathbf{k}}$ on it is the maximum number of of linearly independent functions that can be obtained from $\{S_1|\mathbf{w}_1\}\tilde{u}_{\mathbf{k}}(\mathbf{r}), \{S_2|\mathbf{w}_2\}\tilde{u}_{\mathbf{k}}(\mathbf{r}), \ldots, \{S_b|\mathbf{w}_b\}\tilde{u}_{\mathbf{k}}(\mathbf{r})$. Let this number be t and the independent functions are $\tilde{u}_{\mathbf{k},1}(\mathbf{r}), \tilde{u}_{\mathbf{k},2}(\mathbf{r}), \ldots, \tilde{u}_{\mathbf{k},t}(\mathbf{r})$. Then these t functions form the basis of a representation of little group $G^{\mathbf{k}}$. Let this representation be irreducible (if not then we can choose a subset of these basis functions to get an irrep). Since $G = \{R_1|\mathbf{v}_1\}G^{\mathbf{k}} + \{R_2|\mathbf{v}_2\}G^{\mathbf{k}} + \cdots + \{R_q|\mathbf{v}_q\}G^{\mathbf{k}}$ (with $\{R_1|\mathbf{v}_1\} = \{E|\mathbf{0}\}$), $\{R_i|\mathbf{v}_i\}\tilde{u}_{\mathbf{k},1}(\mathbf{r}), \{R_i|\mathbf{v}_i\}\tilde{u}_{\mathbf{k},2}(\mathbf{r}), \ldots, \{R_i|\mathbf{v}_i\}\tilde{u}_{\mathbf{k},t}(\mathbf{r})$ are linearly independent Bloch functions at $\mathbf{k}_i = \mathbf{R}\mathbf{k}$. Together, the collection of the functions $\{R_i|\mathbf{v}_i\}\tilde{u}_{\mathbf{k},j}$ where $i = 1, \ldots, q$ and $j = 1, \ldots, t$ forms the basis of an irreducible representation of the space group G with dimension tq. This means that to find the representations of the space group G, we will choose $\mathbf{k}$ vectors from the irreducible Brillouin zone and find the irreps $\rho^{\mathbf{k}}$ of the little group $G^{\mathbf{k}}$ and then acting on the basis functions of $\rho^{\mathbf{k}}$ with the coset representatives of $G^{\mathbf{k}}$ in G, we can get the basis functions of the irreps of G. The power of this result becomes clear once we realize that the basis functions of the little group $G^{\mathbf{k}}$ are Bloch functions at wave vector $\mathbf{k}$ meaning that the representation matrices for the lattice translations $\{E|\mathbf{t}\}$ are just $\exp(-i\mathbf{k}\cdot\mathbf{t})\mathbb{1}$ meaning that the only nontrivial representation matrices that we have deal with are those corresponding to $\{S_i|\mathbf{w}_i\}$ where $i = 1, \ldots, b$. In the following we describe how to get the irreps of the little groups.

Let $\rho^{\mathbf{k}}$ be an irrep of the little group $G^{\mathbf{k}}$ at wave vector $\mathbf{k}$ with basis functions $\tilde{u}_{\mathbf{k},1}(\mathbf{r}), \tilde{u}_{\mathbf{k},2}(\mathbf{r}), \ldots, \tilde{u}_{\mathbf{k},t}(\mathbf{r})$. Let us call the vector space spanned by these basis functions $V_\rho^{\mathbf{k}}$. As before, we keep the coset decomposition $G^{\mathbf{k}} = \{S_1|\mathbf{w}_1\}T + \{S_2|\mathbf{w}_2\}T + \cdots + \{S_b|\mathbf{w}_b\}T$. Also, let the the representation matrices of irrep $\rho^{\mathbf{k}}$ be denoted as $\mathbf{\Gamma}_\rho^{\mathbf{k}}(\{R|\mathbf{v}\})$ for $\{R|\mathbf{v}\} \in G^{\mathbf{k}}$. Since the basis functions are Bloch functions

we require that $\mathbf{\Gamma}^{\mathbf{k}}_{\rho}(\{E|\mathbf{t}\}) = \exp(-i\mathbf{k}\cdot\mathbf{t})$. Moreover, since $\rho^{\mathbf{k}} : G^{\mathbf{k}} \to GL(V^{\mathbf{k}}_{\rho})$ is a homomorphism, $\mathbf{\Gamma}^{\mathbf{k}}_{\rho}(\{S_i|\mathbf{w}_i\}\{S_j|\mathbf{w}_j\}) = \mathbf{\Gamma}^{\mathbf{k}}_{\rho}(\{S_i|\mathbf{w}_i\})\mathbf{\Gamma}^{\mathbf{k}}_{\rho}(\{S_j|\mathbf{w}_j\})$ where $\{S_i|\mathbf{w}_i\}$ and $\{S_j|\mathbf{w}_j\}$ are any two coset representatives of T in $G^{\mathbf{k}}$. However, $\{S_i|\mathbf{w}_i\}\{S_j|\mathbf{w}_j\} = \{S_iS_j|\mathbf{w}_i + \mathbf{S}_i\mathbf{w}_j\} = \{E|\mathbf{t}_{ij}\}\{S_k|\mathbf{w}_k\}$ where $S_k = S_iS_j$, $\{S_k|\mathbf{w}_k\}$ is a coset representative of T in $G^{\mathbf{k}}$ with rotation (or mirror) part being S_k and $\mathbf{t}_{ij} = \mathbf{w}_i + \mathbf{S}_i\mathbf{w}_j - \mathbf{w}_k$. Note that $\mathbf{t}_{ij}$ has to be a lattice translation, $\mathbf{t}_{ij} \in T$. This means that $\mathbf{\Gamma}^{\mathbf{k}}_{\rho}(\{S_i|\mathbf{w}_i\}\{S_j|\mathbf{w}_j\}) = \mathbf{\Gamma}^{\mathbf{k}}_{\rho}(\{E|\mathbf{t}_{ij}\}\{S_k|\mathbf{w}_k\}) = \mathbf{\Gamma}^{\mathbf{k}}_{\rho}(\{E|\mathbf{t}_{ij}\})\mathbf{\Gamma}^{\mathbf{k}}_{\rho}(\{S_k|\mathbf{w}_k\}) = \exp(-i\mathbf{k}\cdot\mathbf{t}_{ij})\mathbf{\Gamma}^{\mathbf{k}}_{\rho}(\{S_k|\mathbf{w}_k\})$ again using the homomorphism property of $\rho^{\mathbf{k}}$. Therefore, $\mathbf{\Gamma}^{\mathbf{k}}_{\rho}(\{S_i|\mathbf{w}_i\})\mathbf{\Gamma}^{\mathbf{k}}_{\rho}(\{S_j|\mathbf{w}_j\}) = \exp(-i\mathbf{k}\cdot\mathbf{t}_{ij})\mathbf{\Gamma}^{\mathbf{k}}_{\rho}(\{S_k|\mathbf{w}_k\})$. Now, if we define a new matrix $\boldsymbol{D}^{\mathbf{k}}_{\rho}(\{S_i|\mathbf{w}_i\}) \equiv \exp(i\mathbf{k}\cdot\mathbf{w}_i)\mathbf{\Gamma}^{\mathbf{k}}_{\rho}(\{S_i|\mathbf{w}_i\})$, the equation $\mathbf{\Gamma}^{\mathbf{k}}_{\rho}(\{S_i|\mathbf{w}_i\})\mathbf{\Gamma}^{\mathbf{k}}_{\rho}(\{S_j|\mathbf{w}_j\}) = \exp(-i\mathbf{k}\cdot\mathbf{t}_{ij})\mathbf{\Gamma}^{\mathbf{k}}_{\rho}(\{S_k|\mathbf{w}_k\})$ becomes $\exp(-i\mathbf{k}\cdot(\mathbf{w}_i + \mathbf{w}_j))\boldsymbol{D}^{\mathbf{k}}_{\rho}(\{S_i|\mathbf{w}_i\})\boldsymbol{D}^{\mathbf{k}}_{\rho}(\{S_j|\mathbf{w}_j\}) = \exp(-i\mathbf{k}\cdot(\mathbf{t}_{ij} + \mathbf{w}_k))\boldsymbol{D}^{\mathbf{k}}_{\rho}(\{S_k|\mathbf{w}_k\})$ or $\boldsymbol{D}^{\mathbf{k}}_{\rho}(\{S_i|\mathbf{w}_i\})\boldsymbol{D}^{\mathbf{k}}_{\rho}(\{S_j|\mathbf{w}_j\}) = \exp(-i\mathbf{k}\cdot(\mathbf{S}_i\mathbf{w}_j - \mathbf{w}_j))\boldsymbol{D}^{\mathbf{k}}_{\rho}(\{S_k|\mathbf{w}_k\}) = \exp(-i(\mathbf{S}_i^{-1}\mathbf{k} - \mathbf{k})\cdot\mathbf{w}_j)\boldsymbol{D}^{\mathbf{k}}_{\rho}(\{S_k|\mathbf{w}_k\})$. However, since $\{S_i|\mathbf{w}_i\} \in G^{\mathbf{k}}$, $\mathbf{S}_i\mathbf{k} \equiv \mathbf{k}$ or $\mathbf{S}_i^{-1}\mathbf{k} = \mathbf{k} + \mathbf{g}_i$ where $\mathbf{g}_i = c_1\mathbf{K}_1 + c_2\mathbf{K}_2$ is some reciprocal lattice vector. Therefore, $\boldsymbol{D}^{\mathbf{k}}_{\rho}(\{S_i|\mathbf{w}_i\})\boldsymbol{D}^{\mathbf{k}}_{\rho}(\{S_j|\mathbf{w}_j\}) = \exp(-i\mathbf{g}_i\cdot\mathbf{w}_j)\boldsymbol{D}^{\mathbf{k}}_{\rho}(\{S_k|\mathbf{w}_k\})$. The reason we go from $\mathbf{\Gamma}^{\mathbf{k}}_{\rho}$ to $\boldsymbol{D}^{\mathbf{k}}_{\rho}$ matrices becomes clear from the following observation. Let $\{S|\mathbf{w}_1\}$ and $\{S|\mathbf{w}_2\}$ be two elements of the coset $\{S|\mathbf{w}\}T$ of $G^{\mathbf{k}}$. Then, we know that $\mathbf{w}_2 - \mathbf{w}_1 = \mathbf{t}$ is a lattice translation. Then, $\boldsymbol{D}^{\mathbf{k}}_{\rho}(\{S|\mathbf{w}_2\}) = \exp(i\mathbf{k}\cdot\mathbf{w}_2)\mathbf{\Gamma}^{\mathbf{k}}_{\rho}(\{S|\mathbf{w}_2\}) = \exp(i\mathbf{k}\cdot\mathbf{w}_2)\mathbf{\Gamma}^{\mathbf{k}}_{\rho}(\{S|\mathbf{w}_1 + \mathbf{t}\}) = \exp(i\mathbf{k}\cdot\mathbf{w}_2)\mathbf{\Gamma}^{\mathbf{k}}_{\rho}(\{E|\mathbf{t}\}\{S|\mathbf{w}_1\}) = \exp(i\mathbf{k}\cdot\mathbf{w}_2)\mathbf{\Gamma}^{\mathbf{k}}_{\rho}(\{E|\mathbf{t}\})\mathbf{\Gamma}^{\mathbf{k}}_{\rho}(\{S|\mathbf{w}_1\}) = \exp(i\mathbf{k}\cdot\mathbf{w}_2)\exp(-i\mathbf{k}\cdot\mathbf{t})\exp(-i\mathbf{k}\cdot\mathbf{w}_1)\boldsymbol{D}^{\mathbf{k}}_{\rho}(\{S|\mathbf{w}_1\}) = \boldsymbol{D}^{\mathbf{k}}_{\rho}(\{S|\mathbf{w}_1\})$. Therefore, the matrices $\boldsymbol{D}^{\mathbf{k}}_{\rho}$ are same for all elements of a coset. Therefore, we can think of $\boldsymbol{D}^{\mathbf{k}}_{\rho}$ as matrix valued function on the quotient group $G^{\mathbf{k}}/T \cong \bar{G}^{\mathbf{k}}$, where $\cong$ symbol was used to show that the groups are isomorphic. Therefore, $\boldsymbol{D}^{\mathbf{k}}_{\rho}$ is a function on $\bar{G}^{\mathbf{k}}$ satisfying the condition $\boldsymbol{D}^{\mathbf{k}}_{\rho}(S_i)\boldsymbol{D}^{\mathbf{k}}_{\rho}(S_j) = \exp(-i\mathbf{g}_i\cdot\mathbf{w}_j)\boldsymbol{D}^{\mathbf{k}}_{\rho}(S_k)$ where $S_iS_j = S_k$. Now, $\boldsymbol{D}^{\mathbf{k}}_{\rho}$ is a homomorphism if (i) all $\mathbf{w}_j$ are $\mathbf{0}$ or lattice translations $\mathbf{t}$, (ii) $\mathbf{g}_i = S_i^{-1}\mathbf{k} - \mathbf{k} = 0$ that is $\mathbf{k}$ is a interior point of the irreducible Brillouin zone. Therefore, in these two cases, the $\boldsymbol{D}^{\mathbf{k}}_{\rho}$

matrices are representation matrices of the little co-group $\bar{G}^{\mathbf{k}}$. Therefore, in these two cases, we need to find the irreps of $\bar{G}^{\mathbf{k}}$, and that will immediately give the irreps of $G^{\mathbf{k}}$ since $\mathbf{\Gamma}^{\mathbf{k}}_{\rho}(\{S_i|\mathbf{w}_i\}) = \exp(-i\mathbf{k}\cdot\mathbf{w}_i)\boldsymbol{D}^{\mathbf{k}}_{\rho}(\{S_i|\mathbf{w}_i\})$.

When the factor $\exp(-i\mathbf{g}_i\cdot\mathbf{w}_j) \neq 1$ that is when the space group is nonsymmorphic and wave vector $\mathbf{k}$ is at the edge of the Brillouin zone, finding the irreps $\mathbf{\Gamma}^{\mathbf{k}}_{\rho}$ is a bit more complicated. In this case, we need to introduce the concept of *projective representations*. A nonsingular matrix function Δ on a group H is called projective representation of H if $\Delta(H_i)\Delta(H_j) = \mu(H_i,H_j)\Delta(H_iH_j)$ for all $H_i, H_j \in H$ where $\mu(H_i,H_j)$ is a scalar function satisfying $\mu(H_i,H_jH_k)\mu(H_j,H_k) = \mu(H_i,H_j)\mu(H_iH_j,H_k)$. The function μ is called the *factor system* of the projective representation Δ. In our problem $\mu(S_i,S_j) = \exp(-i\mathbf{g}_i\cdot\mathbf{w}_j)$ with properties $\mu(E,S_j) = \mu(S_j,E) = \mu(E,E) = 1$ as well as $\mu(S_j^{-1},S_j) = \exp(-i(\mathbf{S}_j\mathbf{k}-\mathbf{k})\cdot\mathbf{w}_j) = \exp(-i(\mathbf{S}_j\mathbf{k}-\mathbf{k})\cdot\mathbf{w}_j) = \exp(-i(\mathbf{k}-\mathbf{S}_j^{-1}\mathbf{k})\cdot(\mathbf{S}_j^{-1}\mathbf{w}_j)) = \exp(-i(\mathbf{S}_j^{-1}\mathbf{k}-\mathbf{k})\cdot(-\mathbf{S}_j^{-1}\mathbf{w}_j)) = \mu(S_j,S_j^{-1})$. For 2 dimensional nonsymmorphic space groups, $\mathbf{w}_j$ is half a lattice translation since it is the translation part of a glide symmetry. In 3 dimensional space groups, $\mathbf{w}_j$ can be $1/n$ of a lattice translation corresponding to a $2\pi/n$ screw rotation where $n = 2, 3, 4,$ or 6. Therefore, since for any reciprocal lattice vector $\mathbf{g}$ and any lattice translation vector $\mathbf{t}$, $\mathbf{g}\cdot\mathbf{t} = 2\pi m$ where $m \in \mathbb{Z}$, the factor $\mu(S_i,S_j)$ can always be written as $\mu(S_i,S_j) = \exp(-i\mathbf{g}_i\cdot\mathbf{w}_j) = \exp(2\pi i a(S_i,S_j)/n)$ where $n = 2, 3, 4,$ or 6 and $a(S_i,S_j) \in \mathbb{Z}$ with the constraint $0 \leq a(S_i,S_j) \leq n-1$. Moreover, for our problem $a(S_i,S_j)$ satisfies the following the properties: $a(S_i,E) = a(E,S_i) = a(E,E) = 0$ and $a(S_i,S_i^{-1}) = a(S_i^{-1},S_i)$. To get the projective representation of $\bar{G}^{\mathbf{k}}$, let us define another group $\bar{G}^{\mathbf{k}}_*$ with number of elements $|\bar{G}^{\mathbf{k}}_*| = n|\bar{G}^{\mathbf{k}}| = nb$ such that the elements of this new group are of the form (S_i,α) where $S_i \in \bar{G}^{\mathbf{k}}$ and $\alpha \in \mathbb{Z}_n$. Note that $\mathbb{Z}_n$ is the cyclic group consisting of elements $0, 1, \ldots, n-1$ with group product being just the addition modulo n. Moreover, we define the product for $|\bar{G}^{\mathbf{k}}_*|$ as $(S_i,\alpha)(S_j,\beta) = (S_iS_j, \alpha+\beta+a(S_i,S_j))$. Clearly the identity

element of $\bar{G}^{\mathbf{k}}_*$ is $(E,0)$. The inverse of an element (S_i,α) is $(S_i^{-1},-\alpha-a(S_i,S_i^{-1}))$. Also, $(E,\alpha)(S_i,\beta) = (S_i,\alpha+\beta) = (S_i,\beta)(E,\alpha)$. Since (E,α) commutes with all elements of $\bar{G}^{\mathbf{k}}_*$, for any irrep ρ_* of $\bar{G}^{\mathbf{k}}_*$, $\mathbf{\Gamma}_{\rho_*}((E,\alpha))$ is a scalar multiply of the identity matrix due to Schur's lemma discussed previously. Suppose there exists an irrep $\rho^{\mathbf{k}}_*$ of $\bar{G}^{\mathbf{k}}_*$ such that $\mathbf{\Gamma}^{\mathbf{k}}_{\rho_*}((E,\alpha)) = \exp(2\pi i\alpha/n)\mathbb{1}$. Then, $\mathbf{\Gamma}^{\mathbf{k}}_{\rho_*}((S_i,\alpha)) = \mathbf{\Gamma}^{\mathbf{k}}_{\rho_*}((S_i,0)(E,\alpha)) = \mathbf{\Gamma}^{\mathbf{k}}_{\rho_*}((S_i,0))\mathbf{\Gamma}^{\mathbf{k}}_{\rho_*}((E,\alpha)) = \mathbf{\Gamma}^{\mathbf{k}}_{\rho_*}((S_i,0))\exp(2\pi i\alpha/n)$. If we now write $\mathbf{\Gamma}^{\mathbf{k}}_{\rho_*}((S_i,0)) = \boldsymbol{D}^{\mathbf{k}}_{\rho}(S_i)$, then we have $\boldsymbol{D}^{\mathbf{k}}_{\rho}(S_i)\boldsymbol{D}^{\mathbf{k}}_{\rho}(S_j) = \mathbf{\Gamma}^{\mathbf{k}}_{\rho_*}((S_i,0))\mathbf{\Gamma}^{\mathbf{k}}_{\rho_*}((S_j,0)) = \mathbf{\Gamma}^{\mathbf{k}}_{\rho_*}((S_i,0)(S_j,0)) = \mathbf{\Gamma}^{\mathbf{k}}_{\rho_*}((S_iS_j,a(S_i,S_j))) = \mathbf{\Gamma}^{\mathbf{k}}_{\rho_*}((S_iS_j,0))\mathbf{\Gamma}^{\mathbf{k}}_{\rho_*}((E,a(S_i,S_j))) = \boldsymbol{D}^{\mathbf{k}}_{\rho}(S_iS_j)\exp(2\pi i a(S_i,S_j)) = \exp(-i\mathbf{g}_i\cdot\mathbf{w}_j)\boldsymbol{D}^{\mathbf{k}}_{\rho}(S_iS_j)$. This is exactly what we wanted. In summary, to get the projective representations $\boldsymbol{D}^{\mathbf{k}}_{\rho}$ of the little co-group $\bar{G}^{\mathbf{k}}$ at wave vector $\mathbf{k}$ at the edge of the Brillouin zone of a nonsymmorphic space group G, we have to construct the group $\bar{G}^{\mathbf{k}}_*$ and look for its representations $\mathbf{\Gamma}^{\mathbf{k}}_{\rho_*}$ which satisfy condition that $\mathbf{\Gamma}^{\mathbf{k}}_{\rho_*}((E,\alpha)) = \exp(2\pi i\alpha/n)\mathbb{1}$.

Once we get the irreps $\rho^{\mathbf{k}}$ of the little group $G^{\mathbf{k}}$ at wave vector $\mathbf{k}$ following the procedure outlined above, we can find the representations of the space group G in the following way. As before, the coset decomposition of the little group is $G^{\mathbf{k}} = \{S_1|\mathbf{w}_1\}T + \{S_2|\mathbf{w}_2\}T + \cdots + \{S_b|\mathbf{w}_b\}T$, and the basis functions of t-dimensional irrep $\rho^{\mathbf{k}}$ are $\tilde{u}_{\mathbf{k},1}(\mathbf{r}), \tilde{u}_{\mathbf{k},2}(\mathbf{r}), \ldots, \tilde{u}_{\mathbf{k},t}(\mathbf{r})$. We write the coset decomposition $G = \{E|\mathbf{0}\}G^{\mathbf{k}} + \{R_2|\mathbf{v}_2\}G^{\mathbf{k}} + \cdots + \{R_q|\mathbf{v}_q\}G^{\mathbf{k}}$. As noted earlier, any element of the coset can be a representative of the coset, but here we fix the coset representatives to be $\{E|\mathbf{0}\}, \{R_2|\mathbf{v}_2\}, \ldots, \{R_q|\mathbf{v}_q\}$, and index these with greek letters as $\{R_\alpha|\mathbf{v}_\alpha\}$ with $\alpha = 1,\ldots,q$. The readers can convince themselves that any element g of the space group G can be uniquely written as $g = \{R_\alpha|\mathbf{v}_\alpha\}\{S_n|\mathbf{v}_n\}$ where $\{R_\alpha|\mathbf{v}_\alpha\} \in \{\{E|\mathbf{0}\}, \{R_2|\mathbf{v}_2\}, \ldots, \{R_q|\mathbf{v}_q\}\}$ and $\{S_n|\mathbf{v}_n\} \in G^{\mathbf{k}}$. We define $\tilde{u}_{\mathbf{R}_\alpha\mathbf{k},i}(\mathbf{r}) = \{R_\alpha|\mathbf{v}_\alpha\}\tilde{u}_{\mathbf{k},i}(\mathbf{r})$ which are the basis functions at wave vector $R_\alpha\mathbf{k}$ in the star of $\mathbf{k}$. Then, the set of functions $\{\tilde{u}_{\mathbf{R}_\alpha\mathbf{k},i}(\mathbf{r})\}$ forms the basis of the representation of space group G induced from $\rho^{\mathbf{k}}$. We denote this induced representation as $\rho^{\mathbf{k}} \uparrow G$, and

the representation matrices $\mathbf{\Gamma}_{(\rho^{\mathbf{k}}\uparrow G)}(g)$ of $(\rho^{\mathbf{k}} \uparrow G)$ can be obtained from the representation matrices $\mathbf{\Gamma}^{\mathbf{k}}_{\rho}$ of $\rho^{\mathbf{k}}$ as follows. Writing any $g \in G$ in the unique form $g = \{R_\alpha|\mathbf{v}_\alpha\}\{S_n|\mathbf{v}_n\}$ as mentioned above, we get

$$\begin{aligned}
(\rho^{\mathbf{k}} \uparrow G)(g)\tilde{u}^{(\beta)}_{\mathbf{R}_\beta\mathbf{k},i}(\mathbf{r}) &= g\{R_\beta|\mathbf{v}_\beta\}\tilde{u}_{\mathbf{k},i}(\mathbf{r}) \\
&= \{R_\alpha|\mathbf{v}_\alpha\}\{S_n|\mathbf{v}_n\}\{R_\beta|\mathbf{v}_\beta\}\tilde{u}_{\mathbf{k},i}(\mathbf{r}) \\
&= \{R_\gamma|\mathbf{v}_\gamma\}\{S_m|\mathbf{v}_m\}\tilde{u}_{\mathbf{k},i}(\mathbf{r}) \\
&= \{R_\gamma|\mathbf{v}_\gamma\}\tilde{u}_{\mathbf{k},j}(\mathbf{r})\mathbf{\Gamma}^{\mathbf{k}}_{\rho}(\{S_m|\mathbf{v}_m\})_{ji} \\
&= \tilde{u}^{(\gamma)}_{\mathbf{R}_\gamma\mathbf{k},j}(\mathbf{r})\mathbf{\Gamma}^{\mathbf{k}}_{\rho}(\{S_m|\mathbf{v}_m\})_{ji} \\
\Rightarrow \mathbf{\Gamma}_{(\rho^{\mathbf{k}}\uparrow G)}(g)_{\gamma\beta,ji} &= \mathbf{\Gamma}^{\mathbf{k}}_{\rho}(\{S_m|\mathbf{v}_m\})_{ji}\delta_{\gamma,(g\beta)} = \mathbf{\Gamma}^{\mathbf{k}}_{\rho}(\{R_\gamma|\mathbf{v}_\gamma\}^{-1}g\{R_\beta|\mathbf{v}_\beta\})_{ji}\delta_{\gamma,(g\beta)},
\end{aligned} \tag{4.10}$$

where in the third equality we used that fact that $g\{R_\beta|\mathbf{v}_\beta\} = \{R_\alpha|\mathbf{v}_\alpha\}\{S_n|\mathbf{v}_n\}\{R_\beta|\mathbf{v}_\beta\}$ is an element of G and can be uniquely written as $\{R_\gamma|\mathbf{v}_\gamma\}\{S_m|\mathbf{v}_m\}$, where $\{R_\gamma|\mathbf{v}_\gamma\}$ is one of the fixed coset representatives mentioned above and $\{S_m|\mathbf{v}_m\} \in G^{\mathbf{k}}$. In the last line we introduced a the kronecker delta function $\delta_{\gamma,(g\beta)}$ which is 1 when $g\{R_\beta|\mathbf{v}_\beta\} \in \{R_\gamma|\mathbf{v}_\gamma\}G^{\mathbf{k}}$ and 0 otherwise. The notation $\mathbf{\Gamma}_{(\rho^{\mathbf{k}}\uparrow G)}(g)_{\gamma\beta,ji}$ is understood in the following way. The basis functions are arranged in a row vector in the same order as we order the coset representatives: $\{\tilde{u}_{\mathbf{k},1}(\mathbf{r}),\ \ldots,\ \tilde{u}_{\mathbf{k},t}(\mathbf{r}),\ \tilde{u}_{\mathbf{R}_2\mathbf{k},1}(\mathbf{r}),\ \ldots,\ \tilde{u}_{\mathbf{R}_2\mathbf{k},t}(\mathbf{r}), \ldots, \tilde{u}_{\mathbf{R}_q\mathbf{k},1}(\mathbf{r}), \ldots, \tilde{u}_{\mathbf{R}_q\mathbf{k},t}(\mathbf{r})\}$. Then the rows and columns of representation matrices $\mathbf{\Gamma}_{(\rho^{\mathbf{k}}\uparrow G)}(g)$ can be broken into blocks corresponding to the wave vectors $R_\alpha\mathbf{k}$ in the star of $\mathbf{k}$. If there are nonzero elements in the block $\gamma\beta$ of $\mathbf{\Gamma}_{(\rho^{\mathbf{k}}\uparrow G)}(g)$, the group element g maps the basis functions at $R_\beta\mathbf{k}$ to the basis functions at $R_\gamma\mathbf{k}$. With this understanding, we can also get the expression for the characters $\chi_{(\rho^{\mathbf{k}}\uparrow G)}$ of the

induced representation $\rho^{\mathbf{k}} \uparrow G$ in terms of the characters $\chi_{\rho^{\mathbf{k}}}$ of the irrep $\rho^{\mathbf{k}}$ of $G^{\mathbf{k}}$:

$$\begin{aligned}
\chi_{(\rho^{\mathbf{k}}\uparrow G)}(g) &= \sum_{\alpha=1}^{q}\sum_{i=1}^{t} \mathbf{\Gamma}_{(\rho^{\mathbf{k}}\uparrow G)}(g)_{\alpha\alpha,ii} \\
&= \sum_{\alpha=1}^{q}\sum_{i=1}^{t} \mathbf{\Gamma}^{\mathbf{k}}_{\rho}(\{R_\alpha|\mathbf{v}_\alpha\}^{-1} g \{R_\alpha|\mathbf{v}_\alpha\})_{ii}\delta_{\alpha,(g\alpha)} \\
&= \sum_{\alpha=1}^{q} \chi_{\rho^{\mathbf{k}}}(\{R_\alpha|\mathbf{v}_\alpha\}^{-1} g \{R_\alpha|\mathbf{v}_\alpha\})\delta_{\alpha,(g\alpha)} \\
&= \sum_{\alpha}{}' \chi_{\rho^{\mathbf{k}}}(\{R_\alpha|\mathbf{v}_\alpha\}^{-1} g \{R_\alpha|\mathbf{v}_\alpha\})
\end{aligned} \tag{4.11}$$

where the sum in the last equality is constrained to those α for which little group $G^{\mathbf{k}_\alpha} = \{R_\alpha|\mathbf{v}_\alpha\} G^{\mathbf{k}} \{R_\alpha|\mathbf{v}_\alpha\}^{-1}$ of wave vector $\mathbf{k}_\alpha = \mathbf{R}_\alpha \mathbf{k}$ contains g.

Before going to the examples in the next subsection let us summarize the procedure of finding characters of finite dimensional representations of space groups, or more precisely, characters of irreducible representations of little group $G^{\mathbf{k}}$ at wave-vector $\mathbf{k}$ in the Brillouin zone of corresponding to some space group G. The steps are given below:

- Find the isogonal group F of space group G consisting of the mirror and rotation parts of the quotient group G/T where T translation subgroup of G.

- Find the elements $R \in F$ such that $\mathbf{R}\mathbf{k} \equiv \mathbf{k}$. The set of these elements form little co-group $\bar{G}^{\mathbf{k}}$.

- If the group is symmorphic or if the point $\mathbf{k}$ not at the edge of the Brillouin zone, find the irreducible representation matrices $\mathbf{D}^{\mathbf{k}}$ corresponding to little co-group $\bar{G}^{\mathbf{k}}$. Then irreducible representation matrices $\mathbf{\Gamma}^{\mathbf{k}}$ corresponding to little group $G^{\mathbf{k}}$ are $\mathbf{\Gamma}^{\mathbf{k}}(\{R|\mathbf{v}\}) = \exp(-i\mathbf{k}\cdot\mathbf{v})\mathbf{D}^{\mathbf{k}}(R)$.

- If the group is nonsymmorphic and the wave vector $\mathbf{k}$ is at the edge of Brillouin zone, instead of finding representations of $\bar{G}^{\mathbf{k}}$, we have to find projective representations.

Symmetry protected degeneracy in frequency bands of elastic structures

In the following you will give examples of representations of different 2 dimensional space groups. We will start with a elastic system corresponding to the maximally symmetric space group $p4mm$ with square Bravais lattice. We will plot the eigenvalues ω of the Eq. 4.4 as function of wave vector $\mathbf{k}$, i.e. the band structure, along high symmetry lines in the Brillouin zone. We will find degeneracies in the band structures at some wave vectors $\mathbf{k}$ corresponding to 2 dimensional irreps of the little group of $\mathbf{k}$. Then, we will change the elastic structure perturbatively to get a structure with a lower space group symmetry. We will find that some of the symmetry protected degeneracies will be lifted for these elastic structures with lower symmetry. Note that band structures and eigenfunctions shown here are obtained using finite element simulations.

***p4mm*:** The unit cell, band structure and some of the eigenfunctions of the elastic structure is shown in Fig. 4.4(a). The elliptic inclusions all have major axis $0.3a$ and minor axis $0.15a$ where a is the length of the sides of the unit cell. Any element of the group $p4mm$ can be written as an element of the point group C_{4v} followed by a lattice translation with two fundamental lattice translations $\mathbf{t}_1$ and $\mathbf{t}_2$ being of same length but in the mutually perpendicular directions. The elements $\{E, C_4, C_4^2, C_4^3, \sigma_v, \sigma_v', \sigma_d, \sigma_d'\}$ of the point group C_{4v} can be understood in the following way. C_4 is the rotation about the center of the cell by an angle $\pi/2$ in the anticlockwise direction. Then, C_4^2 and C_4^3 are then rotations around the point by angles π and $3\pi/2$. The two vertical mirrors σ_v and σ_v' are the mirrors with normals along $\mathbf{t}_1$ and

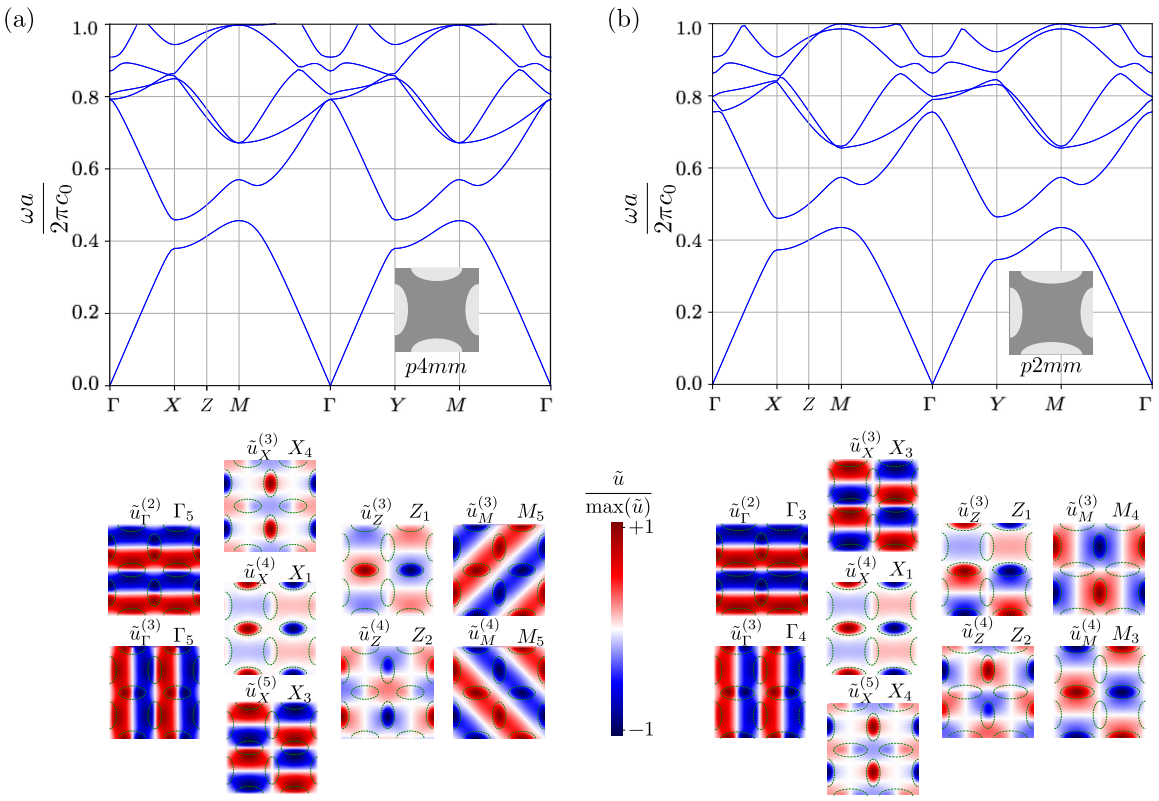

Figure 4.4: Anti-plane shear wave band structures and eigenfunctions of elastic systems $p4mm$ (a) and $p2mm$ (b). The unit cells are shown inset with the band structures. The elastic matrix with shear modulus μ_0 and densityρ_0 is shown in dark grey and the elliptic inclusions with shear modulus μ_i and densityρ_i are shown in light grey, where $\mu_i/\mu_0 = 1/10$ and $\rho_i/\rho_0 = 1/2$. The sizes of the inclusions are given in the text. See Fig. 4.2(a) for the specifics of the points in the horizontal axes of band structures. The eigenfrequency ω was normalized by $2\pi c_0/a$ where $c_0 = \sqrt{\mu_0/\rho_0}$ is the speed of shear wave inside the elastic matrix and a is length of the sides of the unit cells. A few eigenfunctions $\tilde{u}_{\mathbf{k}}^{(i)}$ for $\mathbf{k} = \Gamma, X, Z$ and M are plotted over four adjacent unit cells below each band structures, where i in $\tilde{u}_{\mathbf{k}}^{(i)}$ denotes the band number counted from the lowest band at that point $\mathbf{k}$. At the top right of each eigenfunction the little group irrep it belongs to is written.

$\mathbf{t}_2$ respectively. The two diagonal mirrors σ_d and σ_d' are the ones with normals along $\mathbf{t}_1 - \mathbf{t}_2$ and $\mathbf{t}_1 + \mathbf{t}_2$, respectively. To make the notations for the mirrors clearer, we will denote a mirror as σ_{mn} if its normal is along $m\mathbf{t}_1 + n\mathbf{t}_2$ direction from here onward. In this notation, $\sigma_v \equiv \sigma_{10}$, $\sigma_v' \equiv \sigma_{01}$, $\sigma_d \equiv \sigma_{1\bar{1}}$ and $\sigma_d' \equiv \sigma_{11}$. The isogonal group of $p4mm$ is just $F = C_{4v}$. The Brillouin zone and some spacial points in the Brillouin

zone are shown in Fig. 4.2(a). In the following we will treat some of the points in the Brillouin zone in detail.

Γ: Clearly, the point Γ with wave vector $\mathbf{k} = \mathbf{0}$ is invariant under the application of any element of $F = C_{4v}$. Therefore, the little co-group of point Γ is $\bar{G}^{\Gamma} = C_{4v}$, and the little group is $G^{\Gamma} = \{E|\mathbf{0}\}T + \{C_4|\mathbf{0}\}T + \{C_4^2|\mathbf{0}\}T + \{C_4^3|\mathbf{0}\}T + \{\sigma_{10}|\mathbf{0}\}T + \{\sigma_{01}|\mathbf{0}\}T + \{\sigma_{1\bar{1}}|\mathbf{0}\}T + \{\sigma_{11}|\mathbf{0}\}T$ where $T = \{m\mathbf{t}_1 + n\mathbf{t}_2 | m, n \in \mathbb{Z}\}$. Then, using the recipe explained above, we can first find the irreps $\mathbf{D}^{\Gamma}$ of $\bar{G}^{\Gamma} = C_{4v}$ (since $p4mm$ is symmorphic). Once we find that, the irreps of little group G^{Γ} are $\mathbf{\Gamma}^{\Gamma}(\{R|\mathbf{t}\}) = \exp(-i\mathbf{0}\cdot\mathbf{t})\mathbf{D}^{\Gamma}(R) = \mathbf{D}^{\Gamma}(R)$. Now, the matrices $\mathbf{\Gamma}^{\Gamma}(\{R|\mathbf{t}\}) = \mathbf{D}^{\Gamma}(R)$ may vary depending on the choice of the basis functions, but the characters (trace) are independent of this choice. Moreover, the character table of $\bar{G}^{\Gamma} = C_{4v}$ is easily available [68]. We reproduce the character table for completeness in Table 4.4. From

Table 4.4: Character table of C_{4v}

	$\{E\}$	$\{C_4, C_4^3\}$	$\{C_2\}$	$\{\sigma_{10}, \sigma_{01}\}$	$\{\sigma_{1\bar{1}}, \sigma_{11}\}$
A_1	$+1$	$+1$	$+1$	$+1$	$+1$
A_2	$+1$	$+1$	$+1$	-1	-1
B_1	$+1$	-1	$+1$	$+1$	-1
B_2	$+1$	-1	$+1$	-1	$+1$
E	$+2$	0	-2	0	0

this character table of the little co-group $\bar{G}^{\Gamma}$, the characters of the matrices $\mathbf{\Gamma}^{\Gamma}$ of the little group G^{Γ} can be easily obtained (since $\mathbf{\Gamma}^{\Gamma}(\{R|\mathbf{t}\}) = \mathbf{D}^{\Gamma}(R)$), which we show in Table 4.5. Note that this table does not contain the composite elements (combi-

Table 4.5: Characters of irrep matrices $\mathbf{\Gamma}^{\Gamma}$ of little group G^{Γ} of $p4mm$

	$\{\{E\|m\mathbf{t}_1 + n\mathbf{t}_2\}\}$	$\{\{C_4\|\mathbf{0}\}, \{C_4^3\|\mathbf{0}\}\}$	$\{\{C_4^2\|\mathbf{0}\}\}$	$\{\{\sigma_{10}\|\mathbf{0}\}, \{\sigma_{01}\|\mathbf{0}\}\}$	$\{\{\sigma_{1\bar{1}}\|\mathbf{0}\}, \{\sigma_{11}\|\mathbf{0}\}\}$
Γ_1	$+1$	$+1$	$+1$	$+1$	$+1$
Γ_2	$+1$	$+1$	$+1$	-1	-1
Γ_3	$+1$	-1	$+1$	$+1$	-1
Γ_4	$+1$	-1	$+1$	-1	$+1$
Γ_5	$+2$	0	-2	0	0

nation of point group operation and translation) of G^{Γ}. However, matrices of those

composite operations can be obtained multiplying matrices of point group operations and translation operations due to homomorphism. More importantly, since irrep Γ_5 is 2 dimensional (this clear from the fact that the trace of the irrep matrix of the identity element $\{E|\mathbf{0}\}$ is 2), there can be degeneracies at the Γ point in the band structure. Consider the eigenfunctions $\tilde{u}^{(2)}_\Gamma$ and $\tilde{u}^{(3)}_\Gamma$ in Fig. 4.4(a). Under lattice translations, the remain invariant. Under π rotation about the center of the unit cell, they become $-\tilde{u}^{(2)}_\Gamma$ and $-\tilde{u}^{(3)}_\Gamma$. Under $\pi/2$ rotation, though, $\tilde{u}^{(2)}_\Gamma$ and $\tilde{u}^{(3)}_\Gamma$ transform to $-\tilde{u}^{(3)}_\Gamma$ and $\tilde{u}^{(2)}_\Gamma$, respectively. Under mirror σ_{10}, $\tilde{u}^{(2)}_\Gamma$ and $\tilde{u}^{(3)}_\Gamma$ transform to $\tilde{u}^{(2)}_\Gamma$ and $-\tilde{u}^{(3)}_\Gamma$, respectively. Under mirror σ_{01}, $\tilde{u}^{(2)}_\Gamma$ and $\tilde{u}^{(3)}_\Gamma$ transform to $-\tilde{u}^{(2)}_\Gamma$ and $\tilde{u}^{(3)}_\Gamma$, respectively. Under mirror $\sigma_{1\bar{1}}$, $\tilde{u}^{(2)}_\Gamma$ and $\tilde{u}^{(3)}_\Gamma$ transform to $\tilde{u}^{(3)}_\Gamma$ and $\tilde{u}^{(2)}_\Gamma$, respectively. Lastly, under mirror σ_{11}, $\tilde{u}^{(2)}_\Gamma$ and $\tilde{u}^{(3)}_\Gamma$ transform to $-\tilde{u}^{(3)}_\Gamma$ and $\tilde{u}^{(2)}_\Gamma$, respectively. Therefore, $\tilde{u}^{(2)}_\Gamma$ and $\tilde{u}^{(3)}_\Gamma$ form a representation of G^Γ with matrices:

$$
\begin{aligned}
&\mathbf{\Gamma}^\Gamma(\{E|m\mathbf{t}_1+n\mathbf{t}_2\}) = \begin{pmatrix} 1 & 0 \\ 0 & 1 \end{pmatrix}, \mathbf{\Gamma}^\Gamma(\{C_4|\mathbf{0}\}) = \begin{pmatrix} 0 & 1 \\ -1 & 0 \end{pmatrix}, \\
&\mathbf{\Gamma}^\Gamma(\{C_4^3|\mathbf{0}\}) = \begin{pmatrix} 0 & -1 \\ 1 & 0 \end{pmatrix}, \mathbf{\Gamma}^\Gamma(\{C_4^2|\mathbf{0}\}) = \begin{pmatrix} -1 & 0 \\ 0 & -1 \end{pmatrix}, \\
&\mathbf{\Gamma}^\Gamma(\{\sigma_{10}|\mathbf{0}\}) = \begin{pmatrix} 1 & 0 \\ 0 & -1 \end{pmatrix}, \mathbf{\Gamma}^\Gamma(\{\sigma_{01}|\mathbf{0}\}) = \begin{pmatrix} -1 & 0 \\ 0 & 1 \end{pmatrix}, \\
&\mathbf{\Gamma}^\Gamma(\{\sigma_{1\bar{1}}|\mathbf{0}\}) = \begin{pmatrix} 0 & 1 \\ 1 & 0 \end{pmatrix}, \mathbf{\Gamma}^\Gamma(\{\sigma_{11}|\mathbf{0}\}) = \begin{pmatrix} 0 & 1 \\ -1 & 0 \end{pmatrix}.
\end{aligned}
\tag{4.12}
$$

The traces of these matrices reveal that this corresponds to irrep Γ_5, which is 2 dimensional. That is why we see that $\tilde{u}^{(2)}_\Gamma$ and $\tilde{u}^{(3)}_\Gamma$ have the same eigenfrequency (Fig. 4.4)(a).

M: Since any element of C_{4v} brings the wave vector $\mathbf{k} = (\mathbf{K}_1 + \mathbf{K}_2)/2$, where $\mathbf{K}_1$ and $\mathbf{K}_2$ are the fundamental reciprocal lattice vectors, to an equivalent wave vector, the little co-group of the M point is also $\bar{G}^M = C_{4v}$. The M point is a vertex of Brillouin zone. However, since $p4mm$ is a symmorphic group, the matrices $\mathbf{D}^M$ are irrep matrices (as opposed to projective representation matrices) of little co-group $\bar{G}^M$. However, unlike for Γ point, for M point the relation between irrep matrices $\mathbf{\Gamma}^M$ of the little group G^M and irrep matrices $\mathbf{D}^M$ of the little co-group $\bar{G}^M$ is $\mathbf{\Gamma}^M(\{R|\mathbf{t}\}) = \exp(-i(\mathbf{K}_1/2 + \mathbf{K}_2/2) \cdot \mathbf{t})\mathbf{D}^M(R) = \exp(-i\pi(m+n))\mathbf{D}^M(R)$, where $\mathbf{t} = m\mathbf{t}_1 + n\mathbf{t}_2$. Using the character table of C_{4v}, the characters of the irrep matrices of little group G^M can be easily evaluated and given in Table 4.6. Again,

Table 4.6: Characters of irrep matrices $\mathbf{\Gamma}^M$ of little group G^M of $p4mm$

	$\{\{E\|m\mathbf{t}_1 + n\mathbf{t}_2\}\}$	$\{\{C_4\|\mathbf{0}\}, \{C_4^3\|\mathbf{0}\}\}$	$\{\{C_4^2\|\mathbf{0}\}\}$	$\{\{\sigma_{10}\|\mathbf{0}\}, \{\sigma_{01}\|\mathbf{0}\}\}$	$\{\{\sigma_{1\bar{1}}\|\mathbf{0}\}, \{\sigma_{11}\|\mathbf{0}\}\}$
M_1	$\exp(-i\pi(m+n))$	$+1$	$+1$	$+1$	$+1$
M_2	$\exp(-i\pi(m+n))$	$+1$	$+1$	-1	-1
M_3	$\exp(-i\pi(m+n))$	-1	$+1$	$+1$	-1
M_4	$\exp(-i\pi(m+n))$	-1	$+1$	-1	$+1$
M_5	$2\exp(-i\pi(m+n))$	0	-2	0	0

there is one 2 dimensional irrep: M_5. Consider the eigenfunctions $\tilde{u}_M^{(3)}$ and $\tilde{u}_M^{(4)}$ as shown in Fig. 4.4(a). Eigenfunctions $\tilde{u}_M^{(3)}$ and $\tilde{u}_M^{(4)}$ transform to $-\tilde{u}_M^{(3)}$ and $-\tilde{u}_M^{(4)}$, respectively, under each of the translations $\mathbf{t}_1$ and $\mathbf{t}_2$, but to $\tilde{u}_M^{(3)}$ and $\tilde{u}_M^{(4)}$, respectively, under translation $\mathbf{t}_1 + \mathbf{t}_2$. Moreover, it can be easily verified by inspection that the

representation matrices of the point group operations in the basis $\tilde{u}_M^{(3)}$ and $\tilde{u}_M^{(4)}$ are:

$$\mathbf{\Gamma}^M(\{C_4|\mathbf{0}\}) = \begin{pmatrix} 0 & 1 \\ -1 & 0 \end{pmatrix}, \mathbf{\Gamma}^M(\{C_4^3|\mathbf{0}\}) = \begin{pmatrix} 0 & -1 \\ 1 & 0 \end{pmatrix}, \mathbf{\Gamma}^M(\{C_4^2|\mathbf{0}\}) = \begin{pmatrix} -1 & 0 \\ 0 & -1 \end{pmatrix},$$
$$\mathbf{\Gamma}^M(\{\sigma_{10}|\mathbf{0}\}) = \begin{pmatrix} 0 & 1 \\ 1 & 0 \end{pmatrix}, \mathbf{\Gamma}^M(\{\sigma_{01}|\mathbf{0}\}) = \begin{pmatrix} 0 & -1 \\ -1 & 0 \end{pmatrix},$$
$$\mathbf{\Gamma}^M(\{\sigma_{1\bar{1}}|\mathbf{0}\}) = \begin{pmatrix} -1 & 0 \\ 0 & 1 \end{pmatrix}, \mathbf{\Gamma}^M(\{\sigma_{11}|\mathbf{0}\}) = \begin{pmatrix} 1 & 0 \\ 0 & -1 \end{pmatrix}. \tag{4.13}$$

From all this, clearly, $\tilde{u}_M^{(3)}$ and $\tilde{u}_M^{(4)}$ form the basis of irrep M_5, and unsurprisingly the eigenfrequencies for these two eigenfunctions are same giving rise to symmetry protected degeneracy.

X: The point X or wave vector $\mathbf{k} = \mathbf{K}_1/2$ (where $\mathbf{K}_1$ is the fundamental reciprocal lattice vector in the horizontal direction) remain invariant under elements C_2, σ_{01} and transform to an equivalent point under σ_{10}. Therefore, the little co-group of point X is $\bar{G}^X = C_{2v}$. The X point is at the edge of Brillouin zone. The character table of irreps of $\bar{G}^X = C_{2v}$ is given in Table 4.7. Then, using the relation

Table 4.7: Character table of C_{2v}

	$\{E\}$	$\{C_2\}$	$\{\sigma_{10}\}$	$\{\sigma_{01}\}$
A_1	$+1$	$+1$	$+1$	$+1$
A_2	$+1$	$+1$	-1	-1
B_1	$+1$	-1	$+1$	-1
B_2	$+1$	-1	-1	$+1$

$\mathbf{\Gamma}^X(\{R|\mathbf{t}\}) = \exp(-i(\mathbf{K}_1/2)\cdot\mathbf{t})\mathbf{D}^X(R) = \exp(-im\pi)\mathbf{D}^X(R)$, where $\mathbf{t} = m\mathbf{t}_1 + n\mathbf{t}_2$ between irrep matrices $\mathbf{\Gamma}^X$ of little group G^X and irrep matrices $\mathbf{D}^X$ of little co-group $\bar{G}^X$, the characters of irrep matrices $\mathbf{\Gamma}^X$ can be obtained and given in Table 4.8. Note that there are no multidimensional irrep. Therefore, there is no symmetry protected

Table 4.8: Characters of irrep matrices $\mathbf{\Gamma}^X$ of little group G^X of $p4mm$ and $p2mm$

	$\{\{E\|m\mathbf{t}_1+n\mathbf{t}_2\}\}$	$\{\{C_2\|\mathbf{0}\}\}$	$\{\{\sigma_{10}\|\mathbf{0}\}\}$	$\{\{\sigma_{01}\|\mathbf{0}\}\}$
X_1	$\exp(-im\pi)$	$+1$	$+1$	$+1$
X_2	$\exp(-im\pi)$	$+1$	-1	-1
X_3	$\exp(-im\pi)$	-1	$+1$	-1
X_4	$\exp(-im\pi)$	-1	-1	$+1$

degeneracies at the X point. Consider the eigenfunctions $\tilde{u}_X^{(3)}$, $\tilde{u}_X^{(4)}$ and $\tilde{u}_X^{(5)}$ shown in Fig. 4.4(a). The eigenfunction $\tilde{u}_X^{(3)}$ transform to $-\tilde{u}_X^{(3)}$, $-\tilde{u}_X^{(3)}$ and $\tilde{u}_X^{(3)}$ under C_2, σ_{10} and σ_{01} respectively. Therefore, $\tilde{u}_X^{(3)}$ is the basis of 1 dimensional irrep X_4. The eigenfunction $\tilde{u}_X^{(4)}$ transform to $\tilde{u}_X^{(4)}$, $\tilde{u}_X^{(4)}$ and $\tilde{u}_X^{(4)}$ under C_2, σ_{10} and σ_{01} respectively. Therefore, $\tilde{u}_X^{(4)}$ is the basis of 1 dimensional irrep X_1. The eigenfunction $\tilde{u}_X^{(5)}$ transform to $-\tilde{u}_X^{(5)}$, $\tilde{u}_X^{(5)}$ and $-\tilde{u}_X^{(5)}$ under C_2, σ_{10} and σ_{01} respectively. Therefore, $\tilde{u}_X^{(5)}$ is the basis of 1 dimensional irrep X_3.

Z: The wave vectors $\mathbf{K}_1/2+u\mathbf{K}_2$ with $0<u<1/2$ are denoted as Z, and remain invariant only under the application the identity E and σ_{10} (σ_{10} brings the Z to an equivalent wave vector) among all the elements of C_{4v}. Therefore, for these wave vectors, the little co-group is $\bar{G}^Z=\{E,\sigma_{10}\}=C_{1v}$. The points Z are at the edge of the Brillouin zone, however, since $p4mm$ is a symmorphic group, the irreps of little group G^Z can be obtained from the irreps of little co-group $\bar{G}^Z$. The character table of C_{1v} is given Table 4.9. The characters of The relation between irrep

Table 4.9: Character table of C_{1v}

	$\{E\}$	$\{\sigma\}$
A_1	$+1$	$+1$
A_2	$+1$	-1

matrices $\mathbf{\Gamma}^Z$ of the little group G^Z and irrep matrices $\boldsymbol{D}^Z$ of the little co-group $\bar{G}^Z$ is $\mathbf{\Gamma}^Z(\{R|\mathbf{t}\})=\exp(-i(\mathbf{K}_1/2+u\mathbf{K}_2)\cdot\mathbf{t})\mathbf{D}^Z(R)=\exp(-i\pi(m+2un))\mathbf{D}^Z(R)$, where $\mathbf{t}=m\mathbf{t}_1+n\mathbf{t}_2$. Using this, we can find the characters of matrices $\mathbf{\Gamma}^Z$, and they are given in Table 4.10. There is no multidimensional irrep of G^Z, and therefore there

can be no symmetry protected degeneracies. Let us consider the eigenfunctions $\tilde{u}_Z^{(3)}$

Table 4.10: Characters of irrep matrices $\mathbf{\Gamma}^Z$ of little group G^Z of $p4mm$

	$\{\{E\|m\mathbf{t}_1+n\mathbf{t}_2\}\}$	$\{\{\sigma_{10}\|\mathbf{0}\}\}$
Z_1	$\exp(-i\pi(m+2un))$	$+1$
Z_2	$\exp(-i\pi(m+2un))$	-1

and $\tilde{u}_Z^{(4)}$ shown in Fig. 4.4(a) (we chose $u = 1/4$). Under mirror σ_{10}, $\tilde{u}_Z^{(3)}$ and $\tilde{u}_Z^{(4)}$ transform to $\tilde{u}_Z^{(3)}$ and $-\tilde{u}_Z^{(4)}$, respectively. Therefore, $\tilde{u}_Z^{(3)}$ and $\tilde{u}_Z^{(4)}$ form the basis of Z_1 and Z_2, respectively.

A more instructive way of thinking about the irrep label of the 3rd and 4th bands at wave vectors Z comes from the observation that the little co-group C_{1v} of the Z points is subgroup of the little co-group C_{2v} at point X and little co-group C_{4v} at point M. Let the irrep E of C_{4v} restricted to subgroup C_{1v} breaks into $E^{C_{4v}}\big|_{C_{1v}} = a_1 A_1^{C_{1v}} \oplus a_2 A_2^{C_{1v}}$. Then using the formula $a_\alpha = \frac{1}{|C_{1v}|}\sum_{g\in C_{1v}} \left(\chi_\alpha^{C_{1v}}(g)\right)^* \chi_E^{C_{4v}}(g)$, we find $E^{C_{4v}}\big|_{C_{1v}} = A_1^{C_{1v}} \oplus A_2^{C_{1v}}$. Therefore, $M_5|_{G^Z} = Z_1 \oplus Z_2$. Let the irrep A_1 of C_{2v} restricted to subgroup C_{1v} breaks into $A_1^{C_{2v}}\big|_{C_{1v}} = a_1 A_1^{C_{1v}} \oplus a_2 A_2^{C_{1v}}$. Then using the formula $a_\alpha = \frac{1}{|C_{1v}|}\sum_{g\in C_{1v}} \left(\chi_\alpha^{C_{1v}}(g)\right)^* \chi_{A_1}^{C_{2v}}(g)$, we find $A_1^{C_{2v}}\big|_{C_{1v}} = A_1^{C_{1v}}$. Therefore, $X_1|_{G^X} = Z_1$. Similarly, if the irrep B_2 of C_{2v} restricted to subgroup C_{1v} breaks into $B_2^{C_{2v}}\big|_{C_{1v}} = a_1 A_1^{C_{1v}} \oplus a_2 A_2^{C_{1v}}$, using the formula $a_\alpha = \frac{1}{|C_{1v}|}\sum_{g\in C_{1v}} \left(\chi_\alpha^{C_{1v}}(g)\right)^* \chi_{B_2}^{C_{2v}}(g)$, we find $B_2^{C_{2v}}\big|_{C_{1v}} = A_2^{C_{1v}}$. Therefore, $X_4|_{G^Z} = Z_2$. Therefore, 3rd goes from X_4 irrep at point X to Z_2 at points Z, whereas 4th goes from X_1 irrep at point X to Z_1 at points Z. However, a closer look at the band structure in Fig. 4.4(a) shows that the 3rd and 4th bands cross near between X and M near point X. then, to the right of the crossing the 3rd band has irrep label Z_1 and the 4th band has irrep label Z_2. This is exactly what we found in the last paragraph. This means that just by knowing the irrep labels at the high symmetry points X and M, the irrep label on the line connecting them is completely determined. Moreover, the band crossing near point

X is accidental, not symmetry protected because there is no multidimensional irrep of the little group G^Z.

***p2mm*:** As shown in Fig. 4.4(b), by changing the major axes of the top and bottom ellipses to $0.37a$, we obtain an elastic structure with $p2mm$ space group symmetry. In changing the sizes of the top and bottom ellipses, we broke C_4, C_4^3, $\sigma_{1\bar{1}}$ and σ_{11} point group symmetries. Therefore, any element of group $p2mm$ can be written as an element of the point group $C_{2v} = \{E, C_2, \sigma_{10}, \sigma_{01}\}$ about the center of the unit cell followed by a lattice translation. Note that since we did not change the size of the unit cell, the fundamental lattice translations $\mathbf{t}_1$ and $\mathbf{t}_2$ and fundamental reciprocal lattice vectors $\mathbf{K}_1$ and $\mathbf{K}_2$ remain the same as in the $p4mm$ case in our example. As a result, the Brillouin zone remain the same as in $p4mm$.

Γ: The point Γ with wave vector $\mathbf{k} = \mathbf{0}$ is invariant under the application of any element of C_{4v}. The characters of the irreps $\mathbf{D}^\Gamma$ of little co-group $\bar{G}^\Gamma = C_{2v}$ are given in Table 4.7. Then, using the relation $\mathbf{\Gamma}^\Gamma(R|\mathbf{t}) = \exp(-i\mathbf{0}\cdot\mathbf{t})\mathbf{D}^\Gamma(R) = \mathbf{D}^\Gamma(R)$ between irrep matrices $\mathbf{\Gamma}^\Gamma$ of the little group G^Γ and irrep matrices $\mathbf{D}^\Gamma$ of the little co-group $\bar{G}^\Gamma$, the characters of irrep matrices $\mathbf{\Gamma}^\Gamma(R|\mathbf{t})$ can be obtained and are given in Table 4.11. Now, it is worth noting that there is no multidimensional

Table 4.11: Characters of irrep matrices $\mathbf{\Gamma}^\Gamma$ of little group G^Γ of $p2mm$

	$\{\{E\|m\mathbf{t}_1 + n\mathbf{t}_2\}\}$	$\{\{C_2\|\mathbf{0}\}\}$	$\{\{\sigma_{10}\|\mathbf{0}\}\}$	$\{\{\sigma_{01}\|\mathbf{0}\}\}$
Γ_1	$+1$	$+1$	$+1$	$+1$
Γ_2	$+1$	$+1$	-1	-1
Γ_3	$+1$	-1	$+1$	-1
Γ_4	$+1$	-1	-1	$+1$

irrep at the Γ point for $p2mm$. This means that coming from $p4mm$ to $p2mm$ by perturbatively changing the sizes of two of the ellipses in the unit cell, we lift the degeneracies at the Γ point. Now, our goal is to learn which irrep of little group

G^{Γ}_{p2mm} the 2 dimensional irrep Γ_5^{p4mm} of the little group G^{Γ}_{p4mm} breaks into. Let $\Gamma_5^{p4mm}\big|_{p2mm} = a_1\Gamma_1^{p2mm} \oplus a_2\Gamma_2^{p2mm} \oplus a_3\Gamma_3^{p2mm} \oplus a_4\Gamma_4^{p2mm}$. This is equivalent to writing $E^{C_{4v}}\big|_{C_{2v}} = a_1A_1^{C_{2v}} \oplus a_2A_2^{C_{2v}} \oplus a_3B_1^{C_{2v}} \oplus a_4B_2^{C_{2v}}$. We have to determine the coefficients a_1, a_2, a_3 and a_4. To do this we use the formula $a_\alpha = \frac{1}{|C_{2v}|}\sum_{g\in C_{2v}} \left(\chi_\alpha^{C_{2v}}(g)\right)^* \chi_E^{C_{4v}}(g)$ derived earlier. Then $a_1 = (1\times 2 + 1\times(-2))/4 = 0$, $a_2 = (1\times 2 + 1\times(-2))/4 = 0$, $a_3 = (1\times 2 + (-1)\times(-2))/4 = 1$ and $a_4 = (1\times 2 + (-1)\times(-2))/4 = 1$. This implies that $\Gamma_5^{p4mm}\big|_{p2mm} = \Gamma_3^{p2mm} \oplus \Gamma_4^{p2mm}$. Consider the eigenfunctions $\tilde{u}^{(2)}_\Gamma$ and $\tilde{u}^{(3)}_\Gamma$ in Fig. 4.4(b). Eigenfunction $\tilde{u}^{(2)}_\Gamma$ transforms to $-\tilde{u}^{(2)}_\Gamma$, $\tilde{u}^{(2)}_\Gamma$ and $-\tilde{u}^{(2)}_\Gamma$ under C_2, σ_{10} and σ_{01} about the center of the unit cell. Eigenfunction $\tilde{u}^{(3)}_\Gamma$ transforms to $-\tilde{u}^{(3)}_\Gamma$, $-\tilde{u}^{(3)}_\Gamma$ and $\tilde{u}^{(3)}_\Gamma$ under C_2, σ_{10} and σ_{01} about the center of the unit cell. Therefore, $\tilde{u}^{(2)}_\Gamma$ and $\tilde{u}^{(3)}_\Gamma$ correspond to irreps Γ_3^{p2mm} and Γ_4^{p2mm} respectively. This confirms that the 2-fold degeneracy between 2$^{\text{nd}}$ and 3$^{\text{rd}}$ band at Γ point of $p4mm$ corresponding to irrep Γ_5^{p4mm} (Fig. 4.4(a)) breaks into non-degenerate eigenfrequencies at Γ point of $p2mm$ corresponding to irrep Γ_3^{p2mm} and Γ_4^{p2mm} (Fig. 4.4(b)).

M: Since any element of C_{2v} bring the wave vector $\mathbf{k} = (\mathbf{K}_1 + \mathbf{K}_2)/2$, where $\mathbf{K}_1$ and $\mathbf{K}_2$ are the fundamental reciprocal lattice vectors, to an equivalent wave vector, the little co-group of the M point is also $\bar{G}^M = C_{2v}$. The characters of the irreps $\mathbf{D}^\Gamma$ of little co-group $\bar{G}^\Gamma = C_{2v}$ are given in Table 4.7. Then, using the relation $\mathbf{\Gamma}^\Gamma(R|\mathbf{t}) = \exp(-i(\mathbf{K}_1/2 + \mathbf{K}_2/2)\cdot\mathbf{t})\mathbf{D}^\Gamma(R) = \exp(-i\pi(m+n))\mathbf{D}^\Gamma(R)$ (where $\mathbf{t} = m\mathbf{t}_1 + n\mathbf{t}_2$) between irrep matrices $\mathbf{\Gamma}^\Gamma$ of the little group G^Γ and irrep matrices $\mathbf{D}^\Gamma$ of the little co-group $\bar{G}^\Gamma$, the characters of irrep matrices $\mathbf{\Gamma}^\Gamma(R|\mathbf{t})$ can be obtained and are given in Table 4.12. Again, there is no multidimensional irrep at the M point for $p2mm$.

Table 4.12: Characters of irrep matrices $\mathbf{\Gamma}^M$ of little group G^M of $p2mm$

	$\{\{E\|m\mathbf{t}_1 + n\mathbf{t}_2\}\}$	$\{\{C_2\|\mathbf{0}\}\}$	$\{\{\sigma_{10}\|\mathbf{0}\}\}$	$\{\{\sigma_{01}\|\mathbf{0}\}\}$
M_1	$\exp(-i\pi(m+n))$	$+1$	$+1$	$+1$
M_2	$\exp(-i\pi(m+n))$	$+1$	-1	-1
M_3	$\exp(-i\pi(m+n))$	-1	$+1$	-1
M_4	$\exp(-i\pi(m+n))$	-1	-1	$+1$

Since, $E^{C_{4v}}\big|_{C_{2v}} = B_1^{C_{2v}} \oplus B_2^{C_{2v}}$ as we saw before, $M_5^{p4mm}\big|_{p2mm} = M_3^{p2mm} \oplus M_4^{p2mm}$. Consider the eigenfunctions $\tilde{u}_M^{(3)}$ and $\tilde{u}_M^{(4)}$ in Fig. 4.4(b). Eigenfunction $\tilde{u}_M^{(3)}$ transforms to $-\tilde{u}_M^{(3)}$, $-\tilde{u}_M^{(3)}$ and $\tilde{u}_M^{(3)}$ under C_2, σ_{10} and σ_{01} about the center of the unit cell. Eigenfunction $\tilde{u}_M^{(4)}$ transforms to $-\tilde{u}_M^{(4)}$, $\tilde{u}_M^{(4)}$ and $-\tilde{u}_M^{(4)}$ under C_2, σ_{10} and σ_{01} about the center of the unit cell. Therefore, $\tilde{u}_M^{(3)}$ and $\tilde{u}_M^{(4)}$ correspond to irreps M_4^{p2mm} and M_3^{p2mm} respectively. This confirms that the 2-fold degeneracy between 3$^{\text{rd}}$ and 4$^{\text{th}}$ band at M point of $p4mm$ corresponding to irrep M_5^{p4mm} (Fig. 4.4(a)) breaks into non-degenerate eigenfrequencies at M point of $p2mm$ corresponding to irrep M_3^{p2mm} and M_4^{p2mm} (Fig. 4.4(b)).

X: The wave vector $\mathbf{k} = \mathbf{K}_1/2$ corresponding to point X remains invariant under σ_{01}, whereas transforms to an equivalent point under σ_{10} and C_2. Therefore, the little co-group $\bar{G}^X = C_{2v}$. Since the little co-group of point X for $p2mm$ and $p4mm$ are same and both space groups are symmorphic, the characters of the irrep matrices $\mathbf{\Gamma}_{p2mm}^X$ of $p2mm$ equal those of $p4mm$ and given in Table 4.8. Again there are no multidimensional irrep. Therefore, there is no symmetry protected degeneracies at the X point. Consider the eigenfunctions $\tilde{u}_X^{(3)}$, $\tilde{u}_X^{(4)}$ and $\tilde{u}_X^{(5)}$ shown in Fig. 4.4(b). The eigenfunction $\tilde{u}_X^{(3)}$ transform to $-\tilde{u}_X^{(3)}$, $\tilde{u}_X^{(3)}$ and $-\tilde{u}_X^{(3)}$ under C_2, σ_{10} and σ_{01} respectively. Therefore, $\tilde{u}_X^{(3)}$ is the basis of 1 dimensional irrep X_3. The eigenfunction $\tilde{u}_X^{(4)}$ transform to $\tilde{u}_X^{(4)}$, $\tilde{u}_X^{(4)}$ and $\tilde{u}_X^{(4)}$ under C_2, σ_{10} and σ_{01} respectively. Therefore, $\tilde{u}_X^{(4)}$ is the basis of 1 dimensional irrep X_1. The eigenfunction $\tilde{u}_X^{(5)}$ transform to $-\tilde{u}_X^{(5)}$, $-\tilde{u}_X^{(5)}$ and $\tilde{u}_X^{(5)}$ under C_2, σ_{10} and σ_{01} respectively. Therefore, $\tilde{u}_X^{(5)}$ is the basis of 1 dimensional irrep X_4. Note that the eigenvectors at the X point of $p2mm$ and $p4mm$ looked very similar. Moreover, the irrep labels at the X point of band 3, 4 and 5 for $p4mm$ were exactly the same as those for $p2mm$ albeit in a different order. This is because we perturbed the elastic structure with $p4mm$ to get to $p2mm$, and as a result band inversions happened between the three bands.

Z: The Z points of $p2mm$ have the same little co-group as in $p4mm$ and all irreps are 1 dimensional; hence do not permit symmetry protected degeneracy. The degeneracies that we see between 3[rd] and 4[th] band in Fig. 4.4(b) are accidental.

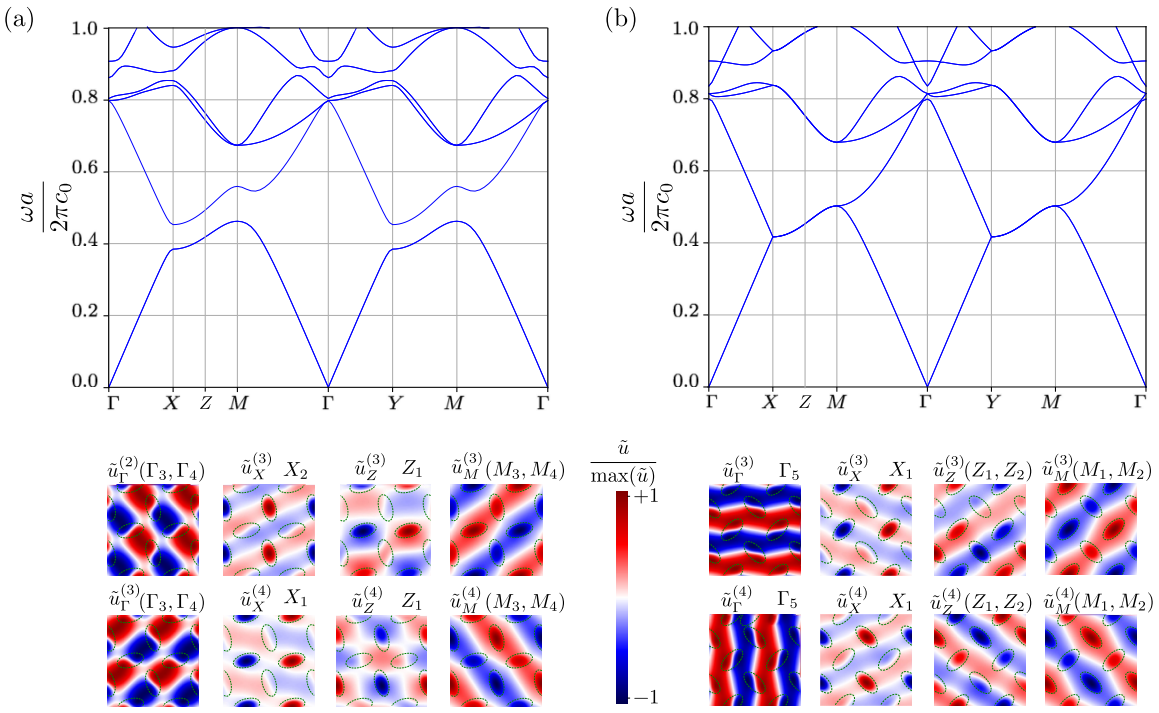

Figure 4.5: Anti-plane shear wave band structures and eigenfunctions of elastic systems $p4$ (a) and $p4gm$ (b). The unit cells are shown inset with the band structures. The elastic matrix with shear modulus μ_0 and densityρ_0 is shown in dark grey and the elliptic inclusions with shear modulus μ_i and densityρ_i are shown in light grey, where $\mu_i/\mu_0 = 1/10$ and $\rho_i/\rho_0 = 1/2$. The sizes of the inclusions are given in the text. See Fig. 4.2(a) for the specifics of the points in the horizontal axes of band structures. The eigenfrequency ω was normalized by $2\pi c_0/a$ where $c_0 = \sqrt{\mu_0/\rho_0}$ is the speed of shear wave inside the elastic matrix and a is length of the sides of the unit cells. A few eigenfunctions $\tilde{u}_{\mathbf{k}}^{(i)}$ for $\mathbf{k} = \Gamma, X, Z$ and M are plotted over four adjacent unit cells below each band structures, where i in $\tilde{u}_{\mathbf{k}}^{(i)}$ denotes the band number counted from the lowest band at that point $\mathbf{k}$. At the top right of each eigenfunction the little group irrep it belongs to is written. In some cases two irreps are written with a parenthesis as for $\tilde{u}_\Gamma^{(2)}$. This means those two irreps together form an irreducible co-representation due to time reversal symmetry, see Sec. 4.3.

***p4*:** As shown in Fig 4.5(a), starting from the elastic structure corresponding to $p4mm$, if we rotate all the ellipse counter clockwise by an angle $0 < \theta < \pi/4$, we

break the mirror symmetries while keeping C_4 rotation symmetry about the center. This means that for $0 < \theta < \pi/4$, the elastic structure has $p4$ space group symmetry. The space group $p4$ is symmorphic. In the specific angle used in Fig 4.5(a) is $\theta = \pi/12$.

$\mathbf{\Gamma}$: Clearly, the point Γ with wave vector $\mathbf{k} = \mathbf{0}$ is invariant under the application of any element of $F = C_4$. Therefore, the little co-group of point Γ is $\bar{G}^\Gamma = C_4$, and the little group is $G^\Gamma = \{E|\mathbf{0}\}T + \{C_4|\mathbf{0}\}T + \{C_4^2|\mathbf{0}\}T + \{C_4^3|\mathbf{0}\}T + \{\sigma_{10}|\mathbf{0}\}T$ where $T = \{m\mathbf{t}_1 + n\mathbf{t}_2 | m, n \in \mathbb{Z}\}$. We can first find the irreps $\mathbf{D}^\Gamma$ of $\bar{G}^\Gamma = C_4$ (since $p4$ is symmorphic). Once we get that, the irreps of little group G^Γ are $\mathbf{\Gamma}^\Gamma(\{R|\mathbf{t}\}) = \exp(-i\mathbf{0}\cdot\mathbf{t})\mathbf{D}^\Gamma(R) = \mathbf{D}^\Gamma(R)$. The character table of point group C_4 is given in Table 4.13. From this character table of the little co-group $\bar{G}^\Gamma$, the characters of the

Table 4.13: Character table of C_4

	$\{E\}$	$\{C_4\}$	$\{C_2\}$	$\{C_4^3\}$
A	$+1$	$+1$	$+1$	$+1$
B	$+1$	-1	$+1$	-1
E_1	$+1$	$+i$	-1	$-i$
E_2	$+1$	$-i$	-1	$+i$

matrices $\mathbf{\Gamma}^\Gamma$ of the little group G^Γ can be easily obtained (since $\mathbf{\Gamma}^\Gamma(\{R|\mathbf{t}\}) = \mathbf{D}^\Gamma(R)$), which we show in Table 4.14. Note that there is no multidimensional irrep. However,

Table 4.14: Characters of irrep matrices $\mathbf{\Gamma}^\Gamma$ of little group G^Γ of $p4$

	$\{\{E|m\mathbf{t}_1 + n\mathbf{t}_2\}\}$	$\{\{C_4|\mathbf{0}\}\}$	$\{\{C_2|\mathbf{0}\}\}$	$\{\{C_4^3|\mathbf{0}\}\}$
Γ_1	$+1$	$+1$	$+1$	$+1$
Γ_2	$+1$	-1	$+1$	-1
Γ_3	$+1$	$+i$	-1	$-i$
Γ_4	$+1$	$-i$	-1	$+i$

the characters corresponding to irreps Γ_3 and Γ_4 are complex. Since we obtained the elastic structure with $p4$ symmetry by perturbatively rotating the ellipses from a structure with $p4mm$ symmetry, we should be able to tell which irrep of $p4mm$ at Γ converts to which irrep of $p4$ at Γ. Our goal is to learn which irrep of little group G^Γ_{p4} the 2 dimensional irrep Γ_5^{p4mm} of the little group G^Γ_{p4mm} breaks into. Let

$\Gamma_5^{p4mm}\big|_{p4} = a_1\Gamma_1^{p4} \oplus a_2\Gamma_2^{p4} \oplus a_3\Gamma_3^{p4} \oplus a_4\Gamma_4^{p4}$. This is equivalent to writing $E^{C_{4v}}\big|_{C_4} = a_1A^{C_4} \oplus a_2B^{C_4} \oplus a_3E_1^{C_4} \oplus a_4E_2^{C_4}$. We have to determine the coefficients a_1, a_2, a_3 and a_4. To do this we use the formula $a_\alpha = \frac{1}{|C_4|}\sum_{g\in C_4}\left(\chi_\alpha^{C_4}(g)\right)^*\chi_E^{C_{4v}}(g)$ derived earlier. Then $a_1 = (1\times 2 + 1\times(-2))/4 = 0$, $a_2 = (1\times 2 + 1\times(-2))/4 = 0$, $a_3 = (1\times 2 + (-1)\times(-2))/4 = 1$ and $a_4 = (1\times 2 + (-1)\times(-2))/4 = 1$. This implies that $\Gamma_5^{p4mm}\big|_{p4} = \Gamma_3^{p4} \oplus \Gamma_4^{p4}$. Consider the eigenfunctions $\tilde{u}_\Gamma^{(2)}$ and $\tilde{u}_\Gamma^{(3)}$ in Fig. 4.5(a). Eigenfunction $\tilde{u}_\Gamma^{(2)}$ transforms to $-\tilde{u}_\Gamma^{(2)}$ under C_2 about the center of the unit cell. Eigenfunction $\tilde{u}_\Gamma^{(3)}$ transforms to $-\tilde{u}_\Gamma^{(3)}$ under C_2 about the center of the unit cell. Therefore, $\tilde{u}_\Gamma^{(2)}$ and $\tilde{u}_\Gamma^{(3)}$ correspond to irreps Γ_3^{p4} and Γ_4^{p4} in no particular order. This confirms that the 2-fold degeneracy between 2$^{\text{nd}}$ and 3$^{\text{rd}}$ band at Γ point of $p4mm$ corresponding to irrep Γ_5^{p4mm} (Fig. 4.4(a)) breaks into eigenfrequencies at Γ point of $p4$ corresponding to irrep Γ_3^{p4} and Γ_4^{p4} (Fig. 4.5(a)). From our discussion until now, since the eigenfunctions $\tilde{u}_\Gamma^{(2)}$ and $\tilde{u}_\Gamma^{(3)}$ correspond to different irreps, they should not be degenerate. But from the band structure in Fig. 4.5(a), we see that the bands 2 and 3 have the frequency at point Γ. This is not an accidental degeneracy; it is rooted in the fact that the characters of Γ_3 and Γ_4 are complex, and the Hamiltonian is time reversal symmetric. We will discuss this in the nex section (Sec 4.3).

M: Clearly, the point M with wave vector $\mathbf{k} = (\mathbf{K}_1 + \mathbf{K}_2)/2$ transforms to an equivalent point under the application of any element in the isogonal group $F = C_4$. Therefore, the little co-group of point M is $\bar{G}^M = C_4$. We can first find the irreps $\mathbf{D}^M$ of $\bar{G}^M = C_4$ (since $p4$ is symmorphic). Once we get that, the irreps of little group G^M are $\mathbf{\Gamma}^M(\{R|\mathbf{t}\}) = \exp(-i(\mathbf{K}_1/2 + \mathbf{K}_2/2)\cdot\mathbf{t})\mathbf{D}^M(R) = \exp(-i\pi(m+n))\mathbf{D}^M(R)$. The character table of point group C_4 is given in Table 4.13. From this character table of the little co-group $\bar{G}^M$, the characters of the matrices $\mathbf{\Gamma}^M$ of the little group G^M can be easily obtained, which we show in Table 4.15. Note that, again, there is no multidimensional irrep; but, the characters corresponding to irreps M_3 and M_4

Table 4.15: Characters of irrep matrices $\mathbf{\Gamma}^M$ of little group G^M of $p4$

	$\{\{E\|m\mathbf{t}_1+n\mathbf{t}_2\}\}$	$\{\{C_4\|\mathbf{0}\}\}$	$\{\{C_2\|\mathbf{0}\}\}$	$\{\{C_4^3\|\mathbf{0}\}\}$
M_1	$\exp(-i\pi(m+n))$	$+1$	$+1$	$+1$
M_2	$\exp(-i\pi(m+n))$	-1	$+1$	-1
M_3	$\exp(-i\pi(m+n))$	$+i$	-1	$-i$
M_4	$\exp(-i\pi(m+n))$	$-i$	-1	$+i$

are complex. Since $E^{C_{4v}}\big|_{C_4} = E_1^{C_4} \oplus E_2^{C_4}$, $M_5^{p4mm}\big|_{p4} = M_3^{p4} \oplus M_4^{p4}$. Consider the eigenfunctions $\tilde{u}_M^{(3)}$ and $\tilde{u}_M^{(3)}$ in Fig. 4.5(a). Eigenfunction $\tilde{u}_M^{(3)}$ transforms to $-\tilde{u}_M^{(3)}$ under C_2 about the center of the unit cell. Eigenfunction $\tilde{u}_M^{(4)}$ transforms to $-\tilde{u}_M^{(4)}$ under C_2 about the center of the unit cell. Therefore, $\tilde{u}_M^{(3)}$ and $\tilde{u}_M^{(4)}$ correspond to irreps M_3^{p4} and M_4^{p4} in no particular order. This confirms that the 2-fold degeneracy between 3$^{\text{nd}}$ and 4$^{\text{rd}}$ band at M point of $p4mm$ corresponding to irrep M_5^{p4mm} (Fig. 4.4(a)) breaks into eigenfrequencies at M point of $p4$ corresponding to irrep M_3^{p4} and M_4^{p4} (Fig. 4.5(a)). From our discussion until now, since the eigenfunctions $\tilde{u}_M^{(3)}$ and $\tilde{u}_M^{(4)}$ correspond to different irreps, they should not be degenerate. But from the band structure in Fig. 4.5(a), we see that the bands 3 and 4 have the frequency at point M. This is not an accidental degeneracy; it is rooted in the fact that the characters of M_3 and M_4 are complex, and the Hamiltonian is time reversal symmetric. We will discuss this in the nex section (Sec 4.3).

X: The point X with wave vector $\mathbf{k} = \mathbf{K}_1/2$ transform into an equivalent point under C_2 rotation. The little co-group is $\bar{G}^X = C_2 = \{E, C_2\}$. The characters of irrep matrices $\mathbf{D}^X$ of point group C_2 are given in Table 4.16. Then, using the relation

Table 4.16: Character table of C_2

	$\{E\}$	$\{C_2\}$
A	$+1$	$+1$
B	$+1$	-1

$\mathbf{\Gamma}^X(\{R|\mathbf{t}\}) = \exp(-i(\mathbf{K}_1/2)\cdot\mathbf{t})\mathbf{D}^X(R) = \exp(-im\pi)\mathbf{D}^X(R)$, where $\mathbf{t} = m\mathbf{t}_1 + n\mathbf{t}_2$ between irrep matrices $\mathbf{\Gamma}^X$ of little group G^X and irrep matrices $\mathbf{D}^X$ of little co-group

$\bar{G}^X$, the characters of irrep matrices $\mathbf{\Gamma}^X$ can be obtained and given in Table 4.17. Note

Table 4.17: Characters of irrep matrices $\mathbf{\Gamma}^X$ of little group G^X of $p4$

	$\{\{E\|m\mathbf{t}_1+n\mathbf{t}_2\}\}$	$\{\{C_2\|\mathbf{0}\}\}$
X_1	$\exp(-im\pi)$	$+1$
X_2	$\exp(-im\pi)$	-1

that there is no multidimensional irreps and all characters are real. Therefore, there should not be any degeneracies. Consider the eigenfunctions $\tilde{u}_X^{(3)}$ and $\tilde{u}_X^{(4)}$ shown in Fig. 4.5(a). The eigenfunction $\tilde{u}_X^{(3)}$ transform to $-\tilde{u}_X^{(3)}$ under C_2 rotation. Therefore, $\tilde{u}_X^{(3)}$ is the basis of 1 dimensional irrep X_2. The eigenfunction $\tilde{u}_X^{(4)}$ transform to $\tilde{u}_X^{(4)}$ under C_2 rotation. Therefore, $\tilde{u}_X^{(4)}$ is the basis of 1 dimensional irrep X_1.

Z: The little co-group Z points of $p4$ is trivial $\bar{G}^Z = \{E\}$ because no element of the isogonal group $F = C_4$ brings the wave vector to an equivalent point. Therefore, the irrep is trivial and 1 dimensional.

Table 4.18: Characters of irrep matrices $\mathbf{\Gamma}^Z$ of little group G^Z of $p4$

	$\{\{E\|m\mathbf{t}_1+n\mathbf{t}_2\}\}$
Z_1	$\exp(-i(m+2un)\pi)$

***p4gm*:** Starting from the $p4mm$ unit cell shown in Fig. 4.4(a) a counter clockwise rotation of all the ellipses, as we also did to break the mirrors and obtain $p4$ structure, by angle $\theta = \pi/4$ creates glide planes perpendicular to the fundamental lattice translations but shifted by a quarter of a unit cell from the center of a unit cell as well as mirror planes at angle $\pi/4$ with the fundamental lattice translations (see Fig. 4.1(l)). These are exactly the symmetry elements of space group $p4gm$. As was discussed before, this is a nonsymmorphic space group. However, the isogonal group of $p4gm$ is same as that of $p4mm$: $F = C_{4v}$. As such, finding the irreps of the little groups of

wave vectors at the edge of the Brillouin zone will be more involved as we will discuss below.

Γ: Since the wave vector $\mathbf{k} = \mathbf{0}$ remains invariant under every element of the isogonal group $F = C_{4v}$, the little co-group of the Γ point is $\bar{G}^{\Gamma} = C_{4v}$. Even though $p4gm$ is a nonsymmorphic group, since the point Γ is inside the Brillouin zone, according to our recipe, we can build the irrep matrices $\mathbf{D}^{\Gamma}$ of the little co-group $\bar{G}^{\Gamma}$ and then use the relation $\mathbf{\Gamma}^{\Gamma}(\{R|\mathbf{t}\}) = \exp(-i\mathbf{0}\cdot\mathbf{t})\mathbf{D}^{\Gamma}(R) = \mathbf{D}^{\Gamma}(R)$ between the irrep matrices $\mathbf{\Gamma}^{\Gamma}(\{R|\mathbf{t}\})$ of little group G^{Γ} and the irrep matrices $\mathbf{D}^{\Gamma}(R)$. To that end, the character table of $\bar{G}^{\Gamma} = C_{4v}$ is given in Table 4.4 and the characters of irrep matrices $\mathbf{\Gamma}^{\Gamma}$ are given in Table 4.19. Consider the eigenfunctions $\tilde{u}^{(3)}_{\Gamma}$ and $\tilde{u}^{(4)}_{\Gamma}$ in Fig. 4.5(b).

Table 4.19: Characters of irrep matrices $\mathbf{\Gamma}^{\Gamma}$ of little group G^{Γ} of $p4gm$. The Seitz notation $\{R|1/2, 1/2\}$ is the shorthand for $\{R|\mathbf{t}_1/2 + \mathbf{t}_2/2\}$

	$\{\{E\|m\mathbf{t}_1 + n\mathbf{t}_2\}\}$	$\{\{C_4\|\mathbf{0}\}, \{C_4^3\|\mathbf{0}\}\}$	$\{\{C_4^2\|\mathbf{0}\}\}$	$\{\{\sigma_{10}\|1/2, 1/2\}, \{\sigma_{01}\|1/2, 1/2\}\}$	$\{\{\sigma_{1\bar{1}}\|1/2, 1/2\}, \{\sigma_{11}\|1/2, 1/2\}\}$
Γ_1	+1	+1	+1	+1	+1
Γ_2	+1	+1	+1	−1	−1
Γ_3	+1	−1	+1	+1	−1
Γ_4	+1	−1	+1	−1	+1
Γ_5	+2	0	−2	0	0

Under lattice translations, they remain invariant. Under π rotation about the center of the unit cell, they become $-\tilde{u}^{(3)}_{\Gamma}$ and $-\tilde{u}^{(4)}_{\Gamma}$. Under $\pi/2$ rotation, though, $\tilde{u}^{(3)}_{\Gamma}$ and $\tilde{u}^{(4)}_{\Gamma}$ transform to $-\tilde{u}^{(4)}_{\Gamma}$ and $\tilde{u}^{(3)}_{\Gamma}$, respectively. Under mirror $\{\sigma_{10}|\mathbf{t}_1/2+\mathbf{t}_2/2\}$, $\tilde{u}^{(3)}_{\Gamma}$ and $\tilde{u}^{(4)}_{\Gamma}$ transform to $-\tilde{u}^{(3)}_{\Gamma}$ and $\tilde{u}^{(4)}_{\Gamma}$, respectively. Under mirror $\{\sigma_{01}|\mathbf{t}_1/2+\mathbf{t}_2/2\}$, $\tilde{u}^{(3)}_{\Gamma}$ and $\tilde{u}^{(4)}_{\Gamma}$ transform to $\tilde{u}^{(3)}_{\Gamma}$ and $-\tilde{u}^{(4)}_{\Gamma}$, respectively. Under mirror $\{\sigma_{1\bar{1}}|\mathbf{t}_1/2+\mathbf{t}_2/2\}$, $\tilde{u}^{(3)}_{\Gamma}$ and $\tilde{u}^{(4)}_{\Gamma}$ transform to $-\tilde{u}^{(4)}_{\Gamma}$ and $-\tilde{u}^{(3)}_{\Gamma}$, respectively. Lastly, under mirror $\{\sigma_{11}|\mathbf{t}_1/2+\mathbf{t}_2/2\}$, $\tilde{u}^{(3)}_{\Gamma}$ and $\tilde{u}^{(4)}_{\Gamma}$ transform to $-\tilde{u}^{(4)}_{\Gamma}$ and $\tilde{u}^{(3)}_{\Gamma}$, respectively. Therefore, $\tilde{u}^{(3)}_{\Gamma}$ and $\tilde{u}^{(4)}_{\Gamma}$ form

a representation of G^{Γ} with matrices:

$$\mathbf{\Gamma}^{\Gamma}(\{E|m\mathbf{t}_1+n\mathbf{t}_2\})=\begin{pmatrix}1&0\\0&1\end{pmatrix},\mathbf{\Gamma}^{\Gamma}(\{C_4|\mathbf{0}\})=\begin{pmatrix}0&1\\-1&0\end{pmatrix},\mathbf{\Gamma}^{\Gamma}(\{C_4^3|\mathbf{0}\})=\begin{pmatrix}0&-1\\1&0\end{pmatrix},$$
$$\mathbf{\Gamma}^{\Gamma}(\{C_4^2|\mathbf{0}\})=\begin{pmatrix}-1&0\\0&-1\end{pmatrix},\mathbf{\Gamma}^{\Gamma}(\{\sigma_{10}|\mathbf{t}_1/2+\mathbf{t}_2/2\})=\begin{pmatrix}-1&0\\0&1\end{pmatrix},$$
$$\mathbf{\Gamma}^{\Gamma}(\{\sigma_{01}|\mathbf{t}_1/2+\mathbf{t}_2/2\})=\begin{pmatrix}1&0\\0&-1\end{pmatrix},\mathbf{\Gamma}^{\Gamma}(\{\sigma_{1\bar{1}}|\mathbf{t}_1/2+\mathbf{t}_2/2\})=\begin{pmatrix}0&-1\\-1&0\end{pmatrix},$$
$$\mathbf{\Gamma}^{\Gamma}(\{\sigma_{11}|\mathbf{t}_1/2+\mathbf{t}_2/2\})=\begin{pmatrix}0&1\\-1&0\end{pmatrix}. \tag{4.14}$$

The traces of these matrices reveal that this corresponds to irrep Γ_5, which is 2 dimensional. That is why we see that $\tilde{u}_{\Gamma}^{(3)}$ and $\tilde{u}_{\Gamma}^{(4)}$ have the same eigenfrequency (Fig. 4.5)(b).

M: Since any element of C_{4v} brings the wave vector $\mathbf{k}=(\mathbf{K}_1+\mathbf{K}_2)/2$, where $\mathbf{K}_1$ and $\mathbf{K}_2$ are the fundamental reciprocal lattice vectors, to an equivalent wave vector, the little co-group of the M point is also $\bar{G}^M=C_{4v}$. The M point is a vertex of Brillouin zone. Since $p4gm$ is a nonsymmorphic group, the matrices $\mathbf{D}^M$ form projective representations of the little co-group C_{4v}. To this end we first build the little group $G^M=\{E|\mathbf{0}\}T+\{C_4|\mathbf{0}\}T+\{C_2|\mathbf{0}\}T+\{C_4^3|\mathbf{0}\}T+\{\sigma_{10}|\mathbf{t}_1/2+\mathbf{t}_2/2\}T+\{\sigma_{01}|\mathbf{t}_1/2+\mathbf{t}_2/2\}T+\{\sigma_{1\bar{1}}|\mathbf{t}_1/2+\mathbf{t}_2/2\}T+\{\sigma_{11}|\mathbf{t}_1/2+\mathbf{t}_2/2\}T$ fixing the coset representative as those shown. The factor group G^M/T is $G^M/T=\{\{E|\mathbf{0}\},\{C_4|\mathbf{0}\},\{C_2|\mathbf{0}\},\{C_4^3|\mathbf{0}\},\{\sigma_{10}|\mathbf{t}_1/2+\mathbf{t}_2/2\},\{\sigma_{01}|\mathbf{t}_1/2+\mathbf{t}_2/2\},\{\sigma_{1bar1}|\mathbf{t}_1/2+\mathbf{t}_2/2\},\{\sigma_{11}|\mathbf{t}_1/2+\mathbf{t}_2/2\}\}\cong C_{4v}$. According to recipe laid out earlier, we find the factor system $\mu=\exp(-i\mathbf{g}_i\cdot\mathbf{w}_j)$ first. Clearly, $\mu(E,S)=\mu(S,E)=1$ for

any $S \in \bar{G}^M$. Also, for any element of the form $\{S_0|\mathbf{0}\} \in G^M/T$, $\mu(S, S_0) = 1$ for any element $S \in \bar{G}^M$. This means $\mu(C_4, C_4) = \mu(C_2, C_4) = \mu(C_4^3, C_4) = \mu(\sigma_{10}, C_4) = \mu(\sigma_{01}, C_4) = \mu(\sigma_{1\bar{1}}, C_4) = \mu(\sigma_{11}, C_4) = \mu(C_4, C_2) = \mu(C_2, C_2) = \mu(C_4^3, C_2) = \mu(\sigma_{10}, C_2) = \mu(\sigma_{01}, C_2) = \mu(\sigma_{1\bar{1}}, C_2) = \mu(\sigma_{11}, C_2) = \mu(C_4, C_4^3) = \mu(C_2, C_4^3) = \mu(C_4^3, C_4^3) = \mu(\sigma_{10}, C_4^3) = \mu(\sigma_{01}, C_4^3) = \mu(\sigma_{1\bar{1}}, C_4^3) = \mu(\sigma_{11}, C_4^3) = 1$. Moreover, since the point M remains under mirror $\sigma_{1\bar{1}}$, the wave vector $\mathbf{g}_i = \mathbf{0}$ for $\sigma_{1\bar{1}}$. As a consequence, $\mu(\sigma_{1\bar{1}}, S) = 1$ for any $S \in \bar{G}^M$. Furthermore, since the wave vector $(\mathbf{K}_1 + \mathbf{K}_2)/2$ corresponding to point M goes to $-(\mathbf{K}_1 + \mathbf{K}_2)/2$ under C_2 and σ_{11}, the wave vector $\mathbf{g}_i$ corresponding to these two elements is $\mathbf{g}_i = \mathbf{K}_1 + \mathbf{K}_2$. However, since the translation part of any element in G^M/T with nontrivial translation is $\mathbf{w}_j = (\mathbf{t}_1 + \mathbf{t}_2)/2$, $\mathbf{g}_i \cdot \mathbf{w}_j = 2\pi(1/2 + 1/2) = 2\pi$. This implies that for any $S_0 \in \{\sigma_{11}, C_2\}$ and any $S \in \bar{G}^M$, $\mu(S_0, S) = 1$. The only nontrivial values of the factor system are $\mu(C_4, \sigma_{10}) = \mu(C_4, \sigma_{01}) = \mu(C_4, \sigma_{1\bar{1}}) = \mu(C_4, \sigma_{11}) = \exp(i\mathbf{K}_1 \cdot (\mathbf{t}_1 + \mathbf{t}_2)/2) = \exp(i\pi) = -1$, $\mu(C_4^3, \sigma_{10}) = \mu(C_4^3, \sigma_{01}) = \mu(C_4^3, \sigma_{1\bar{1}}) = \mu(C_4^3, \sigma_{11}) = \exp(i\mathbf{K}_2 \cdot (\mathbf{t}_1 + \mathbf{t}_2)/2) = \exp(-i\pi) = -1$, $\mu(\sigma_{10}, \sigma_{10}) = \mu(\sigma_{10}, \sigma_{01}) = \mu(\sigma_{10}, \sigma_{1\bar{1}}) = \mu(\sigma_{10}, \sigma_{11}) = \exp(i\mathbf{K}_1 \cdot (\mathbf{t}_1 + \mathbf{t}_2)/2) = \exp(i\pi) = -1$, $\mu(\sigma_{01}, \sigma_{10}) = \mu(\sigma_{01}, \sigma_{01}) = \mu(\sigma_{01}, \sigma_{1\bar{1}}) = \mu(\sigma_{01}, \sigma_{11}) = \exp(i\mathbf{K}_2 \cdot (\mathbf{t}_1 + \mathbf{t}_2)/2) = \exp(i\pi) = -1$. Therefore, for any $S_i, S_j \in \bar{G}^M$, the factor system can be written as $\mu(S_i, S_j) = \exp(2\pi i a(S_i, S_j)/n)$ with $n = 2$ and $a(S_i, S_j) = 0$ when $\mu(S_i, S_j) = 1$ and $a(S_i, S_j) = 1$ when $\mu(S_i, S_j) = -1$. Now we can form the group $\bar{G}_*^M$ with elements (S_i, α) with $S_i \in \bar{G}^M$ and $\alpha \in \mathbb{Z}_2$ with multiplication rule $(S_i, \alpha)(S_j, \beta) = (S_i, S_j, (\alpha + \beta + a(S_i, S_j)) \mod 2)$. For completeness, we give the multiplication table of the group $\bar{G}_*^M$ is given in Table 4.29. From the table it is clear that $(C_4, 0)^4 = (C_4, 1)^4 = (C_4^3, 0)^4 = (C_4^3, 1)^4 = (\sigma_{10}, 0)^4 = (\sigma_{10}, 1)^4 = (\sigma_{01}, 0)^4 = (\sigma_{01}, 1)^4 = (E, 1)^2 = (C_2, 0)^2 = (C_2, 1)^2 = (\sigma_{1\bar{1}}, 0)^2 = (\sigma_{1\bar{1}}, 1)^2 = (\sigma_{11}, 0)^2 = (\sigma_{11}, 1)^2 = (E, 0)$. Denoting $(C_4, 0) = P$, $(C_2, 1) = Q$ and $(\sigma_{1\bar{1}}, 0) = R$, we see that $P^4 = Q^2 = R^2 = (E, 0)$, the identity element. All the

other elements of $\bar{G}^M_*$ can be generated from these three elements. Moreover, these three elements satisfy the following identities: $PQ = (C_4, 0)(C_2, 1) = (C_4^3, 1) = (C_2, 1)(C_4, 0) = QP$, $QR = (C_2, 1)(\sigma_{1\bar{1}}, 0) = (\sigma_{11}, 1) = (\sigma_{1\bar{1}}, 0)(C_2, 1) = RQ$, $PQR = (C_4, 0)(C_2, 1)(\sigma_{1\bar{1}}, 0) = (C_4^3, 1)(\sigma_{1\bar{1}}, 0) = (\sigma_{01}, 0) = (\sigma_{1\bar{1}}, 0)(C_4, 0) = RP$. This is the abstract group $G_1 6^{10}$ and its character table is given in Table 4.30 (see [68], page 234). Among these irreps only the ones with irrep matrices $\mathbf{\Gamma}^M_{\rho*}((E, 1)) = -\mathbb{1}$ will be accepted. This means only R_5, R_6, R_7, R_8 and R_9 correspond to the projective representations of $\bar{G}^M$. Hence, the character table of the projective reps of $\bar{G}^M$ is given in Table 4.20. Now, using the relation $\mathbf{\Gamma}^M(\{R|\mathbf{v}\}) = \exp(-i(\mathbf{K}_1/2+\mathbf{K}_2/2)\cdot\mathbf{v})\mathbf{D}^M(R)$,

Table 4.20: Character table of projective reps of $\bar{G}^M$ of $p4gm$.

	$\{E\}$	$\{C_2\}$	$\{\sigma_{1\bar{1}}\}$	$\{\sigma_{11}\}$	$\{C_4\}$	$\{C_4^3\}$	$\{\sigma_{01}\}$	$\{\sigma_{10}\}$
R_5	$+1$	-1	$+1$	-1	$+i$	$-i$	$+i$	$-i$
R_6	$+1$	-1	$+1$	-1	$-i$	$+i$	$-i$	$+i$
R_7	$+1$	-1	-1	$+1$	$-i$	$+i$	$+i$	$-i$
R_8	$+1$	-1	-1	$+1$	$+i$	$-i$	$-i$	$+i$
R_9	$+2$	$+2$	0	0	0	0	0	0

we can find the characters of the irrep matrices $\mathbf{\Gamma}^M$ of little group G^M; they are given in Table 4.21.

Table 4.21: Character table of irreps of G^M of $p4gm$. The Seitz notation $\{R|1/2, 1/2\}$ is the shorthand for $\{R|\mathbf{t}_1/2 + \mathbf{t}_2/2\}$

	$\{E\|m\mathbf{t}_1 + n\mathbf{t}_2\}$	$\{C_2\|\mathbf{0}\}$	$\{\sigma_{1\bar{1}}\|1/2, 1/2\}$	$\{\sigma_{11}\|1/2, 1/2\}$	$\{C_4\|\mathbf{0}\}$	$\{C_4^3\|\mathbf{0}\}$	$\{\sigma_{01}\|1/2, 1/2\}$	$\{\sigma_{10}\|1/2, 1/2\}$
M_1	$\exp(-i\pi(m+n))$	-1	-1	$+1$	$+i$	$-i$	$-i$	$+i$
M_2	$\exp(-i\pi(m+n))$	-1	-1	$+1$	$-i$	$+i$	$+i$	$-i$
M_3	$\exp(-i\pi(m+n))$	-1	$+1$	-1	$-i$	$+i$	$-i$	$+i$
M_4	$\exp(-i\pi(m+n))$	-1	$+1$	-1	$+i$	$-i$	$+i$	$-i$
M_5	$2\exp(-i\pi(m+n))$	$+2$	0	0	0	0	0	0

Consider the eigenfunction $\tilde{u}^{(3)}_M$ shown in Fig. 4.5(b). It transforms to $-\tilde{u}^{(3)}_\Gamma$, $-\tilde{u}^{(3)}_\Gamma$ and $\tilde{u}^{(3)}_\Gamma$ under $\{C_2|\mathbf{0}\}$, $\{\sigma_{1\bar{1}}|(\mathbf{t}_1 + \mathbf{t}_2)/2\}$ and $\{\sigma_{11}|(\mathbf{t}_1 + \mathbf{t}_2)/2\}$ respectively. On the other hand, the eigenfunction $\tilde{u}^{(4)}_M$, shown in Fig. 4.5(b), transforms to $-\tilde{u}^{(4)}_\Gamma$, $-\tilde{u}^{(4)}_\Gamma$ and $\tilde{u}^{(4)}_\Gamma$ under $\{C_2|\mathbf{0}\}$, $\{\sigma_{1\bar{1}}|(\mathbf{t}_1+\mathbf{t}_2)/2\}$ and $\{\sigma_{11}|(\mathbf{t}_1+\mathbf{t}_2)/2\}$ respectively. Then, $\tilde{u}^{(3)}_M$ and $\tilde{u}^{(4)}_M$ can correspond to irrep M_1 or M_2. From Table 4.15, we see that M_1 and M_2 are 1 dimensional. However, the band 3 and 4 are degenerate at point M. In fact, all

bands in the band structure of Fig. 4.5(b) are doubly degenerate at M. This is due to time reversal symmetry which we will discuss in the next section.

X: Since any element of $C_{2v} = E, C_2, \sigma_{10}, \sigma_{01}$ brings the wave vector $\mathbf{k} = \mathbf{K}_1/2$ to an equivalent wave vector, the little co-group of the X point is also $\bar{G}^X = C_{2v}$. The X point is at the edge of Brillouin zone. Since $p4gm$ is a nonsymmorphic group, the matrices $\mathbf{D}^X$ form projective representations of the little co-group C_{2v}. To this end we first build the little group $G^X = \{E|\mathbf{0}\}T + \{C_2|\mathbf{0}\}T + \{\sigma_{10}|\mathbf{t}_1/2 + \mathbf{t}_2/2\}T + \{\sigma_{01}|\mathbf{t}_1/2 + \mathbf{t}_2/2\}T$ fixing the coset representative as those shown. The factor group G^X/T is $G^X/T = \{\{E|\mathbf{0}\}, \{C_2|\mathbf{0}\}, \{\sigma_{10}|\mathbf{t}_1/2 + \mathbf{t}_2/2\}, \{\sigma_{01}|\mathbf{t}_1/2 + \mathbf{t}_2/2\} \cong C_{2v}$. According to recipe laid out earlier, we find the factor system $\mu = \exp(-i\mathbf{g}_i \cdot \mathbf{w}_j)$ first. Clearly, $\mu(E, S) = \mu(S, E) = 1$ for any $S \in \bar{G}^X$. Also, for any element of the form $\{S_0|\mathbf{0}\} \in G^X/T$, $\mu(S, S_0) = 1$ for any element $S \in \bar{G}^X$. This means $\mu(C_2, C_2) = \mu(\sigma_{10}, C_2) = \mu(\sigma_{01}, C_2) = 1$. Moreover, since the point X remains under mirror σ_{01}, the wave vector $\mathbf{g}_i = \mathbf{0}$ for σ_{01}. As a consequence, $\mu(\sigma_{01}, S) = 1$ for any $S \in \bar{G}^M$. The only nontrivial values of the factor system are $\mu(C_2, \sigma_{10}) = \mu(C_2, \sigma_{01}) = \exp(i\mathbf{K}_1 \cdot (\mathbf{t}_1 + \mathbf{t}_2)/2) = \exp(i\pi) = -1$, $\mu(\sigma_{10}, \sigma_{10}) = \mu(\sigma_{10}, \sigma_{01}) = \exp(i\mathbf{K}_1 \cdot (\mathbf{t}_1 + \mathbf{t}_2)/2) = \exp(i\pi) = -1$. Therefore, for any $S_i, S_j \in \bar{G}^X$, the factor system can be written as $\mu(S_i, S_j) = \exp(2\pi i a(S_i, S_j)/n)$ with $n = 2$ and $a(S_i, S_j) = 0$ when $\mu(S_i, S_j) = 1$ and $a(S_i, S_j) = 1$ when $\mu(S_i, S_j) = -1$. Now we can form the group $\bar{G}^X_*$ with elements (S_i, α) with $S_i \in \bar{G}^X$ and $\alpha \in \mathbb{Z}_2$ with multiplication rule $(S_i, \alpha)(S_j, \beta) = (S_i, S_j, (\alpha + \beta + a(S_i, S_j)) \mod 2)$. For completeness, we give the multiplication table of the group $\bar{G}^X_*$ is given in Table 4.22. We see that $(\sigma_{10}, 0)^4 = (\sigma_{10}, 1)^4 = (\sigma_{01}, 0)^2 = (\sigma_{01}, 1)^2 = (C_2, 0)^2 = (C_2, 1)^2 = (E, 1)^2 = (E, 0)$, the identity element. Denoting $(\sigma_{10}, 0) = P$ and $(C_2, 1) = Q$, we find the following identity: $QP = (C_2, 1)(\sigma_{10}, 0) = (\sigma_{01}, 0) = (\sigma_{10}, 1)(C_2, 1) = (\sigma_{10}, 0)^3(C_2, 1) = P^3Q$. This is the abstract group G^4_8 (isomorphic to C_{4v} if we identify $C_4 \cong (\sigma_{10}, 0)$ and $\sigma_{10} \cong (C_2, 1)$), and the character

Table 4.22: Multiplication table of $\bar{G}^X_*$ of group $p4gm$

	$(E,0)$	$(E,1)$	$(C_2,0)$	$(C_2,1)$	$(\sigma_{10},0)$	$(\sigma_{10},1)$	$(\sigma_{01},0)$	$(\sigma_{01},1)$
(E,0)	$(E,0)$	$(E,1)$	$(C_2,0)$	$(C_2,1)$	$(\sigma_{10},0)$	$(\sigma_{10},1)$	$(\sigma_{01},0)$	$(\sigma_{01},1)$
$(E,1)$	$(E,1)$	$(E,0)$	$(C_2,1)$	$(C_2,0)$	$(\sigma_{10},1)$	$(\sigma_{10},0)$	$(\sigma_{01},1)$	$(\sigma_{01},0)$
$(C_2,0)$	$(C_2,0)$	$(C_2,1)$	$(E,0)$	$(E,1)$	$(\sigma_{01},1)$	$(\sigma_{01},0)$	$(\sigma_{10},1)$	$(\sigma_{10},0)$
$(C_2,1)$	$(C_2,1)$	$(C_2,0)$	$(E,1)$	$(E,0)$	$(\sigma_{01},0)$	$(\sigma_{01},1)$	$(\sigma_{10},0)$	$(\sigma_{10},1)$
$(\sigma_{10},0)$	$(\sigma_{10},0)$	$(\sigma_{10},1)$	$(\sigma_{01},0)$	$(\sigma_{01},1)$	$(E,1)$	$(E,0)$	$(C_2,1)$	$(C_2,0)$
$(\sigma_{10},1)$	$(\sigma_{10},1)$	$(\sigma_{10},0)$	$(\sigma_{01},1)$	$(\sigma_{01},0)$	$(E,0)$	$(E,1)$	$(C_2,0)$	$(C_2,1)$
$(\sigma_{01},0)$	$(\sigma_{01},0)$	$(\sigma_{01},1)$	$(\sigma_{10},0)$	$(\sigma_{10},1)$	$(C_2,0)$	$(C_2,1)$	$(E,0)$	$(E,1)$
$(\sigma_{01},1)$	$(\sigma_{01},1)$	$(\sigma_{01},0)$	$(\sigma_{10},1)$	$(\sigma_{10},0)$	$(C_2,1)$	$(C_2,0)$	$(E,1)$	$(E,0)$

table for this group is given in Table 4.23. We only consider the irrep of $\bar{G}^X_*$ that

Table 4.23: Character table of G^4_8

	$\{(E,0)\}$	$\{(E,1)\}$	$\{(\sigma_{10},0),(\sigma_{10},1)\}$	$\{(C_2,0),(C_2,1)\}$	$\{\sigma_{01},0),(\sigma_{01},1)\}$
R_1	$+1$	$+1$	$+1$	$+1$	$+1$
R_2	$+1$	$+1$	$+1$	-1	-1
R_3	$+1$	$+1$	-1	$+1$	-1
R_4	$+1$	$+1$	-1	-1	$+1$
R_5	$+2$	-2	0	0	0

has the property $\mathbf{\Gamma}^X_{\rho*}((E,1)) = -\mathbb{1}$. That is only satisfied by R_5. Therefore, the characters of the only projective irrep of $\bar{G}^X$ are given in Table 4.24. Now, using the

Table 4.24: Character table of projective reps of $\bar{G}^X$ of $p4gm$

	$\{E\}$	$\{\sigma_{10}\}$	$\{C_2\}$	$\{\sigma_{01}\}$
R_5	$+2$	0	0	0

relation $\mathbf{\Gamma}^X(\{R|\mathbf{v}\}) = \exp(-i(\mathbf{K}_1/2)\cdot\mathbf{v})\mathbf{D}^X(R)$, we can find the characters of the irrep matrices $\mathbf{\Gamma}^X$ of little group G^X; they are given in Table 4.25.

Table 4.25: Character table of irreps of G^X of $p4gm$

	$\{E\|m\mathbf{t}_1+n\mathbf{t}_2\}$	$\{\sigma_{10}\|(\mathbf{t}_1+\mathbf{t}_2)/2\}$	$\{C_2\|\mathbf{0}\}$	$\{\sigma_{01}\|(\mathbf{t}_1+\mathbf{t}_2)/2\}$
X_1	$+2\exp(-im\pi)$	0	0	0

Consider the eigenfunctions $\tilde{u}^{(3)}_\Gamma$ and $\tilde{u}^{(4)}_\Gamma$ in Fig. 4.5(b). Under lattice translations in the vertical direction, they remain invariant. Under fundamental lattice translation in the horizontal direction, they become $-\tilde{u}^{(3)}_\Gamma$ and $-\tilde{u}^{(4)}_\Gamma$ respectively. Under π

rotation about the center of the unit cell, they become $-\tilde{u}_\Gamma^{(3)}$ and $\tilde{u}_\Gamma^{(4)}$. Under operation $\{\sigma_{10}|\mathbf{t}_1/2+\mathbf{t}_2/2\}$, $\tilde{u}_\Gamma^{(3)}$ and $\tilde{u}_\Gamma^{(4)}$ transform to $\tilde{u}_\Gamma^{(4)}$ and $\tilde{u}_\Gamma^{(3)}$, respectively. Under operation $\{\sigma_{01}|\mathbf{t}_1/2+\mathbf{t}_2/2\}$, $\tilde{u}_\Gamma^{(3)}$ and $\tilde{u}_\Gamma^{(4)}$ transform to $\tilde{u}_\Gamma^{(4)}$ and $-\tilde{u}_\Gamma^{(3)}$, respectively. Therefore, $\tilde{u}_\Gamma^{(3)}$ and $\tilde{u}_\Gamma^{(4)}$ form a representation of G^Γ with matrices:

$$\mathbf{\Gamma}^\Gamma(\{E|m\mathbf{t}_1+n\mathbf{t}_2\})=\begin{pmatrix}\exp(-im\pi) & 0\\ 0 & \exp(-im\pi)\end{pmatrix},\mathbf{\Gamma}^\Gamma(\{C_2|\mathbf{0}\})=\begin{pmatrix}-1 & 0\\ 0 & 1\end{pmatrix},$$
$$\mathbf{\Gamma}^\Gamma(\{\sigma_{10}|\mathbf{t}_1/2+\mathbf{t}_2/2\})=\begin{pmatrix}0 & 1\\ 1 & 0\end{pmatrix},\mathbf{\Gamma}^\Gamma(\{\sigma_{01}|\mathbf{t}_1/2+\mathbf{t}_2/2\})=\begin{pmatrix}0 & -1\\ 1 & 0\end{pmatrix}. \tag{4.15}$$

The traces of these matrices reveal that this corresponds to irrep X_1, which is 2 dimensional. That is why we see that $\tilde{u}_\Gamma^{(3)}$ and $\tilde{u}_\Gamma^{(4)}$ have the same eigenfrequency (Fig. 4.5)(b).

Z: Since any element of $C_{1v}=E,\sigma_{10}$ brings the wave vector $\mathbf{k}=\mathbf{K}_1/2+u\mathbf{K}_2$ ($0<u<1/2$) to an equivalent wave vector, the little co-group of the Z point is $\bar{G}^Z=C_{1v}$. The Z point is at the edge of Brillouin zone. Since $p4gm$ is a nonsymmorphic group, the matrices $\mathbf{D}^Z$ form projective representations of the little co-group C_{1v}. To this end we first build the little group $G^X=\{E|\mathbf{0}\}T+\{\sigma_{10}|\mathbf{t}_1/2+\mathbf{t}_2/2\}T$ fixing the coset representative as those shown. The factor group G^Z/T is $G^Z/T=\{\{E|\mathbf{0}\},\{\sigma_{10}|\mathbf{t}_1/2+\mathbf{t}_2/2\}\cong C_{1v}$. According to recipe laid out earlier, we find the factor system $\mu=\exp(-i\mathbf{g}_i\cdot\mathbf{w}_j)$ first. Clearly, $\mu(E,S)=\mu(S,E)=1$ for any $S\in\bar{G}^Z$. The only nontrivial values of the factor system are $\mu(\sigma_{10},\sigma_{10})=\exp(i\mathbf{K}_1\cdot(\mathbf{t}_1+\mathbf{t}_2)/2)=\exp(i\pi)=-1$. Therefore, for any $S_i,S_j\in\bar{G}^Z$, the factor system can be written as $\mu(S_i,S_j)=\exp(2\pi i a(S_i,S_j)/n)$ with $n=2$ and $a(S_i,S_j)=0$ when $\mu(S_i,S_j)=1$ and $a(S_i,S_j)=1$ when $\mu(S_i,S_j)=-1$. Now we can form the group $\bar{G}_*^Z$ with elements (S_i,α) with $S_i\in\bar{G}^Z$ and $\alpha\in\mathbb{Z}_2$ with multiplication rule $(S_i,\alpha)(S_j,\beta)=(S_i,S_j,(\alpha+$

$\beta+a(S_i,S_j))\mod 2$). For completeness, we give the multiplication table of the group $\bar{G}^Z_*$ is given in Table 4.26. We see that $(\sigma_{10},0)^4=(\sigma_{10},1)^4=(E,1)^2=(E,0)$, the

Table 4.26: Multiplication table of $\bar{G}^Z_*$ of group $p4gm$

	$(E,0)$	$(E,1)$	$(\sigma_{10},0)$	$(\sigma_{10},1)$
(E,0)	$(E,0)$	$(E,1)$	$(\sigma_{10},0)$	$(\sigma_{10},1)$
$(E,1)$	$(E,1)$	$(E,0)$	$(\sigma_{10},1)$	$(\sigma_{10},0)$
$(\sigma_{10},0)$	$(\sigma_{10},0)$	$(\sigma_{10},1)$	$(E,1)$	$(E,0)$
$(\sigma_{10},1)$	$(\sigma_{10},1)$	$(\sigma_{10},0)$	$(E,0)$	$(E,1)$

identity element. Denoting $(\sigma_{10},0)=P$, $(E,1)=P^2$ and $(\sigma_{10},1)=P^3$ meaning this group is isomorphic to C_4 if we identify $(\sigma_{10},0)=C_4$, $(E,1)=C_2$, $(\sigma_{10},1)=C_4^3$, and the character table for this group is given in Table 4.13. We only consider the irrep of $\bar{G}^Z_*$ that has the property $\mathbf{\Gamma}^Z_{\rho*}((E,1))=-\mathbb{1}$. That is only satisfied by E_1 and E_2. Therefore, the characters of the only projective irrep of $\bar{G}^Z$ are given in Table 4.27. Now, using the relation $\mathbf{\Gamma}^Z(\{R|\mathbf{v}\})=\exp(-i(\mathbf{K}_1/2+u\mathbf{K}_2)\cdot\mathbf{v})\mathbf{D}^Z(R)$, we can find the

Table 4.27: Character table of projective reps of $\bar{G}^Z$ of $p4gm$

	$\{E\}$	$\{\sigma_{10}\}$
E_1	$+1$	$+i$
E_2	$+1$	$-i$

characters of the irrep matrices $\mathbf{\Gamma}^Z$ of little group G^Z; they are given in Table 4.28.

Table 4.28: Character table of irreps of G^Z of $p4gm$

	$\{E\|m\mathbf{t}_1+n\mathbf{t}_2\}$	$\{\sigma_{10}\|(\mathbf{t}_1+\mathbf{t}_2)/2\}$
Z_1	$\exp(-i\pi(m+2un))$	$\exp(-iu\pi)$
Z_2	$\exp(-i\pi(m+2un))$	$-\exp(-iu\pi)$

Again, the irreps of the little group G^Z are 1 dimensional, whereas all bands in the band structure shown in Fig. 4.5(b) are doubly degenerate at points Z. This is again due to time reversal symmetry and will be explained in the next section.

Table 4.29: Multiplication table of $\bar{G}_*^M$ of group $p4gm$

	$(E,0)$	$(E,1)$	$(C_4,0)$	$(C_4,1)$	$(C_2,0)$	$(C_2,1)$	$(C_4^3,0)$	$(C_4^3,1)$	$(\sigma_{10},0)$	$(\sigma_{10},1)$	$(\sigma_{01},0)$	$(\sigma_{01},1)$	$(\sigma_{1\bar{1}},0)$	$(\sigma_{1\bar{1}},1)$	$(\sigma_{11},0)$	$(\sigma_{11},1)$
$(E,0)$	$(E,0)$	$(E,1)$	$(C_4,0)$	$(C_4,1)$	$(C_2,0)$	$(C_2,1)$	$(C_4^3,0)$	$(C_4^3,1)$	$(\sigma_{10},0)$	$(\sigma_{10},1)$	$(\sigma_{01},0)$	$(\sigma_{01},1)$	$(\sigma_{1\bar{1}},0)$	$(\sigma_{1\bar{1}},1)$	$(\sigma_{11},0)$	$(\sigma_{11},1)$
$(E,1)$	$(E,1)$	$(E,0)$	$(C_4,1)$	$(C_4,0)$	$(C_2,1)$	$(C_2,0)$	$(C_4^3,1)$	$(C_4^3,0)$	$(\sigma_{10},1)$	$(\sigma_{10},0)$	$(\sigma_{01},1)$	$(\sigma_{01},0)$	$(\sigma_{1\bar{1}},1)$	$(\sigma_{1\bar{1}},0)$	$(\sigma_{11},1)$	$(\sigma_{11},0)$
$(C_4,0)$	$(C_4,0)$	$(C_4,1)$	$(C_2,0)$	$(C_2,1)$	$(C_4^3,0)$	$(C_4^3,1)$	$(E,0)$	$(E,1)$	$(\sigma_{11},1)$	$(\sigma_{11},0)$	$(\sigma_{1\bar{1}},1)$	$(\sigma_{1\bar{1}},0)$	$(\sigma_{10},1)$	$(\sigma_{10},0)$	$(\sigma_{01},1)$	$(\sigma_{01},0)$
$(C_4,1)$	$(C_4,1)$	$(C_4,0)$	$(C_2,1)$	$(C_2,0)$	$(C_4^3,1)$	$(C_4^3,0)$	$(E,1)$	$(E,0)$	$(\sigma_{11},0)$	$(\sigma_{11},1)$	$(\sigma_{1\bar{1}},0)$	$(\sigma_{1\bar{1}},1)$	$(\sigma_{10},0)$	$(\sigma_{10},1)$	$(\sigma_{01},0)$	$(\sigma_{01},1)$
$(C_2,0)$	$(C_2,0)$	$(C_2,1)$	$(C_4^3,0)$	$(C_4^3,1)$	$(E,0)$	$(E,1)$	$(C_4,0)$	$(C_4,1)$	$(\sigma_{01},0)$	$(\sigma_{01},1)$	$(\sigma_{10},0)$	$(\sigma_{10},1)$	$(\sigma_{11},0)$	$(\sigma_{11},1)$	$(\sigma_{1\bar{1}},0)$	$(\sigma_{1\bar{1}},1)$
$(C_2,1)$	$(C_2,1)$	$(C_2,0)$	$(C_4^3,1)$	$(C_4^3,0)$	$(E,1)$	$(E,0)$	$(C_4,1)$	$(C_4,0)$	$(\sigma_{01},1)$	$(\sigma_{01},0)$	$(\sigma_{10},1)$	$(\sigma_{10},0)$	$(\sigma_{11},1)$	$(\sigma_{11},0)$	$(\sigma_{1\bar{1}},1)$	$(\sigma_{1\bar{1}},0)$
$(C_4^3,0)$	$(C_4^3,0)$	$(C_4^3,1)$	$(E,0)$	$(E,1)$	$(C_4,0)$	$(C_4,1)$	$(C_2,0)$	$(C_2,1)$	$(\sigma_{1\bar{1}},1)$	$(\sigma_{1\bar{1}},0)$	$(\sigma_{11},1)$	$(\sigma_{11},0)$	$(\sigma_{01},1)$	$(\sigma_{01},0)$	$(\sigma_{10},1)$	$(\sigma_{10},0)$
$(C_4^3,1)$	$(C_4^3,1)$	$(C_4^3,0)$	$(E,1)$	$(E,0)$	$(C_4,1)$	$(C_4,0)$	$(C_2,1)$	$(C_2,0)$	$(\sigma_{1\bar{1}},0)$	$(\sigma_{1\bar{1}},1)$	$(\sigma_{11},0)$	$(\sigma_{11},1)$	$(\sigma_{01},0)$	$(\sigma_{01},1)$	$(\sigma_{10},0)$	$(\sigma_{10},1)$
$(\sigma_{10},0)$	$(\sigma_{10},0)$	$(\sigma_{10},1)$	$(\sigma_{1\bar{1}},0)$	$(\sigma_{1\bar{1}},1)$	$(\sigma_{01},0)$	$(\sigma_{01},1)$	$(\sigma_{11},0)$	$(\sigma_{11},1)$	$(E,1)$	$(E,0)$	$(C_2,1)$	$(C_2,0)$	$(C_4,1)$	$(C_4,0)$	$(C_4^3,1)$	$(C_4^3,0)$
$(\sigma_{10},1)$	$(\sigma_{10},1)$	$(\sigma_{10},0)$	$(\sigma_{1\bar{1}},1)$	$(\sigma_{1\bar{1}},0)$	$(\sigma_{01},1)$	$(\sigma_{01},0)$	$(\sigma_{11},1)$	$(\sigma_{11},0)$	$(E,0)$	$(E,1)$	$(C_2,0)$	$(C_2,1)$	$(C_4,0)$	$(C_4,1)$	$(C_4^3,0)$	$(C_4^3,1)$
$(\sigma_{01},0)$	$(\sigma_{01},0)$	$(\sigma_{01},1)$	$(\sigma_{11},0)$	$(\sigma_{11},1)$	$(\sigma_{10},0)$	$(\sigma_{10},1)$	$(\sigma_{1\bar{1}},0)$	$(\sigma_{1\bar{1}},1)$	$(C_2,1)$	$(C_2,0)$	$(E,1)$	$(E,0)$	$(C_4^3,1)$	$(C_4^3,0)$	$(C_4,1)$	$(C_4,0)$
$(\sigma_{01},1)$	$(\sigma_{01},1)$	$(\sigma_{01},0)$	$(\sigma_{11},1)$	$(\sigma_{11},0)$	$(\sigma_{10},1)$	$(\sigma_{10},0)$	$(\sigma_{1\bar{1}},1)$	$(\sigma_{1\bar{1}},0)$	$(C_2,0)$	$(C_2,1)$	$(E,0)$	$(E,1)$	$(C_4^3,0)$	$(C_4^3,1)$	$(C_4,0)$	$(C_4,1)$
$(\sigma_{1\bar{1}},0)$	$(\sigma_{1\bar{1}},0)$	$(\sigma_{1\bar{1}},1)$	$(\sigma_{01},0)$	$(\sigma_{01},1)$	$(\sigma_{11},0)$	$(\sigma_{11},1)$	$(\sigma_{10},0)$	$(\sigma_{10},1)$	$(C_4^3,0)$	$(C_4^3,1)$	$(C_4,0)$	$(C_4,1)$	$(E,0)$	$(E,1)$	$(C_2,0)$	$(C_2,1)$
$(\sigma_{1\bar{1}},1)$	$(\sigma_{1\bar{1}},1)$	$(\sigma_{1\bar{1}},0)$	$(\sigma_{01},1)$	$(\sigma_{01},0)$	$(\sigma_{11},1)$	$(\sigma_{11},0)$	$(\sigma_{10},1)$	$(\sigma_{10},0)$	$(C_4^3,1)$	$(C_4^3,0)$	$(C_4,1)$	$(C_4,0)$	$(E,1)$	$(E,0)$	$(C_2,1)$	$(C_2,0)$
$(\sigma_{11},0)$	$(\sigma_{11},0)$	$(\sigma_{11},1)$	$(\sigma_{10},0)$	$(\sigma_{10},1)$	$(\sigma_{1\bar{1}},0)$	$(\sigma_{1\bar{1}},1)$	$(\sigma_{10},0)$	$(\sigma_{10},1)$	$(C_4,0)$	$(C_4,1)$	$(C_4^3,0)$	$(C_4^3,1)$	$(C_2,0)$	$(C_2,1)$	$(E,0)$	$(E,1)$
$(\sigma_{11},1)$	$(\sigma_{11},1)$	$(\sigma_{11},0)$	$(\sigma_{10},1)$	$(\sigma_{10},0)$	$(\sigma_{1\bar{1}},1)$	$(\sigma_{1\bar{1}},0)$	$(\sigma_{10},1)$	$(\sigma_{10},0)$	$(C_4,1)$	$(C_4,0)$	$(C_4^3,1)$	$(C_4^3,0)$	$(C_2,1)$	$(C_2,0)$	$(E,1)$	$(E,0)$

Table 4.30: Character table of G_{16}^{10}

	$\{(E,0)\}$	$\{(C_2,1)\}$	$\{(C_2,0)\}$	$\{(E,1)\}$	$\{(\sigma_{1\bar{1}},0),(\sigma_{11},1)\}$	$\{(\sigma_{11},0),(\sigma_{1\bar{1}},1)\}$	$\{(C_4,0),(C_4^3,1)\}$	$\{(C_4^3,0),(C_4,1)\}$	$\{\sigma_{10},1),(\sigma_{01},0)\}$	$\{\sigma_{01},1),(\sigma_{10},0)\}$
R_1	$+1$	$+1$	$+1$	$+1$	$+1$	$+1$	$+1$	$+1$	$+1$	$+1$
R_2	$+1$	$+1$	$+1$	$+1$	-1	-1	-1	-1	$+1$	$+1$
R_3	$+1$	$+1$	$+1$	$+1$	$+1$	$+1$	-1	-1	-1	-1
R_4	$+1$	$+1$	$+1$	$+1$	-1	-1	$+1$	$+1$	-1	-1
R_5	$+1$	$+1$	-1	-1	$+1$	-1	$+i$	$-i$	$+i$	$-i$
R_6	$+1$	$+1$	-1	-1	$+1$	-1	$-i$	$+i$	$-i$	$+i$
R_7	$+1$	$+1$	-1	-1	-1	$+1$	$-i$	$+i$	$+i$	$-i$
R_8	$+1$	$+1$	-1	-1	-1	$+1$	$+i$	$-i$	$-i$	$+i$
R_9	$+2$	-2	$+2$	-2	0	0	0	0	0	0
R_{10}	$+2$	-2	-2	$+2$	0	0	0	0	0	0

4.3 Time reversal symmetry, co-representations and associated degeneracies

There is another symmetry of Eq. 4.4 that we have not discussed yet. Let us define the complex conjugation operation Θ. When it acts on a complex number or a complex function, it gives the complex conjugate of them. Applying this operator on both sides of Eq. 4.4, we get $\Theta\hat{H}\tilde{u}_z = \Theta\boldsymbol{\nabla}\cdot\mu\boldsymbol{\nabla}\tilde{u}_z = \boldsymbol{\nabla}\cdot\mu\boldsymbol{\nabla}\tilde{u}_z^* = \boldsymbol{\nabla}\cdot\mu\boldsymbol{\nabla}\Theta\tilde{u}_z = -\Theta\rho\omega^2\tilde{u}_z = -\rho\omega^2\tilde{u}_z^* = -\rho\omega^2\Theta\tilde{u}_z$, where we assumed the fact that material properties μ, ρ are real and positive (which also implies $\omega^2 > 0$ as shown in Eq. 4.5). This means that the modified Hamiltonian $\tilde{H} = \frac{1}{\rho}\hat{H}$ commutes with operator Θ: $[\tilde{H}, \Theta] = 0$. From the discussion on the definition of a symmetry in Section 4.2.2, we know then that Θ is a symmetry of the Hamiltonian. This symmetry is called time reversal symmetry due to mainly quantum mechanical reasons [144]. Time reversal operator is clearly an antilinear operator because $\Theta(c_1 f_1(\mathbf{x}) + c_2 f_2(\mathbf{x})) = c_1^*\Theta f_1(\mathbf{x}) + c_2^*\Theta f_2(\mathbf{x})$. It is also an antiunitary operator: $\langle(\Theta f_1)|(\Theta f_2)\rangle = \int dx\, dy\, \rho(\Theta f_1)^*(\Theta f_2) = \int dx\, dy\, \rho(f_1^*)^* f_2^* = \int dx\, dy\, \rho\, f_1 f_2^* = \langle f_1|f_2\rangle^* = \langle f_2|f_1\rangle$. Note that $\Theta^2 = \mathbb{1}$ and it is a local operator; it commutes any spatial operator.

In the following we discuss how addition of this symmetry to the space group symmetries affect the representations of the group elements and thus the degeneracies in the frequency bands (for a thorough discussion, see [145, 68, 146]).

4.3.1 Magnetic groups and co-representations

The addition of operator Θ to the spatial symmetry group G enlarges the symmetry group of the Hamiltonian. This enlarged group is called *magnetic group* M. There are three kinds of magnetic groups. The magnetic groups of *first kind* (M_I) are the ones which do not have any antiunitary symmetry Θ, that is $M_I = G$. The magnetic groups of *second kind* M_{II} can be defined by the theoretical sum $M_{II} = G + \Theta G$. This means

that the spatial symmetry group g is an invariant subgroup of M_{II} with index 2. The magnetic group of *third kind* does not contain the complex conjugation operation Θ as a separate element, but contains composite elements: $M_{III} = N + \Theta(G \setminus N)$ where N is normal subgroup of G with index 2: $G = N + a'N$ with $a' \in (G \setminus N)$. Then M_{III} can be written as $M_{III} = N + (\Theta a')N$. Note that both M_{II} and M_{III} can be written as $M_{II/III} = \mathcal{G} + r\mathcal{G}$ where $\mathcal{G} = G$ and $r = \Theta$ for magnetic groups of second kind, $\mathcal{G} = N$ and $r = \Theta a'$ for magnetic groups of third kind. Note that since product of two antiunitary operators is unitary, the product of any two elements in $r\mathcal{G}$ is an element of $\mathcal{G}$. In the following we denote the elements of $\mathcal{G}$ as $a, b, c, \ldots$, whereas the elements of $r\mathcal{G}$ as $r, s, t, \ldots$. Now, let ρ be an d dimensional irrep of $\mathcal{G}$ with basis functions $\mathbf{f} = \{f_1, f_2, \ldots, f_d\}$. Let the representation matrices in this basis be $\mathbf{\Gamma}_\rho(a)$ for $a \in \mathcal{G}$; $\rho(a) f_i = f_j \mathbf{\Gamma}_\rho(a)_{ji}$. This can be written in a more compact form as follows: $\rho(a)\mathbf{f} = \mathbf{f}\,\mathbf{\Gamma}_\rho(a)$. To extend this to the whole magnetic group M, we denote the action of the group elements on the functions as ρ_M with its restriction to $\mathcal{G}$ being irrep ρ. Note that the action ρ_M of any element in $r\mathcal{G}$ needs to be antilinear and antiunitary. Let the action of element $r \in r\mathcal{G}$ (r can be any element in $r\mathcal{G}$, however once we choose it, we keep it fixed) on the basis functions f_i of ρ be $\rho_M(r) f_i = g_i$ or $\rho_M(r)\mathbf{f} = \mathbf{g}$. Now, action of an element $a \in \mathcal{G}$ on $\mathbf{g}$ gives $\rho_M(a)\mathbf{g} = \rho_M(ar)\mathbf{f} = \rho_M(rr^{-1}ar)\mathbf{f} = \rho_M(r)\rho_M(r^{-1}ar)\mathbf{f} = \rho_M(r)\mathbf{f}\,\mathbf{\Gamma}_\rho(r^{-1}ar) = \mathbf{g}\,\mathbf{\Gamma}^*_\rho(r^{-1}ar)$ where we used that fact that $r^{-1}ar \in \mathcal{G}$ and the action of r is antilinear. Therefore,

$$\rho_M(a)\{\mathbf{f}, \mathbf{g}\} = \{\mathbf{f}, \mathbf{g}\} \begin{bmatrix} \mathbf{\Gamma}_\rho(a) & 0 \\ 0 & \mathbf{\Gamma}^*_\rho(r^{-1}ar) \end{bmatrix} \equiv \{\mathbf{f}, \mathbf{g}\}\mathbf{\Gamma}_{\rho_M}(a) \text{ for } a \in \mathcal{G}. \tag{4.16}$$

The matrix $\mathbf{\Gamma}_{\rho_M}(a)$ is block diagonal. On the other hand, an element $s \in r\mathcal{G}$, which can be written as $s = rb$ with $b \in \mathcal{G}$, acts in the following way:

$$\begin{aligned}
\rho_M(s)\{\mathbf{f},\mathbf{g}\} &= \{\rho_M(s)\mathbf{f}, \rho_M(s)\mathbf{g}\} = \{\rho_M(rb)\mathbf{f}, \rho_M(rb)\mathbf{g}\} \\
&= \{\rho_M(r)\rho_M(a)\mathbf{f}, \rho_M(ra)\rho_M(r)\mathbf{f}\} = \{\rho_M(r)\mathbf{f}\,\mathbf{\Gamma}_\rho(b), \rho_M(rbr)\mathbf{f}\} \\
&= \{\rho_M(r)\mathbf{f}\,\mathbf{\Gamma}_\rho(b), \mathbf{f}\,\mathbf{\Gamma}_{\rho_M}(rbr)\} = \{\mathbf{g}\,\mathbf{\Gamma}^*_\rho(b), \mathbf{f}\,\mathbf{\Gamma}_\rho(rbr)\} \\
&= \{\mathbf{f},\mathbf{g}\} \begin{bmatrix} 0 & \mathbf{\Gamma}_\rho(sr) \\ \mathbf{\Gamma}^*_\rho(r^{-1}s) & 0 \end{bmatrix} \equiv \Gamma_{\rho_M}(s) \text{ for } s \in r\mathcal{G}.
\end{aligned} \tag{4.17}$$

Clearly, the vector space spanned by the basis $\{\mathbf{f},\mathbf{g}\}$ is invariant under the action ρ_M of the elements of M. Furthermore, the matrix corresponding to the product of two elements $a, b \in \mathcal{G}$ can be written as

$$\begin{aligned}
\mathbf{\Gamma}_{\rho_M}(ab) = \begin{bmatrix} \mathbf{\Gamma}_\rho(ab) & 0 \\ 0 & \mathbf{\Gamma}^*_\rho(r^{-1}abr) \end{bmatrix} &= \begin{bmatrix} \mathbf{\Gamma}_\rho(a) & 0 \\ 0 & \mathbf{\Gamma}^*_\rho(r^{-1}ar) \end{bmatrix} \begin{bmatrix} \mathbf{\Gamma}_\rho(b) & 0 \\ 0 & \mathbf{\Gamma}^*_\rho(r^{-1}br) \end{bmatrix} \\
&= \mathbf{\Gamma}_{\rho_M}(a)\mathbf{\Gamma}_{\rho_M}(b)
\end{aligned} \tag{4.18}$$

where we used the facts that $ab \in \mathcal{G}$ and ρ is representation and consequently it is a homomorphism: $\mathbf{\Gamma}_\rho(ab) = \mathbf{\Gamma}_\rho(a)\mathbf{\Gamma}_\rho(b)$. Similarly, the matrix corresponding to the product of $a \in \mathcal{G}$ and $s \in r\mathcal{G}$ is given by $\mathbf{\Gamma}_{\rho_M}(as) = \mathbf{\Gamma}_{\rho_M}(a)\mathbf{\Gamma}_{\rho_M}(s)$. However, the matrix corresponding to the product $sa \in r\mathcal{G}$ is

$$\begin{aligned}
\mathbf{\Gamma}_{\rho_M}(sa) = \begin{bmatrix} 0 & \mathbf{\Gamma}_\rho(sar) \\ \mathbf{\Gamma}^*_\rho(r^{-1}sa) & 0 \end{bmatrix} &= \begin{bmatrix} 0 & \mathbf{\Gamma}_\rho(sr) \\ \mathbf{\Gamma}^*_\rho(r^{-1}s) & 0 \end{bmatrix} \begin{bmatrix} \mathbf{\Gamma}^*_\rho(a) & 0 \\ 0 & \mathbf{\Gamma}_\rho(r^{-1}ar) \end{bmatrix} \\
&= \mathbf{\Gamma}_{\rho_M}(s)\mathbf{\Gamma}^*_{\rho_M}(a),
\end{aligned} \tag{4.19}$$

where we again use the homomorphism of ρ. It is also easy to see that for $s, t \in r\mathcal{G}$, $\mathbf{\Gamma}_{\rho_M}(st) = \mathbf{\Gamma}_{\rho_M}(s)\mathbf{\Gamma}^*_{\rho_M}(t)$. Notice that $\mathbf{\Gamma}_{\rho_M}(sa) = \mathbf{\Gamma}_{\rho_M}(s)\mathbf{\Gamma}^*_{\rho_M}(a) \neq \mathbf{\Gamma}_{\rho_M}(s)\mathbf{\Gamma}_{\rho_M}(a)$. Therefore, the action ρ_M is not a representation. However, if we choose the basis functions $\mathbf{f}$ orthogonal and equinorm, and as a consequence the representation matrices $\mathbf{\Gamma}_\rho$ of ρ unitary, then the matrices $\mathbf{\Gamma}_{\rho_M}$ of ρ_M are also unitary. ρ_M is called *co-representation* of $M = \mathcal{G} + r\mathcal{G}$ derived from representation ρ of $\mathcal{G}$.

Since the matrices corresponding to the elements of $r\mathcal{G}$ are off diagonal, it would seem that the addition of the antiunitary operator in the symmetry group doubles the dimension of the vector space invariant under the space group. However, for that to be true, some matrices have to be non-block-diagonal in any basis. To check if all the matrices diagonalizable to the same block-diagonal form, we first show how the matrices $\mathbf{\Gamma}_{\rho_M}$ transform under unitary transformation of the basis $\{\mathbf{f}, \mathbf{g}\} \to \{\mathbf{f}', \mathbf{g}'\} = \{\mathbf{f}, \mathbf{g}\}\mathbf{S}$. Then, the co-representation matrices $\mathbf{\Gamma}'_{\rho_M}$ in this basis are

$$\begin{aligned}
&\rho_M(a)\{\mathbf{f}', \mathbf{g}'\} = \rho_M(a)\{\mathbf{f}, \mathbf{g}\}\mathbf{S} = \{\mathbf{f}, \mathbf{g}\}\mathbf{\Gamma}_{\rho_M}(a)\mathbf{S} = \{\mathbf{f}', \mathbf{g}'\}\mathbf{S}^{-1}\mathbf{\Gamma}_{\rho_M}(a)\mathbf{S} \\
&\quad \Rightarrow \mathbf{\Gamma}'_{\rho_M}(a) = \mathbf{S}^{-1}\mathbf{\Gamma}_{\rho_M}(a)\mathbf{S} \text{ for } a \in \mathcal{G}, \\
&\rho_M(s)\{\mathbf{f}', \mathbf{g}'\} = \rho_M(s)\{\mathbf{f}, \mathbf{g}\}\mathbf{S} = \{\mathbf{f}, \mathbf{g}\}\mathbf{\Gamma}_{\rho_M}(s)\mathbf{S}^* = \{\mathbf{f}', \mathbf{g}'\}\mathbf{S}^{-1}\mathbf{\Gamma}^*_{\rho_M}(s)\mathbf{S} \\
&\quad \Rightarrow \mathbf{\Gamma}'_{\rho_M}(s) = \mathbf{S}^{-1}\mathbf{\Gamma}^*_{\rho_M}(s)\mathbf{S}^* \text{ for } s \in r\mathcal{G},
\end{aligned} \tag{4.20}$$

where in the second line we used the fact that $s \in r\mathcal{G}$ is antilinear. With these transformation rules for the co-representation matrices, we can think about reducibility of co-representations, i.e., if it is possible to decompose the space spanned by basis $\{\mathbf{f}, \mathbf{g}\}$ into subspaces which will remain invariant under the action of the elements of M. It turns out that the reducibility of the co-representation ρ_M depends on the equivalence of the irrep $\rho(a)$ with matrices $\mathbf{\Gamma}_\rho(a)$ and irrep $\bar{\rho}(a)$ with matrices $\mathbf{\Gamma}^*_\rho(r^{-1}ar)$ of group $\mathcal{G}$ (given irrep ρ of $\mathcal{G}$ with matrices $\mathbf{\Gamma}_\rho(a)$ for $a \in \mathcal{G}$, it can be easily checked that $\bar{\rho}$ with matrices $\mathbf{\Gamma}^*_\rho(r^{-1}ar)$ is an irrep). There are two cases in this regard:

1. ρ and $\bar{\rho}$ are equivalent, i.e., there exists a matrix $\mathbf{S}$ such that $\mathbf{\Gamma}_\rho(a) = \mathbf{S}\mathbf{\Gamma}^*_\rho(r^{-1}ar)\mathbf{S}^{-1}$ for all $a \in \mathcal{G}$. Then, since $r^2 \in \mathcal{G}$, $\mathbf{\Gamma}_\rho(r^2) = \mathbf{S}\mathbf{\Gamma}^*_\rho(r^{-1}r^2r)\mathbf{S}^{-1}$ or $\mathbf{\Gamma}_\rho(r^2) = \mathbf{S}\mathbf{\Gamma}^*_\rho(r^2)\mathbf{S}^{-1}$. Also, $\mathbf{\Gamma}^*_\rho(a) = \mathbf{S}^*\mathbf{\Gamma}_\rho(r^{-1}ar)\mathbf{S}^{*-1}$ for all $a \in \mathcal{G}$, and if we replace a with $r^{-1}ar$, we get $\mathbf{\Gamma}^*_\rho(r^{-1}ar) = \mathbf{S}^*\mathbf{\Gamma}_\rho(r^{-2}ar^2)\mathbf{S}^{*-1} = \mathbf{S}^*\mathbf{\Gamma}_\rho(r^{-2})\mathbf{\Gamma}_\rho(a)\mathbf{\Gamma}_\rho(r^2)\mathbf{S}^{*-1}$ using the homomorphism of ρ. Now, we can replace this expression for $\mathbf{\Gamma}^*_\rho(r^{-1}ar)$ in the first equation of equivalence to get $\mathbf{\Gamma}_\rho(a) = \mathbf{S}\mathbf{S}^*\mathbf{\Gamma}_\rho(r^{-2})\mathbf{\Gamma}_\rho(a)\mathbf{\Gamma}_\rho(r^2)\mathbf{S}^{*-1}\mathbf{S}^{-1} = (\mathbf{S}\mathbf{S}^*\mathbf{\Gamma}^{-1}_\rho(r^2))\mathbf{\Gamma}_\rho(a)(\mathbf{S}\mathbf{S}^*\mathbf{\Gamma}^{-1}_\rho(r^2))^{-1}$ where we used the fact that $\mathbf{\Gamma}_\rho(r^{-2}) = \mathbf{\Gamma}^{-1}_\rho(r^2)$. This implies that the commutator $[\mathbf{\Gamma}_\rho(a), \mathbf{S}\mathbf{S}^*\mathbf{\Gamma}^{-1}_\rho(r^2)] = 0$ for all $a \in \mathcal{G}$. Then, sing Schur's first lemma tells us that $\mathbf{S}\mathbf{S}^*\mathbf{\Gamma}^{-1}_\rho(r^2) = \lambda\mathbb{1}$ for some complex number λ. Rewriting this as $\mathbf{\Gamma}_\rho(r^2) = \frac{1}{\lambda}\mathbf{S}\mathbf{S}^*$ and recalling that $\mathbf{\Gamma}_\rho(r^2) = \mathbf{S}\mathbf{\Gamma}^*_\rho(r^2)\mathbf{S}^{-1}$, we get $\frac{1}{\lambda}\mathbf{S}\mathbf{S}^* = \frac{1}{\lambda^*}\mathbf{S}\mathbf{S}^*\mathbf{S}\mathbf{S}^{-1}$, or $\lambda = \lambda^*$ or λ is real. Now, since $\mathbf{\Gamma}_\rho(r^2)$ and $\mathbf{S}$ are both unitary (which can always true for orthogonal equinorm basis), $|\lambda| = 1$. This implies that $\lambda = \pm 1$ or $\mathbf{S}\mathbf{S}^* = \pm\mathbf{\Gamma}_\rho(r^2)$. We are met with two choices again. To see how the two choices are different, we first do a unitary transformation of the matrices $\mathbf{\Gamma}_{\rho_M}$ for convenience:

$$
\begin{aligned}
\mathbf{\Gamma}'_{\rho_M}(a) = \mathbf{U}^{-1}\mathbf{\Gamma}_{\rho_M}(a)\mathbf{U} &= \begin{bmatrix} \mathbb{1} & \mathbf{0} \\ \mathbf{0} & \mathbf{S} \end{bmatrix} \begin{bmatrix} \mathbf{\Gamma}_\rho(a) & 0 \\ 0 & \mathbf{\Gamma}^*_\rho(r^{-1}ar) \end{bmatrix} \begin{bmatrix} \mathbb{1} & \mathbf{0} \\ \mathbf{0} & \mathbf{S}^{-1} \end{bmatrix} \\
&= \begin{bmatrix} \mathbf{\Gamma}_\rho(a) & 0 \\ 0 & \mathbf{S}\mathbf{\Gamma}^*_\rho(r^{-1}ar)\mathbf{S}^{-1} \end{bmatrix} = \begin{bmatrix} \mathbf{\Gamma}_\rho(a) & 0 \\ 0 & \mathbf{\Gamma}_\rho(a) \end{bmatrix} \text{ for } a \in \mathcal{G}, \\
\mathbf{\Gamma}'_{\rho_M}(r) = \mathbf{U}^{-1}\mathbf{\Gamma}_{\rho_M}(r)\mathbf{U}^* &= \begin{bmatrix} \mathbb{1} & \mathbf{0} \\ \mathbf{0} & \mathbf{S} \end{bmatrix} \begin{bmatrix} 0 & \mathbf{\Gamma}_\rho(r^2) \\ \mathbb{1} & 0 \end{bmatrix} \begin{bmatrix} \mathbb{1} & \mathbf{0} \\ \mathbf{0} & \mathbf{S}^{*-1} \end{bmatrix} \\
&= \begin{bmatrix} 0 & \mathbf{\Gamma}_\rho(r^2)\mathbf{S}^{*-1} \\ \mathbf{S} & 0 \end{bmatrix}.
\end{aligned}
\tag{4.21}
$$

Note that since all elements $s \in r\mathcal{G}$ are of the form $s = ra$, they can be written as $s = ra = (rar^{-1})r = \tilde{a}r$ where $\tilde{a} = (rar^{-1}) \in \mathcal{G}$. Hence, if we can simultaneously diagonalize $\mathbf{\Gamma}'_{\rho_M}(a)$ for all $a \in \mathcal{G}$ and $\mathbf{\Gamma}'_{\rho_M}(r)$ to the same block diagonal form, we diagonalize $\mathbf{\Gamma}'_{\rho_M}(s)$ for all $s \in r\mathcal{G}$ because $\mathbf{\Gamma}'_{\rho_M}(s) = \mathbf{\Gamma}'_{\rho_M}(\tilde{a}r) = \mathbf{\Gamma}'_{\rho_M}(\tilde{a})\mathbf{\Gamma}'_{\rho_M}(r)$. Now, $\mathbf{\Gamma}'_{\rho_M}(a)$ is already block diagonal for all $a \in \mathcal{G}$. To diagonalize $\mathbf{\Gamma}'_{\rho_M}(r)$, we try a unitary matrix $\mathbf{V}^{-1} = \begin{bmatrix} \boldsymbol{\alpha} & \boldsymbol{\beta} \\ \boldsymbol{\gamma} & \boldsymbol{\delta} \end{bmatrix}$. However, under this transformation $\mathbf{\Gamma}'_{\rho_M}(a)$ need to remain block diagonal for all $a \in \mathcal{G}$:

$$\begin{aligned} \mathbf{\Gamma}'_{\rho_M}(a)\mathbf{V}^{-1} &= \mathbf{V}^{-1}\mathbf{\Gamma}'_{\rho_M}(a) \\ \Rightarrow \begin{bmatrix} \mathbf{\Gamma}_\rho(a)\boldsymbol{\alpha} & \mathbf{\Gamma}_\rho(a)\boldsymbol{\beta} \\ \mathbf{\Gamma}_\rho(a)\boldsymbol{\gamma} & \mathbf{\Gamma}_\rho(a)\boldsymbol{\delta} \end{bmatrix} &= \begin{bmatrix} \boldsymbol{\alpha}\mathbf{\Gamma}_\rho(a) & \boldsymbol{\beta}\mathbf{\Gamma}_\rho(a) \\ \boldsymbol{\gamma}\mathbf{\Gamma}_\rho(a) & \boldsymbol{\delta}\mathbf{\Gamma}_\rho(a) \end{bmatrix} \text{ for all } a \in \mathcal{G}. \end{aligned} \tag{4.22}$$

Then, again using Schur's first lemma we know that $\boldsymbol{\alpha} = c_\alpha \mathbb{1}$, $\boldsymbol{\beta} = c_\beta \mathbb{1}$, $\boldsymbol{\gamma} = c_\gamma \mathbb{1}$ and $\boldsymbol{\delta} = c_\delta \mathbb{1}$ where $c_\alpha, c_\beta, c_\gamma, c_\delta$ are complex numbers. Now, applying this unitary transformation of $\mathbf{\Gamma}'_{\rho_M}(r)$ we get,

$$\begin{aligned} \mathbf{\Gamma}''_{\rho_M}(r) = \mathbf{V}^{-1}\mathbf{\Gamma}'_{\rho_M}(r)\mathbf{V}^* &= \begin{bmatrix} c_\alpha \mathbb{1} & c_\beta \mathbb{1} \\ c_\gamma \mathbb{1} & c_\delta \mathbb{1} \end{bmatrix} \begin{bmatrix} 0 & \mathbf{\Gamma}_\rho(r^2)\mathbf{S}^{*-1} \\ \mathbf{S} & 0 \end{bmatrix} \begin{bmatrix} c_\alpha \mathbb{1} & c_\gamma \mathbb{1} \\ c_\beta \mathbb{1} & c_\delta \mathbb{1} \end{bmatrix} \\ &= \begin{bmatrix} c_\alpha c_\beta \mathbf{S} + c_\alpha c_\beta \mathbf{\Gamma}_\rho(r^2)\mathbf{S}^{*-1} & c_\gamma c_\beta \mathbf{S} + c_\alpha c_\delta \mathbf{\Gamma}_\rho(r^2)\mathbf{S}^{*-1} \\ c_\alpha c_\delta \mathbf{S} + c_\gamma c_\beta \mathbf{\Gamma}_\rho(r^2)\mathbf{S}^{*-1} & c_\gamma c_\delta \mathbf{S} + c_\gamma c_\delta \mathbf{\Gamma}_\rho(r^2)\mathbf{S}^{*-1} \end{bmatrix}, \end{aligned} \tag{4.23}$$

where we used that fact that $\mathbf{V}$ is unitary, hence $\mathbf{V}^* = (\mathbf{V}^\dagger)^T = (\mathbf{V}^{-1})^T$. To make $\mathbf{\Gamma}''_{\rho_M}(r)$ diagonal we need to choose $c_\alpha, c_\beta, c_\gamma, c_\delta$ such that the off-diagonal

blocks are zero:

$$\begin{aligned} c_\gamma c_\beta \mathbf{S} + c_\alpha c_\delta \mathbf{\Gamma}_\rho(r^2)\mathbf{S}^{*-1} = \mathbf{0} &\Rightarrow c_\gamma c_\beta \mathbb{1} + c_\alpha c_\delta \mathbf{S}^{-1}\frac{1}{\lambda}\mathbf{S}\mathbf{S}^*\mathbf{S}^{*-1} = \mathbf{0} \\ &\Rightarrow (\lambda c_\gamma c_\beta + c_\alpha c_\delta)\mathbb{1} = \mathbf{0} \\ c_\alpha c_\delta \mathbf{S} + c_\gamma c_\beta \mathbf{\Gamma}_\rho(r^2)\mathbf{S}^{*-1} = \mathbf{0} &\Rightarrow c_\alpha c_\delta \mathbb{1} + c_\gamma c_\beta \mathbf{S}^{-1}\frac{1}{\lambda}\mathbf{S}\mathbf{S}^*\mathbf{S}^{*-1} = \mathbf{0} \\ &\Rightarrow (\lambda c_\alpha c_\delta + c_\gamma c_\beta)\mathbb{1} = \mathbf{0}. \end{aligned} \tag{4.24}$$

Now remembering $\lambda = \pm 1$, to satisfy these equation we need $(c_\alpha c_\delta + c_\gamma c_\beta) = 0$ when $\lambda = 1$, and $(c_\alpha c_\delta - c_\gamma c_\beta) = 0$ when $\lambda = -1$. However, since $\mathbf{V}^{-1}$ is unitary, the determinant of it is $\det(\mathbf{V}^{-1}) = c_\alpha c_\delta - c_\gamma c_\beta \neq 0$. This means that there are two cases:

(i) $\lambda = 1$: we can diagonalize $\mathbf{\Gamma}'_{\rho_M}(a)$ and $\mathbf{\Gamma}'_{\rho_M}(r)$ to the same block diagonal form. The co-representation ρ_M reduces to two irreducible co-representations of dimension d.

(ii) $\lambda = -1$: we cannot diagonalize $\mathbf{\Gamma}'_{\rho_M}(a)$ and $\mathbf{\Gamma}'_{\rho_M}(r)$ to the same block diagonal form. We have irreducible co-representation of dimension $2d$.

2. ρ and $\bar{\rho}$ are inequivalent. In this case, since the off-diagonal blocks of $\mathbf{\Gamma}_{\rho_M}(s)$ for $s \in r\mathcal{G}$ are inequivalent, it is not possible to diagonalize both $\mathbf{\Gamma}_{\rho_M}(a)$ for $a \in \mathcal{G}$ and $\mathbf{\Gamma}_{\rho_M}(s)$ for $s \in r\mathcal{G}$ to have the same block diagonal form. Therefore, in this case, we have irreducible co-representation of dimension $2d$.

From the above discussion, we see that in the cases 1.(ii) and 2., the dimension of irreducible co-representation ρ_M is twice that of the irreducible representation ρ from which ρ_M is derived. However, we still need to find an easy way to detect which case ρ_M falls under once we are given ρ and r. It turns out that there is an indicator, which is easy to compute for finite magnetic groups, that can differentiate between

the three cases. We first give the expression of the indicator and then prove it.

$$\frac{1}{|\mathcal{G}|}\sum_{s\in r\mathcal{G}}\chi_\rho(s^2)=\begin{cases}+1, & 1.(\text{i})\\ -1, & 1.(\text{ii})\\ \ 0, & 2\end{cases} \tag{4.25}$$

where $\chi_\rho(s^2)$ is the character of the matrices $\mathbf{\Gamma}_\rho(s^2)$ (recall that if $s\in r\mathcal{G}$, $s^2\in\mathcal{G}$). When ρ and $\bar{\rho}$ are equivalent (case 1):

$$\begin{aligned}\sum_{s\in r\mathcal{G}}\chi_\rho(s^2)&=\sum_{a\in\mathcal{G}}\chi_\rho(rara)=\sum_{a\in\mathcal{G}}\chi_\rho(r^2(r^{-1}ar)a)=\sum_{a\in\mathcal{G}}\mathrm{Tr}(\mathbf{\Gamma}_\rho(r^2(r^{-1}ar)a))\\
&=\sum_{a\in\mathcal{G}}\mathrm{Tr}(\mathbf{\Gamma}_\rho(r^2)\mathbf{\Gamma}_\rho(r^{-1}ar)\mathbf{\Gamma}_\rho(a))=\sum_{a\in\mathcal{G}}\mathbf{\Gamma}_\rho(r^2)_{ij}\mathbf{\Gamma}_\rho(r^{-1}ar)_{jk}\mathbf{\Gamma}_\rho(a)_{ki}\\
&=\mathbf{\Gamma}_\rho(r^2)_{ij}\sum_{a\in\mathcal{G}}\mathbf{\Gamma}_\rho(r^{-1}ar)_{jk}\mathbf{\Gamma}_\rho(a)_{ki}=\mathbf{\Gamma}_\rho(r^2)_{ij}\sum_{a\in\mathcal{G}}\mathbf{S}^{*-1}_{jl}\mathbf{\Gamma}^*_\rho(a)_{lm}\mathbf{S}^*_{mk}\mathbf{\Gamma}_\rho(a)_{ki}\\
&=\mathbf{\Gamma}_\rho(r^2)_{ij}\mathbf{S}^{*-1}_{jl}\mathbf{S}^*_{mk}\sum_{a\in\mathcal{G}}\mathbf{\Gamma}^\dagger_\rho(a)_{ml}\mathbf{\Gamma}_\rho(a)_{ki}=\mathbf{\Gamma}_\rho(r^2)_{ij}\mathbf{S}^{*-1}_{jl}\mathbf{S}^*_{mk}\frac{|\mathcal{G}|}{d}\delta_{mi}\delta_{kl}\\
&=\frac{|\mathcal{G}|}{d}\mathbf{\Gamma}_\rho(r^2)_{ij}\mathbf{S}^*_{ik}\mathbf{S}^{*-1}_{jk}=\frac{|\mathcal{G}|}{d}\mathbf{\Gamma}_\rho(r^2)_{ij}\mathbf{S}^{*-1}_{jk}\mathbf{S}^{*T}_{ki}\\
&=\frac{|\mathcal{G}|}{d}\mathbf{\Gamma}_\rho(r^2)_{ij}(\mathbf{S}^{*-1}\mathbf{S}^\dagger)_{ji}=\frac{|\mathcal{G}|}{d}\mathbf{\Gamma}_\rho(r^2)_{ij}(\mathbf{S}^{*-1}\mathbf{S}^{-1})_{ji}=\frac{|\mathcal{G}|}{d}\mathbf{\Gamma}_\rho(r^2)_{ij}(\mathbf{S}\mathbf{S}^*)^{-1}_{ji}\\
&=\lambda\frac{|\mathcal{G}|}{d}\mathbf{\Gamma}_\rho(r^2)_{ij}\mathbf{\Gamma}^{-1}_\rho(r^2)_{ji}=\lambda|\mathcal{G}|,\end{aligned} \tag{4.26}$$

where we used the relation between $\mathbf{\Gamma}_\rho(r^2)$ and $\mathbf{S}$, the orthogonality theorem of representation matrices, and the facts that ρ is homomorphism and $\mathbf{S}$ is unitary. This proves the first two cases of Eq. 4.25 When ρ and $\bar{\rho}$ are inequivalent, we follow the same steps to get:

$$\sum_{s\in r\mathcal{G}}\chi_\rho(s^2)=\mathbf{\Gamma}_\rho(r^2)_{ij}\sum_{a\in\mathcal{G}}\mathbf{\Gamma}_\rho(r^{-1}ar)_{jk}\mathbf{\Gamma}_\rho(a)_{ki}=\mathbf{\Gamma}_\rho(r^2)_{ij}\sum_{a\in\mathcal{G}}(\mathbf{\Gamma}^*_\rho(r^{-1}ar))^*_{jk}\mathbf{\Gamma}_\rho(a)_{ki}=0, \tag{4.27}$$

where once again we used the orthogonality theorem which says the sum of over all elements of $\mathcal{G}$ should be zero because $\mathbf{\Gamma}_\rho(a)$ and $\mathbf{\Gamma}^*_\rho(r^{-1}ar)$ are representations matrices of inequivalent irreps. This proves third condition of Eq. 4.25.

Corepresentations of magnetic space groups

As we discussed above in detail, a space magnetic space group can be written as $M = \mathcal{G} + r\mathcal{G}$. There are four kind of magnetic space groups. The first kind is where there is no antiunitary symmetry meaning that $M = G$ where G is the space group. The second kind is where $r = \Theta$ and $\mathcal{G} = G$, that is $M = G + \Theta G$. The third kind is where $\mathcal{G}$ is a normal subgroup of G i.e., the coset decomposition of G is $G = N + aN$ with $a \in G$ but $a \notin N$, and $M = N + \Theta aN = N + rN$ where $r = \Theta a$. The fourth kind of magnetic space group is where $\mathcal{G} = G$ but $r = \Theta\{E|\mathbf{t}_0\}$ where $\{E|\mathbf{t}_0\}$ is a translation which is not in G: $\{E|\mathbf{t}_0\} \notin G$. In simple elasticity problems, the third and fourth kind of magnetic space groups do not arise. Therefore, we will mainly stick to magnetic space groups of the second kind in our discussion. Now, Let us assume that we have found an irrep of space group $\mathcal{G}$. By that we mean that for some wave vector $\mathbf{k}$ in the irreducible Brillouin zone, we got the projected representation of the little co-group $\bar{\mathcal{G}}^{\mathbf{k}}$, from that we obtained the irrep $\rho^{\mathbf{k}}$ of the little group $\mathcal{G}^{\mathbf{k}}$, from which we got the induced representation $(\rho^{\mathbf{k}} \uparrow \mathcal{G})$ of G (these steps were outlined in Section 4.2). Now, we can use the expression of the character of $(\rho^{\mathbf{k}} \uparrow \mathcal{G})$ as given in Eq. 4.11 to investigate which of the cases in Eq. 4.25 the representation $(\rho^{\mathbf{k}} \uparrow \mathcal{G})$ falls under. If it falls under either 1.(ii) or 2., the co-representation derived from $(\rho^{\mathbf{k}} \uparrow \mathcal{G})$ will have twice the dimension as the dimension of $(\rho^{\mathbf{k}} \uparrow \mathcal{G})$. Therefore, we need to

evaluate the following:

$$\begin{aligned}\frac{1}{|\mathcal{G}|}\sum_{s\in r\mathcal{G}}\chi_{(\rho^{\mathbf{k}}\uparrow\mathcal{G})}(s^2) &= \frac{1}{|\mathcal{G}|}\sum_{a\in\mathcal{G}}\chi_{(\rho^{\mathbf{k}}\uparrow\mathcal{G})}(rara)\\ &= \frac{1}{|\mathcal{G}|}\sum_{a\in\mathcal{G}}{\sum_{\alpha}}'\chi_{\rho^{\mathbf{k}}}(\{R_\alpha|\mathbf{v}_\alpha\}^{-1}rara\{R_\alpha|\mathbf{v}_\alpha\}) \text{ (using Eq. 4.11)}\\ &= \frac{1}{|\mathcal{G}|}\sum_{\alpha}{\sum_{a\in\mathcal{G}}}'\chi_{\rho^{\mathbf{k}}}(\{R_\alpha|\mathbf{v}_\alpha\}^{-1}rara\{R_\alpha|\mathbf{v}_\alpha\})\end{aligned} \tag{4.28}$$

where α goes over the wave vectors in the star of $\mathbf{k}$, and the second sum in the second equality is constrained to those α for which the little co-group $\mathcal{G}^{\mathbf{k}_\alpha} = \{R_\alpha|\mathbf{v}_\alpha\}\mathcal{G}^{\mathbf{k}}\{R_\alpha|\mathbf{v}_\alpha\}^{-1}$ of wave vector $\mathbf{k}_\alpha = \mathbf{R}_\alpha\mathbf{k}$ contains $rara$, and the second sum in the last equality is constrained to those a which $rara \in \mathcal{G}^{\mathbf{k}_\alpha}$. Defining $rb = \{R_\alpha|\mathbf{v}_\alpha\}^{-1}ra\{R_\alpha|\mathbf{v}_\alpha\}$ with $b \in \mathcal{G}$, we have $rbrb = \{R_\alpha|\mathbf{v}_\alpha\}^{-1}rara\{R_\alpha|\mathbf{v}_\alpha\} \in \mathcal{G}^{\mathbf{k}}$. However for every $a \in \mathcal{G}$ such that $rara \in \mathcal{G}^{\mathbf{k}_\alpha}$, there is $a' = r^{-1}\{R_\alpha|\mathbf{v}_\beta\}\{R_\alpha|\mathbf{v}_\alpha\}^{-1}ra$ $\{R_\alpha|\mathbf{v}_\alpha\}\{R_\alpha|\mathbf{v}_\beta\}^{-1} \in \mathcal{G}$ such that $ra'ra' \in \mathcal{G}^{\mathbf{k}_\beta}$, and $\chi_{\rho^{\mathbf{k}}}(\{R_\alpha|\mathbf{v}_\alpha\}^{-1}rara\{R_\alpha|\mathbf{v}_\alpha\}) = \chi_{\rho^{\mathbf{k}}}(\{R_\beta|\mathbf{v}_\alpha\}^{-1}ra'ra'\{R_\alpha|\mathbf{v}_\beta\}) = \chi_{\rho^{\mathbf{k}}}(rbrb)$. Therefore we can evaluate $\sum_{a\in\mathcal{G}}{}'$ $\chi_{\rho^{\mathbf{k}}}(\{R_\alpha|\mathbf{v}_\alpha\}^{-1}rara\{R_\alpha|\mathbf{v}_\alpha\})$ for one α and multiply the number q of wave vectors in the star of $\mathbf{k}$ to get $\sum_\alpha\sum_{a\in\mathcal{G}}{}'\chi_{\rho^{\mathbf{k}}}(\{R_\alpha|\mathbf{v}_\alpha\}^{-1}rara\{R_\alpha|\mathbf{v}_\alpha\})$. Without loss of generality, we can choose $\alpha = 1$ with $\{R_1|\mathbf{v}_1\} = \{E|\mathbf{0}\}$. Therefore, $\sum_\alpha\sum_{a\in\mathcal{G}}{}'\chi_{\rho^{\mathbf{k}}}(\{R_\alpha|\mathbf{v}_\alpha\}^{-1}rara\{R_\alpha|\mathbf{v}_\alpha\}) = q\sum_{b\in\mathcal{G}}{}'\chi_{\rho^{\mathbf{k}}}(rbrb)$ where the sum is restricted to those $b \in \mathcal{G}$ such that $rbrb \in \mathcal{G}^{\mathbf{k}}$. Hence, we have the following:

$$\frac{1}{|\mathcal{G}|}\sum_{s\in r\mathcal{G}}\chi_{(\rho^{\mathbf{k}}\uparrow\mathcal{G})}(s^2) = \frac{q}{|\mathcal{G}|}\sum_{b\in\mathcal{G}}{}'\chi_{\rho^{\mathbf{k}}}(rbrb) = \frac{1}{|\mathcal{G}^{\mathbf{k}}|}\sum_{b\in\mathcal{G}}{}'\chi_{\rho^{\mathbf{k}}}(rbrb). \tag{4.29}$$

Now, recall that the space group $\mathcal{G}$ can be written in the form of coset decomposition $\mathcal{G} = \{R_1|\mathbf{v}_1\}T + \{R_2|\mathbf{v}_2\}T + \cdots + \{R_h|\mathbf{v}_h\}T$ with T being the translation subgroup, and theoretical sum of those cosets for which the rotation part $S_1, S_2, \ldots, S_b$ satisfies $\mathbf{S}_i\mathbf{k} \equiv \mathbf{k}$ forms the little group $\mathcal{G}^{\mathbf{k}}$. Recall that we can choose any element of a coset

to represent the coset. Let us assume that we have chosen one representative from each coset in the two coset decompositions above, and fixed them. Since, $b \in \mathcal{G}$, $b = \{R_i|\mathbf{v}_i\}\{E|\mathbf{t}\}$, where $\{R_i|\mathbf{v}_i\}$ is one of the coset representatives chosen for the decomposition of $\mathcal{G}$ and $\{E|\mathbf{t}\} \in T$. With definition $r\{R_i|\mathbf{v}_i\} = \Theta\{R'_i|\mathbf{v}'_i\}$, we have

$$\begin{aligned} rbrb &= \{R'_i|\mathbf{v}'_i\}\{E|\mathbf{t}\}\{R'_i|\mathbf{v}'_i\}\{E|\mathbf{t}\} = \{R'_i|\mathbf{v}'_i\}^2(\{R'_i|\mathbf{v}'_i\}^{-1}\{E|\mathbf{t}\}\{R'_i|\mathbf{v}'_i\} \\ &= \{R'_i|\mathbf{v}'_i\}^2\{E|\mathbf{R}'^{-1}\mathbf{t}\}\{E|\mathbf{t}\}, \end{aligned} \tag{4.30}$$

since Θ commutes with spatial symmetry elements and $\Theta^2 = 1$. Clearly, $\{E|\mathbf{R}'^{-1}\mathbf{t}\} = \{R'_i|\mathbf{v}'_i\}^{-1}\{E|\mathbf{t}\}\{R'_i|\mathbf{v}'_i\} = (r\{R_i|\mathbf{v}_i\})^{-1}\{E|\mathbf{t}\}(r\{R_i|\mathbf{v}_i\}) \in \mathcal{G}$, and hence $\{E|\mathbf{R}'^{-1}\mathbf{t}\} \in T$. Moreover, since $rbrb \in \mathcal{G}^{\mathbf{k}}$, $\{R'_i|\mathbf{v}'_i\}^2 \in \mathcal{G}^{\mathbf{k}}$ and $R'^2_i \in \bar{\mathcal{G}}^{\mathbf{k}}$. Also, with the definition $r\{R_i|\mathbf{v}_i\} = \Theta\{R'_i|\mathbf{v}'_i\}$, $r\mathcal{G} = \Theta\{R'_1|\mathbf{v}'_1\}T + \Theta\{R'_2|\mathbf{v}'_2\}T + \cdots + \Theta\{R'_h|\mathbf{v}'_h\}T$. Defining the set $F' = \{R'_1, R'_2, \ldots, R'_h\}$, we can break the sum over b in Eq. 4.29 into a sum over the elements R' of set F' such that $R'^2 \in \bar{\mathcal{G}}^{\mathbf{k}}$ and another sum over the elements of the translation subgroup T as follows

$$\begin{aligned} \frac{1}{|\mathcal{G}|}\sum_{s\in r\mathcal{G}}\chi_{(\rho^{\mathbf{k}}\uparrow\mathcal{G})}(s^2) &= \frac{1}{|\mathcal{G}^{\mathbf{k}}|}{\sum_{b\in\mathcal{G}}}'\chi_{\rho^{\mathbf{k}}}(rbrb) = \frac{1}{|\mathcal{G}^{\mathbf{k}}|}\sum_{\substack{R'\in F'\\ R'^2\in\bar{\mathcal{G}}^{\mathbf{k}}}}\sum_{\mathbf{t}\in T}\chi_{\rho^{\mathbf{k}}}(\{R'_i|\mathbf{v}'_i\}^2\{E|\mathbf{R}'^{-1}\mathbf{t}+\mathbf{t}\}) \\ &= \frac{1}{|\mathcal{G}^{\mathbf{k}}|}\sum_{\substack{R'\in F'\\ R'^2\in\bar{\mathcal{G}}^{\mathbf{k}}}}\sum_{\mathbf{t}\in T}\chi_{\rho^{\mathbf{k}}}(\{R'_i|\mathbf{v}'_i\}^2)\chi_{\rho^{\mathbf{k}}}(\{E|\mathbf{R}'^{-1}\mathbf{t}+\mathbf{t}\}) \\ &= \frac{1}{|\mathcal{G}^{\mathbf{k}}|}\sum_{\substack{R'\in F'\\ R'^2\in\bar{\mathcal{G}}^{\mathbf{k}}}}\chi_{\rho^{\mathbf{k}}}(\{R'_i|\mathbf{v}'_i\}^2)\sum_{\mathbf{t}\in T}e^{-i\mathbf{k}\cdot(\mathbf{R}'^{-1}\mathbf{t}+\mathbf{t})} \\ &= \frac{1}{|\mathcal{G}^{\mathbf{k}}|}\sum_{\substack{R'\in F'\\ R'^2\in\bar{\mathcal{G}}^{\mathbf{k}}}}\chi_{\rho^{\mathbf{k}}}(\{R'_i|\mathbf{v}'_i\}^2)\sum_{\mathbf{t}\in T}e^{-i(\mathbf{R}'\mathbf{k}+\mathbf{k})\cdot\mathbf{t}}. \end{aligned} \tag{4.31}$$

Now, $\sum_{\mathbf{t}\in T}e^{-i(\mathbf{R}'\mathbf{k}+\mathbf{k})\cdot\mathbf{t}}$ is nonzero only when $(\mathbf{R}'\mathbf{k}+\mathbf{k})$ is a reciprocal lattice vector $\mathbf{K}$ or $\mathbf{R}'\mathbf{k} \equiv -\mathbf{k}$. Moreover, when $\mathbf{R}'\mathbf{k} \equiv -\mathbf{k}$, $\sum_{\mathbf{t}\in T}e^{-i(\mathbf{R}'\mathbf{k}+\mathbf{k})\cdot\mathbf{t}} = \sum_{\mathbf{t}\in T}1 = |T|$.

Therefore,

$$\frac{1}{|\mathcal{G}|}\sum_{s\in r\mathcal{G}}\chi_{(\rho^{\mathbf{k}}\uparrow\mathcal{G})}(s^2)=\frac{|T|}{|\mathcal{G}^{\mathbf{k}}|}\sum_{\substack{R'\in F'\\ \mathbf{R}'\mathbf{k}\equiv-\mathbf{k}\\ R'^2\in\bar{\mathcal{G}}^{\mathbf{k}}}}\chi_{\rho^{\mathbf{k}}}(\{R'_i|\mathbf{v}'_i\}^2)=\frac{1}{|\bar{\mathcal{G}}^{\mathbf{k}}|}\sum_{\substack{R'\in F'\\ \mathbf{R}'\mathbf{k}\equiv-\mathbf{k}\\ R'^2\in\bar{\mathcal{G}}^{\mathbf{k}}}}\chi_{\rho^{\mathbf{k}}}(\{R'_i|\mathbf{v}'_i\}^2). \quad (4.32)$$

Hence, the criterion Eq. 4.25 for the co-representation of M derived from $(\rho^{\mathbf{k}}\uparrow G)$ can be simplified to

$$\frac{1}{|\bar{\mathcal{G}}^{\mathbf{k}}|}\sum_{\substack{R'\in F'\\ \mathbf{R}'\mathbf{k}\equiv-\mathbf{k}\\ R'^2\in\bar{\mathcal{G}}^{\mathbf{k}}}}\chi_{\rho^{\mathbf{k}}}(\{R'_i|\mathbf{v}'_i\}^2)=\begin{cases}+1, & 1.(\mathrm{i})\\ -1, & 1.(\mathrm{ii})\\ 0, & 2\end{cases}. \quad (4.33)$$

This criterion called *Herring criterion*.

Time reversal symmetry protected degeneracy in frequency bands of elastic structures

In the previous section we saw that in the case of $p4$ space group, we could not explain the degeneracies at points Γ and M, whereas in case of $p4gm$ space group, we could not explain the degeneracies at points M and Z just by using spatial symmetries. Note that in our elasticity problems the antiunitary operator simply is $r=\Theta$ and the group $\mathcal{G}$ is just the space group.

p4: The isogonal group is $F=\{E,C_4,C_2,C_4^3\}$. The elements of this set are the only point group symmetry elements. Since $r=\Theta$, $F'=\{E,C_4,C_2,C_4^3\}$. The coset decomposition of the space group $\mathcal{G}=G=\{E|\mathbf{0}\}T+\{C_4|\mathbf{0}\}T+\{C_2|\mathbf{0}\}T+\{C_4^3|\mathbf{0}\}T$. We fix this coset representatives and will not change in the discussion below.

Γ: We have seen in Table 4.14 that there are 4 irreps. Moreover, the number of elements in the little co-group $\bar{G}^{\Gamma}=C_4$ is 4. Using Eq. 4.33, we will see if any of the

irreps gives multidimensional co-representations.

$$\frac{1}{4}\sum_{\substack{R'\in F'\\ \mathbf{R}'\mathbf{k}\equiv-\mathbf{k}\\ R'^2\in\bar{\mathcal{G}}^{\mathbf{k}}}}\chi_{\Gamma_1}(\{R'_i|\mathbf{v}'_i\}^2)=\frac{1}{4}\left(\chi_{\Gamma_1}(\{E|\mathbf{0}\}^2)+\chi_{\Gamma_1}(\{C_4|\mathbf{0}\}^2)+\chi_{\Gamma_1}(\{C_2|\mathbf{0}\}^2)+\chi_{\Gamma_1}(\{C_4^3|\mathbf{0}\}^2)\right)$$
$$=\frac{1}{4}\left(2\chi_{\Gamma_1}(\{E|\mathbf{0}\})+2\chi_{\Gamma_1}(\{C_2|\mathbf{0}\})\right)=1 \tag{4.34a}$$

$$\frac{1}{4}\sum_{\substack{R'\in F'\\ \mathbf{R}'\mathbf{k}\equiv-\mathbf{k}\\ R'^2\in\bar{\mathcal{G}}^{\mathbf{k}}}}\chi_{\Gamma_2}(\{R'_i|\mathbf{v}'_i\}^2)=\frac{1}{4}\left(\chi_{\Gamma_2}(\{E|\mathbf{0}\}^2)+\chi_{\Gamma_2}(\{C_4|\mathbf{0}\}^2)+\chi_{\Gamma_2}(\{C_2|\mathbf{0}\}^2)+\chi_{\Gamma_2}(\{C_4^3|\mathbf{0}\}^2)\right)$$
$$=\frac{1}{4}\left(2\chi_{\Gamma_2}(\{E|\mathbf{0}\})+2\chi_{\Gamma_2}(\{C_2|\mathbf{0}\})\right)=1 \tag{4.34b}$$

$$\frac{1}{4}\sum_{\substack{R'\in F'\\ \mathbf{R}'\mathbf{k}\equiv-\mathbf{k}\\ R'^2\in\bar{\mathcal{G}}^{\mathbf{k}}}}\chi_{\Gamma_3}(\{R'_i|\mathbf{v}'_i\}^2)=\frac{1}{4}\left(\chi_{\Gamma_3}(\{E|\mathbf{0}\}^2)+\chi_{\Gamma_3}(\{C_4|\mathbf{0}\}^2)+\chi_{\Gamma_3}(\{C_2|\mathbf{0}\}^2)+\chi_{\Gamma_3}(\{C_4^3|\mathbf{0}\}^2)\right)$$
$$=\frac{1}{4}\left(2\chi_{\Gamma_3}(\{E|\mathbf{0}\})+2\chi_{\Gamma_3}(\{C_2|\mathbf{0}\})\right)=0 \tag{4.34c}$$

$$\frac{1}{4}\sum_{\substack{R'\in F'\\ \mathbf{R}'\mathbf{k}\equiv-\mathbf{k}\\ R'^2\in\bar{\mathcal{G}}^{\mathbf{k}}}}\chi_{\Gamma_4}(\{R'_i|\mathbf{v}'_i\}^2)=\frac{1}{4}\left(\chi_{\Gamma_4}(\{E|\mathbf{0}\}^2)+\chi_{\Gamma_4}(\{C_4|\mathbf{0}\}^2)+\chi_{\Gamma_4}(\{C_2|\mathbf{0}\}^2)+\chi_{\Gamma_4}(\{C_4^3|\mathbf{0}\}^2)\right)$$
$$=\frac{1}{4}\left(2\chi_{\Gamma_4}(\{E|\mathbf{0}\})+2\chi_{\Gamma_4}(\{C_2|\mathbf{0}\})\right)=0 \tag{4.34d}$$

Therefore, the co-representations induced from Γ_1 or Γ_2 of $p4$ belong to case 1.(i) and the dimension of the co-representations obtained from these two irreps is 1. However, the co-representations induced from Γ_3 or Γ_4 of $p4$ belong to case 2. This means that irreps $\Gamma_3 \not\equiv \bar{\Gamma}_3$ and $\Gamma_4 \not\equiv \bar{\Gamma}_4$. However, since $\bar{\Gamma}_3$ and $\bar{\Gamma}_4$ are also irreps of little group

G^Γ, it must be that $\bar{\Gamma}_3 = \Gamma_4$ and $\bar{\Gamma}_4 = \Gamma_3$. Therefore, Γ_3 and Γ_4 of little group G^Γ of space group $p4$ together make a 2 dimensional co-representation. We saw in our discussion about the eigenfunctions $\tilde{u}^{(2)}_\Gamma$ and $\tilde{u}^{(3)}_\Gamma$ in Fig. 4.5(a) in the previous section that they belong to Γ_3 or Γ_4, but could not explain the degeneracy between band 2 and 3. Since the irreps Γ_3 and Γ_4 together make the 2-dimensional co-representation of the magnetic group, we see degeneracy between bands 2 and 3 at the Γ point in the band structure of Fig. 4.5(a).

M: We have seen in Table 4.15 that there are 4 irreps. Moreover, the number of elements in the little co-group $\bar{G}^M = C_4$ is 4. Using Eq. 4.33, we will see if any of the irreps gives multidimensional co-representations. Noting that $(\mathbf{K}_1 + \mathbf{K}_2)/2 \equiv -(\mathbf{K}_1 + \mathbf{K}_2)/2$, we find

$$\begin{aligned}\frac{1}{4}\sum_{\substack{R'\in F'\\ \mathbf{R}'\mathbf{k}\equiv-\mathbf{k}\\ R'^2\in\bar{\mathcal{G}}^{\mathbf{k}}}}\chi_{M_1}(\{R'_i|\mathbf{v}'_i\}^2) &= \frac{1}{4}\left(\chi_{M_1}(\{E|\mathbf{0}\}^2)+\chi_{M_1}(\{C_4|\mathbf{0}\}^2)+\chi_{M_1}(\{C_2|\mathbf{0}\}^2)+\chi_{M_1}(\{C_4^3|\mathbf{0}\}^2)\right)\\ &= \frac{1}{4}\left(2\chi_{M_1}(\{E|\mathbf{0}\})+2\chi_{M_1}(\{C_2|\mathbf{0}\})\right)=1\end{aligned} \tag{4.35a}$$

$$\begin{aligned}\frac{1}{4}\sum_{\substack{R'\in F'\\ \mathbf{R}'\mathbf{k}\equiv-\mathbf{k}\\ R'^2\in\bar{\mathcal{G}}^{\mathbf{k}}}}\chi_{M_2}(\{R'_i|\mathbf{v}'_i\}^2) &= \frac{1}{4}\left(\chi_{M_2}(\{E|\mathbf{0}\}^2)+\chi_{M_2}(\{C_4|\mathbf{0}\}^2)+\chi_{M_2}(\{C_2|\mathbf{0}\}^2)+\chi_{M_2}(\{C_4^3|\mathbf{0}\}^2)\right)\\ &= \frac{1}{4}\left(2\chi_{M_2}(\{E|\mathbf{0}\})+2\chi_{M_2}(\{C_2|\mathbf{0}\})\right)=1\end{aligned} \tag{4.35b}$$

$$\frac{1}{4}\sum_{\substack{R'\in F'\\ \mathbf{R}'\mathbf{k}\equiv-\mathbf{k}\\ R'^2\in\bar{\mathcal{G}}^{\mathbf{k}}}}\chi_{M_3}(\{R'_i|\mathbf{v}'_i\}^2)=\frac{1}{4}\left(\chi_{M_3}(\{E|\mathbf{0}\}^2)+\chi_{M_3}(\{C_4|\mathbf{0}\}^2)+\chi_{M_3}(\{C_2|\mathbf{0}\}^2)+\chi_{M_3}(\{C_4^3|\mathbf{0}\}^2)\right)$$
$$=\frac{1}{4}\left(2\chi_{M_3}(\{E|\mathbf{0}\})+2\chi_{M_3}(\{C_2|\mathbf{0}\})\right)=0 \tag{4.35c}$$

$$\frac{1}{4}\sum_{\substack{R'\in F'\\ \mathbf{R}'\mathbf{k}\equiv-\mathbf{k}\\ R'^2\in\bar{\mathcal{G}}^{\mathbf{k}}}}\chi_{M_4}(\{R'_i|\mathbf{v}'_i\}^2)=\frac{1}{4}\left(\chi_{M_4}(\{E|\mathbf{0}\}^2)+\chi_{M_4}(\{C_4|\mathbf{0}\}^2)+\chi_{M_4}(\{C_2|\mathbf{0}\}^2)+\chi_{M_4}(\{C_4^3|\mathbf{0}\}^2)\right)$$
$$=\frac{1}{4}\left(2\chi_{M_4}(\{E|\mathbf{0}\})+2\chi_{M_4}(\{C_2|\mathbf{0}\})\right)=0 \tag{4.35d}$$

Therefore, the co-representations induced from M_1 or M_2 of $p4$ belong to case 1.(i) and the dimension of the co-representations obtained from these two irreps is 1. However, the co-representations induced from M_3 or M_4 of $p4$ belong to case 2. This means that irreps $M_3 \not\equiv \bar{M}_3$ and $M_4 \not\equiv \bar{M}_4$. However, since $\bar{M}_3$ and $\bar{M}_4$ are also irreps of little group G^M, it must be that $\bar{M}_3 = M_4$ and $\bar{M}_4 = M_3$. Therefore, M_3 and M_4 of little group G^M of space group $p4$ together make a 2 dimensional co-representation. We saw in our discussion about the eigenfunctions $\tilde{u}_M^{(3)}$ and $\tilde{u}_M^{(4)}$ in Fig. 4.5(a) in the previous section that they belong to M_3 or M_4, but could not explain the degeneracy between band 3 and 4. Since the irreps M_3 and M_4 together make the 2-dimensional co-representation of the magnetic group, we see degeneracy between bands 3 and 4 at the M point in the band structure of Fig. 4.5(a).

***p4gm*:** The isogonal group is $F = \{E, C_4, C_2, C_4^3, \sigma_{10}, \sigma_{01}, \sigma_{1\bar{1}}, \sigma_{11}\}$. The elements of this set are the only point group symmetry elements. Since $r = \Theta$, $F' = \{E, C_4, C_2, C_4^3, \sigma_{10}, \sigma_{01}, \sigma_{1\bar{1}}, \sigma_{11}\}$. The coset decomposition of the space group $\mathcal{G} = G = \{E|\mathbf{0}\}T + \{C_4|\mathbf{0}\}T + \{C_2|\mathbf{0}\}T + \{C_4^3|\mathbf{0}\}T + \{\sigma_{10}|\mathbf{t}_1/2+\mathbf{t}_2/2\}T + \{\sigma_{01}|\mathbf{t}_1/2+$

$\mathbf{t}_2/2\}T + \{\sigma_{1\bar{1}}|\mathbf{t}_1/2 + \mathbf{t}_2/2\}T + \{\sigma_{11}|\mathbf{t}_1/2 + \mathbf{t}_2/2\}T$. We fix this coset representatives and will not change in the discussion below.

M: We have seen in Table 4.21 that there are 5 irreps. Moreover, the number of elements in the little co-group $\bar{G}^M = C_{4v}$ is 8. Using Eq. 4.33, we will see if any of the irreps gives multidimensional co-representations.

$$\begin{aligned}\frac{1}{8}\sum_{\substack{R'\in F'\\ \mathbf{R}'\mathbf{k}\equiv-\mathbf{k}\\ R'^2\in\bar{\mathcal{G}}^{\mathbf{k}}}}\chi_{M_1}(\{R'_i|\mathbf{v}'_i\}^2) &= \frac{1}{8}\big(\chi_{M_1}(\{E|\mathbf{0}\}^2) + \chi_{M_1}(\{C_4|\mathbf{0}\}^2) + \chi_{M_1}(\{C_2|\mathbf{0}\}^2) + \chi_{M_1}(\{C_4^3|\mathbf{0}\}^2 + \chi_{M_1}(\{\sigma_{10}|\mathbf{t}_1/2+\mathbf{t}_2/2\}^2)\\ &\quad + \chi_{M_1}(\{\sigma_{01}|\mathbf{t}_1/2+\mathbf{t}_2/2\}^2) + \chi_{M_1}(\{\sigma_{1\bar{1}}|\mathbf{t}_1/2+\mathbf{t}_2/2\}^2) + \chi_{M_1}(\{\sigma_{11}|\mathbf{t}_1/2+\mathbf{t}_2/2\}^2)\big)\\ &= \frac{1}{8}\big(2\chi_{M_1}(\{E|\mathbf{0}\}) + 2\chi_{M_1}(\{C_2|\mathbf{0}\}) + \chi_{M_1}(\{E|\mathbf{t}_2\}) + \chi_{M_1}(\{E|\mathbf{t}_1\})\\ &\quad + \chi_{M_1}(\{E|\mathbf{t}_1+\mathbf{t}_2\}) + \chi_{M_1}(\{E|0\})\big)\\ &= \frac{1}{8}(2\times 1 + 2\times(-1) + (-1) + (-1) + 1 + 1) = 0\end{aligned} \tag{4.36a}$$

$$\begin{aligned}\frac{1}{8}\sum_{\substack{R'\in F'\\ \mathbf{R}'\mathbf{k}\equiv-\mathbf{k}\\ R'^2\in\bar{\mathcal{G}}^{\mathbf{k}}}}\chi_{M_2}(\{R'_i|\mathbf{v}'_i\}^2) &= \frac{1}{8}\big(\chi_{M_2}(\{E|\mathbf{0}\}^2) + \chi_{M_2}(\{C_4|\mathbf{0}\}^2) + \chi_{M_2}(\{C_2|\mathbf{0}\}^2) + \chi_{M_2}(\{C_4^3|\mathbf{0}\}^2 + \chi_{M_2}(\{\sigma_{10}|\mathbf{t}_1/2+\mathbf{t}_2/2\}^2)\\ &\quad + \chi_{M_2}(\{\sigma_{01}|\mathbf{t}_1/2+\mathbf{t}_2/2\}^2) + \chi_{M_2}(\{\sigma_{1\bar{1}}|\mathbf{t}_1/2+\mathbf{t}_2/2\}^2) + \chi_{M_2}(\{\sigma_{11}|\mathbf{t}_1/2+\mathbf{t}_2/2\}^2)\big)\\ &= \frac{1}{8}\big(2\chi_{M_2}(\{E|\mathbf{0}\}) + 2\chi_{M_2}(\{C_2|\mathbf{0}\}) + \chi_{M_2}(\{E|\mathbf{t}_2\}) + \chi_{M_2}(\{E|\mathbf{t}_1\})\\ &\quad + \chi_{M_2}(\{E|\mathbf{t}_1+\mathbf{t}_2\}) + \chi_{M_2}(\{E|0\})\big)\\ &= \frac{1}{8}(2\times 1 + 2\times(-1) + (-1) + (-1) + 1 + 1) = 0\end{aligned} \tag{4.36b}$$

$$\begin{aligned}\frac{1}{8}\sum_{\substack{R'\in F'\\ \mathbf{R}'\mathbf{k}\equiv-\mathbf{k}\\ R'^2\in\bar{\mathcal{G}}^{\mathbf{k}}}}\chi_{M_3}(\{R'_i|\mathbf{v}'_i\}^2) &= \frac{1}{8}\big(\chi_{M_3}(\{E|\mathbf{0}\}^2) + \chi_{M_3}(\{C_4|\mathbf{0}\}^2) + \chi_{M_3}(\{C_2|\mathbf{0}\}^2) + \chi_{M_3}(\{C_4^3|\mathbf{0}\}^2 + \chi_{M_3}(\{\sigma_{10}|\mathbf{t}_1/2+\mathbf{t}_2/2\}^2)\\ &\quad + \chi_{M_3}(\{\sigma_{01}|\mathbf{t}_1/2+\mathbf{t}_2/2\}^2) + \chi_{M_3}(\{\sigma_{1\bar{1}}|\mathbf{t}_1/2+\mathbf{t}_2/2\}^2) + \chi_{M_3}(\{\sigma_{11}|\mathbf{t}_1/2+\mathbf{t}_2/2\}^2)\big)\\ &= \frac{1}{8}\big(2\chi_{M_3}(\{E|\mathbf{0}\}) + 2\chi_{M_3}(\{C_2|\mathbf{0}\}) + \chi_{M_3}(\{E|\mathbf{t}_2\}) + \chi_{M_3}(\{E|\mathbf{t}_1\})\\ &\quad + \chi_{M_3}(\{E|\mathbf{t}_1+\mathbf{t}_2\}) + \chi_{M_3}(\{E|0\})\big)\\ &= \frac{1}{8}(2\times 1 + 2\times(-1) + (-1) + (-1) + 1 + 1) = 0\end{aligned} \tag{4.36c}$$

$$\frac{1}{8}\sum_{\substack{R'\in F'\\ \mathbf{R}'\mathbf{k}\equiv-\mathbf{k}\\ R'^2\in\bar{\mathcal{G}}^{\mathbf{k}}}}\chi_{M_4}(\{R'_i|\mathbf{v}'_i\}^2)=\frac{1}{8}\big(\chi_{M_4}(\{E|\mathbf{0}\}^2)+\chi_{M_4}(\{C_4|\mathbf{0}\}^2)+\chi_{M_4}(\{C_2|\mathbf{0}\}^2)+\chi_{M_4}(\{C_4^3|\mathbf{0}\}^2+\chi_{M_4}(\{\sigma_{10}|\mathbf{t}_1/2+\mathbf{t}_2/2\}^2)$$

$$+\chi_{M_4}(\{\sigma_{01}|\mathbf{t}_1/2+\mathbf{t}_2/2\}^2)+\chi_{M_4}(\{\sigma_{1\bar{1}}|\mathbf{t}_1/2+\mathbf{t}_2/2\}^2)+\chi_{M_4}(\{\sigma_{11}|\mathbf{t}_1/2+\mathbf{t}_2/2\}^2)\big)$$

$$=\frac{1}{8}\big(2\chi_{M_4}(\{E|\mathbf{0}\})+2\chi_{M_4}(\{C_2|\mathbf{0}\})+\chi_{M_4}(\{E|\mathbf{t}_2\})+\chi_{M_4}(\{E|\mathbf{t}_1\})$$

$$+\chi_{M_4}(\{E|\mathbf{t}_1+\mathbf{t}_4\})+\chi_{M_4}(\{E|0\})\big)$$

$$=\frac{1}{8}(2\times1+2\times(-1)+(-1)+(-1)+1+1)=0 \tag{4.36d}$$

$$\frac{1}{8}\sum_{\substack{R'\in F'\\ \mathbf{R}'\mathbf{k}\equiv-\mathbf{k}\\ R'^2\in\bar{\mathcal{G}}^{\mathbf{k}}}}\chi_{M_5}(\{R'_i|\mathbf{v}'_i\}^2)=\frac{1}{8}\big(\chi_{M_5}(\{E|\mathbf{0}\}^2)+\chi_{M_5}(\{C_4|\mathbf{0}\}^2)+\chi_{M_5}(\{C_2|\mathbf{0}\}^2)+\chi_{M_5}(\{C_4^3|\mathbf{0}\}^2+\chi_{M_5}(\{\sigma_{10}|\mathbf{t}_1/2+\mathbf{t}_2/2\}^2)$$

$$+\chi_{M_5}(\{\sigma_{01}|\mathbf{t}_1/2+\mathbf{t}_2/2\}^2)+\chi_{M_5}(\{\sigma_{1\bar{1}}|\mathbf{t}_1/2+\mathbf{t}_2/2\}^2)+\chi_{M_5}(\{\sigma_{11}|\mathbf{t}_1/2+\mathbf{t}_2/2\}^2)\big)$$

$$=\frac{1}{8}\big(2\chi_{M_5}(\{E|\mathbf{0}\})+2\chi_{M_5}(\{C_2|\mathbf{0}\})+\chi_{M_5}(\{E|\mathbf{t}_2\})+\chi_{M_5}(\{E|\mathbf{t}_1\})$$

$$+\chi_{M_5}(\{E|\mathbf{t}_1+\mathbf{t}_2\})+\chi_{M_5}(\{E|0\})\big)$$

$$=\frac{1}{8}(2\times2+2\times2+2\times(-1)+2\times(-1)+2\times1+2\times1)=1 \tag{4.36e}$$

Therefore, the co-representation induced from M_5 of $p4gm$ belongs to case 1.(i) and the dimension of the co-representations obtained from this irrep is 2. However, the co-representations induced from M_1, M_2, M_3 and M_4 of $p4$ belong to case 2. This means that irreps $M_1 \not\equiv \bar{M}_1$, $M_2 \not\equiv \bar{M}_2$, $M_3 \not\equiv \bar{M}_3$ and $M_4 \not\equiv \bar{M}_4$. However, $\bar{M}_1$, $\bar{M}_2$, $\bar{M}_3$ and $\bar{M}_4$ are also irreps of little group G^M. Now, it requires a little more work to find which of $\bar{M}_1$, $\bar{M}_2$, $\bar{M}_3$ and $\bar{M}_4$ is equivalent to which of M_1, M_2, M_3 and M_4. This we do in the next paragraph.

Since (i) $\Theta\tilde{u}_{\mathbf{k}}(\mathbf{x}) = \Theta(\hat{u}_{\mathbf{k}}(\mathbf{x})e^{i\mathbf{k}\cdot\mathbf{x}}) = \hat{u}^*_{\mathbf{k}}(\mathbf{x})e^{-i\mathbf{k}\cdot\mathbf{x}}$, (ii) $\hat{u}^*_{\mathbf{k}}(\mathbf{x})e^{-i\mathbf{k}\cdot\mathbf{x}}$ is a Bloch function with wave vector $-\mathbf{k}$, (iii) for $\mathbf{k} = (\mathbf{K}_1 + \mathbf{K}_2)/2$, $\mathbf{k} \equiv -\mathbf{k}$, the operator Θ transforms one Bloch function at point M to another Bloch function at the same point. Moreover, $[\tilde{H}, \Theta] = 0$, the Hamiltonian restricted to eigenfunctions at wave vector $\mathbf{k} = (\mathbf{K}_1 + \mathbf{K}_2)/2$ (we will be denoting that as $\tilde{H}|_M$) has Θ as

one of its symmetries. More succinctly, $[\tilde{H}|_M, \Theta] = 0$. Clearly, the space group symmetry of this Hamiltonian $\tilde{H}|_M$ is the little group G^M of the total Hamiltonian $\tilde{H}$. The magnetic group associated with $\tilde{H}|_M$ is $M = G^M + \Theta G^M$. Recall that the matrices $\mathbf{\Gamma}_{\bar{\rho}}$ corresponding to irrep $\bar{\rho}$ are related to the matrices $\mathbf{\Gamma}_{\rho}$ corresponding to irrep ρ by the relation $\mathbf{\Gamma}_{\bar{\rho}}(a) = \mathbf{\Gamma}^*_{\rho}(r^{-1}ar)$ and $r = \Theta$. This means that $\mathbf{\Gamma}_{\bar{M}_1}(\{C_4|\mathbf{0}\}) = \mathbf{\Gamma}^*_{M_1}(\Theta^{-1}\{C_4|\mathbf{0}\}\Theta) = \mathbf{\Gamma}^*_{M_1}(\{C_4|\mathbf{0}\}) = (+i)^* = -i$, where we used that fact that the element Θ commutes with any spatial symmetry element. Similarly, $\mathbf{\Gamma}_{\bar{M}_1}(\{C_4^3|\mathbf{0}\}) = \mathbf{\Gamma}^*_{M_1}(\{C_4^3|\mathbf{0}\}) = (-i)^* = +i$, $\mathbf{\Gamma}_{\bar{M}_1}(\{\sigma_{01}|(\mathbf{t}_1+\mathbf{t}_2)/2\}) = \mathbf{\Gamma}^*_{M_1}(\{\sigma_{01}|(\mathbf{t}_1+\mathbf{t}_2)/2\}) = (-i)^* = +i$, $\mathbf{\Gamma}_{\bar{M}_1}(\{\sigma_{10}|(\mathbf{t}_1+\mathbf{t}_2)/2\}) = \mathbf{\Gamma}^*_{M_1}(\{\sigma_{10}|(\mathbf{t}_1+\mathbf{t}_2)/2\}) = (+i)^* = -i$, $\mathbf{\Gamma}_{\bar{M}_1}(\{\sigma_{1\bar{1}}|(\mathbf{t}_1+\mathbf{t}_2)/2\}) = \mathbf{\Gamma}^*_{M_1}(\{\sigma_{1\bar{1}}|(\mathbf{t}_1+\mathbf{t}_2)/2\}) = (-1)^* = -1$, $\mathbf{\Gamma}_{\bar{M}_1}(\{\sigma_{11}|(\mathbf{t}_1+\mathbf{t}_2)/2\}) = \mathbf{\Gamma}^*_{M_1}(\{\sigma_{11}|(\mathbf{t}_1+\mathbf{t}_2)/2\}) = (+1)^* = +1$, $\mathbf{\Gamma}_{\bar{M}_1}(\{E|m\mathbf{t}_1+n\mathbf{t}_2\}) = \mathbf{\Gamma}^*_{M_1}(\{E|m\mathbf{t}_1+n\mathbf{t}_2\}) = (\exp(-i\pi(m+n)))^* = \exp(i\pi(m+n)) = \exp(-i\pi(m+n))$. Therefore, $\bar{M}_1 = M_2$. Also, $\mathbf{\Gamma}_{\bar{M}_3}(\{C_4|\mathbf{0}\}) = \mathbf{\Gamma}^*_{M_3}(\{C_4|\mathbf{0}\}) = (-i)^* = +i$, $\mathbf{\Gamma}_{\bar{M}_3}(\{C_4^3|\mathbf{0}\}) = \mathbf{\Gamma}^*_{M_3}(\{C_4^3|\mathbf{0}\}) = (+i)^* = -i$, $\mathbf{\Gamma}_{\bar{M}_3}(\{\sigma_{01}|(\mathbf{t}_1+\mathbf{t}_2)/2\}) = \mathbf{\Gamma}^*_{M_3}(\{\sigma_{01}|(\mathbf{t}_1+\mathbf{t}_2)/2\}) = (-i)^* = +i$, $\mathbf{\Gamma}_{\bar{M}_3}(\{\sigma_{10}|(\mathbf{t}_1+\mathbf{t}_2)/2\}) = \mathbf{\Gamma}^*_{M_3}(\{\sigma_{10}|(\mathbf{t}_1+\mathbf{t}_2)/2\}) = (+i)^* = -i$, $\mathbf{\Gamma}_{\bar{M}_3}(\{\sigma_{1\bar{1}}|(\mathbf{t}_1+\mathbf{t}_2)/2\}) = \mathbf{\Gamma}^*_{M_3}(\{\sigma_{1\bar{1}}|(\mathbf{t}_1+\mathbf{t}_2)/2\}) = (+1)^* = +1$, $\mathbf{\Gamma}_{\bar{M}_3}(\{\sigma_{11}|(\mathbf{t}_1+\mathbf{t}_2)/2\}) = \mathbf{\Gamma}^*_{M_3}(\{\sigma_{11}|(\mathbf{t}_1+\mathbf{t}_2)/2\}) = (-1)^* = -1$, $\mathbf{\Gamma}_{\bar{M}_3}(\{E|m\mathbf{t}_1+n\mathbf{t}_2\}) = \mathbf{\Gamma}^*_{M_3}(\{E|m\mathbf{t}_1+n\mathbf{t}_2\}) = (\exp(-i\pi(m+n)))^* = \exp(i\pi(m+n)) = \exp(-i\pi(m+n))$. Therefore, $\bar{M}_1 = M_2$. Hence, $\bar{M}_3 = M_4$. Therefore, M_1 and M_2 of little group G^M of space group $p4gm$ together make a 2 dimensional co-representation. We saw in our discussion about the eigenfunctions $\tilde{u}^{(3)}_M$ and $\tilde{u}^{(4)}_M$ in Fig. 4.5(b) in the previous section that they belong to M_1 or M_2, but could not explain the degeneracy between band 3 and 4. Since the irreps M_1 and M_2 together make the 2-dimensional co-representation of the magnetic group, we see degeneracy between bands 3 and 4 at the M point in the band structure of Fig. 4.5(b).

Z: We have seen in Table 4.28 that there are 2 irreps. Moreover, the number of elements in the little co-group $\bar{G}^Z = C_{1v} = \{E, \sigma_{10}\}$ is 2. Using Eq. 4.33, we will see if any of the irreps gives multidimensional co-representations.

$$\begin{aligned}
\frac{1}{2}\sum_{\substack{R'\in F'\\ \mathbf{R}'\mathbf{k}\equiv-\mathbf{k}\\ R'^2\in\bar{\mathcal{G}}^{\mathbf{k}}}} \chi_{Z_1}(\{R'_i|\mathbf{v}'_i\}^2) &= \frac{1}{2}\left(\chi_{Z_1}(\{C_2|\mathbf{0}\}^2) + \chi_{Z_1}(\{\sigma_{01}|(\mathbf{t}_1+\mathbf{t}_2)/2\}^2)\right)\\
&= \frac{1}{2}\left(\chi_{Z_1}(\{E|\mathbf{0}\}) + \chi_{Z_1}(\{E|\mathbf{t}_1\})\right) = \frac{1}{2}(1+\exp(-i\pi)) = 0\\
\frac{1}{2}\sum_{\substack{R'\in F'\\ \mathbf{R}'\mathbf{k}\equiv-\mathbf{k}\\ R'^2\in\bar{\mathcal{G}}^{\mathbf{k}}}} \chi_{Z_2}(\{R'_i|\mathbf{v}'_i\}^2) &= \frac{1}{2}\left(\chi_{Z_2}(\{C_2|\mathbf{0}\}^2) + \chi_{Z_2}(\{\sigma_{01}|(\mathbf{t}_1+\mathbf{t}_2)/2\}^2)\right)\\
&= \frac{1}{2}\left(\chi_{Z_2}(\{E|\mathbf{0}\}) + \chi_{Z_2}(\{E|\mathbf{t}_1\})\right) = \frac{1}{2}(1+\exp(-i\pi)) = 0.
\end{aligned} \tag{4.37}$$

This means $\bar{Z}_1 \not\equiv Z_1$ and $\bar{Z}_2 \not\equiv Z_2$. Since, $\bar{Z}_1$ and $\bar{Z}_2$ are also irreps of little group G^Z, it must be that $\bar{Z}_1 = Z_2$ and $\bar{Z}_2 = Z_1$. To see this concretely, we note that the operator Θ transforms a Bloch function at wave vector $\mathbf{k}$ to a Bloch function at $-\mathbf{k}$ (as we saw in the discussion on the M in the previous subparagraph). However, the spatial operator $\{C_2|\mathbf{0}\} \in G = p4gm$ also transforms a Bloch function at wave vector $\mathbf{k}$ to a Bloch function $-\mathbf{k}$. Therefore, the composite operator $\Theta\{C_2|\mathbf{0}\}$ transforms a Bloch function at wave vector $\mathbf{k}$ to a Bloch function at wave vector $\mathbf{k}$. Since both Θ and $\{C_2|\mathbf{0}\}$ are symmetries of the hamiltonian $\tilde{H}$, the composite operator $\Theta\{C_2|\mathbf{0}\}$ is also a symmetry of $\tilde{H}$. Then, the Hamiltonian restricted to eigenfunctions at point Z ($\tilde{H}|_Z$) has the antiunitary operator $\Theta\{C_2|\mathbf{0}\}$ as its symmetry. The space group symmetry of $\tilde{H}|_Z$ is clearly the little group $G^Z = \{E|\mathbf{0}\}T + \{\sigma_{10}|(\mathbf{t}_1+\mathbf{t}_2)/2\}T$ of the total Hamiltonian $\tilde{H}$. The magnetic space group associated with $\tilde{H}|_Z$ is $M = G^Z + \Theta\{C_2|\mathbf{0}\}G^Z$. Recall that the matrices $\mathbf{\Gamma}_{\bar{\rho}}$ corresponding to irrep $\bar{\rho}$ are related to the matrices $\mathbf{\Gamma}_\rho$ corresponding to irrep ρ by the relation $\mathbf{\Gamma}_{\bar{\rho}}(a) = \mathbf{\Gamma}^*_\rho(r^{-1}ar)$ and $r = \Theta$. This means that $\mathbf{\Gamma}_{\bar{Z}_1}(\{\sigma_{10}|(\mathbf{t}_1+\mathbf{t}_2)/2\}) = \mathbf{\Gamma}^*_{Z_1}(\{C_2|\mathbf{0}\}^{-1}\Theta^{-1}\{\sigma_{10}|(\mathbf{t}_1+\mathbf{t}_2)/2\}\Theta\{C_2|\mathbf{0}\}) =$

$\mathbf{\Gamma}^*_{Z_1}(\{C_2|\mathbf{0}\}\{\sigma_{10}|(\mathbf{t}_1+\mathbf{t}_2)/2\}\{C_2|\mathbf{0}\}) = \mathbf{\Gamma}^*_{Z_1}(\{\sigma_{01}|-(\mathbf{t}_1+\mathbf{t}_2)/2\}\{C_2|\mathbf{0}\}) = \mathbf{\Gamma}^*_{Z_1}(\{\sigma_{10}|-(\mathbf{t}_1+\mathbf{t}_2)/2\}) = \mathbf{\Gamma}^*_{Z_1}(\{\sigma_{10}|(\mathbf{t}_1+\mathbf{t}_2)/2\})\mathbf{\Gamma}^*_{Z_1}(\{E|-(\mathbf{t}_1+\mathbf{t}_2)\}) = \exp(+iu\pi)\exp(-i\pi(1+2u)) = -\exp(-iu\pi)$, where we used that fact that the element Θ commutes with any spatial symmetry element and the fact the irrep matrices $\mathbf{\Gamma}_{Z_1}$ satisfy homomorphism. Similarly, $\mathbf{\Gamma}_{\bar{Z}_1}(\{E|m\mathbf{t}_1+n\mathbf{t}_2\}) = \mathbf{\Gamma}^*_{Z_1}(\{C_2|\mathbf{0}\}^{-1}\Theta^{-1}\{E|m\mathbf{t}_1+n\mathbf{t}_2\}\Theta\{C_2|\mathbf{0}\}) = \mathbf{\Gamma}^*_{Z_1}(\{C_2|\mathbf{0}\}\{E|m\mathbf{t}_1+n\mathbf{t}_2\}\{C_2|\mathbf{0}\}) = \mathbf{\Gamma}^*_{Z_1}(\{E|-m\mathbf{t}_1-n\mathbf{t}_2\}) = \exp(-i\pi(m+2un))$. These imply that $\bar{Z}_1 = Z_2$. Since there are only two irreps of G^Z and together they form a 2 dimensional co-representation, all bands at points Z are doubly degenerate as can be seen in the band structure in Fig. 4.5(b).

4.4 Conclusion

This chapter is a tutorial for the group theoretic characterization of symmetry protected degeneracies in the band structures of elastic systems. In particular, it explains how to obtain the irreducible representations of the symmetry groups at different points of the Brillouin zones corresponding to different space groups. If there exists a multidimensional irrep at a wave vector, there will be symmetry protected degeneracies at that point in the Brillouin zone. When some of the symmetries are broken due to structural alterations, and if the new symmetry group does not have a multidimensional irrep at the point in Brillouin zone under consideration, the degeneracy will be lifted creating a band gap at that point. To help the reader get familiar with the theory, we give examples of different space groups showing how going from higher to lower symmetry group may create band gaps.

In addition to being important for designing tunable band gap elastic metamaterials, symmetry characterization of frequency bands in elastic systems is also important for designing topological metamaterials [147, 148, 149, 150, 151, 152, 153, 154, 155, 156, 157], which, being able to transport at their boundary wave without scat-

tering from defects, are important for waveguides [158], acoustic antenna [159], delay lines [160], etc. It has been shown that if a set of bands of a periodic system with certain space group symmetry have certain irrep labels at the high symmetry points in the Brillouin zone, those bands are topological [161, 162, 163]. This article will help researchers interested in this field get acquainted with the concepts of representation theory which may help them designing topological mechanical systems.

Chapter 5

Statistical mechanics of nanotubes

Here we investigate the statistical mechanics of thin single-walled nanotubes at low temperatures within shallow shell approximation [164, 165, 166]. Due to the presence of the curvature in nanotubes, the radial fluctuations along the axial direction costs both bending and stretching energy, whereas the radial fluctuations along the circumferential direction only costs bending energy. This competition between stretching and bending costs associated with height fluctuations introduces a characteristic elastic length scale ($\ell_{\rm el} \sim \sqrt{Rt}$) [107, 167], which is proportional to the geometric mean of the radius and effective thickness. In typical carbon naotubes, this length is $\ell_{\rm el} \lesssim 3$nm. We show that below this length, the bending rigidity and in-plane stiffness constants scales the same way as for flat membranes mentioned above. As will be discussed in detail in this article, beyond the elastic length scale, the in-plane elastic constants stop renormalizing in the axial direction, while they continue to renormalize in the circumferential direction beyond the elastic length scale albeit with different universal exponents. The bending rigidity, however, stops renormalizing in the circumferential direction at the elastic length scale. We verify our theoretical findings with molecular dynamics simulations.

5.1 Elastic energy of deformation

The elastic energy of a deformed cylindrical shell can be estimated with shallow shell theory. To this end, let us consider a cylindrical shell with radius R and length L in its undeformed configuration. [1] Then, any point on the undeformed shell can be written as $\bar{\mathbf{X}} = (R\cos\varphi, R\sin\varphi, z)$ in cartesian coordinates where the axis of the cylinder is in the z direction. Since the radius R is a constant, the shell can be parametrized by $(R\varphi, z)$ coordinates. The tangent vectors at any point on the shell can be written as $\bar{\mathbf{t}}_\varphi = \partial_\varphi \bar{\mathbf{X}} = (-\sin\varphi, \cos\varphi, 0)$ and $\bar{\mathbf{t}}_z = \partial_z \bar{\mathbf{X}} = (0, 0, 1)$, whereas the normal is $\bar{\mathbf{N}} = (\cos\varphi, \sin\varphi, 0)$. Note that here we used short-hands $\partial_\varphi \equiv \frac{1}{R}\frac{\partial}{\partial\varphi}$ and $\partial_z \equiv \frac{\partial}{\partial z}$. The reference metric is $\bar{g}_{ij} = \bar{\mathbf{t}}_i \cdot \bar{\mathbf{t}}_j = \delta_{ij}$ and curvature tensor is $\bar{b}_{ij} = \bar{\mathbf{N}} \cdot \partial_i \bar{\mathbf{t}}_j = -\frac{1}{R}\delta_{ij}\delta_{i\varphi}$ where $i \in \{\phi, z\}$. Then, in the deformed configuration, the displacement of each point can be decomposed into tangential components $u_i(R\varphi, z)$ (where $i \in \{\varphi, z\}$) and radial component $h(R\varphi, z)$ (see Fig. 5.1(a)) such that the coordinates of the points in deformed configuration are given by $\mathbf{X} = \bar{\mathbf{X}} + \mathbf{u}_\varphi \bar{\mathbf{t}}_\varphi + \mathbf{u}_z \bar{\mathbf{t}}_z + h\bar{\mathbf{N}}$. The tangent vectors in the deformed configuration are $\mathbf{t}_\varphi = \partial_\varphi \mathbf{X} = \bar{\mathbf{t}}_\varphi + \bar{\mathbf{t}}_\varphi \partial_\varphi u_\varphi - \frac{1}{R}u_\varphi \bar{\mathbf{N}} + \bar{\mathbf{t}}_z \partial_\varphi u_z + \bar{\mathbf{N}}\partial_\varphi h + \frac{1}{R}h\bar{\mathbf{t}}_\varphi$ and $\mathbf{t}_z = \partial_z \bar{\mathbf{X}} = \bar{\mathbf{t}}_z + \bar{\mathbf{t}}_\varphi \partial_z \mathbf{u}_\varphi + \bar{\mathbf{t}}_z \partial_z \mathbf{u}_z + \bar{\mathbf{N}}\partial_z h$. Then, the metric and the curvature tensors in the deformed configuration are:

$$\begin{aligned} g_{ij} &\approx \delta_{ij} + \partial_i u_j + \partial_j u_i + (\partial_i h)(\partial_j h) + \frac{2}{R} h \delta_{ij}\delta_{i\varphi}, \\ b_{ij} &\approx -\frac{1}{R}\delta_{ij}\delta_{i\varphi} + \partial_i \partial_j h, \end{aligned} \tag{5.1}$$

where we only kept only the relevant terms (in the sense of Wilsonian renormalization [168]) in displacements and their derivatives. This is the Donnell-Mushtari-Vlasov approximation [165, 164, 166]. The in-plane strain and bending strain tensors are defined as $u_{ij} \equiv (g_{ij} - \bar{g}_{ij})/2$ and $K_{ij} \equiv (b_{ij} - \bar{b}_{ij})$, respectively [164]. Then, from

[1] In principle, a cylindrical shell should have different inner and outer radii since it can have finite thickness, for atomatically thin nanotubes thickness is not defined. However, as we will see later, an effective thickness can be defined in terms of its bending rigidity and in-plane stiffness constants.

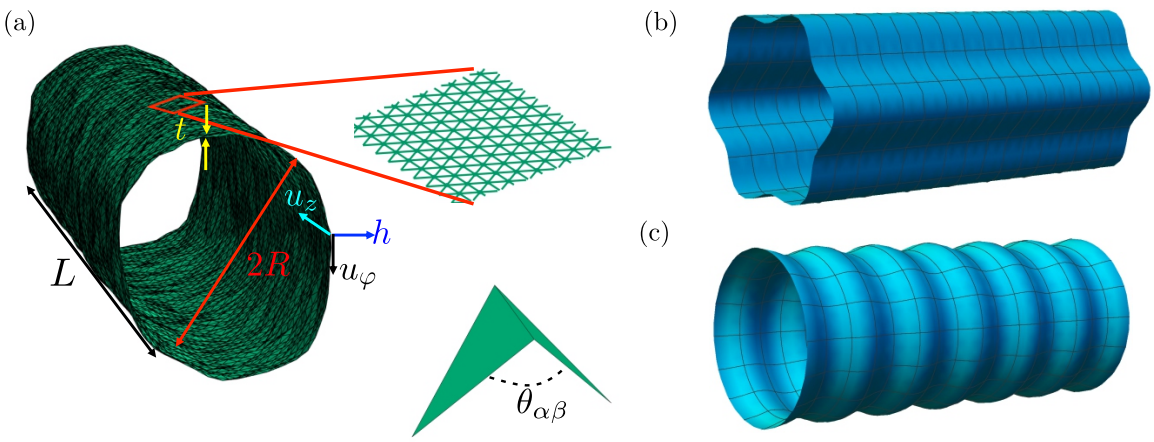

Figure 5.1: (a) A snaphot of a thermally fluctuating cylindrical shell. The length L, diameter $2R$, thickness t, in-plane displacements u_φ and u_z, radial displacement h are shown. A small segment (shown in red box) on the shell is zoomed in to show that in simulations, the shell is modeled with triangular lattice of point masses connected by harmonic springs (green lines). At bottom right corner, the angle $\theta_{\alpha\beta}$ between two adjacent triangles of the triangular lattice is shown. (b) A deformed cylindrical shell with only nonzero $\tilde{h}(q_\varphi \neq 0, q_z = 0)$ and $\tilde{h}(q_\varphi = 0, q_z = 0)$ does not cost stretching energy if the change in the length of circumference due to $\tilde{h}(q_\varphi \neq 0, q_z = 0)$ is compensated by $\tilde{h}(q_\varphi = 0, q_z = 0)$. (c) A deformed cylindrical shell with nonzero $\tilde{h}(q_\varphi = 0, q_z \neq 0)$ and $\tilde{h}(q_\varphi = 0, q_z = 0)$ costs stretching energy different positions along the axis of the cylindrical shell have different circumference length.

Eq. 5.1, we find

$$\begin{aligned} u_{ij} &= (\partial_i u_j + \partial_j u_i + \partial_i h \partial_j h)/2 + \frac{h}{R}\delta_{ij}\delta_{i\varphi}, \\ K_{ij} &= \partial_i \partial_j h, \end{aligned} \tag{5.2}$$

where $i, j \in \{\varphi, z\}$. Notice that first term inside the parenthesis in the expression of in-plane strain u_{ij} is the same as in flat sheets. However, the second term is new, and it shows the coupling between in-plane strains and radial undulation field h due to curvature $1/R$. The free energy cost of the shell deformation is given by:

$$F = \int_A dA \frac{1}{2}\left[\kappa_0 (K_{ii})^2 + \lambda_0 (u_{ii})^2 + 2\mu_0 (u_{ij})^2\right], \tag{5.3}$$

where the first term accounts for the bending energy and the last two terms are the in-plane stretching energy. Note that we did not consider the term consisting of the Gaussian curvature because we are interested in periodic boundary condition, where the integral of the Gaussian curvature is zero due Gauss-Bonnet theorem. Here, κ_0 is the microscopic (bare) bending rigidity of the material and has the dimension of energy, whereas λ_0 and μ_0 are the microscopic (bare) Lamé coefficients and has the dimension of energy per area, $dA = d\varphi dz R$ is infinitesimal area element, $A = 2\pi RL$, ds is the infinitesimal line element at the boundary, ∂A is the boundary of the cylinder, $\mathbf{T}$ is the traction force at the boundary. The components of the traction force can be written as $T_i = n_j \sigma_{ij}$ where σ_{ij} is the homogeneous stress tensor and n_j is the in-plane normal to at the boundary. Replacing this expression of the traction force T_i and using Stokes' theorem we get:

$$\begin{aligned}\int_{\partial A} ds\, T_i u_i &= \int_{\partial A} ds\, n_j \sigma_{ij} u_i = \int_A dA \partial_j(\sigma_{ij} u_i) = \int_A dA \sigma_{ij} \partial_j u_i \\ &= \sigma_{ij} \int_A dA \frac{1}{2}(\partial_j u_i + \partial_i u_j), \\ F &= \int_A dA\, \frac{1}{2}\left[\kappa_0 (\nabla^2 h)^2 + \lambda_0 (u_{ii})^2 + 2\mu_0 (u_{ij})^2 - \sigma_{ij}(\partial_j u_i + \partial_i u_j)\right],\end{aligned} \tag{5.4}$$

where we used the facts that $\sigma_{ij} = \sigma_{ji}$ and $K_{ii} = \nabla^2 h$. Also, we assume that the microscopic material is isotropic which is reasonable for carbon nanotubes. However, inspection of the last term in the expression of u_{ij} in Eq. 5.2 shows that it is anisotropic. This means that as we integrate small wavelength degrees of freedom to investigate long wavelength behavior, the stiffness constants may become anisotropic. Keeping this in mind, we write the more general form of the free energy is given below:

$$F = \int_A dA\, \frac{1}{2}\left[B^0_{ijkl}(\partial_i \partial_j h)(\partial_k \partial_l h) + C^0_{ijkl} u_{ij} u_{kl} - \sigma_{ij}(\partial_j u_i + \partial_i u_j)\right], \tag{5.5}$$

where B^0_{ijkl} and C^0_{ijkl} are the most general bare bending rigidity and in-plane elastic tensors, respectively. However, because of the mirror planes $x - y$ and $r - z$, the

anisotropy can be at most orthorhombic, meaning that $B_{\varphi\varphi\varphi z} = B_{\varphi zzz} = C_{\varphi\varphi\varphi z} = C_{\varphi zzz} = 0$. This along with the major and minor symmetries of B_{ijkl} and C_{ijkl} tensors mean that the only independent constants are $B_{\varphi\varphi\varphi\varphi}$, $B_{\varphi\varphi zz}$, B_{zzzz}, $C_{\varphi\varphi\varphi\varphi}$, $C_{\varphi\varphi zz}$, $C_{\varphi z\varphi z}$ and C_{zzzz}. For isotropic bare rigidities, $B^0_{ijkl} = \kappa_0\delta_{ij}\delta_{kl}$ and $C^0_{ijkl} = \lambda_0\delta_{ij}\delta_{kl} + \mu_0(\delta_{ik}\delta_{jl} + \delta_{il}\delta_{jk})$.

5.2 Thermal fluctuations

The effect of thermal fluctuations can be seen in the correlation functions obtained from the functional integrals:

$$\langle h\rangle \equiv \langle h(\mathbf{x})\rangle = \frac{1}{Z}\int \mathcal{D}[u_i, h]h(\mathbf{x})e^{-F/k_BT}, \tag{5.6a}$$

$$G_{hh}(\mathbf{x}_2 - \mathbf{x}_1) \equiv \langle \delta h(\mathbf{x}_2)\delta h(\mathbf{x}_1)\rangle = \frac{1}{Z}\int \mathcal{D}[u_i, h]\delta h(\mathbf{x}_2)\delta h(\mathbf{x}_1)e^{-F/k_BT}, \tag{5.6b}$$

$$G_{u_iu_j}(\mathbf{x}_2 - \mathbf{x}_1) \equiv \langle u_i(\mathbf{x}_2)u_j(\mathbf{x}_1)\rangle = \frac{1}{Z}\int \mathcal{D}[u_i, h]u_i(\mathbf{x}_2)u_j(\mathbf{x}_1)e^{-F/k_BT}, \tag{5.6c}$$

$$Z = \int \mathcal{D}[u_i, h]e^{-F/k_BT}, \tag{5.6d}$$

where T is the temperature, k_B is the Boltzmann's constant, Z is the partition function, $\delta h(\mathbf{x}) = h(\mathbf{x}) - \langle h\rangle$, $\mathbf{x} \equiv (R\varphi, z)$, and in Eqs. 5.6a, 5.6b and 5.6c , we used the fact the system is translationally invariant.

In the following, we decompose the radial displacement field as $h(\mathbf{x}) = h_0 + \tilde{h}(\mathbf{x})$, where $h_0 = (1/A)\int dA\, h(\mathbf{x})$ is the homogeneous part of the undulation field, and $(1/A)\int dA\, \tilde{h}(\mathbf{x}) = 0$. Then, $\langle h_0\rangle = (1/A)\int dA\langle h(\mathbf{x})\rangle = \langle h\rangle$. With this knowledge then, $\delta h(\mathbf{x}) = \tilde{h}(\mathbf{x}) + h_0 - \langle h_0\rangle$. Similarly, the in-plane strain fields can be decomposed

into $u_{ij}(\mathbf{x}) = u^0_{ij} + \tilde{u}_{ij}(\mathbf{x})$. However, the homogeneous strain $u^0_{\varphi\varphi}$ and the zero mode of the radial fluctuation h_0 are related by $u^0_{\varphi\varphi} = h_0/R$ because increasing the length in azimuthal direction effectively increases the radius. Integrating out the homogeneous fields h_0 and u^0_{ij}, we obtain the following effective free energy:

$$\begin{aligned}
F_{\text{eff},1} &= -k_B T \ln\left(\int \mathcal{D}[u^0_{\varphi z}, h_0, u^0_{zz}] e^{-F/k_B T}\right) \\
&= \int_A dA\, \frac{1}{2}\left[B^0_{ijkl}(\partial_i\partial_j\tilde{h})(\partial_k\partial_l\tilde{h}) + C^0_{ijkl}\tilde{u}_{ij}\tilde{u}_{kl} + \sigma_{ij}(\partial_i\tilde{h})(\partial_j\tilde{h})\right] \\
&= F_0 + F_I, \\
F_0/A &= \int_A dA\, \frac{1}{2}\left[B^0_{ijkl}(\partial_i\partial_j\tilde{h})(\partial_k\partial_l\tilde{h}) + \frac{C^0_{\varphi\varphi\varphi\varphi}}{R^2}\tilde{h}^2 + \sigma_{ij}(\partial_i\tilde{h})(\partial_j\tilde{h})\right] \\
&\quad + \int_A dA\, \frac{1}{2}\left[C^0_{ijkl}(\partial_i\tilde{u}_j)(\partial_k\tilde{u}_l) + C^0_{ij\varphi\varphi}(\partial_i\tilde{u}_j)\frac{\tilde{h}}{R}\right], \\
F_I/A &= \int_A dA\, \frac{1}{2}\left[C^0_{ijkl}\partial_i\tilde{u}_j(\partial_k\tilde{h})(\partial_l\tilde{h}) + C^0_{\varphi\varphi kl}\frac{\tilde{h}}{R}(\partial_k\tilde{h})(\partial_l\tilde{h})\right] \\
&\quad + \int_A dA\, \frac{1}{8}C^0_{ijkl}(\partial_i\tilde{h})(\partial_j\tilde{h})(\partial_k\tilde{h})(\partial_l\tilde{h}),
\end{aligned} \tag{5.7}$$

where F_0 and F_I are the harmonic and anharmonic parts of the effective free energy $F_{\text{eff},1}$. A similar functional integral shows that the average radial and axial extensions are:

$$\frac{\langle h\rangle}{R} = \frac{\langle h_0\rangle}{R} = \frac{\sigma_{\varphi\varphi}}{Y^0_{\varphi\varphi}} - \frac{\nu^0_{\varphi\varphi}\sigma_{zz}}{Y^0_{\varphi\varphi}} - \frac{1}{2}\langle(\partial_\varphi\tilde{h})^2\rangle, \tag{5.8a}$$

$$\frac{\langle \Delta L\rangle}{L} = \langle u^0_{zz}\rangle = \frac{\sigma_{zz}}{Y^0_{zz}} - \frac{\nu^0_{zz}\sigma_{\varphi\varphi}}{Y^0_{zz}} - \frac{1}{2}\langle(\partial_z\tilde{h})^2\rangle, \tag{5.8b}$$

where $Y^0_{\varphi\varphi} = C_{\varphi\varphi\varphi\varphi} - C^2_{\varphi\varphi zz}/C_{zzzz}$ and $Y^0_{zz} = C_{zzzz} - C^2_{\varphi\varphi zz}/C_{\varphi\varphi\varphi\varphi}$ are the 2-dimensional Young's moduli in azimuthal and axial directions respectively, and $\nu_{\varphi\varphi} = C_{\varphi\varphi zz}/C_{zzzz}$ and $\nu_{zz} = C_{\varphi\varphi zz}/C_{\varphi\varphi\varphi\varphi}$ are the Poisson's ratios in azimuthal and axial directions respectively. For isotropic microscopic properties, $Y^0_{\varphi\varphi} = Y^0_{zz} = 4\mu_0(\lambda_0+\mu_0)/(\lambda_0+2\mu_0) \equiv Y_0$, and $\nu^0_{\varphi\varphi} = \nu^0_{zz} = \lambda_0/(\lambda_0+2\mu_0) \equiv \nu^0_{\text{iso}}$.

The last terms in Eqs. 5.8a and 5.8b are negative meaning that in absence of any normal stress ($\sigma_{\varphi\varphi} = \sigma_{zz} = 0$), the radius and the length of the cylindrical shell shrink under thermal fluctuations. This is because nonuniform radial fluctuations $\tilde{h}(\mathbf{x})$ at fixed radius would increase the integrated area, with a large stretching energy cost. The system prefers to wrinkle and shrink its radius to gain entropy while keeping the integrated area of the convoluted shell approximately constant.

For renormalization group calculations, it is sometimes helpful to integrate out the in-plane phonons completely and write an effective free energy as a functional of radial undulations:

$$
\begin{aligned}
F_{\text{eff}} &= -k_B T \ln\left(\int \mathcal{D}[u_\varphi, u_z] e^{-F_{\text{eff},1}/k_B T}\right) = F^0_{\text{eff}} + F^I_{\text{eff}},\\
F^0_{\text{eff}}/A &= \sum_{\mathbf{q}\neq\mathbf{0}} \frac{1}{2}\left[B^0_{ijkl} q_i q_j q_k q_l + \frac{N(C^0_{ijkl}) q_z^4}{R^2 D(C^0_{ijkl};\mathbf{q})} + \sigma_{ij} q_i q_j\right] \tilde{h}(\mathbf{q})\tilde{h}(-\mathbf{q}),\\
F^I_{\text{eff}}/A &= \sum_{\mathbf{q}_1+\mathbf{q}_2=-\mathbf{q}\neq\mathbf{0}} \frac{q_z^2}{2q^2}[q_{1i} P^T_{ij}(\mathbf{q}) q_{2j}] \frac{N(C^0_{ijkl}) q^4}{R D(C^0_{ijkl};\mathbf{q})} \tilde{h}(\mathbf{q})\tilde{h}(\mathbf{q}_1)\tilde{h}(\mathbf{q}_2)\\
&\quad + \sum_{\substack{\mathbf{q}_1+\mathbf{q}_2=\mathbf{q}\neq\mathbf{0}\\ \mathbf{q}_3+\mathbf{q}_4=-\mathbf{q}\neq\mathbf{0}}} \frac{1}{8}[q_{1i} P^T_{ij}(\mathbf{q}) q_{2j}][q_{3i} P^T_{ij}(\mathbf{q}) q_{4j}] \frac{N(C^0_{ijkl}) q^4}{D(C^0_{ijkl};\mathbf{q})} \tilde{h}(\mathbf{q}_1)\tilde{h}(\mathbf{q}_2)\tilde{h}(\mathbf{q}_3)\tilde{h}(\mathbf{q}_4),
\end{aligned}
\tag{5.9}
$$

$$
\begin{aligned}
N(C_{ijkl}) &= \det(C_{ijkl})/4 = C_{\varphi\varphi\varphi\varphi} C_{\varphi z\varphi z} C_{zzzz} - C^2_{\varphi\varphi zz} C_{\varphi z\varphi z},\\
D(C_{ijkl};\mathbf{q}) &= \det(C_{kilj} q_k q_l) = \frac{1}{2}(\varepsilon_{i_1 i_2}\varepsilon_{j_1 j_2} C_{k_1 i_1 l_1 j_1} C_{k_2 i_2 l_2 j_2} q_{k_1} q_{k_2} q_{l_1} q_{l_2})\\
&= C_{\varphi\varphi\varphi\varphi} C_{\varphi z\varphi z} q_\varphi^4 + (C_{\varphi\varphi\varphi\varphi} C_{zzzz} - 2C_{\varphi\varphi zz} C_{\varphi z\varphi z} - C^2_{\varphi\varphi zz}) q_\varphi^2 q_z^2\\
&\quad + C_{zzzz} C_{\varphi z\varphi z} q_z^4,
\end{aligned}
$$

where $P^T_{ij}(\mathbf{q}) = (\delta_{ij} - q_i q_j/q^2)$, ε_{ij} is the permutation symbol, and we took Fourier transform of the radial undulation field $\tilde{h}(\mathbf{q}) = \int_A (dA/A)\tilde{h}(\mathbf{x}) e^{-i\mathbf{q}\cdot\mathbf{x}}$. Note that in the isotropic case, $Nq^4/D(C^0_{ijkl};\mathbf{q}) = Y_0$. Note that F^0_{eff} and F^I_{eff} are the harmonic and anharmonic part of the effective free energy F_{eff}. Then, within harmonic approximation one can read off the Fourier transform $G^0_{hh}(\mathbf{q}) = \int_A (dA/A) G^0_{hh}(\mathbf{x}) e^{-i\mathbf{q}\cdot\mathbf{x}}$ of the

correlation function $G^0_{hh}(\mathbf{x})$ (the superscript "0" is for harmonic approximation):

$$G^0_{hh}(\mathbf{q}) \equiv \langle|\tilde{h}(\mathbf{q})|^2\rangle_0 = \frac{k_BT/A}{B^0_{ijkl}q_iq_jq_kq_l + \frac{N(C^0_{ijkl})q_z^4}{R^2D(C^0_{ijkl};\mathbf{q})} + \sigma_{ij}q_iq_j} \overset{\text{isotropic}}{=} \frac{k_BT/A}{\kappa_0 q^4 + \frac{Y_0q_z^4}{R^2q^4} + \sigma_{ij}q_iq_j}, \tag{5.10}$$

where $\langle\rangle_0$ is the harmonic average. The effect of the anharmonic terms is to replace the bare parameters B^0_{ijkl}, C^0_{ijkl} and σ_{ij} with scale dependent renormalized parameters $B^R_{ijkl}(\mathbf{q})$, $C^R_{ijkl}(\mathbf{q})$ and σ^R_{ij}:

$$G_{hh}(\mathbf{q}) \equiv \langle|\tilde{h}(\mathbf{q})|^2\rangle = \frac{k_BT/A}{B^R_{ijkl}(\mathbf{q})q_iq_jq_kq_l + \frac{N(C^R_{ijkl}(\mathbf{q}))q_z^4}{R^2D(C^R_{ijkl}(\mathbf{q});\mathbf{q})} + \sigma^R_{ij}q_iq_j}. \tag{5.11}$$

Before going into the details of renormalization, it is useful to gain some insights from the Green's function in Eq. 5.10. In the limit $R \to \infty$, it gives back the Green's function for isotropic sheets $G^{s,0}_{hh}(\mathbf{q}) = \frac{k_BT/A}{\kappa_0q^4+\sigma_{ij}q_iq_j}$. Because of the presence of anisotropic curvature in the cylindrical shell, we have, in the denominator, an extra direction dependent term $(Y_0q_z^4)/(R^2q^4)$ which suppresses the amplitude of the radial fluctuations in the axial direction. This because the Fourier modes of radial fluctuations which are in axial direction necessarily cost stretching energy along with bending energy, whereas the Fourier modes of radial fluctuations which are in azimuthal direction only cost bending energy (see Fig. 5.1(b) and (c)) [167]. Furthermore, setting external stresses to zero $\sigma_{ij} = 0$ and equating the two remaining terms in the denominator of Eq. 5.10, we obtain a characteristic wave vector:

$$q^0_{\text{el}} \equiv \frac{\pi}{\ell^0_{\text{el}}} = \left(\frac{Y_0}{\kappa_0R^2}\right)^{\frac{1}{4}} = \frac{\gamma^{\frac{1}{4}}}{R}, \tag{5.12}$$

where $\gamma = Y_0R^2/\kappa_0$ is the Föppl-von Karman number. In the theory of shallow shells, bending rigidity $\kappa_0 \sim Et^3$ and $Y_0 \sim Et$, where E is 3-dimensional Young's modulus

of the material and t is the thickness of shell. In atomically thin systems thickness is not well defined; however, we can define an effective thickness as $t \sim \sqrt{\kappa_0/Y_0}$ Then, the Föppl-von Karman number $\gamma \sim R^2/t^2$ meaning that the larger γ is, the larger the radius R is with respect to the thickness t. The length scale $\ell_{\rm el}^0$ obtained from this is what we will call the "elastic length scale." The superscript "0" is for harmonic approximation; we will see later that when we take renormalization of the parameters due to the anharmonic terms into account, the expression of $\ell_{\rm el}$ changes slightly. As we will see in the next section, the effect of the curvature on the renormalization of the material parameters is negligible for scales smaller the elastic length scale $\ell_{\rm el}$ and will be important at scales larger than this. Another important length scale that is important for both isotropic sheets and cylindrical shells comes from the form of the Green's function: $G^0_{hh} \sim \frac{k_BT}{A\kappa_0 q^4}$ when $\sigma_{ij} = 0$ and $q \gg q^0_{\rm el}$. Therefore, the largest amplitude of the radial (height in case of sheets) fluctuations occur when $q \sim 1/L$ and $A \sim L^2$ (where is the system size) giving largest amplitude of the radial fluctuation as $h_{\rm th} \sim L\sqrt{k_BT/\kappa_0} = L\tau^{1/2}$ ($\tau \equiv k_BT/\kappa_0$ is the nondimensional temperature). Anharmonic terms become important when this amplitude is of the order of the thickness $h_{\rm th} \sim t \sim \sqrt{\kappa_0/Y_0}$. This gives us a length $\ell_{\rm th} \sim \sqrt{\kappa_0^2/(k_BTY_0)}$ called thermal length scale [169] (we will get a better estimate of $\ell_{\rm th}$ later in Eq. 5.20). The effect of the anharmonic terms are only important when the system size is larger than the thermal length scale $\ell_{\rm th}$. These two length scales $\ell_{\rm th}$ and $\ell_{\rm el}$ divides the scales dependence of the material parameters into three regimes. We will be interested in the limit where $\ell_{\rm th} \ll \ell_{\rm el}$ because as we discussed above below $\ell_{\rm th}$ the anharmonic terms are not important the theory is trivial. Therefore, keeping this length smaller than other important length scales enables us to see all possible nontrivial scalings due to the anharmonic terms. We will comment on the other limit later. Also, we will be interested in zero external stress limit $\sigma_{ij} = 0$.

5.3 Renormalization group and scaling analysis

The effect of the anharmonic terms in Eq. 5.7 at a given scale $\ell^* \equiv \pi/q^*$ can be obtained by systematically integrating out all degrees of freedom on smaller scales (i.e., larger wave vectors). This can be done by splitting the displacement fields into pieces: $g_<(\mathbf{r}) = \sum_{|\mathbf{q}|<q^*} e^{i\mathbf{q}\cdot\mathbf{r}} g(\mathbf{q})$ and $g_>(\mathbf{r}) = \sum_{\Lambda>|\mathbf{q}|>q^*} e^{i\mathbf{q}\cdot\mathbf{r}} g(\mathbf{q})$, where $g \in \{\tilde{u}_i, \tilde{h}\}$ and $a \equiv \pi/\Lambda$ is a microscopic cutoff, and integrating out $g_>$ as

$$\begin{aligned} F_{\text{eff},1}(\ell^*) &= -k_B T \ln\left(\int \mathcal{D}[\tilde{u}_{i,>}, \tilde{h}_>] e^{-F_{\text{eff},1}/k_B T}\right), \\ F_{\text{eff}}(\ell^*) &= -k_B T \ln\left(\int \mathcal{D}[\tilde{h}_>] e^{-F_{\text{eff},1}/k_B T}\right). \end{aligned} \tag{5.13}$$

5.3.1 Scaling analysis for $\ell^* \ll \ell_{\text{el}}$

- $\ell^* \ll \ell_{\text{th}} \ll \ell^0_{\text{el}}$: we have $C^0_{\varphi\varphi\varphi\varphi}|\tilde{h}(\mathbf{q})|^2/R^2 \ll \kappa_0 (q^*)^4 |\tilde{h}(\mathbf{q})|^2$, meaning that we can ignore the term $C^0_{\varphi\varphi\varphi\varphi}\tilde{h}^2/R^2$ from Eq. 5.7, and similarly we can ignore the term $N(C^0_{ijkl})q_z^4/(R^2 D(C^0_{ijkl};\mathbf{q}))\tilde{h}(\mathbf{q})\tilde{h}(-\mathbf{q}) \sim Y_0 q_z^4/(R^2 q^4)\tilde{h}(\mathbf{q})\tilde{h}(-\mathbf{q})$ from Eq. 5.9. Since $\ell^* \ll \ell_{\text{th}}$, the anharmonic terms are not important as was discussed in the last section. Therefore, the effective harmonic free energy is

$$F_{\text{eff}}(\ell^*) = \sum_{\substack{\mathbf{q}\neq\mathbf{0} \\ q<q^*}} \frac{A}{2}\left[B^0_{ijkl} q_i q_j q_k q_l + \sigma_{ij} q_i q_j\right] = \sum_{\substack{\mathbf{q}\neq\mathbf{0} \\ q<q^*}} \frac{A}{2}\left[\kappa_0 q^4 + \sigma_{ij} q_i q_j\right] \tilde{h}(\mathbf{q})\tilde{h}(-\mathbf{q}). \tag{5.14}$$

This Free energy is isotropic and the material parameters remain the same as their bare values. The naïve (Gaussian or harmonic) dimensions of the quantities $\tilde{h}(\mathbf{q})$ and σ_{ij} requiring that $[F_{\text{eff}}] = 0$ and $[\kappa_0] = 0$ and expressing dimensionality in wave-vector units [170]:

$$[\tilde{h}(\mathbf{q})] = -1 = (D-4)/2 \equiv -\zeta_h, [\sigma_{ij}] = 2, \tag{5.15}$$

where $D = 2$ is the dimension of the system. The meaning of these dimensions is that under scale transformation $\mathbf{q} \to \mathbf{q}' = b\mathbf{q}$ or $\mathbf{x} \to \mathbf{x}' = b^{-1}\mathbf{x}$, if we transform $\tilde{h}(\mathbf{q}) \to \tilde{h}'(\mathbf{q}') = b^{[\tilde{h}(\mathbf{q})]}\tilde{h}(b\mathbf{q}) = b^{-1}\tilde{h}(b\mathbf{q})$ and $\sigma_{ij} \to \sigma'_{ij} = b^{[\sigma_{ij}]}\sigma_{ij} = b^2\sigma_{ij}$, the harmonic theory remain invariant. With these dimensions we go back to $F_{\text{eff},1}$ in Eq. 5.7 and find the naïve dimensions of the following quantities:

$$[C^0_{ijkl}] = 2 = 4 - D, [\tilde{u}_i] = -1 = D - 3 = 1 - 2\zeta_h, [1/R] = 1 = D/2. \quad (5.16)$$

This means that under scale transformation $\mathbf{q} \to \mathbf{q}' = b\mathbf{q}$, $C'^0_{ijkl} = b^{4-D}C^0_{ijkl}$ meaning as we zoom out of the system C'^0_{ijkl} grows for dimensions $D < 4$. Since C^0_{ijkl} are the coefficients of the anharmonic terms in Eq. 5.7, the anharmonic terms are important for dimensions $D \leq 4$. This implies that the upper critical dimension of the theory in Eq. 5.7 is $D_u = 4$ and the anharmonic terms are relevant in the physical dimension $D = 2$. This means that the anharmonic terms will renormalize the parameters B^0_{ijkl} and C^0_{ijkl} at least in the regime $\ell_{\text{th}} < \ell^* \ll \ell^0_{\text{el}}$ which we discuss next.

- $\ell_{\text{th}} < \ell^* \ll \ell^0_{\text{el}}$: In this regime, the anharmonic renomrmalize the parameters B^0_{ijkl} and C^0_{ijkl} to parameters $B^R_{ijkl}(\mathbf{q}^*)$ and $C^R_{ijkl}(\mathbf{q}^*)$ at scale q^*. However, for $\ell^* \gtrsim \ell_{\text{th}}$ when the parameters are only mildly renormalized, the anisotropic term $N^R(\mathbf{q})q_z^4/(R^2D^R(\mathbf{q}))$ in the denominator Green's function in Eq. 5.11 is still small w.r.t. the first term and the Green's function is still approximately isotropic (we will show the consistency of this once we obtain the renormalization group flow equations). Therefore, we can implement isotropic (circular) momentum-shell renormalization group scheme. We first integrate out all Fourier modes in a thin momentum shell $\Lambda/b/ < q < \Lambda$ and $b \equiv \ell^*/a = e^s$,

with $s \ll 1$. Next we rescale lengths and fields:

$$\mathbf{r} = b\mathbf{r}',\ \tilde{h}(\mathbf{r}) = b^{\zeta_h}\tilde{h}(\mathbf{r}'),\ \tilde{u}_i(\mathbf{r}) = b^{2\zeta_h - 1}\tilde{u}_i(\mathbf{r}') \tag{5.17}$$

where ζ_h is the field-rescaling exponent. We find it convenient to work directly with a D =2-dimensional cylindrical shell embedded in d =3 space, rather than introducing an expansion in $\epsilon = 4 - D$ [94, 92]. In principle, this is dangerous and can give wrong results because if we work in $D = 2$, $\epsilon = 4 - 2 = 2$ is large and there is no small parameter perturbative renormalization. However, later we show using the molecular dynamics simulations that the results obtained by directly working in $D = 2$ matches with simulations. Finally, we define new elastic constants B'_{ijkl}, C'_{ijkl}, and a new external pressure σ'_{ij}, such that the free-energy functional in Eqs. 5.7 and 5.9 retain the same form after the renormalization group steps. We then write the ordinary differential equations for the parameters w.r.t. s, called β functions [170, 171]. To obtain the contribution to the renormalization of B_{ijkl} from the anharmonic terms, we find it easier to work with the effective free energy F_{eff} where the in-plane phonon are completely integrated out (see Fig. 5.2). However, for C_{ijkl}, it is much simpler to use the free energy $F_{\text{eff},1}$ (see Fig. 5.3). To one-loop order we get:

$$\begin{aligned}\beta_{B_{ijkl}} = \frac{dB'_{ijkl}}{ds} &= 2(\zeta_h - 1)B'_{ijkl} \\ &+ \frac{A}{4\pi^2}\frac{d}{ds}\int_{\Lambda/b<|\mathbf{p}|<\Lambda} d^2\mathbf{p}\,\varepsilon_{im}\varepsilon_{jn}\varepsilon_{kr}\varepsilon_{lt}p_m p_n p_r p_t \frac{N(C'_{ijkl})}{D(C'_{ijkl};\mathbf{p})}G_{hh}(\mathbf{p}) \\ &- \frac{2A^2}{4\pi^2 R'^2 k_B T}\frac{d}{ds}\int_{\Lambda/b<|\mathbf{p}|<\Lambda} d^2\mathbf{p}\,\varepsilon_{im}\varepsilon_{jn}\varepsilon_{kr}\varepsilon_{lt}p_m p_n p_r p_t p_z^4 \frac{N^2(C'_{ijkl})}{D^2(C'_{ijkl};\mathbf{p})}G^2_{hh}(\mathbf{p}),\end{aligned} \tag{5.18a}$$

$$\begin{aligned}\beta_{C_{ijkl}} = \frac{dC'_{ijkl}}{ds} &= 2(2\zeta_h - 1)C'_{ijkl} \\ &- \frac{A^2}{8\pi^2 k_B T}C'_{ijmn}C'_{rtkl}\frac{d}{ds}\int_{\Lambda/b<|\mathbf{p}|<\Lambda} d^2\mathbf{p}\,p_m p_n p_r p_t G^2_{hh}(\mathbf{p}),\end{aligned} \tag{5.18b}$$

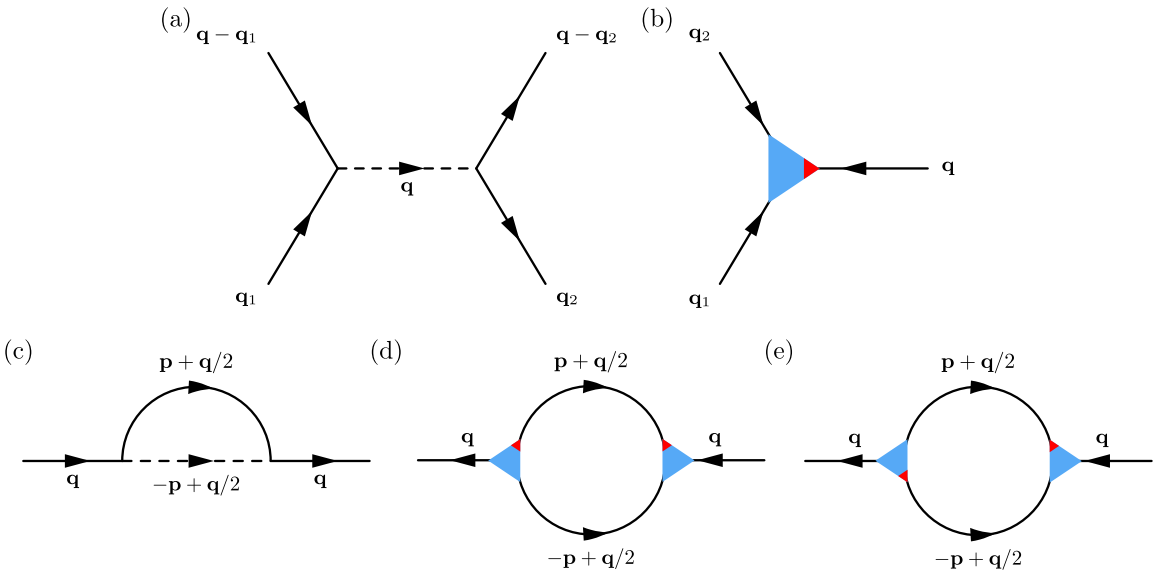

Figure 5.2: Feynman diagrams relevant to the renormalization of bending rigidity. (a) Four-point and (b) three-point vertices describe the quartic and cubic terms in the effective free energy of Eq. 5.9, respectively. the straight legs represent radial displacement fields $\tilde{h}(\mathbf{q})$. The red part of the three-point vertex in (b) connects to the field $\tilde{h}(\mathbf{q})$ corresponding to wave vector which is in the argument of P^T_{ij}. (c–e) One-loop diagrams that contribute to the renormalization flows of the bending rigidities B^R_{ijkl}. The momentum $\mathbf{p}$ in (c), (d), (e) is the loop momentum which is integrated over a shell $\Lambda/b < p < \Lambda$ and whole Fourier space in momentum-shell renormalization and self consistent calculation respectively.

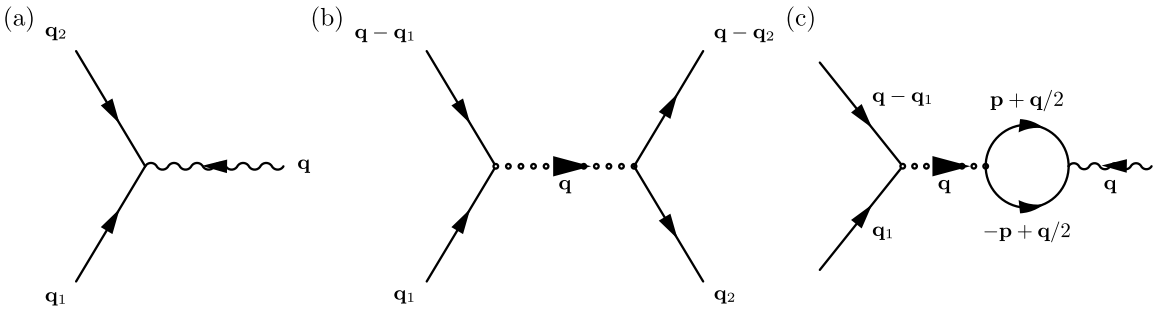

Figure 5.3: Feynman diagrams relevant to the renormalization of in-plane moduli. (a) Three-point (b) four-point vertices describe the cubic $\tilde{u}\tilde{h}\tilde{h}$ and quartic $\tilde{h}\tilde{h}\tilde{h}\tilde{h}$ terms in the free energy of Eq. 5.7, respectively. The wiggly line in (a) is the leg correspoding to in-plane displacement field $\tilde{u}_i(\mathbf{q})$. (c) One-loop diagram that contributes to the renormalization flows of the in-plane stiffnesses C^R_{ijkl} associated with the three-point vertex in (a). The connected legs in these diagrams represent the propagators $G_{hh}(\mathbf{q})$. The momentum $\mathbf{p}$ in (c) is the loop momentum which is integrated over a shell $\Lambda/b < p < \Lambda$ and whole Fourier space in momentum-shell renormalization and self consistent calculation respectively.

$$\beta_{\sigma_{ij}} = \frac{d\sigma'_{ij}}{ds} = 2\zeta_h \sigma'_{ij}, \tag{5.18c}$$

$$\beta_R = \frac{dR'}{ds} = -R', \tag{5.18d}$$

where ε_{ij} is the permutation symbol ($\varepsilon_{11} = \varepsilon_{22} = 0$ and $\varepsilon_{12} = -\varepsilon_{21} = 1$). The scale-dependent parameters B'_{ijkl}, C'_{ijkl}, and σ'_{ij}, obtained by integrating the differential equations in Eqs. 5.18 up to a scale $s = \ln(\ell^*/a)$ with initial conditions $B'_{ijkl}(0) = \kappa_0 \delta_{ij}\delta_{kl}$, $C_{ijkl}(0) = \lambda_0 \delta_{ij}\delta_{kl} + \mu_0(\delta_{ik}\delta_{jl} + \delta_{il}\delta_{jk})$ and $\sigma_{ij}(0) = 0$, are related to the scale-dependent renormalized parameters as $B^R_{ijkl}(s) = B'_{ijkl}(s)e^{(2-2\zeta_h)s} = B'_{ijkl}(s)$, $C^R_{ijkl}(s) = C'_{ijkl}(s)e^{(2-4\zeta_h)s} = C'_{ijkl}(s)e^{-2s}$ and $\sigma^R_{ij}(s) = \sigma'_{ij}(s)e^{-2s}$, since $\zeta_h = 1$.

With the initial conditions just mentioned, the only term that can make the RG flow anisotropic is the last term in Eq. 5.18a. In the limit $\ell_{\text{th}} < \ell^* \ll \ell^0_{\text{el}}$, the second and third terms in Eq. 5.18a are $\sim k_B T Y'/(\kappa' \Lambda^2)$ and $\sim k_B T Y'^2/(\kappa'^2 R'^2 \Lambda^6)$ respectively. Third term is of the order of the second terms when:

$$\begin{aligned} k_B T Y'/(\kappa' \Lambda^2) &\lesssim k_B T Y'^2/(\kappa'^2 R'^2 \Lambda^6) \\ \Rightarrow k_B T Y_R(s) e^{2s} a^2/\kappa_R(s) &\lesssim k_B T Y_R^2(s) e^{4s} a^6/(\kappa_R^2(s) R^2 e^{-2s}) \\ \Rightarrow 1 &\lesssim Y_R(s)(\ell/a)^4 a^4/(\kappa_R(s) R^2) \\ \Rightarrow \ell &\gtrsim (\kappa_R(s) R^2/Y_R(s))^{1/4} \end{aligned} \tag{5.19}$$

Comparing the right hand side of the last line of Eq. 5.19 with Eq. 5.12, we define a new elastic length scale as

$$\ell_{\rm el} \equiv \frac{\pi}{q_{\rm el}} = \pi \left(\frac{\kappa_R(\ell_{\rm el}) R^2}{Y_R(\ell_{\rm el})} \right)^{\frac{1}{4}}, \tag{5.20}$$

where $\kappa_R(\ell_{\rm el})$ and $Y_R(ell_{\rm el})$ are themselves dependent on the elastic length scale. We will give a better estimate of elastic length later. From, Eq. 5.19, we see that the third term in Eq. 5.18a, which makes anisotropic contribution, is negligible compared to the isotropic second term in the regime $\ell_{\rm th} < \ell^* \ll \ell_{\rm el}$, and can be ignored. Therefore, in this region the material parameters remain isotropic. In this limit, the *beta*-functions are exactly the same as those for a thermally fluctuating isotropic sheet [169]. Hence, in this regime, the scale dependence of the isotropic material parameters is the same as in case of isotropic sheets:

$$\begin{aligned} \frac{\kappa_R(\ell)}{\kappa_0} &\approx (\ell/\ell_{\rm th})^{\eta}, \ell_{\rm th} \ll \ell \ll \ell_{\rm el}, \\ \frac{\lambda_R(\ell)}{Y_0}, \frac{\mu_R(\ell)}{Y_0}, \frac{Y_R(\ell)}{Y_0} &\approx c(\ell/\ell_{\rm th})^{-\eta_u}, \ell_{\rm th} \ll \ell \ll \ell_{\rm el}, \end{aligned} \tag{5.21}$$

where the prefactor c is -0.36, 0.72 and 1.0 for λ_R, μ_R and Y_R respectively [169], $\eta \approx 0.8 - 0.85$ [169, 96, 98], and the exponents η and η_u satisfy the identity $2\eta + \eta_u = 2$, which is a result of infinitesimal rotational symmetry of the system about in-plane axes [92]. Replacing These expressions of $\kappa_R(\ell)$ and $Y_R(\ell)$ in Eq. 5.20 we get the following estimate of elastic length:

$$\ell_{\rm el} = \frac{\pi}{q_{\rm el}} = \left(\frac{\kappa_0 R^2 q_{\rm th}^{\eta+\eta_u}}{Y_0} \right)^{\frac{1}{4-\eta-\eta_u}}. \tag{5.22}$$

A better estimate of the thermal length scale can also be obtained from Eq. 5.18a. The scale $\ell = ae^s$ at which the second term is comparable to the first (Gaussian) term of Eq. 5.18a is the system size where the anharmonicity of

the free energy becomes important, and the length is called the thermal length scale. Then, by simplifying the second term in Eq. 5.18a using the fact that the material parameters are isotropic and using the expressions $\kappa'(s) = \kappa_R(s) \approx \kappa_0$ (the last equality is due to the fact that the parameters only starts to renormalize at the thermal length scale), $Y'(s) = Y_R(s)e^{2s} \approx Y_0 e^{2s} \approx \kappa_0(s)$, $s = \ln(\ell_{\text{th}}/a)$, $\Lambda = \pi/a$, we get [169]:

$$\ell_{\text{th}} \equiv \frac{\pi}{q_{\text{th}}} = \sqrt{\frac{16\pi^3\kappa_0^2}{3k_BTY_0}}. \tag{5.23}$$

5.3.2 Scaling analysis for $\ell^* \gg \ell_{\text{el}}$

From the discussion until now, we have seen that up to elastic length scale the parameters remain isotropic and $B^R_{ijkl}(q_{\text{el}}) \approx \kappa_R(q_{\text{el}})\delta_{ij}\delta_{kl} \approx \delta_{ij}\delta_{kl}\kappa_0(q_{\text{el}}/q_{\text{th}})^{-\eta}$ and $C^R_{ijkl}(q_{\text{el}}) \approx \lambda_R(q_{\text{el}})\delta_{ij}\delta_{kl} + \mu_R(q_{\text{el}})(\delta_{ik}\delta_{jl} + \delta_{il}\delta_{jk}) \approx Y_0(-0.36\delta_{ij}\delta_{kl} + 0.72(\delta_{ik}\delta_{jl} + \delta_{il}\delta_{jk}))(q_{\text{el}}/q_{\text{th}})^{\eta_u}$. Therefore, integrating out the degree of freedom on scales smaller than ℓ_{el}, the free energy takes the form:

$$\begin{aligned} F^0_{\text{eff}}(q_{\text{el}})/A &= \sum_{\substack{\mathbf{q}\neq 0 \\ q<q_{\text{el}}}} \frac{1}{2}\left(B^R_{ijkl}(q_{\text{el}})q_iq_jq_kq_l + \frac{q_z^4 N(C^R_{ijkl}(q_{\text{el}}))}{R^2 D(C^R_{ijkl}(q_{\text{el}});\mathbf{q})}\right)\tilde{h}(\mathbf{q})\tilde{h}(-\mathbf{q}) \\ &\approx \sum_{\substack{\mathbf{q}\neq 0 \\ q<q_{\text{el}}}} \frac{1}{2}\left(\kappa_R(q_{\text{el}})q^4 + \frac{q_z^4 Y_R(q_{\text{el}})}{R^2q^4}\right)\tilde{h}(\mathbf{q})\tilde{h}(-\mathbf{q}), \end{aligned} \tag{5.24a}$$

$$
\begin{aligned}
F^I_{\text{eff}}(q_{\text{el}})/A = &\sum_{\substack{\mathbf{q}_1+\mathbf{q}_2=-\mathbf{q}\neq 0\\ q_1,q_2,q<q_{\text{el}}}} \frac{q_z^2}{2q^2}[q_{1i}P^T_{ij}(\mathbf{q})q_{2j}]\frac{N(C^R_{ijkl}(q_{\text{el}}))q^4}{RD(C^R_{ijkl}(q_{\text{el}});\mathbf{q})}\tilde{h}(\mathbf{q})\tilde{h}(\mathbf{q}_1)\tilde{h}(\mathbf{q}_2)\\
&+\sum_{\substack{\mathbf{q}_1+\mathbf{q}_2=\mathbf{q}\neq 0\\ \mathbf{q}_3+\mathbf{q}_4=-\mathbf{q}\neq 0\\ q_1,q_2,q_3,q_4,q<q_{\text{el}}}} \frac{1}{8}[q_{1i}P^T_{ij}(\mathbf{q})q_{2j}][q_{3i}P^T_{ij}(\mathbf{q})q_{4j}]\frac{N(C^R_{ijkl}(q_{\text{el}}))q^4}{D(C^R_{ijkl}(q_{\text{el}});\mathbf{q})}\tilde{h}(\mathbf{q}_1)\tilde{h}(\mathbf{q}_2)\tilde{h}(\mathbf{q}_3)\tilde{h}(\mathbf{q}_4),\\
\approx &\sum_{\substack{\mathbf{q}_1+\mathbf{q}_2=-\mathbf{q}\neq 0\\ q_1,q_2,q<q_{\text{el}}}} [q_{1i}P^T_{ij}(\mathbf{q})q_{2j}]\frac{Y_R(q_{\text{el}})q_z^2}{2Rq^2}\tilde{h}(\mathbf{q})\tilde{h}(\mathbf{q}_1)\tilde{h}(\mathbf{q}_2)\\
&+\sum_{\substack{\mathbf{q}_1+\mathbf{q}_2=\mathbf{q}\neq 0\\ \mathbf{q}_3+\mathbf{q}_4=-\mathbf{q}\neq 0\\ q_1,q_2,q_3,q_4,q<q_{\text{el}}}} \frac{Y_R(q_{\text{el}})}{8}[q_{1i}P^T_{ij}(\mathbf{q})q_{2j}][q_{3i}P^T_{ij}(\mathbf{q})q_{4j}]\tilde{h}(\mathbf{q}_1)\tilde{h}(\mathbf{q}_2)\tilde{h}(\mathbf{q}_3)\tilde{h}(\mathbf{q}_4).
\end{aligned}
\tag{5.24b}
$$

Starting from this course-grained free energy, the harmonic approximation to the Green's function is:

$$
G^0_{hh}(\mathbf{q};q<q_{\text{el}}) = \frac{k_BT/A}{\kappa_R(q_{\text{el}})q^4+\frac{Y_R(q_{\text{el}})q_z^4}{R^2q^4}}, \tag{5.25}
$$

which is aniostropic for $q < q_{\text{el}}$. Now, following the argument of [172] (section V), the regime of wavevectors that dominates the $\tilde{h}$-fluctuations is $q^8 \approx (q_{\text{el}}q_z)^4$ i.e., $q_z = q_\varphi^2/q_{\text{el}}$. Therefore, for small $q \ll q_{\text{el}}$, $q_z \sim q_\varphi^2 \ll q_\varphi$. This leads to a simplification of the expression of $D(C_{ijkl};\mathbf{q})$ keeping only the lowest order terms in q_φ:

$$
\begin{aligned}
\frac{q_z^4N(C^R_{ijkl}(q_{\text{el}}))}{D(C^R_{ijkl}(q_{\text{el}});\mathbf{q})} &\approx \frac{C^R_{\varphi\varphi\varphi\varphi}(q_{\text{el}})C^R_{\varphi z\varphi z}(q_{\text{el}})C^R_{zzzz}(q_{\text{el}}) - C^R_{\varphi\varphi zz}(q_{\text{el}})^2C^R_{\varphi z\varphi z}(q_{\text{el}})}{C^R_{\varphi\varphi\varphi\varphi}(q_{\text{el}})C^R_{\varphi z\varphi z}(q_{\text{el}})}\frac{q_z^4}{q_\varphi^4}\\
&= Y^R_{zz}(q_{\text{el}})\frac{q_z^4}{q_\varphi^4}.
\end{aligned}
\tag{5.26}
$$

In this regime, if we count the dimension of wave vector component q_φ as $[q_\varphi] = 1$, we have to count the dimension of q_z as $[q_z] = 2$ since $q_z \sim q_\varphi^2$. This happens in strongly anisotropic systems, see for example [173]. Then, the dimension of area A

is $[A] = -1 - 2 = -3$. With these, and requiring that Gaussian part of the effective free energy

$$F^0_{\text{eff}}(q_{\text{el}}) \approx \sum_{\substack{\mathbf{q}\neq 0 \\ q<q_{\text{el}}}} \frac{A}{2}\left(B^R_{ijkl}(q_{\text{el}})q_i q_j q_k q_l + \frac{q_z^4 Y^R_{zz}(q_{\text{el}})}{R^2 q_\varphi^4}\right)\tilde{h}(\mathbf{q})\tilde{h}(-\mathbf{q}) \tag{5.27}$$

dimensionless, we get the following naïve dimensions:

$$[\tilde{h}(\mathbf{q})] = -1/2, [B^R_{\varphi\varphi\varphi\varphi}(q_{\text{el}})] = 0, [B^R_{\varphi\varphi zz}(q_{\text{el}})] = -2, [B^R_{zzzz}(q_{\text{el}})] = -4, [Y^R_{zz}(q_{\text{el}})/R^2] = 0 \tag{5.28}$$

Therefore, the terms $B^R_{\varphi\varphi zz}(q_{\text{el}})q_\varphi^2 q_z^2\tilde{h}(\mathbf{q})\tilde{h}(-\mathbf{q})$, $B^R_{zzzz}(q_{\text{el}})q_z^4\tilde{h}(\mathbf{q})\tilde{h}(-\mathbf{q})$ are irrelevant. Keeping only the relevant terms then the harmonic part of the free energy is:

$$F^0_{\text{eff}}(q_{\text{el}}) \approx \sum_{\substack{\mathbf{q}\neq 0 \\ q<q_{\text{el}}}} \frac{A}{2}\left(B^R_{\varphi\varphi\varphi\varphi}(q_{\text{el}})q_\varphi^4 + \frac{q_z^4 Y^R_{zz}(q_{\text{el}})}{R^2 q_\varphi^4}\right)\tilde{h}(\mathbf{q})\tilde{h}(-\mathbf{q}), \tag{5.29}$$

and the harmonic Green's function can be approximated as:

$$G^0_{hh}(\mathbf{q}; q < q_{\text{el}}) \approx \frac{k_B T/A}{B^R_{\varphi\varphi\varphi\varphi}(q_{\text{el}})q_\varphi^4 + \frac{Y^R_{zz}(q_{\text{el}})q_z^4}{R^2 q_\varphi^4}}. \tag{5.30}$$

To get the naïve dimensions of other constants, first go back to the form of the in-plane strain tensor and require that all the terms in the same component of strain have the same dimension. This way we get:

$$\begin{aligned}
&\tilde{u}_{\varphi\varphi} : [\partial_\varphi \tilde{u}_\varphi] = [\tilde{h}/R] = [(\partial_\varphi \tilde{h})^2] = 1 \Rightarrow [\tilde{u}_\varphi] = 0, [1/R] = 3/2, \\
&\tilde{u}_{zz} : [\partial_z \tilde{u}_z] = [(\partial_z \tilde{h})^2] = 3 \Rightarrow [\tilde{u}_z] = 1, \\
&\tilde{u}_{\varphi z} : [\partial_\varphi \tilde{u}_z] = [\partial_z \tilde{u}_\varphi] = [(\partial_z \tilde{h})(\partial_\varphi \tilde{h})] = 2,
\end{aligned} \tag{5.31}$$

where we used $\tilde{u}_{\varphi\varphi}$ and $\tilde{u}_{zz}$ get the dimensions of $\tilde{u}_\varphi$, $\tilde{u}_z$ and $1/R$, and checked their consistency with $\tilde{u}_{\varphi z}$. With these dimensions, we use the free energy in Eq. 5.7 to

find the dimensions of $C^R_{ijkl}(q_{\rm el})$:

$$[C^R_{\varphi\varphi\varphi\varphi}(q_{\rm el})] = 1, [C^R_{\varphi\varphi zz}(q_{\rm el})] = [C^R_{\varphi z\varphi z}(q_{\rm el})] = -1, [C^R_{zzzz}(q_{\rm el})] = -3. \tag{5.32}$$

This means that only terms with $C^R_{\varphi\varphi\varphi\varphi}(q_{\rm el})$ as coefficient are relevant. Keeping only terms with coefficients $C^R_{\varphi\varphi\varphi\varphi}(q_{\rm el})$ in Eq. 5.7, if we integrate out the in-plane displacements, the interacting part $F^I_{\rm eff}(q_{\rm el})$ of effective free energy is $F^I_{\rm eff}(q_{\rm el}) = 0$. Therefore, the effective free energy:

$$F_{\rm eff}(q_{\rm el}) \approx F^0_{\rm eff}(q_{\rm el}) \approx \sum_{\substack{\mathbf{q}\neq 0 \\ q<q_{\rm el}}} \frac{A}{2}\left(B^R_{\varphi\varphi\varphi\varphi}(q_{\rm el})q^4_\varphi + \frac{q^4_z Y^R_{zz}(q_{\rm el})}{R^2 q^4_\varphi}\right)\tilde{h}(\mathbf{q})\tilde{h}(-\mathbf{q}) \tag{5.33}$$

describes a free field theory and $B^R_{\varphi\varphi\varphi\varphi}(q_{\rm el})$ and $Y^R_{zz}(q_{\rm el})$ do not renormalize any further as we integrate out Fourier modes beyond $q < q_{\rm el}$:

$$B^R_{\varphi\varphi\varphi\varphi}(\mathbf{q}) \approx B^R_{\varphi\varphi\varphi\varphi}(q_{\rm el}) = \kappa_R(q_{\rm el}) \approx \kappa_0(q_{\rm el}/q_{\rm th})^{-\eta}, \tag{5.34a}$$

$$Y^R_{zz}(\mathbf{q}) \approx Y^R_{zz}(q_{\rm el}) = Y_R(q_{\rm el}) \approx Y_0(q_{\rm el}/q_{\rm th})^{\eta_u}. \tag{5.34b}$$

Hence, the Green's function $G_{hh}(\mathbf{q}; q < q_{\rm el}) = G^0_{hh}(\mathbf{q}; q < q_{\rm el})$. However, the free energy in Eq. 5.7 is not a free field theory because $C^R_{\varphi\varphi\varphi\varphi}(q_{\rm el})$ is relevant. Then we can use the Feynman diagram in Fig. 5.3(c) to write a self consistent perturbative

equation (see a similar analysis in [172]):

$$
\begin{aligned}
C^R_{\varphi\varphi\varphi\varphi}(\mathbf{q}) &= C^R_{\varphi\varphi\varphi\varphi}(q_{\rm el}) \\
&\quad - \frac{A^2}{8\pi^2 k_B T}(C^R_{\varphi\varphi\varphi\varphi}(\mathbf{q}))^2 \int_{|\mathbf{p}|<q_{\rm el}} dp_\varphi dp_z\, p_\varphi^2 (p_\varphi - q_\varphi)^2 G_{hh}(\mathbf{p}) G_{hh}(\mathbf{p}-\mathbf{q}) \\
&= C^R_{\varphi\varphi\varphi\varphi}(q_{\rm el}) - \frac{k_B T}{8\pi^2}(C^R_{\varphi\varphi\varphi\varphi}(\mathbf{q}))^2 \int_{|\mathbf{p}|<q_{\rm el}} dp_\varphi dp_z\, p_\varphi^2 (p_\varphi - q_\varphi)^2 \times \\
&\qquad \frac{1}{\left(B^R_{\varphi\varphi\varphi\varphi}(q_{\rm el}) p_\varphi^4 + \frac{Y^R_{zz}(q_{\rm el}) p_z^4}{R^2 p_\varphi^4}\right)\left(B^R_{\varphi\varphi\varphi\varphi}(q_{\rm el})(p_\varphi - q_\varphi)^4 + \frac{Y^R_{zz}(q_{\rm el})(p_z - q_z)^4}{R^2 (p_\varphi - q_\varphi)^4}\right)}.
\end{aligned}
\tag{5.35}
$$

One can extract how the integral scales with q_φ or q_z by non dimensionalizing p_φ and p_z with either q_φ and q_φ^2 or $q_z^{1/2}$ and q_z respectively. By doing this one can find that the integral scales as $q_\varphi^{-1} \sim q_z^{-1/2}$. This observation tells us that the self consistent equation can be solved by the ansatz:

$$
C^R_{\varphi\varphi\varphi\varphi}(\mathbf{q}) = q_\varphi^{\eta_\varphi} \Omega_{\varphi\varphi\varphi\varphi}(q_\varphi/(q_{\rm el} q_z)^z). \tag{5.36}
$$

Using simple power counting, we find that

$$
\eta_\varphi = 1, z = 1/2. \tag{5.37}
$$

From the form of the integral in Eq. 5.35, it is easy to see that the function $\Omega_{\varphi\varphi\varphi\varphi}$ is independent of q_φ when $q_\varphi \to 0$, as well as independent of q_z when $q_z \to 0$. This means the following:

$$
\Omega_{\varphi\varphi\varphi\varphi}(x) \propto \begin{cases} \text{consant}, & x \to \infty \\ x^{-\eta_\varphi}, & x \to 0 \end{cases}. \tag{5.38}
$$

This implies the following:

$$C^R_{\varphi\varphi\varphi\varphi}(\mathbf{q}) \propto \begin{cases} q_\varphi, & q < q_{\rm el} < q_{\rm th} \text{ and } q_\varphi \gg (q_{\rm el} q_z)^{1/2} \\ \sqrt{q_z}, & q < q_{\rm el} < q_{\rm th} \text{ and } q_\varphi \ll (q_{\rm el} q_z)^{1/2} \end{cases}. \tag{5.39}$$

Although the other moduli are irrelevant, we can repeat this same analysis to obtain how they scale. We can check how these moduli scale in our simulations and therefore better verify our theory and provide an understanding of the mechanical properties of nanotubes. We can check for example how the shear modulus should scale:

$$C^R_{\varphi z\varphi z}(\mathbf{q}) = C^R_{\varphi z\varphi z}(q_{\rm el}) - \frac{k_B T}{2\pi^2}(C^R_{\varphi z\varphi z}(\mathbf{q}))^2 \int dp_\varphi dp_z (p_\varphi - q_\varphi)(p_z - q_z) p_\varphi p_z \times \frac{1}{\left(B^R_{\varphi\varphi\varphi\varphi}(q_{\rm el}) p_\varphi^4 + \frac{Y^R_{zz}(q_{\rm el}) p_z^4}{R^2 p_\varphi^4}\right)\left(B^R_{\varphi\varphi\varphi\varphi}(q_{\rm el})(p_\varphi - q_\varphi)^4 + \frac{Y^R_{zz}(q_{\rm el})(p_z - q_z)^4}{R^2 (p_\varphi - q_\varphi)^4}\right)}. \tag{5.40}$$

By non dimensionalizing p_φ and p_z with either q_φ and q_φ^2 respectively, we find the integral scales as $q_\varphi \sim q_z^{1/2} \to 0$ as $q \to 0$. This implies that $C^R_{\varphi z\varphi z}(\mathbf{q}) \approx C^R_{\varphi z\varphi z}(q_{\rm el})$:

$$C^R_{\varphi z\varphi z}(\mathbf{q}) \approx C^R_{\varphi z\varphi z}(q_{\rm el}),\ q < q_{\rm el} < q_{\rm th}. \tag{5.41}$$

Similarly, for $C^R_{zzzz}(\mathbf{q})$, we have the following self-consistent equation:

$$C^R_{zzzz}(\mathbf{q}) = C^R_{zzzz}(q_{\rm el}) - \frac{k_B T}{8\pi^2}(C^R_{zzzz}(\mathbf{q}))^2 \int dp_\varphi dp_z (p_z - q_z)^2 p_z^2 \times \frac{1}{\left(B^R_{\varphi\varphi\varphi\varphi}(q_{\rm el}) p_\varphi^4 + \frac{Y^R_{zz}(q_{\rm el}) p_z^4}{R^2 p_\varphi^4}\right)\left(B^R_{\varphi\varphi\varphi\varphi}(q_{\rm el})(p_\varphi - q_\varphi)^4 + \frac{Y^R_{zz}(q_{\rm el})(p_z - q_z)^4}{R^2 (p_\varphi - q_\varphi)^4}\right)}. \tag{5.42}$$

By non dimensionalizing p_φ and p_z with either q_φ and q_φ^2 respectively, we find the integral scales as $q_\varphi^3 \sim q_z^{3/2} \to 0$ as $q \to 0$. This implies that $C^R_{zzzz}(\mathbf{q}) \approx C^R_{zzzz}(q_{\text{el}})$:

$$C^R_{zzzz}(\mathbf{q}) \approx C^R_{zzzz}(q_{\text{el}}),\ q < q_{\text{el}} < q_{\text{th}}. \tag{5.43}$$

Lastly, for $C^R_{zzzz}(\mathbf{q})$, we have the following self-consistent equation:

$$C^R_{\varphi\varphi zz}(\mathbf{q}) = C^R_{\varphi\varphi zz}(q_{\text{el}}) - \frac{k_B T}{8\pi^2}\int dp_\varphi dp_z \frac{[C^R_{\varphi\varphi\varphi\varphi}(\mathbf{q})(p_\varphi - q_\varphi)^2 + C^R_{\varphi\varphi zz}(\mathbf{q})(p_z - q_z)^2][C^R_{\varphi\varphi zz}(\mathbf{q})p_\varphi^2 + C^R_{zzzz}(\mathbf{q})p_z^2]}{\left(B^R_{\varphi\varphi\varphi\varphi}(q_{\text{el}})p_\varphi^4 + \frac{Y^R_{zz}(q_{\text{el}})p_z^4}{R^2 p_\varphi^4}\right)\left(B^R_{\varphi\varphi\varphi\varphi}(q_{\text{el}})(p_\varphi - q_\varphi)^4 + \frac{Y^R_{zz}(q_{\text{el}})(p_z - q_z)^4}{R^2(p_\varphi - q_\varphi)^4}\right)}. \tag{5.44}$$

The integral multiplied to $C^R_{\varphi\varphi\varphi\varphi}(\mathbf{q})C^R_{\varphi\varphi zz}(\mathbf{q})$ scales as q_φ^{-1}, the integral multiplied to $C^R_{\varphi\varphi\varphi\varphi}(\mathbf{q})C^R_{zzzz}(\mathbf{q})$ scales as q_φ, the integral multiplied to $C^R_{\varphi\varphi zz}(\mathbf{q})C^R_{\varphi\varphi zz}(\mathbf{q})$ scales as q_φ, and the integral multiplied to $C^R_{\varphi\varphi zz}(\mathbf{q})C^R_{zzzz}(\mathbf{q})$ scales as q_φ^3. The only term among these that does not vanish as $q_\varphi \to 0$ is the term whose coefficient is $C^R_{\varphi\varphi\varphi\varphi}(\mathbf{q})C^R_{\varphi\varphi zz}(\mathbf{q})$. However, as we have seen before, $C^R_{\varphi\varphi\varphi\varphi}(\mathbf{q}) \sim q_\varphi$. This means that self consistent equation gives the following:

$$C^R_{\varphi\varphi zz}(\mathbf{q}) \approx C^R_{\varphi\varphi zz}(q_{\text{el}}) + \text{const.} \times C^R_{\varphi\varphi zz}(\mathbf{q}),\ q < q_{\text{el}} < q_{\text{th}}. \tag{5.45}$$

This equation is not sufficient to find the scaling of $C^R_{\varphi\varphi zz}(\mathbf{q})$. However, by solving the differential equations in Eq. 5.18 numerically, we find the following scaling of $C^R_{\varphi\varphi zz}(\mathbf{q})$:

$$C^R_{\varphi\varphi zz}(\mathbf{q}) \propto \begin{cases} q_\varphi, & q < q_{\text{el}} < q_{\text{th}} \text{ and } q_\varphi \gg (q_{\text{el}} q_z)^{1/2} \\ \sqrt{q_z}, & q < q_{\text{el}} < q_{\text{th}} \text{ and } q_\varphi \ll (q_{\text{el}} q_z)^{1/2} \end{cases}. \tag{5.46}$$

Earlier, we found that $Y^R_{zz}(\mathbf{q})$ stops renormalizing in the regime $q < q_{\text{el}} < q_{\text{th}}$. But we know that $Y_{zz} = C_{zzzz} - C^2_{\varphi\varphi zz}/C_{\varphi\varphi\varphi\varphi}$. Since $C^R_{zzzz-} \sim$ constant

and $(C^R_{\varphi\varphi zz})^2/C^R_{\varphi\varphi\varphi\varphi} \sim q_\varphi^2/q_\varphi = q_\varphi \to 0$ as $q_\varphi \to 0$, and therefore $C^R_{zzzz} - (C^R_{\varphi\varphi zz})^2/C^R_{\varphi\varphi\varphi\varphi} \sim$ constant which matches with our result for Y^R_{zz}. Similarly, $Y_{\varphi\varphi} = C_{\varphi\varphi\varphi\varphi} - C^2_{\varphi\varphi zz}/C_{zzzz} \sim q_\varphi$. We summarize these scalings in Table 5.1.

Table 5.1: Scaling functions for $\ell_{\rm th} < \ell_{\rm el} \Rightarrow q_{\rm th} > q_{\rm el}$

Scale	$q > q_{\rm th} > q_{\rm el}$	$q_{\rm th} > q > q_{\rm el}$	$q_{\rm th} > q_{\rm el} > q$
$C^R_{\varphi\varphi\varphi\varphi}/Y_0$	$\frac{1}{1-\nu_0^2}$	$\left(\frac{q}{q_{\rm th}}\right)^{\eta_u}$	$\left(\frac{q_{\rm el}}{q_{\rm th}}\right)^{\eta_u}\left(\frac{q_\varphi}{q_{\rm el}}\right)\Omega_{\varphi\varphi\varphi\varphi}\left(q_\varphi/(q_{\rm el}q_z)^{1/2}\right)$
$C^R_{\varphi\varphi zz}/Y_0$	$\frac{\nu_0}{1-\nu_0^2}$	$\left(\frac{q}{q_{\rm th}}\right)^{\eta_u}$	$\left(\frac{q_{\rm el}}{q_{\rm th}}\right)^{\eta_u}\left(\frac{q_\varphi}{q_{\rm el}}\right)\Omega_{\varphi\varphi zz}\left(q_\varphi/(q_{\rm el}q_z)^{1/2}\right)$
$C^R_{\varphi z\varphi z}/Y_0$	$\frac{1}{2(1+\nu_0)}$	$\left(\frac{q}{q_{\rm th}}\right)^{\eta_u}$	$\left(\frac{q_{\rm el}}{q_{\rm th}}\right)^{\eta_u}$
C^R_{zzzz}/Y_0	$\frac{1}{1-\nu_0^2}$	$\left(\frac{q}{q_{\rm th}}\right)^{\eta_u}$	$\left(\frac{q_{\rm el}}{q_{\rm th}}\right)^{\eta_u}$
$Y^R_{\varphi\varphi}/Y_0$	1	$\left(\frac{q}{q_{\rm th}}\right)^{\eta_u}$	$\left(\frac{q_{\rm el}}{q_{\rm th}}\right)^{\eta_u}\left(\frac{q_\varphi}{q_{\rm el}}\right)\Omega_{Y_{\varphi\varphi}}\left(q_\varphi/(q_{\rm el}q_z)^{1/2}\right)$
Y^R_{zz}/Y_0	1	$\left(\frac{q}{q_{\rm th}}\right)^{\eta_u}$	$\left(\frac{q_{\rm el}}{q_{\rm th}}\right)^{\eta_u}$
$B^R_{\varphi\varphi\varphi\varphi}/\kappa_0$	1	$\left(\frac{q}{q_{\rm th}}\right)^{-\eta}$	$\left(\frac{q_{\rm el}}{q_{\rm th}}\right)^{-\eta}$

In the beginning of this section, we assumed $\ell_{\rm el} \gg \ell_{\rm th}$. However, even if $\ell_{\rm th} > \ell_{el}$, all the analysis starting from the naïve dimensions in Eqs. 5.28 and 5.31 would remain the same in the regime $\ell > \ell_{\rm th} > \ell_{el}$ except the fact that we would our starting course-grained free energy would be $F_{\rm eff}(q_{\rm th})$ instead of $F_{\rm eff}(q_{\rm el})$ in Eq. 5.24 and the material parameters in the course-grained free energy $F_{\rm eff}(q_{\rm th})$ would be $B^R_{ijkl}(q_{\rm th}) \approx B^0_{ijkl} = \kappa_0\delta_{ij}\delta_{kl}$ and $C^R_{ijkl}(q_{\rm th}) \approx C^0_{ijkl} = \lambda_0\delta_{ij}\delta_{kl} + \mu_0(\delta_{ik}\delta_{jl} + \delta_{il}\delta_{jk})$ instead of $B^R_{ijkl}(q_{\rm el})$ and $C^R_{ijkl}(q_{\rm el})$ in $F_{\rm eff}(q_{\rm el})$ since the elastic moduli do not renormalize in the regime $q > q_{\rm th}$. We summarize these scalings in Table 5.2.

Note that the scaling exponents in the regime $q < \min\{q_{\rm th}, q_{\rm el}\}$ hold to all orders of perturbation theory. This is because of the following reason. Since the parameters in the radial correlation function remain constant due to the irrelevance of all anharmonic terms in the effective free enegy $F_{\rm eff}$, the scaling exponents of the in-plane moduli are obtained using simple power counting from self-consistent equations like Eqs. 5.35 and 5.42. This remains the same to all orders in perturbation [172].

Table 5.2: Scaling Exponents for $\ell_{\rm el} < \ell_{\rm th} \Rightarrow q_{\rm el} > q_{\rm th}$

Scale	$q > q_{\rm el} > q_{\rm th}$	$q_{\rm el} > q > q_{\rm th}$	$q_{\rm el} > q_{\rm th} > q$
$C^R_{\varphi\varphi\varphi\varphi}/Y_0$	$\frac{1}{1-\nu_0^2}$	$\frac{1}{1-\nu_0^2}$	$\sim \left(\frac{q_\varphi}{q_{\rm el}}\right) \Omega_{\varphi\varphi\varphi\varphi} \left(q_\varphi/(q_{\rm el}q_z)^{1/2}\right)$
$C^R_{\varphi\varphi zz}/Y_0$	$\frac{\nu_0}{1-\nu_0^2}$	$\frac{\nu_0}{1-\nu_0^2}$	$\sim \left(\frac{q_\varphi}{q_{\rm el}}\right) \Omega_{\varphi\varphi zz} \left(q_\varphi/(q_{\rm el}q_z)^{1/2}\right)$
$C^R_{\varphi z\varphi z}/Y_0$	$\frac{1}{2(1+\nu_0)}$	$\frac{1}{2(1+\nu_0)}$	constant
C^R_{zzzz}/Y_0	$\frac{1}{1-\nu_0^2}$	$\frac{1}{1-\nu_0^2}$	constant
$Y^R_{\varphi\varphi}/Y_0$	1	1	$\sim \left(\frac{q_\varphi}{q_{\rm el}}\right) \Omega_{Y_{\varphi\varphi}} \left(q_\varphi/(q_{\rm el}q_z)^{1/2}\right)$
Y^R_{zz}/Y_0	1	1	constant
$B^R_{\varphi\varphi\varphi\varphi}/\kappa_0$	1	1	constant

5.4 Comparison with molecular dynamics simulations

To test our results tabulated in Tables 5.1 and 5.2, we compared with molecular dynamics (MD) simulations. Instead of using a fully atomistic model to simulate a nanotube, we used a convenient coarse-grained discrete model made of a triangular lattice of point masses with nearest neighbors are connected by harmonic springs (see Fig. 5.1(a)). Then the stretching part in the free energy in Eq. 5.3 can be modeled by assigning the equilibrium length of the springs to be a_0 and a spring constant K_b:

$$F_{\rm stretch} = \frac{1}{2} K_b \sum_{\langle i,j \rangle} (|\mathbf{x}_i - \mathbf{x}_j| - a_0)^2, \tag{5.47}$$

where $\mathbf{x}_i$ is the position of $i^{\rm th}$ mass and the sum is over nearest neighbor point masses i and j. The energy cost of bending in Eq. 5.3 can be modeled as [174, 103]:

$$F_{\rm bending} = K_d \sum_{(\alpha,\beta)} (1 - \cos(\theta_{\alpha\beta} - \theta^0_{\alpha\beta})), \tag{5.48}$$

where $\theta_{\alpha\beta}$ is the angle between two adjacent triangles α and β as shown in Fig. 5.1(a) and $\theta^0_{\alpha\beta}$ is the value of this angle at minimum bending energy configuration. Note that $\theta^0_{\alpha\beta}$ depends on the curvature of the nanotube and fineness of the discretization.

The parameters K_b and K_d are related to the continuum material parameters as follows [174]:

$$Y_0 = \frac{2}{\sqrt{3}}K_b, \lambda_0 = \mu_0 = \frac{\sqrt{3}}{4}K_b, \nu_0 = \frac{1}{3}, \kappa_0 = \frac{\sqrt{3}}{2}K_d. \tag{5.49}$$

The simulations were done with LAMMPS package [175, 176]. As will be discussed later, the simulations were done in isobaric-isothermal (NPT) or canonical (NVT) ensemble. Temperature and pressure were controlled using Nosé-Hoover type thermostat and barostat [177]. The parameters K_d, K_b, T, the aspect ration $L/(2\pi R)$ and number point masses were varied to probe different scaling regimes. The time steps were chosen to be one tenth of the smallest of the characteristic time scales of the system:

$$\tau_T = a\sqrt{\frac{m}{k_B T}}, \tau_b = \sqrt{\frac{m}{K_b}}, \tau_d = a_0\sqrt{\frac{m}{K_d}}, \tag{5.50}$$

where m is the mass of each point mass, and τ_T is characteristic time a point mass takes to cover one atomic length at thermal velocity, τ_b is characteristic time of the spring-mass system, τ_d is characteristic time of the dihedral bond-mass system. A simulation generally ran for approximately $1.6\text{x}10^8 - 10^9$ time steps. For each simulation, the equilibration was checked using autocorrelation time of different parameters such as radial fluctuations, length of the shell, etc.

First, simulations were done with periodic boundary condition along the axial direction and the simulation box was allowed to change its size in the axial direction maintaining zero pressure condition so that the cylindrical shell could fluctuate freely. From these simulations, the radial displacements were calculated. The Fourier transform of the correlation function $\langle|\tilde{h}(q_\varphi, q_z = 0)|^2\rangle$ and $\langle|\tilde{h}(q_\varphi = 0, q_z)|^2\rangle$ of radial displacement are plotted in Fig. 5.4. Fig. 5.4(a) shows the collapse around q_{th}. The dotted lines for $\langle|\tilde{h}(q_\varphi, q_z = 0)|^2\rangle$ and $\langle|\tilde{h}(q_\varphi = 0, q_z)|^2\rangle$ coincide with each other in the region $q > q_{\text{el}}$ for each parameter set. This is because in this regime the effect of

anisotropic curvature is negligible in this regime. Furthermore, in this regime, we see that the correlation function goes as $\sim q^{-4}$ when $q > q_{\text{th}}$ and $\sim q^{-3.2}$ when $q < q_{\text{th}}$. This is because in the former case the effect of the anharmonic terms are not important and the system is in the harmonic regime, whereas in the latter case the anharmonic terms are important and since $q > q_{\text{el}}$ we see the exponent $-4 + \eta = -3.2$. However, in the regime $q < q_{\text{el}}$ they diverge from each other. To understand this regime better, scaling collapse around q_{el} is done in Fig. 5.4(b) keeping $q_{\text{el}} \leq q_{\text{th}}$ for all simulations. Again, for $q > q_{\text{el}}$, $\langle|\tilde{h}(q_\varphi, q_z = 0)|^2\rangle$ and $\langle|\tilde{h}(q_\varphi = 0, q_z)|^2\rangle$ coincide with each other and scale as $\sim q^{-3.2}$ because here $q_{\text{el}} < q < q_{\text{th}}$. However, for $q < q_{\text{el}} < q_{\text{th}}$, we see new scaling laws. In the φ direction the correlation function scales as $\sim q_\varphi^{-4}$, whereas in the z direction the correlation function scales as $\sim q_z^{-1/2}$. These observations can be justified using the Green's function in Eq. 5.11 and Table 5.1 in the following way:

$$\langle|\tilde{h}(q_\varphi, q_z = 0)|^2\rangle = \frac{k_B T/A}{B^R_{\varphi\varphi\varphi\varphi}(\mathbf{q}) q_\varphi^4} = \frac{k_B T/A}{\kappa_R(\mathbf{q}) q_\varphi^4} \approx \frac{k_B T/A}{\kappa_0 (q_{\text{el}}/q_{\text{th}})^{-\eta} q_\varphi^4} \text{ for } q_\varphi < q_{\text{el}} < q_{\text{th}}, \tag{5.51a}$$

$$\begin{aligned}\langle|\tilde{h}(q_\varphi = 0, q_z)|^2\rangle &= \frac{k_B T/A}{B^R_{zzzz}(\mathbf{q}) q_z^4 + \frac{Y^R_{\varphi\varphi}(\mathbf{q})}{R^2}} \approx \frac{k_B T/A}{Y^R_{\varphi\varphi}(\mathbf{q})/R^2} \\ &\approx \frac{k_B T/A}{Y_0 (q_{\text{el}}/q_{\text{th}})^{\eta_u} (q_z/q_{\text{el}})^{1/2}/R^2} \text{ for } q_z < q_{\text{el}} < q_{\text{th}}.\end{aligned} \tag{5.51b}$$

In total, both panels of Fig. 5.4 can be understood using the following equations:

$$\langle|\tilde{h}(q_\varphi, q_z = 0)|^2\rangle = \frac{k_B T/A}{B^R_{\varphi\varphi\varphi\varphi}(\mathbf{q}) q_\varphi^4} \approx \begin{cases} \frac{k_B T/A}{\kappa_0 q_\varphi^4}, & q_{\text{el}} < q_{\text{th}} < q_\varphi \\ \frac{k_B T/A}{\kappa_0 (q_\varphi/q_{\text{th}})^{-\eta} q_\varphi^4}, & q_{\text{el}} < q_\varphi < q_{\text{th}} \\ \frac{k_B T/A}{\kappa_0 (q_{\text{el}}/q_{\text{th}})^{-\eta} q_\varphi^4}, & q_\varphi < q_{\text{el}} < q_{\text{th}} \end{cases}, \tag{5.52a}$$

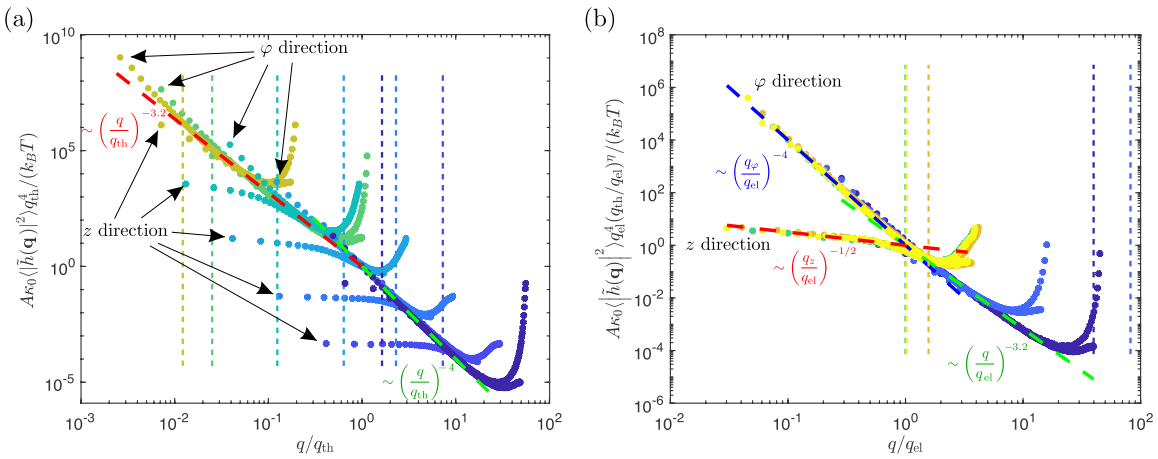

Figure 5.4: Scaling collapse for radial displacement correlation function $\langle|\tilde{h}(\mathbf{q})|^2\rangle$ for molecular dynamics simulations with zero pressure condition in the axial direction. (a) Correlation function $\langle|\tilde{h}(q_\varphi, q_z = 0)|^2\rangle$ and $\langle|\tilde{h}(q_\varphi = 0, q_z)|^2\rangle$ collapsed around q_{th} plotted in dots. For a single parameter set, the same color was used to plot the correlation function in both φ and z direction. The dotted lines of different colors correspond to different parameter sets. The vertical dashed lines of different colors show $q_{\text{el}}/q_{\text{th}}$ corresponding to the dotted curves of same color. The red and green slanted dashed lines are $(q_\varphi/q_{\text{th}})^{-3.2}$ and $(q_\varphi/q_{\text{th}})^{-4}$ respectively. (b) Correlation functions $\langle|\tilde{h}(q_\varphi, q_z = 0)|^2\rangle$ and $\langle|\tilde{h}(q_\varphi = 0, q_z)|^2\rangle$ collapsed around q_{el} plotted in dots. For a single parameter set, the same color was used to plot the correlation function in both φ and z direction. The vertical dashed lines of different colors show q_{th}/q_{el} corresponding to the dotted curves of same color. The red, blue and green slanted dashed lines are $(q_z/q_{\text{th}})^{-1/2}$, $(q_\varphi/q_{\text{th}})^{-1/2}$ and $(q/q_{\text{th}})^{-3.2}$ respectively. In both panels, the curling up of the tails of the simulation curves corresponds to wave vectors close to the edge of the first Brillouin zone.

$$\langle|\tilde{h}(q_\varphi = 0, q_z)|^2\rangle = \frac{k_BT/A}{B^R_{zzzz}(\mathbf{q})q_z^4 + \frac{Y^R_{\varphi\varphi}(\mathbf{q})}{R^2}} \approx \begin{cases} \frac{k_BT/A}{\kappa_R(\mathbf{q})q_z^4}, & q_{\text{el}} < q_z \\ \frac{k_BT/A}{Y^R_{\varphi\varphi}(\mathbf{q})/R^2}, & q_z < q_{\text{el}} \end{cases}$$

$$\approx \begin{cases} \frac{k_BT/A}{\kappa_0 q_\varphi^4}, & q_{\text{el}} < q_{\text{th}} < q_z \\ \frac{k_BT/A}{\kappa_0 (q_z/q_{\text{el}})^{-\eta} q_z^4}, & q_{\text{el}} < q_z < q_{\text{th}} \\ \frac{k_BT/A}{Y_0 (q_{\text{el}}/q_{\text{th}})^{\eta_u} (q_z/q_{\text{el}})^{1/2}/R^2}, & q_z < q_{\text{el}} < q_{\text{th}} \end{cases} \tag{5.52b}$$

This confirms the nontrivial scaling of $Y_{\varphi\varphi}$ in the regime $q < q_{\rm el} < q_{\rm th}$ as we predicted in Section 5.3.2.

To probe the Young's modulus Y_{zz} in the axial direction, we performed simulations changing the length of the box in steps and at each step letting the shell equilibrate under thermal fluctuation. This ensemble is canonical (NVT) since we fixed the volume of the system at each step. Then, at each value of box length we recorded the pressure on the box in the axial direction. From that, we extracted the normal stress in the axial direction σ_{zz} (to get the stress from the pressure, we multiply the pressure with the area of the wall and divide by the perimeter of the nanotube) and plotted the average value of that as function of strain (defined as the relative change of length from the size of the box at the minimum energy configuration) for different values of temperature T in Fig. 5.5(a). Note that in the figure, the strain at which the average stress is zero is different for different temperatures. This is because under thermal fluctuation, the shell shrinks (see Eq. 5.8b) in equilibrium (at zero external stress condition on the average). More importantly, we notice that the slope of the stress vs. strain curves change with temperature. The slope of the stress vs. strain curve at zero stress is defined as the Young's modulus Y_{zz} in the axial direction. We plotted the normalized Young's modulus Y_{zz}/Y_0, extracted this way, as function of $\ell_{\rm el}/\ell_{\rm th}$ in Fig. 5.5(b) for two different parameter sets. The Young's moduli for these two parameter sets decrease with increasing system size meaning that they renormalize with increasing system size, but only collapse on top of each other when the horizontal axis is $\ell_{\rm el}/\ell_{\rm th}$ in fig. 5.5(b). This implies that Y_{zz} stops renormalize at the elastic length scale $\ell_{\rm el}$ confirming Eq. 5.34b. Furthermore, from Fig. 5.5(b), we see that the Y^R_{zz} scales as $\sim (\ell_{\rm el}/\ell_{\rm th})^{-0.37} = (\ell_{\rm el}/\ell_{\rm th})^{-\eta_u}$ confirming the scaling law in the regime $\ell_{\rm th} < \ell < \ell_{\rm el}$.

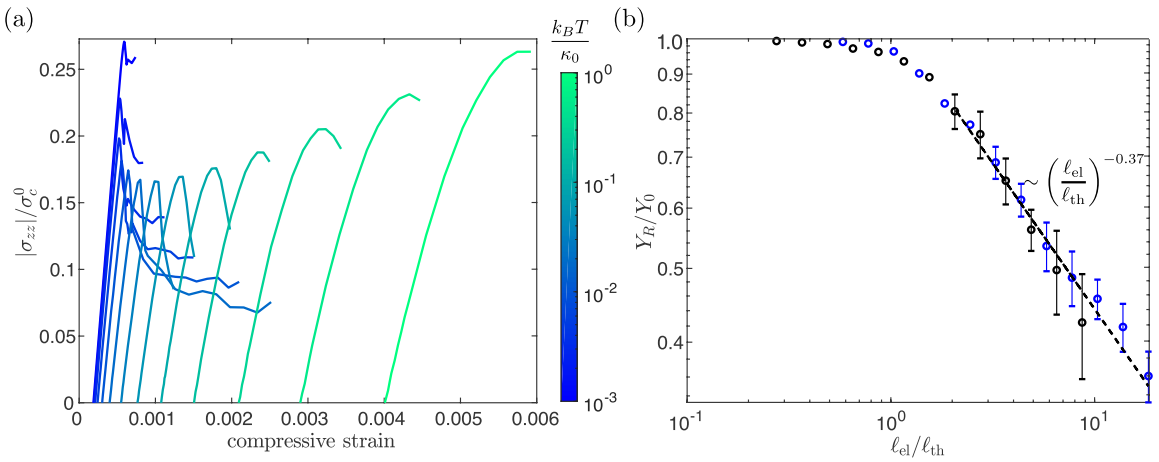

Figure 5.5: Simulation results from NVT simulations fixing the length of the cylindrical shell. (a) Stress vs. strain curves for a fixed parameter set $\gamma = 2 \times 10^6$, $L/2\pi R = 2$, $2\pi R/a_0 = 48$ at different temperatures (the colorbar shows k_B/κ_0). The vertical axis of the plot is $|\sigma_{zz}|/\sigma_c^0$, where $\sigma_c^0 = 2\sqrt{Y_0\kappa_0}/R$ is the critical buckling load for classical cylindrical shell [178]. The maximum of the curve at each temperature is the critical buckling load for molecular dynamics, which is smaller than the classical buckling load σ_c^0 because of the discrete nature and corresponding non-ideality of our model. (b) Young's modulus extracted from the slope of the strain vs. strain curves (example shown in (a)) at zero stress plotted as a function of ℓ_{el}/ℓ_{th}. The black dots correspond to the parameter set $\gamma = Y_0R^2/\kappa_0 = 1 \times 10^5$, $L/2\pi R = 1$, $2\pi R/a_0 = 48$, $L/\ell_{el} \approx 35$. The blue dots correspond to the parameter set $\gamma = Y_0R^2/\kappa_0 = 2 \times 10^6$, $L/2\pi R = 2$, $2\pi R/a_0 = 48$, $L/\ell_{el} \approx 126$. The black dashed line shows $(\ell_{el}/\ell_{th})^{-0.37}$.

5.5 Conclusion

We have studied mechanical properties of thermally fluctuating nanotubes. We have shown that the presence of length scales ℓ_{th} and ℓ_{el} gives different scaling regimes. In particular, at scales larger than both ℓ_{th} and ℓ_{el}, we find that the stiffness moduli become anisotropic. Moreover, in this regime, we obtain new scaling exponents for the elastic moduli. For $\ell_{th} < \ell_{el}$ and scales between these two lengths, however, we recover the same scaling exponents as in isotropic flat solid membranes.

One immediate extension of this work can be to study the effect of thermal fluctuations on the critical axial buckling load. We see from Fig. 5.5(a), the critical buckling load initially reduces with increasing temperature (see the bluer curves), but starts increasing (see the greener curves) as the with temperature at higher temperatures.

We anticipate that the initial dip is due to thermal activation of energy barrier crossing to the buckled state, but the later increase is due to renormalization of elastic moduli. However, deeper investigation is required for better understanding.

Chapter 6

Conclusion and outlook

Mechanics problems such as designing metamaterials for novel applications, understanding the mechanics of biological membranes and tissues, designing micro-scale origami and kirigami structures for self-foldable micro-robots are hard and requires multidisciplinary expertise. To that end, in this thesis, we focused on using concepts and techniques from physics and combining them to existing theories in mechanics to better understand problems ranging from static boundary value problems to dynamical wave propagation problems to thermal fluctuations of thin shells. In the following we summarize each of these and discuss possible extensions.

6.1 Elastic multipole method: towards more complicated geometries

We used concept of induction and method of multipole expansion from electrostatics to develop an elastic multipole method to describe deformations of infinite elastic systems with circular holes and inclusions. This method is not only intuitive, but also gives quantitatively accurate results. We demonstrated that error in the results obtained with this method decreases exponentially with increasing highest order of

multipole considered. The agreement between our method and finite element simulations and experiments are also very good. To extend this method to finite elastic systems with boundaries, we used the concept of image charges from electrostatics. We demonstrated how images of the elastic multipoles can be obtained for several different boundary conditions such as flat traction free edge, flat rigid edge, circular traction free edge, circular rigid edge and circular edge with allowed slippage. Results obtained with our method are in good agreement with finite element simulations and experiments.

The elastic multipole method can also be straightforwardly extended to include defects inside elastic materials by adding their contributions to the Airy stress functions (see Sec. 2.1). Note, however, that the linear elasticity breaks down in the vicinity of defects, where the displacement fields are singular (see Table 2.2). This can be remedied via strain gradient elasticity [179, 180, 181]. The elastic multipole method can in principle also be generalized to describe deformations of curved thin shells with inclusions. The local force balance can still be satisfied by representing stresses in terms of the Airy stress function [123]. However, in order to find the Airy stress functions for the monopoles and higher order multipoles, one also needs to include the bending moment balance equation and appropriately modify the compatibility conditions by taking into account the Gaussian curvature of the shell [182, 183, 184].

While the elastic multipole method presented here focused only on linear deformation, similar concepts can also be useful for describing the post-buckling deformation of mechanical metamaterials. Previously, it was demonstrated that the buckled patterns of structures with periodic arrays of holes [128, 185, 27, 186], square frames [187, 188] and kirigami slits [187] can be qualitatively described with interacting quadrupoles. Furthermore, the approach with elastic quadrupoles has recently been extended to the nonlinear regime of compressed structures with periodic arrays

of holes, which can estimate the initial linear deformation, the critical buckling load, as well as the buckling mode [127]. The accuracy of these results could be further improved by expanding the induced fields to higher-order multipoles. Thus, the elastic multipole method has the potential to significantly advance our understanding of deformation patterns in structures with holes and inclusions.

The analysis for elastic disks in Section 3.2.4 could be directly extended to the analysis for linear deformation of an elastic annulus with circular holes and inclusion by constructing an infinite set of image multipoles similarly as was done for the elastic strip in Section 3.2.2. For structures with other geometries, the first step is to identify the Airy stress function for the image of disclination, which is directly related to the Green's function for biharmonic equation (see Section 3.1). The Green's function for a rectangular geometry can be obtained with a Fourier series [1]. The Green's function for an infinite elastic wedge with traction-free boundary conditions was previously obtained by Gregory in Ref. [189]. Interestingly, for a sufficiently small wedge angle the Airy stress functions exhibit an infinite number of oscillations near the wedge tip [190, 191, 192, 189]. Once the Airy stress functions for the images of disclinations are found, then the Airy stress functions for images of all other multipoles can be obtained by following the procedure outlined in Section 3.1. These results could then be used to analyze deformations of structures with holes and inclusions, where external load induces elastic multipoles at the center of holes and inclusions, which further induce image multipoles to satisfy boundary conditions at the outer boundaries of these structures. The amplitudes of induced multipoles can then be obtained from the continuity of tractions and displacements at the boundary of each hole as described in Section 3.2.1.

6.2 Symmetry characters of elastic wave eigenmodes: designing topological metamaterials

Using representation theory we analyzed anti-plane shear wave bands corresponding to periodic elastic media with different space group symmetry. In particular, we showed how to find the irreducible representation (irrep) labels at different high symmetry points in the Brillouin zone. We showed using examples that when there are multidimensional irreps, there can be degeneracies at that point. Moreover, we gave examples to show when the some of the symmetries are broken the multidimensional irreps can break into single dimensional irreps, and when that happens the degeneracies are lifted and directional band gap open up.

Representation labels of bands at high symmetry points in the Brillouin zone have been shown to be a very good indicator of if the band is topological [161, 162, 163, 193, 194]. Not long ago, using the fact that the space group $p6mm$ has two independent 2-dimensional irreps at the Γ point of its Brillouin zone, Wu and Hu [195] engineered a photonic structure, which behave like spin-1/2 $\mathbb{Z}_2$ topological insulator even though photonic system are spin-1 systems. They showed that this structure can support helical edge states where edge states with opposite angular momenta travel in opposite one way direction without being scattered. Although there was debate if these edge modes are stable [196], this discovery has led to several similar works in the field of phononics [197, 198, 199]. However, not much have been explored in the realm of the newly discovered topological phases such as fragile topology [193, 200], higher-order topology [201, 202] where instead of stable edge modes, one finds corner and hinge modes. One way to detect these topological bands is through symmetry labels [193, 194]. For example, consider the bands 2 and 3 in Figs. 6.1(a) and (b) of periodic elastic systems with space group symmetry $p6mm$. The symmetry labels for the anti-plane shear wave bands are $\Gamma_6 + M_3 + M_4 + K_3$

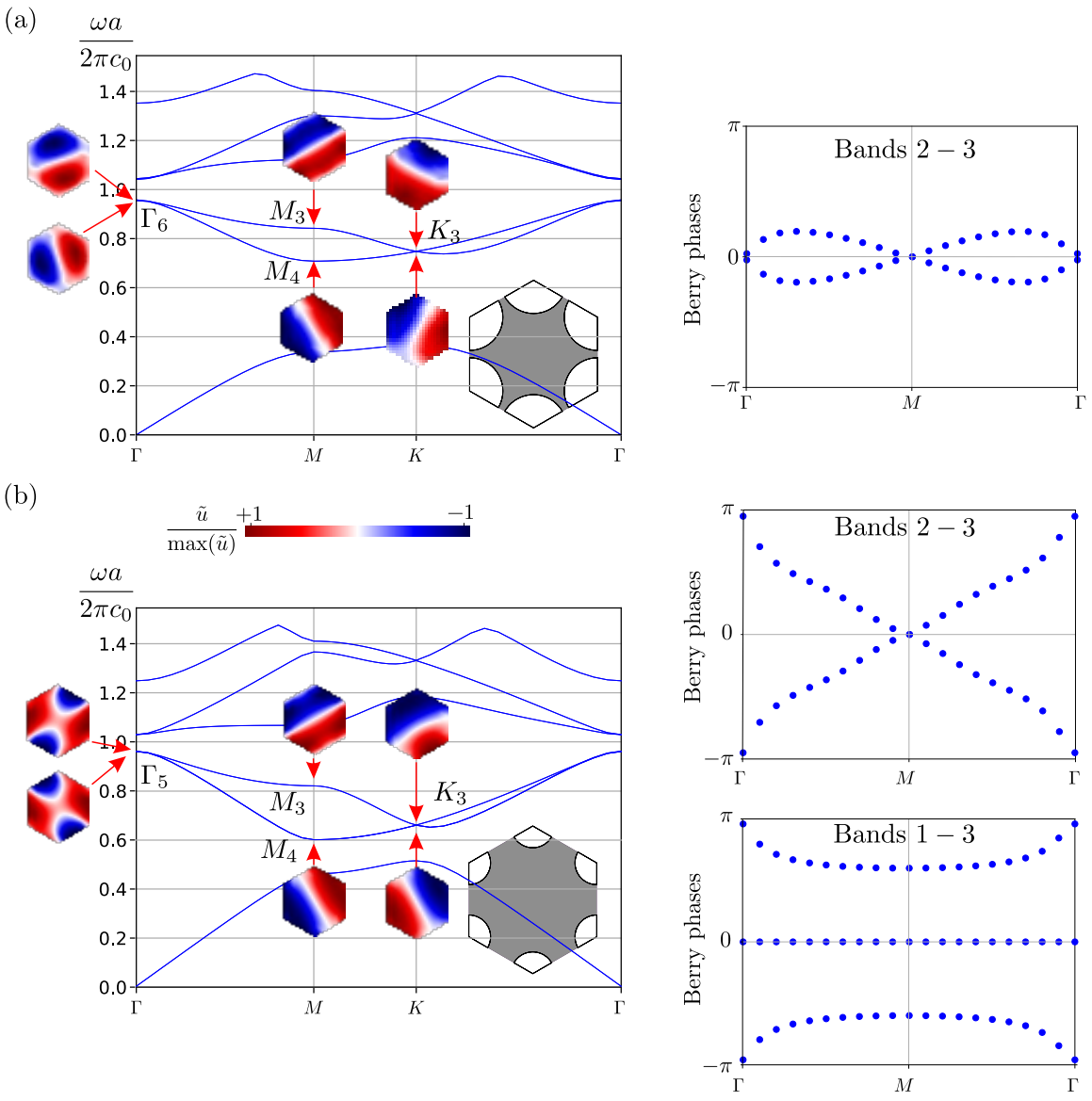

Figure 6.1: Fragile topology of anti-plane shear wave bands in elastic systems with space group symmetry $p6mm$. (a) Trivial system, (b) fragile topological system. In both panels the band structures along with the eigenfunctions (real parts) and their symmetry irrep labels are shown on the left. The unit cells are shown inset with the elastic matrix (shear modulus μ_0, density ρ_0) shown in dark grey and the holes shown in white. The radius R to lattice spacing a ratio are $R/a = 0.26$ for (a) and $R/a = 0.17$ for (b). The eigenfrequencies on the y-axis of the band structures are normalized by $2\pi c_0/a$, where $c_0 = \sqrt{\mu_0/\rho_0}$ is the velocity of shear wave inside the elastic matrix. On the right, the flow of non-Abelian Berry phases along a reciprocal lattice vector are shown for bands $2+3$ for (a), and $2+3$ and $1+2+3$ for (b).

in Fig. 6.1(a) whereas are $\Gamma_5 + M_3 + M_4 + K_3$ in Fig. 6.1(b) (see [203] for the irrep labels of little groups at high symmetry points of the Brillouin zone of space group

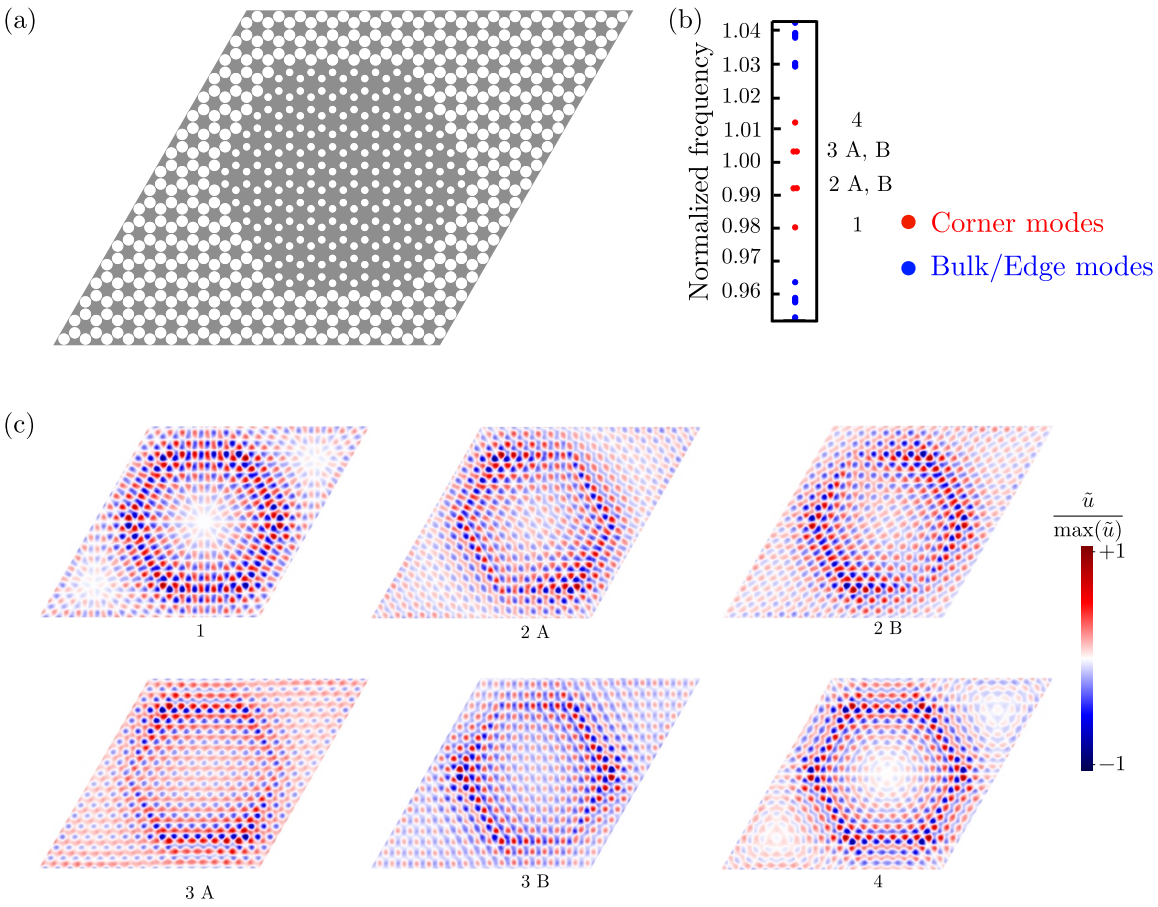

Figure 6.2: Corner modes at the boundary of fragile topological systems. (a) shows the 6-fold rotational symmetric super-cell made with the fragile topological system of Fig. 6.1(b) inside trivial system of Fig. 6.1(a). (b) shows frequencies of the 6 corner modes in red and bulk/edge modes in blue. (c) eigenfunctions of the corner modes. The 6 identical corner modes at the 6 corners of inner system couple together to break into irreps A_2 corresponding to mode 1, E_1 corresponding to modes $2A$ and $2B$, E_2 corresponding to modes $3A$ and $3B$, and B_1 corresponding to mode 4 of point group C_{6v} (see the character table of C_{6v} Table C.3). Since, $2A$ and $2B$ correspond to 2-dimensional irrep E_1, they have the same eigenfrequency. Similarly, $3A$ and $3B$ have the same eigenfrequency because they correspond to 2-dimensional irrep E_2.

$p6mm$). From the supplementary material of article [193], we find that a set of band with symmetry labels $\Gamma_5 + M_3 + M_4 + K_3$ must be fragile topological and we find that a set of band with symmetry labels $\Gamma_6 + M_3 + M_4 + K_3$ is trivial. The non-Abelian Berry phases [204, 205] for bands $2 + 3$ show winding in case of Fig. 6.1(b) and no winding in Fig. 6.1(a) showing nontrivial topology in the former case and trivial topology in the latter case. However, non-Abelian Berry phases for bands

$1+2+3$ of Fig. 6.1(b) shows no winding, meaning that the topology of bands $2+3$ in Fig. 6.1(b) is fragile. This confirms the prediction just by looking at the symmetry representation labels at the high symmetry points. In Fig. 6.2, we see that when a boundary is created between the fragile topological system (Fig. 6.1(b)) and the trivial system (Fig. 6.1(a)), eigenmodes localized to corners show up in the common bandgap region $\omega a/(2\pi c_0) = 0.95 - 1.04$ of the two systems.

We hope that our work enables researchers in the field of mechanics and elasticity to use representation theory to design and detect topological phases in phononics and use them in novel applications.

6.3 Thermalized nanotubes: under external load, at extreme limits of aspect ratios, and multi-walled structures

Using renormalization group from statistical field theory we analyzed scale dependent renormalization of elastic moduli of thermalized nanotubes. Beyond elastic length which is approximately the geometric mean of radius and effective thickness of the shell, we found new scaling laws due to presence of the curvature. In particular, the in-plane elastic moduli become anisotropic with Young's modulus in the axial direction becoming a constant whereas Young's modulus in the azimuthal direction renormalizing with a new scaling exponent. We confirmed this results with molecular dynamics simulations. We also found evidence from molecular dynamics that axial critical buckling load changes nontrivially with changing temperature.

In the future, it will be interesting to study (theoretically and using simulations) the response of thermalized nanotubes under axial load, axisymmetric pressure and torsion. In the classical theory of shells, in each of these cases interesting buckling

instabilities occur. It would be fascinating to investigating thermal fluctuations affect these instabilities

The theory presented in Chapter 5 is limited to shells with length L to circumference $2\pi R$ ratio of order 1. However, shells with $L \gg 2\pi R$ or $L \ll 2\pi R$ may also be importance. In both cases, one can, in principle, integrate out the Fourier modes in the shorter direction and study the effectively 1-dimensional system. In the case $L \gg 2\pi R$, we expect the shell to behave like a polymer chain [206] and do random walk when the length is larger than its persistence length. In the case $L \ll 2\pi R$, we expect the shell to behave like an elastic ring which also does random walk beyond a persistence length [207] and can show interesting instabilities under axisymmetric pressure [208].

While the results presented in Chapter 5 are for single-walled nanotubes, similar studies can also be done with multi-walled nanotubes. Whereas a realistic model with van der Waals interactions between layers may be too difficult for analytical methods, a phenomenological elasticity-like model as described in [209] adapted for cylindrical shells may be more amenable to analytical studies.

Appendix A

Details of linear finite element simulations in Chapter 2

Linear analyses in finite element simulations were performed with the commercial software Ansys® Mechanical, Release 17.2. Geometric models of plates with holes and inclusions were discretized with 2D eight-node, quadratic elements of type PLANE183 set to the plane stress state option. The material for plates and inclusions was modeled as a linear isotropic elastic material. To minimize the effect of boundaries for the comparison with the elastic multipole method, which considers an infinite domain, we chose a sufficiently large square-shaped domain of size $L = 400d$, where d is the diameter of inclusions. To ensure high accuracy, we used a fine mesh with 360 quadratic elements evenly spaced around the circumference of each inclusion. To keep the total number of elements at a manageable number, the size of the elements increased at a rate of 2% per element, when moving away from inclusions, up to the largest elements at the domain boundaries with an edge length of $L/200$. To prevent rigid body motions of the whole structure, we fixed the following 3 degrees of freedom: the displacement vector at the center of the square domain was specified to be zero ($u_x(0,0) = 0$, $u_y(0,0) = 0$); the midpoint of the left edge of the square domain

was constrained to move only in the x-direction ($u_y(-L/2, 0) = 0$). For consistency with finite element simulations, we imposed the same set of constraints ($u_x(0, 0) = 0$, $u_y(0, 0) = 0$, $u_y(-L/2, 0) = 0$) for the elastic multipole method. This was done in two steps. After obtaining the displacement field ($u_x^{\mathrm{EMP}}(x, y), u_y^{\mathrm{EMP}}(x, y)$) with the elastic multipole method, we first subtracted the displacement ($u_x^{\mathrm{EMP}}(0, 0), u_y^{\mathrm{EMP}}(0, 0)$) at each point

$$u'^{\mathrm{EMP}}_x(x, y) = u_x^{\mathrm{EMP}}(x, y) - u_x^{\mathrm{EMP}}(0, 0), \tag{A.1a}$$

$$u'^{\mathrm{EMP}}_y(x, y) = u_y^{\mathrm{EMP}}(x, y) - u_y^{\mathrm{EMP}}(0, 0), \tag{A.1b}$$

to ensure that the center of the square domain is fixed ($u'^{\mathrm{EMP}}_x(0, 0) = u'^{\mathrm{EMP}}_y(0, 0) = 0$). For this updated displacement field, the coordinates of points in the deformed configuration are $x'(x, y) = x + u'^{\mathrm{EMP}}_x(x, y)$ and $y'(x, y) = y + u'^{\mathrm{EMP}}_y(x, y)$. To impose the last constraint ($u_y(-L/2, 0) = 0$), this new deformed configuration was then rotated anticlockwise by the angle $\theta = \tan^{-1}(u'^{\mathrm{EMP}}_y(-L/2, 0)/[L/2 - u'^{\mathrm{EMP}}_x(-L/2, 0)])$ around the origin of the coordinate system as

$$x''(x, y) = x'(x, y)\cos\theta - y'(x, y)\sin\theta \equiv x + u''^{\mathrm{EMP}}_x(x, y), \tag{A.2a}$$

$$y''(x, y) = x'(x, y)\sin\theta + y'(x, y)\cos\theta \equiv y + u''^{\mathrm{EMP}}_y(x, y). \tag{A.2b}$$

The set of displacement fields $u''^{\mathrm{EMP}}_x(x, y)$ and $u''^{\mathrm{EMP}}_y(x, y)$ was then used for comparison with finite element simulations.

Appendix B

Additional details of linear finite element simulations and experiments in Chapter 3

B.1 Linear finite element simulations

Linear analyses in finite element simulations were performed with the commercial software Ansys® Mechanical Release 17.2. Geometric models of 2D plates with holes and inclusions were discretized with 2D eight-node, quadratic elements of type PLANE183 set to the plane stress option. The material for plates and inclusions was modeled as a linear isotropic elastic material. To ensure high accuracy, we used a fine mesh with 360 quadratic elements evenly spaced around the circumference of each hole and each inclusion, and elements of similar sizes were also used inside the inclusions. To keep the number of elements at a manageable level, the size of elements was allowed to increase at a rate of approximately 2% per element, when moving away from inclusions.

For the simulation of a single hole with radius R embedded in a compressed plate near a traction-free edge in Fig. 3.4, we used a sufficiently large rectangular domain of size $L \times w$ with length $L = 800R$ and width $w = 400R$ to minimize the effect of boundaries far away from the hole. Along the left and right boundaries, we prescribed tractions $\sigma_{xx}(\pm L/2, y) = \sigma_{xx}^{\text{ext}}$ and $\sigma_{xy}(\pm L/2, y) = 0$, and along the top and bottom boundaries, we prescribed tractions $\sigma_{xy}(x, \pm w/2) = \sigma_{yy}(x, \pm w/2) = 0$. To prevent rigid body motions of the structure, the midpoints of the left and right edges of the domain were constrained to move only in the x-direction ($u_y(\pm L/2, 0) = 0$), while the midpoint of the bottom edge of the domain was fixed in the x-direction ($u_x(0, -w/2) = 0$).

For comparison with the experiment of the sample with one hole near a traction-free edge in Fig. 3.6 we simulated a plate of length $L = 100$ mm and width $w = 100$ mm. To mimic experimental conditions, the plate was compressed by prescribing a uniform horizontal displacement on the left and right surfaces ($u_x(\pm L/2, y) = \pm L/2\varepsilon_{xx}^{\text{ext}}$), while allowing the nodes on these surfaces to move freely in the y-direction ($\sigma_{xy}(\pm L/2, y) = 0$). The top and bottom boundaries were traction-free ($\sigma_{xy}(x, \pm w/2) = \sigma_{yy}(x, \pm w/2) = 0$). The midpoints of the left and right edges were again constrained ($u_y(\pm L/2, 0) = 0$) to prevent rigid body translation in the y-direction.

For the simulation of elastic strips of length $L = 100$ mm and width w in Figs. 3.8 and 3.10 we used a uniform external pressure load at the two ends of the strip ($\sigma_{xx}(\pm L/2, y) = \sigma_{xx}^{\text{ext}}$, $\sigma_{xy}(\pm L/2, y) = 0$), while the other boundaries were traction-free ($\sigma_{xy}(x, \pm w/2) = \sigma_{yy}(x, \pm w/2) = 0$). To prevent rigid body motions of the strip we restricted 3 degrees of freedom ($u_x(0, -w/2) = 0$, $u_y(0, -w/2) = 0$, $u_x(0, +w/2) = 0$).

For the simulation of a single hole with radius R located near a straight rigid edge in Fig. 3.12, we used a domain of length $L = 800R$ and width $w = 400R$. Points on

the top boundary of the domain were fixed ($u_x(x, +w/2) = u_y(x, +w/2) = 0$) and the sample was compressed by applying uniform displacement in the y-direction on the bottom boundary of the plate ($u_y(x, -w/2) = w\varepsilon_{yy}^{\text{ext}}$, $\sigma_{xy}(x, -w/2) = 0$). Points on the left and right boundaries were constrained to move only in the y-direction ($u_x(\pm L/2, y) = 0$ and $\sigma_{xy}(\pm L/2, y) = 0$).

For the simulations of elastic disks with radius R in Figs. 3.14 and 3.16 we considered three different boundary conditions: hydrostatic ($\sigma_{\text{tot},rr}^{\text{out}}(r = R, \varphi) = \sigma_{rr}^{\text{ext}}$, $\sigma_{\text{tot},r\varphi}^{\text{out}}(r = R, \varphi) = 0$), no-slip ($u_{\text{tot},r}^{\text{out}}(r = R, \varphi) = u_r^{\text{ext}}$, $u_{\text{tot},\varphi}^{\text{out}}(r = R, \varphi) = 0$), and slip ($u_{\text{tot},r}^{\text{out}}(r = R, \varphi) = u_r^{\text{ext}}$, $\sigma_{\text{tot},r\varphi}^{\text{out}}(r = R, \varphi) = 0$). To prevent the rigid-body motions of elastic discs with holes, we fixed 3 degrees of freedom for the hydrostatic load ($u_x(x = 0, y = 0) = u_y(x = 0, y = 0) = u_x(x = 0, y = R) = 0$) and 1 degree of freedom for the slip boundary condition ($u_x(x = 0, y = R) = 0$). No additional constraints were needed for the no-slip boundary condition.

B.2 Experimental Methods

Experimental samples were prepared by casting Elite Double 32 (Zhermack) elastomers with a measured Young's modulus $E_0 = 0.97$ MPa and assumed Poisson's ratio $\nu = 0.49$ [28]. Molds were fabricated from 5 mm thick acrylic plates with laser cut circular holes, which were then filled with acrylic cylinders in the assembled molds to create cylindrical holes in elastomer samples. Approximately 30 min after casting, molds were disassembled and solid samples were placed in a convection oven at 40 °C for 12 hours for further curing. The cylindrical inclusions made from acrylic (Young's modulus $E = 2.9$ GPa, Poisson's ratio $\nu = 0.37$ [130]) were inserted into the holes in elastomer samples and glued by a cyanoacrylate adhesive where required.

We designed a custom testing system for extracting the contours of deformed holes and inclusions in compressed experimental samples. The system comprises a

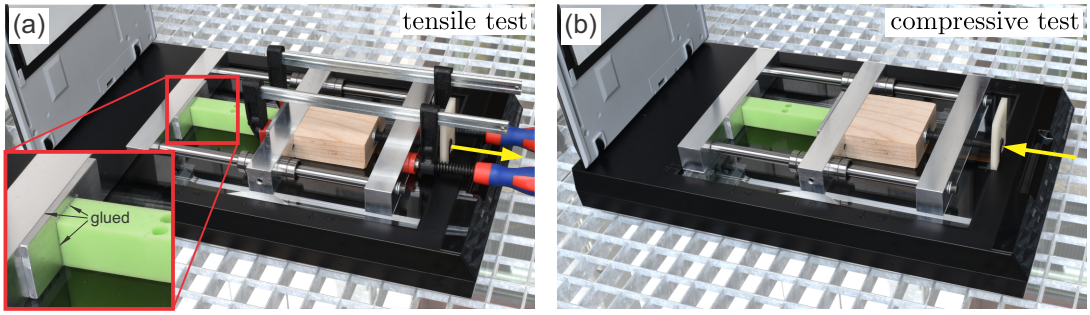

Figure B.1: Experimental systems for displacement controlled (a) tensile and (b) compressive tests for thin strips with holes and inclusions. The mechanism sits on a scanning device, which is used to extract the contours of deformed holes and inclusions. The two ends of the strip were glued to the aluminum plates (see the zoomed-in photo in (a)) to prevent bending due to the asymmetric position of holes/inclusion for both tensile and compressive loading. F-clamps were used to apply the tensile load to the elastic strip in (a). A 3D printed plastic wrench was used to precisely control the screw turns to achieve the desired compression in (b).

custom-made loading mechanism and a flatbed photo scanner (see Fig. B.1). For the experiment in Section 3.2.1, the sample was placed between aluminum plates and silicone oil was applied to reduce friction. Compressive displacement loading was applied incrementally in 1/3 mm steps via 120° turns of the M10x1 screw (metric thread with 10 mm diameter and 1 mm pitch) in the mechanism controlled by a 3D printed plastic wrench (see Fig. B.1b). For the experiments with elastic strips in Section 3.2.2, samples were glued to aluminum plates to prevent bending due to the asymmetric position of holes/inclusions (see Fig. B.1a). Compressive loading was applied as described above. For the tensile displacement loading, we again turned the M10x1 screw in increments of 1/3 mm. The outward movement of the screw created a gap between the screw and the wooden block, which was then closed by applying compression with F-style clamps (see Fig. B.1a).

The loading mechanism was placed on an Epson V550 photo scanner to scan the surface of deformed samples and silicone oil was applied between the sample and the glass surface of the scanner to reduce friction between them. Scanned images were post-processed with the Corel PHOTO-PAINT X8 and Image Processing Toolbox in

MATLAB 2018b. First, the dust particles and air-bubbles trapped in a thin silicone oil film were digitally removed from scanned images. Scanned grayscale images were then converted to black and white binary images from which the contours were extracted with MATLAB. Note that when samples were mounted in the loading mechanism they could be slightly compressed even before we start turning the screw to apply additional loads. To identify the value of this offset, we fitted contours of holes/inclusions/edges for each sample in experiments to those obtained with finite elements at a specific wrench position (usually, at the third increment, i.e. ~ 1.0 mm displacement). This offset was then used when we compared experiments to the multipole method and simulations at a different value of the applied load.

We designed another testing system for capturing the displacement and strain fields in compressed samples via digital image correlation (DIC) technique (see Fig. 9b in Ref. [49]). Black and white speckle patterns were sprayed onto the surface of samples with slow-drying acrylic paint to prevent the pattern from hardening too quickly, which could lead to delamination under applied compressive loads. Using a Zwick Z050 universal material testing machine, we applied a compressive displacement in 0.2 mm increments, where again a silicone oil was applied between the steel plates and the elastomer samples to prevent sticking and to reduce friction. A Nikon D5600 photo camera was used at each step to take a snapshot of the compressed sample. These photos were then used to calculate the displacements and strains fields via Ncorr, an open-source 2D DIC MATLAB based software. [131]

Appendix C

Additional definitions, theorems and results required for Chapter 4

C.1 Definitions and results from group theory

This section is based on books such as [67, 68, 70].

A group is a set G with a binary operation, called product, such that (i) product of any two elements $A, B \in G$ their product AB is also in G, (ii) the product is associative, i.e., for any three elements $A, B, C \in G$, $A(BC) = (AB)C$, (iii) there exists a unique identity $E \in G$ such that for any element $A \in G$, $AE = EA = A$, (iv) for any element $A \in G$, there exists a unique element $A^{-1} \in E$, called the inverse of A, such that $AA^{-1} = A^{-1}A = E$.

It is clear from the above definition that all that is needed to define a group is to write down the multiplication table. An example of such a group multiplication table is given in Table C.1. This group is called the C_{6v} group. The name represent a crystallographic group and comes from the action of the group on Euclidean space. The nomenclature of crystallographic groups will be discussed in the next section. The number of elements in a group G is called the *order of the group* $|G|$. The C_{6v}

group is of order 12. A little inspection shows that all the elements of this group as well as the whole multiplication table can be obtained from the relations that $P_1^6 = E$, $P_6^2 = E$ and $P_6P_1 = P_1^5P_6$. The other can be generated from P_1 and P_6 in the following manner: $P_2 = P_1^2$, $P_3 = P_1^3$, $P_4 = P_1^4$, $P_5 = P_1^5$, $P_7 = P_1P_6$, $P_8 = P_1^2P_6$, $P_9 = P_1^3P_6$, $P_{10} = P_1^4P_6$ and $P_{11} = P_1^5P_6$. In this case, P_1 and P_6 are called the *generators of the group*, and the three above mentioned relations are called *defining relations*. One can check that for the C_{6v} group, the product is not commutative,

Table C.1: Multiplication table of the C_{6v} group

	E	P_1	P_2	P_3	P_4	P_5	P_6	P_7	P_8	P_9	P_{10}	P_{11}
E	E	P_1	P_2	P_3	P_4	P_5	P_6	P_7	P_8	P_9	P_{10}	P_{11}
P_1	P_1	P_2	P_3	P_4	P_5	E	P_7	P_8	P_9	P_{10}	P_{11}	P_6
P_2	P_2	P_3	P_4	P_5	E	P_1	P_8	P_9	P_{10}	P_{11}	P_6	P_7
P_3	P_3	P_4	P_5	E	P_1	P_2	P_9	P_{10}	P_{11}	P_6	P_7	P_8
P_4	P_4	P_5	E	P_1	P_2	P_3	P_{10}	P_{11}	P_6	P_7	P_8	P_9
P_5	P_5	E	P_1	P_2	P_3	P_4	P_{11}	P_6	P_7	P_8	P_9	P_{10}
P_6	P_6	P_{11}	P_{10}	P_9	P_8	P_7	E	P_5	P_4	P_3	P_2	P_1
P_7	P_7	P_6	P_{11}	P_{10}	P_9	P_8	P_1	E	P_5	P_4	P_3	P_2
P_8	P_8	P_7	P_6	P_{11}	P_{10}	P_9	P_2	P_1	E	P_5	P_4	P_3
P_9	P_9	P_8	P_7	P_6	P_{11}	P_{10}	P_3	P_2	P_1	E	P_5	P_4
P_{10}	P_{10}	P_9	P_8	P_7	P_6	P_{11}	P_4	P_3	P_2	P_1	E	P_5
P_{11}	P_{11}	P_{10}	P_9	P_8	P_7	P_6	P_5	P_4	P_3	P_2	P_1	E

e.g. $P_1P_6 \neq P_6P_1$. In general, the product is not commutative. However, if for all $A, B \in G$, $AB = BA$, G is called an *Abelian group*. An example of Abelian group is the set of integers $\mathcal{Z}$ with the binary operation being addition. The identity is 0 and inverse of any element $a \in \mathcal{Z}$ is $-a$.

In a finite group G, when any element $A \in G$ is multiplied enough number of times to itself, the identity element E should be obtained because otherwise the group cannot be finite. For any element A in a finite group G, the smallest positive integer n for which $A^n = E$ is called *order of element* A. In the case of the C_{6v} group (Tab. C.1), it can be seen that the order of each element is 6, except E and P_2, which have order 1 and 2 respectively. If a subset G_s of a group G itself forms a

group, the subset G_s is called *subgroup* of G. The subgroups of the C_{6v} group are: (i) the group itself, (ii) $C_6 = \{E, P_1, P_2, P_3, P_4, P_5\}$, (iii) $C_{3v}(1) = \{E, P_2, P_4, P_6, P_8, P_{10}\}$, (iv) $C_{3v}(2) = \{E, P_2, P_4, P_7, P_9, P_{11}\}$, (v) $C_{2v} = \{E, P_3, P_6, P_9\}$, (vi) $C_3 = \{E, P_2, P_4\}$, (vii) $C_2 = \{E, P_3\}$, (viii) $C_s(1) = \{E, P_6\}$ (or $\{E, P_8\}$ or $\{E, P_{10}\}$), (ix) $C_s(2) = \{E, P_7\}$ (or $\{E, P_9\}$ or $\{E, P_{11}\}$) and (x) $\{E\}$. Clearly, for any group, the subset containing only the identity element and the group itself are subgroups of the group. These are called *improper subgroups*, the other subgroups of a group are called *proper subgroups*. The C_{6v} group has 8 proper subgroups. It is interesting to note that in each of the subgroups (ii), (vi), (vii), (viii) and (ix), there is one element (P_1, P_2, P_3, P_6 and P_9, respectively) whose powers generate all other terms in that subgroup. For example, in subgroup (ii), $P_2 = P_1^2$, $P_3 = P_1^3$, $P_4 = P_1^4$, $P_5 = P_1^5$ and $E = P_4^6$. Such a set of elements $\{E, A, \ldots, A^{n-1}\}$, where $A \in G$ and n is order of the element A, is called the *period* of A. Note that the period of any element $A \in G$ form an Abelian subgroup of G.

Two elements A and B of a group G are called *conjugate* of each other if there exists another element $C \in G$ such that $A = CBC^{-1}$. For example, in the C_{6v} group P_1 and P_5 are conjugate of each other because $P_5 = P_6 P_1 P_6^{-1}$. Let two elements A and B of a group G are conjugate of each other, i.e., there exists $X_1 \in G$ such that $A = X_1 B X_1^{-1}$. Moreover, B and C ($\in G$) are also conjugate of each other, i.e., there exists $X_2 \in G$ such that $B = X_2 C X_2^{-1}$. Then, $A = X_1 B X_1^{-1} = X_1 X_2 C X_2^{-1} X_1^{-1} = (X_1 X_2) C (X_1 X_2)^{-1}$. This implies that A and C are also conjugate of each other since $X_1 X_2$ is also an element of G. This means that conjugacy is a *transitive* relation. A *conjugacy class* is the set of all elements that can be obtained from one element of the group by conjugation. Then, due to transitivity of conjugacy, all elements of the same class are conjugate of each other and elements from different classes cannot be conjugate of one another. Moreover, the set containing only the identity element is a class for any Group. In the example of C_{6v} group, the conjugacy classes are

$\mathcal{C}_1 = \{E\}$, $\mathcal{C}_2 = \{P_3\}$, $\mathcal{C}_3 = \{P_1, P_5\}$ ($P_5 = P_6 P_1 P_6^{-1}$), $\mathcal{C}_4 = \{P_2, P_4\}$ ($P_4 = P_6 P_2 P_6^{-1}$), $\mathcal{C}_5 = \{P_6, P_8, P_{10}\}$ ($P_8 = P_1 P_6 P_1^{-1}$ and $P_{10} = P_5 P_6 P_5^{-1}$) and $\mathcal{C}_6 = \{P_7, P_9, P_{11}\}$ ($P_9 = P_1 P_7 P_1^{-1}$ and $P_{11} = P_5 P_7 P_5^{-1}$). An interesting property of the elements of a class is that they all have the same order. It is worth noting that in an Abelian group, each element is in a conjugacy class by itself, i.e., the number of conjugacy classes is equal to the number of elements in an Abelian group.

If G_s is a subgroup of group G, for any element $A \in G$, the subset $G_s A$ is called *right coset* of G_s, where $G_s A$ consists of the elements of G_s multiplied by A from the right. Similarly, one can multiply A from the left and get a subset AG_s, which is called *left coset* of G_s. Note that a coset (left or right) is in general not a subgroup. Some important properties of the right cosets are listed below. (i) If B is an element of $G_s A$, $G_s B = G_s A$. This is because B can be written as $B = XA$ for some element $X \in G_s$. Then, for any element $CA \in G_s A$ ($C \in G_s$), $CA = CX^{-1}XA = CX^{-1}B$ implying $G_s A \subset G_s B$ since $CX^{-1} \in G_s$. Also, for any element $CB \in G_s B$ ($C \in G_s$), $CB = CXX^{-1}B = CXA$ implying $G_s B \subset G_s A$ since $CX \in G_s$. Together, they imply $G_s B = G_s A$. (ii) All cosets of $G_s A$ have same number of elements as G_s. (iii) Any element A of G is in some coset of G_S. The proof is simple. Since the identity $E \in G_s$, $A = EA \in G_s A$. (iv) Any two right cosets of a subgroup G_s are either equal or they have no element in common. We prove this by contradiction. Let there be two cosets $G_s B$ and $G_s A$ with $0 < |G_s B \cap G_s A| < |G_s|$ (recall that for a group G, $|G|$ is the order of G or the number of elements in the group). Let C be an element of $G_s B \cap G_s A$. Then it can be written as $C = X_1 A = X_2 B$ for some elements $X_1, X_2 \in G_s$. Then any element $P \in G_s A$ can be written as $P = (PA^{-1})A = (PA^{-1}X_1^{-1})X_1 A = (PA^{-1}X_1^{-1})X_2 B = (PA^{-1}X_1^{-1}X_2)B \in G_s B$ since by definition $PA^{-1}, PA^{-1}X_1^{-1}, PA^{-1}X_1^{-1}X_2 \in G_s$. This implies $G_s A \subset G_s B$. Also any element $Q \in G_s B$ can be written as $Q = (QB^{-1})B = (QB^{-1}X_2^{-1})X_2 B = (QB^{-1}X_2^{-1})X_1 A = (QB^{-1}X_2^{-1}X_1)A \in G_s A$ since by

definition $QB^{-1}, QB^{-1}X_2^{-1}, QB^{-1}X_2^{-1}X_1 \in G_s$. This implies $G_sB \subset G_sA$. Together they imply $G_sA = G_sB$ meaning $|G_sB \cap G_sA| = |G_sA| = |G_sB| = |G_s|$ which contradicts the our assumption $0 < |G_sB \cap G_sA| < |G_s|$. (v) Let there be n distinct cosets of G_s. This means that the group G is union of the all the distinct cosets of G_s. Then from the above properties $|G| = n|G_s|$. This implies that the order of a subgroup is a divisor of the order of the group. The number n is called the *index* of G_s in G. All these properties are also true for left cosets. In our example of C_{6v}, clearly, the order of C_6 is 6 a divisor of 12, the order of group C_{6v} with index 2. Therefore, there are two distinct right cosets of C_6, C_6E and C_6P_6. The coset decomposition of C_{6v} is $C_{6v} = C_6E + C_6P_6$. Note that the distinct left and right cosets of C_6 are equal; $EC_6 = C_6E$ and $P_6C_6 = C_6P_6$. A subgroup $\mathcal{N}$ of group G for which $A\mathcal{N} = \mathcal{N}A$ for any $A \in G$ is called a *normal subgroup*. In other words, if $\mathcal{N}$ is a subgroup of G such that $\mathcal{N} = A\mathcal{N}A^{-1}$ for any $A \in G$, i.e., for any $N \in \mathcal{N}$ and $A \in G$, $ANA^{-1} \in \mathcal{N}$, $\mathcal{N}$ is a normal subgroup of G. It can be seen immediately that any subgroup of index 2 is a normal subgroup. Therefore, C_6, $C_{3v}(1)$ and $C_{3v}(2)$ are all normal subgroups of C_{6v}. Direct inspection shows that C_3 and C_2 are also normal subgroups of C_{6v}. It is interesting to note that the set of all right (or left, which are the same as the right ones) cosets of a normal subgroup $\mathcal{N}$ of a group G forms a group. To see this, let there be elements $N_1 \in \mathcal{N}A$ and $N_2 \in \mathcal{N}B$. By definition, $N_1A^{-1}, A^{-1}N_1, N_2B^{-1}, B^{-1}N_2 \in \mathcal{N}$. Then, $N_1N_2 = N_1A^{-1}AN_2B^{-1}B = (N_1A^{-1}N_3)AB \in \mathcal{N}AB$, where $N_3 = AN_2B^{-1}A^{-1} \in \mathcal{N}$. Hence, if we define $(\mathcal{N}A)(\mathcal{N}B)$ to be the set consisting of elements N_1N_2 for all elements $N_1 \in \mathcal{N}A$ and $N_2 \in \mathcal{N}B$, then $(\mathcal{N}A)(\mathcal{N}B) \subset \mathcal{N}AB$. Conversely, for any element $N \in \mathcal{N}AB$, since $N(AB)^{-1} \in \mathcal{N}$, $N = N(AB)^{-1}AB = (EA)((A^{-1}N(AB)^{-1}A)B) \in (\mathcal{N}A)(\mathcal{N}B)$. This is because $EA \in (\mathcal{N}A)$, and since $N(AB)^{-1} \in \mathcal{N}$, $(A^{-1}N(AB)^{-1}A) \in \mathcal{N}$ implying $((A^{-1}N(AB)^{-1}A)B) \in (\mathcal{N}B)$. (i) Therefore, we can define the product on the set of cosets in the following way: $(\mathcal{N}A)(\mathcal{N}B) = \mathcal{N}AB$, which is also a coset of $\mathcal{N}$. (ii) The associative property holds

because it holds for the elements of G. (iii) The identity is the normal subgroup $\mathcal{N}$ itself since $(\mathcal{N}A)\mathcal{N} = \mathcal{N}(\mathcal{N}A) = \mathcal{N}A$. (iv) The inverse of a coset $\mathcal{N}A$ ($A \in G$) is $\mathcal{N}A^{-1}$, since $(\mathcal{N}A)(\mathcal{N}A^{-1}) = \mathcal{N}AA^{-1} = \mathcal{N}E = \mathcal{N}$. This group is called the quotient group of $\mathcal{N}$ and denoted by $G/\mathcal{N}$. For example, the quotient group of C_3 in C_{6v} is $C_{6v}/C_3 = \{C_3, C_3P_1, C_3P_6, C_3P_7\}$ with the multiplication table shown in Table C.2. This is exactly like the multiplication table of the subgroup C_{2v} with the identifica-

Table C.2: Multiplication table of the quotient group C_{6v}/C_3

	C_3	C_3P_1	C_3P_6	C_3P_7
C_3	C_3	C_3P_1	C_3P_6	C_3P_7
C_3P_1	C_3P_1	C_3	C_3P_7	C_3P_6
C_3P_6	C_3P_6	C_3P_7	C_3	C_3P_1
C_3P_7	C_3P_7	C_3P_6	C_3P_1	C_3

tion that C_3, C_3P_1, C_3P_6 and C_3P_7 corresponding to E, P_3, P_6 and P_9 respectively (one can read of the multiplication table of C_{2v} from the Table C.1 by just taking the appropriate rows and columns). To make the similarity between C_{2v} and C_{6v}/C_3 concrete we nee the concept of homomorphism and isomorphism which we discuss in the next paragraph.

A *homomorphism* is a mapping f from a group G_1 to another group G_2 such that for any two elements $A, B \in G_1$, $f(G_1)f(G_2) = f(G_1G_2)$. In other words, a homomorphism is a mapping from one group to another such that the product is preserved. When this mapping is bijective (one-one and onto), it is called *isomorphism* and the two groups are said to isomorphic to each other. Therefore, if we define the mapping $f : C_{6v}/C_3 \to C_{6v}$ such that $f(C_3) = E$, $f(C_3P_1) = P_3$, $f(C_3P_6) = P_6$ and $f(C_3P_7) = P_9$, it is clearly a homomorphism. However, if we restrict the mapping to $f : C_{6v}/C_3 \to C_{2v}$, it is an isomorphism because it is one-one and onto. We write $C_{6v}/C_3 \cong C_{2v}$ to show that these two groups are isomorphic. Intuitively, the group C_{6v} can be obtained by "multiplying" all the elements of C_3 and C_{2v}. The corresponding concept is that of semi-direct product. If G_1 and G_2 are two subgroups of group G

such that (i) $AG_1 = G_1A$ for any $A \in G_2$, (ii) any element $C \in G$ can expressed as $C = BA$ with $B \in G_1$ and $A \in G_2$ and (iii) $G_1 \cap G_2 = \{E\}$, then G is called the *semi-direct product* of G_1 and G_2 and is written as $G = G_1 \wedge G_2$. Note that by definition G_1 is a normal subgroup of G in this case. An example of semi-direct product is $C_{6v} = C_3 \wedge C_{2v}$.

Another kind of product between groups that will be important later in this article is *outer direct product*. Let G be a group with subgroups H and K such that (i) $H \cap K = \{E\}$, (ii) for any $A \in H$ and $B \in K$, $AB = BA$ and (iii) any element $C \in G$ can be written uniquely as product $C = AB$ such that $A \in H$ and $B \in K$. Then G is called outer direct product of H and K, and is denoted as $G = H \otimes K$. Clearly, H and K are normal subgroups of G. Furthermore, let there be conjugacy classes $\mathcal{C}_H$ and $\mathcal{C}_K$ of subgroups H and K. Let us consider the set $\mathcal{C}_{HK}$ of all elements A_cB_c such that $A_c \in \mathcal{C}_H$ and $B_c \in \mathcal{C}_K$. Then conjugation with any element $C \in G$ on A_cB_c gives $CA_cB_cC^{-1} = (AB)A_cB_c(AB)^{-1} = ABA_cB_cB^{-1}A^{-1} = AA_c(BB_cB^{-1})A^{-1} = (AA_cA^{-1})(BB_cB^{-1})$ where $C = AB$ with $A \in H$ and $B \in K$. Since A_c is in conjugacy class $\mathcal{C}_H$, so is (AA_cA^{-1}) by definition. Similarly, $(BB_cB^{-1}) \in \mathcal{C}_K$. Therefore, the set $\mathcal{C}_{HK}$ is invariant under conjugacy operation with any element of G; in other words $\mathcal{C}_{HK}$ is a conjugacy class of G. It is easy to see from this that the number of classes in G is product of the number of classes in H and K.

This introduction to group theory is no way complete. However, here we restrict ourselves to only the definitions that we need. A more thorough description of group theory can be found in [68, 67, 140].

C.1.1 Point groups

This introduction to group theory is no way complete. However, here we restrict ourselves to only the definitions that we need. A more thorough description of group

theory can be found in [68, 67, 140] With this introduction to groups, in the next two subsections we describe how spatial symmetries form groups.

Point Group

A point group is a group of symmetry operations that act on Euclidean space keeping a point (let us call that point O) in the n dimensional Euclidean space fixed and preserving all angles and distances. Let there be two points with position vectors $\mathbf{x}_1$ and $\mathbf{x}_2$ measured from point O with lengths $|\mathbf{x}_1|$ and $|\mathbf{x}_2|$ respectively and the angle between them be θ. Then, the inner product of these vectors is $\mathbf{x}_1 \cdot \mathbf{x}_2 = |\mathbf{x}_1||\mathbf{x}_2| \cos\theta$ which depends only on the lengths of the two vectors and the angle between them. Let the symmetry be R. Under the action of the symmetry operation the two vectors will transform to $\mathbf{y}_1 = \mathbf{R}\mathbf{x}_1$ and $\mathbf{y}_2 = \mathbf{R}\mathbf{x}_2$, where $\mathbf{R}$ is an $n \times n$ matrix. Since all distances and angles are preserved under the operation, $\mathbf{y}_1 \cdot \mathbf{y}_2 = \mathbf{R}\mathbf{x}_1 \cdot \mathbf{R}\mathbf{x}_2 = \mathbf{x}_1 \cdot \mathbf{R}^T\mathbf{R}\mathbf{x}_2 = \mathbf{x}_1 \cdot \mathbf{x}_2$. This implies that $\mathbf{R}^T\mathbf{R} = \mathbb{1}$, or $\mathbf{R}$ is an orthogonal matrix. This means that group all possible symmetry operation which keep a point O fixed is isomorphic to the group of orthogonal matrices $O(n)$. Among these symmetry operations, the ones with determinant $+1$ are called proper rotations and the ones with determinant -1 are called improper rotations. If only all possible proper rotations are symmetries, the group is isomorphic to $SO(n)$ (special orthogonal group). In odd dimensional Euclidean spaces, inversion operation I (which transforms any position vector $\mathbf{x}$ to $-\mathbf{x}$) has determinant -1. Thus, in 3 dimensions the set of all proper rotations ($SO(3)$) along with their products with inversion make the group of all rotations ($O(3)$). It is interesting to note that in 2 dimensions, inversion is equivalent to rotation by an angle π meaning that inversion operation has determinant $+1$ in 2D. However, a reflection has determinant of -1. Therefore, in 2D, the group of all rotations consists of all proper rotation and their product with a reflection. In 2D, every subgroup of the group of all rotations $O(2)$ is a point group. An example of a point group is shown in

Fig. C.1. The hexagon shown in the figure has six fold rotation symmetry about its

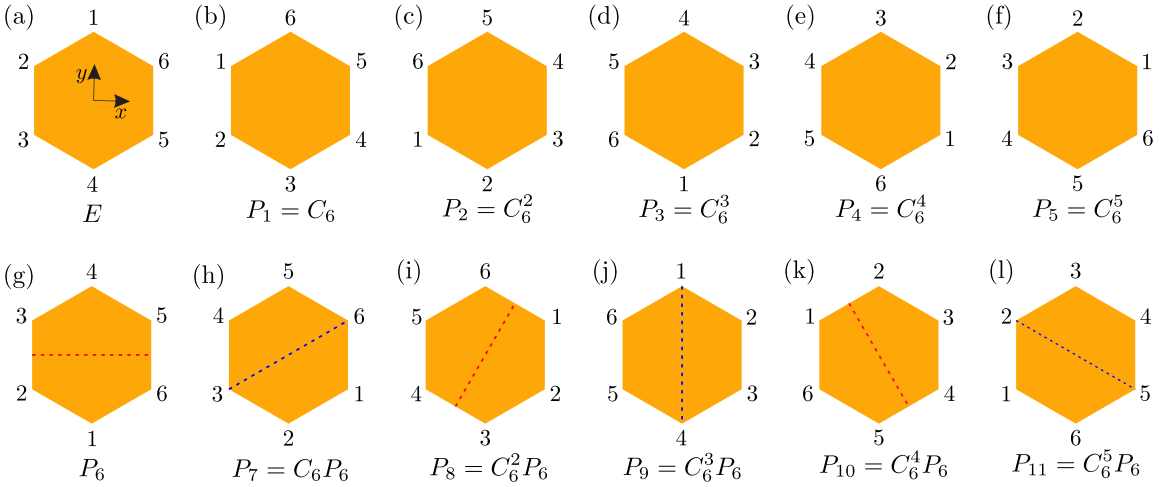

Figure C.1: Action of the elements of the group C_{6v} on a hexagon with labeled vertices. (a) is the identity element E which keeps the vertices at their original position. The axes x and y are shown for future reference. (b)-(f) show the transformation of the hexagon under rotation C_6 by multiples of $2\pi/6$ around its center. (g) shows the reflection around the horizontal mirror passing through the center shown in red dashed line. (h)-(l) show the composition of the reflection followed by rotations mentioned above. The elements in (g), (i) and (k) are equivalent to mirrors which cut two opposite sides of the hexagon shown with red dashed lines. These three elements form a conjugacy class of C_{6v}. The elements in (h), (j) and (l) are equivalent to mirrors which passes two opposite vertices of the hexagon shown with blue dashed lines. These three elements form a conjugacy class of C_{6v}.

center O. Therefore, rotations of $\pi/3$, $2\pi/3$, π, $4\pi/3$ and $5\pi/3$ about the z axis (out-of-plane direction) are (Fig. C.1(b)-(f)) all symmetries of the hexagon. Moreover, a reflection about the $x-z$ plane is also a symmetry (Fig. C.1(g)). Therefore, a reflection about $x-z$ plane followed by any of the above mentioned rotation is also a symmetry (Fig. C.1(h)-(l)). Note that such composite operation is equivalent to a reflection about a different plane. For example, a reflection about $x-z$ plane followed by a rotation of $\pi/3$ about the z axis is equivalent to a reflection about a plane containing the z axis and the dashed line shown in Fig. C.1(h). A rotation of $2\pi/n$ is denoted by C_n in *Schoenflies notation* and by n in *international notation*. In our example, the rotations are C_6, $C_6^2 = C_3$, $C_6^3 = C_2$, $C_6^4 = C_3^2$ and C_6^5. A vertical reflection plane is denoted by σ_v and m in Schoenflies and international notation

respectively. Clearly, if we identify C_6 with P_1 and the reflection about $x-z$ plane with P_6, this point group shown in Fig. C.1 is the same as the group in Table C.1. Now the name of the group is clear. Since the group is generated by C_6 rotation and reflection about vertical mirror plane $x-z$, it is called C_{6v} in Schoenflies notation. In international notation, this group is called $6mm$ because there are two inequivalent sets of 3 mirrors which are $\pi/3$ rotated from each other (shown in blue and red dashed lines in Fig. C.1(g)-(l)).

There are infinitely many point groups in 3 dimensions. However, only finite number of them are compatible with discrete translational symmetry of a crystal. In fact, the only point group operations that are compatible with discrete translational symmetry are 1, 2, 3, 4 and 6 fold rotations, inversion and reflection about a plane [56, 68]. This means that in 2D, the points groups are either just C_n or $C_{nv} = C_n + \sigma_v C_n$ with $n = 1, 2, 3, 4$ or 6 (note that C_n can mean rotation by an angle $2\pi/n$ or the group $\{E, C_n, C_n^2, \ldots, C_n^{n-1}\}$, in this case we mean the second one); therefore there are 10 2D point groups compatible with discrete translational symmetry. These are called *crystallographic point groups*. There are 32 crystallographic point groups in 3D [68]. In the rest of the text we restrict ourselves to 2D systems.

C.2 Definitions and results from group representations

Having introduced group theory and specified the groups that we are interested in, now we are at a place to describe the action of groups on a vector space. Let there be a finite dimensional vector space V over the complex field. The set of all nonsingular linear operators on V forms a group called general linear group $GL(V)$. A *representation of a group* G is a homomorphism ρ from a group to the group of nonsingular linear operators $GL(V)$ on a finite dimensional vector space V. Since ρ is homomor-

phism, for any two elements $A, B \in G$, $\rho(A)\rho(B) = \rho(AB)$ meaning that for any vector $\mathbf{v} \in V$, $\rho(A)(\rho(B)\mathbf{v}) = \rho(AB)\mathbf{v}$. Moreover, $\rho(E)\mathbf{v} = \mathbf{v}$ where E is the identity element of G, and $\rho(A)^{-1}\mathbf{v} = \rho(A^{-1})\mathbf{v}$ for any $A \in G$ and $\mathbf{v} \in V$. Now, let a basis of the d dimensional vector space V be $V_b = \{\mathbf{v}_1, \mathbf{v}_2, \ldots, \mathbf{v}_d\}$. Then, for any element $A \in G$, since $\rho(A)\mathbf{v}_i \in V$, it can be written as a linear combination of all the vectors in the basis

$$\rho(A)\mathbf{v}_i = \mathbf{v}_j \mathbf{\Gamma}_\rho(A)_{ji}, \tag{C.1}$$

where $\mathbf{\Gamma}_\rho(A)_{ji}$ is the coefficient of $\mathbf{v}_j$ and obviously depends on the group element A. Note that sum over repeated index j is implied. We say that the square matrix $\mathbf{\Gamma}_\rho(A)$ of dimension $d \times d$ is the matrix representing A in the basis V_b. Since for any $A \in G$, $\mathbf{\Gamma}_\rho(A) = \mathbf{\Gamma}_\rho(AE) = \mathbf{\Gamma}_\rho(A)\mathbf{\Gamma}_\rho(E)$, $\mathbf{\Gamma}_\rho(E) = \mathbb{1}$ the identity matrix of dimensionality d. Moreover, $\mathbb{1} = \mathbf{\Gamma}_\rho(E) = \mathbf{\Gamma}_\rho(AA^{-1}) = \mathbf{\Gamma}_\rho(A)\mathbf{\Gamma}_\rho(A^{-1})$ implies that $\mathbf{\Gamma}_\rho(A^{-1}) = \mathbf{\Gamma}_\rho(A)^{-1}$. It is not hard to realize that the set of all distinct matrices $\mathbf{\Gamma}_\rho(G)$ form a group Δ. Moreover, the mapping $\mathbf{\Gamma}_\rho : G \to \Delta$ is a homomorphism. Let us take the example of C_{6v}. Let the position vectors of points i be $\mathbf{a}_i$ for $i = 1, \ldots, 6$ where the origin is O in Fig. C.1. We take our vector space to be the plane of the hexagon. The dimension of the vector space is $d = 2$, and let us choose the basis to be $\{\mathbf{a}_1, \mathbf{a}_2\}$. The other position vectors can be written in terms of the basis as follows: $\mathbf{a}_3 = \mathbf{a}_2 - \mathbf{a}_1$, $\mathbf{a}_4 = -\mathbf{a}_1$, $\mathbf{a}_5 = -\mathbf{a}_2$ and $\mathbf{a}_6 = \mathbf{a}_1 - \mathbf{a}_2$. The representation ρ of the two generators P_1 and P_6 of C_{6v} are anticlockwise rotation by angle $\pi/3$ about O and reflection about the horizontal line passing through O respectively. Therefore $\rho(P_1)\mathbf{a}_1 = \mathbf{a}_2$, $\rho(P_1)\mathbf{a}_2 = \mathbf{a}_3 = \mathbf{a}_2 - \mathbf{a}_1$, $\rho(P_6)\mathbf{a}_1 = \mathbf{a}_2$ and $\rho(P_6)\mathbf{a}_2 = \mathbf{a}_1$. Hence the matrices representing these two group elements in the aforementioned basis are then

$$\mathbf{\Gamma}_\rho(P_1) = \begin{pmatrix} 0 & -1 \\ 1 & 1 \end{pmatrix}, \ \mathbf{\Gamma}_\rho(P_6) = \begin{pmatrix} 0 & 1 \\ 1 & 0 \end{pmatrix}. \tag{C.2}$$

A mirror reflection about the horizontal axis (P_6) followed by an anticlockwise rotation of $\pi/3$ (P_1) gives $\rho(P_1P_6)\mathbf{a}_1 = \mathbf{a}_3 = \mathbf{a}_2 - \mathbf{a}_1$ and $\rho(P_1P_6)\mathbf{a}_2 = \mathbf{a}_2$ implying

$$\mathbf{\Gamma}_\rho(P_1P_6) = \begin{pmatrix} -1 & 0 \\ 1 & 1 \end{pmatrix} = \mathbf{\Gamma}_\rho(P_1)\mathbf{\Gamma}_\rho(P_6) \tag{C.3}$$

showing the homomorphism explicitly. Note that the representative matrices are in general not unitary (orthogonal in the case of real matrices). They are only unitary if we choose the basis functions to be orthogonal and restrict them to have the same norm. Now, if we choose a different basis $V_b' = \{\mathbf{v}_1', \mathbf{v}_2', \ldots \mathbf{v}_d'\}$ which is related to V_b by the following relation

$$\mathbf{v}_i' = \mathbf{v}_k \mathbf{S}_{ki}, \tag{C.4}$$

the action of any group element $A \in G$ on these new basis vectors are

$$\rho(A)\mathbf{v}_i' = \rho(A)(\mathbf{v}_k\mathbf{S}_{ki}) = (\rho(A)\mathbf{v}_k)\mathbf{S}_{ki} = \mathbf{v}_j\mathbf{\Gamma}_\rho(A)_{jk}\mathbf{S}_{ki} = \mathbf{v}_l'\mathbf{S}^{-1}_{lk}\mathbf{\Gamma}_\rho(A)_{jk}\mathbf{S}_{ki}. \tag{C.5}$$

We say that the set of representative matrices Δ and $\mathbf{S}^{-1}\Delta\mathbf{S}$ are equivalent and the transformation $\Delta \to \mathbf{S}^{-1}\Delta\mathbf{S}$ an *equivalence transformation*. In the above example, if we choose $\mathbf{a}_1' = \mathbf{a}_1$ and $\mathbf{a}_2' = (2\mathbf{a}_2 - \mathbf{a}_1)/\sqrt{3}$, then,

$$\mathbf{S} = \begin{pmatrix} 1 & -\frac{1}{\sqrt{3}} \\ 0 & \frac{2}{\sqrt{3}} \end{pmatrix},\ \mathbf{S}^{-1}\mathbf{\Gamma}(P_1)\mathbf{S} = \begin{pmatrix} \frac{1}{2} & -\frac{\sqrt{3}}{2} \\ \frac{\sqrt{3}}{2} & \frac{1}{2} \end{pmatrix},\ \mathbf{S}^{-1}\mathbf{\Gamma}(P_6)\mathbf{S} = \begin{pmatrix} \frac{1}{2} & \frac{\sqrt{3}}{2} \\ \frac{\sqrt{3}}{2} & -\frac{1}{2} \end{pmatrix}. \tag{C.6}$$

Note that with the new choice of basis vectors, both representative matrices have become unitary (orthogonal) because the new basis is orthonormal. It is noted that every matrix representation can be brought to unitary representation by a change of basis, and every matrix group is equivalent to a unitary matrix group. The *character of a matrix group* Δ is a function $\chi : \Delta \to \mathbb{C}$, such that for any element

$\mathbf{R} \in \Delta$, $\chi(\mathbf{R}) = \mathrm{tr}(\mathbf{R})$, where $\mathrm{tr}(\mathbf{R})$ is the trace of the matrix $\mathbf{R}$. Clearly, under equivalence transformation $\Delta \to \mathbf{S}^{-1}\Delta\mathbf{S}$, the characters remain invariant. Moreover, if two group elements A and B in group G are in the same conjugacy class (i.e. there exists a $C \in G$ such that $A = CBC^{-1}$), their matrix representatives in any basis under representation ρ are equal since $\chi_\rho(A) \equiv \mathrm{tr}(\mathbf{\Gamma}_\rho(A)) = \mathrm{tr}(\mathbf{\Gamma}_\rho(CBC^{-1})) = \mathrm{tr}(\mathbf{\Gamma}_\rho(C)\mathbf{\Gamma}_\rho(B)\mathbf{\Gamma}_\rho(C^{-1})) = \mathrm{tr}(\mathbf{\Gamma}_\rho(B)) \equiv \chi_\rho(B)$. In the example of representations ρ of group C_{6v} to the group of nonsingular linear operators on the 2 dimensional Euclidean space, the characters of different elements of C_{6v} are $\chi_\rho(E) = 2$, $\chi_\rho(P_1) = \chi_\rho(P_5) = 1$, $\chi_\rho(P_2) = \chi_\rho(P_4) = -1$, , $\chi_\rho(P_3) = -2$, $\chi_\rho(P_6) = \chi_\rho(P_8) = \chi_\rho(P_{10}) = 0$ and $\chi_\rho(P_7) = \chi_\rho(P_9) = \chi_\rho(P_{11}) = 0$. Since, for any $A \in G$, $\chi_\rho(A^{-1}) = \mathrm{tr}(\mathbf{\Gamma}_\rho(A^{-1})) = \mathrm{tr}(\mathbf{\Gamma}_\rho(A)^{-1}) = \mathrm{tr}(\mathbf{S}\mathbf{\Gamma}_\rho(A)^{-1}\mathbf{S}^{-1}) = \mathrm{tr}((\mathbf{S}^{-1}\mathbf{\Gamma}_\rho(A)\mathbf{S})^{-1})$ for any nonsingular matrix $\mathbf{S}$ and we can always choose $\mathbf{S}$ such that $\mathbf{S}^{-1}\mathbf{\Gamma}_\rho(A)\mathbf{S}$ becomes unitary, then with such a choice of $\mathbf{S}$, $\chi_\rho(A^{-1}) = \mathrm{tr}((\mathbf{S}^{-1}\mathbf{\Gamma}_\rho(A)\mathbf{S})^{-1}) = \mathrm{tr}((\mathbf{S}^{-1}\mathbf{\Gamma}_\rho(A)\mathbf{S})^\dagger) = \mathrm{tr}(\mathbf{S}^\dagger\mathbf{\Gamma}_\rho(A)^\dagger(\mathbf{S}^{-1})^\dagger) = \mathrm{tr}(\mathbf{S}^\dagger\mathbf{\Gamma}_\rho(A)^\dagger(\mathbf{S}^\dagger)^{-1}) = \mathrm{tr}(\mathbf{\Gamma}_\rho(A)^\dagger) = \mathrm{tr}(\mathbf{\Gamma}_\rho(A))^* = \chi_\rho(A)^*$ where † stands for Hermitian conjugate operation and * stands for complex conjugation. This can be seen from our example of the representation of C_{6v}: $\chi_\rho(P_1^{-1}) = \chi_\rho(P_5) = 1 = \chi_\rho(P_1) = (\chi_\rho(P_1))^*$.

If there is a subspace U of the vector space V such that for a representation ρ of a group G and any vector $\mathbf{u} \in U$, $\rho(A)\mathbf{u} \in U$ for all $A \in G$, U is called an *invariant subspace* of V under representation ρ of group G. In this case, the representation ρ is said to be *reducible*. If there are no invariant proper subspace of V under representation ρ of G, ρ is called *irreducible representation* of G. In this case the dimension of the vector space V is called the dimension of the representation ρ. In the example of representation of C_{6v}, since rotation of angle $\pi/3$ brings one basis vector ($\mathbf{a}_1$) to the other ($\mathbf{a}_2$), there is no invariant proper subspace of the 2 dimensional Euclidean space. Therefore, the representation ρ in this case is irreducible with dimenion 2. However, if we take the representation of the subgroup C_2 of group C_{6v}, the transformations of the basis functions $\mathbf{a}_1$ and $\mathbf{a}_2$ under P_3 (rotation by angle π)

are $\rho'(P_3)\mathbf{a}_1 = -\mathbf{a}_1$ and $\rho'(P_3)\mathbf{a}_2 = -\mathbf{a}_2$. Therefore, the one dimensional subspaces $\{c\,\mathbf{a}_1|\, c \in \mathbb{R}\}$ and $\{c\,\mathbf{a}_2|\, c \in \mathbb{R}\}$ are invariant under the representation ρ' of group C_2. Therefore, the representation ρ' is reducible.

Next we state some important theorems without giving proofs. The interested reader can consult any book on group theory ([67]) for the proofs. (1)*Schur's first lemma*: A representation ρ of a group G is irreducible if and only if the only matrices that commute with all matrices $\mathbf{\Gamma}_\rho(A)$ $(A \in G)$ are constant multiples of the identity matrix. (2)*Schur's first lemma*: If there exist two irreducible representations ρ and ρ' of G such that $\mathbf{\Gamma}_\rho(A)\mathbf{S} = \mathbf{S}\mathbf{\Gamma}_{\rho'}(A)$ for all $A \in G$ and a matrix $\mathbf{S}$, then either $\mathbf{S} = \mathbf{0}$ or $\mathbf{S}$ is nonsingular and the representations ρ and ρ' are equivalent. Clearly, if two representations are equivalent, their dimensions are equal. (3) (*Orthogonality theorem*) If there are two irreducible representations ρ_α and ρ_β of group G with dimensions d_α and d_β and matrix representatives $\mathbf{\Gamma}_\alpha$ and $\mathbf{\Gamma}_\beta$ respectively, the following identity holds

$$\sum_{A\in G} \mathbf{\Gamma}_\alpha(A)_{ij}\mathbf{\Gamma}_\beta(A^{-1})_{mn} = \frac{|G|}{d_\alpha}\delta_{\alpha\beta}\delta_{in}\delta_{jm}, \tag{C.7}$$

where δ_{ij} is the Kronecker delta function. Note that here we considered all equivalent representations to be be the same representation. A series of corollaries can be obtained from this last theorem.

(i) If we construct $|G|$ dimensional vectors out of these matrix elements in the following manner: $\mathbf{v}^\alpha_{ij} = \{\mathbf{\Gamma}_\alpha(G_1)_{ij}, \mathbf{\Gamma}_\alpha(G_2)_{ij}, \ldots, \mathbf{\Gamma}_\alpha(G_{|G|})_{ij}\}$ (G_ns are the distinct elements of group G, $n = 1, \ldots, |G|$), as we go over all α, i and j we get $\sum_\alpha d_\alpha^2$ number of orthonormal vectors. Therefore $\sum_\alpha d_\alpha^2 \leq |G|$. This also means that there are finitely many distinct representations of a finite group G.

(ii) $\sum_{A\in G} \chi_\alpha(A)\chi_\beta(A)^* = \sum_{A\in G} \chi_\alpha(A)\chi_\beta(A^{-1}) = \sum_{A\in G} \mathbf{\Gamma}_\alpha(A)_{ii}\mathbf{\Gamma}_\beta(A^{-1})_{mm} = \frac{|G|}{d_\alpha}\delta_{\alpha\beta}\delta_{im}\delta_{im} = |G|\delta_{\alpha\beta}$. Here sum over repeated indices is implied. Since, the elements in the same conjugacy class have equal characters, this result can be rewritten as

$\sum_i |\mathcal{C}_i| \chi_\alpha(\mathcal{C}_i) \chi_\beta(\mathcal{C}_i)^* = |G| \delta_{\alpha\beta}$, where the sum is over number of distinct conjugacy classes and $|\mathcal{C}|$ is the number of elements in class $\mathcal{C}$.

(iii) Two irreducible representations are equivalent if and only if their characters are same. The necessary condition that if the irreducible representations are equivalent, then the characters are same is clear. Conversely, let the characters χ_1 and χ_2 of two irreducible representations ρ_1 and ρ_2 of a group are same. If they are not equivalent, we know that $\sum_{A \in G} \mathbf{\Gamma}_1(A)_{ij} \mathbf{\Gamma}_2(A^{-1})_{mn} = 0 \Rightarrow \sum_{A \in G} \chi_1(A) \chi_2(A^{-1}) = 0 \Rightarrow \sum_{A \in G} \chi_1(A) \chi_2(A)^* = 0 \Rightarrow \sum_{A \in G} |\chi_1(A)|^2 = 0$ which is impossible. Therefore, the sufficient condition is proved.

(iii) Let ρ be an arbitrary representation of G with representative matrices $\mathbf{\Gamma}_\rho(A)$ for $A \in G$. Let $\rho_1, \rho_2, \ldots \rho_r$ be the distinct irreducible representations of G. Obviously, ρ is direct sum of these irreducible representations: $\rho = a_\alpha \rho_\alpha$. Then, the character χ_ρ for any conjugacy class $\mathcal{C}$ of G can be written as $\chi_\rho(\mathcal{C}) = a_\alpha \chi_\alpha(\mathcal{C})$ where χ_α is the character of irreducible representation ρ_α. The sum $\sum_i |\mathcal{C}_i| \chi_\alpha(\mathcal{C}_i)^* \chi_\rho(\mathcal{C}_i) = \sum_i |\mathcal{C}_i| \chi_\alpha(\mathcal{C}_i)^* a_\beta \chi_\beta(\mathcal{C}_i) = a_\beta |G| \delta_{\alpha\beta} = a_\alpha |G|$ implies that $a_\alpha = \frac{1}{|G|} \sum_i |\mathcal{C}_i| \chi_\alpha(\mathcal{C}_i)^* \chi_\rho(\mathcal{C}_i)$. This not only proves that the reduction of a representation ρ to irreducible representations ρ_α is unique but also gives the coefficients a_α.

(iv) The number of distinct irreducible representations is less than or equal to the number of distinct conjugacy classes in a group. The proof is simple. We know that $\sum_i |\mathcal{C}_i| \chi_\alpha(\mathcal{C}_i) \chi_\beta(\mathcal{C}_i)^* = |G| \delta_{\alpha\beta}$. Rearranging this equation, we get $\sum_i (\sqrt{|\mathcal{C}_i|/|G|} \chi_\alpha(\mathcal{C}_i)) (\sqrt{|\mathcal{C}_i|/|G|} \chi_\beta(\mathcal{C}_i))^* = \delta_{\alpha\beta}$. Then, if there are c number of classes, we can construct c dimensional vectors $\mathbf{v}_\alpha = \{\sqrt{|\mathcal{C}_1|/|G|} \chi_\alpha(\mathcal{C}_1), \ldots, \sqrt{|\mathcal{C}_c|/|G|} \chi_\alpha(\mathcal{C}_c)\}$. If there are r distinct irreducible representations, we get r distinct orthonormal vectors in this manner. Since number of orthonormal vectors can not be larger than the dimension of the vector space, $r \leq c$.

The two inequalities in (i) and (iv) are in fact equalities. This can be proven with the help of special type of representation called *regular representation* ρ_R which repre-

sents the action of group G on itself. This representation is defined by $\rho_R(G_m)G_n \equiv G_mG_n = G_p\mathbf{\Gamma}_R(G_m)_{pn}$ for $G_m, G_n, G_p \in G$. Clearly, this matrix shows the rearrangement of the group elements under the multiplication of G_m to the them on the left. If $G_mG_n = G_q$, in the n^{th} column of $\mathbf{\Gamma}_R(G_m)$ all elements are zero except the element in the q^{th} row which is 1. This non zero element is diagonal only when G_m is the identity element E. Therefore, the characters of non-identity element $\chi_R(G_m) = 0$ $(G_m \neq E)$, and $\chi_R(E) = |G|$. If we reduce the regular representation into the irreducible representation ρ_α of G $\rho_R = a_\alpha\rho_\alpha$, the coefficients a_α are given by $a_\alpha = \frac{1}{|G|}\sum_{A\in G}\chi_\alpha(A)^*\chi_R(A) = \frac{1}{|G|}|G|\chi_\alpha(E)^* = \chi_\alpha(E) = d_\alpha$ the dimension of representation ρ_α. This implies that $|G| = \chi_R(E) = a_\alpha\chi_\alpha(E) = \sum_\alpha d_\alpha^2$. Therefore, the vectors $\mathbf{v}_{ij}^\alpha$ defined in (i) span the $|G|$ dimensional vector space. So, any vector $\mathbf{v}$ in this space can be written as $\mathbf{v} = \sum_{\alpha ij} c_{\alpha ij}\mathbf{v}_{ij}^\alpha$ where $c_{\alpha ij}$ are the coefficients of basis vectors. We call $v_m = \sum_{\alpha ij} c_{\alpha ij}\mathbf{\Gamma}_\alpha(G_m)_{ij}$ the component $\mathbf{v}$ in the "direction" m. Now, in the case of the specific vectors $\mathbf{v}$, for which all "directions" corresponding to the elements of the same class are equal meaning that $v_m = v_n$ if $G_n = G_p^{-1}G_mG_p$ for any $G_p \in G$, v_m can be written as

$$
\begin{aligned}
v_m &= \frac{1}{|G|}\sum_{p=1}^{|G|} v_n \text{ with } G_n = G_p^{-1}G_mG_p \\
&= \frac{1}{|G|}\sum_{p=1}^{|G|}\sum_{\alpha ij} c_{\alpha ij}\mathbf{\Gamma}_\alpha(G_p^{-1}G_mG_p)_{ij} \\
&= \frac{1}{|G|}\sum_{p=1}^{|G|}\sum_{\alpha ij} c_{\alpha ij}\mathbf{\Gamma}_\alpha(G_p^{-1})_{ik}\mathbf{\Gamma}_\alpha(G_m)_{kl}\mathbf{\Gamma}_\alpha(G_p)_{lj} \\
&= \frac{1}{|G|}\sum_{\alpha ij} c_{\alpha ij}\mathbf{\Gamma}_\alpha(G_m)_{kl}\frac{|G|}{d_\alpha}\delta_{ij}\delta_{kl} \text{ using Eq. C.7} \\
&= \sum_{\alpha i}\frac{1}{d_\alpha}c_{\alpha ii}\mathbf{\Gamma}_\alpha(G_m)_{ll} \\
&= \sum_{\alpha i}\frac{1}{d_\alpha}c_{\alpha ii}\chi_\alpha(G_m).
\end{aligned}
\tag{C.8}
$$

Note that if number of classes is c, these special type of vectors $\mathbf{v}$ form an c dimensional vector subspace. However, from Eq. C.8 we see that these vectors can be spanned by the character vectors $\mathbf{v}_\alpha$, which are a set of r (number of irreducible representations) orthonormal vectors defined in (iv). This implies $r \geq c$. Therefore, in total $r = c$.

Establishing the fact that there are $r = c$ number of orthonormal vectors $\mathbf{v}_\alpha$ with $c = r$ number of components, we can construct a matrix $\mathbf{U}$ whose α^{th} row is the vector vector $\mathbf{v}_\alpha$. Then, $(\mathbf{U}\mathbf{U}^\dagger)_{\alpha\beta} = \sum_{i=1}^{c} \mathbf{v}_{\alpha i}\mathbf{v}^*_{\beta i} = \sum_{i=1}^{c}(|\mathcal{C}_i|/|G|)\chi_\alpha(\mathcal{C}_i)\chi_\beta(\mathcal{C}_i)^* = \delta_{\alpha\beta}$ implying that $\mathbf{U}$ is a unitary matrix. Therefore, $(\mathbf{U}^\dagger\mathbf{U})_{ij} = \delta_{ij} = \sum_\alpha(\sqrt{|\mathcal{C}_i||\mathcal{C}_j|}/|G|)$ $\chi_\alpha(\mathcal{C}_i)\chi_\alpha(\mathcal{C}_j)^*$ giving the identity $\sum_\alpha \chi_\alpha(\mathcal{C}_i)\chi_\alpha(\mathcal{C}_j)^* = \delta_{ij}|G|/|\mathcal{C}_i|$.

From the technical discussion above, it is clear an irreducible representation (from here on we will call them *irreps*) of a finite group can be recognized up to an equivalence solely from its characters. Let us go back to our example group C_{6v}. We know that it has 6 conjugacy classes. Therefore, it has 6 inequivalent irreps. Since C_{6v} has 12 elements, $\sum_{\alpha=1}^{6} d_\alpha^2 = 12$ where $d_\alpha \geq 1, d_\alpha \in \mathbb{Z}$ are the dimensions of the irreps. if there is a $d_6 = 3$ dimensional irrep, $\sum_{\alpha=1}^{5} d_\alpha^2 = 12 - 9 = 3$ which is not possible. Also, all 1 dimensional irreps is not possible because $\sum_{\alpha=1}^{6} d_\alpha^2 = 6 < 12$. Only one 2 dimensional irrep and five 1 dimensional irreps give $\sum_{\alpha=1}^{6} d_\alpha^2 = 9$. Similarly, three or more 2 dimensional representations is not possible because $3 \times 2^2 = 12$. Therefore, the possibility is four 1 dimensional irreps and two 2 dimensional irreps ($4\times1^2+2\times2^2 = 12$). One of the 1 dimensional irreps has all characters to be 1. To see this, let us choose the z axis passing through point O in Fig. C.1 as our vector space. All vectors in this vector space remain invariant under rotations and mirror reflection mentioned above. Therefore, the representation matrices of all the elements of C_{6v} are 1 meaning that all characters are 1. In fact, for any finite dimensional group, there is one representation with all characters being 1. One 2 dimensional irrep of C_{6v} is the one that we encountered above with the action of C_{6v} on the 2 dimensional Euclidean space. We show the characters of all 6 irreps in Table C.3 (the 6 rows correspond

to the 6 different irreps). These tables are called *character table*. In the table, each column corresponds to a conjugacy class (recall that all elements of the same conjugacy class have same character). Moreover, since the matrix representation of the

Table C.3: Character table of group C_{6v}

	$\mathcal{C}_1$	$\mathcal{C}_2$	$\mathcal{C}_3$	$\mathcal{C}_4$	$\mathcal{C}_5$	$\mathcal{C}_6$
A_1	$+1$	$+1$	$+1$	$+1$	$+1$	$+1$
A_2	$+1$	$+1$	$+1$	$+1$	-1	-1
B_1	$+1$	-1	-1	$+1$	$+1$	-1
B_2	$+1$	-1	-1	$+1$	-1	$+1$
E_1	$+2$	-2	$+1$	-1	0	0
E_2	$+2$	$+2$	-1	-1	0	0

identity element is always the identity matrix, the character of the class containing (only) the identity element is the dimension of the irrep. The orthonormality of the character vectors can be checked easily. The left column in the table shows the names (based on [210]) of the irreps. The character tables of all the 2 dimensional and 3 dimensional point groups are given in many books [68, 67, 211] and also listed in Bilbao Crystallographic Server (BCS) [203, 212, 213].

Before moving on to the representations of the specific groups we are interested in, we discuss a specific example to show how the symmetry operations act on functions on a manifold, and thus have representations on the function space. Let there be function on 2 dimensional Euclidean space $f : \mathbb{R}^2 \to \mathbb{R}$. If we perform the action of a point group element (R) on the function, we get a new a function that we write as $f' = \rho(R)f$ and $f'(\mathbf{r}) = \rho(R)f(\mathbf{r}) = f(\mathbf{R}^{-1}\mathbf{r})$ where $\mathbf{R}$ is the representative matrix of the symmetry group element R in the chosen basis for the vector space that is 2 dimensional Euclidean space. Let us take the symmetry group to be C_s which contains identity (E) and a mirror reflection M about a straight line in the 2 dimensional plane. Therefore, $\rho(E)f(\mathbf{r}) = f(\mathbf{r})$ and $\rho(M)f(\mathbf{r}) = f(\mathbf{M}^{-1}\mathbf{r})$. Since $M^2 = E$, $f(\mathbf{r}) = \rho(E)f(\mathbf{r}) = \rho(M^2)f(\mathbf{r}) = f(\mathbf{M}^{-1}\mathbf{M}^{-1}\mathbf{r})$ implying $\mathbf{M}^{-2} = \mathbb{1} = \mathbf{M}^2$. We define two functions $f^{\mathrm{e}}(\mathbf{r}) = f(\mathbf{r}) + \rho(M)f(\mathbf{r})$ and $f^{\mathrm{o}}(\mathbf{r}) = f(\mathbf{r}) - \rho(M)f(\mathbf{r})$. Let us also

define a vector space V containing all functions g on $\mathbb{R}^2$ which are linear combinations of f^{e} and f^{o}; $V = \{g | g = c_{\mathrm{e}} f^{\mathrm{e}} + c_{\mathrm{o}} f^{\mathrm{o}}, c_{\mathrm{e}}, c_{\mathrm{o}} \in \mathbb{C}\}$ with inner product of functions $g_1, g_2 \in V$ given by $\langle g_1 | g_2 \rangle = \int d^2\mathbf{r} g_1^*(\mathbf{r}) g_2(\mathbf{r})$. With this definition of the vector space and inner product, f^{e} and f^{o} are orthogonal: $\langle f^{\mathrm{e}} | f^{\mathrm{o}} \rangle = \langle f + \rho(M) f | f - \rho(M) f \rangle = \langle f | f \rangle + \langle \rho(M) f | f \rangle - \langle f | \rho(M) f \rangle - \langle \rho(M) f | \rho(M) f \rangle = 0$ since

$$\begin{aligned}
\langle \rho(M) f | \rho(M) f \rangle &= \int d^2\mathbf{r} f(\mathbf{M}^{-1}\mathbf{r})^* f(\mathbf{M}^{-1}\mathbf{r}) \\
&= \int d^2(\mathbf{M}\mathbf{r}') f(\mathbf{M}^{-1}\mathbf{M}\mathbf{r}')^* f(\mathbf{M}^{-1}\mathbf{M}\mathbf{r}') \text{ where } \mathbf{M}\mathbf{r}' = \mathbf{r} \\
&= \int d^2\mathbf{r}' f(\mathbf{r}')^* f(\mathbf{r}') \\
&= \langle f | f \rangle, \\
\langle \rho(M) f | f \rangle &= \int d^2\mathbf{r} f(\mathbf{M}^{-1}\mathbf{r})^* f(\mathbf{r}) \\
&= \int d^2(\mathbf{M}^{-1}\mathbf{r}') f(\mathbf{M}^{-1}\mathbf{M}^{-1}\mathbf{r}')^* f(\mathbf{M}^{-1}\mathbf{r}') \text{ where } \mathbf{M}^{-1}\mathbf{r}' = \mathbf{r} \\
&= \int d^2\mathbf{r}' f(\mathbf{r}')^* f(\mathbf{M}^{-1}\mathbf{r}') \text{ since } \mathbf{M}^{-2} = \mathbb{1} \\
&= \langle f | \rho(M) f \rangle.
\end{aligned}$$

Note that in the second to last equality we replaced $\int d^2(\mathbf{M}^{-1}\mathbf{r}')$ with $\int d^2\mathbf{r}'$ because the determinant of the Jacobian of the this transformation is -1 and the limits of integration of one of the two coordinates get flipped too giving another $-$ sign. Therefore, V is a two dimensional vector space with f^{e} and f^{o} forming a basis. Moreover, $\rho(M) f^{\mathrm{e}} = \rho(M) f + \rho(M^2) f = f + \rho(M) f = f^{\mathrm{e}}$ and $\rho(M) f^{\mathrm{o}} = \rho(M) f - \rho(M^2) f = -(f - \rho(M) f) = -f^{\mathrm{o}}$. Therefore, in this basis the representative matrices of the group are:

$$\mathbf{\Gamma}(E) = \begin{pmatrix} 1 & 0 \\ 0 & 1 \end{pmatrix} \text{ and } \mathbf{\Gamma}(M) = \begin{pmatrix} 1 & 0 \\ 0 & -1 \end{pmatrix}. \tag{C.9}$$

Since under the group action, $f^{\rm e}$ and $f^{\rm o}$ do not mix, vector space V has to invariant subspaces: $V_{\rm e} = \{g | g = c_{\rm e} f^{\rm e}, c_{\rm e} \in \mathbb{C}\}$ and $V_{\rm o} = \{g | g = c_{\rm o} f^{\rm o}, c_{\rm o} \in \mathbb{C}\}$. Looking at the character table of C_s group on Bilbao Crystallography Server shows that there are two irreps of C_s named A' and A''. The subspaces $V_{\rm e}$ and $V_{\rm o}$ transform under irreps A' and A'' respectively.

Now, let us go back to the C_{6v} group in Fig. C.1 where the origin O has all 12 symmetries and each of the vertices has only a mirror reflection symmetry. The mirror that passes through origin O and vertex 1 corresponds to the element P_{11}; the group of symmetries of vertex 1 is $C_s = \{E, P_{11}\}$. The decomposition of C_{6v} into cosets of C_s gives

$$C_{6v} = (E = P_1^0)C_s + (P_1 = P_1^1)C_s + (P_2 = P_1^2)C_s + (P_3 = P_1^3)C_s + (P_4 = P_1^4)C_S + (P_5 = P_1^5)C_s, \tag{C.10}$$

where P_1 stands for rotation by an angle $\pi/3$ about origin O. Let there be basis functions $f_{11}(\mathbf{r})$ and $f_{12}(\mathbf{r})$ centered at vertex 1 with $\rho(P_{11})f_{11} = f_{11}$ (even) and $\rho(P_{11})f_{12} = -f_{12}$ (odd) and the vector space is $V_1 = \{g_1 | g_1 = c_{11}f_{11} + c_{12}f_{12}, c_{11}, c_{12} \in \mathbb{C}\}$. From these two basis functions, we can get basis functions around any other vertex by rotating the basis at vertex 1 around origin O: $f_{i\alpha}(\mathbf{r}) = \rho(P_1^{i-1})f_{1\alpha}(\mathbf{r})$. From the 12 independent basis functions, we can then construct a vector space V of functions of the form $f(\mathbf{r}) = \sum_{i=1}^{6}\sum_{\alpha=1}^{2} c_{i\alpha} f_{i\alpha}(\mathbf{r})$ where $c_{i\alpha} \in \mathbb{C}$. We are going to consider the representation ρ of C_{6v} on this vector space. With this choice of basis, the element P_n (anticlockwise rotation by angle $n\pi/3$ where $n = 1, 2, 3, 4, 5$) is represented by $\rho(P_n)f_{i\alpha} = f_{((i \mod 6)+n)\alpha}$ meaning that the representative matrix for P_n has no diagonal element implying $\chi_\rho(P_n) = 0$. Each of the mirror operations that pass through the vertices (P_7, P_9 or P_{11}) has two $+1$ (-1) diagonal elements for the even (odd) basis functions at the vertices it crosses. This implies $\chi_\rho(P_7) = \chi_\rho(P_9) = \chi_\rho(P_{11}) = 0$. Also, none of the other mirror operations (P_6, P_8 and P_{10}) keep the functions at their place. Therefore $\chi_\rho(P_6) = \chi_\rho(P_8) = \chi_\rho(P_{10}) = 0$. Obviously

$\chi_\rho(E) = 12$. The coefficients of decomposition of this representation ρ into the irreps of C_{6v} can be easily obtained using the formula in (*iii*); $a_{A_1} = (1 \times 12 \times 1)/12 = 1$, $a_{A_2} = (1 \times 12 \times 1)/12 = 1$, $a_{B_1} = (1 \times 12 \times 1)/12 = 1$, $a_{B_2} = (1 \times 12 \times 1)/12 = 1$, $a_{E_1} = (1 \times 12 \times 2)/12 = 2$ and $a_{E_2} = (1 \times 12 \times 2)/12 = 2$. Let us summarize what we have done so far in this example. We started with representation of C_s on vector space V_1 which is clearly a direct sum of even (irrep A') and odd (irrep A'') subspaces of V_1. In group theory language, this is written as $A' \oplus A''$. Acting 6-fold rotations on the basis of V_1 we created a 12 dimensional vector space V on which the group C_{6v} acts. We found that the representation of C_{6v} on this vector space is a direct sum of 1 A_1, 1 A_2, 1 B_1, 1 B_2, 2 E_1 and 2 E_2 irreps; $A_1 \oplus A_2 \oplus B_1 \oplus B_2 \oplus 2E_1 \oplus 2E_2$. This representation of C_{6v} is constructed from a specific chosen representation of subgroup C_s. Construction of a representation ρ_G of a group G from a representation ρ_H of its subgroup H is called *induction of representation* and written as $\rho_H \uparrow G$. In our example, it is $(A' \oplus A'') \uparrow C_{6v} = (A_1 \oplus A_2 \oplus B_1 \oplus B_2 \oplus 2E_1 \oplus 2E_2)$. The next step is to find the basis for invariant subspaces of the vector space V. Clearly, the function $\sum_{i=1}^{6} f_{i1}$ is constant under any symmetry operation in C_{6v}; therefore $\sum_{i=1}^{6} f_{i1}$ is the basis of irrep A_1. Similarly, $\sum_{i=1}^{6} f_{i2}$ forms the basis of the irrep A_2, since it is constant under any rotation but gives a $-$ sign under any reflection. By similar inspections, the readers can convince themselves that the functions $f_{12} - f_{22} + f_{32} - f_{42} + f_{52} - f_{62}$ and $f_{11} - f_{21} + f_{31} - f_{41} + f_{51} - f_{61}$ are basis functions of irreps B_1 and B_2 respectively. To get the basis functions for 2 dimensional irreps of C_{6v}, we start with a function which is takes into account the dominant symmetry (6-fold rotation) of the group: $\sum_{i=n}^{6} \omega^{n-1} f_{n1}$, where $\omega = e^{i2\pi/6}$, $\omega^6 = 1$. Then, $\rho(P_1) \sum_{i=n}^{6} \omega^{n-1} f_{n1} = \sum_{i=n}^{6} \omega^{n-1} f_{((n \mod 6)+1)1} = \omega^{-1} \sum_{i=n}^{6} \omega^{n} f_{((n \mod 6)+1)1} = \omega^{5} \sum_{i=n}^{6} \omega^{n-1} f_{n1}$. Therefore, under any allowed rotation $\sum_{i=n}^{6} \omega^{n-1} f_{n1}$ transforms into a function proportional to itself. However, under the reflection P_{11}, it gives $\rho(P_{11}) \sum_{i=n}^{6} \omega^{n-1} f_{n1} = \sum_{n=1}^{6} \omega^{7-n} f_{n1}$. Therefore, $\sum_{i=n}^{6} \omega^{n-1} f_{n1}$ and $\sum_{i=n}^{6} \omega^{7-n} f_{n1}$

form an invariant subspace which by inspection transforms under E_1. Similarly, one can show that $\{\sum_{n=1}^{6}\omega^{2n-2}f_{n1}, \sum_{n=1}^{6}\omega^{2-2n}f_{n1}\}$, $\{\sum_{n=1}^{6}\omega^{n-1}f_{n2}, \sum_{n=1}^{6}\omega^{7-n}f_{n2}\}$ and $\{\sum_{n=1}^{6}\omega^{2n-2}f_{n2}, \sum_{n=1}^{6}\omega^{2-2n}f_{n2}\}$ are the basis of the other three irreps E_2, E_1 and E_2 respectively.

Publications and presentations

Publications

published

- S. Sarkar, M. Čebron, M. Brojan, and A. Košmrlj, *Method of image charges for describing deformation of bounded two-dimensional solids with circular inclusions*, **Phys. Rev. E 103** 053004 (2021).
- S. Sarkar, M. Čebron, M. Brojan, and A. Košmrlj, *Elastic multipole method for describing deformation of infinite two-dimensional solids with circular inclusions*, **Phys. Rev. E 103** 053003 (2021).

in preparation

- S. Sarkar, T. Dethe, P. Zhilkina, and A. Košmrlj, *Symmetry based classification of phonon bands in periodic elastic media.*
- S. Sarkar, M.E.H. Bahri, A. Košmrlj, *Statistical mechanics of cylindrical shells.*
- M.E.H. Bahri, S. Sarkar, A. Košmrlj, *Statistical mechanics of thermalized sheets under uniaxial tension.*

Talks and Presentations

Contibuted Talks

2021

- S. Sarkar, M.E.H. Bahri, and A. Košmrlj, *"Statistical mechanics of nanotubes"*, **Virtual APS March meeting**, March 2021.

2020

- S. Sarkar, M.E.H. Bahri, and A. Košmrlj, *"Statistical mechanics of nanotubes"*, **Society of Engineering Science (SES) virtual annual technical meeting**, September 2020.

- S. Sarkar, M.E.H. Bahri, and A. Košmrlj, *"Statistical mechanics of nanotubes*"*, **APS March meeting**, Denver CO, March 2020.
  *APS March Meeting was canceled due to the COVID-19 pandemic.

2019

- S. Sarkar and A. Košmrlj, *"Mechanical properties of thermalized cylindrical shells"*, **Soft Materials Coffee Hour, Princeton University**, Princeton, NJ, November 2019.

- S. Sarkar, M. Čebron, M. Brojan, and A. Košmrlj, *"Elastic multipole method for describing deformation of 2D solid structures with circular holes and inclusions"*, **APS March Meeting**, Boston, MA, March 2019.

2018

- S. Sarkar, and A. Košmrlj, *"Image charges in 2D linear elasticity"*, **APS March Meeting**, Los Angeles, CA, March 2018

- S. Sarkar and A. Košmrlj, *"Image charges in 2D linear elasticity"*, **8th Northeast Complex Fluids and Soft Matter Workshop**, Columbia University, New York, NJ, January 2018.

2017

- S. Sarkar and A. Košmrlj, *"Elastic multipole method for describing deformation of 2D solid structures"*, **APS March Meeting**, New Orleans, LA, March 2017.

- S. Sarkar and A. Košmrlj, *"Elastic multipole method for describing deformation of 2D solid structures"*, **6th Northeast Complex Fluids and Soft Matter Workshop**, Stevens Institute of Technology, Hoboken, NJ, January 2017.

Poster Presentations

2019

- S. Sarkar and A. Košmrlj, *"Buckling of thermalized cylindrical shells"*, **56th Society of Engineering Science (SES) annual technical meeting**, St. Louis, MO, October 2019.

- S. Sarkar and A. Košmrlj, *"Mechanical properties of thermalized cylindrical shells"*, **USACM Workshop "Recent Advances in the Modeling and Simulation of the Mechanics of Nanoscale Materials"**, University of Pennsylvania, Philadelphia, PA, August 2019.

- S. Sarkar and A. Košmrlj, *"Buckling of Thermalized Cylindrical Shells"*, **Frontiers in Applied & Computational Mathematics held jointly with the 11th Northeast Complex Fluids and Soft Matter Workshop**, New Jersey Institute of Technology, Newark, NJ, May 2019.

2018

- S. Sarkar and A. Košmrlj, *"Elastic multipole method for describing deformation of 2D solid structures"*, **Summer School on Soft Solids and Complex Fluids**, University of Massachusetts Amherst, Amherst, MA, May 2018.

- S. Sarkar and A. Košmrlj, *"Elastic multipole method for describing deformation of 2D solid struc- tures"*, **Princeton Institute for the Science and Technology of Materials Annual Research Symposium**, Princeton University, Princeton, NJ, March 2018.

- S. Sarkar and A. Košmrlj, *"Elastic multipole method for describing deformation of 2D solid struc- tures"*, **Princeton Center for Complex Materials Poster Night**, Princeton University, Princeton, NJ, February 2018.

2017

- S. Sarkar and A. Košmrlj, *"Elastic multipole method for describing deformation of 2D solid structures"*, **Summer School on Soft Solids and Complex Fluids**, University of Massachusetts Amherst, Amherst, MA, May 2017.

2016

- S. Sarkar and A. Košmrlj, *"Elastic multipole method for describing patterns in mechanically deformed structures"*, **Summer School on Physics and Mechanics of Soft Complex Materials**, Cargese, France, August 2016.

Bibliography

[1] J. R. Barber, *Elasticity*. Solid Mechanics and Its Applications, Springer Netherlands, 2002.

[2] K. Bertoldi, V. Vitelli, J. Christensen, and M. van Hecke, "Flexible mechanical metamaterials," *Nature Reviews Materials*, vol. 2, no. 11, p. 17066, 2017.

[3] R. M. Neville, F. Scarpa, and A. Pirrera, "Shape morphing kirigami mechanical metamaterials," *Scientific Reports*, vol. 6, p. 31067, 2016.

[4] T. Bückmann, M. Thiel, M. Kadic, R. Schittny, and M. Wegener, "An elasto-mechanical unfeelability cloak made of pentamode metamaterials," *Nature Communications*, vol. 5, p. 4130, 2014.

[5] Q. Wang, J. A. Jackson, Q. Ge, J. B. Hopkins, C. M. Spadaccini, and N. X. Fang, "Lightweight mechanical metamaterials with tunable negative thermal expansion," *Physical Review Letters*, vol. 117, p. 175901, 2016.

[6] J. Liu, T. Gu, S. Shan, S. H. Kang, J. C. Weaver, and K. Bertoldi, "Harnessing buckling to design architected materials that exhibit effective negative swelling," *Advanced Materials*, vol. 28, no. 31, pp. 6619–6624, 2016.

[7] P. Wang, J. Shim, and K. Bertoldi, "Effects of geometric and material nonlinearities on tunable band gaps and low-frequency directionality of phononic crystals," *Physical Review B*, vol. 88, p. 014304, 2013.

[8] K. S. Kim, J. Neu, and G. Oster, "Curvature-mediated interactions between membrane proteins," *Biophysical Journal*, vol. 75, no. 5, pp. 2274–2291, 1998.

[9] O. Kahraman, P. D. Koch, W. S. Klug, and C. A. Haselwandter, "Bilayer-thickness-mediated interactions between integral membrane proteins," *Physical Review E*, vol. 93, no. 4, p. 042410, 2016.

[10] H. Agrawal, M. Zelisko, L. Liu, and P. Sharma, "Rigid proteins and softening of biological membranes—with application to HIV-induced cell membrane softening," *Scientific Reports*, vol. 6, p. 25412, 2016.

[11] J.-H. Na, A. A. Evans, J. Bae, M. C. Chiappelli, C. D. Santangelo, R. J. Lang, T. C. Hull, and R. C. Hayward, "Programming reversibly self-folding

origami with micropatterned photo-crosslinkable polymer trilayers," *Advanced Materials*, vol. 27, no. 1, pp. 79–85, 2015.

[12] M. K. Blees, A. W. Barnard, P. A. Rose, S. P. Roberts, K. L. McGill, P. Y. Huang, A. R. Ruyack, J. W. Kevek, B. Kobrin, D. A. Muller, *et al.*, "Graphene kirigami," *Nature*, vol. 524, no. 7564, pp. 204–207, 2015.

[13] K. Malachowski, M. Jamal, Q. Jin, B. Polat, C. J. Morris, and D. H. Gracias, "Self-folding single cell grippers," *Nano letters*, vol. 14, no. 7, pp. 4164–4170, 2014.

[14] Q. Liu, W. Wang, M. F. Reynolds, M. C. Cao, M. Z. Miskin, T. A. Arias, D. A. Muller, P. L. McEuen, and I. Cohen, "Micrometer-sized electrically programmable shape-memory actuators for low-power microrobotics," *Science Robotics*, vol. 6, no. 52, 2021.

[15] M. Z. Miskin, A. J. Cortese, K. Dorsey, E. P. Esposito, M. F. Reynolds, Q. Liu, M. Cao, D. A. Muller, P. L. McEuen, and I. Cohen, "Electronically integrated, mass-manufactured, microscopic robots," *Nature*, vol. 584, no. 7822, pp. 557–561, 2020.

[16] J. D. Eshelby, "The determination of the elastic field of an ellipsoidal inclusion, and related problems," *Proceedings of the Royal Society of London A: Mathematical, Physical and Engineering Sciences*, vol. 241, no. 1226, pp. 376–396, 1957.

[17] Z. Hashin and S. Shtrikman, "A variational approach to the theory of the elastic behaviour of multiphase materials," *Journal of the Mechanics and Physics of Solids*, vol. 11, no. 2, pp. 127–140, 1963.

[18] P. P. Castañeda and J. R. Willis, "The effect of spatial distribution on the effective behavior of composite materials and cracked media," *Journal of the Mechanics and Physics of Solids*, vol. 43, no. 12, pp. 1919–1951, 1995.

[19] S. Torquato, *Random Heterogeneous Materials: Microstructure and Macroscopic Properties*. Interdisciplinary applied mathematics, vol. 16, Springer, 2002.

[20] B. J. Reynwar, G. Illya, V. A. Harmandaris, M. M. Müller, K. Kremer, and M. Deserno, "Aggregation and vesiculation of membrane proteins by curvature-mediated interactions," *Nature*, vol. 447, pp. 461–464, 2007.

[21] E. Siéfert, E. Reyssat, J. Bico, and B. Roman, "Bio-inspired pneumatic shape-morphing elastomers," *Nature Materials*, vol. 18, no. 1, pp. 24–28, 2019.

[22] T. Bückmann, M. Kadic, R. Schittny, and M. Wegener, "Mechanical cloak design by direct lattice transformation," *Proceedings of the National Academy of Sciences*, vol. 112, no. 16, pp. 4930–4934, 2015.

[23] S. A. Cummer, J. Christensen, and A. Alù, "Controlling sound with acoustic metamaterials," *Nature Reviews Materials*, vol. 1, no. 3, p. 16001, 2016.

[24] R. F. Almgren, "An isotropic three-dimensional structure with Poisson's ratio $= -1$," *Journal of Elasticity*, vol. 15, pp. 427–430, 1985.

[25] R. Lakes, "Foam structures with a negative Poisson's ratio," *Science*, vol. 235, pp. 1038–1041, 1987.

[26] K. Bertoldi, P. M. Reis, S. Willshaw, and T. Mullin, "Negative Poisson's ratio behavior induced by an elastic instability," *Advanced Materials*, vol. 22, no. 3, pp. 361–366, 2010.

[27] J. Shim, S. Shan, A. Košmrlj, S. H. Kang, E. R. Chen, J. C. Weaver, and K. Bertoldi, "Harnessing instabilities for design of soft reconfigurable auxetic/chiral materials," *Soft Matter*, vol. 9, pp. 8198–8202, 2013.

[28] S. Babaee, J. Shim, J. C. Weaver, E. R. Chen, N. Patel, and K. Bertoldi, "3D soft metamaterials with negative Poisson's ratio," *Advanced Materials*, vol. 25, no. 36, pp. 5044–5049, 2013.

[29] L. Wu, B. Li, and J. Zhou, "Isotropic negative thermal expansion metamaterials," *ACS Applied Materials & Interfaces*, vol. 8, no. 27, pp. 17721–17727, 2016.

[30] H. Zhang, X. Guo, J. Wu, D. Fang, and Y. Zhang, "Soft mechanical metamaterials with unusual swelling behavior and tunable stress-strain curves," *Science Advances*, vol. 4, no. 6, 2018.

[31] M. Curatolo, "Effective negative swelling of hydrogel-solid composites," *Extreme Mechanics Letters*, vol. 25, pp. 46–52, 2018.

[32] K. Bertoldi and M. C. Boyce, "Mechanically triggered transformations of phononic band gaps in periodic elastomeric structures," *Physical Review B*, vol. 77, p. 052105, 2008.

[33] J. Shim, P. Wang, and K. Bertoldi, "Harnessing instability-induced pattern transformation to design tunable phononic crystals," *International Journal of Solids and Structures*, vol. 58, pp. 52–61, 2015.

[34] A. E. Green, "General bi-harmonic analysis for a plate containing circular holes," *Proceedings of the Royal Society of London A: Mathematical, Physical and Engineering Sciences*, vol. 176, no. 964, pp. 121–139, 1940.

[35] R. A. W. Haddon, "Stresses in an infinite plate with two unequal circular holes," *The Quarterly Journal of Mechanics and Applied Mathematics*, vol. 20, no. 3, pp. 277–291, 1967.

[36] V. G. Ukadgaonker, "Stress analysis of a plate containing two circular holes having tangential stresses," *AIAA Journal*, vol. 18, no. 1, pp. 125–128, 1980.

[37] K. Ting, K. T. Chen, and W. S. Yang, "Applied alternating method to analyze the stress concentration around interacting multiple circular holes in an infinite domain," *International Journal of Solids and Structures*, vol. 36, no. 4, pp. 533–556, 1999.

[38] S. K. Hoang and Y. N. Abousleiman, "Extended Green's solution for the stresses in an infinite plate with two equal or unequal circular holes," *Journal of Applied Mechanics*, vol. 75, no. 3, p. 031016, 2008.

[39] J. H. Michell, "On the direct determination of stress in an elastic solid, with application to the theory of plates," *Proceedings of the London Mathematical Society*, vol. s1-31, no. 1, pp. 100–124, 1899.

[40] M. Goulian, R. Bruinsma, and P. Pincus, "Long-range forces in heterogeneous fluid membranes," *EPL (Europhysics Letters)*, vol. 22, no. 2, pp. 145–150, 1993.

[41] J.-M. Park and T. Lubensky, "Interactions between membrane inclusions on fluctuating membranes," *Journal de Physique I France*, vol. 6, no. 9, pp. 1217–1235, 1996.

[42] R. Golestanian, M. Goulian, and M. Kardar, "Fluctuation-induced interactions between rods on a membrane," *Physical Review E*, vol. 54, no. 6, p. 6725, 1996.

[43] R. Golestanian, M. Goulian, and M. Kardar, "Fluctuation-induced interactions between rods on membranes and interfaces," *EPL (Europhysics Letters)*, vol. 33, no. 3, pp. 241–246, 1996.

[44] T. R. Weikl, M. M. Kozlov, and W. Helfrich, "Interaction of conical membrane inclusions: effect of lateral tension," *Physical Review E*, vol. 57, no. 6, p. 6988, 1998.

[45] C. Yolcu and M. Deserno, "Membrane-mediated interactions between rigid inclusions: an effective field theory," *Physical Review E*, vol. 86, no. 3, p. 031906, 2012.

[46] C. Yolcu, R. C. Haussman, and M. Deserno, "The effective field theory approach towards membrane-mediated interactions between particles," *Advances in Colloid and Interface Science*, vol. 208, pp. 89–109, 2014.

[47] X. Liang and P. K. Purohit, "A method to compute elastic and entropic interactions of membrane inclusions," *Extreme Mechanics Letters*, vol. 18, pp. 29–35, 2018.

[48] W. R. Smythe, "Two-dimensional potential distributions," in *Static and Dynamic Electricity*, ch. 4, pp. 63–120, Taylor & Francis, 1988.

[49] S. Sarkar, M. c. v. Čebron, M. Brojan, and A. Košmrlj, "Elastic multipole method for describing deformation of infinite two-dimensional solids with circular inclusions," *Phys. Rev. E*, vol. 103, p. 053003, May 2021.

[50] S. Sarkar, M. c. v. Čebron, M. Brojan, and A. Košmrlj, "Method of image charges for describing deformation of bounded two-dimensional solids with circular inclusions," *Phys. Rev. E*, vol. 103, p. 053004, May 2021.

[51] K. Bertoldi and M. C. Boyce, "Wave propagation and instabilities in monolithic and periodically structured elastomeric materials undergoing large deformations," *Physical Review B*, vol. 78, no. 18, p. 184107, 2008.

[52] L. Wang and K. Bertoldi, "Mechanically tunable phononic band gaps in three-dimensional periodic elastomeric structures," *International Journal of Solids and Structures*, vol. 49, no. 19, pp. 2881–2885, 2012. Proceedings of International Union of Theoretical and Applied Mechanics Symposium.

[53] M. S. Kushwaha, P. Halevi, L. Dobrzynski, and B. Djafari-Rouhani, "Acoustic band structure of periodic elastic composites," *Phys. Rev. Lett.*, vol. 71, pp. 2022–2025, Sep 1993.

[54] J. Jensen, "Phononic band gaps and vibrations in one and two-dimensional mass–spring structures," *Journal of Sound and Vibration*, vol. 266, no. 5, pp. 1053–1078, 2003.

[55] P. G. Martinsson and A. B. Movchan, "Vibrations of Lattice Structures and Phononic Band Gaps," *The Quarterly Journal of Mechanics and Applied Mathematics*, vol. 56, pp. 45–64, 02 2003.

[56] N. W. Ashcroft, N. D. Mermin, *et al.*, *Solid state physics*, vol. 2005. holt, rinehart and winston, new york London, 1976.

[57] C. Kittel, P. McEuen, and P. McEuen, *Introduction to solid state physics*, vol. 8. Wiley New York, 1996.

[58] J. Joannopoulos, S. Johnson, J. Winn, and R. Meade, *Photonic Crystals: Molding the Flow of Light - Second Edition*. Princeton University Press, 2011.

[59] F. Casadei, L. Dozio, M. Ruzzene, and K. A. Cunefare, "Periodic shunted arrays for the control of noise radiation in an enclosure," *Journal of Sound and Vibration*, vol. 329, no. 18, pp. 3632–3646, 2010.

[60] F. Casadei, B. S. Beck, K. A. Cunefare, and M. Ruzzene, "Vibration control of plates through hybrid configurations of periodic piezoelectric shunts," *Journal of Intelligent Material Systems and Structures*, vol. 23, no. 10, pp. 1169–1177, 2012.

[61] F. Javid, P. Wang, A. Shanian, and K. Bertoldi, "Architected materials with ultra-low porosity for vibration control," *Advanced Materials*, vol. 28, no. 28, pp. 5943–5948, 2016.

[62] J. O. Vasseur, A.-C. Hladky-Hennion, B. Djafari-Rouhani, F. Duval, B. Dubus, Y. Pennec, and P. A. Deymier, "Waveguiding in two-dimensional piezoelectric phononic crystal plates," *Journal of Applied Physics*, vol. 101, no. 11, p. 114904, 2007.

[63] W. Cheng, J. Wang, U. Jonas, G. Fytas, and N. Stefanou, "Observation and tuning of hypersonic bandgaps in colloidal crystals," *Nature Materials*, vol. 5, pp. 830–836, 2006.

[64] K. Jim, C. W. Leung, S. Lau, S. Choy, and H. Chan, "Thermal tuning of phononic bandstructure in ferroelectric ceramic/epoxy phononic crystal," *Applied Physics Letters*, vol. 94, no. 19, p. 193501, 2009.

[65] S. Babaee, N. Viard, P. Wang, N. X. Fang, and K. Bertoldi, "Harnessing deformation to switch on and off the propagation of sound," *Advanced Materials*, vol. 28, no. 8, pp. 1631–1635, 2016.

[66] S. Shan, S. H. Kang, P. Wang, C. Qu, S. Shian, E. R. Chen, and K. Bertoldi, "Harnessing multiple folding mechanisms in soft periodic structures for tunable control of elastic waves," *Advanced Functional Materials*, vol. 24, no. 31, pp. 4935–4942, 2014.

[67] M. Dresselhaus, G. Dresselhaus, and A. Jorio, *Group Theory: Application to the Physics of Condensed Matter*. Springer Berlin Heidelberg, 2007.

[68] T. Bradley, C. Bradley, and A. Cracknell, *The Mathematical Theory of Symmetry in Solids: Representation Theory for Point Groups and Space Groups*. Clarendon Press, 1972.

[69] W. Hergert, M. Däne, and D. Ködderitzsch, "6. symmetry properties of electronic and photonic band structures," in *Computational Materials Science: From Basic Principles to Material Properties* (W. Hergert, M. Däne, and A. Ernst, eds.), pp. 103–125, Berlin, Heidelberg: Springer Berlin Heidelberg, 2004.

[70] W. Hergert and R. Geilhufe, *Group Theory in Solid State Physics and Photonics: Problem Solving with Mathematica*. Wiley, 2018.

[71] K. S. Novoselov, D. Jiang, F. Schedin, T. Booth, V. Khotkevich, S. Morozov, and A. K. Geim, "Two-dimensional atomic crystals," *Proceedings of the National Academy of Sciences*, vol. 102, no. 30, pp. 10451–10453, 2005.

[72] S. Iijima, "Helical microtubules of graphitic carbon," *Nature*, vol. 354, pp. 56–58, 1991.

[73] D. Lembke, S. Bertolazzi, and A. Kis, "Single-layer mos2 electronics," *Accounts of Chemical Research*, vol. 48, no. 1, pp. 100–110, 2015.

[74] G. Bhimanapati, N. Glavin, and J. Robinson, "Chapter three - 2d boron nitride: Synthesis and applications," in *2D Materials* (F. Iacopi, J. J. Boeckl, and C. Jagadish, eds.), vol. 95 of *Semiconductors and Semimetals*, pp. 101–147, Elsevier, 2016.

[75] L. Joly-Pottuz and M. Iwaki, "14 - superlubricity of tungsten disulfide coatings in ultra high vacuum," in *Superlubricity* (A. Erdemir and J.-M. Martin, eds.), pp. 227–236, Amsterdam: Elsevier Science B.V., 2007.

[76] C. Gao, E. Donath, S. Moya, V. Dudnik, and H. Möhwald, "Elasticity of hollow polyelectrolyte capsules prepared by the layer-by-layer technique," *The European Physical Journal E*, vol. 5, pp. 21–28, 2001.

[77] V. D. Gordon, X. Chen, J. W. Hutchinson, A. R. Bausch, M. Marquez, and D. A. Weitz, "Self-assembled polymer membrane capsules inflated by osmotic pressure," *Journal of the American Chemical Society*, vol. 126, no. 43, pp. 14117–14122, 2004.

[78] V. V. Lulevich, D. Andrienko, and O. I. Vinogradova, "Elasticity of polyelectrolyte multilayer microcapsules," *The Journal of Chemical Physics*, vol. 120, no. 8, pp. 3822–3826, 2004.

[79] J. Lidmar, L. Mirny, and D. R. Nelson, "Virus shapes and buckling transitions in spherical shells," *Phys. Rev. E*, vol. 68, p. 051910, Nov 2003.

[80] I. L. Ivanovska, P. J. de Pablo, B. Ibarra, G. Sgalari, F. C. MacKintosh, J. L. Carrascosa, C. F. Schmidt, and G. J. L. Wuite, "Bacteriophage capsids: Tough nanoshells with complex elastic properties," *Proceedings of the National Academy of Sciences*, vol. 101, no. 20, pp. 7600–7605, 2004.

[81] J. P. Michel, I. L. Ivanovska, M. M. Gibbons, W. S. Klug, C. M. Knobler, G. J. L. Wuite, and C. F. Schmidt, "Nanoindentation studies of full and empty viral capsids and the effects of capsid protein mutations on elasticity and strength," *Proceedings of the National Academy of Sciences*, vol. 103, no. 16, pp. 6184–6189, 2006.

[82] S. Wang, H. Arellano-Santoyo, P. A. Combs, and J. W. Shaevitz, "Actin-like cytoskeleton filaments contribute to cell mechanics in bacteria," *Proceedings of the National Academy of Sciences*, vol. 107, no. 20, pp. 9182–9185, 2010.

[83] D. R. Nelson, "Biophysical dynamics in disorderly environments," *Annual Review of Biophysics*, vol. 41, no. 1, pp. 371–402, 2012.

[84] A. Amir, F. Babaeipour, D. B. McIntosh, D. R. Nelson, and S. Jun, "Bending forces plastically deform growing bacterial cell walls," *Proceedings of the National Academy of Sciences*, vol. 111, no. 16, pp. 5778–5783, 2014.

[85] R. Waugh and E. Evans, "Thermoelasticity of red blood cell membrane," *Biophysical Journal*, vol. 26, no. 1, pp. 115–131, 1979.

[86] Y. Park, C. A. Best, K. Badizadegan, R. R. Dasari, M. S. Feld, T. Kuriabova, M. L. Henle, A. J. Levine, and G. Popescu, "Measurement of red blood cell mechanics during morphological changes," *Proceedings of the National Academy of Sciences*, vol. 107, no. 15, pp. 6731–6736, 2010.

[87] E. Evans, "Bending elastic modulus of red blood cell membrane derived from buckling instability in micropipet aspiration tests," *Biophysical Journal*, vol. 43, no. 1, pp. 27–30, 1983.

[88] D. Nelson and L. Peliti, "Fluctuations in membranes with crystalline and hexatic order," *Journal de physique*, vol. 48, no. 7, pp. 1085–1092, 1987.

[89] Y. Kantor and D. R. Nelson, "Crumpling transition in polymerized membranes," *Physical review letters*, vol. 58, no. 26, p. 2774, 1987.

[90] M. Paczuski, M. Kardar, and D. R. Nelson, "Landau theory of the crumpling transition," *Phys. Rev. Lett.*, vol. 60, pp. 2638–2640, 1988.

[91] F. David and E. Guitter, "Crumpling transition in elastic membranes: Renormalization group treatment," *EPL*, vol. 5, no. 8, pp. 709–713, 1988.

[92] E. Guitter, F. David, S. Leibler, and L. Peliti, "Thermodynamical behavior of polymerized membranes," *Journal de Physique*, vol. 50, no. 14, pp. 1787–1819, 1989.

[93] J. Aronovitz, L. Golubovic, T. C. Lubensky, and L. Golubovi0107, "Fluctuations and lower critical dimensions of crystalline membranes fluctuations and lower critical dimensions of crystalline membranes," *Journal de Physique*, vol. 50, no. 6, pp. 609–631, 1989.

[94] J. A. Aronovitz and T. C. Lubensky, "Fluctuations of solid membranes," *Physical review letters*, vol. 60, no. 25, p. 2634, 1988.

[95] L. Radzihovsky and D. R. Nelson, "Statistical mechanics of randomly polymerized membranes," *Physical Review A*, vol. 44, no. 6, pp. 3525–3542, 1991.

[96] P. Le Doussal and L. Radzihovsky, "Self-consistent theory of polymerized membranes," *Phys. Rev. Lett.*, vol. 69, pp. 1209–1212, Aug 1992.

[97] P. Le Doussal and L. Radzihovsky, "Anomalous elasticity, fluctuations and disorder in elastic membranes," *Annals of Physics*, vol. 392, pp. 340–410, 2018.

[98] J.-P. Kownacki and D. Mouhanna, "Crumpling transition and flat phase of polymerized phantom membranes," *Phys. Rev. E*, vol. 79, p. 040101, 2009.

[99] F. L. Braghin and N. Hasselmann, "Thermal fluctuations of free-standing graphene," *Phys. Rev. B*, vol. 82, p. 035407, 2010.

[100] N. Hasselmann and F. L. Braghin, "Nonlocal effective-average-action approach to crystalline phantom membranes," *Phys. Rev. E*, vol. 83, p. 031137, 2011.

[101] A. Košmrlj and D. R. Nelson, "Thermal excitations of warped membranes," *Phys. Rev. E*, vol. 89, p. 022126, 2014.

[102] J. H. Los, A. Fasolino, and M. I. Katsnelson, "Scaling behavior and strain dependence of in-plane elastic properties of graphene," *Phys. Rev. Lett.*, vol. 116, p. 015901, 2016.

[103] M. J. Bowick, A. Košmrlj, D. R. Nelson, and R. Sknepnek, "Non-hookean statistical mechanics of clamped graphene ribbons," *Phys. Rev. B*, vol. 95, p. 104109, Mar 2017.

[104] A. Morshedifard, M. Ruiz-García, M. J. Abdolhosseini Qomi, and A. Košmrlj, "Buckling of thermalized elastic sheets," *Journal of the Mechanics and Physics of Solids*, vol. 149, p. 104296, 2021.

[105] G. López-Polín, C. Gómez-Navarro, V. Parente, F. Guinea, M. I. Katsnelson, F. Pérez-Murano, and J. Gómez-Herrero, "Increasing the elastic modulus of graphene by controlled defect creation," *Nature Physics*, vol. 11, pp. 26–31, 2015.

[106] J. Paulose, G. A. Vliegenthart, G. Gompper, and D. R. Nelson, "Fluctuating shells under pressure," *Proceedings of the National Academy of Sciences*, vol. 109, no. 48, pp. 19551–19556, 2012.

[107] A. Košmrlj and D. R. Nelson, "Statistical mechanics of thin spherical shells," *Phys. Rev. X*, vol. 7, p. 011002, Jan 2017.

[108] T. Tombler, C. Zhou, L. Alexseyev, J. Kong, H. Dai, L. Liu, C. Jayanthi, M. Tang, and S.-Y. Wu, "Reversible electromechanical characteristics of carbon nanotubes under local-probe manipulation," *Nature*, vol. 405, no. 6788, pp. 769–772, 2000.

[109] M.-F. Yu, O. Lourie, M. J. Dyer, K. Moloni, T. F. Kelly, and R. S. Ruoff, "Strength and breaking mechanism of multiwalled carbon nanotubes under tensile load," *Science*, vol. 287, no. 5453, pp. 637–640, 2000.

[110] R. S. Ruoff and D. C. Lorents, "Mechanical and thermal properties of carbon nanotubes," *carbon*, vol. 33, no. 7, pp. 925–930, 1995.

[111] C. W. Tan, K. H. Tan, Y. T. Ong, A. R. Mohamed, S. H. S. Zein, and S. H. Tan, "Energy and environmental applications of carbon nanotubes," *Environmental Chemistry Letters*, vol. 10, no. 3, pp. 265–273, 2012.

[112] S. G. Noyce, J. L. Doherty, Z. Cheng, H. Han, S. Bowen, and A. D. Franklin, "Electronic stability of carbon nanotube transistors under long-term bias stress," *Nano Letters*, vol. 19, no. 3, pp. 1460–1466, 2019.

[113] V. A. Kobzev, N. G. Chechenin, K. A. Bukunov, E. A. Vorobyeva, and A. V. Makunin, "Structural and functional properties of composites with carbon nanotubes for space applications," *Materials Today: Proceedings*, vol. 5, no. 12, Part 3, pp. 26096–26103, 2018.

[114] R. Shuey and H. Beyeler, "The elastic fields and interactions of point defects in isotropic and cubic media," *Zeitschrift für angewandte Mathematik und Physik ZAMP*, vol. 19, no. 2, pp. 278–300, 1968.

[115] E. Clouet, C. Varvenne, and T. Jourdan, "Elastic modeling of point-defects and their interaction," *Computational Materials Science*, vol. 147, pp. 49–63, 2018.

[116] J. M. Rickman and D. J. Srolovitz, "Defect interactions on solid surfaces," *Surface Science*, vol. 284, no. 1, pp. 211–221, 1993.

[117] S. A. Zhou, R. K. T. Hsieh, and G. A. Maugin, "Electric and elastic multipole defects in finite piezoelectric media," *International Journal of Solids and Structures*, vol. 22, no. 12, pp. 1411–1422, 1986.

[118] S.-A. Zhou, "A material multipole theory of elastic dielectric composites," *International Journal of Solids and Structures*, vol. 28, no. 4, pp. 423–447, 1991.

[119] J. P. Nowacki and R. K. T. Hsieh, "Lattice defects in linear isotropic dielectrics," *International Journal of Engineering Science*, vol. 24, no. 10, pp. 1655–1666, 1986.

[120] Z. Wang, N. Ghoniem, and R. LeSar, "Multipole representation of the elastic field of dislocation ensembles," *Physical Review B*, vol. 69, p. 174102, 2004.

[121] J. D. Jackson, *Classical electrodynamics*. Wiley New York, 3rd ed., 1999.

[122] P. M. Chaikin and T. C. Lubensky, *Principles of Condensed Matter Physics*. Cambridge University Press, 2000.

[123] M. Moshe, E. Sharon, and R. Kupferman, "The plane stress state of residually stressed bodies: a stress function approach," *arXiv preprint arXiv:1409.6594*, 2014.

[124] C. Amrouche, P. G. Ciarlet, L. Gratie, and S. Kesavan, "On Saint Venant's compatibility conditions and Poincaré's lemma," *Comptes Rendus Mathematique*, vol. 342, no. 11, pp. 887 – 891, 2006.

[125] R. Kupferman, M. Moshe, and J. P. Solomon, "Metric description of singular defects in isotropic materials," *Archive for Rational Mechanics and Analysis*, vol. 216, no. 3, pp. 1009–1047, 2015.

[126] M. Moshe, E. Sharon, and R. Kupferman, "Elastic interactions between two-dimensional geometric defects," *Physical Review E*, vol. 92, no. 6, p. 062403, 2015.

[127] Y. Bar-Sinai, G. Librandi, K. Bertoldi, and M. Moshe, "Geometric charges and nonlinear elasticity of two-dimensional elastic metamaterials," *Proceedings of the National Academy of Sciences*, vol. 117, no. 19, pp. 10195–10202, 2020.

[128] E. A. Matsumoto and R. D. Kamien, "Elastic-instability triggered pattern formation," *Physical Review E*, vol. 80, no. 2, p. 021604, 2009.

[129] D. Gottlieb and S. A. Orszag, *Numerical Analysis of Spectral Methods*. Society for Industrial and Applied Mathematics, 1977.

[130] http://www.matweb.com/search/datasheet.aspx?bassnum=O1303. Accessed in March 2020.

[131] J. Blaber, B. Adair, and A. Antoniou, "Ncorr: open-source 2D digital image correlation MATLAB software," *Experimental Mechanics*, vol. 55, no. 6, pp. 1105–1122, 2015.

[132] L. Yu and B. Pan, "The errors in digital image correlation due to overmatched shape functions," *Measurement Science and Technology*, vol. 26, no. 4, p. 045202, 2015.

[133] M. A. Sutton, J. H. Yan, V. Tiwari, H. W. Schreier, and J. J. Orteu, "The effect of out-of-plane motion on 2D and 3D digital image correlation measurements," *Optics and Lasers in Engineering*, vol. 46, no. 10, pp. 746–757, 2008.

[134] W. E. Langlois and M. O. Deville, *Slow viscous flow*. Springer, 2014.

[135] L. D. Landau, L. P. Pitaevskii, A. M. Kosevich, and E. M. Lifshitz, *Theory of Elasticity*. Butterworth-Heinemann, 3 ed., Dec 2012.

[136] J. Dundurs and G. P. Sendeckyj, "Behavior of an edge dislocation near a bimetallic interface," *Journal of Applied Physics*, vol. 36, no. 10, pp. 3353–3354, 1965.

[137] K. Adeerogba, "On eigenstresses in dissimilar media," *Philosophical Magazine*, vol. 35, no. 2, pp. 281–292, 1977.

[138] R. C. J. Howland, "Stress systems in an infinite strip," *Proceedings of the Royal Society of London. Series A, Containing Papers of a Mathematical and Physical Character*, vol. 124, no. 793, pp. 89–119, 1929.

[139] N. Ogbonna, "A representation theorem for the circular inclusion problem," *ZAMM - Journal of Applied Mathematics and Mechanics / Zeitschrift für Angewandte Mathematik und Mechanik*, vol. 95, no. 12, pp. 1514–1520, 2015.

[140] W. Ludwig and C. Falter, *Symmetries in Physics: Group Theory Applied to Physical Problems*. Lecture Notes in Mathematics, Springer-Verlag, 1988.

[141] M. Brun, S. Guenneau, and A. B. Movchan, "Achieving control of in-plane elastic waves," *Applied Physics Letters*, vol. 94, no. 6, p. 061903, 2009.

[142] J. Conway, H. Burgiel, and C. Goodman-Strauss, *The Symmetries of Things*. Ak Peters Series, Taylor & Francis, 2008.

[143] J. Elliott and P. Dawber, *Symmetry in Physics*. No. v. 1 in Symmetry in Physics, Oxford University Press, 1979.

[144] B. Bernevig and T. Hughes, *Topological Insulators and Topological Superconductors*. Princeton University Press, 2013.

[145] D. B. Litvin, "Magnetic group tables: 1-, 2- and 3-dimensional magnetic subperiodic groups and magnetic space groups," 2013.

[146] A. Shubnikov, N. Belov, and W. Holser, *Colored Symmetry*. Macmillan, 1964.

[147] M. Xiao, G. Ma, Z. Yang, P. Sheng, Z. Zhang, and C. T. Chan, "Geometric phase and band inversion in periodic acoustic systems," *Nature Physics*, vol. 11, no. 3, pp. 240–244, 2015.

[148] Z. Yang, F. Gao, X. Shi, X. Lin, Z. Gao, Y. Chong, and B. Zhang, "Topological acoustics," *Physical review letters*, vol. 114, no. 11, p. 114301, 2015.

[149] X. Ni, C. He, X.-C. Sun, X.-p. Liu, M.-H. Lu, L. Feng, and Y.-F. Chen, "Topologically protected one-way edge mode in networks of acoustic resonators with circulating air flow," *New Journal of Physics*, vol. 17, no. 5, p. 053016, 2015.

[150] A. B. Khanikaev, R. Fleury, S. H. Mousavi, and A. Alu, "Topologically robust sound propagation in an angular-momentum-biased graphene-like resonator lattice," *Nature communications*, vol. 6, no. 1, pp. 1–7, 2015.

[151] S. H. Mousavi, A. B. Khanikaev, and Z. Wang, "Topologically protected elastic waves in phononic metamaterials," *Nature communications*, vol. 6, no. 1, pp. 1–7, 2015.

[152] R. Fleury, A. B. Khanikaev, and A. Alu, "Floquet topological insulators for sound," *Nature communications*, vol. 7, no. 1, pp. 1–11, 2016.

[153] C. Kane and T. Lubensky, "Topological boundary modes in isostatic lattices," *Nature Physics*, vol. 10, no. 1, pp. 39–45, 2014.

[154] D. Z. Rocklin, B. G.-g. Chen, M. Falk, V. Vitelli, and T. Lubensky, "Mechanical weyl modes in topological maxwell lattices," *Physical review letters*, vol. 116, no. 13, p. 135503, 2016.

[155] L. Zhang and X. Mao, "Fracturing of topological maxwell lattices," *New Journal of Physics*, vol. 20, no. 6, p. 063034, 2018.

[156] X. Mao and T. C. Lubensky, "Maxwell lattices and topological mechanics," *Annual Review of Condensed Matter Physics*, vol. 9, pp. 413–433, 2018.

[157] J. Paulose, B. G.-g. Chen, and V. Vitelli, "Topological modes bound to dislocations in mechanical metamaterials," *Nature Physics*, vol. 11, no. 2, pp. 153–156, 2015.

[158] Y. Liu, Y. Xu, S.-C. Zhang, and W. Duan, "Model for topological phononics and phonon diode," *Physical Review B*, vol. 96, no. 6, p. 064106, 2017.

[159] Z. Zhang, Y. Tian, Y. Wang, S. Gao, Y. Cheng, X. Liu, and J. Christensen, "Directional acoustic antennas based on valley-hall topological insulators," *Advanced Materials*, vol. 30, no. 36, p. 1803229, 2018.

[160] Z. Zhang, Y. Tian, Y. Cheng, Q. Wei, X. Liu, and J. Christensen, "Topological acoustic delay line," *Physical Review Applied*, vol. 9, no. 3, p. 034032, 2018.

[161] B. Bradlyn, L. Elcoro, J. Cano, M. Vergniory, Z. Wang, C. Felser, M. Aroyo, and B. A. Bernevig, "Topological quantum chemistry," *Nature*, vol. 547, no. 7663, pp. 298–305, 2017.

[162] J. Cano, B. Bradlyn, Z. Wang, L. Elcoro, M. Vergniory, C. Felser, M. Aroyo, and B. A. Bernevig, "Building blocks of topological quantum chemistry: Elementary band representations," *Physical Review B*, vol. 97, no. 3, p. 035139, 2018.

[163] M. Vergniory, L. Elcoro, Z. Wang, J. Cano, C. Felser, M. Aroyo, B. A. Bernevig, and B. Bradlyn, "Graph theory data for topological quantum chemistry," *Physical Review E*, vol. 96, no. 2, p. 023310, 2017.

[164] J. L. Sanders, "Nonlinear theories for thin shells," *Quarterly of Applied Mathematics*, vol. 21, no. 1, pp. 21–36, 1963.

[165] L. H. Donnell, "Stability of thin-walled tubes under torsion," *NACA Technical Report 479*, 1933.

[166] K. Mushtari and K. Galimov, *Non-linear Theory of Thin Elastic Shells*. Israel program for scientific translations, 1961.

[167] S. Komura and R. Lipowsky, "Fluctuations and stability of polymerized vesicles," *Journal de Physique II*, vol. 2, no. 8, pp. 1563–1575, 1992.

[168] M. Peskin, *An introduction to quantum field theory*. CRC press, 2018.

[169] A. Košmrlj and D. R. Nelson, "Response of thermalized ribbons to pulling and bending," *Phys. Rev. B*, vol. 93, p. 125431, 2016.

[170] D. Amit, *Field Theory, The Renormalization Group And Critical Phenomena (2nd Edition)*. International series in pure and applied physics, World Scientific Publishing Company, 1984.

[171] H. Kleinert and V. Schulte-Frohlinde, *Critical Properties of ϕ^4-theories*. World Scientific, 2001.

[172] L. Radzihovsky and J. Toner, "Elasticity, shape fluctuations, and phase transitions in the new tubule phase of anisotropic tethered membranes," *Phys. Rev. E*, vol. 57, pp. 1832–1863, Feb 1998.

[173] H. W. Diehl and M. Shpot, "Critical behavior at m-axial lifshitz points: Field-theory analysis and ϵ-expansion results," *Phys. Rev. B*, vol. 62, pp. 12338–12349, 2000.

[174] H. S. Seung and D. R. Nelson, "Defects in flexible membranes with crystalline order," *Physical Review A*, vol. 38, pp. 1005–1018, Jul 1988.

[175] S. Plimpton, "Fast parallel algorithms for short-range molecular dynamics," *Journal of Computational Physics*, vol. 117, no. 1, pp. 1–19, 1995.

[176] http://lammps.sandia.gov. Accessed in November 2019.

[177] M. Tuckerman, *Statistical Mechanics: Theory and Molecular Simulation*. Oxford Graduate Texts, Oxford University Press, 2010.

[178] S. Timoshenko and J. Gere, *Theory of Elastic Stability*. Dover Civil and Mechanical Engineering, Dover Publications, 2012.

[179] A. C. E. Reid and R. J. Gooding, "Inclusion problem in a two-dimensional nonlocal elastic solid," *Phys. Rev. B*, vol. 46, pp. 6045–6049, Sep 1992.

[180] X. Zhang and P. Sharma, "Inclusions and inhomogeneities in strain gradient elasticity with couple stresses and related problems," *International Journal of Solids and Structures*, vol. 42, no. 13, pp. 3833 – 3851, 2005.

[181] X. Zhang, K. Jiao, P. Sharma, and B. Yakobson, "An atomistic and non-classical continuum field theoretic perspective of elastic interactions between defects (force dipoles) of various symmetries and application to graphene," *Journal of the Mechanics and Physics of Solids*, vol. 54, no. 11, pp. 2304 – 2329, 2006.

[182] A. E. Green, "On the linear theory of thin elastic shells," *Proceedings of the Royal Society of London. Series A, Mathematical and Physical Sciences*, vol. 266, no. 1325, pp. 143–160, 1962.

[183] P. G. Ciarlet, C. Mardare, and M. Shen, "Saint Venant compatibility equations in curvilinear coordinates," *Analysis and Applications*, vol. 05, no. 03, pp. 231–251, 2007.

[184] P. G. Ciarlet, L. Gratie, C. Mardare, and M. Shen, "Saint Venant compatibility equations on a surface – application to intrinsic shell theory," *Mathematical Models and Methods in Applied Sciences*, vol. 18, no. 02, pp. 165–194, 2008.

[185] E. A. Matsumoto and R. D. Kamien, "Patterns on a roll: A method of continuous feed nanoprinting," *Soft Matter*, vol. 8, no. 43, pp. 11038–11041, 2012.

[186] G. Librandi, M. Moshe, Y. Lahini, and K. Bertoldi, "Porous mechanical metamaterials as interacting elastic charges," *arXiv preprint arXiv:1709.00328*, 2017.

[187] M. Moshe, E. Esposito, S. Shankar, B. Bircan, I. Cohen, D. R. Nelson, and M. J. Bowick, "Kirigami mechanics as stress relief by elastic charges," *Physical Review Letters*, vol. 122, p. 048001, 2019.

[188] M. Moshe, E. Esposito, S. Shankar, B. Bircan, I. Cohen, D. R. Nelson, and M. J. Bowick, "Nonlinear mechanics of thin frames," *Physical Review E*, vol. 99, p. 013002, 2019.

[189] R. D. Gregory, "Green's functions, bi-linear forms, and completeness of the eigenfunctions for the elastostatic strip and wedge," *Journal of Elasticity*, vol. 9, pp. 283–309, Jul 1979.

[190] H. K. Moffatt, "Viscous and resistive eddies near a sharp corner," *Journal of Fluid Mechanics*, vol. 18, no. 1, pp. 1–18, 1964.

[191] S. Osher, "On green's function for the biharmonic equation in a right angle wedge," *Journal of Mathematical Analysis and Applications*, vol. 43, no. 3, pp. 705 – 716, 1973.

[192] J. B. Seif, "On the green's function for the biharmonic equation in an infinite wedge," *Transactions of the American Mathematical Society*, vol. 182, pp. 241–260, 1973.

[193] Z.-D. Song, L. Elcoro, and B. A. Bernevig, "Twisted bulk-boundary correspondence of fragile topology," *Science*, vol. 367, no. 6479, pp. 794–797, 2020.

[194] M. G. Vergniory, B. J. Wieder, L. Elcoro, S. S. Parkin, C. Felser, B. A. Bernevig, and N. Regnault, "All topological bands of all stoichiometric materials," *arXiv preprint arXiv:2105.09954*, 2021.

[195] L.-H. Wu and X. Hu, "Scheme for achieving a topological photonic crystal by using dielectric material," *Physical review letters*, vol. 114, no. 22, p. 223901, 2015.

[196] M. Proctor, P. A. Huidobro, B. Bradlyn, M. B. de Paz, M. G. Vergniory, D. Bercioux, and A. García-Etxarri, "Robustness of topological corner modes in photonic crystals," *Physical Review Research*, vol. 2, no. 4, p. 042038, 2020.

[197] C. He, X. Ni, H. Ge, X.-C. Sun, Y.-B. Chen, M.-H. Lu, X.-P. Liu, and Y.-F. Chen, "Acoustic topological insulator and robust one-way sound transport," *Nature physics*, vol. 12, no. 12, pp. 1124–1129, 2016.

[198] Z. Zhang, Q. Wei, Y. Cheng, T. Zhang, D. Wu, and X. Liu, "Topological creation of acoustic pseudospin multipoles in a flow-free symmetry-broken metamaterial lattice," *Phys. Rev. Lett.*, vol. 118, p. 084303, Feb 2017.

[199] Y. Chen, F. Meng, and X. Huang, "Creating acoustic topological insulators through topology optimization," *Mechanical Systems and Signal Processing*, vol. 146, p. 107054, 2021.

[200] H. C. Po, H. Watanabe, and A. Vishwanath, "Fragile topology and wannier obstructions," *Phys. Rev. Lett.*, vol. 121, p. 126402, Sep 2018.

[201] W. A. Benalcazar, B. A. Bernevig, and T. L. Hughes, "Electric multipole moments, topological multipole moment pumping, and chiral hinge states in crystalline insulators," *Physical Review B*, vol. 96, no. 24, p. 245115, 2017.

[202] F. Schindler, A. M. Cook, M. G. Vergniory, Z. Wang, S. S. Parkin, B. A. Bernevig, and T. Neupert, "Higher-order topological insulators," *Science advances*, vol. 4, no. 6, p. eaat0346, 2018.

[203] M. I. Aroyo, J. M. Perez-Mato, D. Orobengoa, E. Tasci, G. De La Flor, and A. Kirov, "Crystallography online: Bilbao crystallographic server," *Bulgarian Chemical Communications*, vol. 43, no. 2, pp. 183–197, 2011.

[204] A. Alexandradinata, X. Dai, and B. A. Bernevig, "Wilson-loop characterization of inversion-symmetric topological insulators," *Physical Review B*, vol. 89, no. 15, p. 155114, 2014.

[205] B. Bradlyn, Z. Wang, J. Cano, and B. A. Bernevig, "Disconnected elementary band representations, fragile topology, and wilson loops as topological indices: An example on the triangular lattice," *Physical Review B*, vol. 99, no. 4, p. 045140, 2019.

[206] P.-G. De Gennes and P.-G. Gennes, *Scaling concepts in polymer physics*. Cornell university press, 1979.

[207] Y. Rabin and S. Panyukov, "Thermal fluctuations of elastic ring," *arXiv preprint arXiv:cond-mat/0010488*, 2000.

[208] E. Katifori, S. Alben, and D. R. Nelson, "Collapse and folding of pressurized rings in two dimensions," *Phys. Rev. E*, vol. 79, p. 056604, May 2009.

[209] A. Mauri, D. Soriano, and M. I. Katsnelson, "Thermal ripples in bilayer graphene," *Phys. Rev. B*, vol. 102, p. 165421, Oct 2020.

[210] R. S. Mulliken, "Electronic structures of polyatomic molecules and valence. iv. electronic states, quantum theory of the double bond," *Physical Review*, vol. 43, no. 4, p. 279, 1933.

[211] G. Koster, J. Dimmock, R. Wheeler, and H. Statz, *Properties of the Thirty-two Point Groups*. Massachusetts Institute of Technology Cambridge, Mass: Research monographs, M.I.T. Press, 1963.

[212] M. I. Aroyo, J. M. Perez-Mato, C. Capillas, E. Kroumova, S. Ivantchev, G. Madariaga, A. Kirov, and H. Wondratschek, "Bilbao crystallographic server: I. databases and crystallographic computing programs," *Zeitschrift für Kristallographie - Crystalline Materials*, vol. 221, no. 1, pp. 15–27, 2006.

[213] M. I. Aroyo, A. Kirov, C. Capillas, J. M. Perez-Mato, and H. Wondratschek, "Bilbao Crystallographic Server. II. Representations of crystallographic point groups and space groups," *Acta Crystallographica Section A*, vol. 62, pp. 115–128, Mar 2006.